

# REPORT DOCUMENTATION PAGE

Form Approved  
OMB No. 0704-0188

The public reporting burden for this collection of information is estimated to average 1 hour per response, including the time for reviewing instructions, searching existing data sources, gathering and maintaining the data needed, and completing and reviewing the collection of information. Send comments regarding this burden estimate or any other aspect of this collection of information, including suggestions for reducing the burden, to Department of Defense, Washington Headquarters Services, Directorate for Information Operations and Reports (0704-0188), 1215 Jefferson Davis Highway, Suite 1204, Arlington, VA 22202-4302. Respondents should be aware that notwithstanding any other provision of law, no person shall be subject to any penalty for failing to comply with a collection of information if it does not display a currently valid OMB control number.

PLEASE DO NOT RETURN YOUR FORM TO THE ABOVE ADDRESS.

1. REPORT DATE (DD-MM-YYYY) 30-11-12		2. REPORT TYPE Final Technical		3. DATES COVERED (From - To) June 2009 to August 2012	
4. TITLE AND SUBTITLE Collaborative University Research on Corrosion OSD Education Initiative				5a. CONTRACT NUMBER W9132T-09-2-0020	
				5b. GRANT NUMBER	
				5c. PROGRAM ELEMENT NUMBER	
				5d. PROJECT NUMBER	
6. AUTHOR(S) Scully, John R. (PI), Kelly, Robert G. (co-PI), Gangloff, Richard P. (co-PI). Co-Authors: J.T. Burns, B. Kannan, A.D. King, E.B. Neiser, B.E. Risteen, E.J. Schindelholz, Y. Shi, M.L. Tayler, Y. Wan, J.S. Warner				5e. TASK NUMBER	
				5f. WORK UNIT NUMBER	
7. PERFORMING ORGANIZATION NAME(S) AND ADDRESS(ES) The Rector and Visitors of the University of Virginia, 1001 N. Emmet Street, Charlottesville, VA 22904				8. PERFORMING ORGANIZATION REPORT NUMBER	
9. SPONSORING/MONITORING AGENCY NAME(S) AND ADDRESS(ES) ERDC-CERL, P.O. Box 9005, Champaign, IL 61826-9005				10. SPONSOR/MONITOR'S ACRONYM(S)	
				11. SPONSOR/MONITOR'S REPORT NUMBER(S)	
12. DISTRIBUTION/AVAILABILITY STATEMENT This material is based on research sponsored by ERDC- U.S. Army Construction Engineering Research Laboratory under agreement number W9132T-09-2-0020. The U.S. Government is authorized to reproduce and distribute reprints for Governmental purposes notwithstanding any copyright notation thereon. The views and conclusions contained herein are those of the authors and should not					
13. SUPPLEMENTARY NOTES					
14. ABSTRACT This work is in support of a pilot program for the Corrosion Policy and Oversight Office within the Office of the Undersecretary for Acquisition, Technology and Logistics, Corrosion Policy and Oversight. The research and technological investigations within have several objectives. One is to support graduate student research and education in the field of corrosion. This objective is met by the training of graduate students in the Materials Science and Engineering discipline to conduct the research listed and the subsequent placement of a high portion of them in US DoD, national laboratory, governments and industry professional positions. A second objective is the conduct of research studies that will support the implementation of other Corrosion Policy and Oversight Office projects that have been completed or are in progress. A third objective is to plan and conduct targeted studies that within about a 2 year period have a significant probability of delivering "products" to DoD interested end users that could begin along a path to implementation.					
15. SUBJECT TERMS Corrosion					
16. SECURITY CLASSIFICATION OF:			17. LIMITATION OF ABSTRACT  UU	18. NUMBER OF PAGES  305	19a. NAME OF RESPONSIBLE PERSON Robert R. Merhige IV
a. REPORT Unclassified	b. ABSTRACT Unclassified	c. THIS PAGE Unclassified			19b. TELEPHONE NUMBER (Include area code) 434-924-6142

20130118323



## **CORROSION PILOT PROGRAM**

### **Collaborative University Research on Corrosion OSD Education Initiative**

**J. R. Scully (PI), R. G. Kelly (co-PI), and R. P. Gangloff (co-PI)**

**Co-authors: J.T. Burns, B. Kannan, A.D. King, E.B. Neiser, B.E. Risteen, E.J. Schindelholz, Y. Shi, M.L. Tayler, Y. Wan, J.S. Warner**

**Center for Electrochemical Science and Engineering  
Department of Materials Science and Engineering  
School of Engineering and Applied Science  
University of Virginia  
Charlottesville VA 22904  
jrs8d@virginia.edu**

**November 30, 2012**

**Final Report**

**DISTRIBUTION STATEMENT A. Approved for public release; distribution is unlimited.**

**© 2012 University of Virginia**

This material is based on research sponsored by ERDC- U.S. Army Construction Engineering Research Laboratory under agreement number W9132T-09-2-0020. The U.S. Government is authorized to reproduce and distribute reprints for Governmental purposes notwithstanding any copyright notation thereon. The views and conclusions contained herein are those of the authors and should not be interpreted as necessarily representing the official policies and endorsements, either expressed or implied of ERDC- U.S. Army Construction Engineering Research Laboratory or the US Government.

**Office of the Under Secretary of Defense  
Acquisition, Technology and Logistics  
DoD Corrosion Policy and Oversight  
3000 Defense Pentagon  
Washington, DC 20301**

## Abstract

This work is in support of a pilot program for the Corrosion Policy and Oversight Office within the Office of the Undersecretary for Acquisition, Technology and Logistics, Corrosion Policy and Oversight. The research and technological investigations within have several objectives. One is to support graduate student research and education in the field of corrosion. This objective is met by the training of graduate students in the Materials Science and Engineering discipline to conduct the research listed and the subsequent placement of a high portion of them in US DoD, national laboratory, governments and industry professional positions. A second objective is the conduct of research studies that will support the implementation of other Corrosion Policy and Oversight Office projects that have been completed or are in progress. A third objective is to plan and conduct targeted studies that within about a 2 year period have a significant probability of delivering "products" to DoD interested end users that could begin along a path to implementation.

All of the projects were conducted at the University Of Virginia, Department of Materials Science and Engineering, Center for Electrochemical Science and Engineering and at various exposure sites around the world on behalf of the U.S. Army Construction Engineering Research Laboratory over the period from June 23, 2009 – August 31, 2012. All projects focused on the research thrust areas of great interest to the Corrosion Policy and Oversight Office and Innovative Corrosion Control needs of CERL (CERL-12). This work was in support of ERDC efforts in Innovative Corrosion Control. Specifically, this report addresses topics in (a) coatings, (c) advanced materials, and (e) remote corrosion assessment and management. These include:

*Research to Better Define the Needs for Future Accelerated Corrosion Test Method Development*

*Development and Causes for Discrepancies Between Field And Laboratory Testing on Bare and Coated Metals.*

*Chromate Replacement Coatings and Specialized Coating Applications with other Functions*

*Innovative Coatings for Corrosion Cracking Resistance*

Findings from each project task are discussed in sections 1.2 to 1.10 below. In general, output included multiple student graduations and placements in US DoD, Academia, and/or industry technical positions (3 placements from this project co-author list). Each report topic includes an introduction, lessons learned, technical investigations, experimental results, conclusions, implementation plans, and in some cases a description of possible economic impacts (enclosed and detailed below). Public dissemination of information occurred by both the research reports (enclosed), publication of research papers in the archival literature (6), student posters and oral presentations as well as placement of soft copies of selected reports on the CORR-Defense Web site.

## Table of Contents

<u>Section</u>	<u>Page</u>
Table of Contents.....	iii
List of Tables .....	vii
List of Figures .....	viii
1.1 Front Matter .....	xxi
1.1.1 Forward .....	xxi
1.1.2 Preface .....	xxii
1.1.3 Acknowledgements.....	xxiii
1.1.4 Introduction and Background .....	xxiii
1.2 Factors Controlling the Atmospheric Corrosion of Silver in Natural and Accelerated Test Environments (R. G. Kelly, E. B. Neiser, Y. Wan) .....	26
1.2.1 Summary .....	26
1.2.2 Introduction and Background .....	26
1.2.3 Lessons Learned .....	27
1.2.4 Technical Investigations .....	27
1.2.5 Experimental Results.....	30
1.2.6 Discussion .....	38
1.2.7 Economic Summary.....	41
1.2.8 Implementation .....	41
1.2.9 Conclusion.....	41
1.2.10 Bibliography .....	41
1.3 Analysis of Relative Importance of Surface Environment Components and Dynamics (R. G. Kelly, B. Risteen, E. J. Schindelholz) .....	44
1.3.1 Summary .....	44
1.3.2 Introduction and Background .....	44
1.3.3 Lessons Learned .....	44
1.3.4 Technical Investigations .....	45
1.3.5 Experimental Results.....	47
1.3.6 Discussion .....	52
1.3.7 Economic Summary.....	53
1.3.8 Implementation .....	53
1.3.9 Conclusion.....	54
1.3.10 Bibliography .....	54
1.4 Galvanic Interactions Between AA7075-T6 and Noble Materials (R. G. Kelly, Y. Shi) .....	55
1.4.1 Summary .....	55
1.4.2 Introduction and Background .....	55



1.4.3 Lessons Learned .....	55
1.4.4 Technical Investigations .....	56
1.4.5 Experimental Results.....	57
1.4.6 Discussion .....	65
1.4.7 Economic Summary.....	65
1.4.8 Implementation .....	65
1.4.9 Conclusion.....	66
1.4.10 Bibliography.....	66
1.5 Scientific Advances Enabling Next Generation Management of Corrosion Induced Fatigue (Burns, J.T. and Gangloff, R.P.) .....	67
1.5.1 Summary .....	67
1.5.2 Introduction and Background .....	67
1.5.3 Lessons Learned .....	68
1.5.4 Experimental Results and Discussion .....	68
1.5.5 Implementation .....	74
1.5.6 Conclusions .....	74
1.5.7 Bibliography.....	75
1.6 Effect of Atmospheric Exposure on Environmental Fatigue Crack Propagation and Inhibition in Precipitation Hardened Al-Cu-Li (Warner, J.S. and Gangloff, R.P.) .....	78
1.6.1 Summary .....	78
1.6.2 Introduction.....	78
1.6.3 Lessons Learned .....	81
1.6.4 Experimental Procedures.....	81
1.6.5 Results .....	88
1.6.6 Discussion .....	99
1.6.7 Conclusions .....	109
1.6.8 Bibliography.....	110
1.7 Blistering Phenomena in Early Generation Mg-Rich Primer Coatings on AA2024-T351 and the Effects of CO <sub>2</sub> (King, A. D. and Scully, J. R.).....	115
1.7.1 Summary .....	115
1.7.2 Introduction and Background .....	115
1.7.3 Lessons Learned .....	117
1.7.4 Technical Investigations .....	118
1.7.5 Experimental Results.....	120
1.7.6 Discussion .....	139
1.7.7 Economic Summary.....	147
1.7.8 Implementation .....	147

1.7.9 Conclusion.....	147
1.7.10 Appendices.....	148
1.7.11 Bibliography.....	148
1.8 Environmental Degradation of a Mg-Rich Primer: Comparison of Selected Field Environments with Laboratory Exposures (King, A. D., Kannan, B. and Scully, J. R.).....	152
1.8.1 Summary.....	152
1.8.2 Introduction.....	153
1.8.3 Lessons Learned .....	156
1.8.4 Technical Investigations .....	157
1.8.5 Experimental Results.....	167
1.8.6 Discussion .....	207
1.8.7 Economic Summary.....	211
1.8.8 Implementation .....	212
1.8.9 Conclusion.....	212
1.8.10 Bibliography.....	214
1.9 Underpaint Corrosion on Chromate –Free Organic- Coated AA2024-T351 as a Function of Accelerated Testing Variables Compared with Natural Exposures (Tayler, M.L. and Scully, J.R.) .....	219
1.9.1 Summary.....	219
1.9.2 Introduction: Necessary Development of LALTs for Chromate Free Coatings.....	220
Ozone.....	224
Chloride.....	225
Time of Wetness and Relative Humidity .....	225
Cycling .....	226
1.9.3 Lessons Learned .....	231
1.9.4 Technical Investigations .....	232
1.9.5 Experimental Results.....	237
1.9.6 Discussion .....	270
1.9.7 Economic Summary.....	274
1.9.8 Implementation .....	274
1.9.9 Conclusions.....	275
1.9.10 Appendices.....	275
1.9.11 Bibliography.....	275
1.10 Molybdate Inhibition of Corrosion Fatigue Crack Propagation in Precipitation Hardened Al- Cu-Li (Warner, J.S. and Gangloff, R.P.).....	280
1.10.1 Summary .....	280
1.10.2 Introduction.....	280
1.10.3 Lessons Learned .....	282

1.10.4 Experimental Procedures.....	282
1.10.5 Results .....	283
1.10.6 Discussion .....	290
1.10.7 Conclusions.....	300
1.10.8 Bibliography.....	301

## List of Tables

Table 1. Intensity of UVA light irradiated in the locations of Figure 2, W/m <sup>2</sup> .....	32
Table 2. Parameters in the field sites and magnifying capability of the parameters of the MB11733	
Table 3. Species, subdomain concentration and diffusion coefficients <sup>5</sup> .....	57
Table 4 . Pitting initiation predicted by modeling result at pH11 .....	63
Table 5: Ambient Concentrations of CO <sub>2</sub> in Various Environments .....	119
Table 6: Equilibrium Concentrations of CO <sub>3</sub> <sup>2-</sup> , according to Henry's Law, in an Aqueous Environment under various partial pressures of CO <sub>2</sub> .....	134
Table 7. Exposure conditions in field and lab accelerated life testing environments. ....	161
Table 8. Fitting results of EIS measured on AA2024-T351 panels coated with MgRP (MgPVC = 45%) after field exposure at Kennedy Space Center 30 m lot for 0, 2, 6, 12, and 24 weeks. Tested in ambiently aerated 5% NaCl Solution. Equivalent electric circuit model used shown in Figure 105. ....	176
Table 9. Fitting results of EIS measured on AA2024-T351 panels coated with MgRP (MgPVC = 45%) after field exposure at Charlottesville, VA for 0, 2, 6, 12, and 24 weeks. Tested in ambiently aerated 5% NaCl Solution. Equivalent electric circuit model used shown in Figure 105.....	185
Table 10. Fitting results of EIS measured on AA2024-T351 panels coated with MgRP (MgPVC = 45%) after LALT in ASTM B117 for 0, 168, 384, 744, and 984 hours. Tested in ambiently aerated 5% NaCl Solution. Equivalent electric circuit model used shown in Figure 105. ....	194
Table 11. Fitting results of EIS measured on AA2024-T351 panels coated with MgRP (MgPVC = 45%) after LALT in ASTM B117 modified with artificial sea water for 0, 192, 408, 698 and 1000 hours. Tested in ambiently aerated 5% NaCl Solution. Equivalent electric circuit model used shown in Figure 105. ....	203
Table 12. Summary of observations made after environmental exposure in various environments. ....	211
Table 13. List of all standard LALTs used in this study.....	236
Table 14. List of all non-standard LALTs used in this study.....	236
Table 15. Environmental severity factors for field sites.....	237
Table 16. Acceleration factors for LALTs with respect to KSC based on scribe creep length. ....	243
Table 17. Summary of Image Analysis of Pitting on bare AA2024-T351.....	248
Table 18. Acceleration factors for AA2024-T351 based on low frequency impedance (Z <sub>0.01</sub> )..	261
Table 19. Acceleration factors for AA2024-T351 based on saddle frequency.....	263
Table 20. DSC and MDSC results showing the glass transition temperature for eponol exposed to various conditions. ....	270
Table 21. TGA results on Eponol films showing the amounts of residual solvents, organic material and inorganic material. ....	270

## List of Figures

Figure 1. Schematic view of the MB117 chamber. ....	28
Figure 2. The selected physical locations (1-18) in the MB117 used for the measurement of the UVA light intensity and the ozone concentration. "Pair a" and "Pair b" are two pairs of UVA lamps and can be moved along y- and z- directions in the racks (red dashed lines).....	29
Figure 3 Reduction curves from exposures with added formic acid. Both exposures' reductions differ very little from the reductions of clean samples, suggesting that no corrosion resulted from either exposure. ....	31
Figure 4. Spectrum of the UVA lamp used in the MB117. ....	32
Figure 5 . The concentration of ozone in the MB117 chamber when the flow of cleaned compressed air was (a) 2 SLPM with measurements at several locations; (b) 10 SLPM for location 8. Physical locations are shown in Figure 2.....	34
Figure 6. X-ray diffraction pattern of silver after exposed in (a) Coconut Island for 6 months and (b) the MB117 with 23ppm ozone for 3 days. ....	35
Figure 7. Image (a) and element distributions (b and c) of different areas spots on the surfaces of the samples after exposure at Coconut Island, HI for 6 months. ....	36
Figure 8. Coulometric reduction curves for the silver samples after exposure to: (a) the MB117 with 23 ppm ozone and UV light ( $33 \text{ W/m}^2$ ) for 15 days, and (b) Daytona Beach for 3 months. The reduction electrolytes was 0.1 M $\text{Na}_2\text{SO}_4$ (pH=10) solution and were deaerated 1 hour in advance. ....	37
Figure 9. Reduction charge and the fitting curves for AgCl produced on silver exposed in the MB117 with different ozone concentration and different exposure times. ....	38
Figure 10. Acceleration factors of the MB117 to the fields, calculated assuming corrosion of silver in those conditions obeys linear kinetics, and all the reduction charges are scaled to an exposure of one month from Figure 8. ....	40
Figure 11. (a) Photograph of ink jet system, including programmable xy-stage and cabinet for controlled humidity. ....	45
Figure 12. Photomicrograph of interdigitated sensor for wetting/drying experiments. ....	46
Figure 13. Pattern of printing used for deposition of salt droplets. Within the $1 \text{ cm}^2$ area, 16,000 droplets were printed. ....	46
Figure 14. Flow diagram for analyses of optical profilometry data after processing with MountainsMap software to produce a text file of the appropriate parameters.....	47
Figure 15. Impedance at 574 kHz as a function of RH for wetting and drying of (a) NaCl (b) $\text{NaNO}_3$ , and (c) $\text{NaCl} + \text{NaNO}_3$ on the interdigitated sensor. Impedance values are those measured after 1 hour at a given RH.....	48
Figure 16. Impedance at 574 kHz as a function of RH for wetting and drying of (a) $\text{MgCl}_2$ , (b) $\text{MgSO}_4$ on the interdigitated sensor.....	49
Figure 17. Sample images from optical profilometry of samples printed with NaCl droplets and exposed to constant RH for 30 days. ....	50
Figure 18. Corrosion rate (from volume loss and 7-day exposure time) as a function of RH for NaCl deposition. Predictions of corrosivity based on ISO 9223 are also shown. ....	50



Figure 19. Mean volume loss per sample as a function of time and RH for NaCl deposition. Note the logarithmic volume loss scale. ....	51
Figure 20. Mean volume loss per sample as a function of time and RH for ASTM Ocean Water deposition. Note the logarithmic volume loss scale. ....	51
Figure 21. Mean volume loss per sample as a function of time and RH for $MgCl_2$ deposition. Note the logarithmic volume loss scale. ....	52
Figure 22. Fastened joint geomerty of AA7075-T6 and noble materials coupled system .....	57
Figure 23. Effect of $[Cl^-]$ on Ag cathodic kinetics.....	58
Figure 24. Effect of pH on Ag cathodic kinetics .....	58
Figure 25. Effect of $[Cl^-]$ on Ni cathodic kinetics.....	58
Figure 26. Effect of pH on Ni cathodic kinetics. ....	58
Figure 27. Effect of $[Cl^-]$ on BMI cathodic kinetics.....	58
Figure 28. Effect of pH on BMI cathodic kinetics .....	58
Figure 29. Effect of pH on AA7075-T6 anodic kinetics. ....	59
Figure 30. Effect of $[Cl^-]$ on AA7075-T6 anodic kinetics.....	59
Figure 31. Effect of $AlCl_3$ on AA7075-T6 anodic kinetics used for propagation boundary conditions .....	60
Figure 32. Corrosion interaction for Ag-AA7075-T6 coupled system with 0.01 M NaCl, pH 11 and gap of 2 mm.....	63
Figure 33. Corrosion interaction along Ag-AA7075-T6 interface with 0.01 M NaCl, pH 11 and gap 2 mm.....	63
Figure 34. Current density along Ag-AA7075-T6 interface with gap of 2 mm under propagation condition, Ag was selected under 0.1 M NaCl , pH11 condition, AA7075 was selected with 0.5 M $AlCl_3$ .....	64
Figure 35. Effect of gap width on Peak Current density. Both Ag and BMI were selected under 0.1 M NaCl , pH11 condition, AA7075 was selected with 0.5 M $AlCl_3$ .....	64
Figure 36. $[Al^{3+}]$ distribution along Ag-AA7075-T6 interface as a function of gap width under propagation condition, 100 second after the propagation begin. Ag was selected under 0.1 M NaCl, pH11 condition, AA7075 was selected with 0.5 M $AlCl_3$ .....	64
Figure 37. $[Cl^-]$ distribution along Ag-AA7075-T6 interface as a function of gap width under propagation condition, 100 second after the propagation begin. Ag was selected under 0.1 M NaCl , pH11 condition, AA7075 was selected with 0.5 M $AlCl_3$ .....	64
Figure 38. Effect of L-T or L-S surface EXCO, ANCIT, or LJSS corrosion pre-exposure on the fatigue life of 7075-T6511 stressed in water vapor saturated $N_2$ at $R=0.1$ and $\sigma_{max}=150$ MPa [12]. Cross-sections of corrosion damage are inset. ....	70
Figure 39. Comparison of measured (lines) and predicted (points) crack formation cycles (black) and total cycles to 500 $\mu m$ (red), plotted versus maximum concentrated macro-stress.....	71
Figure 40. Fatigue crack growth rate from marker-band measurements vs. $\Delta K$ from various controlled pit specimens tested at either $\sigma_{max} = 100, 200, \text{ or } 300$ MPa and $R = 0.5$ in water vapor saturated $N_2$ [15]. Also included are long crack CT and SEN results. ....	73

Figure 41. Fatigue crack growth rate versus $\Delta K$ data from marker-band analysis of 7075-T651 controlled pits tested at $\sigma_{max} = 200$ MPa and $R = 0.5$ in water saturated $N_2$ , and dry $N_2$ at $-50^\circ\text{C}$ and $-90^\circ\text{C}$ [13].	75
Figure 42. The bounding conditions for electrolyte deliquescence under atmospheric conditions.	80
Figure 43. Environmental cell used for fatigue testing which maintain constant RH. The outer cup holds a saturated $K_2SO_4$ which maintains an RH of 97.3%.	83
Figure 44. The effect of surface preparation and environment control on NaCl solution wetting on a C47A-T86 SEN specimen surface which was not plasma cleaned.	86
Figure 45. The effect of surface preparation and environment control on NaCl solution wetting on a C47A-T86 SEN specimen surface which was plasma cleaned.	87
Figure 46. Photographs of salt deposited surfaces of SEN specimens with different applied DCPD currents. The temperature of the specimen at which the picture was taken and applied current are listed under each image.	89
Figure 47. Exposure dependence of $da/dN$ for C433-T351 (L-T orientation) stressed at a $\Delta K$ of 7 MPa $\sqrt{m}$ and $R$ of 0.58.	90
Figure 48. Loading frequency dependence of $da/dN$ for C47A-T86 (L-T orientation) stressed at a constant $\Delta K$ of 7 MPa $\sqrt{m}$ and $R$ of 0.58.	91
Figure 49. Crack length versus cycles data for C47A-T86 (L-T) loaded at $\Delta K$ of 7 MPa $\sqrt{m}$ , $R$ of 0.58, and $f$ of 0.2 Hz under atmospheric conditions producing heterogeneous NaCl droplets with a total surface electrolyte volume of 0.1 L/m <sup>2</sup> and $[NaCl] = 0.79M$ .	92
Figure 50. Crack length versus cycles data for C47A-T86 (L-T) loaded at $\Delta K$ of 7 MPa $\sqrt{m}$ , $R$ of 0.58, and $f$ of 30 Hz under atmospheric conditions producing homogeneous NaCl droplets with a total surface electrolyte volume of 0.1 L/m <sup>2</sup> and $[NaCl] = 0.79M$ .	93
Figure 51. Loading frequency dependence of $da/dN$ for C47A-T86 (L-T) stressed at $\Delta K$ of 7 MPa $\sqrt{m}$ and $R$ of 0.58 under:	94
Figure 52. Crack length versus loading cycles data for C47A-T86 (L-T) loaded at $\Delta K$ of 7 MPa $\sqrt{m}$ , $R$ of 0.58, and $f$ of 0.2 Hz under atmospheric conditions corresponding to those in Figure 51 where heterogeneous NaCl + $Na_2MoO_4$ droplets (☆) were produced.	95
Figure 53. Crack length versus cycles data for C47A-T86 (L-T) loaded at $\Delta K$ of 7 MPa $\sqrt{m}$ , $R$ of 0.58, and $f$ of 0.2 Hz under atmospheric conditions with a NaCl + $Na_2MoO_4$ deposited specimen covered by homogeneous deliquesced droplets.	96
Figure 54. Crack length versus cycles data for C47A-T86 (L-T) loaded at $\Delta K$ of 7 MPa $\sqrt{m}$ , $R$ of 0.58, and $f$ of 0.2 Hz under atmospheric conditions with a NaCl + $Na_2MoO_4$ deposited specimen and homogeneous deliquesced droplets.	97
Figure 55. Crack length versus loading cycles data for C47A-T86 (L-T orientation) loaded at a constant $\Delta K$ of 7 MPa $\sqrt{m}$ , $R$ of 0.58, and $f$ of 30 Hz under atmospheric conditions	98
Figure 56. Crack length versus cycles data for C47A-T86 (L-T) loaded at $\Delta K$ of 7 MPa $\sqrt{m}$ , $R$ of 0.58, and $f$ of 30 Hz under atmospheric conditions with a NaCl + $Na_2MoO_4$ deposited specimen and homogeneous deliquesced droplets.	99
Figure 57. Exposure dependence of $da/dN$ for C47A-T86 (L-T) loaded at constant $\Delta K$ of 7 MPa $\sqrt{m}$ and $R$ of 0.58.	102

Figure 58. Scanning electron micrograph of cross sectioned AA2024-T351 coated with (a) MgRP Sample ID:493-039-A-P-P22 (b) MgRP + Topcoat Sample ID: T65f. Spot markers indicate approximate location of EDS analysis. ....	121
Figure 59. AA2024-T351 coated with (a) MgRP (PVC = 0%) and Aerodur 5000 Topcoat after 840 hrs in ASTM B-117 (b) MgRP (PVC = 45%) and Aerodur 5000 Topcoat after 840 hrs in ASTM B-117 (c) MgRP (PVC = 0%) and Aerodur 5000 Topcoat after 1 yr exposure at Daytona Beach, FL. ....	122
Figure 60. Montage of SEM cross-sections of blisters on AA2024-T351 coated with Akzo Nobel MgRP (PVC = 0%) and Aerodur 5000 Topcoat after environmental exposure at Dayton Beach, FL for 1 yr. Sample ID: unknown. ....	123
Figure 61. SEM cross-section and EDS analysis of blisters on AA2024-T351 coated with Akzo Nobel MgRP and Aerodur 5000 Topcoat after environmental exposure. ....	123
Figure 62. Optical images of AA2024-T351 coated with a model organic epoxy polymer coating after 72 hours exposure in ASTM B-117 with ambient aeration. ....	124
Figure 63. SEM cross-section and EDS analysis of AA2024-T351 coated with Akzo Nobel MgRP after potentiostatic hold at -0.8 V vs. SCE in 50 mM NaCl with ambient aeration for approximately 90 hours. ....	125
Figure 64. Optical images of AA2024-T351 after 1 week immersion in 50 mM NaCl with ambient aeration and Mg shavings. ....	127
Figure 65. Optical images of AA2024-T351 after 72 hours immersion in 50 mM NaCl with ambient aeration and Mg powder. ....	127
Figure 66. Optical images of AA2024-T351 after (a) 1 hour potentiostatic hold at -1.5 V vs. SCE in 50 mM NaCl with ambient aeration. (b) 1 hour galvanic couple with Mg in 50 mM NaCl solution with ambient aeration. ....	128
Figure 67. Small electrolyte cell setup. (a & b) schematic of sample setup (b & c) optical images of cell setup during experiment (e & f) pH indicator paper measurements, labels indicate location of measurement. ....	129
Figure 68. $E_{\text{couple}}$ data and Optical images of AA2024-T351 after 1 hour galvanic couple between AA2024-T351 coated with Eponol and Mg coated with Eponol (a) both electrodes coated with Eponol (b) AA2024-T351 scratched (c) both electrodes scratched (d) $E_{\text{couple}}$ for conditions a-c. ....	130
Figure 69. Optical images of panels of AA2024-T351 coated with MgRP and Aerodur 5000 Topcoat PVC = 45% after about 800 hours of environmental exposure in ASTM B-117. ....	132
Figure 70. XRD Normalized Mg Peak Intensities vs. environmental exposure time in ASTM B-117 for panels of AA2024-T351 coated with MgRP PVC = 45% (a) in ambient $\text{CO}_2$ environment 450 ppm (b) in $\text{CO}_2$ -rich environment 6000 ppm. ....	133
Figure 71. XRD Normalized Mg Peak Intensities vs. environmental exposure time in ASTM B-117 for panels of AA2024-T351 coated with MgRP and Aerodur 5000 Topcoat PVC = 45% (a) in ambient $\text{CO}_2$ environment 450 ppm (b) in $\text{CO}_2$ -rich environment 6000 ppm. ....	133
Figure 72. The E-pH diagrams for carbonate with metal ion concentration of $10^{-6}$ M and 3 different partial pressures of atmospheric $\text{CO}_2$ . (a) $P_{\text{CO}_2} = 0.0005$ atm therefore $[\text{CO}_3^{2-}]$	

= 0.000017 M (b) $P_{CO_2} = .005$ atm therefore $[CO_3^{2-}] = 0.00017$ M and (c) $P_{CO_2} = 1$ atm therefore $[CO_3^{2-}] = 0.034$ M .....	136
Figure 73. Solution pH of 50 mM NaCl with and without dissolved Mg and CO <sub>2</sub> sparging.....	137
Figure 74. Optical images of AA2024-T351 after 1 week immersion in 50 mM NaCl with Mg shavings and bubbled CO <sub>2</sub> . .....	137
Figure 75. Anodic potentiodynamic scans of AA2024-T351 in various solutions. ....	138
Figure 76. Optical images of AA2024-T351 after (a) 1 hour galvanic couple with Mg in 50 mM NaCl solution with bubbled CO <sub>2</sub> (b) 1 hr potentiostatic hold at -1.5 V vs. SCE in 50 mM NaCl with bubbled CO <sub>2</sub> .....	139
Figure 77. Schematic of proposed blistering mechanism: anodic disbondment through anodic undermining and hydrogen production.....	140
Figure 78. Potential-pH equilibrium diagram for Al-H <sub>2</sub> O system at 25°C assuming an ion concentration of 10 <sup>-6</sup> pH indications:.....	142
Figure 79. Potentiodynamic scans of bare electrodes and AA2024-T351 coated with Akzo Nobel MgRP + Aerodur 5000 topcoat exposed in 50 mM NaCl solution for 10 min, ambient aeration.....	143
Figure 80. Schematic showing the Ohmic resistances that exist between the Mg pigment and the electrolyte (ionic) as well as between the Mg pigment and the substrate (electrical).(Interfacial resistances are omitted).....	143
Figure 81. Mixed potential theory modeling based upon polarization scans of bare Mg and bare AA2024-T351.....	144
Figure 82. Galvanic couple potential ( $E_{couple}$ ) of bare AA2024 in a galvanic couple with bare Mg (a) Effect on $E_{couple}$ by adding electrical resistance using a variable resistor. (b) Effect on $E_{couple}$ by adding ionic resistance using an organic polymer coating of Eponol. ..	144
Figure 83. Al oxide stability diagram <sup>42</sup> .....	146
Figure 84. Schematic of AA2024-T351 panels coated with Mg-rich primer coating. ....	157
Figure 85. Optical micrograph of AA2024-T351 panels coated with MgRP that have not been environmentally exposed. ....	158
Figure 86. Scanning electron micrograph (a) and EDS (b) of AA2024-T351 pretreated with Prekote and coated with MgRP (MgPVC = 45%) as applied before environmental exposure. Spot markers indicate approximate location of EDS analysis. ....	159
Figure 87. SEM micrograph (a) far away from and (b) near the scribe and (c) EDS of cross-sectioned MgRP (initial MgPVC = 45%) on AA2024-T351 pretreated with Prekote. Spot markers indicate approximate location of EDS analysis in (a).....	159
Figure 88. Picture of (a) QFog Cyclic Corrosion Tester Model: CCT 1100 (b) MgRP-coated AA2024-T351 samples mounted for exposure in the QFog Cyclic Corrosion Tester at t = 0 hrs. ....	160
Figure 89. Picture of (a) test rack and (b) MgRP-coated AA2024-T351 samples on exposure at Kennedy Space Center, FL 30 m site at t = 0 hrs. (28.59406°N, 80.58283°W, elevation = 0 m).....	162



Figure 90. Picture of (a) test rack and (b) MgRP-coated AA2024-T351 samples on exposure at Birdwood GC in Charlottesville, VA at $t = 0$ hrs. (38.0402°N, 78.54.27°W, elevation = 172 m) .....	163
Figure 91. Labeled (a) schematic and (b) picture of electrochemical flat cell with 1 cm <sup>2</sup> window used for full immersion exposure and post-mortem characterization. ....	164
Figure 92. First-order approximation of XRD penetration depth as a function of $2\theta$ in (a) pure Al and (b) pure Mg. The penetration depths responsible for 50%, 90%, and 99% of the diffracted intensity are shown. ....	165
Figure 93. Schematic of EDS penetration depth (a) and plot of first-order approximation <sup>69</sup> of EDS penetration depth in various materials (b). ....	166
Figure 94. Simulated Energy dispersive X-ray (EDS) spectra for bulk samples of various relevant to the MgRP/AA2024-T351 system and environmental exposure. <sup>70</sup> .....	166
Figure 95. Simulated Energy dispersive X-ray (EDS) spectra for a sphere of (a) metallic Mg and (b) CaCO <sub>3</sub> with various diameter, D, on top of a bulk substrate of Al. <sup>70</sup> .....	167
Figure 96. Optical micrograph of AA2024-T351 panels coated with MgRP (initial MgPVC = 45%) that have been exposed at Kennedy Space Center at 30 m lot for (a) 0 weeks (b) 12 weeks (c) 24 weeks .....	169
Figure 97. Optical micrograph of AA2024-T351 panels coated with MgRP (initial MgPVC = 45%) that have been exposed at Kennedy Space Center at 30 m lot for (a) 0 weeks (b) 12 weeks (c) 24 weeks .....	170
Figure 98. Scanning electron micrograph of AA2024-T351 pretreated with Prekote and coated with MgRP (initial MgPVC = 45%) after environmental exposure in the field at KSC for 24 weeks. ....	170
Figure 99. Scanning electron micrograph of AA2024-T351 pretreated with Prekote and coated with MgRP (initial MgPVC = 45%) after environmental exposure in the field at KSC for (a) 12 weeks and (b) 24 weeks. ....	171
Figure 100. Higher magnification scanning electron micrograph (planar view) of scribed AA2024-T351 pretreated with Prekote and coated with MgRP (initial MgPVC = 45%) after field exposure at Kennedy Space Center 30 m lot for (a) 12 weeks and (b) 24 weeks. ....	171
Figure 101. SEM micrograph (planar view) of scribed AA2024-T351 pretreated with Prekote and coated with MgRP (initial MgPVC = 45%) after field exposure in the field at KSC for 24 weeks. Spot markers indicate approximate location of EDS analysis shown in (b). ....	172
Figure 102. Scanning electron micrograph of cross sectioned AA2024-T351 pretreated with Prekote and coated with MgRP (initial MgPVC = 45%) after field exposure at Kennedy Space Center for (a,b) 12 weeks and (c,d) 24 weeks. Spot markers indicate approximate location of EDS analysis shown in (b) and (d). ....	173
Figure 103. Scanning electron micrograph of cross sectioned AA2024-T351 pretreated with Prekote and coated with MgRP (initial MgPVC = 45%) after environmental exposure in the field at KSC for (a) 12 weeks and (b) 24 weeks. ....	174
Figure 104. X-Ray diffraction spectra of AA2024-T351 panels coated with MgRP (initial MgPVC = 45%) after field exposure at Kennedy Space Center 30 m lot for 0, 12, and 24 weeks. Dotted lines indicate the position of the most intense diffraction peak for (a) MgCO <sub>3</sub> (b) MgCl <sub>2</sub> (c) Al <sub>2</sub> O <sub>3</sub> and (d) Mg(OH) <sub>2</sub> . ....	174



Figure 105. EIS equivalent circuit for a polymer coated metal used for fitting analysis. ....	174
Figure 106. (a) Bode and (b) Nyquist plots of EIS of AA2024-T351 panels coated with MgRP (initial MgPVC = 45%) after field exposure at Kennedy Space Center 30 m lot for 0, 2, 6, 12, and 24 weeks. Tested in ambiently aerated 5% NaCl Solution. Fit results in Table 8.....	175
Figure 107. Optical micrograph of AA2024-T351 panels coated with MgRP (initial MgPVC = 45%) that have been exposed at Charlottesville, VA for (a) 0 weeks (b) 12 weeks and (c) 24 weeks. ....	178
Figure 108. Optical micrograph of AA2024-T351 panels coated with MgRP (initial MgPVC = 45%) that have been exposed at Charlottesville, VA for (a) 0 weeks (b) 12 weeks and (c) 24 weeks. ....	178
Figure 109. Scanning electron micrograph of AA2024-T351 pretreated with Prekote and coated with MgRP (initial MgPVC = 45%) after environmental exposure in the field at Charlottesville, VA for (a) 12 weeks and (b) 24 weeks. ....	179
Figure 110. Scanning electron micrograph of AA2024-T351 pretreated with Prekote and coated with MgRP (initial MgPVC = 45%) after environmental exposure in the field at Charlottesville, VA for (a) 12 weeks and (b) 24 weeks. ....	179
Figure 111. Higher magnification scanning electron micrograph (planar view) of scribed AA2024-T351 pretreated with Prekote and coated with MgRP (initial MgPVC = 45%) after field exposure at Charlottesville, VA for (a) 12 weeks and (b) 24 weeks. ....	180
Figure 112. SEM micrograph (planar view) of scribed AA2024-T351 pretreated with Prekote and coated with MgRP (initial MgPVC = 45%) after field exposure at Charlottesville, VA for 24 weeks. Spot markers indicate approximate location of EDS analysis shown in (b). ....	181
Figure 113. Scanning electron micrograph of cross sectioned AA2024-T351 pretreated with Prekote and coated with MgRP (initial MgPVC = 45%) after field exposure at Charlottesville, VA for (a,b) 12 weeks and (c,d) 24 weeks. Spot markers indicate approximate location of EDS analysis shown in (b) and (d). ....	182
Figure 114. Scanning electron micrograph of cross sectioned AA2024-T351 pretreated with Prekote and coated with MgRP (initial MgPVC = 45%) after environmental exposure in the field at Charlottesville, VA for (a) 12 weeks and (b) 24 weeks. ....	183
Figure 115. X-Ray diffraction spectra of AA2024-T351 panels coated with MgRP (initial MgPVC = 45%) after field exposure at Charlottesville, VA for 0, 12, and 24 weeks. Dotted lines indicate the position of the most intense diffraction peak for (a) $\text{MgCO}_3$ (b) $\text{MgCl}_2$ (c) $\text{Al}_2\text{O}_3$ and (d) $\text{Mg}(\text{OH})_2$ . ....	183
Figure 116. (a) Bode and (b) Nyquist plots of EIS of AA2024-T351 panels coated with MgRP (initial MgPVC = 45%) after field exposure at Charlottesville, VA for 0, 2, 6, 12, and 24 weeks. Tested in ambiently aerated 5% NaCl Solution. Fit results in Table 9.....	184
Figure 117. Optical micrograph of AA2024-T351 panels coated with MgRP (initial MgPVC = 45%) after lab accelerated life testing in ASTM B117 for (a) T = 0 hrs (b) T = 384 hrs (c) T = 984 hrs ....	187
Figure 118. Optical micrograph of AA2024-T351 panels coated with MgRP (initial MgPVC = 45%) after lab accelerated life testing in ASTM B117 for (a) T = 0 hrs (b) T = 384 hrs (c) T = 984 hrs ....	188

Figure 119. Scanning electron micrograph (planar view) of scribed AA2024-T351 pretreated with Prekote and coated with MgRP (initial MgPVC = 45%) after lab accelerated life testing in ASTM B117 for (a) 384 hrs and (b) 984 hrs. ....	188
Figure 120. Scanning electron micrograph (planar view) of scribed AA2024-T351 pretreated with Prekote and coated with MgRP (initial MgPVC = 45%) after lab accelerated life testing in ASTM B117 for (a) 384 hrs and (b) 984 hrs. ....	189
Figure 121. Scanning electron micrograph (planar view) of scribed AA2024-T351 pretreated with Prekote and coated with MgRP (initial MgPVC = 45%) after lab accelerated life testing in ASTM B117 for (a) 384 hrs and (b) 984 hrs. ....	189
Figure 122. SEM micrograph (planar view) of scribed AA2024-T351 pretreated with Prekote and coated with MgRP (initial MgPVC = 45%) after lab accelerated life testing in ASTM B117 for 984 hrs. Spot markers indicate approximate location of EDS analysis shown in (b). ....	190
Figure 123. Scanning electron micrograph of cross sectioned AA2024-T351 pretreated with Prekote and coated with MgRP (initial MgPVC = 45%) after lab accelerated life testing in ASTM B117 for (a,b) 384 hrs and (c,d) 984 hrs. Spot markers indicate approximate location of EDS analysis shown in (b) and (d). ....	191
Figure 124. Scanning electron micrograph of cross sectioned AA2024-T351 pretreated with Prekote and coated with MgRP (initial MgPVC = 45%) after lab accelerated life testing in ASTM B117 for (a) 384 hrs and (b) 984 hrs. ....	192
Figure 125. X-Ray diffraction spectra of AA2024-T351 panels coated with MgRP (initial MgPVC = 45%) that have been environmentally exposed in ASTM B117 for 0, 384 and 984 hours. Dotted lines indicate the position of the most intense diffraction peak for (a) $MgCO_3$ (b) $MgCl_2$ (c) $Al_2O_3$ and (d) $Mg(OH)_2$ . ....	192
Figure 126. (a) Bode and (b) Nyquist plots of EIS of AA2024-T351 panels coated with MgRP (initial MgPVC = 45%) that have been environmentally exposed in ASTM B117 for 0, 168, 384, 744, and 984 hours. Tested in ambiently aerated 5% NaCl Solution. Fit results shown in Table 10. ....	193
Figure 127. Optical micrograph of AA2024-T351 panels coated with MgRP (initial MgPVC = 45%) after lab accelerated life testing in ASTM B117 modified with artificial sea water. (a) T = 0 hrs (b) T = 408 hrs (c) T = 1000 hrs. ....	196
Figure 128. Optical micrograph of AA2024-T351 panels coated with MgRP (initial MgPVC = 45%) after lab accelerated life testing in ASTM B117 modified with artificial sea water. (a) T = 0 hrs (b) T = 408 hrs (c) T = 1000 hrs. ....	197
Figure 129. Scanning electron micrograph (planar view) of scribed AA2024-T351 pretreated with Prekote and coated with MgRP (initial MgPVC = 45%) after lab accelerated life testing in ASTM B117 modified with artificial sea water for (a) 408 hrs and (b) 1000 hrs. ....	197
Figure 130. Scanning electron micrograph (planar view) of scribed AA2024-T351 pretreated with Prekote and coated with MgRP (initial MgPVC = 45%) after lab accelerated life testing in ASTM B117 modified with artificial sea water for (a) 408 hrs and (b) 1000 hrs. ....	198
Figure 131. Higher magnification scanning electron micrograph (planar view) of scribed AA2024-T351 pretreated with Prekote and coated with MgRP (initial MgPVC = 45%)	

after lab accelerated life testing in ASTM B117 modified with artificial sea water for (a) 408 hrs and (b) 1000 hrs.....	198
Figure 132. SEM micrograph (planar view) of scribed AA2024-T351 pretreated with Prekote and coated with MgRP (initial MgPVC = 45%) after after lab accelerated life testing in ASTM B117 modified with artificial sea water for 1000 hrs. Spot markers indicate approximate location of EDS analysis shown in (b).....	199
Figure 133. Scanning electron micrograph of cross sectioned AA2024-T351 pretreated with Prekote and coated with MgRP (initial MgPVC = 45%) after lab accelerated life testing in ASTM B117 modified with artificial sea water for (a,b) 408 hrs and (c,d) 1000 hrs. Spot markers indicate approximate location of EDS analysis shown in (b) and (d). ....	200
Figure 134. Scanning electron micrograph of cross sectioned AA2024-T351 pretreated with Prekote and coated with MgRP (initial MgPVC = 45%) after lab accelerated life testing in ASTM B117 modified with artificial sea water for (a) 408 hrs (b) 1000 hrs.	201
Figure 135. X-Ray diffraction spectra of AA2024-T351 panels coated with MgRP (initial MgPVC = 45%) after lab accelerated life testing in ASTM B117 modified with artificial sea water for 0, 408 and 1000 hours. Dotted lines indicate the position of the most intense diffraction peak for (a) $MgCO_3$ (b) $MgCl_2$ (c) $Al_2O_3$ and (d) $Mg(OH)_2$ . ....	201
Figure 136. (a) Bode and (b) Nyquist plots of EIS of AA2024-T351 panels coated with MgRP (initial MgPVC = 45%) after lab accelerated life testing in ASTM B117 modified with artificial sea water for 0, 192, 408, 698 and 1000 hours. Tested in ambiently aerated 5% NaCl Solution. Fit results shown in Table 11. ....	202
Figure 137. Integrated Mg peak ( $Mg <200> 2\theta = 36.6170^\circ$ ) intensity vs. environmental exposure time in various lab and field exposure environments for panels of AA2024-T351 coated with MgRP (initial MgPVC = 45%). Dotted line indicates initial integrated Mg peak intensity of an unexposed panel. XRD Detection limit is estimated to be 3 – 5% of samples by volume. <sup>3</sup> .....	204
Figure 138. Galvanic protection potential of AA2024-T351 coated with MgRP (initial MgPVC = 45%) in ambiently aerated 5% NaCl solution vs. environmental exposure time in various lab and field exposure environments. ....	205
Figure 139. Correlation between integrated Mg peak ( $Mg <200> 2\theta = 36.6170^\circ$ ) intensity vs. galvanic protection potential of AA2024-T351 coated with MgRP (initial MgPVC = 45%) in ambiently aerated 5% NaCl solution after exposure in various environments.	205
Figure 140. Magnitude of electrochemical impedance at 0.01 Hz in ambiently aerated 5% NaCl solution vs. environmental exposure time in various exposure environments for panels of AA2024-T351 coated with MgRP (initial MgPVC = 45%). ....	206
Figure 141. Breakpoint frequency in ambiently aerated 5% NaCl solution vs. environmental exposure time in various exposure environments for panels of AA2024-T351 coated with MgRP (initial MgPVC = 45%). ....	206
Figure 142. Schematic of AA2024-T351 coated with MgRP depicting MgRP sacrificial cathodic protection function under full immersion.....	208
Figure 143. Schematic of AA2024-T351 coated with MgRP depicting MgRP sacrificial cathodic protection function under thin-layer electrolyte conditions found in high TOW exposure environments such as ASTM B-117 or during specific situations in the field such as during heavy precipitation, immersion or dewing.....	208

Figure 144. Schematic of AA2024-T351 coated with MgRP depicting MgRP sacrificial cathodic protection function under droplet electrolyte geometry conditions likely found in the lab in RH cabinet exposures and in the field during light precipitation or deliquescence of deposited salts due to moderate RH.....	208
Figure 145. Mean hourly solar radiation at Kennedy Space Center, FL over the dates 11/7/2012 – 11/9/2012.....	210
Figure 146. Schematic of filiform corrosion on an aluminum alloy <sup>17</sup> .....	222
Figure 147. The pore resistance for polyester resin coated galvanized and phosphated steel as a function of immersion time. Three different UV irradiation times are shown. The samples were immersed in 5% sodium chloride solution <sup>27</sup> .....	223
Figure 148. Graph showing the relative material loss of pure aluminum exposed to different pollutant gases (left), and a table showing the pH of the surface water films produced in each exposure environment (right) after 4 weeks of exposure <sup>31</sup> .....	224
Figure 149. Molecular structure of Eponol.....	229
Figure 150. Schematic of Eponol coated and scribed AA2024-T351 sample. The sample is a square that is 2.5 cm on a side. ....	230
Figure 151. Schematic of Eponol coated and scribed AA2024-T351 sample. The substrate is roughly 1 mm thick and the Eponol topcoat is 30±5 µm. The scribe line is 150±50 µm in width. ....	230
Figure 152. Schematic showing locations where EIS was performed on coated and scribed samples. ....	231
Figure 153. Optical Images of scribe creep over time for Eponol coated AA2024-T351 exposed at KSC. ....	238
Figure 154. Optical Images of scribe creep over time for Eponol coated AA2024-T351 exposed at BRD. ....	238
Figure 155. Optical images of Eponol coated AA2024-T351 exposed in ASTM B-117.....	239
Figure 156. Optical Images of scribe creep over time for Eponol coated AA2024-T351 exposed to ASTM G-85 Annex 3.....	239
Figure 157. Optical images of the scribe on Eponol coated AA2024-T351 exposed to ASTM G-85 Annex 5. ....	240
Figure 158. Optical images of the scribe on Eponol coated AA2024-T351 exposed to ASTM D-5894. ....	240
Figure 159. Optical images of the scribe on Eponol coated AA2024-T351 exposed to CC+O <sub>3</sub> (0.7-2.5 ppm). ....	241
Figure 160. Optical images of eponol coated AA2024-T351 exposed in various LALTs showing the extent of scribe creep after 15 days. ....	241
Figure 161. Optical images of eponol coated AA2024-T351 exposed at various field sites showing the extent of corrosion and scribe creep over time. ....	242
Figure 162. Scribe creep length over time for eponol coated AA2024-T351 for all LALTs and field sites. The KSC and BRD data points correspond to the upper X axis, as indicated by the arrows. ....	242



Figure 163. Optical image (left) and CSLM image (right) of pitting on bare AA2024 exposed to CC+O <sub>3</sub> (10-25 ppm) for 5 days. All samples rinsed in DI water before imaging. ....	243
Figure 164. Optical images of pitting on bare AA2024-T351 exposed in CC+O <sub>3</sub> (0.7-2.5 ppm) for 15 days (left) and CC+O <sub>3</sub> (10-25 ppm) for 5 days (right). All samples rinsed in DI water before imaging. ....	244
Figure 165. Optical image (left) and CLSM image (right) of pitting on bare AA2024 exposed at LA for 9 months. All samples rinsed in DI water before imaging. ....	244
Figure 166. Optical images of pitting on bare AA2024-T351. a) unexposed sample, b) exposed at BRD for 1 month, c) Exposed at BRD for 3 months, d) Exposed at KSC for 1 month, e) exposed at KSC for 3 months, f) exposed at KSC for 3 months. All samples rinsed in DI water before imaging. ....	245
Figure 167. Optical images of pitting on bare AA2024-T351 a) unexposed, b) exposed at LA for 9 months, c) exposed at KSC for 3 months, d) exposed at PJ for 9 months. All samples rinsed in DI water before imaging. ....	246
Figure 168. Optical images of pitting on bare AA2024-T351 a) unexposed, b) exposed in ASTM D-5894 for 1 cycle (14 days), c) exposed in ASTM D-4587 for 15 days, d) exposed in ASTM G-85 Annex 5 for 10 days, e) exposed in ASTM G-85 Annex 3 for 15 days, f) exposed in ASTM B-117 for 15 days. All samples rinsed in DI water before imaging. ....	247
Figure 169. Optical image (left) and binary image (right) of pitting on bare AA2024-T351 exposed to CC+UV+O <sub>3</sub> (0.7-2.5 ppm) for 15 days. All samples rinsed in DI water before imaging. ....	248
Figure 170. Histogram of pit area for bare AA2024-T351 exposed at KSC for 3 months. ....	249
Figure 171. Histograms of pit area for bare AA2024-T351 exposed in ASTM D-5894 for 1 cycle (14 days) (left) and for samples exposed at KSC for 3 months (right). Note that the x axis scales are equal in this figure and that the x axis scales for samples exposed at KSC is different in this figure compared with Figure 170. ....	249
Figure 172. Histogram of pit area for bare AA2024-T351 exposed in ASTM B-117 for 15 days. ....	250
Figure 173. Optical image of AA2024-T351 exposed in CC+O <sub>3</sub> (10-25 ppm) for 5 days showing open pits, copper replating and oxide filled pits. Sample was rinsed with DI water before imaging. ....	251
Figure 174. SEM image of pit that is filled with oxide. Sample exposed in CC+O <sub>3</sub> (10-25 ppm) for 5 days. Sample was rinsed with DI water before imaging. ....	251
Figure 175. EDS linescan of oxide filled pit of sample exposed in CC+O <sub>3</sub> (10-25 ppm) for 5 days. The spectra on the left show the relative abundances of oxygen, magnesium, aluminum and copper. The image on the right shows the length and direction of the scan. Sample was rinsed with DI water before imaging. ....	252
Figure 176. Images of small pits growing by undercutting the surface oxide layer on AA2024-T351 exposed to CC+O <sub>3</sub> (10-25 ppm) for 5 days. Sample was rinsed with DI water before imaging. ....	252
Figure 177. SEM images of AA2024-T351 exposed in CC+UV+O <sub>3</sub> (0.7-2.5 ppm) for 15 days and then immersed in 60% nitric acid solution to remove the surface oxide. Sample was rinsed with DI water before imaging. ....	253
Figure 178. SEM images of AA2024-T351 exposed to CC+UV+O <sub>3</sub> (0.7-2.5 ppm) for 15 days showing oxide particles on the surface of the sample. The particles were absent from	



samples exposed in other conditions. Sample was rinsed with DI water before imaging. ....	254
Figure 179. SEM images of AA2024-T351 exposed at LA for nine months showing pit morphology characteristic of samples exposed at field sites. Sample was rinsed with DI water before imaging. ....	254
Figure 180. EDS spectra (right) of a pit on AA2024-T351 exposed at LA field site for 9 months. The image on the right shows the direction of the scan. Sample was rinsed with DI water before imaging. ....	255
Figure 181. EIS data for coated AA2024 exposed at Kennedy Space Center, FL. Left is near and right is far. ....	256
Figure 182. EIS data for coated AA2024 exposed at Birdwood Golf Course, Charlottesville VA (BRD). Left is near and right is far. ....	256
Figure 183. EIS data for coated AA2024 exposed to ASTM B-117. Left is near and right is far. ....	257
Figure 184. EIS data for coated AA2024 exposed to ASTM G-85 Annex 3. Left is near and right is far. ....	257
Figure 185. EIS data for coated AA2024 exposed to ASTM G-85 Annex 5. Left is near and right is far. ....	258
Figure 186. EIS data for coated AA2024 exposed in ASTM D-5894. Left is near and right is far. ....	258
Figure 187. EIS data for coated AA2024 exposed to CC. Left is near and right is far. ....	259
Figure 188. EIS data for coated AA2024 exposed to CC+UV. Left is near and right is far. ....	259
Figure 189. EIS data for coated AA2024 exposed to CC+O <sub>3</sub> (0.7-2.5ppm). Left is near and right is far. ....	260
Figure 190. EIS data for coated AA2024 exposed to CC+UV+O <sub>3</sub> (0.7-2.5ppm). Left is near and right is far. ....	260
Figure 191. The equivalent circuit model for an organically coated metal. R(soln) is the solution resistance, R(pore) is the resistance of the pores in the coating, R <sub>dl</sub> is the double layer resistance, CPE2 is the coating capacitance and CPE1 is the double layer capacitance. ....	261
Figure 192. Example of the data that can be obtained from EIS. Saddle frequency decreases as R <sub>pore</sub> decreases. For this simulation, R <sub>s</sub> was 10 Ω-cm <sup>2</sup> , R <sub>pore</sub> varied from 10 <sup>12</sup> to 10 <sup>3</sup> Ω-cm <sup>2</sup> , R <sub>dl</sub> varied from 10 <sup>8</sup> to 10 <sup>4</sup> Ω-cm <sup>2</sup> , and the total area was 1 cm <sup>2</sup> . ....	262
Figure 193. Saddle frequency plots for coated AA2024 exposed to various environments. The top plot is data taken from the Near location. The bottom plot is data taken from the Far location. Open symbols represent data for samples exposed at field sites; time is on the top axis for the field sites. ....	263
Figure 194. EIS data and equivalent circuit fit Eponol coated AA2024-T351 exposed to CC+O <sub>3</sub> (0.7-2.5 ppm) for 3 days. Data taken at the far location (see Figure 152). ....	264
Figure 195. R <sub>pore</sub> values for Eponol coated AA2024-T351 exposed in CC+O <sub>3</sub> (0.7-2.5 ppm). EIS data was taken at near and far locations and then fit to an equivalent circuit to obtain R <sub>pore</sub> . ....	265
Figure 196. Graph of Equation 14 showing the increase in electrical defect area associated with the decrease of R <sub>pore</sub> . ....	266

Figure 197. Plot of saddle frequency and high and low breakpoint frequency ( $f_{45}$ ) for the model presented in Figure 192. The parameters are identical; $R_s$ was $10 \Omega\text{-cm}^2$ , $R_{\text{pore}}$ varied from $10^{12}$ to $10^3 \Omega\text{-cm}^2$ , $R_{\text{dl}}$ varied from $10^8$ to $10^4 \Omega\text{-cm}^2$ , and the area was $1 \text{ cm}^2$ .	267
Figure 198. FTIR spectra of Eponol films exposed in ASTM B-117 and G-85 A5 for 15 days. Data taken at UVA.	268
Figure 199. FTIR spectra of Eponol films exposed in various conditons. Data taken at USM.	269
Figure 200. FTIR spectra of Eponol films on inert polypropylene substrates exposed in various conditions. Arrows indicate peaks that are expected to change with exposure to UV.	272
Figure 201. Optical images showing the comparison of pitting/corrosion morphology on bare AA2024-T351 exposed at KSC (left) and in CC+UV+O <sub>3</sub> (0.7-2.5 ppm) (right).	273
Figure 202. Loading frequency dependence of $da/dN$ for C47A-T86 (L-T) stressed in aqueous solutions of chloride and chloride-molybdate at a constant $\Delta K$ of $7 \text{ MPa}\sqrt{\text{m}}$ and $R$ of 0.58.	284
Figure 203. Loading frequency and applied potential dependencies of $da/dN$ for C47A-T86 (L-T) stressed in aqueous chloride and chloride-molybdate solutions at constant $\Delta K$ of $7 \text{ MPa}\sqrt{\text{m}}$ and $R$ of 0.58.	285
Figure 204. Crack length versus fatigue loading cycles for C47A-T86 (L-T) stressed in $0.06\text{M NaCl} + 0.6\text{M Na}_2\text{MoO}_4$ with polarization of $-400 \text{ mV}_{\text{SCE}}$ at constant $\Delta K$ of $7 \text{ MPa}\sqrt{\text{m}}$ , $R$ of 0.58, and $f$ of 3 Hz.	286
Figure 205. SEM image of the fatigue crack surface morphology for a specimen of C47A-T86 stressed in $0.06\text{M NaCl} + 0.6\text{M Na}_2\text{MoO}_4$ (near-OCP polarization of $-500 \text{ mV}_{\text{SCE}}$ ) at $\Delta K$ of $7 \text{ MPa}\sqrt{\text{m}}$ , $R$ of 0.58, and $f$ of 3 Hz. The direction of crack growth is from bottom to top.	287
Figure 206. SEM images of the fatigue crack surface morphology for a specimen of C47A-T86 stressed in $0.06\text{M NaCl} + 0.6\text{M Na}_2\text{MoO}_4$ at $\Delta K$ of $7 \text{ MPa}\sqrt{\text{m}}$ , $R$ of 0.58, and 0.3 Hz. a) $-500 \text{ mV}_{\text{SCE}}$ and b) $-400 \text{ mV}_{\text{SCE}}$ . The direction of crack growth is from bottom to top.	288
Figure 207. a) EDS spectrum of fatigue crack surface reaction product produced during stressing in $0.06\text{M NaCl} + 0.6\text{M Na}_2\text{MoO}_4$ ( $\Delta K = 7 \text{ MPa}\sqrt{\text{m}}$ , $R = 0.58$ , $f = 3 \text{ Hz}$ ) at near-OCP of $-500 \text{ mV}_{\text{SCE}}$ .	289
Figure 208. SEM images of the fatigue crack surface morphology for C47A-T86 stressed in $0.06\text{M NaCl} + 0.6\text{M Na}_2\text{MoO}_4$ at $\Delta K$ of $7 \text{ MPa}\sqrt{\text{m}}$ , $R$ of 0.58, $f$ of 0.3 Hz, and $-600 \text{ mV}_{\text{SCE}}$ .	290
Figure 209. Crack length versus fatigue loading cycles for C47A-T86 (L-T) stressed in $0.06\text{M NaCl} + 0.6\text{M Na}_2\text{MoO}_4$ at constant $\Delta K$ of $7 \text{ MPa}\sqrt{\text{m}}$ and $R$ of 0.58 with polarizations and $f$ of (a) $-500 \text{ mV}_{\text{SCE}}$ and 10 Hz, (b) $-500 \text{ mV}_{\text{SCE}}$ and 0.3 Hz, and (c) $-600 \text{ mV}_{\text{SCE}}$ and 3 Hz.	292
Figure 210. Water vapor exposure dependence of $da/dN$ for C47A-T86 and 7075-T651 at a $\Delta K$ of $7 \text{ MPa}\sqrt{\text{m}}$ and $R$ of 0.58.	295
Figure 211. Loading frequency dependence of $da/dN$ for C47A-T86 (L-T) stressed in solutions of chloride and chloride-molybdate, replotted from Figure 202.	297
Figure 212. Summary of results from Ro et. Al <sup>14-16, 39, 43</sup> for measured crack surface crystallography as a function of water vapor exposure for the lot of Al-Cu-Li alloy used in the present study.	299

## 1.1

## Front Matter

### 1.1.1 Forward

All of the projects were conducted at the University of Virginia, Department of Materials Science and Engineering, Center for Electrochemical Science and Engineering and various exposure sites under the project period covered by this grant from June 23, 2009 – August 31, 2012. The project thrust areas selected and the subtasks chosen for investigations were based on technical discussions and collaborations with the Corrosion Policy and Oversight Office, Dr. Bill Abbott of Battelle Memorial Labs, Mr. Dick Kenzie and Mr. David Robertson formerly from the Air Force Corrosion Control Office, Bill Nickerson and Craig Matzdorf of NAVAIR, Rich Hayes, formerly of Naval Surface Warfare Center NSWC-CD, Vincent Hock, Richard Lampo and Michael McInerney from CERL, the Corrosion Policy and Oversight Office, as well as numerous others.

The project topic areas lie in four general research thrust areas of great interest to the Corrosion Policy and Oversight Office. These include:

*Research to Better Define the Needs for Future Accelerated Corrosion Test Development*

*Chromate Replacement Coatings and Specialized Coating Applications with other Functions*

*Development and Causes for Discrepancies Between Field and Laboratory Testing on Bare and Coated Metals.*

*Innovative Coatings for Corrosion Cracking Resistance*

These categories were further refined as follows with individual topic projects in each of these two areas in this report. The two areas are (1) Environmental Severity and Accelerated Testing, and (2) Managing Corrosion and Cracking Through the Use of Coatings. Findings from each project task are discussed in sections 1.2-1.10 below.

Projects task reports under Environmental Severity and Accelerated Testing that are reported here include:

- Factors Controlling the Atmospheric Corrosion of Silver in Natural and Accelerated Test Environments, (R.G. Kelly, E.B. Neiser and Y. Wan)
- Analysis of Relative Importance of Surface Environment Components and Dynamics, (R.G. Kelly, B. Risteen, and E.J. Schindelholz)
- Galvanic Interactions Between AA7075-T6 and Noble Materials, (R. G. Kelly, Y. Shi)

Under Atmospheric Environment Effects on Cracking and Structural Integrity:

- Scientific Advances Enabling Next Generation Management of Corrosion Induced Fatigue (J.T. Burns and R. P. Gangloff)

- Effect of Atmospheric Exposure on Environmental Fatigue Crack Propagation and Inhibition in Precipitation Hardened Al-Cu-Li (J. S. Warner, R. P. Gangloff)

Project tasks reported under Managing Corrosion Through the Use of Coatings specifically Chromate Replacement Coatings and Specialized Coating Applications with other Functions as well as Innovative Coatings for Corrosion Cracking Resistance include:

Under Evaluation of the Performance of A Magnesium Rich, Non-Chrome Primer and Discrepancies With Laboratory Data

- Blistering Phenomena in Early Generation Mg-Rich Primer Coatings on AA2024-T351 and the Effects of CO<sub>2</sub> (A.D. King and J.R. Scully)
- Environmental Degradation of a Mg-Rich Primer: Comparison of Selected Field Environments with Laboratory Exposures, (A.D. King and J.R. Scully)

Under Managing Corrosion Through the Use of Coatings, Chromate Replacement Coatings and Specialized Coating Applications with other Functions:

- Underpaint Corrosion on Chromate-Free Organic Coated AA2024-T351 as a Function of Accelerated Testing Variables Compared with Natural Exposures (M.L. Tayler and J.R. Scully)

Regarding Smart Coating System Synthesis and Coating/Corrosion Attributes for Inhibitor Release and Inhibition of Corrosion/Cracking, the single report on this topic is:

- Molybdate Inhibition of Corrosion Fatigue Crack Propagation in Precipitation Hardened Al-Cu-Li (J.S. Warner, and R.P. Gangloff)

### 1.1.2 Preface

The research and technological investigations within this final report have several objectives. One is to support graduate student research and education in the field of corrosion. This objective is met by the training of graduate students in the Materials Science and Engineering discipline to conduct the research listed and the subsequent placement of a high portion of them in US DoD, national laboratory, government and industry professional positions. A second objective is the conduct of research studies that will support the implementation of other Corrosion Policy and Oversight Office projects that have been completed or are in progress. A third objective is to plan and conduct targeted studies within about a 2 year period and that have a significant probability of delivering "products" to DoD interested end users that could begin along a path to implementation. Findings from each project task are discussed in sections 1.2-1.10 below. In general, output included multiple student graduations and placements in US DoD, Academia, and/or industry technical positions (3 placements from this project co-author list). Each report topic includes an introduction, lessons learned, technical investigations, experimental results, conclusions, implementation plans, and a description of possible economic impacts (enclosed and detailed below).



### 1.1.3 Acknowledgements

In addition to funding by the Corrosion Policy and Oversight Office, brainstorming sessions with the Corrosion Policy and Oversight Office, Dr. William Abbott of Battelle Memorial Labs, Richard Kenzie and David Robertson, formerly from the Air Force Corrosion Control Office, Bill Nickerson and Craig Matzdorf, NAVAIR, Rich Hayes, formerly of the NSWC-CD and the Corrosion Policy and Oversight Office, The Naval Research Laboratories, the Center for Structural Aircraft Life Extension (CASTLE) at the US Air Force Academy, Vincent Hock, Richard Lampo and Michael McInerney from CERL, Scott Fawaz (SAFE) and numerous other collaborators contributed to the technical progress enclosed below.

Numerous DoD and non-DoD agencies provided coatings and treatments. Battelle Memorial Labs – Mr. William Abbott, NASA Kennedy Space Flight Center, Alcoa – Francine Bovard and James Moran and the University of Hawaii – Professor Lloyd Hihara provided invaluable assistance by providing access to field exposure sites for material/coating panel deployments, maintenance of field exposure sites, and return of exposed panels. Professor James Rawlins and Michael Blanton provided assistance with organic coatings for testing, coating evaluation, and the packaging and release of ionic inhibitors in coatings.

### 1.1.4 Introduction and Background

Individual topic project reports are enclosed in each of these two areas. The two areas are (1) CERL-12 Area: research to define the needs of accelerated test development and (2) CERL-12 Area: Coatings: causes for discrepancies between field and laboratory testing on bare and coated metals, chromate replacement coatings and specialized coating applications with other functions and innovative coatings for corrosion cracking resistance.

The first topic in area (1) sought to *Understand the Factors Controlling the Atmospheric Corrosion of Silver in Natural and Accelerated Test Environments* (1.2). The objectives were to quantify the kinetics of the atmospheric corrosion of silver used as a corrosion sensor in the field and their dependence on critical parameters and to assess the ability of gas-phase laboratory exposures to replicate the corrosion products observed under field exposures. Silver has been used for a number of years as a measure of the corrosivity of natural environments. After exposure, cathodic reduction of the corroded silver surfaces in the laboratory has indicated the ubiquitous presence of silver chloride, even in locations far from the seacoast or other sources of chloride ion. In standard salt spray testing, there is little, if any, silver chloride formed. This paradox formed the driving force for a preliminary OUSD project that has investigated the role of salt, humidity, ozone, and UV light on the atmospheric corrosion of silver. The work built on previous results reported in the September 30, 2012 report. The second topic in this subject area concerns the *Analysis of Relative Importance of Surface Environment Components and Dynamics* (1.3). The overarching objective of this task was the quantitative assessment of the roles of relevant chemical species on the corrosivity of natural atmospheres including the species identified. The third task was to develop and understanding of *Galvanic Interactions Between AA7075-T6 and Noble Materials* under various geometric, physical; and chemical scenarios relevant to field exposures of noble metal high strength aluminum alloy joints and provide the test methodology for the same (1.4). The last two tasks in this project area concern (a) *A Summary of Scientific Advances Enabling Next Generation Management of Corrosion Induced Fatigue* (1.5) and (b) *Effect of Atmospheric Exposure on Environmental Fatigue Crack Propagation and Inhibition in Precipitation Hardened Al-Cu-Li* (1.6). The objectives of this subtask were to (1) outline the scientific challenges associated with modeling crack formation and growth from corrosion damage, (2) assess the engineering impact of recent high fidelity



experimentation and modeling of this behavior, (3) identify remaining deficiencies, (4) develop a test method for quantifying atmospheric environment exposure effects on fatigue crack growth, and (5) interpret the results of item 4 in the context of scientific understanding of full immersion and gaseous environment effects. The background, objectives, results and findings of each task along with the conclusions, lessons learned, implementation plan and economic summary are discussed in sections 1.2 to 1.6.

The projects under managing corrosion and cracking through the use of coatings include two follow-on tasks on Evaluation of the Performance of a Magnesium Rich, Non-Chrome Primer that was first reported in September 30<sup>th</sup>, 2012. In the first task report in this final report, (1.7) a field lab discrepancy regarding blistering in early generation coatings in standard laboratory accelerated tests are examined. This section is titled *Blistering Phenomena in Early Generation Mg-Rich Primer Coatings on AA2024-T351 and the Effects of CO<sub>2</sub>*. This task report defines the role of atmospheric CO<sub>2</sub> and defines two kinds of blisters. The second task reported (1.8) involves *Environmental Degradation of a Mg-Rich Primer: Comparison of Selected Field Environments with Laboratory Exposures*. The over-arching objective of this task is to conduct appropriate laboratory accelerated life tests (LALT), simulated field exposures, as well as various modeling studies to understand factors both controlling coating performance and limiting the lifetime of the sacrificial corrosion protection function associated with Mg rich primer coating. Secondly the project sought to understand primer coating performance when Mg is "used up" as well as the origins of difference in failure modes in field versus lab tests. The ultimate goal was to predict/estimate the useful life of this and analogous coatings and to explain any field-lab discrepancies. The remaining task in this project area with focus on chromate replacement coatings and managing corrosion through coatings was on the subject of *Studies of Corrosion Along Scribe Lines On Non-chromated Painted Systems* (1.9). In a previous report, results for coatings on steel were developed. Here the results for AA 2024-T351 are reported. The overarching objective of this task was to better control and characterize the underpaint environments, electrochemical behavior and related physical properties that develop under polymer coatings and then elucidate effect of environmental chemistry variables on scribe creep and filiform corrosion on 2024-T351. The objective of the report enclosed was to understand the influence of environmental chemistry, as a function of the bulk environment on the mechanism and rates of scribe creep and filiform attack on 2024-T351 painted and scratched panels. This task compared standard laboratory accelerated exposure tests to assess lifetimes (LALT) to selected natural field environments using high level surveillance methods. This information can then ultimately enable new accelerated tests or smart choice of existing tests.

The final set of tasks under this subject area covered the general topic of Specialized Coating Applications with other Functions and Innovative Coatings for Corrosion Cracking Resistance. The ultimate objective was to develop new smart coatings with various packaged inhibitor strategies and on-demand release mechanisms that inhibit surface corrosion, the pit to crack transition, and either sustained load or cyclic load macroscopic cracking in high performance metals such as precipitation hardened Al alloys. Here, the effects of an ionic inhibitor (molybdate) on the corrosion fatigue properties of an Al-Cu-Li alloy are reported (1.10). An Al-Zn-Mg-Cu alloy was investigated in a previous report. In this case, results are extended to a different alloy system. As a preliminary step in identifying ionic inhibitors for release from a smart coating, investigations first identified ionic additions to sodium chloride solution. This work was guided by significant literature on cracking inhibitors defined from full immersion studies. Addition of molybdate (MoO<sub>4</sub><sup>2-</sup>) to aqueous chloride solution effectively inhibited environmental fatigue crack propagation (EFCP) in peak aged Al-2.6Cu-1.6Li (wt pct, C47A-T86) which also exhibits alloy-induced inhibition in pure chloride solution. MoO<sub>4</sub><sup>2-</sup> inhibited EFCP at frequencies below an upper bound and eliminated the effect of environment at sufficiently low loading

frequencies by yielding crack growth rates equivalent to those for fatigue in ultra-high vacuum. Ion assisted inhibition was attributed to  $\text{MoO}_4^{2-}$  stabilizing a crack tip passive film which reduced  $\text{H}$  production and uptake due to a diffusion barrier film, reduced crack acidification by hydrolysis, and buffered pH. Inhibition was governed by the balance between passive film rupture by crack tip strain and repassivation. As such, inhibition was promoted by reduced loading frequency and potentials at or anodic to free corrosion; each of which favors passivity over film rupture. The inhibiting effect of molybdate for this Al-Cu-Li alloy paralleled chromate and molybdate inhibition of EFCP in 7075-T651, establishing molybdate as a viable chromate replacement inhibitor. The background, object, results and findings of each task along with the conclusion, lessons learned, implementation plan and economic summary are discussed in sections 1.6 to 1.10.

## **1.2 Factors Controlling the Atmospheric Corrosion of Silver in Natural and Accelerated Test Environments (R. G. Kelly, E. B. Neiser, Y. Wan)**

### **1.2.1 Summary**

Laboratory salt spray testing has been used for many years to accelerate natural atmospheric exposures with limited success. The corrosion of silver represents a stark example of the failings of such testing. In virtually any field environment, silver corrodes measurably in a month, but after 4 months in a standard salt spray test, no corrosion of silver is observed. The present work is concerned with the modification of the conventional salt spray corrosion test and its correlation to field measurements of silver. Two subsystems were designed and constructed to modify a conventional salt spray chamber. One subsystem consisted of Ultraviolet A (UVA) lamps mounted on a movable rack which allows them to be positioned to achieve the desired UVA light intensity. The other subsystem consisted of an ozone system based on a commercial ozone generator and a distribution manifold that allowed a uniform concentration of ozone to be maintained throughout the chamber. As constructed, the system can produce 50 W/m<sup>2</sup> of UVA light and ozone concentrations up to 23.2 ppm. The system was then used to modify the protocol of ASTM B117. The results from the modified B117 test are correlated with the corrosion behavior and performance observed in field exposures. The corrosion products formed during the modified B117 exposure are the same as those observed after field exposures. AgCl was the main dominant corrosion product. Non-uniform corrosion occurred, and metallic silver grains were observed on the surface. The large acceleration factors obtained demonstrate that both ozone and UVA light can be used to replicate the type of corrosion found on silver at a wide range of geolocations. The extent of the acceleration can be controlled by the ozone concentration and the intensity of the UVA light. It was also shown that formic acid has no effect on the corrosion of silver in the presence or absence of UVA light.

### **1.2.2 Introduction and Background**

Silver has been used for a number of years as a measure of the corrosivity of natural environments. After exposure, cathodic reduction of the corroded silver surfaces in the laboratory has indicated the ubiquitous presence of silver chloride, even in locations far from the seacoast or other sources of chloride ion. In standard salt spray testing, there is little, if any, silver chloride formed. This paradox formed the driving force for a preliminary OUSD project that has preliminarily investigated the role of salt, humidity, ozone, and UV light on the atmospheric corrosion of silver.

Conventional accelerated corrosion tests (e.g., ASTM standard B117<sup>1</sup>) are often used to accelerate the natural marine atmospheric corrosion of materials for material selection or quality control. However, results from ASTM standard B117 testing often do not correlate well with field exposures<sup>2,8</sup>, requiring caution in using the results for prediction, as pointed out by the standard<sup>1</sup>. A prime example of the shortcoming of this testing is the corrosion of silver. When silver is exposed to actual atmospheric environments, it forms an AgCl film with a thickness that depends on the corrosivity of the exposure site and exposure time, with measurable amounts forming in less than 30 days<sup>2,9</sup>. In contrast, when silver is exposed to the standard B117 test protocol, no AgCl forms even after four months of continuous testing<sup>2</sup>. Clearly, there must be some atmospheric factors that affect corrosion of silver and are not present in the standard B117 testing. This silver paradox implies that natural atmospheres are more oxidizing than the atmosphere created in standard salt spray testing. Note that silver is a material of interest as it

is being increasingly used as a means of rapidly measuring the corrosivity of natural environments, and the corrosion rate of silver is used as an input to a predictive model of steel corrosion<sup>9</sup>.

Atmospheric corrosion of silver is known to be affected by a number of environmental variables, such as temperature, UV light, and pollutant gases<sup>2,10,11</sup>. Although silver is thermodynamically unstable relative to silver oxide under ambient atmospheric conditions, the kinetics of silver oxide formation under these conditions is negligible<sup>12</sup>. However, silver has been shown to corrode in the presence of 5 mol % ozone ( $O_3$ ) in  $O_2$  at 300K and ambient pressure<sup>13,14</sup>. UVA light (295-365 nm) splits ozone to form atomic oxygen, which is a highly reactive species<sup>15,16</sup> that attacks silver. Recent work<sup>2,10</sup> has also shown that the more oxidizing character of natural environments relative to the B117 can be reproduced in the laboratory testing via the introduction of UVA light and ozone to the test environment. The results showed that UVA light and ozone have important accelerating effects on the corrosion of silver. These studies were performed in custom-made exposure chambers.

The goal of this study was to extend the previous work<sup>2,10</sup> by modifying a commercial accelerated corrosion test chamber to allow for the controlled introduction of both ozone and UVA light. The modified chamber was then characterized in terms of the range of ozone and UVA light illumination that can be controlled. A series of tests were performed to evaluate the relative effects of ozone and UVA light on the corrosion of silver, and comparisons were made to data from field exposures at several geolocations that covered a wide range of corrosivity. Finally, a modification to the B117 test protocol is recommended that provides reasonable acceleration factors for silver for a wide range of geolocation corrosivities.

### 1.2.3 Lessons Learned

- (a) Modification of the ASTM B117 standard by the introduction of ozone and UV light can lead to extensive corrosion of silver during the salt spray, unlike the case when the standard is followed, in which no corrosion of silver occurs, even after months of exposure.
- (b) Silver does not appear to react with organic acids that are typical of atmospheric conditions, even in the presence of UV light.

### 1.2.4 Technical Investigations

Silver samples of 75mm×15mm×0.25mm and 99.95% purity were obtained from Lucas-Milhaupt, Inc. (Cudahy, WI) and were wet abraded with 600 grit SiC grinding paper. The samples were then cleaned with methanol and deionized water and air dried before being tested.

#### 1.2.4.1 Small Chamber Studies of Atmospheric Corrosion in the Presence of Formic Acid

Formic acid was introduced to the chamber in an attempt to identify and utilize other species present in natural environments for accelerated tests. Formic acid was selected as it is one of the most abundant atmospheric acids. Formic acid is also considered to be the most aggressive straight-chain organic acid. Formic acid was introduced using a permeation tube in the gas mixer.



#### 1.2.4.2 Modification of the ASTM Standard B117 Method

A salt spray corrosion test chamber (Model CCT 1100, Q-Lab Corporation, Ohio, USA) amenable for conducting ASTM standard B117, was used in this work. A continuous salt spray is created by the atomization of 5 wt. % sodium chloride (NaCl) solution through a nozzle by the pumping compressed air and solution. Compressed air is humidified by passage through a bubble tower on its way to the nozzle. Freshly prepared salt solution is placed in the reservoir as specified by ASTM B117<sup>1</sup>. The modification of the CCT 1100, referred to hereafter as the MB117, involved the design and construction of two subsystems, as shown in Figure 1. One subsystem was designed and constructed to produce a range of UVA light intensity with the desired spectrum in the chamber. The other subsystem was designed and constructed to generate ozone and distribute it uniformly throughout the chamber.

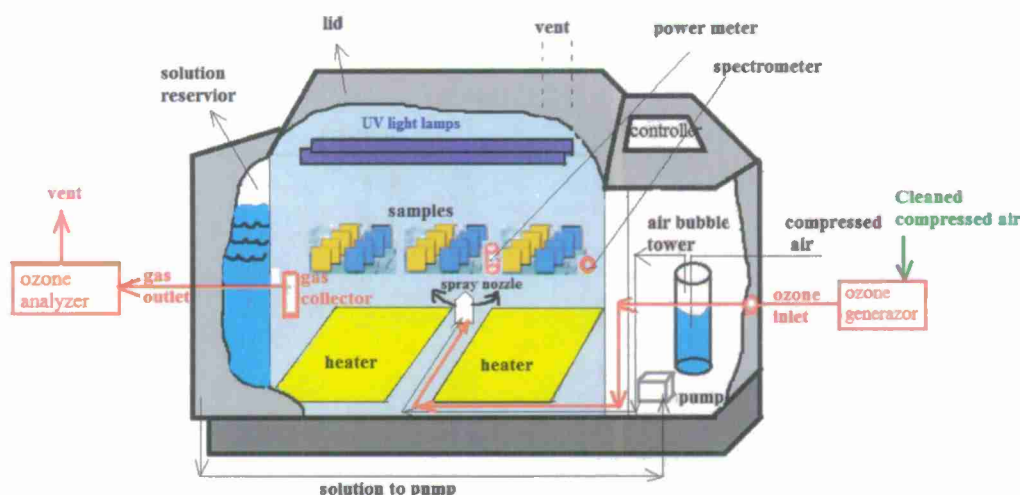


Figure 1. Schematic view of the MB117 chamber.

The UVA lamps (Model UVA-340, Q-Lab Corporation, Ohio, USA) were chosen to simulate sunlight in the critical short-wave UV region from 365 nm down to the solar cutoff of 295 nm. The UVA lamps were used in pairs. Two pairs of lamps were used, referred to as 'Pair a' and 'Pair b'. They are mounted on a movable rack (shown in Figure 2), which allows them to be translated along both the y- and z-directions to create a desired UVA light intensity at a given specimen location. The removable rack is made of structural fiberglass. Reflectors were included the lamps to direct as much of the UVA light towards the samples as possible. The maximum UVA intensity is controlled by the total number and positions of UVA lamps being used. A spectrometer (Model JAZ, Ocean Optics Incorporation, Florida, USA) was used to measure the spectrum of the UVA light, and a 1918-c Newport power meter (Model 1918-c, Newport Corporation, California, USA) was used to measure the UVA light intensity.



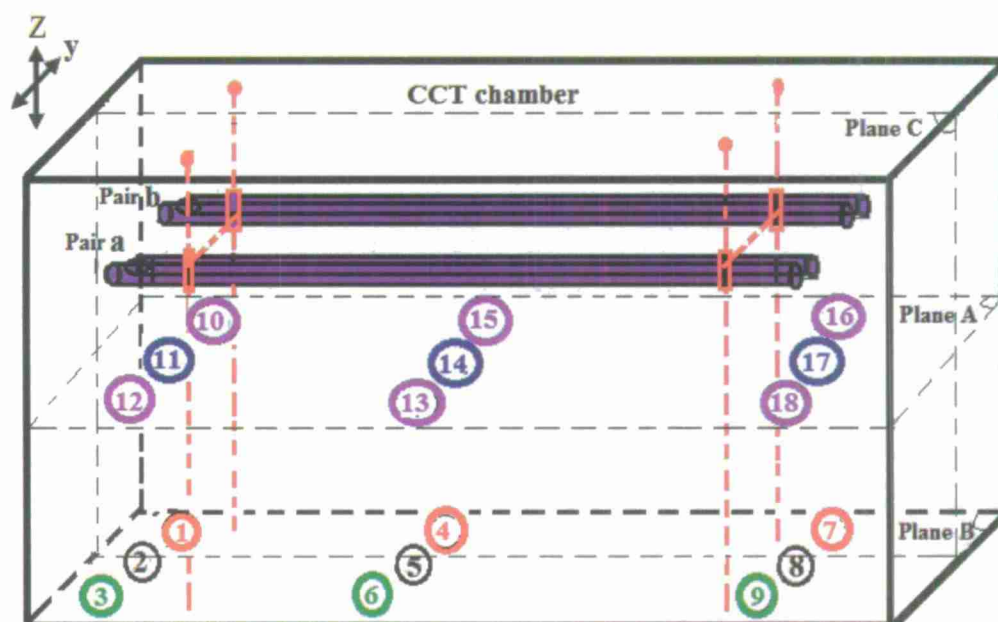


Figure 2. The selected physical locations (1-18) in the MB117 used for the measurement of the UVA light intensity and the ozone concentration. "Pair a" and "Pair b" are two pairs of UVA lamps and can be moved along y- and z- directions in the racks (red dashed lines).

A commercial ozone generator (Model 1000, Jelight Company Inc., California, USA) was used to produce ozone on-line from clean air, which had been created by passing compressed air through a silica gel desiccant and an activated carbon cartridge. The generator used a 12" x 2" cell containing an ozone-producing double-bore lamp to create ozone from high intensity UV light. The ozone was introduced into the chamber via a custom-made baffle to ensure a uniform spatial distribution. The concentration of ozone was recorded with an ozone analyzer (Model 49i, Thermo Scientific Inc., Connecticut, USA), which is a dual-cell, UV photometric gas analyzer generally used for monitoring ambient air. The ozone analyzer has a precision 1.0 ppb and can measure ozone concentrations in the air from 0.05 to 200 ppm.

Figure 2 shows the locations chosen to characterize the distribution of UVA light intensity within the MB117 chamber. Eighteen locations in two horizontal planes (Plane A and Plane B) were chosen. Plane A was in the middle of the chamber, whereas Plane B was at the level of the diffuser, which near the bottom of the chamber. Three triplicate samples, exposed at one time, were used. The surface of the samples were angled 20° from the vertical, and parallel to the principal direction of flow of spray through the chamber. The MB117 test was a continuous exposure to a 5 mass % salt spray (pH was 6.8) at 35°C as described in the ASTM standard B117 protocol.

Field exposures of silver was conducted by W. Abbott<sup>9</sup> and L. Hihara<sup>17</sup> at six geolocations: Coconut Island, HI, Daytona Beach, FL, Whidbey Island, WA, West Jefferson, OH, Lyon Arboretum, HI, and Trenton, NJ. These sites provided a wide range of corrosivities and location types. Coconut Island and Daytona Beach are marine atmospheres, Whidbey Island is a rural marine atmosphere, West Jefferson is a mild urban atmosphere, Lyon Arboretum is a rainforest atmosphere, and Trenton is an urban atmosphere.

Specimens (75mm×12mm×0.5mm and were 99.9% pure) exposed to field sites were mounted onto plastic test cards in slots which could accept at least 4 plastic test cards. The slots were kept in a card cage, which consisted of an open plastic frame. The package was then placed in position to provide free and natural airflow around the samples. The entire process of sample placement and removal can be done within minutes. This need for minimal manpower and/or reporting requirements was also found to be critical to implementation<sup>9</sup>.

After the exposure, corrosion products of silver formed during the field exposure and the MB117 exposure were analyzed with coulometric reduction, which was performed in a three-electrode cell. An area of 1 cm<sup>2</sup> of the exposed silver sample served as the working electrode, a platinum-plated niobium mesh served as the counter electrode, and a saturated mercury/mercurous sulfate reference electrode was used as the reference electrode. Before introduction into the cell, the 0.1M sodium sulfate (Na<sub>2</sub>SO<sub>4</sub>, pH=10) reduction electrolyte was deaerated<sup>2,10</sup> for at least one hour by bubbling nitrogen. A constant cathodic current density of -0.1 mA/cm<sup>2</sup> was applied immediately to the silver sample by a PCI4 card potentiostats (Gamry, Pennsylvania, USA) after addition of the solution to the cell. The voltage was monitored until the voltage dropped to approximately -1.7 V (vs. MSE), at which hydrogen was evolved. Two values are extracted from each reduction curve<sup>18,19</sup>: the reduction potential and the reduction charge. The reduction potentials serve to identify the chemical composition of the corrosion products and were determined as the potential of the curve at the midpoint of an invariant portion of the reduction curve. The total reduction charge passed at one potential represents the amount of that compound present on the sample. The thickness of the corrosion product layer of silver can be calculated from the reduction charge, assuming that the corrosion product film forms with theoretical density. The reduction charges (per unit area, the same below) from field and the modified B117 represented the means of triplicate samples, standard deviations ranging from 1% to 8.5% (not shown).

The images of the samples were characterized by scanning electron microscopy (SEM) (JEOL JSM-6700F) equipped with energy dispersive X-ray spectroscopy (EDS) modes. X-ray diffraction (XRD) measurements were carried out with a Panalytical X'Pert Pro MPD X-ray diffractometer using a focused and monochromatized Cu K<sub>α</sub> source ( $\lambda = 1.540598$ ). The data were collected with a position sensitive detector in a 2 $\theta$  range of 10 to 110° with a resolution of 0.0083556°.

## 1.2.5 Experimental Results

### 1.2.5.1 Atmospheric Corrosion of Silver in Presence of Formic Acid

Formic acid was added to two exposures: one with only formic acid, and one with formic acid and UV illumination. Both were performed at 90 % relative humidity. For both exposures, the amount of formic acid released was calculated to be 230 ppb at the oven temperature of 70° C. This figure is derived from the permeation rates provided by the permeation tube manufacturer and were not measured in this study.

The reduction curves from the exposures with added formic acid are shown below in Figure 3. The reduction curves of both exposures are virtually identical to those of freshly-polished samples, indicating that no corrosion occurred during the exposures.

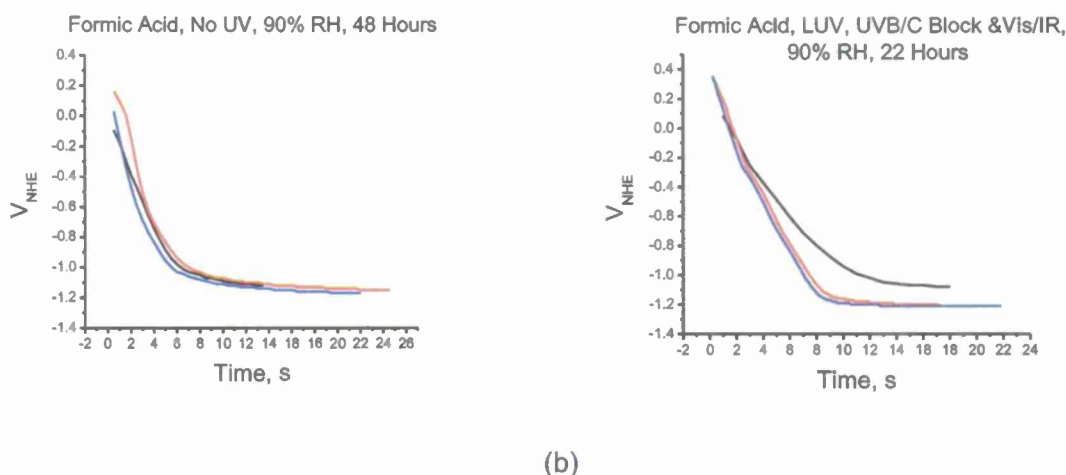


Figure 3 Reduction curves from exposures with added formic acid. Both exposures' reductions differ very little from the reductions of clean samples, suggesting that no corrosion resulted from either exposure.

(a) reductions after an exposure with added formic acid, (b) reductions from an exposure with formic acid and UV.

Although a significant contributor to precipitation acidity, and ubiquitous in worldwide environments, adding formic acid to exposures with silver did not accelerate silver corrosion. Figure 3 shows the reductions for the formic acid exposures and demonstrates their similarity to reductions of freshly cleaned samples.

Typical ground concentrations of formic acid are well below 30 ppb, so the concentration used for these exposures, 230 ppb, represents a significant increase from natural levels. The exposure shown in Figure 3, with only added formic acid and no illumination, lasted 48 hours, more than double the standard 22 hour exposure. Because no corrosion is observed even in this longer exposure, the addition of formic acid does not accelerate silver corrosion significantly enough to be an addition to an accelerated test.

Based on these results, no further exposures to organic acids were done for silver.

#### 1.2.5.2 Modification to ASTM Standard B117 Method

The spectrum of the UVA lamp, with peak emission at 340 nm, was recorded and shown in Figure 3 when the lamps were positioned in the topmost plane and 'Pair a' and 'Pair b' lamps (Figure 2) were in the forward most and backward most positions respectively in the MB117 chamber. Figure 3 shows the main radiation of the lamps to have wavelengths in the region from 300 to 400nm, which is appropriate for UVA light. This spectrum is similar to that of natural sunlight in the UVA light region<sup>20</sup>.

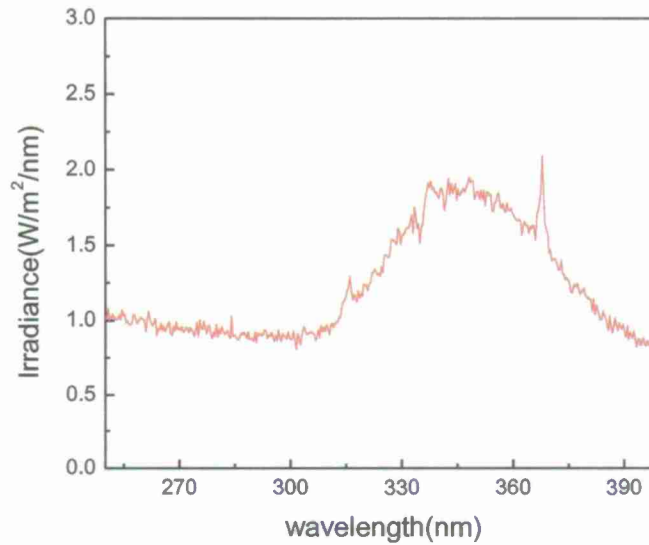


Figure 4. Spectrum of the UVA lamp used in the MB117.

The UVA light intensities in the locations of Figure 2 are shown in Table 1, which demonstrates that the intensities were affected by the quantities of the lamps and the distance between the location of the sample and the UVA lamps. As expected, the more lamps present, the stronger was the UVA light intensity, and the closer the specimen location was to the lamps, the stronger was the UVA light intensity at the location. The UVA light intensity was the lowest at  $0.5 \text{ W/m}^2$  when there was only one pair of lamps and the lamps were mounted in the opposite, topmost edges of the chamber from the samples. The highest UVA intensity,  $50 \text{ W/m}^2$ , was present just below the lamps when both pairs of lamps were next to one another in the middle vertical plane (Plane C) of the chamber. The UVA light intensities in the MB117 can be 100x higher than those of UV light at the studied natural locations, in which the intensities of UV light ranged from 0 to  $0.46 \text{ W/m}^2$ <sup>21</sup>, which was shown in Table 2.

Table 1. Intensity of UVA light irradiated in the locations of Figure 2,  $\text{W/m}^2$

	"Pair a" is in the front edge	"Pair b" is in the back edge	"Pair a" and "Pair b" are in the plane C and close to the location 11, 14 and 17	"Pair a" is at the front edge and "Pair b" is at the back edge	
Location	1, 4 and 7	3, 6 and 9	11, 14 and 17	10, 12, 16 and 18	2, 5 and 8
Intensity	0.5	0.5	50	33	1.5



Table 2. Parameters in the field sites and magnifying capability of the parameters of the MB117

Location	Coconut Island	Daytona Beach	Whidbey Island	West Jefferson	Lyon Arboretum	Trenton
Type of environment	Marine	Marine	Rural marine	Mild urban	Rainforest	Urban
Average UVA intensity, W/m <sup>2</sup>	0.46[20]	0.18	0.07	0.11	0.33 [20]	
Maximum magnification of UVA intensity in the MB117 to field	109	278	714	455	152	
Average annual O <sub>3</sub> concentration, ppb <sup>21</sup>	52	70	56	70	43 [22]	27
Maximum magnification of ozone in the MB117 to field sites	446	331	414	331	540	860

### 1.2.5.3 Concentration and Uniformity of Ozone

In order to measure the distribution of ozone in the MB117, the ozone concentrations in the five locations of the MB117 was recorded. The concentration distribution of ozone in the MB117 is plotted for the different chamber locations (Figure 2) of MB117 in Figure 5a. The ozone concentrations increased from 0 to about 14 ppm, and remaining stable after the ozone generator had been running approximately 1.2 hours when the flow of cleaned air was 2 SLPM (standard liter per minute). The average concentration of ozone and the standard deviation between locations in the MB117 under these conditions were 14.17 ppm and 0.16 ppm, respectively. The standard deviations over time for locations 18, 16, 14, 12 and 10 were 0.05 ppm, 0.01 ppm, 0.04 ppm, 0.02 ppm and 0.06 ppm, respectively. These results show that ozone can be distributed uniformly throughout the chamber and the concentrations maintained to a tight tolerance. At the exposure sites, the average monthly ozone concentration ranged from 0 to 591 ppb<sup>21</sup>, while the annual average concentration of ozone ranged from 27 to 70 ppb<sup>22,23</sup> as shown in Table 2. Therefore, the ozone concentration in the MB117 could be 40x and 330x higher than the maximum average monthly and annual average ozone concentrations at the studied locations, respectively.

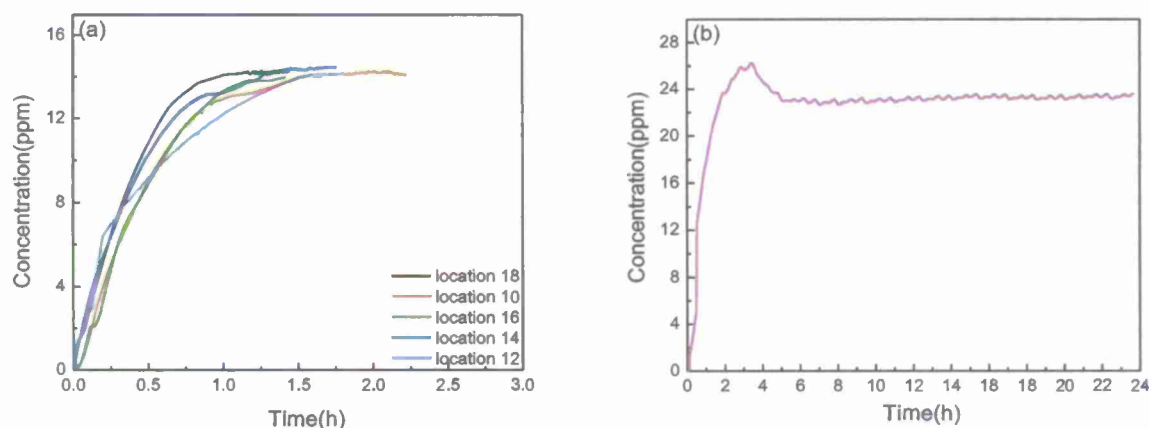
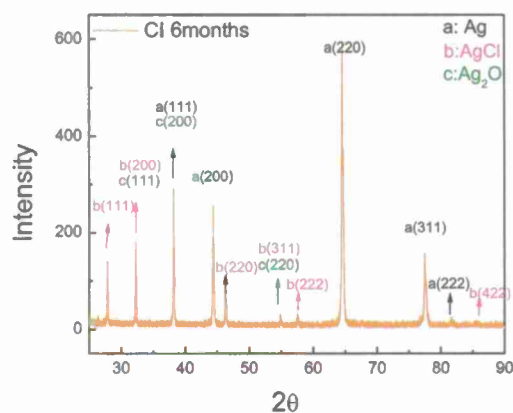


Figure 5 . The concentration of ozone in the MB117 chamber when the flow of cleaned compressed air was (a) 2 SLPM with measurements at several locations; (b) 10 SLPM for location 8. Physical locations are shown in Figure 2.

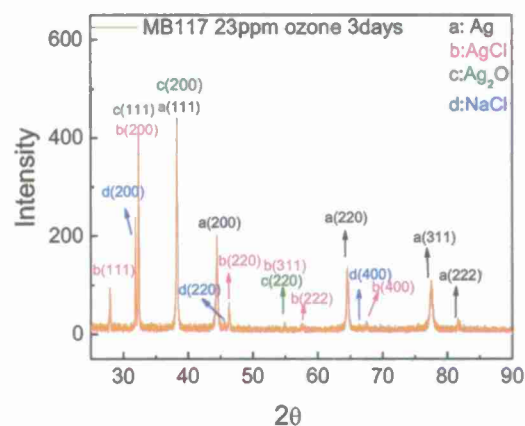
Ozone concentrations in the MB117 were adjusted by adjusting the flow rate of compressed, purified air. The maximum concentration of ozone that could be stably maintained with the present configuration was 23.2 ppm after the generator had been running for approximately 4 hours with a flow rate of cleaned air of 10 SLPM, as shown in Figure 5b. The standard deviation over time for the maximum concentration of ozone was 0.2 ppm, obtained by a series of sampling from 4.7 hours to 23.6 hours of exposure. Note that much higher ozone concentrations could be achieved if compressed oxygen were used to produce ozone rather than air, but this change would complicate the experimental arrangement, especially for long-term exposures.

#### 1.2.5.4 Corrosion of Silver in the field and In the Modified B117 Chamber

In order to investigate the correlation between results from MB117 and the field exposures, the corroded silver surfaces from each were analyzed with the goal of identifying the corrosion products of silver. Due to limitations of individual techniques, a suite of complementary analytical techniques were used. Figure 6 shows the XRD results from samples exposed to the MB117 testing or a six-month exposure at Coconut Island, HI. The series of peaks when  $2\theta$  was approximately 27.8°, 32.2°, 46.2°, 54.8°, 57.5°, 85.7° belonged to AgCl. The peaks when  $2\theta$  was about 38.1°, 44.3°, 64.4°, 81.6° belonged to metallic Ag. The peaks of Ag<sub>2</sub>O are known to be at 32.2°, 38.1° and 54.8°, which overlap peaks for AgCl and metallic Ag. However, the XRD patterns for samples from the field and the MB117 chamber were the same, although the relative intensities of the peaks of the compounds on the surfaces of silver were different.



(a)



(b)

Figure 6. X-ray diffraction pattern of silver after exposed in (a) Coconut Island for 6 months and (b) the MB117 with 23ppm ozone for 3 days.

Figure 7 shows SEM images and EDS results for silver exposed in the MB117 as well as for a sample exposed at Coconut Island, representative of all the field exposure sites examined. The EDS indicates that AgCl was the main corrosion product. The images clearly show Ag grains on the surfaces and the non-uniform corrosion that occurred in both the MB117 chamber and the field exposure.

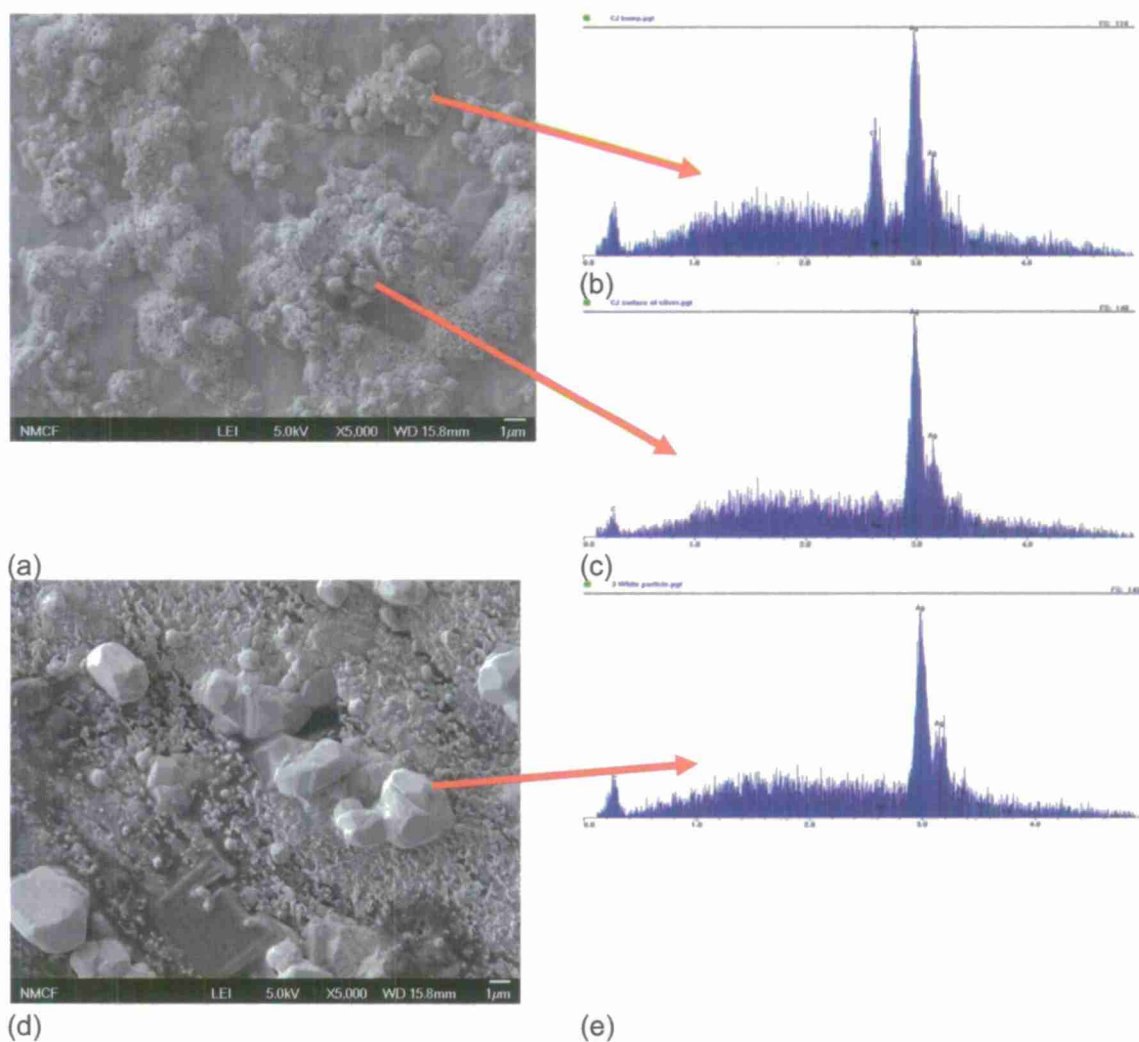


Figure 7. Image (a) and element distributions (b and c) of different areas spots on the surfaces of the samples after exposure at Coconut Island, HI for 6 months. Image (d) and element distributions (e) of the spots on the surfaces of the samples after exposed in the MB117 with 23 ppm  $O_3$  and UV light for 3 days.

For all silver samples, corrosion product accumulation was assessed via coulometric reduction. Coulometric reduction is an electrolytic method that measures the potential as a function of reduction time and is used to both identify the compound and determine the amount present. By measuring these parameters for known compounds, the potential plateau position can be used to identify the compound and the time during which the plateau is maintained can be related to the amount of corrosion product via Faraday's Second Law.

Figure 8 shows the coulometric reduction curves for silver samples after exposed in the MB117 with 23 ppm ozone and  $50W/m^2$  UV light for 15 days and Daytona Beach for 3 months. The reduction potentials at approximately  $-0.18 V_{MSE}$  and  $-0.3 V_{MSE}$  belong to the reduction potentials of  $Ag_2O$  and  $AgCl$  respectively, as demonstrated by the measurement of standards. Reduction



charges were calculated from the reduction time by multiplying by the current density which was constant ( $-0.1 \text{ mA/cm}^2$ ) in this work. The reduction time was defined as from the beginning to the midpoint between the adjacent two plateaus. For example, for the reduction curve from the MB117 exposure (Figure 8a), the reduction time for  $\text{Ag}_2\text{O}$  is from 0 to the time marked by the first blue dashed line (1,290 seconds), whereas the reduction time for  $\text{AgCl}$  is the time between the two blue dashed lines (12,350 seconds). The main compound was found to be  $\text{AgCl}$  on the sample from Daytona Beach site as well as the sample from the MB117 test. Although small reduction charges for  $\text{Ag}_2\text{S}$  of silver were observed for some outdoor sites, for example, at West Jefferson, OH, we only discuss the reduction charge of  $\text{AgCl}$  of silver in this study.

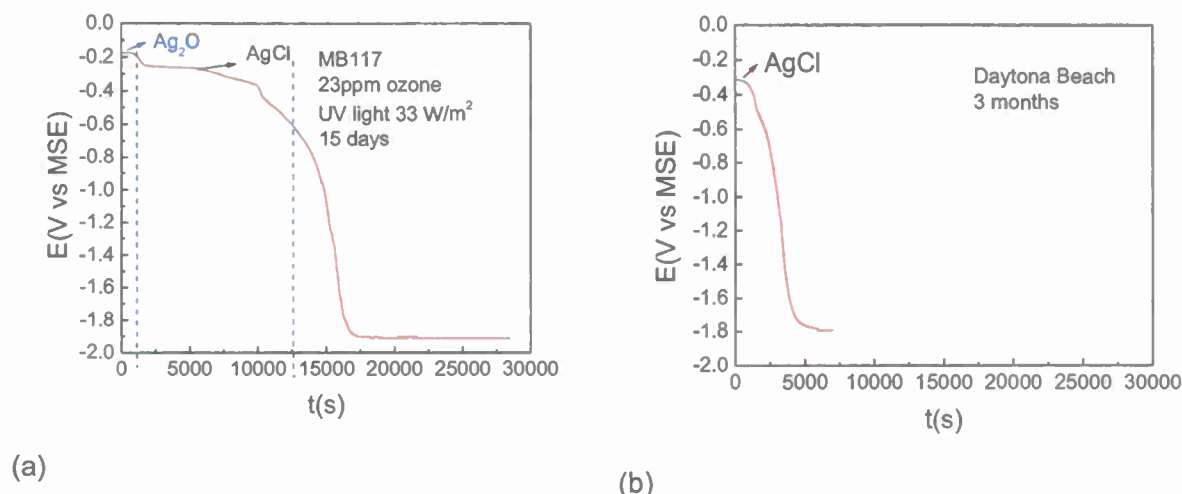


Figure 8. Coulometric reduction curves for the silver samples after exposure to: (a) the MB117 with 23 ppm ozone and UV light ( $33 \text{ W/m}^2$ ) for 15 days, and (b) Daytona Beach for 3 months. The reduction electrolytes was 0.1 M  $\text{Na}_2\text{SO}_4$  (pH=10) solution and were deaerated 1 hour in advance.

Figure 9 depicts the reduction charges for the  $\text{AgCl}$  formed on silver after exposure in the MB117 chamber with varying ozone concentrations and UVA light levels for different times. It shows that silver corroded in all cases of the MB117, in dramatic contrast to the lack of corrosion after four months with the standard B117 method<sup>2</sup>. Higher corrosion rates are observed with higher ozone concentrations. At a constant ozone concentration, higher UVA light intensity increased the rate of attack. The ozone provides sufficient oxidizing ability (above that of molecular oxygen) to corrode silver rapidly. In the presence of UVA light, additional oxidants (such as atomic oxygen<sup>15,16</sup>) are created, increasing the rate of attack. In the presence of  $\text{Cl}^-$ ,  $\text{AgCl}$  is formed. In other work<sup>2,10</sup>, it has been shown that in the absence of chloride, silver oxide is formed in the presence of ozone, with higher rates of oxide formation observed when UVA light is also present.

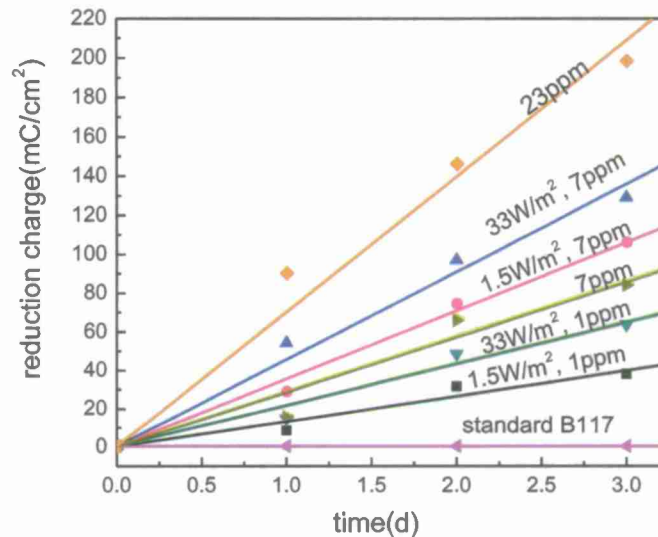


Figure 9. Reduction charge and the fitting curves for AgCl produced on silver exposed in the MB117 with different ozone concentration and different exposure times.

The data in Figure 9 were fit to linear expressions,  $Q = A \cdot t$ . The slope of the linear fit represents the corrosion rate of silver in that environment. All of regression coefficients are larger than 0.975. Corrosion amounts for AgCl of silver increase linearly with exposure time. This constant rate of corrosion has been observed for field exposures<sup>9</sup> and in the laboratory for charge densities of up to  $2 \text{ C/cm}^2$ , corresponding to a AgCl thickness of 5.3 microns, assuming theoretical density ( $5.56 \text{ g/cm}^3$ )<sup>18,24</sup>.

## 1.2.6 Discussion

### 1.2.6.1 Role of Organic Acids in Atmospheric Corrosion of Silver

No corrosion was observed in any of the exposures involving formic acid, even after long exposures. Thus, the addition of formic acid does not accelerate silver corrosion significantly enough to be a useful addition to an accelerated test. Based on these results, no further exposures to organic acids were done for silver.

### 1.2.6.2 Proposed Modified Salt Spray Method

The objective of this work was to extend the work on the atmospheric corrosion of silver from custom-made chambers<sup>2,10</sup> to commercially available salt spray test chambers. By doing so, the so-called "silver paradox" has been resolved. The corrosion of silver observed in virtually any natural atmosphere, but not observed using standard salt spray testing protocols (i.e., ASTM B117), can be reproduced in a commercial test chamber if the chamber and test protocol are appropriately modified. The modifications involve the creation of atmospheres that are as oxidizing (or more oxidizing if acceleration of corrosion is of interest) as natural atmospheres.

Natural atmospheres have many oxidants. Standard salt spray test chambers use laboratory air which is generally highly filtered and the container precludes the presence of UV light. The filtration of the air removes those natural oxidants and the absence of UV light prevents the creation of additional oxidants, making standard B117 protocols far less aggressive in terms of oxidation potential than natural atmospheres. Silver corrosion is primarily driven by the oxidizing potential, and thus standard protocols without oxidizers stronger than molecular oxygen are going to be ineffective in causing silver corrosion. It is interesting to note that in some instances, small amounts of  $\text{Ag}_2\text{S}$  can be observed on silver exposed for many months in standard salt spray testing; it is a measure of the cleanliness of the laboratory air with respect to sulfur compounds, as silver is an outstanding getter for such species.

It is clear from Table 2 that the MB117 protocol can provide UVA light intensities more than 100x and ozone concentration more than 330x those experienced in a range of geolocations, thus creating more oxidizing atmospheres which can accelerate the corrosion of silver. Inspection of Figure 9 shows that the effects of up to  $33 \text{ W/m}^2$  of UVA light were modest relative to increasing ozone concentration in the MB117. The addition of  $1.5 \text{ W/m}^2$  to 7 ppm ozone increased the rate by about 20%, and a further increase to  $33 \text{ W/m}^2$  represented a 60% increase in rate relative to the ozone alone. Inclusion of UVA light may be indicated for testing situations in which higher ozone concentrations are undesirable for other reasons, including ozone production limitations or control issues, or personnel safety.

Based on the results from the coulometric reduction, XRD, SEM images and EDS of the field and the MB117 exposures, the corrosion products and damage morphology produced on silver in presence of NaCl was similar for the field and the MB117 testing exposures. The main corrosion product was AgCl, non-uniform corrosion occurred, and silver grains were found on the surfaces of silver after exposures. According to the lab data in Figure 9 and the field data<sup>9</sup>, the rate of formation of AgCl was constant in the atmospheric environments studied. Therefore, according to the specification of ASTM B117<sup>1</sup>, comparisons between the field data and the MB117 results can be made by considering a common exposure time. For the current purposes, an exposure time of thirty days was used. The reduction charges for each version of the MB117 (i.e., combinations of ozone concentration and UVA light intensity shown in Figure 9) were scaled to 30 days based upon the linear regression equations. The acceleration factor is defined here as the ratio of the reduction charge of the MB117 exposed sample to the charge of the field exposed sample. Calculated acceleration factors for the six geolocations for several different versions of MB117 are shown in Figure 10. It can be seen that the two marine sites are the most corrosive towards silver. It is known that the salt deposition in marine sites, such as Coconut Island and Daytona Beach, is higher than in other areas, the UVA level in Coconut Island is much higher than that in the other sites, and the ozone level in Daytona Beach higher than that in the other sites as well. Recall that no corrosion of silver was observed after four months of the standard ASTM B117 protocol; a combination of NaCl, ozone and/or UV light is required<sup>2,10</sup>.

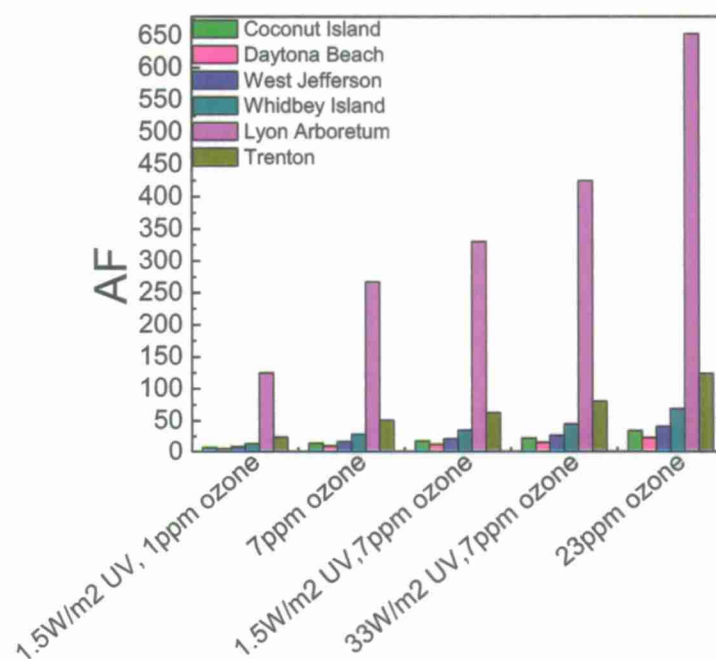


Figure 10. Acceleration factors of the MB117 to the fields, calculated assuming corrosion of silver in those conditions obeys linear kinetics, and all the reduction charges are scaled to an exposure of one month from Figure 8.

The data in Figure 10 show that the MB117 can be tuned to produce a range of desired acceleration factors. Such tuning may be of interest as there is no doubt a trade-off between acceleration and accuracy. Although the MB117 results presented here for silver are consistent with regards to the type of corrosion products formed and the morphology of the corrosion, it is not clear at what combinations of ozone and UVA light that correlation fails. Using Daytona Beach as an example, corrosion of silver could be accelerated in MB117 by up to 20x by adding 23 ppm ozone alone to the standard B117 protocol. In practical terms, this acceleration factor would allow about 6 months of exposure at Daytona Beach to be simulated in one week in the laboratory. If lower ozone concentrations are desired, a very similar acceleration factor can be achieved using 7 ppm ozone and 33 W/m<sup>2</sup> UVA light. The application of the same MB117 conditions for prediction of corrosion at less corrosive geolocations results in much higher acceleration factors, as shown in Figure 10.

The practical implications of these results for the estimation of corrosivity using silver coupons is substantial. Short-term (30-day) exposures of silver have been and are being used to estimate corrosivities of geolocations<sup>9</sup> as well as indoor locations such as control rooms [25], but there has been no means to reproduce that corrosivity in the laboratory using generally available equipment (i.e., commercially available salt spray test chambers). The approach presented here provides such a means. The flexibility of the method provides testers with the ability to tailor their chamber to the degree of acceleration of interest.

It must be noted that all of the work presented here focused on the corrosion of silver. Although silver is used as a corrosivity monitor and is the basis for corrosion rate prediction for steel,



copper and aluminum, the vast majority of interest in accelerated testing is aimed at structural materials and coated structural materials. The testing framework presented here is currently being applied to such materials, but the impact of UVA light and ozone remain to be determined, especially relative to effects of time-of-wetness and salt loading.

#### **1.2.7 Economic Summary**

The economic impact of the work could be substantial if the modified test is better able to quantitatively accelerate the corrosion of metals under marine atmospheric conditions. By allowing more accurate assessments of corrosion rates, more accurate predictions of maintenance and repair intervals could be made.

#### **1.2.8 Implementation**

- (a) The proposed modification to the ASTM B117 standard salt spray test is ready for implementation by DOD and others. The modifications to a commercially available cyclic corrosion test chamber required have been explicitly described.
- (b) While the utility of the modified test has been clearly demonstrated for silver, the extension of the method to structural materials such as steel, aluminum alloys, magnesium alloys, etc., as well as coated metals, needs to be further explored.

#### **1.2.9 Conclusion**

A standard salt spray corrosion test chamber was modified to allow the introduction and control of ozone and UVA light in order to produce an accelerated test that recreates the corrosion of silver observed in geolocations around the world, but heretofore not reproduced in a commercial salt spray corrosion test. The modified test chamber has one subsystem that produces up to 23.2 ppm ozone from cleaned compressed air and another subsystem that produces up to 33 W/m<sup>2</sup> of UVA light intensity.

The results show that silver formed the same corrosion product and had the same damage morphology in the MB117 and field exposures. Ozone accelerates the corrosion of silver during salt spray testing, whereas silver did not corrode measurably using the standard B117 salt spray conditions. The addition of UVA light increases the corrosion rate when ozone is also present. Acceleration factors, based on the comparison of coulometric reduction results from field and MB117 exposures, show that the MB117 can accelerate the atmospheric corrosion of silver substantially relative to natural atmospheres, up to a factor of 20 even for a severe marine environment. Using only ozone at 23 ppm, the corrosion rate of silver in the MB117 was about 20x that of a severe marine location (Daytona Beach, FL), allowing 6 months' worth of corrosion to develop in 1 week. For less locations of lower corrosivity (Trenton, NJ), this version of the MB117 would correspond to acceleration factors of over 120, meaning that 1 week of exposure in the MB117 would correspond to ca. 2 years of field exposure.

Although this work has focused on the corrosion of silver, extension to other materials is envisaged.

#### **1.2.10 Bibliography**

1. ASTM Standard, "Standard practice for operating salt spray apparatus" (West Conshohocken, PA: ASTM B117-03, 2003).
2. D. Liang, H.C. Allen, G.S. Frankel, Z.Y. Chen, R.G. Kelly, Y. Wu, B.E. Wyslouzil, Effects of

- Sodium Chloride Particles, Ozone, UV, and Relative Humidity on Atmospheric Corrosion of Silver, *J. Electrochem. Soc.* 157, 4 (2010): p. C146-C156.
3. F. Deflorian, S. Rossi, L. Fedrizzi, C. Zanella, Comparison of organic coating accelerated tests and natural weathering considering meteorological data, *Prog. Org. Coat.* 59 (2007): p. 244-250.
  4. R.L. Howard, S.B. Lyon, J.D. Scantlebury, Accelerated tests for the prediction of cut-edge corrosion of coil-coated architectural cladding: Part I: cyclic cabinet salt spray, *Prog. Org. Coat.* 37 (1999): p. 91-98.
  5. K.N. Wernstahl, Service life prediction of automotive coatings, correlating infrared measurements and gloss retention, *Polym. Degrad. Stab.* 54 (1996): p. 57-65.
  6. R. Baldwin, C.J.E. Smith, Accelerated corrosion tests for aerospace materials: current limitations and future trends, *Aircr. Eng. Aerosp. Tec.* 71, 3 (1999): p. 239-244.
  7. G.D. Davis, L.A. Krebs, C.M. Dacres, Coating Evaluation and validation of accelerated test conditions using an in-situ corrosion sensor, *J. Coat. Tec.* 74, 935 (2002): p. 69-74
  8. SAE international Surface Vehicle Standard, "Laboratory Cyclic Corrosion Test" (Warrendale, PA: ASE J 2334, 2003).
  9. W.H. Abbott, A Decade of corrosion monitoring in the world's military operating environments-A summary of results, Battelle Columbus operations, (Columbus, Ohio, 2008): p. 2-22, 61 and appendix F.  
<https://www.corrdefense.org/Academia%20Government%20and%20Industry/A%20Decade%20of%20Corrosion%20Monitoring.pdf>
  10. Z.Y. Chen, D. Liang, G. Ma, G.S. Frankel, H.C. Allen, R.G. Kelly, Influence of UV irradiation and ozone on atmospheric corrosion of bare silver, *Corros. Eng. Sci. Tech.* 45, 2 (2010): p. 169-180.
  11. D.W. Rice, P. Peterson, E.B.P. Phipps, R.J. Cappell, R. Tremoureaux, Atmospheric corrosion of Copper and Silver, *J. Electrochem. Soc.* (1981): p. 275-284.
  12. T.E. Graedel, Corrosion Mechanisms for Silver Exposed to the Atmosphere, *J. Electrochem. Soc.* 139 (1992): p. 1963-1970.
  13. G.I.N. Waterhouse, G.A. Bowmaker, J.B. Metson, Oxidation of a polycrystalline silver foil by reaction with ozone, *App. Surf. Sci.* 183 (2001): p. 191-204.
  14. R.O. Suzuki, T. Ogawa, K. Ono, Use of Ozone to Prepare Silver Oxides, *J. Amer. Ceram. Soc.* 82 (1999): p. 2033-2038.
  15. B.J. Finlayson-Pitts, J.N. Pitts, *Chemistry of the Upper and Lower Atmosphere* (Academic Press, San Diego, 2000), p. 86-94.
  16. S. Chapman, The Photochemistry of Atmospheric Oxygen. *Rep. Prog. Phys.* 9 (1942): p. 92-100.
  17. R. Sugamoto, G.A. Hawthorn, L.H. Hihara, "Comparison of Atmospheric Chloride Deposition Measurement Techniques in a Multitude of Microclimates", 2011 DOD Corrosion Conference, (Palm Springs, CA, NACE, 2011).
  18. ASTM Standard, "Standard Test Method for Coulometric Reduction of Surface Films on Metallic Test Samples" (West Conshohocken, PA: ASTM B 825-02, 2002).
  19. S.J. Krumbein, B. Newell, V. Pascucci, Monitoring Environmental Tests by Coulometric Reduction of Metallic Control Samples, *J. Test. Eval.* 17 (1989): p. 357-367.
  20. Q-lab Corporation, "Accelerated weathering tester", [http://www.q-lab.com/EN\\_WebLit/QUV-LU-0805\\_3\\_EN\\_web.pdf](http://www.q-lab.com/EN_WebLit/QUV-LU-0805_3_EN_web.pdf) (2006).
  21. JMA, & NASA-WFF. World Ozone and Ultraviolet Radiation Data Centre (WOUDC) [Data]. <http://www.woudc.org>, (2011).
  22. AIRNOW Tech., <http://www.airnowtech.org> (2011).
  23. J.M. Harris, S.J. Oltmas, E.J. Dlugokencky, P.C. Novelli, An investigation into the source of the springtime tropospheric ozone maximum at Mauna Loa Observatory, *Geophysical research letters*, 25 (1998) 1895-1898.

24. E.B. Neiser, Atmospheric Corrosion of Silver and its relation to Accelerated Corrosion Testing, (Master Thesis, University of Virginia, 2010).
25. W.B.A. Sharp, L. Falat, Krasowski, Corrosion Prevention in Electrical Control Rooms, Tappi J., 72 (10) (1989)

### **1.3 Analysis of Relative Importance of Surface Environment Components and Dynamics** **(R. G. Kelly, B. Risteen, E. J. Schindelholz)**

#### **1.3.1 Summary**

This effort aimed at starting to establish a critical RH range for mild steel whereby electrolyte is present and corrosion significant in a marine environment. Virtually all corrosion models use RH in some way to determine the conditions under which corrosion is possible. Two issues were addressed: the wetting/drying conditions of relevant salt solutions, and the extent of corrosion of carbon steel as a function of RH, with particular focus at quantifying the amount of corrosion that occurs at  $RH < DRH$  (deliquescence RH) of the salt. Wetting and drying of salt solutions was measured by impedance measurements across an interdigitated electrode array with a 5  $\mu m$  spacing. It was found that NaCl, NaNO<sub>3</sub>, MgCl<sub>2</sub> and MgSO<sub>4</sub> all show conductivity at RH up to 40% below their DRH, leading to the possibility of corrosion under those conditions. Corrosion experiments were performed by printing a precise array of salt droplets, exposing those samples to a constant RH, and then evaluating the corrosion damage with quantitative optical profilometry of serial removals. Corrosion was shown to occur at appreciable rates at RH well below 80%, with maximum corrosion rates occurring for NaCl deposits at RH between 71 and 85%, that is, just above the DRH for the salt. All three salt types studied (NaCl, MgCl<sub>2</sub>, and ASTM Ocean Water) showed qualitatively similar behavior with regards to RH, and quantitatively similar corrosion damage. In addition, samples with all three salts showed dramatically slowed corrosion rate with times of greater than 1 week.

#### **1.3.2 Introduction and Background**

Atmospheric corrosion of steel is of widespread importance to virtually all agencies in DOD, across the federal government, as well as in private industry. Despite decades of research, many basic questions remain, including a determination of the conditions of RH under which corrosion can occur. For example, ISO 9223 indicates that at temperatures above freezing, corrosion is negligible below an RH of 80%. The deliquescence RH (DRH) of NaCl is 76%, with other salts having substantially lower DRH, meaning that salt solutions can be present at RH much lower than 80%, and those solutions would tend to be of high concentration. In addition, there is often a kinetically controlled hysteresis in drying of salt solutions, with efflorescence occurring at RH much lower than the DRH<sup>1-4</sup>.

From a practical perspective, the issues are (a) under what RH conditions are corrosive environments present, and (b) under what conditions is the corrosion significant. Considering the diurnal cycle, it is important to know when corrosion turns on, when it turns off, what the time constant for those changes is, and what controls these processes.

#### **1.3.3 Lessons Learned**

- (a) Sustained corrosion detectable well below the deliquescence RH of the salts studied. In the case of NaCl, corrosion was measurable down to 33%RH (~ 40% lower than the DRH). For ASTM Ocean Water, sustained corrosion detectable down to 23%RH, while for MgCl<sub>2</sub>, corrosion was detectable down to 23%, possibly 11%.



- (b) Corrosion loss was found to be most severe in the RH range of 71-85% for NaCl, 64-90% for ASTM Ocean Water, and 53-90% for  $\text{MgCl}_2$ .
- (c) Corrosion takes on a filiform character for all salts from 53-75%. Trails originate from drops.  $\text{MgCl}_2$  exhibits filiform corrosion to 90%, whereas the other salts show sparse, deep pitting above 75%.
- (d) Corrosion confined to under drop areas for  $\text{MgCl}_2$  and seawater below 33%.
- (e) Corrosion rate tapers off with time in all cases.

### 1.3.4 Technical Investigations

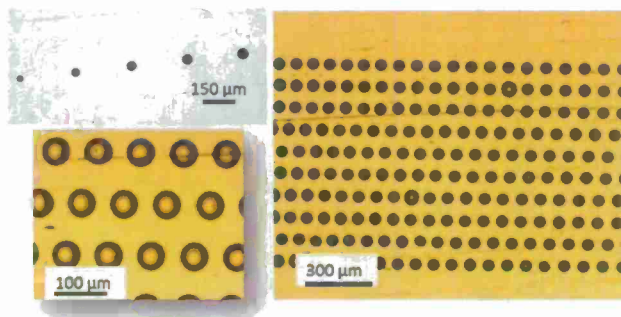
In all experiments, carbon steel coupons were used. They were polished to a mirror finish before being cleaned with water, followed by isopropyl alcohol.

#### 1.3.4.1 Wetting and Drying of Simulated Salt Aerosols

In order to quantitatively assess the role of salt loading density, salt type, and RH on the atmospheric corrosion of steel, it is important to be able to closely control the environment on the metal surface. To accomplish this objective, an ink jet printer (JetLab) was modified in order to provide computer control of the salt pattern as shown in Figure 11. The system is able to produce drops as small as  $35\text{ }\mu\text{m}$  in diameter (representing a volume of 3 pL) with spacing as close as  $< 10\text{ }\mu\text{m}$ , if desired. With the computer-controlled stage, substrates as large as  $230 \times 280 \times 250\text{ mm}$  thick can be printed upon. A custom-made chamber allows the humidity in the chamber to be controlled between  $<1$  to 100 % RH through an external water vapor source. Different salt solutions were deposited and tested for wetting/drying behavior: NaCl,  $\text{NaNO}_3$ , NaCl +  $\text{NaNO}_3$ ,  $\text{MgCl}_2$ , and  $\text{MgSO}_4$ .



(a)



(b)

Figure 11. (a) Photograph of ink jet system, including programmable xy-stage and cabinet for controlled humidity.

Systems specifications: minimum drop size =  $35\text{ }\mu\text{m}$  (substrate), minimum volume = 3 pL, maximum substrate size:  $230 \times 280 \times 250\text{ mm}$  thick. RH control from  $<1$ -100%. In-situ optical microscopy available.

In order to assess the wetting and drying behavior of salt aerosols, the salts of interest were deposited onto interdigitated sensors (Abtech) shown in Figure 12 using the ink jet system above. The spacing of the gold electrodes were spaced  $5\text{ }\mu\text{m}$  apart. The salt-coated sensors were then exposed to controlled humidity steps and the impedance between the interdigitated electrodes was measured at 574 kHz. After each change in the RH, the impedance was monitored periodically for between 1 h and 30 days.

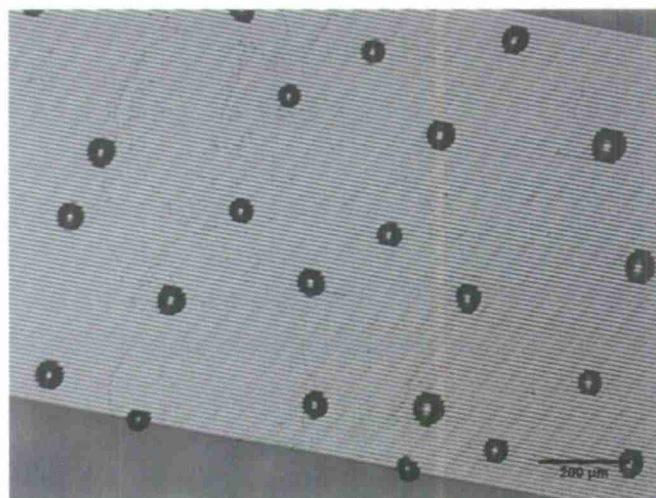


Figure 12. Photomicrograph of interdigitated sensor for wetting/drying experiments.

#### 1.3.4.2 Controlled Salt Deposition for Corrosion Screening

Using the ink jet system, the effects of salt type, RH and time on the corrosion rate of steel was studied by printing the pattern shown in Figure 13. On each 1"x1" coupon, salt was printed on the center area measuring 1 x 1 cm, depositing 16,000 drops, each 35 μm in diameter. The printing solution was either saturated NaCl, saturated MgCl<sub>2</sub>, or concentrated ASTM Ocean Water. The resulting loading density of each printing was 3.9 μg/cm<sup>2</sup> for the NaCl, 7.1 μg/cm<sup>2</sup> for the MgCl<sub>2</sub>, and 7.2 μg/cm<sup>2</sup> for the ASTM Ocean Water.

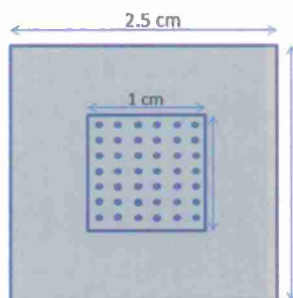


Figure 13. Pattern of printing used for deposition of salt droplets. Within the 1 cm<sup>2</sup> area, 16,000 droplets were printed.

After deposition, the samples were placed in sealed containers in which saturated salt solutions were included in order to control the RH. RH values from 11% to 90% were studied for times between 7 and 30 days.

#### 1.3.4.3 Post-Test Analysis

After each exposure, the samples were cleaned in an aqueous solution of diammonium citrate, and then their surfaces imaged with a Zygo optical profilometer. This quantitative imaging allowed each of the drop areas to be assessed independently for the depth of corrosion.

damage. Thus, each combination of RH and time produced 16,000 points to allow for statistical analyses. The scanning was done using a Zygo NewView 7300 white light interferometer. A 20x objective was used for the scans. The manufacturer-specified z-resolution for the setup used was 1nm and lateral resolution was 0.7  $\mu\text{m}$ .

The data file produced by the imaging was then sent to MountainsMap, a commercial image analysis package. The software converted the image analysis data into a text file of volume, maximum diameter of pits, and maximum pit depth for each drop. As shown in Figure 14, this text file could then be analyzed statistically to determine total volume loss for a coupon, average pit volume, maximum pit volume, maximum pit diameter, and both maximum and average pit depth.

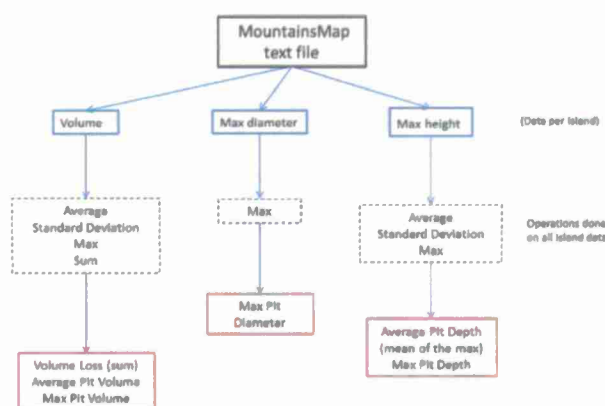


Figure 14. Flow diagram for analyses of optical profilometry data after processing with MountainsMap software to produce a text file of the appropriate parameters.

### 1.3.5 Experimental Results

#### 1.3.5.1 Wetting and Drying Behavior

The conventional wisdom on atmospheric corrosion is that below the deliquescence point of a salt, corrosion is not an issue because the salt would be dry, and thus there would be no aqueous solution present. The physical chemistry literature shows that there is often a hysteresis between the deliquescence and efflorescence RH, as shown in Figure 15a in which the impedance at 574 kHz, which is dominated by the ohmic resistance of the solution layer, as a function of RH for both wetting (deliquescence) and drying (efflorescence).

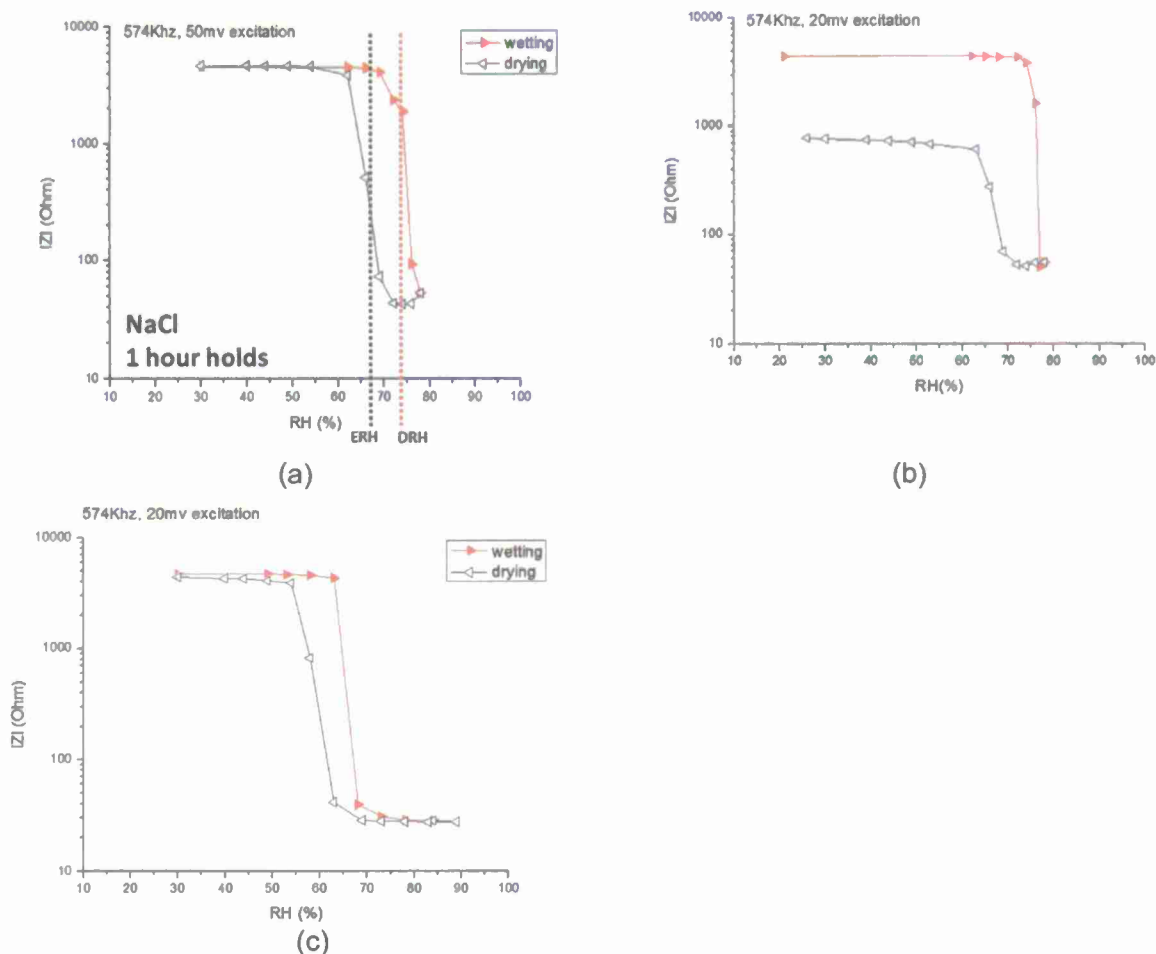


Figure 15. Impedance at 574 kHz as a function of RH for wetting and drying of (a) NaCl (b) NaNO<sub>3</sub>, and (c) NaCl + NaNO<sub>3</sub> on the interdigitated sensor. Impedance values are those measured after 1 hour at a given RH.

The steep drop in measured impedance for each salt on the sensor when elevating the RH correlates well with known deliquescence points. For NaCl, the point at which conductivity drops off is 72-74% RH, compared to the known DRH value of 76%RH. The impedance drops at 74%RH for NaNO<sub>3</sub> which is close to its DRH value of 72%. A similar drop for the mixed salts occurs between 63-68% as would be expected due to the eutectic they form. In the same manner, a sharp rise in impedance back to the initial (starting) impedance during drying is likely indicative of salt efflorescence. Varying amounts of hysteresis are seen between the drying and wetting points of each salt. The efflorescence RH (ERH) of NaCl for levitated aerosols has been reported to be around 43%.<sup>1</sup> The results presented here show the ERH to be nearly equal to the DRH. Given the hysteresis is a kinetic effect due to nucleation and growth phenomena during crystallization, the difference between this result and that referenced above may be due heterogeneous nucleation (drop on a surface) as opposed to homogenous nucleation (levitated drop). Further literature investigation and replication of these results is required for satisfactory interpretation. Literature values for the ERH of NaNO<sub>3</sub> and for the mixed salt have yet to be located.



Figure 16 shows the results for  $\text{MgCl}_2$  and  $\text{MgSO}_4$ . Note the low values of DRH and RH for the  $\text{MgCl}_2$ . The DRH of 31% is well established. The ERH is not found in the literature. In this work, it appears to be approximately 10%. For  $\text{MgSO}_4$ , the impedance dropped abruptly between 80 and 83%. This is very near the published DRH point of the salt, 85%<sup>2</sup>, and within the precision range of the RH sensor used. Interestingly, the deliquesced solution did not appear to dry out when the humidity was brought back to 30%RH, even after holding at 30% for 10 hours. This drying behavior is in accordance with findings by Zhao and coworkers<sup>3</sup>, who have shown this salt to effloresce (to anhydrous form) below 14%RH. In their experiments,  $\text{MgSO}_4$  formed a gel compound below 38%RH during dry-out which was present down to 14%. The presence of electrolyte in deposited sea salt aerosols below 20%RH has been reported by a number of investigators and attributed to the low efflorescence points of magnesium and calcium sulfates, amongst other compounds<sup>4,5</sup>.

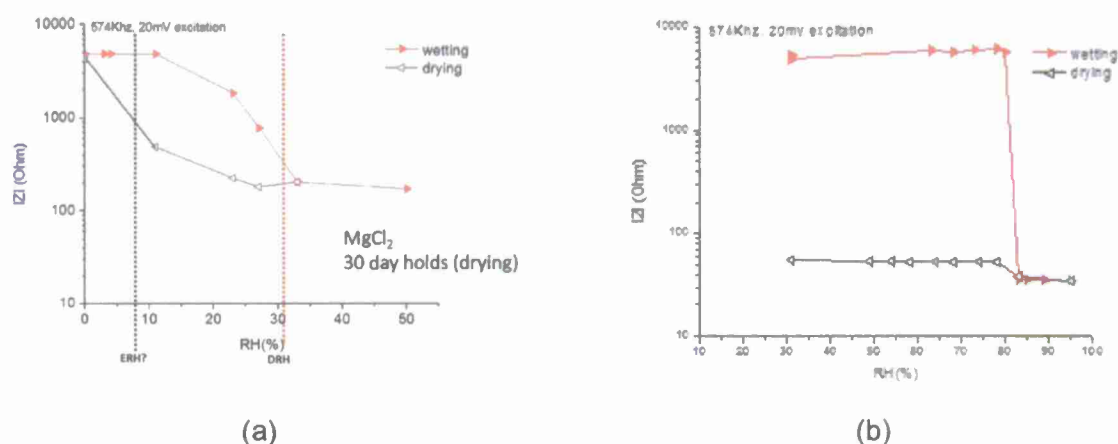


Figure 16. Impedance at 574 kHz as a function of RH for wetting and drying of (a)  $\text{MgCl}_2$ , (b)  $\text{MgSO}_4$  on the interdigitated sensor.

### 1.3.5.2 Corrosion Under Controlled RH and Deposition of Salt: Short-term Exposures

Images from the optical profilometry of samples printed with NaCl and exposed to different RH for 7 days are shown in Figure 17. The false color scale ranges to 80  $\mu\text{m}$ . There appears to be detectable corrosion damage even at the lowest RH shown (33 %). The extent of damage appears to peak at RH < 90%, with sparse, deep pitting occurring above 75%.

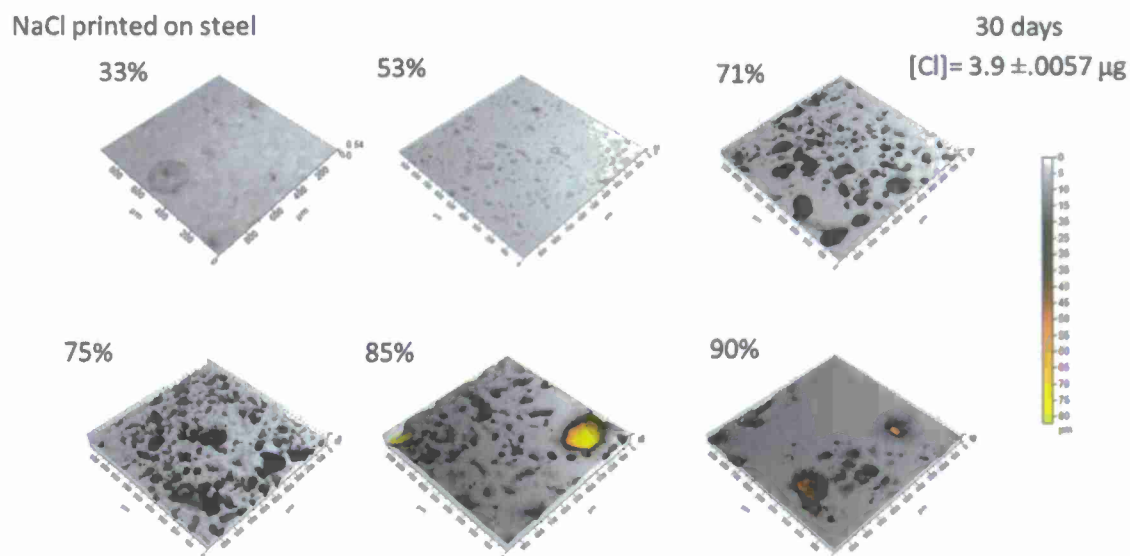


Figure 17. Sample images from optical profilometry of samples printed with NaCl droplets and exposed to constant RH for 30 days.

Figure 18 shows the calculated average corrosion rate, in  $\mu\text{m}/\text{yr}$ , based on normalizing the total volume lost by the exposure time as a function of RH. The ISO 9223 corrosivity category is also shown. It should be noted that for  $\text{RH} < 80\%$ , the ISO standard predicts that the corrosion rate is negligible. However, the current results show that the highest corrosion rates observed during these 7-day exposures occur at 65% RH ( $> 3 \text{ mpy}$ ).

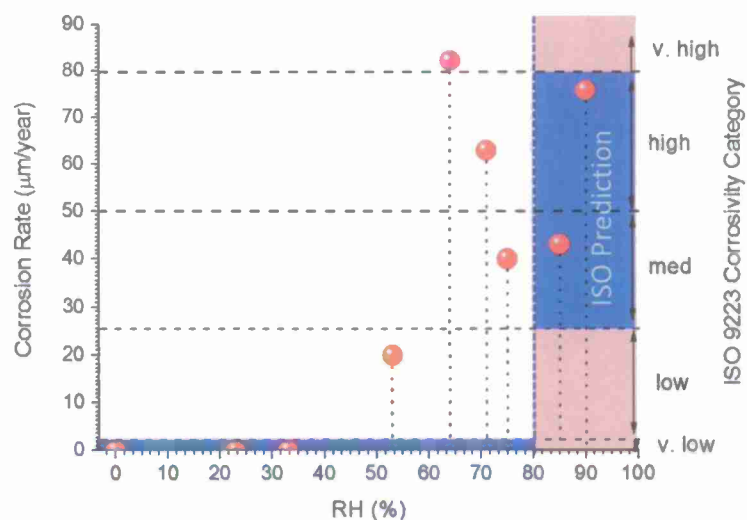


Figure 18. Corrosion rate (from volume loss and 7-day exposure time) as a function of RH for NaCl deposition. Predictions of corrosivity based on ISO 9223 are also shown.

### 1.3.5.3 Corrosion Under Controlled RH and Deposition of Salt: Longer-term Exposures

In order to develop more understanding of the time dependence of the corrosion rate, 30-day exposures were conducted for the three types of salt.

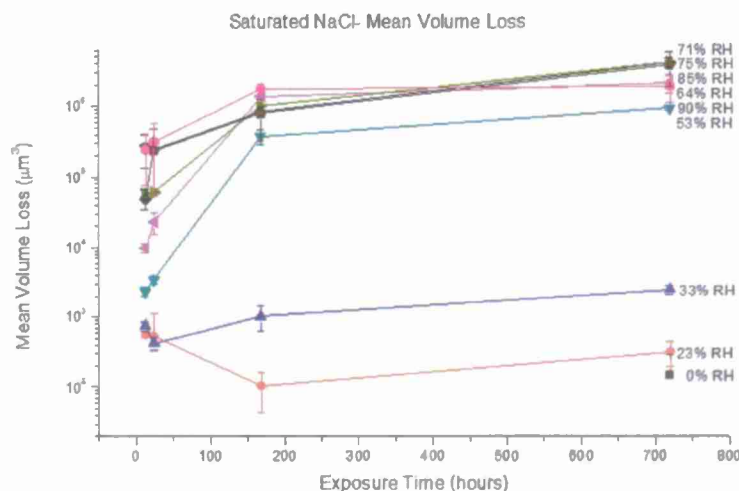


Figure 19. Mean volume loss per sample as a function of time and RH for NaCl deposition. Note the logarithmic volume loss scale.

Longer exposures of NaCl-coated samples at constant RH show similar behavior to that observed in the 7-day exposures, with the highest mean volume loss being observed at between 70 and 85% RH, which measureable corrosion loss at RH as low as 33%. Also note that the corrosion rates drop dramatically after the first week, with further corrosion loss limited.

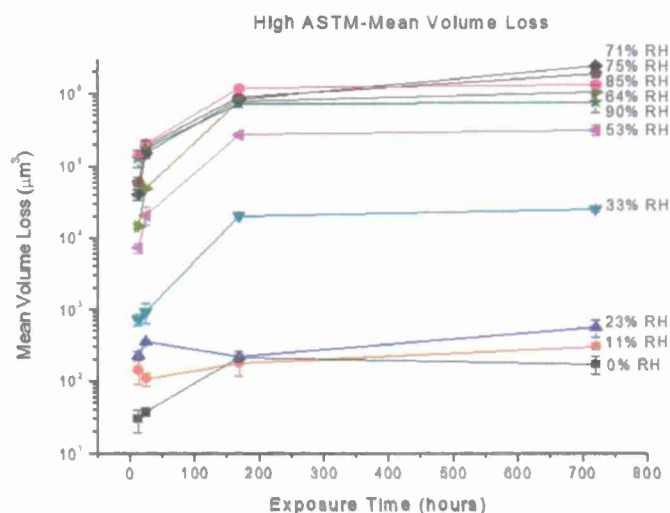


Figure 20. Mean volume loss per sample as a function of time and RH for ASTM Ocean Water deposition. Note the logarithmic volume loss scale.

Figure 20 shows that similar behavior is shown for ASTM Ocean Water deposits: maximum rates at intermediate RH, corrosion rates decreasing dramatically with time, and measurable corrosion damage at RH as low as 33%.

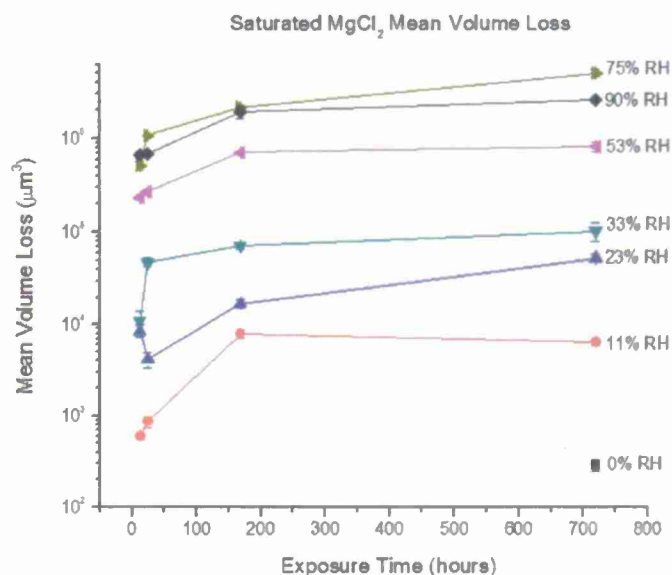


Figure 21. Mean volume loss per sample as a function of time and RH for MgCl<sub>2</sub> deposition. Note the logarithmic volume loss scale.

Figure 21 illustrates the results for MgCl<sub>2</sub> deposits. Although qualitatively similar to the ASTM Ocean Water and NaCl tests, measurable corrosion damage occurs at even lower RH, down to 11 %.

### 1.3.6 Discussion

#### 1.3.6.1 Conductive Aqueous Solutions at RH Well Less than the Deliquescent RH

The importance of the wetting/drying experiments is in trying to establish a critical RH range for mild steel whereby electrolyte is present and corrosion significant in a marine environment. This information would serve as the basis for developing an environment and alloy-specific humidity-based environmental definition. The impedance measurements on interdigitated sensors show that electrolytes with measurable conductivity exist at RH well below the deliquescence RH of the salt in question, and far below the ISO standard for RH that can cause corrosion of 80%.

The application of these results is when considering what occurs during the diurnal cycles which all atmospherically exposed surfaces encounter. For pure NaCl deposits, as long as the RH does not fall below 65%, the solution remains wet, and thus susceptible to corrosion. The results from the corrosion screening testing discussed below demonstrates that the solutions that exist at these intermediate RH are able to corrode steel; in fact, the corrosion rates are higher than at the higher RH.



The results for  $\text{MgCl}_2$  are particularly interesting, in part because  $\text{MgCl}_2$  is a key ingredient in seawater. We were not able to fully dry out  $\text{MgCl}_2$  salt deposits in 30 days at room temperature at RH as low as 11%, which is 20% below the DRH for  $\text{MgCl}_2$  of 33%, indicating that this salt can be corrosive at virtually all naturally observed RH values.

#### **1.3.6.2 Corrosion of Carbon Steel Over a Range of RH, Salt Type, and Time**

This work provides a set of screening tests for the corrosion of carbon steel under a wide range of atmospheric conditions. Three types of salt deposits were studied over a wide range of RH for up to 30 days. For each sample a set of 16,000 identical drops were deposited, and the samples were then allowed to corrode at constant relative humidity. Optical profilometry was used to quantify the corrosion damage statistically. For all three salts, several common observations were made: (a) corrosion damage was maximized at intermediate RH, (b) measurable corrosion damage was observed at RH up to 30% lower than the DRH of the salt in question, and (c) corrosion damage rates decreased substantially after the first week, with the damage accumulation during the final 3 weeks being quite limited. Interestingly, NaCl and  $\text{MgCl}_2$  samples showed very similar amounts of corrosion damage in 30 days ( $\sim 5 \times 10^6 \mu\text{m}^3$ ).

The ramifications of these observations for corrosion modeling of the atmospheric corrosion of steel (and other materials) are clear and broad-reaching. First, models that utilize a minimum RH criterion for when corrosion occurs that is based on either the ISO 9223 definition or the DRH of NaCl are likely greatly underestimating the time during which corrosion occurs. Second, corrosion at  $\text{RH} < \text{DRH}$  can occur at significant rates. Thus, characterization of these rates and their dependence on drop size, salt loading density, temperature, and time is warranted. It is likely that other forms of corrosion can occur at these low RH as well, including pitting, intergranular corrosion, and stress-corrosion cracking. The marked decrease in corrosion rates after the first week of exposure is not well understood at this time, with the formation of protective corrosion products and an increase in the local surface pH with corrosion being prime candidates for its origin.

#### **1.3.7 Economic Summary**

Atmospheric corrosion represents a major corrosion cost for DOD. More accurate models of corrosion of steel would decrease maintenance costs and increase availability. This work will allow the inclusion of an understanding of the conditions under which corrosion can occur where it might not be thought to do so using conventional thinking. In addition to more accurate models, it would also be able to inform under what conditions sheltering would be expected to be helpful, and conditions where such sheltering could possibly be harmful by keeping surface moist longer. Finally, it would allow more accurate assessment of the benefits of dehumidification by setting the RH conditions needed to stop atmospheric corrosion.

#### **1.3.8 Implementation**

Implementation of the results of this work would involve including the fact that corrosion continues to occur below the deliquescence RH into corrosion models used by DOD. Although how this would be included quantitatively would require additional work on the kinetics of the corrosion, a first step could be to use the kinetics reported here in conjunction with the diurnal cycle of RH. Of course, temperature effects would also be needed to be included.

### 1.3.9 Conclusion

This effort aimed at starting to establish a critical RH range for mild steel whereby electrolyte is present and corrosion significant in a marine environment. Virtually all corrosion models use RH in some way to determine the conditions under which corrosion is possible. ISO 9223 uses a threshold RH of 80%, indicating that corrosion at lower RH is negligible. The work presented here shows that such assumptions are not warranted. Corrosion was shown to occur at appreciable rates at RH well below 80%, with maximum corrosion rates occurring for NaCl deposits at RH between 71 and 85%, that is, just above the DRH for the salt. All three salt types studied (NaCl,  $\text{MgCl}_2$ , and ASTM Ocean Water) showed qualitatively similar behavior with regards to RH, and quantitatively similar corrosion damage. In addition, samples with all three salts showed dramatically slowed corrosion rate with times of greater than 1 week.

### 1.3.10 Bibliography

1. Tang, I. N., Deliquescence properties and particle size change of hygroscopic aerosols. Presented at Symposium on Biological Studies of Environmental Pollutants: Aerosol Generation and Exposure Facilities, Honolulu, Hawaii, (1979).
2. Z. Ha, C.K. Chan, The Water Activities of  $\text{MgCl}_2$ ,  $\text{Mg}(\text{NO}_3)_2$ ,  $\text{MgSO}_4$ , and Their Mixtures, *Aerosol Science and Technology*, 31 (1999) 154-169.
3. L.-J. Zhao, Y.-H. Zhang, Z.-F. Wei, H. Cheng, X.-H. Li, Magnesium Sulfate Aerosols Studied by FTIR Spectroscopy: Hygroscopic Properties, Supersaturated Structures, and Implications for Seawater Aerosols, *The Journal of Physical Chemistry A*, 110 (2006) 951-958.
4. H.-S. Xiao, J.-L. Dong, L.-Y. Wang, L.-J. Zhao, F. Wang, Y.-H. Zhang, Spatially Resolved Micro-Raman Observation on the Phase Separation of Effloresced Sea Salt Droplets, *Environmental Science & Technology*, 42 (2008) 8698-8702.
5. D.J. Cziczo, J.B. Nowak, J.H. Hu, J.P.D. Abbatt, Infrared spectroscopy of model tropospheric aerosols as a function of relative humidity: Observation of deliquescence and crystallization, *Journal of Geophysical Research*, 102 (1997) 18843-18850.

## **1.4 Galvanic Interactions Between AA7075-T6 and Noble Materials (R. G. Kelly, Y. Shi)**

### **1.4.1 Summary**

Galvanic interactions between aluminum alloys and noble materials in corrosive environments can cause structural problems in the use of military and commercial assets. The aim of the current work was to determine the conditions that lead to significant localized corrosion by galvanic coupling and to understand its controlling mechanism. The cathodic kinetics of three noble materials (silver, nickel and carbon-fiber reinforced bismaleimide (BMI)) and the dissolution kinetics of aluminum alloy AA7075-T6 were quantitatively investigated and used as boundary conditions for a numerical study. Finite element analyses were used to study the galvanic interactions of AA7075-T6 and noble materials in a geometry modeled to simulate fastened plates as a function of solution pH and chloride concentration  $[Cl^-]$ . The results indicated that both initiation and propagation of localized corrosion were influenced by the galvanic interactions, and these were evaluated as a function of geometry, noble material, and solution composition. Silver was the most aggressive noble metal in that it caused initiation under less severe geometric conditions.

### **1.4.2 Introduction and Background**

Demands for the use of higher performance materials which happen to be noble materials, such as carbon-fiber composites, have exacerbated the instances of galvanic interactions between dissimilar materials in aerospace environments. Localized corrosion of aerospace Al alloys such as AA7075-T6 can be significantly affected by the dissimilar materials with which they may be in contact<sup>1</sup>. By applying mixed potential theory, galvanic corrosion rates can be determined for simple geometries<sup>2</sup>. It is much more difficult to predict the corrosion rate if the coupled system is a complex geometry, including when thin electrolyte layers are present as is the case for atmospheric exposures. Numerical modeling and analyses have been introduced to solve this problem<sup>3</sup>. However, no systematic investigations have addressed galvanic interactions between AA7075-T6 and noble materials that are extensively used in aerospace applications.

The objective of this work was to address the galvanic corrosion of an AA7075-T6/noble materials coupled system in a fastened joint geometry, which is commonly found in engineering structures. The cathodic kinetics of oxygen reduction on the noble materials and the anodic dissolution kinetics of AA7075-T6 were first quantitatively measured as a function of pH and chloride concentration ( $[Cl^-]$ ). These kinetics were then used as boundary conditions in the modeling of galvanic interactions on complex geometries involving atmospheric exposures. By using a commercially available implementation of the finite element method (FEM), the current density and the potential of along the coupled interface were calculated and plotted as a function of geometry. The effect of the fastener gap,  $[Cl^-]$ , and the nature of cathode materials (silver, nickel, and BMI composite) on the initiation of the pitting are discussed. In addition, the corrosion rate and localized chemistry evolution during the pit propagation stage are also predicted.

### **1.4.3 Lessons Learned**

- (a) Galvanic interactions between noble materials used in aerospace structures and AA7075-T6 are sufficient to initiate and propagate localized corrosion on the aluminum alloy under a wide range of conditions.
- (b) A simplified analysis of the current and potential distributions in a simulated fastener geometry allowed the effects of both environmental and geometric variables to be assessed. Simplifying the analyses, the rate of oxygen reduction on the noble materials is a weak function of the chloride ion concentration and the pH.
- (c) Of the three noble materials studied (Ag, Ni, and carbon fiber reinforced bismaleimide (BMI)), the silver was the most deleterious in a galvanic couple with AA7075-T6.
- (d) Tighter gaps at the fastener would be expected to lead to more severe damage of the AA7075-T6 as the attack becomes more focused at the noble material/aluminum alloy interface.

#### 1.4.4 Technical Investigations

Cathodic polarization curves of Ni, Ag, and BMI were measured in NaCl solutions from 0.1 V above to 1 V below the open circuit potential (OCP) with a scan rate of 0.5 mV/s. The selected concentrations of chloride ( $[Cl^-]$ ) were 0.01 M, 0.1 M and 1 M. All solutions contained sulfate at a concentration of 0.1 M in order to simulate the mixed salts that are present on most aerospace structures. The selected pH values were 6, 9 and 11, achieved by the addition of NaOH to the NaCl solutions. Alkaline solutions were studied due to the fact that during galvanic coupling, the pH of the solution adjacent to the cathode surface will tend to increase due to the production of hydroxyl ions ( $OH^-$ ) via reduction of either oxygen or water.

The anodic polarization behavior was determined for AA7075-T6 under conditions meant to simulate the initiation and propagation of localized corrosion to a first order. Initiation of localized corrosion is addressed by determining the kinetics in the same environment as experienced by the cathode. Propagation of localized corrosion was simulated by using acidic  $AlCl_3$  with concentrations ranging from 0.01M to 0.5 M. All the scans ranged from 0.1 V below OCP to 0 V (SCE) with a scan rate of 0.5 mV/s.

COMSOL (Ver. 3.5a and 4.2) software was used to analyze the galvanic coupling between the two materials in a simulated engineering component geometry. The software solves partial differential equations by using the finite element technique. Figure 22 shows the geometry of the modeled system, an approximation of a fastened joint. The width of fastener gap in the model was set at 2 mm, 0.5 mm, or 20  $\mu m$ .

The Nernst–Planck equation<sup>4</sup> was used to describe the transport and mass balance of each species:

$$\nabla \cdot (-z_i u_i F c_i \nabla \phi - D_i \nabla c_i) = R_i \quad [1]$$

where  $D_i$  = diffusion coefficient of species  $i$ ,  $c_i$  = concentration of species  $i$ ,  $z_i$  = charge of species  $i$ ,  $u_i$  = mobility of species  $i$ ,  $R_i$  = reaction rate of species  $i$ ;  $F$  = Faraday's constant;  $\phi$  = the potential of the solution. To simplify the modelling, no homogeneous chemical reactions were considered to occur. The model selected in this study is time-dependent. The species and relevant parameters in the model are listed in Table 3. The boundary conditions used here were obtained by fitting the cathodic/ anodic polarization curves obtained by experimental measurement. Two stages of localized corrosion, initiation and propagation, were considered



separately. The relevant boundary condition for the anode is different for each condition. The details are described in the latter part of the paper.

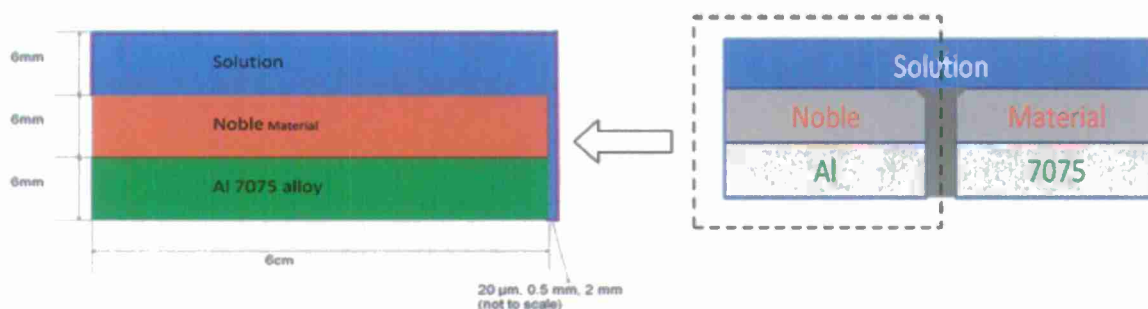


Figure 22. Fastened joint geometry of AA7075-T6 and noble materials coupled system

Table 3. Species, subdomain concentration and diffusion coefficients<sup>5</sup>

Species	Initial Concentration (mol·m <sup>-3</sup> )	Diffusion Coefficient (m <sup>2</sup> s <sup>-1</sup> )
Na <sup>+</sup>	100	1.3 x10 <sup>-9</sup>
Cl <sup>-</sup>	100	2.x10 <sup>-9</sup>
Al <sup>3+</sup>	0	0.54x10 <sup>-9</sup>

#### 1.4.5 Experimental Results

##### 1.4.5.1 Cathode Environment Simulation

Figure 23 shows the cathodic polarization behavior of silver in different chloride concentrations at pH 6. The OCP of the curves are consistent with the reversible potential for



The standard electrode potential against SCE is -0.014V<sup>6</sup>. The OCP changes as the chloride concentration changes. The change of the OCP with [Cl<sup>-</sup>] corresponds well to that calculated from the Nernst equation. AgCl is formed by initial anodic polarization above the OCP potential at the start of the scan. The oxygen reduction rate, as indicated in the curves, does not change much in potential region of interest (-1 to -0.4 V (SCE)) with the different [Cl<sup>-</sup>]. This behavior is as expected due to the limited solubility of oxygen in aqueous solution. The oxygen reduction rate also does not vary much with pH as shown in Figure 24. For nickel, the polarization curves in Figure 25 show that the OCP does not systematically vary with pH, and the oxygen reduction rate is not affected by either pH or [Cl<sup>-</sup>].

Figure 27 shows that OCP of BMI decreased with increasing [Cl<sup>-</sup>]. This decrease may be due to an increase in the anodic reaction of impurities in the water that increase with increasing NaCl. Although the OCP decreased with increasing pH, the oxygen reduction rate of BMI is not significantly affected by either [Cl<sup>-</sup>] or pH as shown in Figure 28. In general, in the potential range of interest, all noble material have similar oxygen reduction rates under fixed conditions, due to the fact that the oxygen reduction rate is under diffusion limitations.

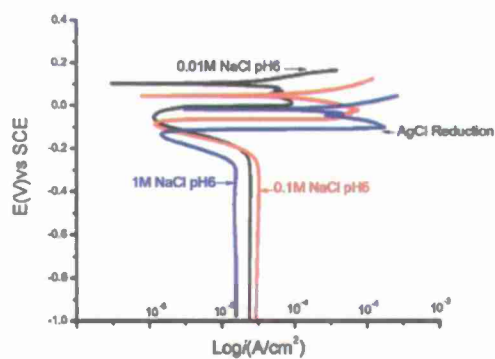


Figure 23. Effect of  $[Cl^-]$  on Ag cathodic kinetics.

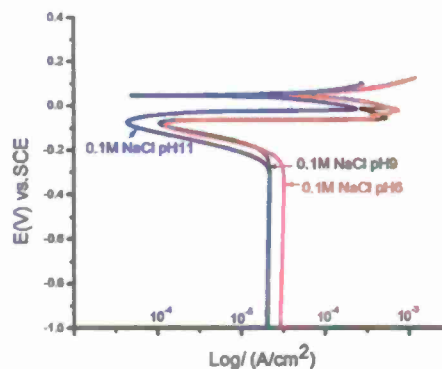


Figure 24. Effect of pH on Ag cathodic kinetics.

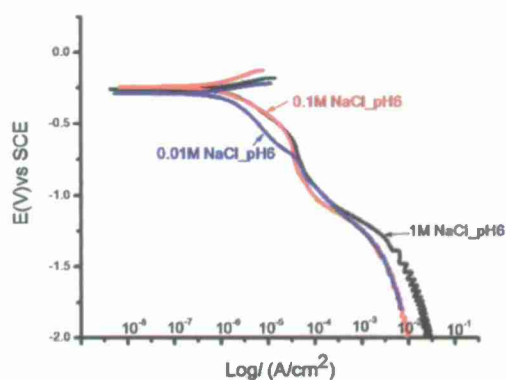


Figure 25. Effect of  $[Cl^-]$  on Ni cathodic kinetics.

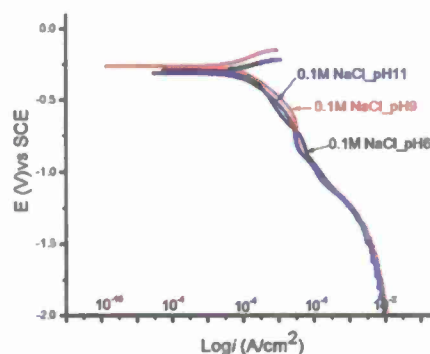


Figure 26. Effect of pH on Ni cathodic kinetics.

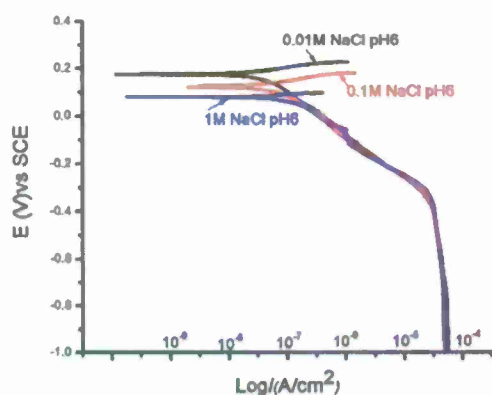


Figure 27. Effect of  $[Cl^-]$  on BMI cathodic kinetics.

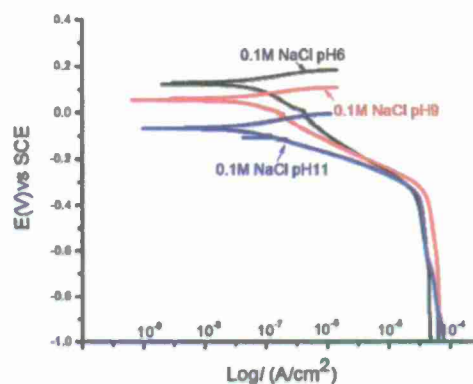


Figure 28. Effect of pH on BMI cathodic kinetics.

#### 1.4.5.2 Anode Environment Simulation

Figure 29 shows the polarization curve of AA7075 with 0.1 M NaCl at different pH. The absence of any passive region for the pH 6 and pH 9 curves indicates that for initiation condition, pitting would be expected to occur spontaneously because the OCP is greater than  $E_{pit}$ , the pitting potential for AA7075. At pH 11, the OCP is much lower, and a distinct passive region is observed, limited by a pitting potential at -0.6 V (SCE). Figure 30 shows that  $E_{pit}$  decreases linearly with the logarithm of the chloride concentration, as expected<sup>7</sup>. The highest  $E_{pit}$  and the lowest OCP appear at pH 11.

For propagation conditions, no passivation behavior is observed in the polarization curves in Figure 31. Acidic solution causes the rapid dissolution of Al alloy. Both the pH and OCP values decrease with increasing  $AlCl_3$  concentration.

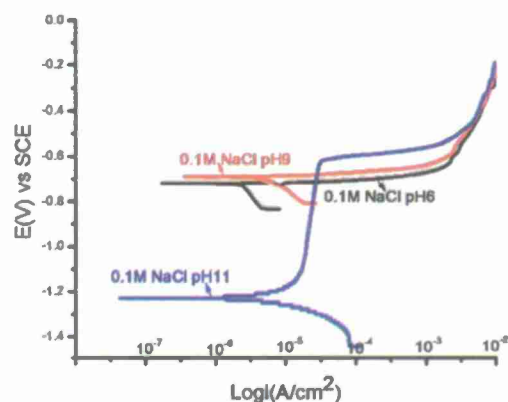


Figure 29. Effect of pH on AA7075-T6 anodic kinetics.

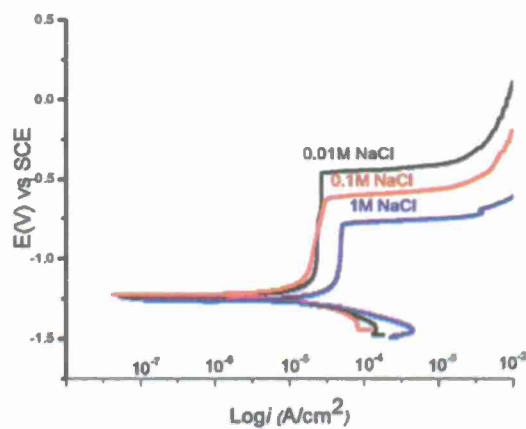


Figure 30. Effect of  $[Cl^-]$  on AA7075-T6 anodic kinetics.

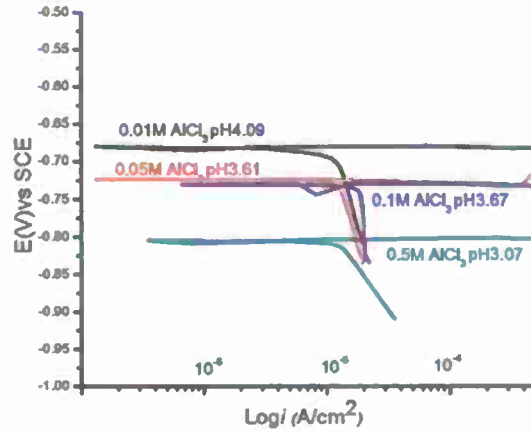


Figure 31. Effect of  $\text{AlCl}_3$  on AA7075-T6 anodic kinetics used for propagation boundary conditions

#### 1.4.5.3 Galvanic Interaction and Numerical Modeling

Using FEM software (COMSOL Ver. 3.5a) the galvanic interactions for the coupled system were studied under different conditions. The present study focuses on discussing the effects of fastened joint geometry,  $[\text{Cl}^-]$ , and the three cathode candidates (Ag, Ni and BMI) for a solution of pH 11. The boundary conditions for both anode and cathode can be characterized by the appropriate current density. The total cathode current density is modeled by:

$$J_C = \frac{1}{\frac{1}{i_c} + \frac{1}{i_l}} \quad [3]$$

where  $i_l$  diffusion limited current density, was obtained from the experimental results, whereas  $i_c$ , the activation controlled current density, is described by Butler-Volmer equation<sup>8</sup>:

$$i_c = i_{C_{corr}} \left[ \exp\left(\frac{E_{C_{corr}} - V}{\alpha_c}\right) - \exp\left(\frac{E_{C_{corr}} - V}{\beta_c}\right) \right] \quad [4]$$

where  $i_{C_{corr}}$  is the cathode corrosion current density,  $E_{C_{corr}}$  is the cathode corrosion potential,  $V$  is the potential in the solution,  $\alpha_c$  is the Tafel slope for the anode, and  $\beta_c$  is the Tafel slope for the cathode.

Under the conditions studied for localized corrosion initiation, the total anodic current is modeled by:



$$Ja = \frac{1}{\frac{1}{i_a} + \frac{1}{i_{pass}} + \frac{1}{i_{a1}}} \quad [5]$$

where  $i_{pass}$  is obtained from the experimental results,  $i_a$  is the exchange current density, and  $i_{a1}$  is current density after pitting is initiated.  $i_a$  and  $i_{a1}$  are determined by Butler-Volmer relations:

$$i_a = i_{acorr} \left[ \exp\left(\frac{Ea_{corr} - V}{\alpha_a}\right) - \exp\left(\frac{Ea_{corr} - V}{\beta_a}\right) \right] \quad [6]$$

$$i_{a1} = i_{a10} \left[ \exp\left(\frac{E_{pit} - V}{\alpha_{a1}}\right) \right] \quad [7]$$

where  $i_{acorr}$  is anode corrosion current density,  $Ea_{corr}$  is anode corrosion potential,  $\alpha_a$  is the anodic coefficient for the anode, and  $\beta_a$  is the cathodic coefficient for the anode.  $i_{a10}$  is the current density at pitting potential,  $E_{pit}$  is pitting potential,  $\alpha_a$  is the anodic coefficient for the anode where the potential is above pitting potential.

Under conditions of localized corrosion propagation, the cathode boundary condition remained the same, whereas the anode became modeled by:

$$i^p_a = i^p_{acorr} \left[ \exp\left(\frac{E^p a_{corr} - V}{\alpha^p_a}\right) - \exp\left(\frac{E^p a_{corr} - V}{\beta^p_a}\right) \right] \quad [8]$$

where  $i^p_{acorr}$  is anode corrosion current density,  $E^p a_{corr}$  is anode corrosion potential,  $\alpha^p_a$  is the anodic coefficient for the anode, and  $\beta^p_a$  is the cathodic coefficient for the anode.

For both initiation and propagation conditions, the dissolution of aluminum,



is considered as the sole reaction along the anode surface. The standard electrode potential relative to SCE is -1.9 V<sup>6</sup>. This dissolution potential varies by the different concentration of AlCl<sub>3</sub>.

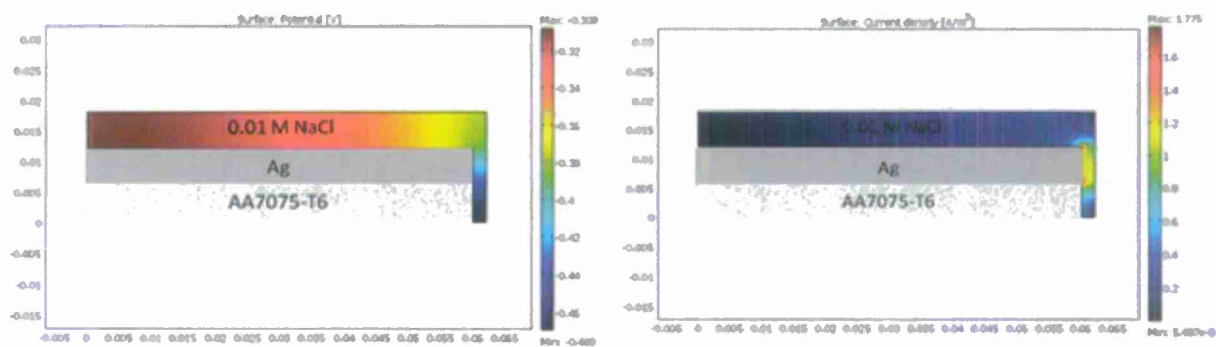
The flux of Al<sup>3+</sup>,  $N_{Al^{3+}}$ , is equal to  $i_a/3F$  at the initiation stage and  $N_{Al^{3+}} = i^p_a/3F$  at the propagation stage in which  $F$  is the Faraday constant which is equal to 96,485 C/equivalent.

Figure 32 shows the potential and current distributions in the Ag-AA7075 coupled system in 0.01 M NaCl, pH 11 with a 2 mm gap under conditions of localized corrosion initiation, where the cathode and anode have the same environment as the bulk solution. Figure 34 shows the potential distribution along the interface of Al alloy and Ag within the fastener gap. The highest

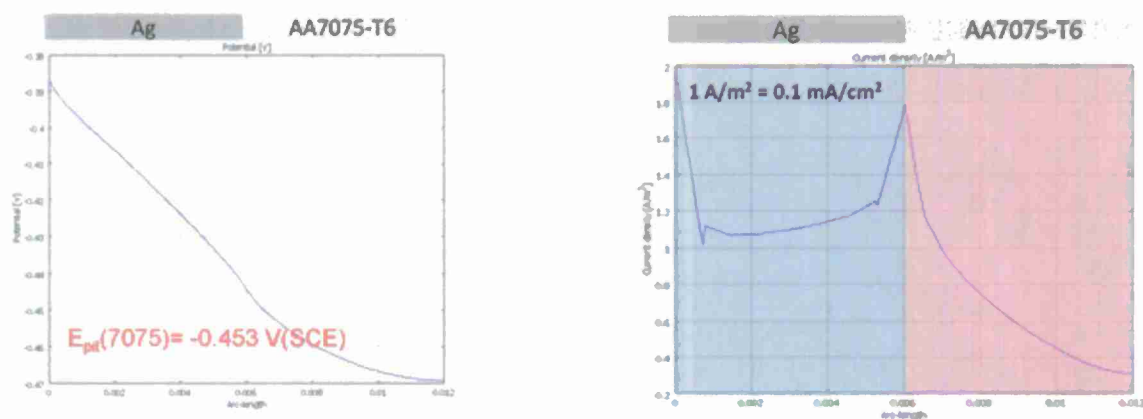
potential on the Al surface is -0.445 V (SCE). Because this potential is higher than -0.453 V (SCE), the pitting potential measured from experiment, the model predicts that pitting can be initiated under this condition. A summary of pitting conditions was generated, as shown in Table 4, by comparing the highest potential at the Al surface within the fastener crevice with the experimentally measured pitting potential under different conditions. According to the summary, Ag causes localized pitting under all the conditions except for 0.01 M  $[\text{Cl}^-]$  in the tightest gap, while Ni does not initiate pitting at all the selected conditions. The pitting for Al alloy coupled with BMI materials varies with the width of the gap and the  $[\text{Cl}^-]$ .

For the propagation simulations, the cathode environment remained the same as in the initiation studies, while the anode environment is changed to acidic  $\text{AlCl}_3$ , with concentrations ranging from 0.01 M to 0.5 M. Figure 35 shows the current distribution along the Ag-AA7075 interface with the same geometry as the initial condition (2mm gap). In this particular case, the boundary condition for Ag is assumed to be 0.1 M NaCl at pH 11, while the boundary condition for AA7075 is assumed to be 0.5 M  $\text{AlCl}_3$ . The peak anodic current density is  $13.1 \text{ A/m}^2$ , which is much higher than  $1.8 \text{ A/m}^2$ , the peak anodic current density calculated for the initiation condition. For BMI, the peak anodic current density under the same propagation conditions is  $14.3 \text{ A/m}^2$ , while the one at initiation condition is  $7.1 \text{ A/m}^2$ . The current density in the propagation condition was also affected by the geometry. In Figure 35, the two curves (Ag and BMI) show the effect of fastener gap on the peak anodic current density under conditions of localized corrosion propagation. The anodic current density at the noble material/aluminum interface is much higher when the fastener gap is decreased to 20 microns.

Figure 36 and Figure 37 show the distribution of  $[\text{Al}^{3+}]$  and  $[\text{Cl}^-]$  along cathode/anode interface as a function of fastener gap. The results shown are for 100 seconds after the propagation began. Although the system has not reached steady state, the results show that the highest concentration for both species appears at the cathode/anode interface. Concentrations decrease due to diffusion as one moves away from the cathode/anode interface. For  $\text{Al}^{3+}$ , as shown in Figure 36, the peak concentration in the tightest gap (20  $\mu\text{m}$ ) is  $24 \text{ mole/m}^3$  (0.024 M). When the gap width increases from 0.5 mm to 2 mm, the peak concentrations do not change remarkably, with  $6 \text{ mole/m}^3$  (for gap width 0.5 mm) and  $4 \text{ mole/m}^3$  (for gap width 2 mm) being calculated. The "bump" shown in Figure 37, where the  $[\text{Cl}^-]$  drops from  $100 \text{ mole/m}^3$  to  $95 \text{ mole/m}^3$  likely occurs because of the substantial quantities of  $\text{OH}^-$  produced at the cathode at this location under these conditions, thus requiring fewer  $\text{Cl}^-$  ions to neutralize the cations in the bulk solution. The distribution of the  $[\text{Cl}^-]$  will be used to better understand and predict the localized corrosion damage on the anode.



(a) (b)  
Figure 32. Corrosion interaction for Ag-AA7075-T6 coupled system with 0.01 M NaCl, pH 11 and gap of 2 mm.



(a) Potential distribution

(b) Current distribution

Figure 33. Corrosion interaction along Ag-AA7075-T6 interface with 0.01 M NaCl, pH 11 and gap 2 mm.

Table 4 . Pitting initiation predicted by modeling result at pH11

	Ag			Ni			BMI		
	2 mm	0.5 mm	20 $\mu$ m	2 mm	0.5 mm	20 $\mu$ m	2 mm	0.5 mm	20 $\mu$ m
[Cl]/Gap									
0.01 M	Y	Y	N	N	N	N	N	N	N
0.1 M	Y	Y	Y	N	N	N	Y	Y	N
1 M	Y	Y	Y	N	N	N	Y	Y	Y

Y: Pitting is initiated. N: Pitting is not initiated.

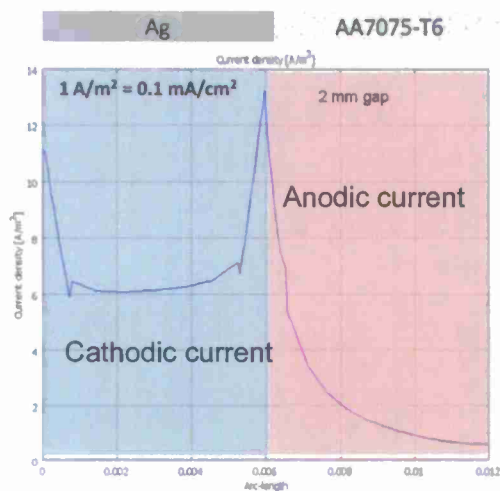


Figure 34. Current density along Ag-AA7075-T6 interface with gap of 2 mm under propagation condition, Ag was selected under 0.1 M NaCl, pH11 condition, AA7075 was selected with 0.5 M  $\text{AlCl}_3$ .

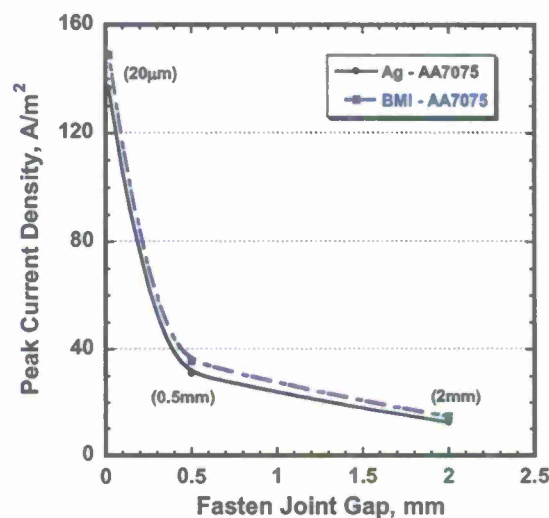


Figure 35. Effect of gap width on Peak Current density. Both Ag and BMI were selected under 0.1 M NaCl, pH11 condition, AA7075 was selected with 0.5 M  $\text{AlCl}_3$ .

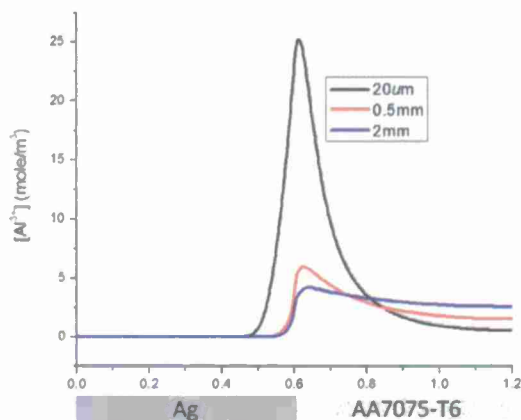


Figure 36.  $[\text{Al}^{3+}]$  distribution along Ag-AA7075-T6 interface as a function of gap width under propagation condition, 100 second after the propagation begin. Ag was selected under 0.1 M NaCl, pH11 condition, AA7075 was selected with 0.5 M  $\text{AlCl}_3$ .

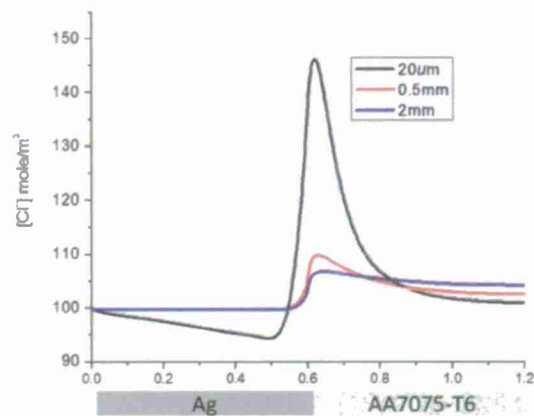


Figure 37.  $[\text{Cl}^-]$  distribution along Ag-AA7075-T6 interface as a function of gap width under propagation condition, 100 second after the propagation begin. Ag was selected under 0.1 M NaCl, pH11 condition, AA7075 was selected with 0.5 M  $\text{AlCl}_3$ .



#### 1.4.6 Discussion

##### 1.4.6.1 Localized Corrosion Initiation

Finite Element Method modeling of a simulated noble material/AA7075-T6 galvanic couple in the form of a fastened panel has shown that Ag is the most deleterious of the three materials studied in terms of initiating localized corrosion. The criterion for initiation was that the potential of any portion of the AA7075-T6 was polarized to above the pitting potential in the chloride concentration of interest. For the case of Ag, all conditions studied, with gaps from 20  $\mu\text{m}$  to 2 mm and chloride concentrations from 0.01 to 1 M led to localized corrosion initiation. At the other end of the spectrum, Ni did not cause initiation in any of the conditions studied, with the BMI composite causing initiation at higher chloride concentrations. Although the criterion for pit initiation is debated, it is clear from this study that Ag, as might be used in RAM coatings, can lead to an increase risk of localized corrosion of 7075-T6. That said, the results also imply that cathodic inhibitors, specifically selected for the noble material of interest, could be useful in mitigating the risk.

##### 1.4.6.2 Localized Corrosion Propagation

To assess the role of geometry and noble material on the propagation of localized corrosion, the solution adjacent to the AA7075-T6 was set to be an  $\text{AlCl}_3$  solution in order to simulate the chemical conditions known to exist in stably propagating localized corrosion sites on Al alloys. The solution in contact with the noble material was set to be the nominal NaCl solution of interest, albeit with an elevated pH to account for the inevitable increase in pH that occurs on a cathode in a galvanic couple. It was shown that under propagation conditions, the dominant effects were geometric, with tighter gaps leading to higher dissolution current densities at the junction between the noble material and the AA7075-T6, with a 20  $\mu\text{m}$  gap having a current density of 140  $\text{A/m}^2$  (14  $\text{mA/cm}^2$ ), nominally independent of the noble material. This peak current density fell 15  $\text{A/m}^2$ .

#### 1.4.7 Economic Summary

There are two means by which this work could have an economic impact. The first is the use of the methodology described in the design phase of aerospace structures. By assessing the effects of material combinations in terms of corrosion, an appropriate trade-off can be made during the design process. Although a structure may be capable of higher performance with a given set of materials, the costs associated with maintenance, risk, and availability need to be considered. The second way in which this work could have an economic impact is in the assessment of the efficacy of proposed mitigation strategies, such as the inclusion of inhibitors in the coatings containing the noble materials. By assessing the effects these inhibitors would have on the electrochemical kinetics, their impact on future costs could be assessed.

#### 1.4.8 Implementation

Implementation of the finite element method described is straightforward; the program used is commercially available. The keys are (a) determination of the geometric details of interest, and (b) establishment of the proper electrochemical boundary conditions. The work described here shows the methodology. For full implementation of the approach into the design/mitigation

process, DOD personnel would need to quantitatively determine the proper geometric details and assess whether the electrochemical boundary conditions used here are appropriate for flight conditions of interest.

#### 1.4.9 Conclusion

The galvanic interactions between AA7075-T6 and three noble materials were investigated. First, the cathodic kinetics of the noble materials were determined as a function of pH and  $[Cl^-]$ . The oxygen reduction rate was not significantly affected by  $[Cl^-]$  and pH for any of the noble materials. The anodic dissolution kinetics of AA7075-T6 was investigated for both localized corrosion initiation and localized corrosion propagation. Localized corrosion was found to be spontaneously initiated at the corrosion potential at pH 6 and pH 9, while at pH 11, localized corrosion only occurred if the potential is higher than pitting potential. The current and potential distributions for the coupled system with a fastener geometry was analyzed by application of the FEM. The effect of geometry,  $[Cl^-]$  and the selection of cathode materials on the galvanic interaction were investigated. For the condition studied in this paper (pH 11, 0.01 M NaCl, gap 2 mm), Ag was the noble material most adept at causing the initiation of localized corrosion, whereas no pitting was expected on AA7075-T6 when coupled with Ni. The corrosion rate and the concentration of the species were also analyzed for localized corrosion propagation. The most severe localized corrosion occurred at the junction between the AA7075-T6 and the noble material, with the tightest gap leading to the highest dissolution rate.

#### 1.4.10 Bibliography

1. G. S. Chen, M. Gao, and R. P. Wei, *Corrosion*, **52**, 8 (1996).
2. J.X. Jia, G.Song, A.Atrems, *Advance Engineering Materials*, **9**, 1-2 (2007).
3. N. Murer, R. Oltra, B. Vuillemin, O.Néel, *Corrosion Science*, **52**, 130–139 (2010).
4. R.W Evitts, J. Postlethwaite and M.K Watson, *Corrosion '92*, (1992).
5. M. Verhoff, R. Alkire, *J. Electrochemical Society*, **147**(4), 1349-1358 (2000).
6. E. McCafferty, *Introduction of Corrosion Science*, p. 97, Springer, New York (2009).
7. G. Sussek, M.Kestern, *Corrosion Science*, **15**, 225 (1975).
8. A. Alavi, R.A. Cottis, *Corrosion Science*, **27**, 443-451 (1987)

## **1.5 Scientific Advances Enabling Next Generation Management of Corrosion Induced Fatigue (Burns, J.T. and Gangloff, R.P.)**

### **1.5.1 Summary**

Recent work on microstructure-scale crack propagation from corrosion damage on a 7000-series alloy in realistic airframe environments is reviewed and its pertinence to airframe prognosis established. The impact of corrosion damage can be accurately modeled by assuming formation life fraction is nil, long crack growth rates, and linear elastic fracture mechanics. An empirically validated corrosion modified-equivalent initial flaw size distribution was established by "back calculation" from measured-total fatigue life; serving as a quantitative descriptor of the deleterious effect of corrosion on fatigue and an initial flaw size input to fracture mechanics modeling. High fidelity characterization of the corrosion pit and fracture surface, coupled with finite element analysis, validated the crack formation and micro-structurally small crack propagation assumptions inherent to fracture mechanics modeling. A large-beneficial effect of low-temperature loading environment was observed; incorporation of this behavior into airframe prognosis could substantially reduce the inspection burden.

### **1.5.2 Introduction and Background**

Aircraft teardowns <sup>1</sup> and failure analyses <sup>2</sup> established the primary importance of fatigue damage formed from localized corrosion for airframe component prognosis. Current corrosion removal-when-detected policies are costly and removal of adjacent-pristine material is possibly more detrimental to structural integrity than the corrosion <sup>3</sup>. Two aspects need to be addressed before a damage tolerant approach to corroded components replaces the remove-when-detected approach. First, a scientifically validated corrosion-topography metric, and a microstructure-scale small crack propagation model, must be developed for the size regime below the current US Air Force damage tolerant flaw size (1,300  $\mu\text{m}$ ) <sup>4</sup>. Second, techniques must be established to elicit the needed corrosion metric for complex service environments that are time and base/airframe-location dependent. This methodology must be scientifically rigorous, but not introduce burdensome inspection or analytical requirements for structural engineers responsible the Aircraft Structural Integrity Program (ASIP).

Researchers demonstrated the large-deleterious effect of water-bearing loading environments on fatigue behavior <sup>5,6</sup>. As such, fracture mechanics codes should incorporate crack growth rates pertinent to airframe loading environments, which can range from salt water spray at sea-level altitudes to cold temperatures and low water-vapor pressures at high altitudes. Furthermore, conversion coatings and primers utilize chromate or other localized corrosion inhibitors; ionic species may leach <sup>7</sup> into a deliquesced surface or crevice-trapped electrolyte layer to retard fatigue crack formation and growth <sup>8,9</sup>. Incorporation of these local environment phenomenon into next generation airframe prognosis would likely decrease the conservatism of current methods due to the beneficial effects of low-temperature <sup>10</sup> and inhibitor affected <sup>8,9</sup> environments.

Airframe component prognosis of microstructure-scale crack progression about corrosion damage in real-world operating environments is challenging and complex. Recent studies have developed a foundation for understanding and modeling such behavior<sup>9, 11-15</sup>.

#### **1.5.2.1 Goal**

The goals of this paper are to: (1) outline the scientific challenges associated with modeling crack formation and growth from corrosion damage, (2) assess the engineering impact of recent high fidelity experimentation and modeling of this behavior, and (3) identify remaining deficiencies.

#### **1.5.3 Lessons Learned**

This paper provides an overview of several detailed studies which have provided firm validation of several assumptions necessarily used to model the impact of corrosion on fatigue life, from the linear-elastic fracture mechanics perspective. These assumptions include: (a) the importance of crack formation life relative to crack propagation life, (b) stress intensity solution accuracy, (c) the proper growth kinetics for microstructure-scale cracks, (d) the impact of H from corrosion on subsequent fatigue life, and (e) the role of the surrounding environment on fatigue life. The detailed results strengthen this fracture mechanics modeling approach. Moreover, a corrosion-modified equivalent initial flaw size (CM-EIFS) parameter is identified. Finally, use of ambient temperature fatigue properties in modeling may be overly conservative for components which are chilled and stressed during high-altitude flight.

#### **1.5.4 Experimental Results and Discussion**

##### **1.5.4.1 Modeling**

Recently, a comprehensive framework was established for modeling fatigue crack progression from constituent particles in a statistically based digital microstructure of 7075-T651. Finite element analyses of local stress and strain were coupled with empirically based damage relationships at the dislocation plasticity scale through microstructure level cracking, long crack growth, crack coalescence, and component failure<sup>16</sup>. Such an approach is at the cutting-edge of the quest for airframe structural health monitoring and fleet management. However, shortcomings in understanding the physics governing fatigue cracking processes hinder application and establish this as a long-term ASIP option<sup>13</sup>.

An attainable near-term advance is extrapolation of current damage tolerant approaches into the microstructure regime of fatigue cracking, which would improve the fidelity of current approaches and enable modeling of surface damage (such as corrosion) with dimensions on the sub-1,300  $\mu\text{m}$  scale. There are four primary technical hurdles in extending linear elastic fracture mechanics (LEFM) to microstructure scale cracking about corrosion damage: (1) How is the crack formation life ( $N_i$ ) quantified? (2) What crack growth rates are used for prediction? (3) What is the initial flaw size? and (4) Will accurate predictions result as LEFM assumptions are possibly violated? Researchers performed LEFM predictions of fatigue life, assuming  $N_i = 0$ , long crack growth rates, and using various metrics for the initial flaw size<sup>17-23</sup>. Such corrosion modified-equivalent initial flaw sizes (CM-EIFS) are either "back-calculated" from known fatigue



lives and/or intermediate crack length measurements<sup>24</sup>, or are a measured crack initiation site metric. The resulting CM-EIFS distributions and/or life predictions were generally encouraging, but tended to vary with stress level and specimen geometry; thus, not representing a material-environment property to broadly quantify corrosion-fatigue resistance.

These deficiencies motivated recent work on EXCO pre-corroded 7075-T6511, to systematically evaluate parameters such as crack formation life, initial microscopic aspect ratio and its evolution, and multiple interacting fatigue cracks. Results from back-calculation showed that accounting for the formation life, using the initial aspect ratio of the pit, and allowing the aspect ratio to evolve based on variable crack front stress intensity (K) resulted in a distribution of CM-EIFS values that were stress independent and correlated well with the crack formation feature sizes<sup>11</sup>.

Despite innovative techniques for crack detection<sup>25, 26</sup>, particularly around corrosion<sup>27</sup>, current technology cannot reliably detect crack features below the damage tolerant-typical flaw size of ~1.3 mm. Furthermore, practical characterization techniques are coarse, providing at best a measure of thickness loss<sup>28</sup> and sophisticated methods, such as confocal scanning laser microscopy or white light interferometry, are not practical for field analysis. These limitations on *a priori* determination of the CM-EIFS distribution via NDI hinder assessing the fitness-for-mission of airframe components.

The CM-EIFS distribution likely depends on the corrosive environment history and resulting surface topography. Fatigue life was measured for 7075-T6511 specimens with precorrosion morphologies produced by different duration EXCO exposures<sup>29</sup>, various corrosion acceleration compositions (ANCIT and LJSS<sup>30</sup>), and different exposure surfaces<sup>12</sup>. The severe-deleterious effect on fatigue life was bounded by a lower trend line as demonstrated in Figure 38<sup>12</sup>. This lower trend leads to an upper-limit CM-EIFS (depth~300  $\mu$ m) that is independent of corrosion morphology or severity. These results are powerful and suggest that limited experiments (similar to those found in Ref. <sup>11, 12</sup>) on service exposed or representative-laboratory exposed coupons can produce a representative CM-EIFS distribution. Such distributions could be coupled with simple NDI measurements of remaining material thickness to allow for LEFM prediction of component life. This methodology is pertinent to known corrosion trouble areas where a fracture mechanics analysis can be accomplished and incorporated in maintenance protocols prior to corrosion detection on a specific component.

Such empirical correspondence is encouraging, but there is a lack of understanding regarding formation life, stress-plastic strain state about different pit morphologies on a broadly corroded surface, and small crack growth kinetics. Moreover, the CM-EIFS approach is a 2-dimensional linear elastic analysis of a single crack; however, the corrosion to fatigue transition is 3-dimensional and likely involves elastic-plastic deformation and crack interactions. Despite the excellent correspondence between model predictions and experimental results<sup>12</sup>, these uncertainties need to be addressed prior to incorporation of such modeling into a prognosis capability.

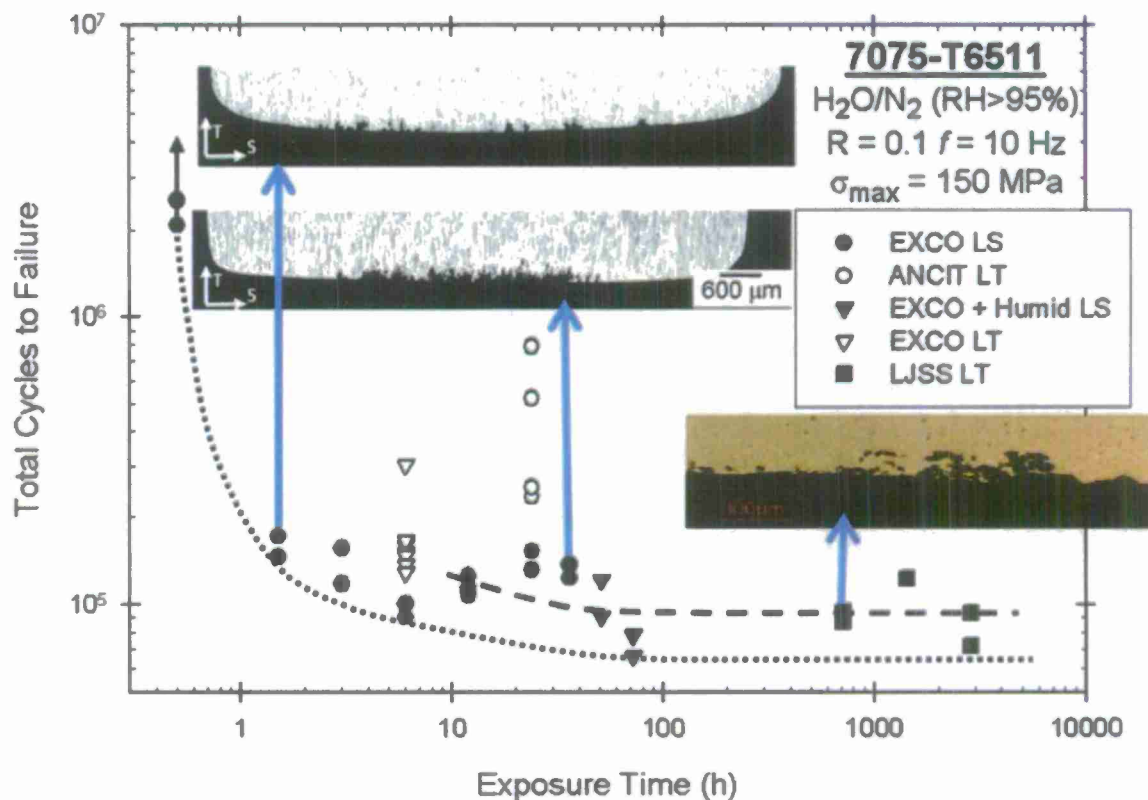


Figure 38. Effect of L-T or L-S surface EXCO, ANCIT, or LJSS corrosion pre-exposure on the fatigue life of 7075-T6511 stressed in water vapor saturated  $N_2$  at  $R=0.1$  and  $\sigma_{max}=150$  MPa [12]. Cross-sections of corrosion damage are inset.

#### 1.5.4.2 Crack Formation

To establish the factors governing crack formation from a corroded surface, and role of formation in component prognosis, constant amplitude fatigue experiments were performed on 7075-T651 specimens pre-corroded with controlled-isolated pits (depth $\approx 250$   $\mu$ m deep; surface length $\approx 650$   $\mu$ m)<sup>14</sup>. A programmed loading sequence was used to mark the fracture surface<sup>11, 12, 24</sup> so as to trace progression of the crack through the microstructure and enable calculation of cycles to form a  $\approx 15$   $\mu$ m crack about the corrosion pit. Coupling high resolution and quantitative physical characterization of the corrosion damage, fracture surface, and underlying microstructure with elastic-plastic finite element analysis (FEA)<sup>14</sup>, provided an experimental basis to refine and validate crack formation models<sup>16, 31</sup>. Results showed that fatigue crack formation involves a complex interaction of driving forces; the distribution of elastic stress concentration due to pit macro-topography interacts with local micro-topographic stress/strain concentration, leading to local plasticity that is further affected by the random distribution of micro-structure (likely constituent particles) proximate to the pit surface<sup>14</sup>. This complex interaction, and the statistically distributed character of corrosion, explains the observed-high

variability in  $N_i$  <sup>14</sup>. Additionally, the limiting fatigue life plateau observed in Figure 38 is explained by the dominant role of micro-topography and underlying microstructure, both of which are similar for all of the macro-corrosion morphologies examined, coupled with corrosion morphology independent intrinsic crack growth rates <sup>15</sup>.

At an engineering level, this work validated the linear-elastic fracture mechanics (LEFM) assumption that formation life is nil at applied stress levels above a material and environment dependent threshold. In this near-threshold regime the empirical Smith, Watson, and Topper model <sup>32</sup> with FEA stress and strain inputs reasonably predicts  $N_i$  <sup>14</sup>. Figure 39 illustrates correspondence between such predictions (yellow-triangles) and experimental crack formation life ranges (black-lines) where right- and left-facing arrows indicate earlier formation or that some pits did not form cracks visible on the fracture surface, respectively. The data are plotted at the maximum center-line concentrated stress (from FEA analysis) for each pit and loading condition <sup>14</sup>. A science-based foundation for prognosis of corrosion initiated fatigue requires coupling this work with analysis of microstructure-scale (<1,300  $\mu\text{m}$ ) crack progression.

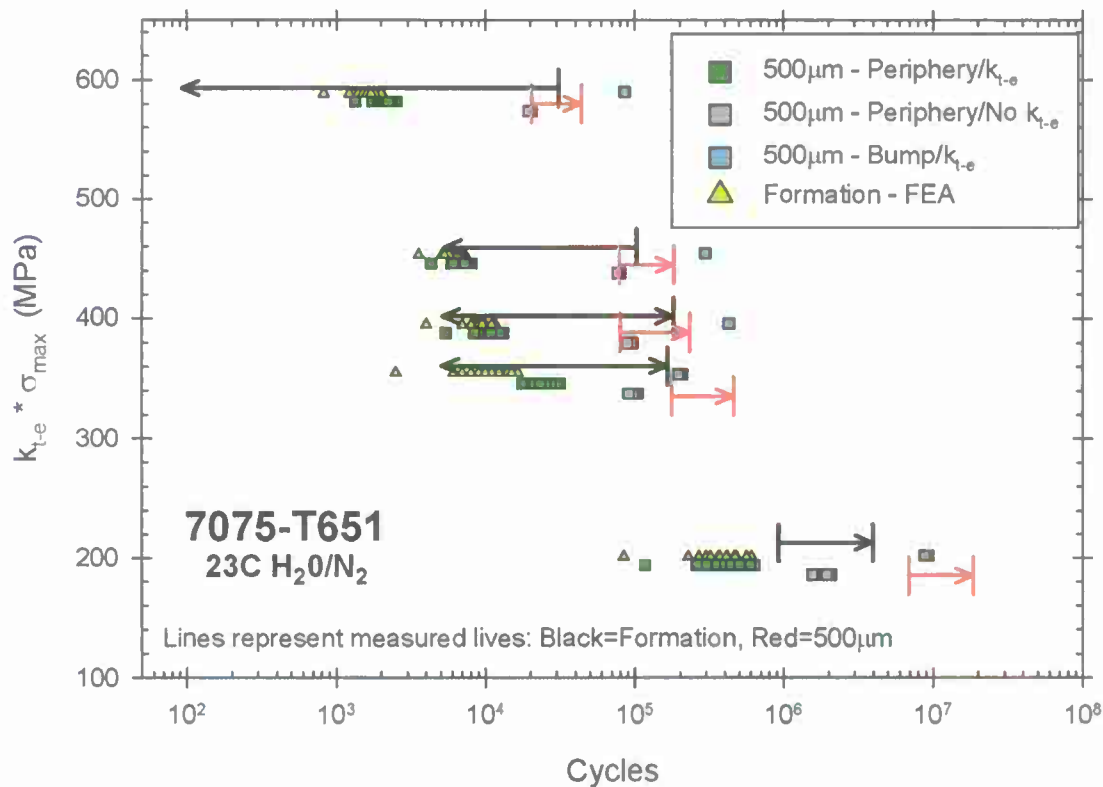


Figure 39. Comparison of measured (lines) and predicted (points) crack formation cycles (black) and total cycles to 500  $\mu\text{m}$  (red), plotted versus maximum concentrated macro-stress. Stresses are computed along the centerline of various controlled pits at  $\sigma_{\text{max}} = 100, 200$ , and 300 MPa for  $R = 0.5$  [15]. The data are offset vertically for clarity. Measured values are from marker analysis of 7075-T651 stressed in humid  $\text{N}_2$  at 23°C.

### 1.5.4.3 Small Crack Propagation

Scientific interest in the mechanisms governing microstructure-sensitive small-fatigue crack behavior that deviates from continuum-long crack trends has been strong for decades<sup>33, 34</sup>. The marker-banding technique was used to develop a unique small crack growth rate ( $da/dN$ ) database that captures crack progression through a complex microstructure in 7075-T651. This method is more rigorous than previously reported small-crack  $da/dN$  data obtained via surface measurement techniques<sup>34-36</sup>. Figure 40 illustrates that marker-band  $da/dN$  for various shapes of controlled pits stressed at  $R=0.5$  and  $\sigma_{max} = 100, 200, \text{ or } 300 \text{ MPa}$  are correlated into a single distribution using complex continuum estimates of stress intensity ( $\Delta K$ )<sup>15</sup>. These driving force estimates account for crack geometry and a local stress concentration gradient due to the 3-D corrosion pit. Also included are CT or SEN long-crack high-constant  $K_{max}$ -decreasing  $\Delta K$  results<sup>15</sup>; marker-band cracking below the apparent long-crack threshold ( $\approx 1.3 \text{ MPa}\sqrt{m}$ ) supports the argument that such threshold is an artifact of the bending-type specimens and K-shedding protocol<sup>37</sup>. These and other results from Ref. <sup>15</sup> show that: (1) moist-environment fatigue is not well described by a single power law relationship, (2) the small-crack  $da/dN$  is not bounded by extrapolation of the mean Paris-regime growth rates (blue-dashed line 2), (3) there is good agreement between long crack and marker-band growth rates in the near-threshold ( $\Delta K=1.8\text{-}3.5 \text{ MPa}\sqrt{m}$ ) regime, and (4)  $da/dN$  variability is high ( $\pm 150\%$ ), particularly for  $\Delta K$  below  $1 \text{ MPa}\sqrt{m}$ .

A common engineering approach to small crack-based life prediction extrapolates Paris-regime  $da/dN$  to very low  $\Delta K$ <sup>37, 38</sup>. However, this is not straightforward (see Figure 40; blue-dashed lines 1, 2 and 3) given the multiple power-law slopes of the CT/SEN data. To predict crack growth from the corrosion pit to  $500 \mu m$ , this assumption (blue-dashed line 2) is coupled with a simple representation of crack geometry and stress state in an LEFM code (AFGROW)<sup>39</sup>. Specifically, the CM-EIFS equals pit size and the crack extends in all directions about the periphery (gray square); concentrated stress due to the pit is not included. (Also shown are predictions that include the pit-induced stress gradient for a periphery crack (green square) and more complex crack shape (blue square)). Figure 39 compares these predictions to marker-band cycles to  $500 \mu m$ , represented by red-lines, where right-facing arrows indicate that some cracks do not progress to  $500 \mu m$  prior. The good correspondence suggests that the CM-EIFS methodology<sup>11, 12</sup> can be extrapolated to model MSC growth<sup>15</sup>. Furthermore, the high fidelity characterization of crack progression, FEA analysis of corrosion pits, and complex stress intensity analysis show that the gross underestimation of  $da/dN$  resulting from Paris-regime extrapolation is negated by the erroneously high  $\Delta K$  values associated with the periphery crack geometry assumption. These findings justify the assumptions inherent in the successful empirical models proposed for use in next generation prognosis of airframe components.



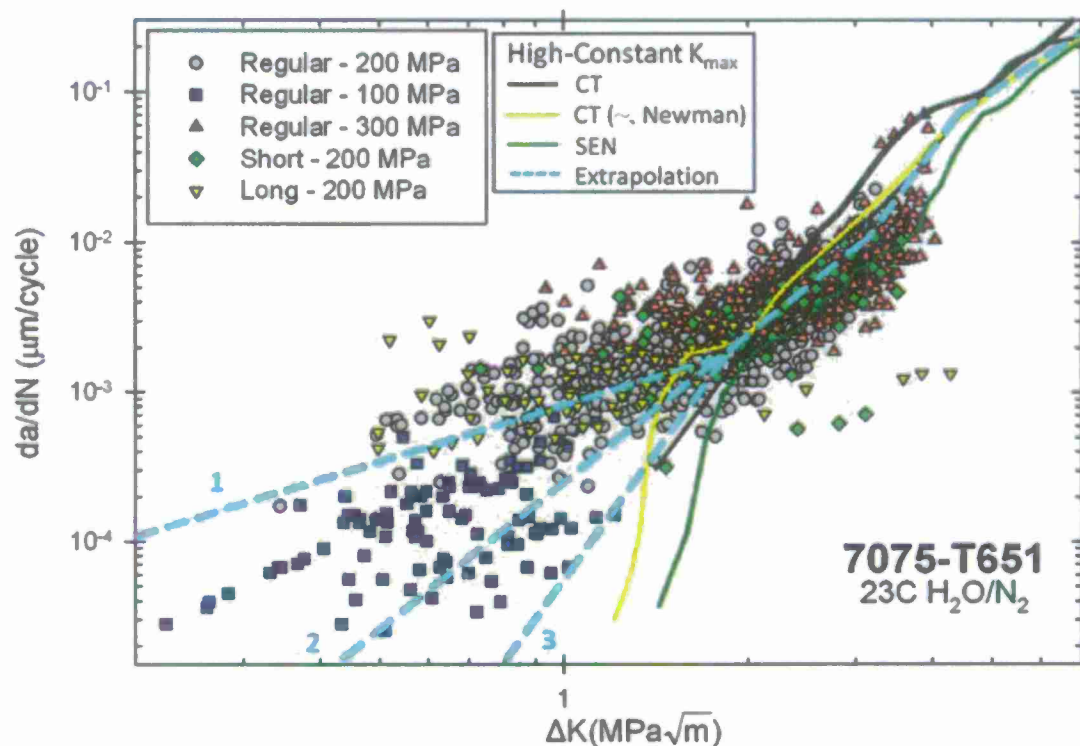


Figure 40. Fatigue crack growth rate from marker-band measurements vs.  $\Delta K$  from various controlled pit specimens tested at either  $\sigma_{\text{max}} = 100, 200$ , or  $300$  MPa and  $R = 0.5$  in water vapor saturated  $\text{N}_2$  [15]. Also included are long crack CT and SEN results.

#### 1.5.4.4 Environmental Effects

Current airframe life prediction models generally use strain/stress-life constants or crack growth rate laws gathered at ambient temperature ( $\sim 23^\circ\text{C}$ ) and humidity (20-70%); water vapor pressure ( $P_{\text{H}_2\text{O}}$ ) is sufficiently high to dominate fatigue damage via H environment embrittlement (HEE) <sup>5</sup>. During high altitude flight, low temperatures decrease local  $P_{\text{H}_2\text{O}}$  and may impede other elements of HEE. Marker-band fatigue testing, identical to that described in Sections 1.2.4.2 and 1.2.4.3, was performed at  $-50^\circ\text{C}$  and  $-90^\circ\text{C}$ ; crack formation life increased 30- and 100-fold, respectively compared to that at  $23^\circ\text{C}$  <sup>13</sup>. Figure 41 shows a strong temperature effect on small crack  $da/dN$ ; for example, at  $\Delta K = 2 \text{ MPa}\sqrt{\text{m}}$ , decreasing temperature to  $-50^\circ\text{C}$  and  $-90^\circ\text{C}$  results in 10-fold and 30-fold decreases in mean  $da/dN$  <sup>13</sup>. Such a reduction in growth rate would lead to high conservatism in current life prediction models. The complexity of modeling crack progression through transient-environment loading must be further studied. However, these results and recent inhibitor findings <sup>8,9</sup> suggest that environment control and modeling have the potential to decrease the inspection burden if integrated into airframe prognosis.

#### 1.5.4.5 Remaining Challenges

Recent work establishes a strong foundation for modeling fatigue cracking from corrosion; however, uncertainties remain. Aging aircraft contain legacy alloys with uncertain microstructure; it is necessary to understand how microstructure affects these modeling efforts. While the approach will be unaffected by microstructure variation, the inputs will be affected. Other important areas include: flight temperature and loading spectra interaction, coating-inhibitor effects, and ground-based corrosion subsequent to crack formation (crack tip blunting, crack wake corrosion induced closure, etc.).

The work detailed above provides crucial experimental data for validation and development of mechanism-based failure criteria and micromechanical models<sup>16, 31</sup>. As a next step, a comprehensive FEA model of the corrosion pit should be coupled with a realistic microstructure model capable of calculating grain-specific stresses/strains. Such a model could be validated with current high-fidelity experimental results to further quantify the contributions of micro-topography and microstructure to local strain. Furthermore the marker-band  $da/dN$  data can be coupled with electron back-scatter diffraction data to quantify the microstructure features that cause the large  $da/dN$  variation in Figure 40 and Figure 41<sup>40</sup>.

#### 1.5.5 Implementation

The implementation path for this work includes: (1) incorporate this modeling capability into AFGROW, (b) obtain information on coupled stresses and temperature for fatigue critical locations in an airframe, and (c) validate model predictions with experiments using a laboratory-scale component that captures the loading and temperature spectra relevant to flight. These tasks are being researched by Professor James Burns at UVA, in close collaboration with Dr. Scott Fawaz (SAFE) and CASTLE personnel; sponsored by OuSD through the United States Air Force Academy under contract to SAFE. The results of these studies will be reported in the final reports associated with these two OuSD grant programs.

#### 1.5.6 Conclusions

Recent work<sup>11-15</sup> has lead to the following conclusions.

- The CM-EIFS distribution from LEFM modeling quantifies the deleterious effect of corrosion on fatigue and provides an initial flaw size for prediction of remaining component life.
- High-fidelity characterization of pit topography, SEM marker band analysis, and elastic-plastic FEA modeling justify the LEFM assumptions concerning crack formation and MSC propagation.
- Fatigue crack formation and growth are substantially reduced at low-temperatures due to reduced HEE. Such behavior justifies work to understand temperature-stress spectra associated with flight spectrum. Control and incorporation of environmental effects on airframe fatigue may significantly reduce the airframe prognosis challenge.
- The factors governing fatigue crack formation, a map of crack growth through microstructure, corrosion morphology characterization, and a major experimental data-base

exist to guide and validate mechanism-based multi-scale modeling which is the future of airframe prognosis.

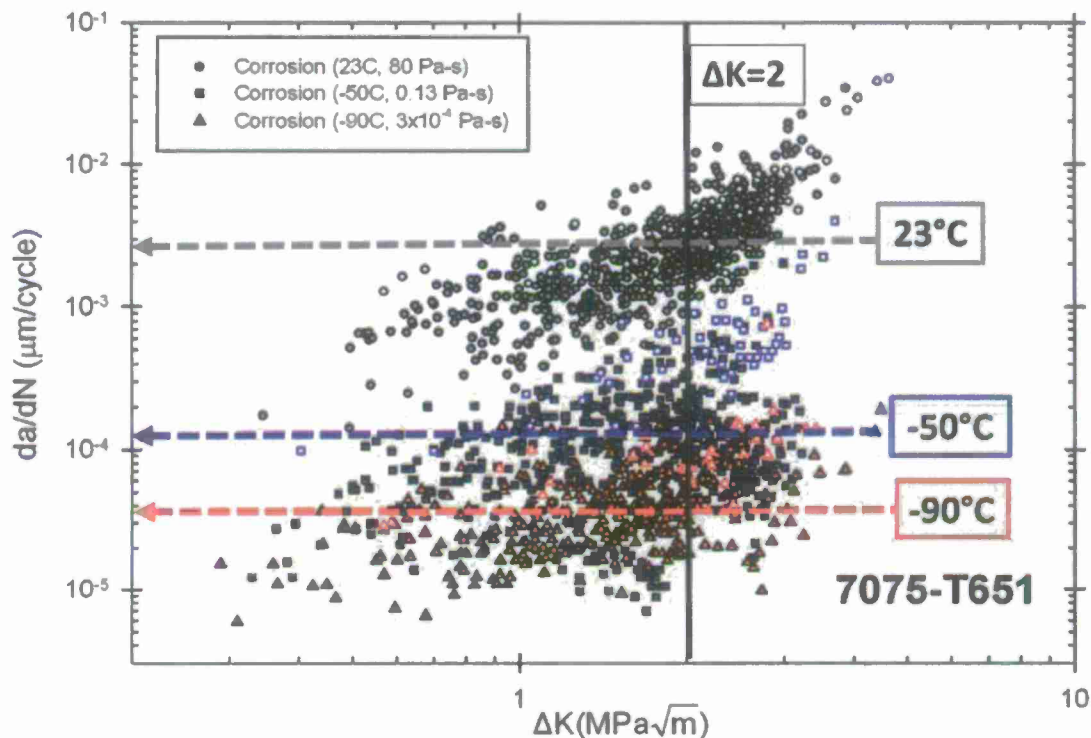


Figure 41. Fatigue crack growth rate versus  $\Delta K$  data from marker-band analysis of 7075-T651 controlled pits tested at  $\sigma_{\max} = 200$  MPa and  $R = 0.5$  in water saturated  $N_2$ , and dry  $N_2$  at  $-50^\circ\text{C}$  and  $-90^\circ\text{C}$  [13].

#### 1.5.7 Bibliography

1. G. A. Shoales, S. A. Fawaz and M. R. Walters, Compilation of damage findings from multiple recent teardown analysis programs, ICAF 2009 - Bridging the Gap Between Theory and Operational Practice, p. 187-207, (Rotterdam, The Netherlands, Springer, 2009).
2. L. Molent, Fatigue crack growth from flaws in combat aircraft, *Int J Fatigue*, 32 (2010), 639-649.
3. M. E. Hoffman and P. C. Hoffman, Corrosion and fatigue research - structural issues and relevance to naval aviation, *Int J Fatigue*, 23 (2001), S1-S10.
4. JSSG-2006 Joint Services Specification Guide - Aircraft Structures. Department of Defense, 1998
5. R. P. Gangloff, Environment sensitive fatigue crack tip processes and propagation in aerospace aluminum alloys, *Fatigue 2002*, (Stockholm, Sweden, EMAS, 2002).

6. J. Petit, G. Henaff and C. Sarrazin-Baudoux, Environmentally assisted fatigue in the gaseous atmosphere, J. Petit and P. Scott, Eds., vol. 6, *Comprehensive Structural Integrity: Environmentally Assisted Fracture*, (New York, NY, Elsevier, 2003, p. 962-970).
7. L. Petry, D. Barrington and J. F. Dante, Evaluation of the inhibitor leaching performance of chromated primers by capillary ion analysis and electrochemical impedance spectroscopy, 2003 Aerospace Coatings Removal and Coatings Conference, (San Antonio, TX, [corrdefense.org](http://corrdefense.org), 2003).
8. Z. M. Gasem and R. P. Gangloff, Rate-limiting processes in environmental fatigue crack propagation in 7000-series aluminum alloys., R. H. Jones, (Ed.), *Chemistry and electrochemistry of corrosion and stress corrosion cracking: A symposium honoring the contributions of R.W. Staehle*, (Warrendale, PA, TMS-AIME, 2001, p. 501-521).
9. J. S. Warner, S. Kim and R. P. Gangloff, Molybdate inhibition of environmental fatigue crack propagation in Al-Zn-Mg-Cu, *Int J Fatigue*, 31 (2009), 1952-1965.
10. C. Gasqueres, C. Sarrazin-Baudoux, J. Petit and D. Dumont, Fatigue crack propagation in an aluminium alloy at 223 K, *Scripta Mater*, 53 (2005), 1333-1337.
11. S. Kim, J. T. Burns and R. P. Gangloff, Fatigue crack formation and growth from localized corrosion in Al-Zn-Mg-Cu, *Eng Fract Mech*, 76 (2009), 651-667.
12. J. T. Burns, S. Kim and R. P. Gangloff, Effect of corrosion severity on fatigue evolution in Al-Zn-Mg-Cu, *Corros Sci*, 52 (2010), 498-508.
13. J. T. Burns, "The Effect of Initiation Feature and Environment on Fatigue Crack Formation and Early Propagation in Al-Zn-Mg-Cu" University of Virginia, 2010).
14. J. T. Burns, J. M. Larsen and R. P. Gangloff, Driving forces for localized corrosion-to-fatigue crack transition in Al-Zn-Mg-Cu, *Fatigue Fract Eng M*, In review (2011).
15. J. T. Burns, J. M. Larsen and R. P. Gangloff, Effect of initiation feature on microstructurally small fatigue crack propagation in Al-Zn-Mg-Cu, *Int J Fatigue*, In review (2011).
16. J. Papazian, E. L. Anagnostou, R. J. Christ, S. J. Engel, D. Fridline, D. Hoitsma, J. Madsen, J. Nardiello, J. Payne, R. P. Silberstein, G. Welsh and J. B. Whiteside, DARPA/NCG structural integrity prognosis system, HR0011-04-C-0003, DARPA, 2009.
17. D. L. DuQuesnay, P. R. Underhill and H. J. Britt, Fatigue crack growth from corrosion damage in 7075-T6511 aluminium alloy under aircraft loading, *Int J Fatigue*, 25 (2003), 371-377.
18. K. M. Gruenberg, B. A. Craig, B. M. Hillberry, R. J. Bucci and A. J. Hinkle, Predicting fatigue life of pre-corroded 2024-T3 aluminum from breaking load tests, *Int J Fatigue*, 26 (2004), 615-627.
19. B. R. Crawford, C. Loader, A. R. Ward, C. Urbani, M. R. Bache, S. H. Spence, D. G. Hay, W. J. Evans, G. Clark and A. J. Stonham, The EIFS distribution for anodized and pre-corroded 7010-T7651 under constant amplitude loading, *Fatigue Fract Eng M*, 28 (2005), 795-808.
20. Y. B. Xiang and Y. M. Liu, EIFS-based crack growth fatigue life prediction of pitting-corroded test specimens, *Eng Fract Mech*, 77 (2010), 1314-1324.
21. J. J. Medved, M. Breton and P. E. Irving, Corrosion pit size distributions and fatigue lives - a study of the EIFS technique for fatigue design in the presence of corrosion, *International Journal of Fatigue*, 26 (2004), 71-80.
22. K. van der Walde and B. M. Hillberry, Initiation and shape development of corrosion-nucleated fatigue cracking, *Int J Fatigue*, 29 (2007), 1269-1281.
23. S. A. Barter, P. K. Sharp, G. Holden and G. Clark, Initiation and early growth of fatigue cracks in an aerospace aluminium alloy, *Fatigue Fract Eng M*, 25 (2002), 111-125.



24. S. A. Fawaz, Equivalent initial flaw size testing and analysis of transport aircraft skin splices, *Fatigue Fract Eng M*, 26 (2003), 279-290.
25. D. S. Forsyth, M. Genest, J. Shaver and T. B. Mills, Evaluation of nondestructive testing methods for the detection of fretting damage, *Int J Fatigue*, 29 (2007), 810-821.
26. Y. Y. Hung, Y. S. Chen, S. P. Ng, L. Liu, Y. H. Huang, B. L. Luk, R. W. L. Ip, C. M. L. Wu and P. S. Chung, Review and comparison of shearography and active thermography for nondestructive evaluation, *Mat Sci Eng R*, 64 (2009), 73-112.
27. E. Tada, Detection of corrosion fatigue cracking through current responses induced by cyclic stressing, *Corros Sci*, 49 (2007), 248-254.
28. J. P. Komorowski, D. S. Forsyth, D. L. Simpson and R. W. Gould, Probability of detection in corrosion in aircraft structures, RTO AVT Workshop - Airframe Inspection Reliability under Field/Depot Conditions, RTO MP-10, (Brussels, Belgium, 1998).
29. ASTM, G34-01: Standard test method for exfoliation corrosion susceptibility in 2xxx and 7xxx series aluminum alloys, Vol 03.02. ASTM International, West Conshohocken, PA, 2007
30. K. S. Ferrer and R. G. Kelly, Development of an aircraft lap joint simulant environment, *Corrosion*, 58 (2002), 452-459.
31. J. M. Papazian, E. L. Anagnostou, S. J. Engel, D. Hoitsma, J. Madsen, R. P. Silberstein, G. Welsh and J. B. Whiteside, A structural integrity prognosis system, *Eng Fract Mech*, 76 (2009), 620-632.
32. K. N. Smith, P. Watson and T. H. Topper, A stress-strain function for the fatigue of metals, *Journal of Materials*, 5 (1970), 167-778.
33. R. O. Ritchie and J. Lankford, Small fatigue cracks : proceedings of the second Engineering Foundation International Conference/Workshop, Santa Barbara, California, January 5-10, 1986, (Warrendale, PA: Metallurgical Society, 1986), p. xi, 665 p.
34. J. M. Larsen and J. E. Allison, Small-crack test methods, *Stp*, (Philadelphia, PA: ASTM, 1992), p. 222 p.
35. K. Shiozawa, Y. Tohda and S. M. Sun, Crack initiation and small fatigue crack growth behaviour of squeeze-cast Al-Si aluminium alloys, *Fatigue Fract Eng M*, 20 (1997), 237-247.
36. R. Jones, S. Pitt and D. Peng, The generalised Frost-Dugdale approach to modelling fatigue crack growth, *Eng Fail Anal*, 15 (2008), 1130-1149.
37. J. C. Newman, A nonlinear fracture mechanics approach to growth of small cracks, Behavior of Short Cracks in Airframe Components - AGARD SP-328, p. 6.1-6.26, (Toronto, CA, AGARD, 1982).
38. W. A. Herman, R. W. Hertzberg and R. Jaccard, A Simplified Laboratory Approach for the Prediction of Short Crack Behavior in Engineering Structures, *Fatigue Fract Eng M*, 11 (1988), 303-320.
39. J. A. Harter, AFGROW Program Version 4.12.15.0, <http://www.stormingmedia.us/13/1340/A134073.html>. AFRL/VASM, WPAFB, OH, 2008
40. V. K. Gupta, R. P. Gangloff and S. R. Agnew, Diffraction characterization of microstructure scale fatigue crack growth in modern Al-Zn-Mg-Cu alloy, *Int J Fatigue*, in review (2011).

## 1.6 Effect of Atmospheric Exposure on Environmental Fatigue Crack Propagation and Inhibition in Precipitation Hardened Al-Cu-Li (Warner, J.S. and Gangloff, R.P.)

### 1.6.1 Summary

A first examination of quantitative environmental fatigue crack propagation (EFCP) and inhibition under atmospheric exposures which create electrolyte droplets on the surface of C47A-T86, an Al-Cu-Li alloy is presented. Fatigue crack propagation rates are not accelerated under high frequency loading by atmospheric exposures producing NaCl-only-electrolyte droplets on the bold surface. This is comparable to full immersion under high frequency when alloy-induced inhibition is not possible. For moderate to low frequency loading, alloy-induced inhibition of Al-Cu alloys is hindered by NaCl containing droplets; and as such, crack growth rates are higher for atmospheric conditions than under full immersion. When molybdate is present in the droplets, ion-assisted inhibition is enhanced. Addition of molybdate to surface NaCl droplets completely eliminated the effect of environment on EFCP by yielding crack growth rates equivalent to ultra high vacuum and crack arrest when loaded at 0.2 Hz. Furthermore,  $da/dN$  was reduced by an order of magnitude under 30 Hz loading, an  $f$  at which molybdate inhibition under full immersion is not possible. The degree to which the crack is filled with solution appears to affect EFCP kinetics by altering anode to cathode separation to influence crack tip potential, pH, and repassivation kinetics and limiting the molybdate to chloride ratio in the crack solution. Ultimately, this study demonstrates that transportation of inhibiting ions to a crack tip and inhibition of EFCP may be possible after inhibitor release from a coating into a surface electrolyte layer or droplets during in-service exposure, and suggests that molybdate or Mo-bearing coatings may provide a vehicle for strong inhibition of EFCP by controlled release of  $MoO_4^{2-}$  in the atmospheric environment.

### 1.6.2 Introduction

Precipitation hardened aluminum alloys including the Al-Cu-Li system used in aerospace structures are susceptible to environmental fatigue crack propagation (EFCP) explained in large part by the hydrogen environment embrittlement (HEE) mechanism<sup>1-17</sup>. Essentially, H is produced by chemical or electrochemical reactions between water molecules and fresh Al surface near the crack tip. Reaction product H absorbed on the crack tip surface diffuses within the fatigue process zone (FPZ) where it interacts with local tensile stresses and dislocation structure from cyclic deformation to cause embrittlement, thereby enhancing fatigue crack propagation rate ( $da/dN$ ) relative to inert gas and vacuum<sup>1, 2, 5, 6, 8-10, 12, 13, 15-17</sup>. Because this process is time/cycle dependant<sup>10, 12, 13, 15</sup>, the H concentration in the FPZ, and therefore  $da/dN$ , can be limited kinetically by one of the following steps: a) transport of the hydrogen producing reaction species from the bulk environment to crack surface reaction sites, b) time for crack surface chemical or electrochemical reaction(s) to produce H, and c) diffusion of atomic reaction product H within the metal to the crack tip FPZ<sup>2, 7, 10, 12, 13, 18</sup>.

Prior research on EFCP has focused on full immersion in aqueous solutions<sup>1, 3, 4, 8, 19-33</sup>, laboratory-moist air<sup>1, 19-21, 26-28, 30, 34-36</sup>, or pure water vapor<sup>2, 5-7, 11, 25, 28, 37</sup>. The environmental driving force for cracking in these environments is well established as being controlled by time

(given by fatigue loading frequency,  $f$ ) and the manner in which H is produced. For pure water vapor, research correlated  $da/dN$  with an exposure parameter, defined by the ratio of water vapor pressure ( $P_{H_2O}$ ) to  $f$ , which describes the environmental driving force for cracking<sup>2, 6, 7, 14-16, 18, 38-43</sup>. The dependence of  $da/dN$  on  $P_{H_2O}/f$  has four regimes of behavior. At low exposures, there is no effect of environment on  $da/dN$ . This behavior transitions to a regime where  $da/dN$  increases rapidly with increasing exposure and is strongly dependent on the environment because of Knudsen flow. In the third regime,  $da/dN$  continues to increase with increasing exposure, but decelerates as the rate limitation changes to H diffusion in the FPZ and/or saturation of the chemical/electrochemical reactions producing H on the crack surface. The fourth regime occurs at a saturation  $P_{H_2O}/f$ , at and above which the environmental effect reaches a maximum and  $da/dN$  no longer increases with increasing  $P_{H_2O}/f$ <sup>14-16</sup>.

For full immersion in aqueous chloride solutions, H is produced electrochemically near an oxygen depleted crack tip by cathodic water reduction and/or dissolution introducing  $Al^{3+}$  which is hydrolyzed to  $H^+$  then cathodically reduced to H<sup>12, 44-46</sup>. The environmental driving force is quantified by: (a)  $f$ ; (b) the overpotential for H production ( $\eta_H$ ), which is a function of crack tip pH and potential ( $E$ ); and (c) passivity which reduces H production and uptake<sup>12</sup>. For aluminum alloys in chloride solutions, the crack tip passive film is broken down allowing reaction rates to be rapid and crack advance to be H-diffusion controlled [3,4,21,22]. Modeling predicts that  $da/dN$  increases with decreasing  $f$  due to increasing time for H to diffuse to the FPZ, then becomes  $f$  and time independent under moderate to low  $f$  loading where neither surface reaction nor H diffusion are rate limiting<sup>3, 4</sup>. This typical time -  $f$  dependence is observed in 7000-series (Al-Zn-Mg) Al alloys in aqueous chloride solutions<sup>3, 4, 22, 25</sup>. For Al-Cu-Mg and Al-Cu-Li alloys (2000-series),  $da/dN$  decreases with decreasing  $f$ <sup>32, 47</sup>. This  $f$  dependence is attributed to alloy-induced inhibition where a crack tip surface passive film is stabilized from: 1) crack flank Cu enrichment following dissolution of anodic Cu-containing GP zones or precipitates and 2) enhanced crack wake cathodic reaction kinetics on these Cu enriched zones which increases crack solution pH to stabilize a native alumina crack tip passive film in the presence of chloride<sup>32, 47</sup>. Crack tip and wake passivity reduce production and uptake of embrittling H through reduced crack hydrolysis and a H-diffusion barrier film<sup>12, 32, 47-50</sup>. The crack tip passive film is destabilized mechanically and rendered incapable of EFCP protection when the strain accumulated at the crack tip exceeds the strain required for film rupture; inhibition resumes once the rupture site(s) repassivate. The decreasing  $da/dN$  with decreasing  $f$  is determined by the interplay between the rate of film rupture, governed by crack tip strain rate, and repassivation. Hence, alloy-induced inhibition in 2000-series Al alloys is promoted by reduced loading frequency, and thus reduced crack tip strain rate, which favors repassivation over film rupture.

Full immersion, laboratory air and pure water vapor environments may not accurately describe the actual conditions encountered by aircraft during flight operations at a range of altitudes<sup>51</sup>. Atmospheric exposure involves gas and particle pollutants dissolved in water vapor, rain, snow, fog, aerosol, etc. These pollutants include oxides of nitrogen (NO, NO<sub>2</sub>, etc.), sulfur dioxide (SO<sub>2</sub>), nitrous oxide (N<sub>2</sub>O<sub>2</sub>), nitric acid (HNO<sub>3</sub>), hydrogen chloride (HCl), hydrogen peroxide (H<sub>2</sub>O<sub>2</sub>), chlorine atoms (Cl), ozone (O<sub>3</sub>), ammonia (NH<sub>3</sub>), chlorine nitrate (ClONO<sub>2</sub>), and hydroxyl (OH) to name a few<sup>52, 53</sup>. Such contaminants collect on a metal surface and absorb moisture to deliquesce an electrolyte layer and/or droplets at  $P_{H_2O}$  lower than expected for pure water condensation on a clean surface. The electrolyte which results from atmospheric exposure may create electrochemical conditions and EFCP rates which differ from those typical of pure water vapor or full immersion as the environmental driving force for cracking may be different or altered. Three bounding conditions are shown in Figure 42. First, the metal surface is fully

hydrophilic and the electrolyte completely wets the metal surface to create a homogeneous electrolyte layer of uniform thickness, as shown in Figure 42a. While the parameters ( $f$ , pH,  $E$ ) controlling the environmental driving force for cracking should be the same as for full immersion, differences exist because the dissolved oxygen diffusion distance from the atmosphere to the cathodic reaction sites on the metal surface is reduced. This can increase cathodic reaction kinetics and open circuit potential at the crack mouth to increase  $\eta_H$ ,  $H$  production/uptake, and  $da/dN$ <sup>47</sup>. The second and third bounding conditions shown in Figure 42 develop when the metal surface is hydrophobic to a varying degree, promoting electrolyte droplets over a uniform electrolyte layer. The scenario shown in Figure 42b occurs when droplets interact with and partially or completely fill the growing crack depending on droplet volume and number intersected. In this scenario, the environmental driving force for cracking will be controlled by  $E$ , pH, and  $f$ , but because electrochemical connection between the crack mouth/bold surface and crack tip is lost, cathodic reaction sites will move into the crack wake and create crack solution  $E$  and pH which differ significantly from those typical of full immersion and Scenario 1 (Figure 42a). If the surface droplets never interact with the crack, then the scenario shown in Figure 42c develops. In this case, EFCP proceeds as if in high humidity air and the environmental driving force for cracking is controlled by  $P_{H_2O}/f$ . The impacts of atmospheric environmental conditions (e.g., Figure 42) on EFCP of aluminum alloys have not been quantitatively established for use in fatigue life prediction and alloy development.

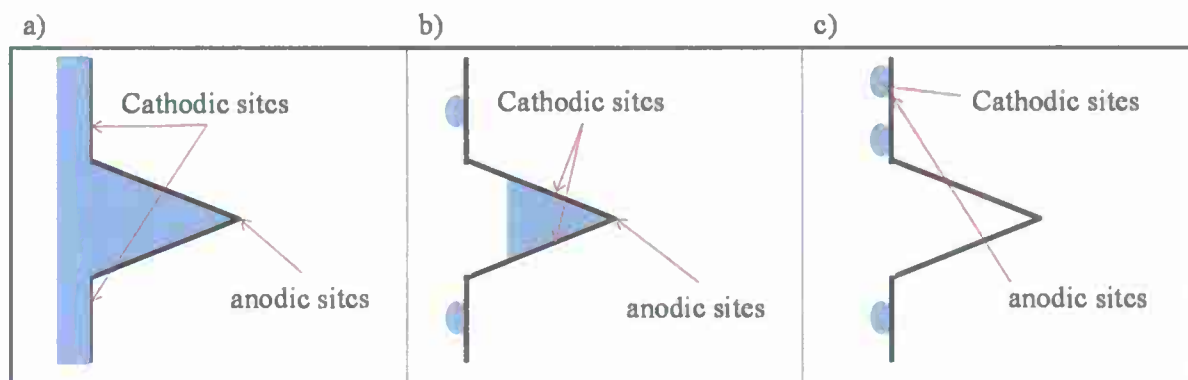


Figure 42. The bounding conditions for electrolyte deliquescence under atmospheric conditions.

a) The electrolyte homogeneously wets a hydrophilic surface and fills the crack. b) Electrolyte droplets form on a hydrophobic surface and (partially) fill the crack. c) Droplets on a hydrophobic surface do not interact with the crack.

Atmospheric exposure conditions may also affect the ability of EFCP inhibitors like chromate and molybdate to transport to a crack tip and inhibit EFCP. Prior research has shown that chromate<sup>3,4</sup> and molybdate<sup>33,47,54</sup> inhibit EFCP via the film rupture-H embrittlement mechanism when added to bulk chloride solution and stressed under full immersion. Inhibition is evidenced by reduced  $da/dN$  compared to that typical of pure chloride solution at a single  $f$  and decreasing  $da/dN$  with decreasing  $f$ . Additionally, molybdate completely eliminated the effect of environment, producing vacuum-level  $da/dN$  at sufficiently low  $f$ <sup>33,47,54</sup>. The thickness



and resistivity of a thin electrolyte layer may affect the ability of an inhibitor to transport to a growing crack tip and provide inhibition to EFCP after release from a corrosion protection system into a small-volume solution. Additionally, electrolyte droplets may alter inhibition due to ion concentration/transport and crack chemistry changes implicit in Figure 42. The extent of self-inhibition, as well as added-ion inhibition, on EFCP of aluminum alloys has not been established for atmospheric-deliquested exposure conditions.

#### 1.6.2.1 Goal

The objective of this work is to quantitatively characterize and understand the effects of atmospheric exposure on EFCP and inhibition, both alloy-induced and molybdate ion-assisted. Particular focus is placed on the importance of electrolyte layer and droplet morphology relative to well studied full immersion and water vapor environments. First,  $da/dN$  is correlated to  $\Delta K$  and  $f$  for atmospheric conditions where a chloride-bearing electrolyte has deliquesced on a boldly exposed Al-Cu-Li alloy surface. Second, the ability of molybdate to inhibit EFCP is established, when present with chloride in a deliquesced surface electrolyte layer and/or droplet.

#### 1.6.3 Lessons Learned

The effect of atmospheric environment on environmental fatigue crack propagation (EFCP) and inhibition is, for the first time, characterized quantitatively for exposures which create electrolyte droplets on the surface of Al-Cu-Li alloy C47A-T86. Fatigue crack propagation rates are not accelerated under high frequency loading by atmospheric exposures producing NaCl-only-electrolyte droplets on the bold surface. For moderate to low frequency loading, alloy-induced inhibition of Al-Cu alloys is hindered by NaCl containing droplets; and as such, crack growth rates are higher for atmospheric conditions than under full immersion. When molybdate is present in the droplets, ion-assisted inhibition is enhanced. Addition of molybdate to surface NaCl droplets completely eliminated the effect of environment on EFCP by yielding crack growth rates equivalent to ultra high vacuum and crack arrest when loaded at 0.2 Hz. Furthermore,  $da/dN$  was reduced by an order of magnitude under 30 Hz loading, an  $f$  at which molybdate inhibition under full immersion is not possible. The degree to which the crack is filled with solution appears to affect EFCP kinetics by altering anode to cathode separation to influence crack tip potential, pH, and repassivation kinetics and limiting the molybdate to chloride ratio in the crack solution. Ultimately, this study demonstrates that transportation of inhibiting ions to a crack tip and inhibition of EFCP may be possible after inhibitor release from a coating into a surface electrolyte layer or droplets during in-service exposure, and suggests that molybdate or Mo-bearing coatings may provide a vehicle for strong inhibition of EFCP by controlled release of  $MoO_4^{2-}$  in the atmospheric environment.

#### 1.6.4 Experimental Procedures

##### 1.6.4.1 Materials

The aluminum alloy used in this study is C47A-T86 which is the registered alloy 2199 designed for improved mechanical property isotropy<sup>55</sup>. The C47A has a composition of Al-2.6Cu-1.6Li-0.6Zn-0.3Mn-0.2Mg-0.06Zr wt% and was provided by Alcoa Technical Center as a 19 mm thick plate in the T36 temper. The as-received material has grain dimensions of 88  $\mu m$  in the

thickness (S) direction and 896  $\mu\text{m}$  in the width (T) direction<sup>15</sup>, and was artificially aged for 36 h at 149°C to simulate the near-peak aged microstructure (T86). A detailed analysis of the microstructure and texture was performed previously<sup>15, 56</sup>: the microstructure contains  $\text{Al}_2\text{LiCu}$  ( $T_1$ ),  $\text{Al}_2\text{Cu}$  ( $\theta$ ), and  $\text{Al}_3\text{Li}$  ( $\delta'$ ) precipitates. The  $\sigma_{ys}$  is 426 MPa.

#### 1.6.4.2 EFCP

For fatigue testing, single edge micronotch tension (SENT) specimens were machined in the L-T orientation with a notch depth of 200  $\mu\text{m}$ , width of 10.2 mm, and thickness of 2.5 mm. (L is parallel to the plate-rolling direction.) The mid portion of the specimen was O-ring sealed in a cylindrical Plexiglas cell with an outer ring-basin which contains a saturated salt solution used to maintain a constant relative humidity (RH) as outlined in the ASTM Standard Practice for Maintaining Constant Relative Humidity by Means of Aqueous Solutions (E104)<sup>57</sup>. This cell is shown in Figure 43. The salt used was  $\text{K}_2\text{SO}_4$ , which maintains an RH of 97.3%  $\pm$  0.5% when in saturated solution at 25°C<sup>57, 58</sup>. High purity-hydrocarbon free air ( $\text{N}_2$  with 19.5%  $\text{O}_2$ , < 2 ppm  $\text{H}_2\text{O}$ , < 0.1 ppm THC, < 0.5 ppm  $\text{CO}_2$ , and < 0.5 ppm CO) was pre-saturated to a RH of 97.3% by passage through two airtight cells containing saturated  $\text{K}_2\text{SO}_4$ , then circulated through the Plexiglas cell throughout each experiment. The threaded SEN specimen was gripped outside the Plexiglas cell to enable unhindered rotation necessary for the stress intensity solution employed<sup>59</sup>. Specimen and cell cap-to-body seals used o-rings, air pre-saturation chambers were Nalgene sterile PETG bottles made for reduced permeability of  $\text{CO}_2$ , and all fittings were rated for the lowest  $\text{CO}_2$  permeability. A positive gas pressure was maintained in the O-ring sealed cell to prevent ambient air entry during fatigue testing. Fatigue crack length was monitored continuously by the Direct Current Potential Difference (DCPD) method<sup>60, 61</sup> utilizing a constant current of  $4.5 \pm 0.005$  ampere. Voltage readings, amplified up to 20,000 times, were collected within 25% of the peak load during each load cycle to eliminate crack wake electrical shorting which may cause a false crack length measurement. Applied current was automatically reversed to eliminate spurious thermally induced voltages. For the constant current power supply and signal averaging employed, the DCPD potential resolution was  $\pm 0.13$   $\mu\text{V}$  and the associated resolvable average crack extension was 4  $\mu\text{m}$ .

Fatigue experiments were conducted using a servo-hydraulic machine operated in load control with a constant amplitude sinusoidal waveform. All specimens were precracked in the test environment under a constant  $\Delta K$  of 7  $\text{MPa}\sqrt{\text{m}}$ ,  $R$  of 0.1 or 0.3, and  $f$  of 1 to 5 Hz to a total notch plus fatigue precrack length of 0.6 mm. All EFCP experiments were performed at a constant  $\Delta K$  of 7  $\text{MPa}\sqrt{\text{m}}$ ,  $K_{\text{max}}$  of 16.5  $\text{MPa}\sqrt{\text{m}}$ ,  $R$  of 0.58, and  $f$  of either 30 or 0.2 Hz. The  $f$  was maintained constant for at least 0.5 mm of crack extension at a constant  $da/dN$  before the next frequency was examined. An average  $da/dN$  was determined by linear regression of the crack length versus load cycle relationship, and the linearity of this relationship provides information on transient versus steady state atmospheric EFCP.

#### 1.6.4.3 Atmospheric Environment/Surface Electrolyte

An electrolyte layer thickness of 100  $\mu\text{m}$  was chosen because corrosion rates were reported to be highest on 2024-T351 at an electrolyte layer thickness of 105  $\mu\text{m}$ <sup>62</sup>. In order to obtain a surface electrolyte layer and/or droplets on the metal surface for atmospheric fatigue testing, the following procedure was used: First, NaCl or NaCl and  $\text{Na}_2\text{MoO}_4$  was deposited onto the SEN plane containing the loading axis (L) and crack propagation direction (T). For NaCl only, a

saturated solution of NaCl in ethanol was transferred onto the specimen surface with a pipette taking care not to include residual salt crystals and to retain all solution on the LT surface. The amount of salt deposited after the ethanol volatilized was determined by knowing the solubility limit of NaCl in ethanol (0.58 g/L) and pipeting a known volume of solution onto a specific area. This process was repeated multiple times for each side of the specimen so as to not pipette too much ethanol at one time to cause overflow loss of NaCl. For both NaCl and Na<sub>2</sub>MoO<sub>4</sub>, Na<sub>2</sub>MoO<sub>4</sub> was deposited first using a super saturated solution of ethanol and Na<sub>2</sub>MoO<sub>4</sub> pipeted onto the specimen. Because the concentration of the super saturated solution was not fixed, the amount of Na<sub>2</sub>MoO<sub>4</sub> deposited on the surface was determined by measuring the change in mass of the specimen. After deposition of Na<sub>2</sub>MoO<sub>4</sub> was complete, NaCl was deposited using the saturated solution technique outlined above. This deposition method was used since Na<sub>2</sub>MoO<sub>4</sub> solubility in ethanol is low (0.075 g/L), and the very small mass changes for the amounts of NaCl deposited require a high precision scale.

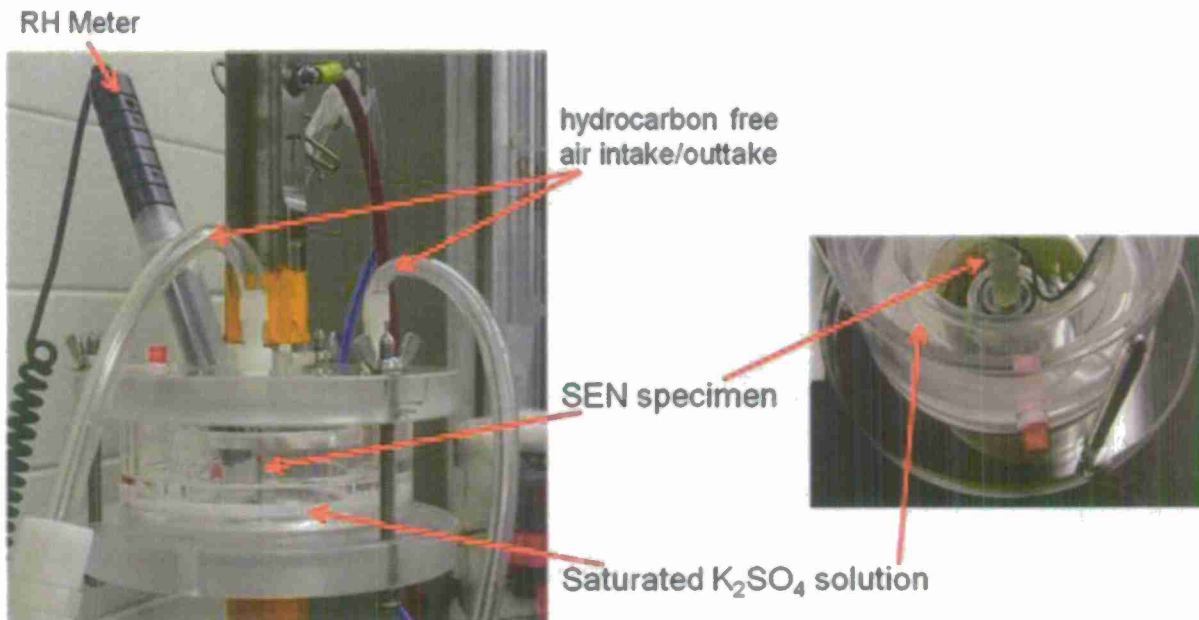


Figure 43. Environmental cell used for fatigue testing which maintain constant RH. The outer cup holds a saturated K<sub>2</sub>SO<sub>4</sub> which maintains an RH of 97.3%.

In order to create a deliquesced electrolyte layer with constant [NaCl] or [NaCl]/[Na<sub>2</sub>MoO<sub>4</sub>] and volume on the surface, constant RH must be maintained about the salt-coated specimen. The equilibrium between RH and [NaCl] was previously established<sup>63</sup> showing when RH is 97.3%, [NaCl] is 0.8 mol/kgH<sub>2</sub>O or 0.79M<sup>63</sup>. The relationship between RH-[NaCl], amount of NaCl deposited ( $c$  in kg/cm<sup>2</sup>), and electrolyte layer thickness ( $\delta$  in meters) is shown in:

$$\frac{cx10^3 (\text{g}/\text{m}^2)}{58.44 (\text{g}/\text{mol})} \rightarrow \frac{(\frac{cx10^3}{58.44}) (\text{mol}/\text{m}^2)}{0.79 (\text{mol}/\text{L})} = \frac{cx10^3 (\text{L}/\text{m}^2)}{46.17} \times \frac{1 \text{ m}^3}{1000 \text{ L}} = \frac{c}{46.17} (\text{m}) = \delta (\text{m}) \quad (1)$$

where the formula weight of NaCl is 58.44 g/mol, and c is the amount of surface NaCl deposited in kg/m<sup>2</sup>. Given this equilibrium and Equation 1, if a known mass of NaCl is deposited on a known surface area of the SEN specimen and a constant RH maintained, then an electrolyte layer of known thickness and constant [NaCl] exists. When electrolyte droplets are present on the surface, is modified to yield the total volume of solution deliquesced on the surface per unit area (v) as shown in Equation 2:

$$\frac{cx10^3(g/m^2)}{58.44(g/mol)} \rightarrow \frac{\left(\frac{cx10^3}{58.44}\right)(mol/m^2)}{0.79(mol/L)} = \frac{cx10^3}{46.17} \left(L/m^2\right) = v \left(L/m^2\right) \quad (2)$$

For surface electrolytes which contain NaCl and Na<sub>2</sub>MoO<sub>4</sub>, the RH versus [NaCl] + [Na<sub>2</sub>MoO<sub>4</sub>] equilibrium relationship was determined by placing solutions of different xM NaCl + yM Na<sub>2</sub>MoO<sub>4</sub> into an airtight container containing an RH meter. When RH remained constant for over 24 h, this value was recorded as the equilibrium RH with the specific solution composition. For the RH used in this study, 97.3%, the equilibrium solution is ~0.06M NaCl + ~0.6M Na<sub>2</sub>MoO<sub>4</sub>. (While other combinations of these salts can produce the same RH, this condition is relevant to comparisons with full immersion ionic inhibition data as considered in the Discussion.) To determine the amount of NaCl and Na<sub>2</sub>MoO<sub>4</sub> to deposit on the surface, were used, respectively with a target of 100 µm.

$$\frac{cx10^3(g/m^2)}{58.44(g/mol)} \rightarrow \frac{\left(\frac{cx10^3}{58.44}\right)(mol/m^2)}{0.06(mol/L)} = \frac{cx10^3}{3.5064} \left(L/m^2\right) \times \frac{1 m^3}{1000 L} = \frac{c}{3.5064} (m) = \delta (m) \quad (3)$$

$$\frac{jx10^3(g/m^2)}{241.95(g/mol)} \rightarrow \frac{\left(\frac{jx10^3}{241.95}\right)(mol/m^2)}{0.6(mol/L)} = \frac{jx10^3}{145.17} \left(L/m^2\right) \times \frac{1 m^3}{1000 L} = \frac{j}{145.17} (m) = \delta (m) \quad (4)$$

"c" in Equation 3 is the mass of NaCl deposited in kg/cm<sup>2</sup>. "j" in Equation 4 is the mass of Na<sub>2</sub>MoO<sub>4</sub> deposited in kg/cm<sup>2</sup>. If droplets are present, the total volume of solution deliquesced on the surface can be calculated from the amount of salt deposited on the surface, analogous to Equation 2.

For scientific investigation, an electrolyte layer which completely wets the metal surface, as in Figure 42a, is ideal as change in the electrolyte layer thickness could be directly related to a change in the oxygen diffusion distance and η<sub>H</sub>. But airframe environments may include homogeneous and heterogeneously distributed droplets for hydrophobic surfaces. Several surface preparation and atmospheric control techniques were investigated to determine effects on Al alloy surface wetting. Salt was deposited on the LT surface of a 13.5 mm x 60 mm coupon with different surface conditions: a) 600 grit polish, b) 1200 grit polish, c) 1 µm polish, d) plasma cleaning prior to salt deposition, e) boiling water anodization prior to salt deposition, f) deposition in laboratory air versus an Ar filled glove box, and g) an automated printing method<sup>64</sup>. Plasma cleaning and salt deposition in Ar were used to remove hydrocarbons from the specimen surface, which can otherwise degrade the wettability of aluminum<sup>65-69</sup>. Salt-coated specimens were placed in the EFCP Plexiglas cell maintained at a constant RH of 97.3% with



saturated  $K_2SO_4$ . High purity, hydrocarbon free air was passed through the cell at all times to ensure hydrocarbon contamination did not compromise the deliquesced electrolyte morphology.

None of the surface preparation combinations examined produced an electrolyte layer which fully wet C47A-T86. Rather, surfaces with heterogeneous-far spaced droplets or homogeneous-closely packed droplets were observed, depending on surface preparation and deposition method. In all cases, the morphology of droplets was unchanging and stable for up to several weeks at which point the specimens were removed from the humidified cell. Based on the results of macrophotographs illustrated in Figure 44 and Figure 45, homogeneous-close packed droplets were attained by printing in air or with salt deposition in a glove box under Ar; each applied to a polished surface. Heterogeneous-far spaced droplets existed for salt deposited on polished surfaces in laboratory air or on the hot-water anodized surface. Such anodization produced particularly large and heterogeneously distributed droplets. Plasma cleaning and surface polish did not significantly affect surface droplet morphology; compare Figure 44 to Figure 45.

Two surface electrolyte layer morphologies were selected for EFCP experiments: homogeneous-close spaced droplets and heterogeneous-far spaced droplets. SEN specimens were cleaned with acetone and 200 proof ethanol to remove residual machining grease. The specimens targeted for homogeneous droplets were plasma cleaned for 5 min using argon gas followed by 5 min using oxygen gas. Plasma cleaned specimens were stored in a glass desiccator under vacuum until salt deposition in an Ar glove box. The coated specimen was loaded into the Plexiglas fatigue cell and sealed under Ar. For heterogeneous droplets, salt deposition and loading into the fatigue cell was performed in lab air. While the coupon study showed that plasma cleaning did not affect droplet morphology for these deposition conditions, it was employed to guarantee a high-reproducible level of surface cleanliness.

The orientation of the SEN specimen surface during fatigue testing affected droplet morphology, as characterized by horizontally mounted coupons (Figure 44 and Figure 45). For heterogeneous droplets, the morphology of the droplets on the surface remained constant throughout experimentation. In contrast the homogeneous droplets slowly moved down the vertically oriented SEN specimen. Such homogeneous droplets were never completely removed from the SEN surface, but the amount of electrolyte along the crack path was less at the end of an experiment than at the beginning. Specifically, a large pool of electrolyte accumulated at the bottom of the deposited surface area and small droplets were more widely dispersed on the SEN surface near the crack propagation path by the end of multi-day fatigue experiments. This behavior provides a mechanism for  $da/dN$  to vary with crack extension and test time. For this reason, all EFCP experiments were conducted at constant  $\Delta K$  to establish the extent of transient crack growth unique to atmospheric exposure.

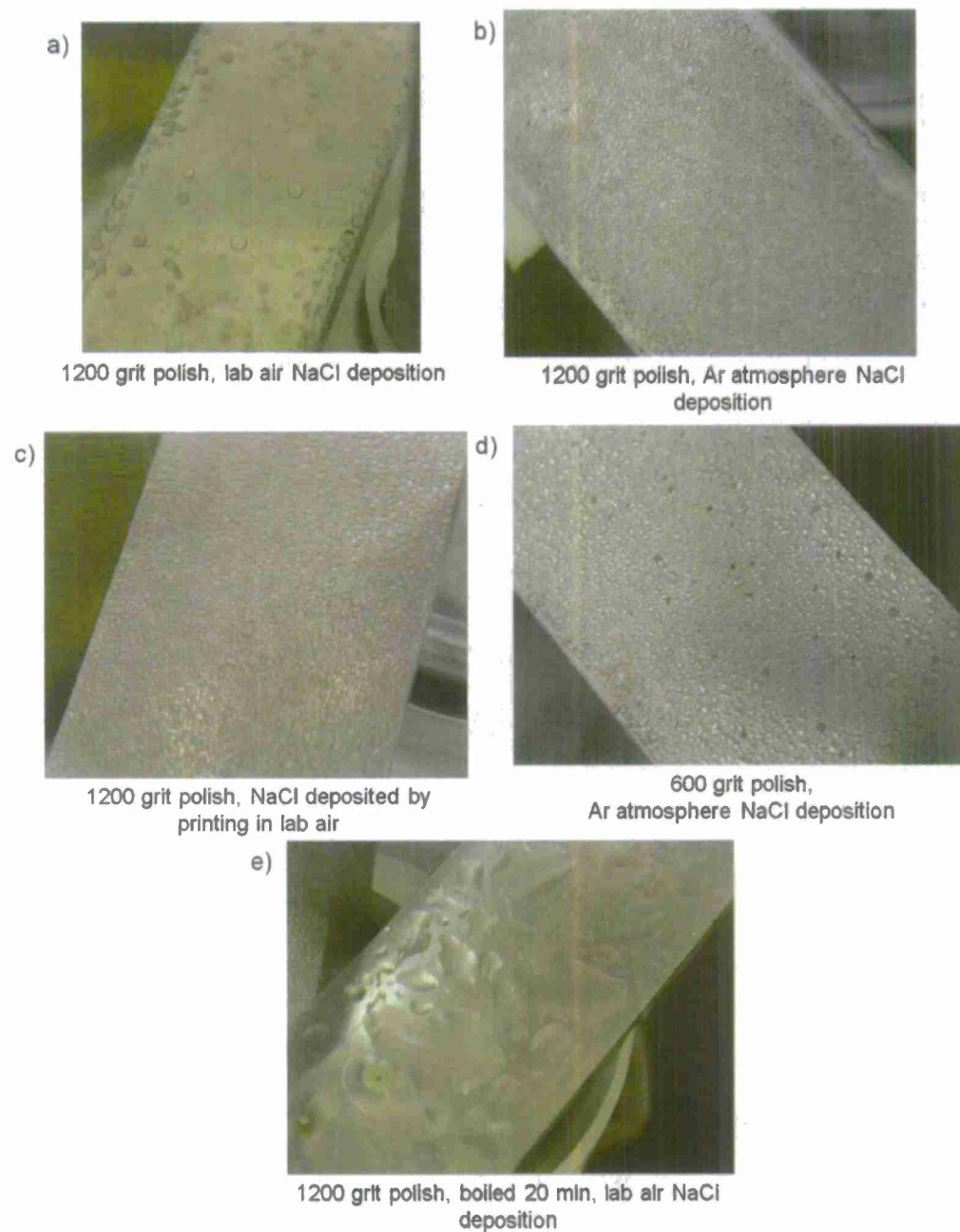


Figure 44. The effect of surface preparation and environment control on NaCl solution wetting on a C47A-T86 SEN specimen surface which was not plasma cleaned.

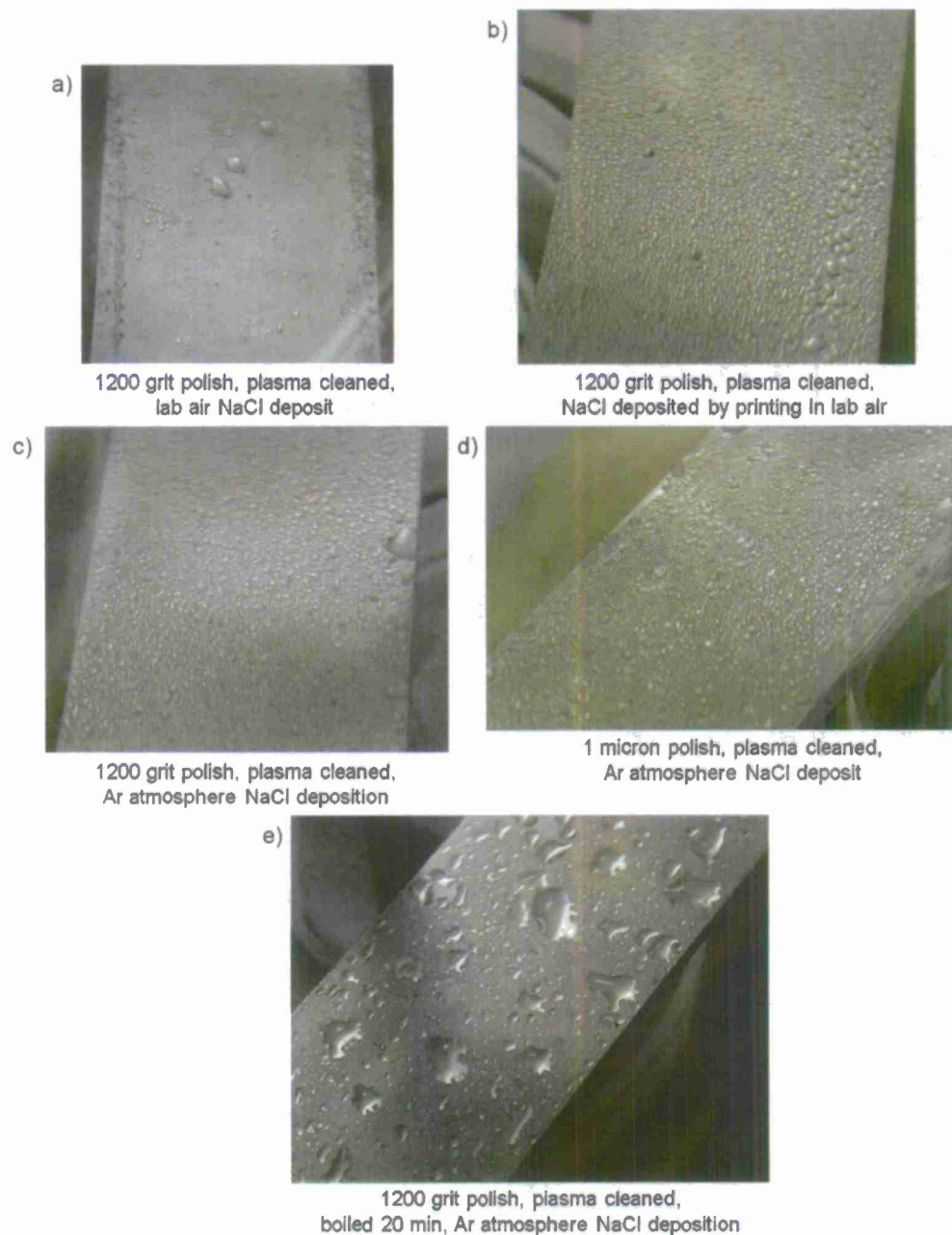


Figure 45. The effect of surface preparation and environment control on NaCl solution wetting on a C47A-T86 SEN specimen surface which was plasma cleaned.

## 1.6.5 Results

### 1.6.5.1 Surface Electrolyte Stability

The stability of surface electrolyte droplets depends on the applied DCPD current because surface heating causes evaporation of the electrolyte. For an applied DCPD current of 6 A and greater, macroscopic observations of the sort shown in Figure 44 and Figure 45 established that the droplets dry during fatigue testing. This drying began as the specimen temperature reached and exceeded  $\sim 28.5^\circ\text{C}$ , as shown in Figure 46. Calculations establish that the condensation temperature of the metal surface is  $27.4^\circ\text{C}$  for a sodium chloride solution, when the external RH is 97% and temperature inside the fatigue cell is  $23^\circ\text{C}$ . As such, surface temperatures of  $27.5^\circ\text{C}$  and higher cause the surface electrolyte to evaporate, at equilibrium, even though RH is above the deliquescent point. At applied currents of 5 A and below, the measured SEN surface temperature never exceeded  $28^\circ\text{C}$ . The DCPD current was maintained at 5 A for all fatigue experiments so that the SEN surface did not exceed this evaporation temperature for all atmospheric experiments reported here.

Figure 47 confirms that the surface electrolyte completely dried at higher DCPD currents. The salt-free data ( $\bullet$ ) in Figure 47 were generated by Ro et al. for Al-Cu-Mg alloy C433-T351 tested under varying levels of high purity water vapor pressure in a high vacuum system<sup>15, 16</sup>. The solid lines represent trends from water molecule transport and H diffusion models<sup>15, 16</sup>. For the atmospheric case, NaCl was deposited on a C433-T351 specimen so as to produce heterogeneous droplets. The specimen was cyclically stressed with an applied current of 12 A; all  $da/dN$  data ( $\circ$ ) fit along the trend line observed by Ro et al. when plotted with the  $P_{\text{H}_2\text{O}}$  corresponding to an RH of 97.3%. This comparison shows that for all data generated on the salt deposited specimen,  $P_{\text{H}_2\text{O}}/f$  is the controlling parameter implying either the electrolyte never interacted with the crack or there is no electrolyte due to drying of the SEN specimen surface. As the crack was grown over 6 mm, an  $a/W$  of 0.6, and crack length versus cycles data were linear, the later is most likely and consistent with the observed droplet evaporation at such high-applied DCPD currents.

### 1.6.5.2 Atmospheric EFCP and Alloy-Induced Inhibition

Constant  $\Delta K$  - varying  $f$  experiments with pure NaCl-coated SEN specimens show that atmospheric conditions producing heterogeneous and homogenous NaCl droplets on a C47A-T86 surface promote EFCP and hinder alloy-induced inhibition at low  $f$ , but do not drastically increase (or decrease) high- $f$  EFCP rates where alloy-induced inhibition does not occur. For loading at 30 Hz, Figure 48 shows that  $da/dN$  values are essentially equal for all environments including: full immersion in pure NaCl ( $\bullet$ ) and NaCl +  $\text{Na}_2\text{MoO}_4$  ( $\circ$ ), atmospheric exposure with pure NaCl ( $\Delta$  &  $\blacktriangle$ ), and salt-free high humidity air ( $x$ ). In contrast loading at 0.2 Hz, where alloy-induced inhibition is established for C47A-T86<sup>32, 47</sup>,  $da/dN$  is accelerated by the presence of NaCl droplets as compared to full immersion in pure chloride solution, but does not exceed  $da/dN$  measured for a salt free surface stressed in high humidity air ( $x$ ). Notably, the EFCP response is similar for the heterogeneous and homogeneous NaCl droplets produced by atmospheric deliquescence, at each loading frequency examined.





no applied current  
T = 24.6°C



8A  
T = 31.5°C



6A  
T = 29.4°C



5A  
T = 27.6°C

Figure 46. Photographs of salt deposited surfaces of SEN specimens with different applied DCPD currents. The temperature of the specimen at which the picture was taken and applied current are listed under each image.

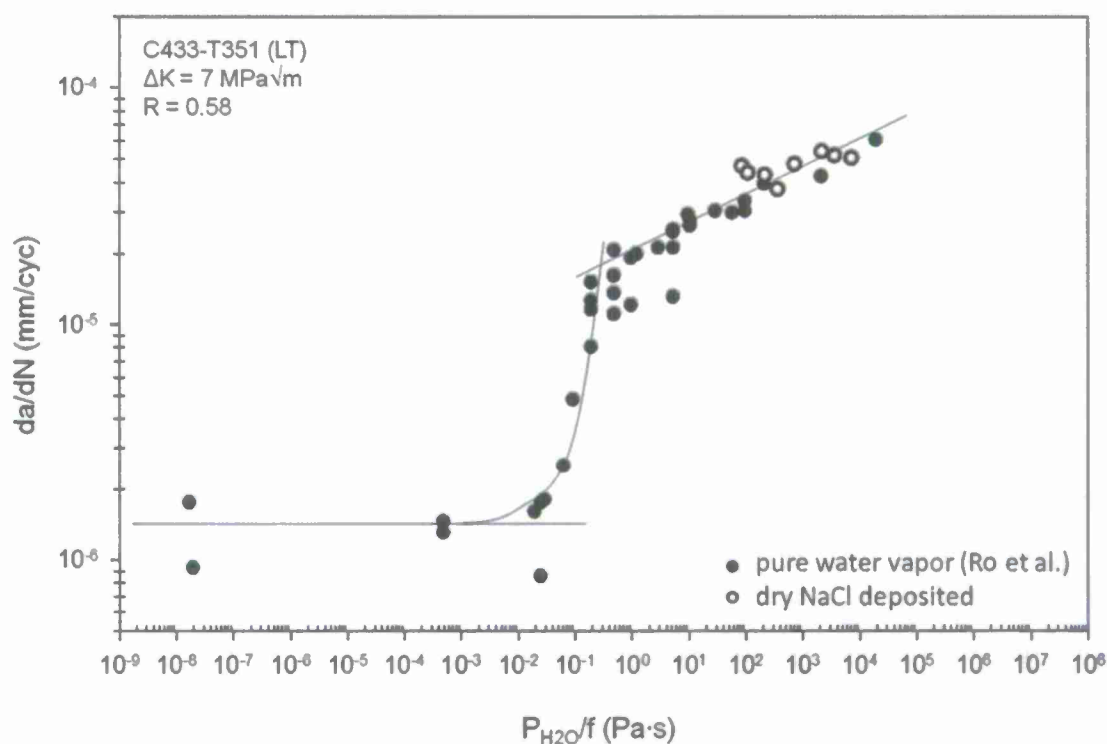


Figure 47. Exposure dependence of  $da/dN$  for C433-T351 (L-T orientation) stressed at a  $\Delta K$  of 7  $\text{MPa}\sqrt{\text{m}}$  and  $R$  of 0.58.

The ● data were generated by Ro et al. in a vacuum fatigue system with additions of pure water vapor<sup>14-16</sup>. The ○ data were for SEN specimens with deposited NaCl and a desired electrolyte layer thickness of 100  $\mu\text{m}$  or volume of 0.1  $\text{L}/\text{m}^2$ , stressed with a maintained pure air RH of 97.3% and applied DCPD current of 12 A.

A wide range of crack growth rates were observed at 0.2 Hz for the NaCl-containing heterogeneous droplets on replicate SEN specimens ( $\Delta$ ). Figure 49 shows a two-fold reduction in  $da/dN$  for crack growth in a single specimen with heterogeneous NaCl droplets under a constant 0.2 Hz  $f$  loading segment. For this loading, two reasonably steady-state growth rate regimes are seen;  $da/dN$  was near that measured for salt free high humidity (x) at  $3.9 \times 10^{-5}$  mm/cyc from a crack depth of 0.8 mm to 2.2 mm over a period of 50 h, when  $da/dN$  changed abruptly to  $1.6 \times 10^{-5}$  mm/cyc which persisted over 60 h to a crack length of 3 mm when the segment was ended. The middle heterogeneous NaCl  $da/dN$  data point ( $\Delta$ ) was measured on a separate specimen and did not show a  $da/dN$  shift during growth in the segment. The occurrence of a range of measured  $da/dN$  and changing  $da/dN$  mid-segment is unique to atmospheric conditions producing both heterogeneous and homogeneous droplets, and was not seen in previous studies under full immersion conditions<sup>32, 33, 47, 54</sup>. Causes for this behavior will be addressed in the Discussion. Figure 50 illustrates steady state EFCP over a crack length change of 1.3 mm for the condition where such behavior is expected; that is, for homogeneous droplets and a very short test time of 0.24 h at 30 Hz. Steady state EFCP was also observed for prolonged loading (57 h) at 0.2 Hz, where a stable  $da/dN$  of  $2.4 \times 10^{-5}$  mm/cyc was maintained over 1 mm of crack extension. This EFCP rate, measured under both homogenous

( $\blacktriangle$ ) and heterogeneous (middle  $\Delta$  at 0.2 Hz) droplet morphologies, is greater than that for alloy-induced inhibition of EFCP on C47A ( $\bullet$ ), but less than that observed for a salt-free high humidity (x) environment.

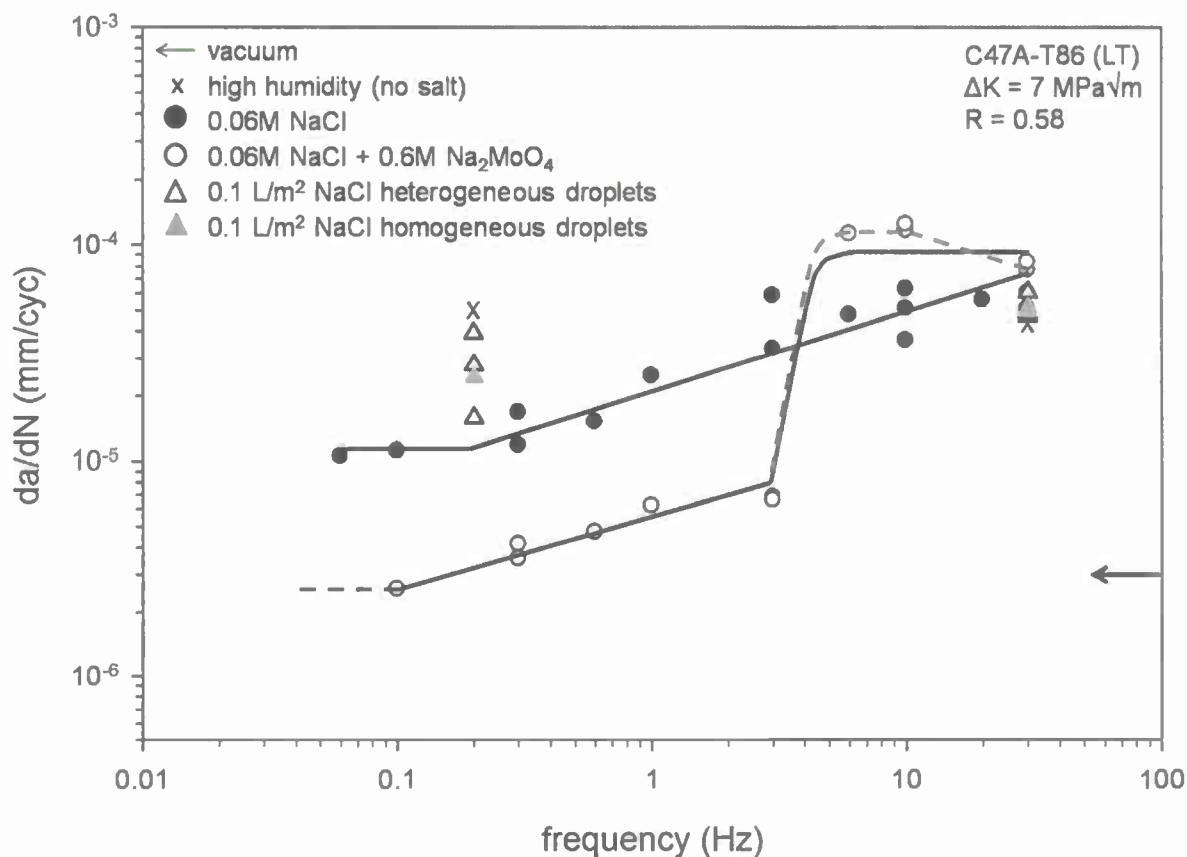


Figure 48. Loading frequency dependence of  $da/dN$  for C47A-T86 (L-T orientation) stressed at a constant  $\Delta K$  of 7 MPa $\sqrt{m}$  and  $R$  of 0.58.

Results were obtained for: (a) full immersion in aqueous chloride-molybdate solutions ( $\bullet$  and  $\circ$ ) and (b) atmospheric conditions at an RH of 97.3% producing heterogeneous ( $\Delta$ ) and homogeneous ( $\blacktriangle$ ) droplets with a total surface electrolyte volume of 0.1 L/m<sup>2</sup> and [NaCl] = 0.79M. The solid and dashed trend lines offer two possible interpretations for the full immersion NaCl + Na<sub>2</sub>MoO<sub>4</sub> data. The viability of these two trends is presented in the Discussion.

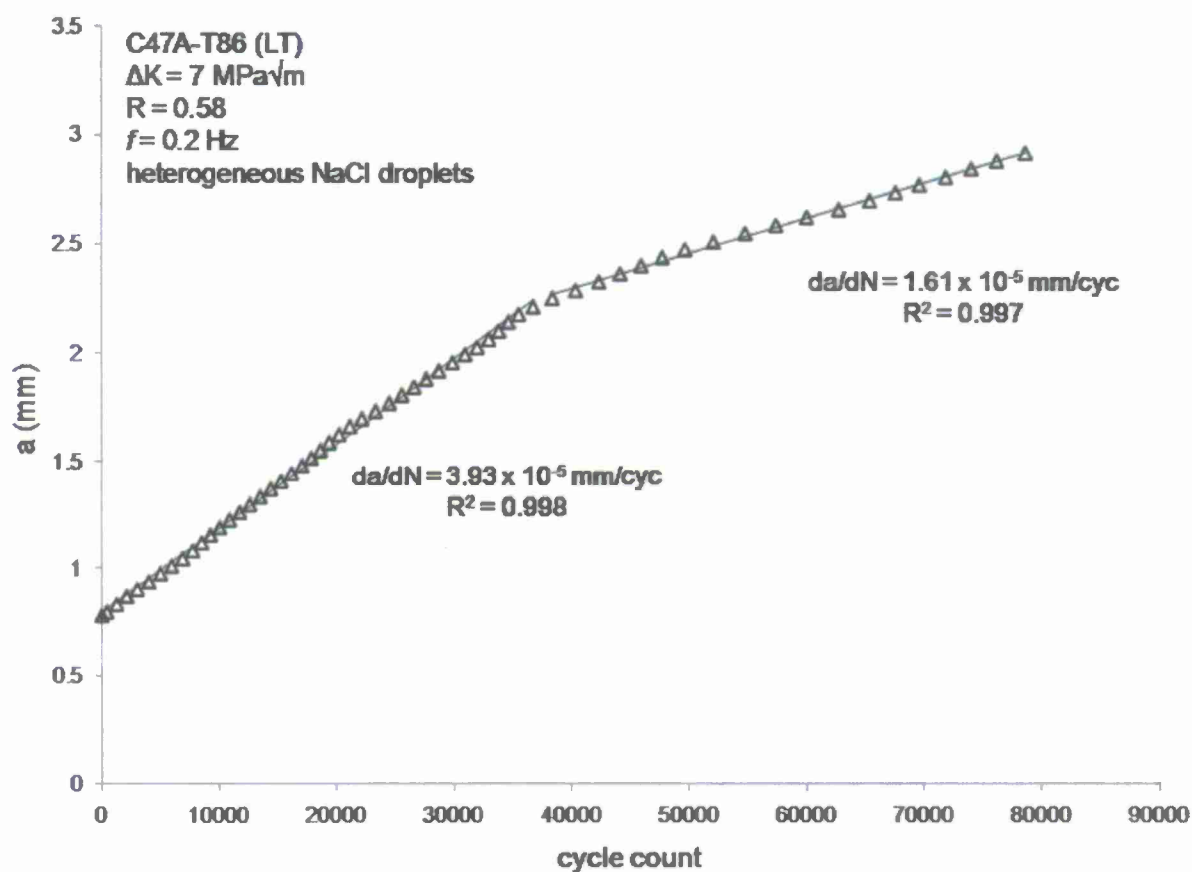


Figure 49. Crack length versus cycles data for C47A-T86 (L-T) loaded at  $\Delta K$  of  $7 \text{ MPa}\sqrt{\text{m}}$ ,  $R$  of  $0.58$ , and  $f$  of  $0.2 \text{ Hz}$  under atmospheric conditions producing heterogeneous NaCl droplets with a total surface electrolyte volume of  $0.1 \text{ L/m}^2$  and  $[\text{NaCl}] = 0.79\text{M}$ . The data shown are for the highest and lowest heterogeneous droplet data points ( $\Delta$ ) in Figure 48 at  $0.2 \text{ Hz}$ .



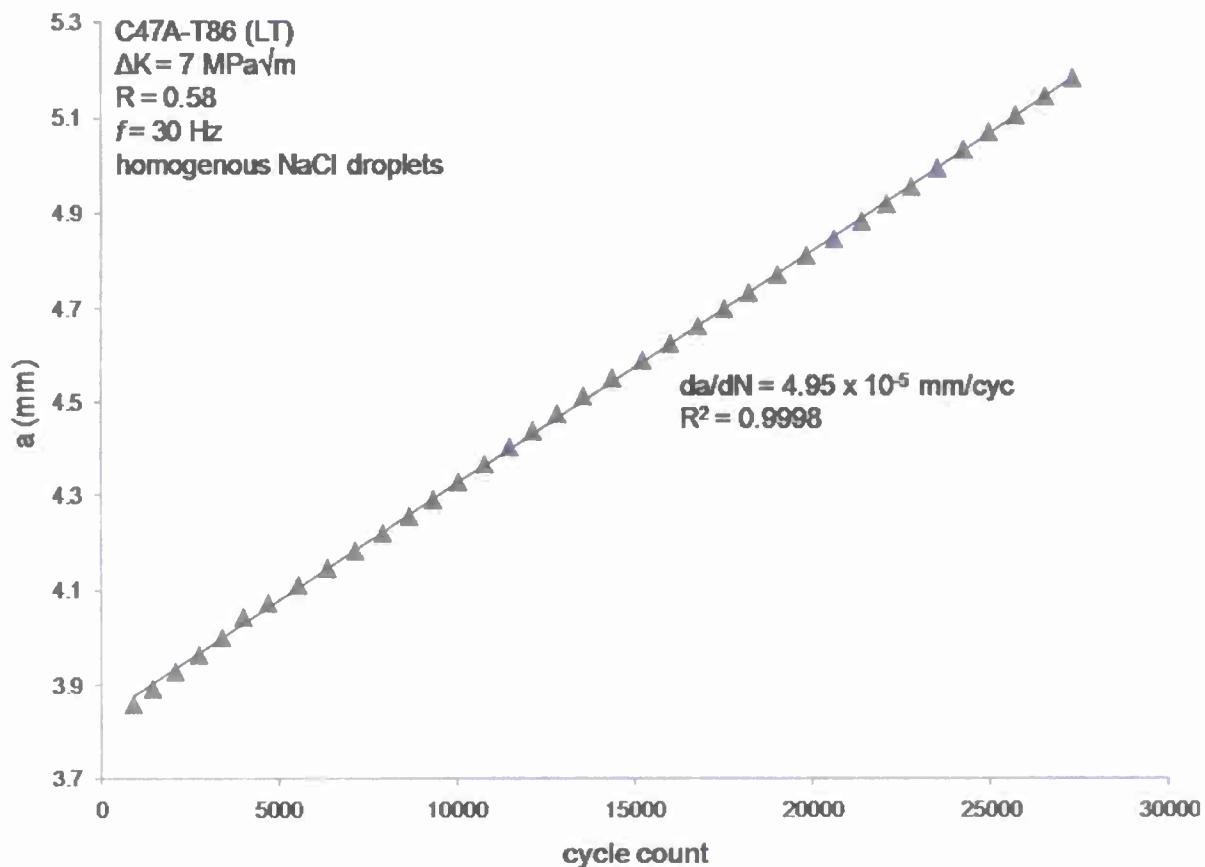


Figure 50. Crack length versus cycles data for C47A-T86 (L-T) loaded at  $\Delta K$  of  $7 \text{ MPa}\sqrt{\text{m}}$ ,  $R$  of 0.58, and  $f$  of 30 Hz under atmospheric conditions producing homogeneous NaCl droplets with a total surface electrolyte volume of  $0.1 \text{ L/m}^2$  and  $[\text{NaCl}] = 0.79\text{M}$ .

### 1.6.5.3 Molybdate Ion-Assisted Inhibition Under Atmospheric Exposure

For the low-loading frequency regime, addition of molybdate to heterogeneous NaCl surface droplets provides mild EFCP inhibition with crack growth rates just below the level observed for full immersion alloy-induced inhibition in pure NaCl. Figure 51 shows that  $da/dN$  for heterogeneous droplets containing both NaCl and  $\text{Na}_2\text{MoO}_4$  ( $\star$ ) is lower than that observed for heterogeneous ( $\Delta$ ) and homogeneous ( $\blacktriangle$ ) NaCl-only droplets, but only marginally below the  $da/dN$  trend for full immersion in pure NaCl ( $\bullet$ ) where alloy-induced inhibition was observed<sup>32, 47</sup>. Crack growth rates for Mo-containing heterogeneous surface droplets ( $\star$ ) are  $\sim 4$  times faster at 0.2 Hz than those for full immersion in  $0.06\text{M NaCl} + 0.6\text{M Na}_2\text{MoO}_4$  ( $\circ$ ). The stability of  $da/dN$  for this 0.2 Hz heterogeneous NaCl +  $\text{Na}_2\text{MoO}_4$  containing droplet environment is shown in Figure 52. Specific values of  $da/dN$  fluctuate slightly around  $8.3 \times 10^{-6} \text{ mm/cyc}$ , but maintain an  $R^2$  value of 0.996 for over 3.5 mm of crack extension during 425 h of loading. This establishes that the experimental technique is stable and steady state EFCP is achieved. Moreover, relative to pure water vapor and pure NaCl, some EFCP inhibition is achieved by the presence of molybdate.

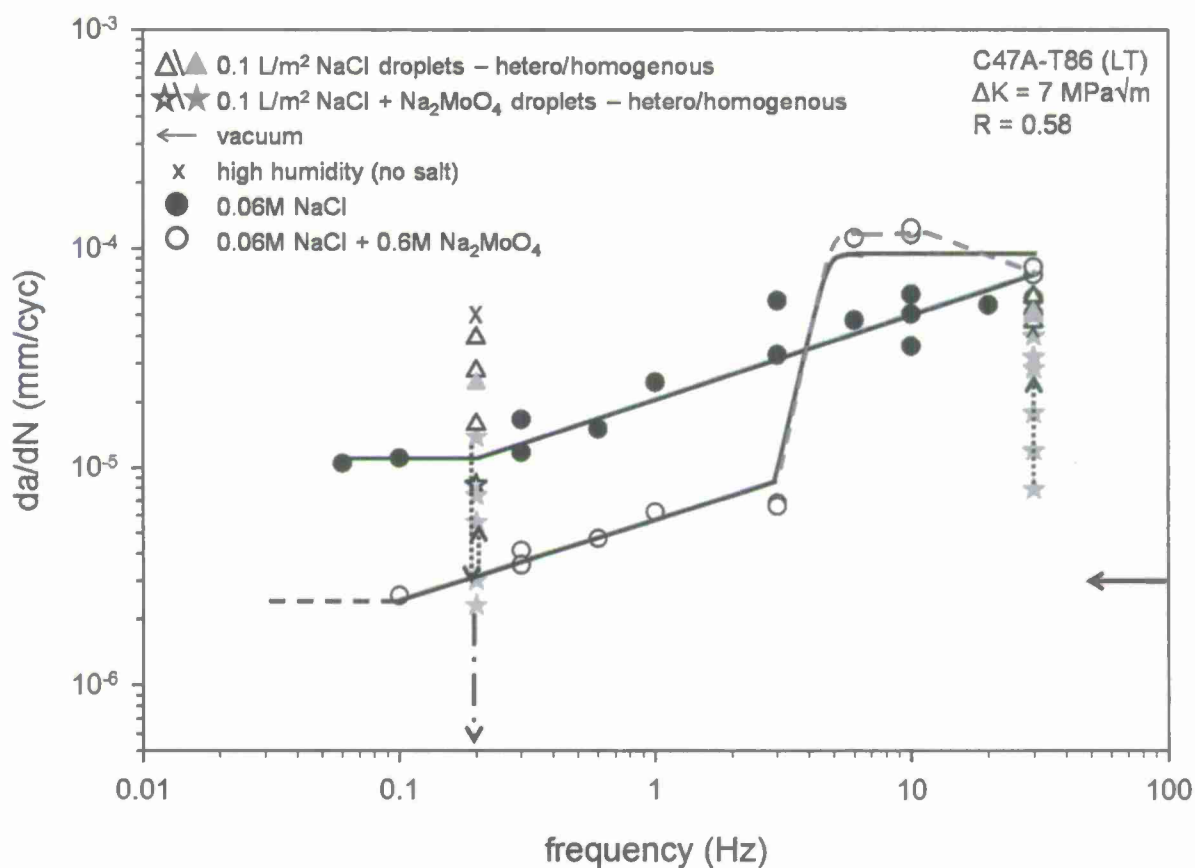


Figure 51. Loading frequency dependence of  $da/dN$  for C47A-T86 (L-T) stressed at  $\Delta K$  of 7 MPa $\sqrt{\text{m}}$  and  $R$  of 0.58 under:

full immersion in: aqueous chloride-molybdate solutions ( $\bullet$  and  $\circ$ ) and under atmospheric conditions at an RH of 97.3% which produce heterogeneous ( $\Delta$ ) and homogeneous ( $\blacktriangle$ ) NaCl droplets (total surface electrolyte volume of 0.1 L/m<sup>2</sup> and [NaCl] = 0.79M) and heterogeneous ( $\star$ ) and homogeneous NaCl + Na<sub>2</sub>MoO<sub>4</sub> ( $\blackstar$ ) (total surface electrolyte volume of 0.1 L/m<sup>2</sup> and [NaCl] = 0.06M and [Na<sub>2</sub>MoO<sub>4</sub>] = 0.6M). The solid and dashed trend lines offer two possible interpretations for the full immersion NaCl + Na<sub>2</sub>MoO<sub>4</sub> data. The viability of these two trends is presented in the Discussion.

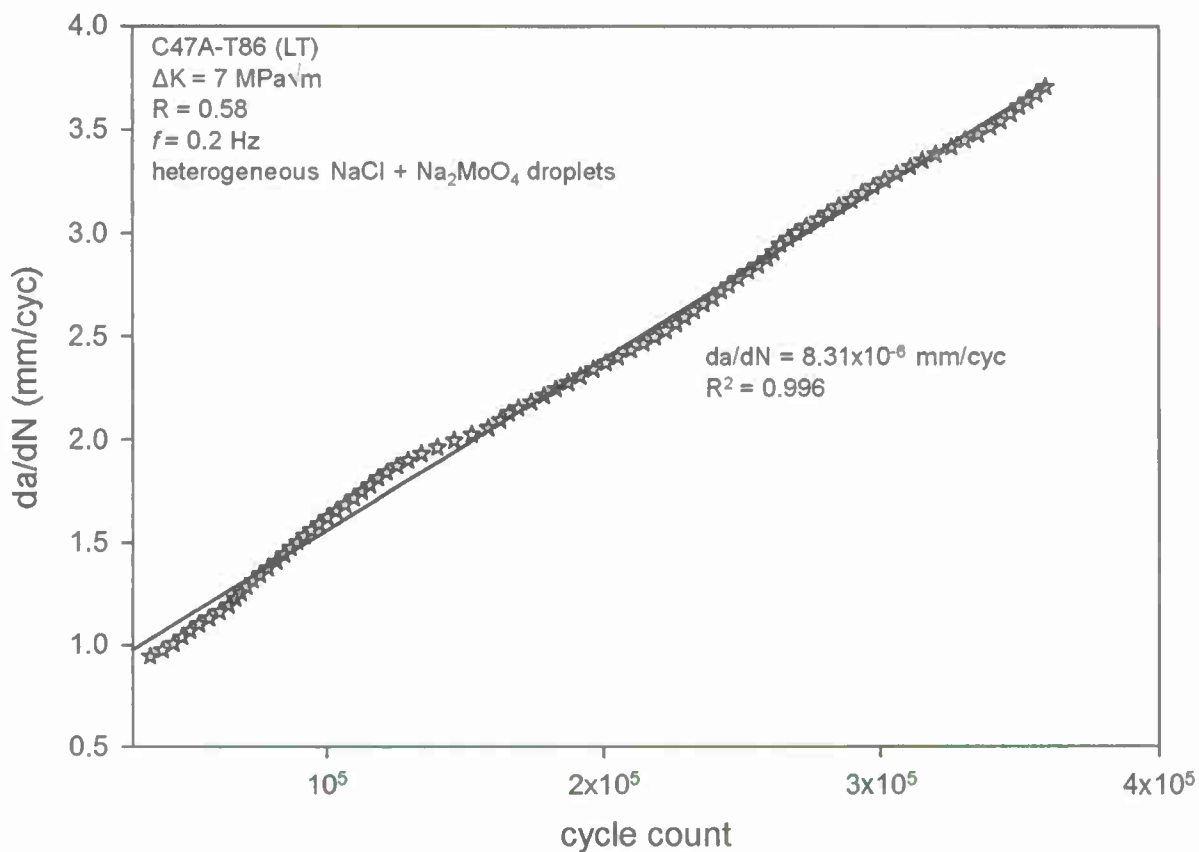


Figure 52. Crack length versus loading cycles data for C47A-T86 (L-T) loaded at  $\Delta K$  of 7 MPa $\sqrt{\text{m}}$ ,  $R$  of 0.58, and  $f$  of 0.2 Hz under atmospheric conditions corresponding to those in Figure 51 where heterogeneous NaCl + Na<sub>2</sub>MoO<sub>4</sub> droplets (☆) were produced.

Molybdate-containing homogeneous droplets effectively inhibit EFCP by completely eliminating the effect of environment at low  $f$  and substantially decreasing  $da/dN$  at a high  $f$  of 30 Hz, as established in Figure 51 (☆). For one segment at 0.2 Hz,  $da/dN$  was initially rapid, then slowed over the first 0.65 mm of extension to that typical of ultra high vacuum ( $3.0 \times 10^{-6} \text{ mm/cyc}$ ); but after 0.5 mm of crack extension at vacuum  $da/dN$ , the growth rate increased to  $5.5 \times 10^{-6} \text{ mm/cyc}$ . This behavior is represented by the dotted arrows at 0.2 Hz in Figure 51 and detailed in Figure 53. For a second SEN experiment at 0.2 Hz, the black dashed-dotted downward arrow in Figure 51 indicates crack arrest, as justified in Figure 54. After crack arrest, which occurred on two separate events, a substantial amount of time under 30 Hz loading was required for crack growth to restart and recover to  $da/dN$  levels typical of the 30 Hz data points in Figure 51.

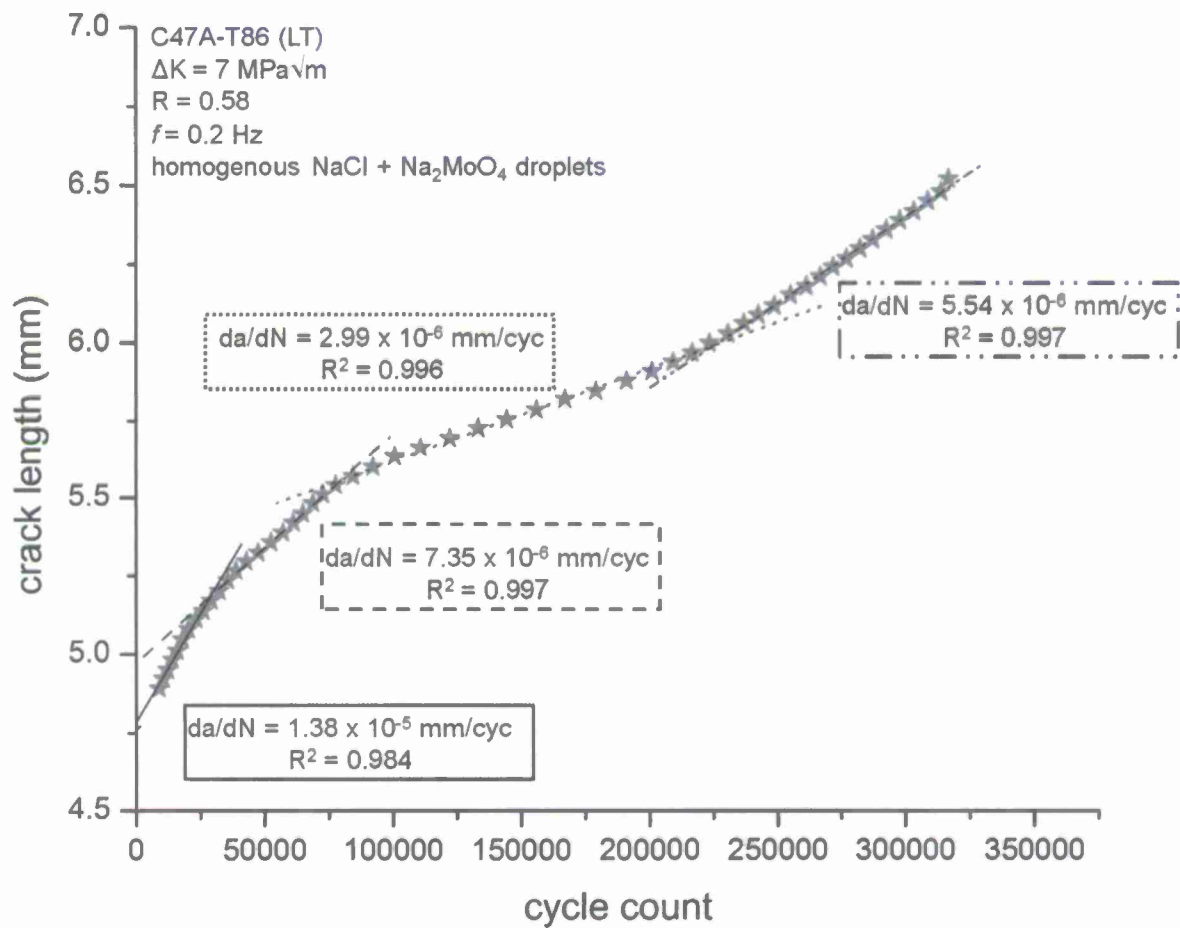


Figure 53. Crack length versus cycles data for C47A-T86 (L-T) loaded at  $\Delta K$  of  $7 \text{ MPa}\sqrt{\text{m}}$ ,  $R$  of 0.58, and  $f$  of 0.2 Hz under atmospheric conditions with a  $\text{NaCl} + \text{Na}_2\text{MoO}_4$  deposited specimen covered by homogeneous deliquesced droplets.

The data correspond to the  $da/dN$  values in Figure 51 connected by the dotted arrow.



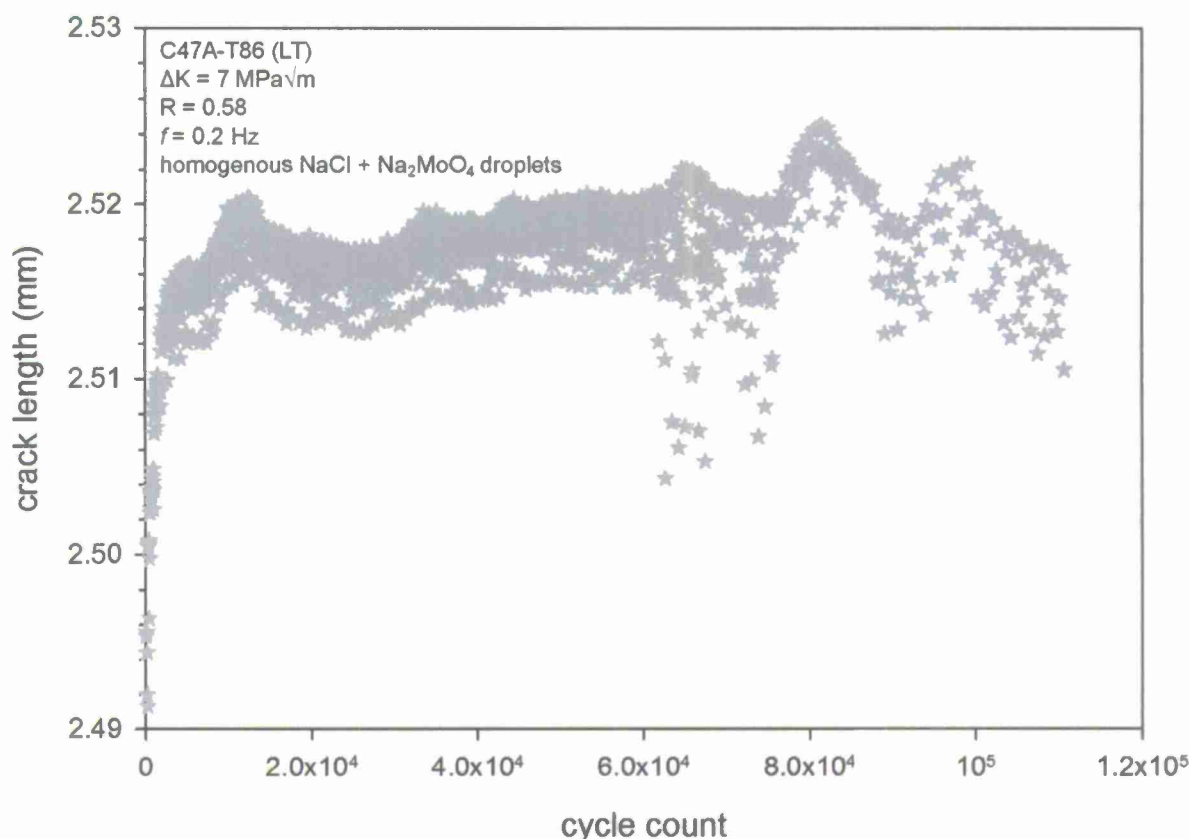


Figure 54. Crack length versus cycles data for C47A-T86 (L-T) loaded at  $\Delta K$  of 7 MPa $\sqrt{m}$ ,  $R$  of 0.58, and  $f$  of 0.2 Hz under atmospheric conditions with a NaCl + Na<sub>2</sub>MoO<sub>4</sub> deposited specimen and homogeneous deliquesced droplets.

The data correspond to the  $da/dN$  value and black dashed downward pointing arrow at 0.2 Hz in Figure 51.

A range in the measured  $da/dN$  was observed under 30 Hz loading for the homogeneous NaCl + Na<sub>2</sub>MoO<sub>4</sub> droplets (★), just as at 0.2 Hz (see Figure 51). The lowest observed  $da/dN$  was  $7.9 \times 10^{-6}$  mm/cyc which is an order of magnitude lower than  $da/dN$  measured at 30 Hz under full immersion in 0.06M NaCl + 0.6M Na<sub>2</sub>MoO<sub>4</sub> (○), while the highest  $da/dN$  was  $4.0 \times 10^{-5}$  mm/cyc which is near that for salt-free high humidity (x) and full immersion in pure NaCl (●) experiments. Figure 55 shows crack length versus loading cycle data for homogeneous Mo-containing droplets where  $da/dN$  is linear for 2 mm of crack extension (0.6 h segment) for this fixed  $\Delta K$  and  $f$ . In contrast Figure 56 shows crack length versus loading cycle data for a specimen which provided the lowest  $da/dN$  at 30 Hz. The crack growth rate was  $7.9 \times 10^{-6}$  mm/cyc for 0.6 mm (0.7 h) and then increased with increasing crack length to between  $1.8 \times 10^{-5}$  and  $2.8 \times 10^{-5}$  mm/cyc for the remaining 1.8 mm (0.8 h) of crack growth in this segment. This behavior is indicated by the dotted arrow at 30 Hz in Figure 51.

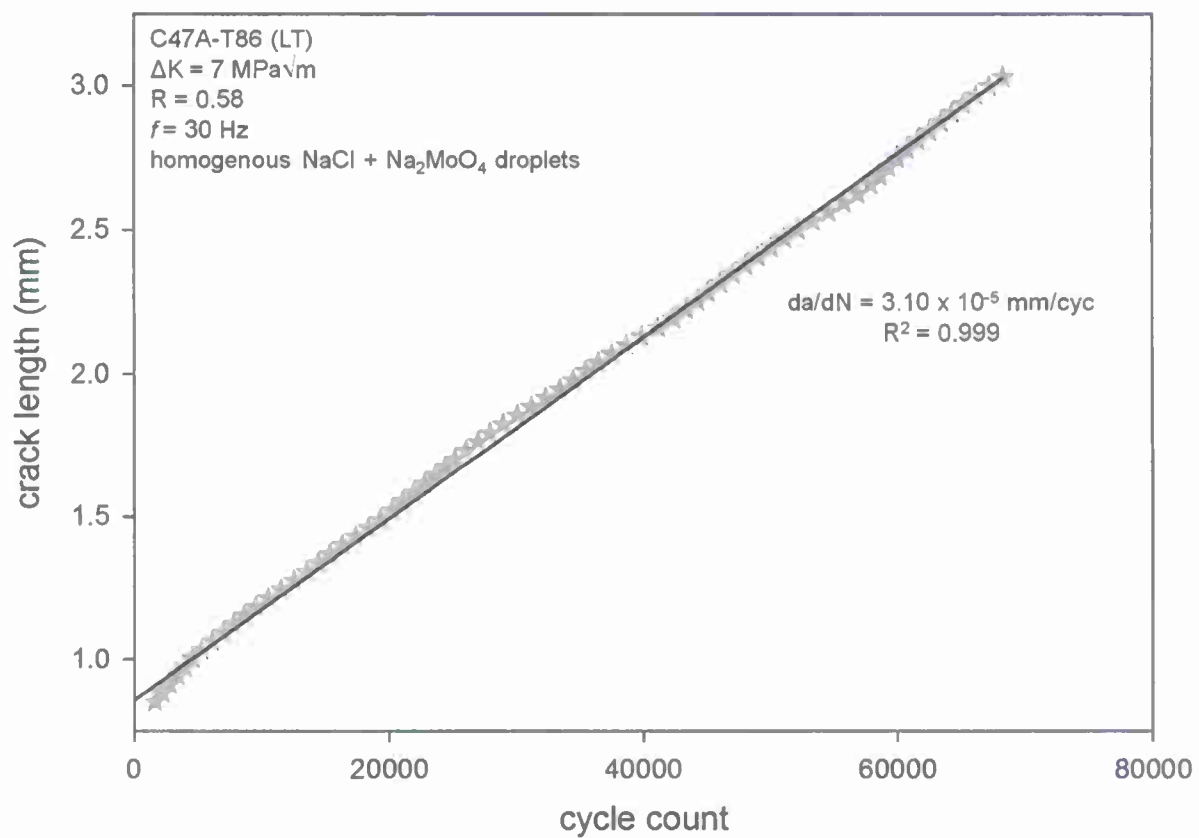


Figure 55. Crack length versus loading cycles data for C47A-T86 (L-T orientation) loaded at a constant  $\Delta K$  of  $7 \text{ MPa}\sqrt{\text{m}}$ ,  $R$  of 0.58, and  $f$  of 30 Hz under atmospheric conditions corresponding to those in Figure 51 for a  $\text{NaCl} + \text{Na}_2\text{MoO}_4$  deposited specimen with homogeneous deliquesced droplets.

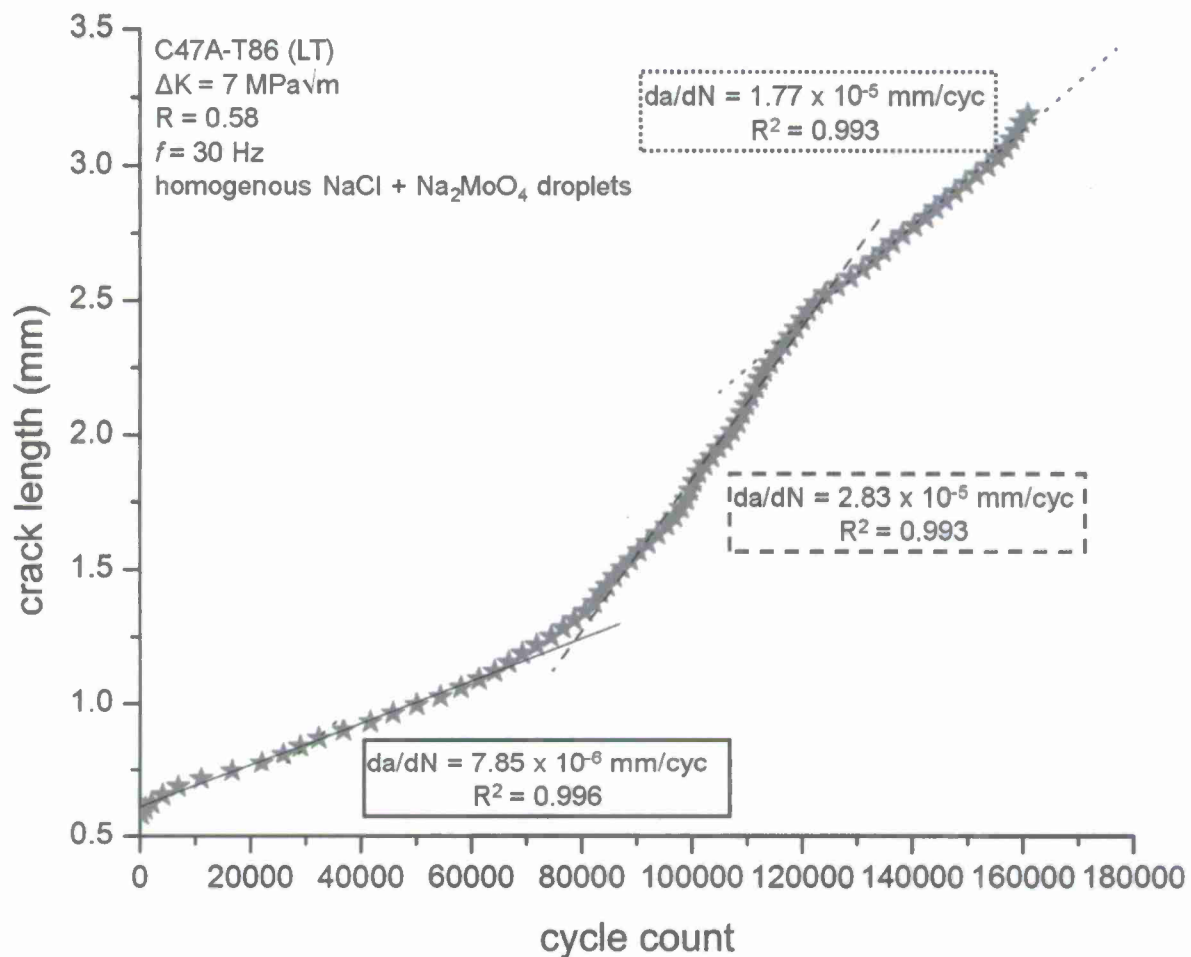


Figure 56. Crack length versus cycles data for C47A-T86 (L-T) loaded at  $\Delta K$  of 7 MPa $\sqrt{\text{m}}$ ,  $R$  of 0.58, and  $f$  of 30 Hz under atmospheric conditions with a NaCl + Na<sub>2</sub>MoO<sub>4</sub> deposited specimen and homogeneous deliquesced droplets. These data correspond to the  $da/dN$  values connected by the dotted arrow in Figure 51 at 30 Hz.

#### 1.6.6 Discussion

This research establishes a technique for quantitatively measuring rates of EFCP under atmospheric conditions which more accurately describe conditions encountered by aircraft than typical laboratory test environments by promoting deliquesced surface electrolyte layers/droplets. The  $da/dN$  results presented in Figure 48 are among the first reported for this important environmental condition. Presently, the existence of surface droplets of varying distribution and size, rather than a uniform electrolyte layer and changes in droplet morphology during long term fatigue loading, limit this type of experimentation to constant stress intensity loading where crack growth rate transients and steady state can be assessed.

Changes in the droplet morphology and/or the degree to which the crack is filled with electrolyte as it intersect droplets during a standard increasing/decreasing  $\Delta K$  experiment can compromise the steady state character of the EFCP kinetics, and use of such transient  $da/dN$ , rather than steady state data in either scientific mechanism studies or fracture mechanics life prediction could lead to erroneous conclusions. A variety of atmospheric-surface conditions were encountered during this well controlled laboratory study suggesting that a range of surface electrolytes may be encountered in various parts of an airframe under flight conditions. Additional test method development and airframe environment characterization are required to address issues of these atmospheric environment characteristics and impacts on crack growth rate. This first examination illustrates the impact of varying surface conditions, resulting from atmospheric exposure, on  $da/dN$  and EFCP inhibition; and establishes a test method that can be used as a start for understanding and quantifying these environments.

#### 1.6.6.1 Atmospheric EFCP

Atmospheric environmental exposure increased fatigue crack growth rates, but only for a single comparison; that is, relative to full immersion exposure to NaCl solution at low loading frequency. At this low loading frequency, atmospheric EFCP was essentially equal to or lower than values typical of humid nitrogen; humid nitrogen produces  $da/dN$  up to 5 times greater than full immersion in NaCl. At high loading frequency, each environment investigated produced  $da/dN$  levels that were essentially similar. These behaviors, as well as nuances in EFCP rates are understood based on time-cycle dependent HEE as described in detail below.

#### High Frequency Behavior

Compared to conventional environments under high frequency loading, atmospheric exposure with chloride does not drastically increase or decrease the rates of EFCP for the peak aged Al-Cu-Li alloy C47A-T86 loaded at 30 Hz,  $\Delta K$  of 7 MPa $\sqrt{m}$ , and R of 0.58. As shown in Figure 48, fatigue crack growth rates in the presence of NaCl-containing droplets, both heterogeneous and homogeneous dispersions ( $\Delta$  &  $\blacktriangle$ ), essentially equal those measured under full immersion in NaCl ( $\bullet$ ) and salt-free high humidity experiments ( $\times$ ). When Na<sub>2</sub>MoO<sub>4</sub> is added to solution in full immersion testing,  $da/dN$  is slightly increased over full immersion NaCl at 10 and 6 Hz, as can be seen in Figure 48 and Figure 51. It has been established that this increase in  $da/dN$  is due to molybdate inhibiting alloy-induced inhibition which occurs in Al-Cu-Mg and Al-Cu-Li alloys<sup>70</sup>. At 30 Hz, at or near the upper bound critical frequency for alloy-induced inhibition where the crack tip strain rate is sufficient to completely destabilize the protective crack tip passive film<sup>70</sup>, all environments tested in this study exhibit comparable crack growth kinetics.

One explanation for this behavior is Scenario c in Figure 42, where electrolyte droplets never interact with the crack. In this case,  $da/dN$  should equal that for a salt-free high humidity experiment where the crack tip contains water vapor or capillary-condensed water only without chloride. However, deliquesced electrolyte likely penetrated the fatigue crack during atmospheric exposure because full immersion in NaCl ( $\bullet$ ) produced a level of  $da/dN$  at 30 Hz equal to the values measured for cracking with both heterogeneous and homogeneous dispersions of NaCl droplets. Moreover, cracking at low frequencies is clearly different for the droplet case compared to moist nitrogen. As such, atmospheric results may be better explained by droplets interacting with the crack to electrochemically produce H available for diffusion to the FPZ.



Invariant  $da/dN$  with changing external environment can be explained by the HEE mechanism. The HEE mechanism predicts that  $da/dN$  for a given loading and environmental exposure depends on three time-dependent steps which establish the FPZ H concentration: a) transport of the environmental species from the bulk environment to the crack tip reaction sites, b) crack tip surface chemical or electrochemical reaction producing H, and c) diffusion of atomic H within the metal to crack tip FPZ damage sites<sup>10</sup>. Even if electrolyte droplets do not interact with the crack, the high humidity in the fatigue cell should ensure that step a) is not rate limiting for the various environments indicated in Figure 48<sup>14</sup>. As such, an environmental exposure independence of  $da/dN$  could be due to: 1) saturation of the surface reaction producing a constant crack surface H concentration for each bulk environment, following Wei et al.<sup>10, 18, 40</sup>; or 2) sufficient H diffusion at a fixed  $\Delta K$ ,  $R$ , and  $f$  providing the required-critical H in the FPZ for maximum damage while surface reaction product  $[H]$  increases<sup>3, 4, 10, 14-16</sup>.

Research by Ro et al. on this same lot of C47A-T86 stressed in pure water vapor at the same constant  $\Delta K$  and  $R$  conditions as this study evidenced exposure independent  $da/dN$  at high  $P_{H_2O}/f$ <sup>14-16</sup>. Ro et al. attributed this exposure independent regime to either saturation of the surface H producing reaction (1 above), or a H diffusion limitation argument where a constant maximum  $[H]$  is achieved in the FPZ at constant  $f$  (2 above)<sup>14-16</sup>. Specific results are shown in Figure 57, including the Ro et al.  $da/dN$  versus  $P_{H_2O}/f$  data ( $\circ$ ), full immersion NaCl and NaCl + Na<sub>2</sub>MoO<sub>4</sub> data ( $\bullet$  and  $\star$ ), and atmospheric  $da/dN$  for heterogeneous ( $\Delta$  and  $\diamond$ ) and homogeneous ( $\blacktriangle$  and  $\blacklozenge$ ) NaCl-only droplets on SEN specimens loaded at 30 Hz. For the full immersion data, an effective  $P_{H_2O}$  was chosen ( $1.7 \times 10^6$  Pa) based on the assumption that this  $P_{H_2O}/f$  is the lowest value possible for a logical-consistent fit of the full immersion with the water vapor  $da/dN$  values from Ro et al.<sup>14-16</sup>. (The decline in  $da/dN$  with increasing exposure parameter for full immersion ( $\bullet$  and  $\star$ ) is attributed to alloy-induced and ion-assisted inhibition reducing H. This is not captured by a single effective  $P_{H_2O}$  due to changing crack surface electrochemistry and H production<sup>47, 70, 71</sup>.) The atmospheric data were plotted as a range bounded by the effective  $P_{H_2O}$  for full immersion ( $\diamond$  and  $\blacklozenge$ ) and the measured RH within in the fatigue cell during testing (97.3%:  $\Delta$  and  $\blacktriangle$ ) which should represent the lowest possible  $P_{H_2O}$ . From examination of Figure 57, the data for full immersion NaCl + Na<sub>2</sub>MoO<sub>4</sub> where alloy-induced and ion-assisted inhibition are not possible (those data points not within the dashed boxes) imply that the exposure independent regime identified by Ro et al. (dashed horizontal black line) does not exist at the exposure levels believed.

Gasem and Gangloff reported a similar plateau  $da/dN$  in the frequency dependence of 7075 loaded under full immersion in aqueous chloride solutions<sup>3, 4</sup>. This constant  $da/dN$  was attributed to sufficient time for the maximum required (critical)  $[H]$  to diffuse to the damage sites within the FPZ at a critical frequency,  $f_{CRIT}$ , defined as the frequency at and below which  $da/dN$  becomes  $f$  independent. Longer times and lower  $f$  had no effect on  $da/dN$  because the critical H concentration required for maximum HEE damage had been reached; and therefore, the rise in FPZ H concentration did not promote additional crack extension increment beyond the critical-distance length set by  $K_{max}$ , independent of the crack tip environmental exposure level<sup>3, 4</sup>. Above  $f_{CRIT}$ ,  $da/dN$  declined due to H diffusion limitation as established by the linear relationship between the plateau  $da/dN$  level and reciprocal  $\sqrt{f_{CRIT}}$ . Figure 48 and Figure 51 show two possible trend lines for the full immersion NaCl + Na<sub>2</sub>MoO<sub>4</sub> data in the solid black and dashed gray lines. These trend lines offer two possible interpretations of the full immersion NaCl-Na<sub>2</sub>MoO<sub>4</sub> data consistent with H diffusion rate limitation: (a) an assumed  $f_{CRIT}$  of 10 Hz, as illustrated by the gray dashed lines, apparent because molybdate inhibited the localized

corrosion process that is responsible for alloy-induced inhibition<sup>47,70,71</sup>; and (b) an assumed  $f_{\text{crit}} > 30$  Hz, illustrated by the black solid lines, with  $da/dN$  differences between 30 Hz,

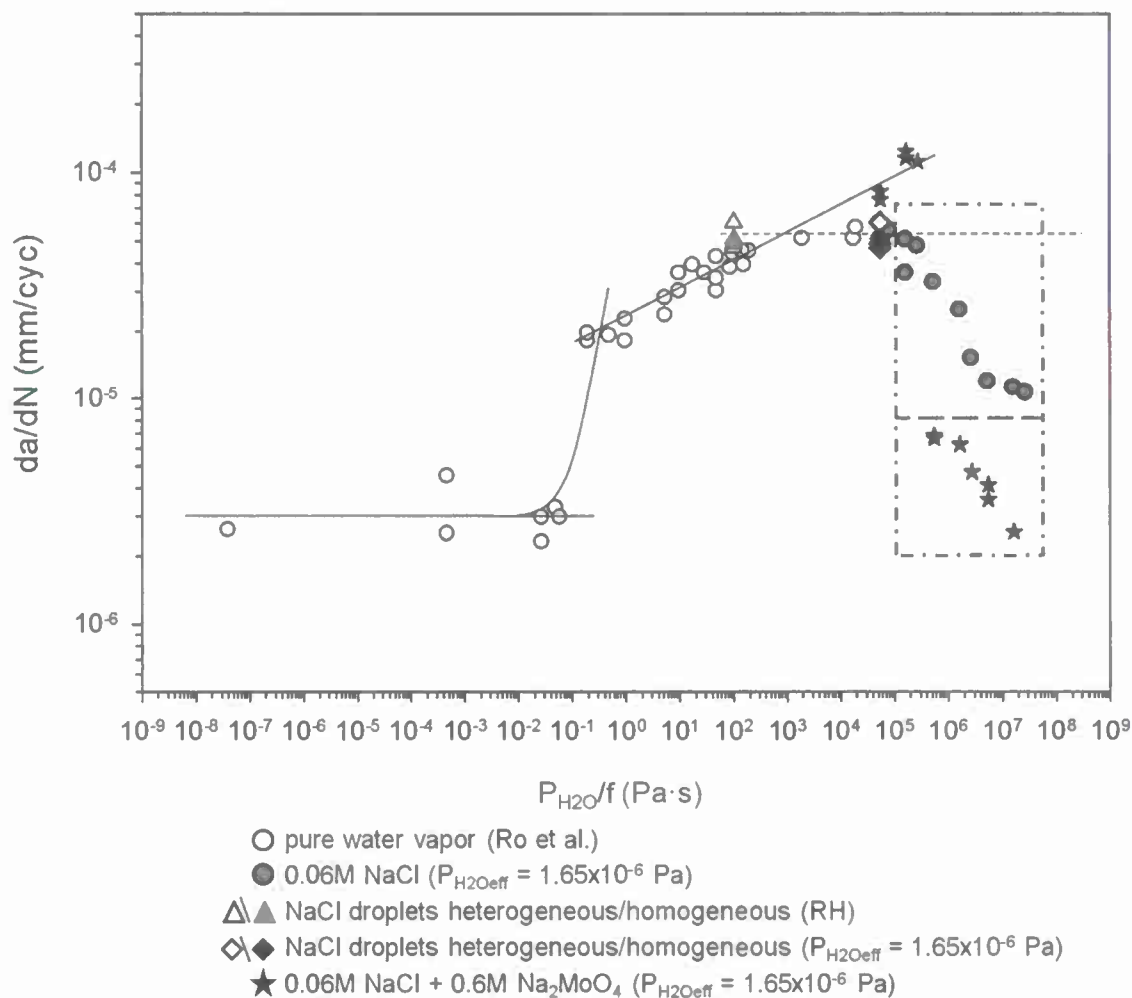


Figure 57. Exposure dependence of  $da/dN$  for C47A-T86 (L-T) loaded at constant  $\Delta K$  of 7  $\text{MPa}\sqrt{\text{m}}$  and  $R$  of 0.58.

The data given by ○ were generated for ultra high vacuum with pure water vapor additions by Ro et al.<sup>14,15</sup>. Full immersion NaCl (●), full immersion NaCl +  $\text{Na}_2\text{MoO}_4$  (★), and atmospheric chloride (△/▲ =  $P_{\text{H}_2\text{O}}$  from RH and ◇/◆ =  $P_{\text{H}_2\text{Oeff}}$ ) data are plotted from Figure 48 with effective  $P_{\text{H}_2\text{O}}$  chosen as described in the Discussion. The boxes enclose full immersion data where alloy-induced<sup>71</sup> or ion-assisted inhibition<sup>70</sup> act to inhibit EFCP and reduce  $da/dN$ . The horizontal dashed line is the exposure independent regime defined by Ro et al.<sup>14-16</sup>.

10 Hz, and 6 Hz loading based on experimental uncertainty. These two interpretations offer different insights regarding the environmental effect at 30 Hz. If  $f_{\text{CRIT}} = 10$  Hz, then the 30 Hz da/dN levels are rate limited by H diffusion to the FPZ damage sites; and as such, all environments (full immersion, high humidity, and atmospheric droplets) must produce similar amounts of crack tip [H] in order to explain the similar degrees of HEE and da/dN which were observed. This interpretation suggests that atmospheric conditions producing electrolyte droplets do not dramatically increase H production and the degree of HEE. If  $f_{\text{CRIT}} > 30$  Hz, then the critical level of FPZ [H] is provided at 30 Hz, independent of the crack surface [H]. As such, crack surface H concentration for the droplet case could be larger, smaller, or equal to the value for full immersion in chloride solution. Additional experiments are required to determine the precise  $f_{\text{CRIT}}$ ; but because Figure 57 indicates that the exposure independent regime does not start at 30 Hz, it is likely at or below 10 Hz. Therefore, the EFCP rates are likely controlled by H diffusion into the FPZ as suggested by the gray dotted lines. This suggests that all environments (full immersion, high humidity, and atmospheric droplets) produce similar degrees of HEE. Stated alternatively, this interpretation suggests that atmospheric conditions producing electrolyte droplets do not dramatically increase H production at the crack tip and thus do not dramatically increase HEE.

### Low Frequency Behavior

Atmospheric EFCP at low frequency is understood based on the interaction of droplets with alloy-induced inhibition which is prevalent for full immersion exposure.

#### *Inhibiting Mechanism*

Inhibition of EFCP for C47A under full immersion chloride solution exposure is critical to the discussion of atmospheric effects with pure chloride and chloride-molybdate droplets. The primary mechanism controlling ion-assisted inhibition by molybdate and alloy-induced inhibition in age-hardenable Al alloys is the film rupture-H embrittlement mechanism<sup>33, 47, 70, 71</sup>. This mechanism attributes inhibition to stabilization of a crack tip passive film which reduces the HEE contribution to fatigue crack propagation by one or more of 3 mechanisms: (a) reduced  $\text{Al}^{+3}$  concentration and hydrolysis resulting in reduced crack acidification and thus a reduced overpotential for H production; (b) reduced exchange current density for cathodic water reduction, owing to the catalytic action of corroding Al and/or the effect of reduced acidification; and (c) acting as a barrier to H uptake<sup>12, 33, 47-50</sup>. Fatigue loading can mechanically destabilize the crack tip passive film by one or more rupture events when the strain accumulated at the crack tip exceeds the critical level required for film rupture (a material property for a given environment); as such, inhibition will cease until sufficient repassivation of the crack tip passive film occurs.

The frequency dependence observed under full immersion, decreasing da/dN with decreasing  $f$ , is a consequence of the interplay between rupture and repassivation of the crack tip passive film. As such, the  $f$ -dependence observed under full immersion can be described as follows: Below  $f_{\text{critLB}}$  (~0.2 Hz for 0.06M NaCl in Figure 48), the crack tip strain rate ( $\dot{\epsilon}_{\text{tip}}$ , which controls the rate of film rupture and is proportional to  $f$  and  $\Delta K^{-3}$ ) is sufficiently low to maintain stability of the crack tip passive film against mechanical damage. For ion-assisted inhibition by molybdate, with isolated rupture events at low frequencies near  $f_{\text{critLB}}$ , crack tip solution conditions are such that molybdate can act as a pH buffer to maintain a neutral to alkaline pH<sup>33, 47</sup>. As  $f$  increases above  $f_{\text{critLB}}$ ,  $\dot{\epsilon}_{\text{tip}}$  is sufficient for mechanical destabilization of the crack tip passive film and rupture occurs leaving the crack tip unprotected until repassivation. As  $\dot{\epsilon}_{\text{tip}}$  increases in this  $f$

regime, repassivation time ( $t_{\text{repass}}$ ) remains the same while the time between rupture events ( $t_{\text{rup}}$ ) decreases causing H production and uptake to increase with increasing  $\dot{\epsilon}_{\text{tip}}$  and  $f$  for a constant  $\Delta K$ . For frequencies at and above  $f_{\text{critUB}}$  (~30 Hz for 0.06M NaCl in Figure 48), the time between rupture events is insufficient to allow a significant amount of the crack tip passive film to repassivate; basically  $t_{\text{repass}}$  is greater than  $t_{\text{rup}}$ , and inhibition is lost. Because the amounts of  $\text{Al}^{3+}$  and  $\text{H}^+$  from hydrolysis increase as  $f$  increases above  $f_{\text{critLB}}$ , pH buffering by molybdate to near neutral pH is overwhelmed and not available to inhibit EFCP<sup>33, 47</sup>.

#### **Atmospheric Alloy-Induced Inhibition**

Crack growth rates, produced at 0.2 Hz loading under atmospheric conditions which produce NaCl-only droplets, ranged from the highest values equivalent to pure water vapor (x) to near those characteristic of alloy inhibited EFCP under full immersion in NaCl (●), as shown in Figure 48. This implies that alloy-induced inhibition of Al-Cu alloys is possible, but less effective, under atmospheric conditions producing NaCl droplets on the bold surface. Alloy-induced inhibition of Al-Cu alloys is attributed to the following electrochemical sequence<sup>47, 71</sup>. For full immersion, dissolution of  $\text{Al}_2\text{CuX}$  precipitates occurs by a dealloying process which first dissolves less noble Al, Mg, and Li resulting in Cu enrichment in and possibly Cu replating onto the crack wake. Crack wake Cu clusters act as strong cathodic reaction sites which increase the cathodic reaction kinetics within the crack and thus increases crack solution  $\text{OH}^-$  concentration. This more alkaline crack pH stabilizes the native passive film which then reduces H production and uptake analogous to the ion-inhibition mechanism<sup>3, 4, 33, 70</sup>. When loaded under full immersion, alloy-induced inhibition was observed for this same lot of C47A-T86 at  $f$  at and below 30 Hz, as shown in Figure 48, Figure 51, and Figure 57<sup>47, 71</sup>.

EFCP associated with NaCl-only droplets loaded at 0.2 Hz (Figure 48) exhibited variable  $da/dN$  and variable degree of alloy-induced inhibition. The ability of 2000-series Al alloys to alloy-induced inhibit EFCP may depend on the degree to which the crack is filled with solution, which is related to the non-ideal wetting conditions which created electrolyte droplets with varying degree of intersection with the growing crack. Figure 49 provides an example of this behavior for heterogeneous NaCl droplets loaded at 0.2 Hz. The  $da/dN$  is initially  $3.9 \times 10^{-5}$  mm/cyc and steady state ( $\Delta$ ), which is equivalent to that measured in a high humidity salt free environment as seen in Figure 48 (x). At a crack depth of ~2.2 mm,  $da/dN$  decreased to  $1.6 \times 10^{-5}$  mm/cyc, approaching the  $da/dN$  expected under full immersion in 0.06M NaCl (● in Figure 48) and showing steady state character. These results imply that the crack was initially void of electrolyte for the first 1.4 mm of cracking, and at ~2.2 mm  $da/dN$  decreased to near that for full immersion inhibition because droplets were intersected and solution filled the crack to some degree.

Variation in the degree of filling can alter H production/uptake and passivity as follows. First, consider changes in H production and uptake, unrelated to passive film stability, as solution volume in the crack changes. As crack-solution volume decreases, the anode to cathode separation is reduced; and therefore, the number of sites producing H near the tip, either by water reduction or proton reduction (after metal ion hydrolysis), will increase. Although the ability of H to diffuse from cathodic reaction sites where produced to the FPZ will limit the impact of anode and cathode separation on  $da/dN$ , cracks which are partially filled will have increased H production near the tip which may at least partially offset the benefit of the crack tip passive film.

The observed variation in alloy-induced inhibition is not likely caused by changes in passive film stability as crack solution volume changes. As both a partially and fully filled crack in C47A-T86



are expected to have a near neutral or even alkaline pH, changes in the degree of filling as a droplet is intersected by a growing crack are not expected to greatly alter the crack pH. (A partially filled crack has near neutral pH because all anodic and cathodic reaction sites are within the crack as explained for scenario b in Figure 42b. A fully filled crack in C47A-T86 has near neutral pH as a result of Cu enrichment along the wake<sup>47, 71</sup>.) Additionally, because the native Al passive film is stable over a wide range of potentials at near neutral pH<sup>72</sup>, changes in crack tip potential as solution volume changes are not expected to affect the stability of the crack tip passive film.

#### ***Atmospheric Ion-Assisted Inhibition***

The results in Figure 51 establish that transport of molybdate to a crack tip from surface electrolyte droplets is possible and subsequent inhibition of EFCP is enhanced for the homogeneous droplet morphology. At 0.2 Hz, molybdate completely eliminated the effect of environment by producing vacuum level da/dN when homogenous droplets containing both NaCl and Na<sub>2</sub>MoO<sub>4</sub> were present on the bold surface (★). Similarly, for homogeneous droplets containing both NaCl and Na<sub>2</sub>MoO<sub>4</sub> under 30 Hz loading, molybdate inhibition was significantly enhanced relative to full immersion as ion-assisted inhibition was not seen for full immersion at 30 Hz ( $f > f_{critUB}$  of 3-6 Hz)<sup>33, 47, 70</sup>. For atmospheric exposures, da/dN was reduced by an order of magnitude at 30 Hz for the lowest measured da/dN. This implies that atmospheric conditions increase  $f_{critUB}$  to above 30 Hz, and  $f_{critLB}$  to above 0.2 Hz; but only under certain circumstances as the results for molybdate inhibition under atmospheric exposures shown in Figure 51 are highly variable.

Enhanced ion-assisted inhibition resulting from atmospheric exposures which produce homogenous droplets on the metal surface may be the result of several factors. First, research shows that under full immersion, ion-assisted inhibition is enhanced by slight anodic polarization of the bold surface<sup>33, 47, 70</sup>. Specifically, a slight anodic polarization resulted in an increased  $f_{critLB}$  and increased  $f$  range over which vacuum level da/dN were observed. If the crack is completely filled with electrolyte, similar to bounding scenario 1 in Figure 42a, the crack tip and crack mouth will be electrochemically connected and anodic polarization will result because the decreased O<sub>2</sub> diffusion distance will increase the potential at the crack mouth<sup>73</sup>. However, while anodic polarization was found to increase  $f_{critLB}$  under full immersion, it had no effect on  $f_{critUB}$ . Therefore, while anodic polarization resulting from complete filling of the crack explains the 0.2 Hz atmospheric results, it does not explain the significantly enhanced inhibition at 30 Hz, and cannot be the sole or primary reason for enhanced inhibition under atmospheric exposures.

Differences in the MoO<sub>4</sub><sup>2-</sup> to Cl<sup>-</sup> concentration ratio between full immersion and atmospheric-surface droplets can explain enhanced inhibition when homogenous droplets are present on the surface. For atmospheric conditions with surface droplets, the Cl<sup>-</sup> and MoO<sub>4</sub><sup>2-</sup> concentrations within the crack solution are controlled by the concentration in an intersected droplet. For 97.3% relative humidity, this droplet concentration is fixed at 0.06M NaCl + 0.6M Na<sub>2</sub>MoO<sub>4</sub>. Therefore, under the atmospheric conditions in this study, the crack tip MoO<sub>4</sub><sup>2-</sup> to Cl<sup>-</sup> concentration ratio is 10. For full immersion, crack tip ion concentrations are due to ion migration, diffusion, and convective mixing. Because of ion migration to maintain electroneutrality, the crack tip becomes supersaturated in Cl<sup>-</sup> and MoO<sub>4</sub><sup>2-</sup>; making the tip MoO<sub>4</sub><sup>2-</sup> to Cl<sup>-</sup> concentration ratio differ from that of the bulk solution<sup>45, 46</sup>. Stress corrosion cracking (SCC) experiments on AA7050 under full immersion in 0.05M NaCl + 0.5M Na<sub>2</sub>CrO<sub>4</sub> measured near crack tip concentrations of Cl<sup>-</sup> and CrO<sub>4</sub><sup>2-</sup> and found 0.4M and 2M respectively<sup>44-46, 74</sup>. So while the bulk has a CrO<sub>4</sub><sup>2-</sup> to Cl<sup>-</sup> concentration ratio of 10, the two times greater mobility of Cl<sup>-</sup> made the ratio 5 at the tip. Chromate has a higher mobility than molybdate (the ionic equivalent

conductance,  $\Lambda$ , for chromate is  $85 \text{ cm}^2/\Omega$  equiv while for molybdate it is  $75 \text{ cm}^2/\Omega$ . Mobility is defined as:  $\Lambda/zF$ ); therefore, this ratio would be even lower if  $\text{MoO}_4^{2-}$  were considered. Additionally, as SCC does not have a convective mixing component in determining crack tip ion concentrations which would increase mixing with the bulk solution; the  $\text{CrO}_4^{2-}$  to  $\text{Cl}^-$  concentration ratio for EFCP may not be as diminished, but still expected to be below that for the bulk solution. Therefore, it is expected that the atmospheric exposures producing surface droplets examined in this study produced a crack tip  $\text{MoO}_4^{2-}$  to  $\text{Cl}^-$  concentration ratio of 10; while the experiments produced under full immersion will have a crack tip  $\text{MoO}_4^{2-}$  to  $\text{Cl}^-$  concentration ratio lower than 10, likely near 5. This higher crack tip solution  $\text{MoO}_4^{2-}$  to  $\text{Cl}^-$  concentration ratio for atmospheric droplets relative to full immersion would be expected to enhance passivation/repassivation and thereby enhance ionic inhibition.

An alternate explanation for enhanced inhibition is that the presence of molybdate ions reduces the overpotential for H production more efficiently than the NaCl-only droplets. This may be possible if crack solution conditions are such that molybdate can buffer to a near-neutral pH over a wider  $f$  range. A chemical buffer maintains a constant pH by consuming or producing  $\text{H}^+$  in order keep equilibrium between the weak acid and conjugate base produced by buffer dissociation. Molybdate acts as a chemical buffer with maximum buffering capacity at a pH  $\sim 7$  or  $\sim 2.7$  (the exact pH depends on the solution concentration of acid and base). However, the ability of molybdate to buffer in the occluded crack is degraded by cations such as  $\text{Al}^{3+}$  produced during dissolution, as hydrolysis can reduce the pH away from the optimal range (6 or 2.7) <sup>75</sup>. While buffering at a pH of 7 will perhaps inhibit EFCP and mitigate HEE by consumption of  $\text{H}^+$  from metal ion hydrolysis, buffering at a pH of 2.7 will not be beneficial as it will have the counter-deleterious effect of maintaining the acidic crack environment through production of  $\text{H}^+$ . For EFCP under full immersion in molybdate solutions, buffering to a near neutral pH at low  $f$  is possible because the stable crack tip passive film maintained low cation concentrations; but for higher  $f$  when the crack tip passive film is rarely intact, cation formation and subsequent hydrolysis is promoted and molybdate buffering to maintain a near neutral pH is overwhelmed by high  $\text{H}^+$  concentration <sup>33, 47</sup>. Under atmospheric-droplet conditions, the crack solution will be less acidic, even at high  $f$ , than for full immersion (for Al alloys near crack tip pH is between 2 and 3 <sup>44, 46</sup>) because all cathodic reactions will take place within the crack along the wake. This less acidic environment may allow molybdate to buffer the crack solution under high  $f$  loading where it was previously overwhelmed under full immersion.

Ion-assisted inhibition may also be enhanced by a more limited anode to cathode separation when the crack is partially filled because the species produced at cathodic reaction sites which are required to balance oxidation (e.g.  $\text{OH}^-$ ) are in higher quantity near the crack tip rupture site(s). This will enhance oxide formation and repassivation kinetics. Therefore, an increased potency of inhibition and  $f_{\text{critUB}}$ , as it represents the point at which  $t_{\text{rup}} \leq t_{\text{repass}}$ , is expected.

The increase in  $f_{\text{critUB}}$  to above 30 Hz implies that the repassivation kinetics for the Mo-bearing passive film at the crack tip are enhanced under atmospheric conditions producing homogeneous electrolyte droplets. Prior research on molybdate inhibition under full immersion on 7075-T651 <sup>33, 47</sup> and C47A-T86 <sup>47, 70</sup> found that  $f_{\text{critUB}}$  was 12 Hz for 7075 at a  $\Delta K$  of  $6 \text{ MPa}\sqrt{\text{m}}$  (R of 0.65 and 0.6M  $\text{Na}_2\text{MoO}_4$ ), and between 3 and 6 Hz for C47A at a  $\Delta K$  of  $7 \text{ MPa}\sqrt{\text{m}}$  (R of 0.58 and 0.6M  $\text{Na}_2\text{MoO}_4$ ). A value of  $t_{\text{repass}}$  can be calculated from  $f_{\text{critUB}}$  by estimating  $t_{\text{rup}}$  at  $f_{\text{critUB}}$ .  $t_{\text{rup}}$  can be estimated by the ratio of the film rupture strain (uncertain value, but likely on the order of 1% for a passive film on Al <sup>76, 77</sup>) to the crack tip strain rate ( $\dot{\epsilon}_{\text{tip}}$ ) <sup>48-50</sup>. Analytical and experimental approaches estimated the average  $\dot{\epsilon}_{\text{tip}}$  during cyclic loading as <sup>12</sup>:

$$\frac{\partial \varepsilon}{\partial t_{tip}} = \beta(\Delta K)^{\lambda} f \quad (5)$$

The material constants,  $\lambda$  and  $\beta$ , were determined for fatigue loading of 7075-T6 using *in situ* SEM stereo-imaging measurements of crack tip opening displacement, and are  $3.2^{78,79}$  and  $1.2 \times 10^{-4}$  respectively,<sup>79</sup>. These constants are relevant to  $\dot{\varepsilon}_{tip}$  in units of  $s^{-1}$  with  $\Delta K$  as  $MPa\sqrt{m}$  and  $f$  as Hz. As the values for these coefficients are unknown for C47A-T86, the 7075-T6 values are used to estimate  $\dot{\varepsilon}_{tip}$  and  $t_{rup}$ , and thus the inferred  $t_{repass}$  for C47A-T86. Therefore,  $t_{repass}$  is 0.022 for 7075-T651 and 0.028 for C47A-T86 loaded under full immersion in 0.06M NaCl + 0.6M  $Na_2MoO_4$ . If 30 Hz is used to estimate  $t_{rup}$  for C47A-T86 under atmospheric-droplet conditions, then  $t_{repass}$  must be less than  $\sim 0.005$  s. A repassivation time of 0.002 s is reported for a fractured surface of pure Al in Cl<sup>-</sup> free 1.2N  $K_2SO_4$  at a pH of 5.6 and -600 mV<sub>SCE</sub><sup>80</sup>, while 0.003s is reported for scratched Al-7% Mg in Cl<sup>-</sup> free 0.5M  $Na_2SO_4$  at a pH of 1 and -700 mV<sub>SCE</sub><sup>81</sup>. As such, the inferred  $t_{repass}$  of  $\sim 0.005$  s is not unreasonable. The combination of a more favorable  $MoO_4^{2-}$  to Cl<sup>-</sup> concentration ratio, enhanced ability to buffer at high  $f$  by molybdate, and reduced anode to cathode separation to enhance oxide formation; may together explain the significant increase in ability to inhibit to  $f$  at and above 30 Hz.

Like EFCP under atmospheric exposures which produced NaCl-only droplets, the ability of molybdate to inhibit EFCP under atmospheric conditions producing surface electrolyte droplets is variable under both 0.2 Hz and 30 Hz loading, as seen by the results in Figure 51 and crack length versus loading cycles data in Figure 52 through Figure 56. This variability in measured  $da/dN$  under constant loading conditions may once again be explained by changes in the degree of filling of the crack with electrolyte as the crack grows.

Changes in the anode to cathode separation as solution volume within the crack changes can alter inhibition in multiple ways. First, similar to that explained for alloy-induced inhibition, reducing the anode to cathode separation by partial filling of the crack increases the amount of H produced near the crack tip and may increase H uptake into the FPZ. Therefore, as anode to cathode separation decreases, H uptake may increase, thereby decreasing the potency of inhibition. Alternatively, as anode to cathode separation increases, it is expected that the potential will decrease slightly due to IR drop and pH will become more acidic. As Cu enrichment (which is responsible for alloy-induced inhibition because it creates near neutral pH conditions within the crack solution) does not occur when  $MoO_4^{2-}$  is in solution (at least for full immersion)<sup>47,70</sup>; a decrease in the crack tip pH will not be mitigated unless buffering by  $MoO_4^{2-}$  is possible. A decrease in the crack tip pH and a slight decrease in potential will increase the overpotential for H production, and likely  $da/dN$ . Therefore, in this consideration, a decrease in the anode to cathode separation will enhance inhibition by decreasing H production. Finally, reduced anode to cathode separation may allow the crack tip oxide to form and repassivate more easily and quickly because the distance that species produced at the cathodic reaction site and required for passivation (e.g. OH<sup>-</sup>) needs to migrate is reduced. As  $f_{critUB}$ , according to the film rupture-H embrittlement mechanism, represents the point at which  $t_{rup} \leq t_{repass}$ ; if the oxide can repassivate more quickly,  $f_{critUB}$  would be expected to increase like that observed in Figure 51.

Potency of ion-assisted inhibition can also be altered by changes in  $MoO_4^{2-}$  containing crack solution volume to crack surface area as degree of filling changes. Prior research on the ability of molybdate to inhibit EFCP under full immersion showed that the ratio of  $MoO_4^{2-}$  containing crack solution volume to crack surface area affected inhibition<sup>33,47</sup>. Essentially, results showed enhanced ability to inhibit EFCP with increasing R. This increased potency to inhibit was



attributed to increasing  $R$  to increase the crack mouth opening displacement (CMOD); and thus, the volume of  $\text{MoO}_4^{2-}$  containing solution to react with the same crack surface area. When a partially filled crack intersects a droplet to increase the volume of solution within the crack, the ratio of crack solution volume to crack surface area interacting with the solution also increases; and based on the results from the prior study under full immersion<sup>33, 47</sup>, this increased ratio as filling increases can enhance inhibition to decrease  $da/dN$  as the crack grows and intersects droplets.

The ability of  $\text{MoO}_4^{2-}$  to buffer the crack tip to near neutral pH and assist inhibition by consuming  $\text{H}^+$  may be affected by changes in the degree to which the crack is filled with solution. Buffering capacity depends on the ratio of  $\text{MoO}_4^{2-}$  to  $\text{H}^+$  concentrations. If the concentration of  $\text{H}^+$  is too high, buffering can be overwhelmed<sup>75</sup>. The ratio of  $\text{MoO}_4^{2-}$  to  $\text{H}^+$  near the crack tip may change as anode to cathode separation and crack solution volume containing  $\text{MoO}_4^{2-}$  change with degree of filling. Therefore, changes in degree of filling likely affect the ability of molybdate to buffer at both low and high  $f$  (buffering is a secondary mechanism for inhibition at low  $f$  under full immersion<sup>33, 47</sup>).

The explanations considered above for variations in the potency of ion-assisted inhibition of EFCP under atmospheric exposures and constant loading conditions affect inhibition and  $da/dN$  in various and often opposing ways. These factors may be playing a role in inhibition of EFCP, and the interplay is likely complex and may explain the crack growth rate slowing and accelerating as the crack grows, as can be seen in Figure 53 and Figure 56.

Under 0.2 Hz loading, crack arrest occurred in some instances, as indicated by the downward pointing dashed/dotted arrow in Figure 51 and a vs  $N$  data in Figure 54. After crack arrest, a substantial amount of time under 30 Hz loading was required to restart crack propagation. This implies that crack closure may be occurring under atmospheric-droplet conditions. This may be due to the limited solution volume which exists under atmospheric conditions. Because there is a limited volume of solution for dissolved ions, super saturation of the crack solution can occur more readily than under full immersion where a bulk external electrolyte is present. Once super saturation of this limited solution volume occurs, precipitation of a hydroxyl-chloride-molybdate phase(s) occurs and which cannot eject into the bulk solution. Thus, corrosion product induced closure ensues and  $da/dN$  and effective  $\Delta K$  are reduced. As most loading segments produced  $da/dN$  which were linear for long periods and/or increased with crack extension, as shown in Figure 52 and Figure 55, corrosion product induced closure is not likely to be compromising all results.

#### 1.6.6.2 Impact

This study has taken the first step toward quantitatively characterizing and understanding the effects of atmospheric conditions on EFCP. This work established a reliable atmospheric EFCP testing procedure, and verified the ability of inhibitors to transport to a crack tip when present in a small solution volume on the metal surface and EFCP inhibition at higher  $f$  than possible under full immersion in aqueous chloride solution. The next logical step in understanding if ion-assisted inhibition is possible after release from a coating, is to design experiments which releasing the ion from an actual coating into a small electrolyte solution volume.

Quantitative and scientific understanding of effects of atmospheric conditions on EFCP in Al-Cu-Li alloy C47A-T86 have been hindered by the surface wetting properties of the aluminum alloy



used in this study. Because a homogeneous water layer which completely wets the metal surface was not attained, a complete scientific understanding of crack chemical and electrochemical conditions linked to the environmental driving force for cracking and comparisons to full immersion EFCP was not possible. Consideration of surface wetting effects, and electrolyte morphology on EFCP must be further investigated.

#### 1.6.6.3 Implementation

Molybdate offers the ability to both eliminate the effect of environment on FCP at sufficiently low  $f$ , and be released in the proper oxidation state through dissolution of metallic Mo<sup>72</sup>; both of which have not been reported for chromate. Additionally, the results from this study suggest that EFCP inhibition for Al-Cu-X alloys can be achieved via release of an ionic inhibitor from a pigmented paint much like the release provided by chromate conversion coatings in use today<sup>82</sup>. The high molybdate concentration studied here is not representative of the low concentrations expected after release from a coating. The leach rate of chromate from a commercial coating varies greatly depending on the primer and pigments used<sup>82</sup>. At the high end, concentrations of chromate leached into small occluded solution volumes like those found in a lap joint may be as high as 0.01 to 0.03M based on leach rates reported by Petry et. Al [80]. The prior 7075 molybdate study showed effective inhibition for molybdate concentrations as low as 0.03M when loading under high stress ratios<sup>33, 47</sup>. For full immersion or large solution volumes, significantly lower inhibitor concentrations would be expected after inhibitor leaching. Experiments are in progress to examine the impact of these low expected inhibitor concentrations on EFCP in aerospace aluminum alloys stressed under either full immersion or with coverage by a thin electrolyte layer.

The long term implementation path for this work requires additional stages of research. First, the effect of very low molybdate and chromate inhibitor concentrations on EFCP must be quantified. Second, coatings must be formulated, and the ionic-inhibitor release kinetics and capacity must be determined. Third, the measurements in these two former tasks must be extended to the case of atmospheric thin-film electrolytes typical of airframe applications. Fourth, the repassivation kinetics pertinent to the proposed inhibition mechanism must be established. This 4<sup>th</sup> aspect of the implementation work is ongoing in a task sponsored by OuSD and lead by Professor Scully. The former three tasks are being researched by Ms. Sarah Galyon Dorman as part of her PhD degree program, sponsored by OuSD through the United States Air Force Academy under contract to SAFE. Professor Robert Kelly is collaborating on these three tasks. The results of these studies will be reported in the final reports associated with each of these OuSD grant programs.

#### 1.6.7 Conclusions

- A deliquesced surface electrolyte containing chloride promotes EFCP in peak aged Al-Cu-Li alloy C47A (registered alloy 2199) relative to inert environment behavior; however, complex surface wetting and droplet changes during long time cyclic loading cause fatigue crack growth rate transients which complicate mechanistic interpretations and component fatigue life prediction.
- For a  $\Delta K$  of 7 MPa $\sqrt{m}$  and loading frequency of 30 Hz, EFCP kinetics for Al-Cu-Li alloy C47A-T86 are not accelerated by the presence of NaCl-only containing surface droplets compared to full immersion in chloride solution. More research needs to be conducted

in order to determine the fundamental reason behind this; building on several reasonable-existing hypotheses associated with crack surface H production and diffusion to crack tip damage sites.

- Pure NaCl-containing surface electrolyte droplets hinder self inhibition of EFCP. This may be due to partial filling of the crack which increases the amount of cathodic reactions occurring and H production near the crack tip.
- Molybdate is capable of transport from a surface electrolyte droplet, be it heterogeneously distributed or homogeneously distributed, to the crack tip and subsequent inhibition of EFCP.
- Molybdate containing homogeneous surface droplets show an enhanced ability to inhibit EFCP by reducing  $da/dN$  at 30 Hz, a relatively high  $f$  at which  $MoO_4^{2-}$  inhibition is not seen under full immersion. This is likely due to molybdate buffering the crack solution, possibly increased repassivation kinetics due to the higher  $MoO_4^{2-}$  to  $Cl^-$  concentration ratio, and possibly to reduced anode to cathode separation.
- For atmospheric conditions producing homogeneous surface droplets loaded under low  $f$ , molybdate is capable of complete elimination of the environmental enhancement of fatigue crack propagation as evidenced by vacuum level  $da/dN$ .
- Surface electrolyte morphology and subsequent crack solution volume likely affect EFCP kinetics and inhibition; the details of this interaction are complex and not well understood but likely due to a combination of crack closure, varying solution volume, and crack chemical and electrochemical considerations.

#### 1.6.8 Bibliography

1. J. A. Feeney, J. C. McMillan and R. P. Wei, Environmental Fatigue Crack Propagation of Aluminum Alloys at Low Stress Intensity Levels, *Metallurgical Transactions*, 1 (1970), 1741-1757.
2. M. Gao, R. P. Wei and P. Pao, Chemical and Metallurgical Aspects of Environmentally Assisted Fatigue Crack Growth in 7075-T651 Aluminum Alloy, *Metallurgical and Materials Transactions A*, 19 (1988), 1739-1750.
3. Z. Gasem and R. P. Gangloff, Rate-Limiting Processes in Environmental Fatigue Crack Propagation in 7000-series Aluminum Alloys, R. H. Jones, (Ed.), *Chemistry and Electrochemistry of Corrosion and Stress Corrosion Cracking*, (Warrendale, PA, TMS-AIME, 2001, p. 501-521).
4. Z. M. Gasem, "Frequency Dependent Environmental Fatigue Crack Propagation in the 7XXX Alloy/Aqueous Chloride System" University of Virginia, 1999).
5. A. Hartman, On the Effect of Oxygen and Water Vapor on the Propagation of Fatigue Cracks in 2024-T3 Alclad Sheet, *International Journal of Fracture Mechanics*, 1 (1965), 167-188.
6. P. S. Pao, M. Gao and R. P. Wei, Environmentally Assisted Fatigue-Crack Growth in 7075 and 7050 Aluminum Alloys, *Scripta Metallurgica*, 19 (1985), 265-270.
7. J. Ruiz and M. Elices, Effect of Water Vapor Pressure and Frequency on Fatigue Behaviour in 7017-T651 Aluminium Alloy Plate, *Acta Materialia*, 45 (1997), 281-293.

8. R. P. Wei, Fatigue-Crack Propagation in a High-Strength Aluminum Alloy, *International Journal of Fracture Mechanics*, 4 (1968), 159-168.
9. R. P. Wei, Some Aspects of Environment-Enhanced Fatigue-Crack Growth, *Engineering Fracture Mechanics*, 1 (1970), 633-651.
10. R. P. Wei and R. P. Gangloff, Environmentally Assisted Crack Growth in Structural Alloys: Perspectives and New Directions, R. P. Wei and R. P. Gangloff, Eds., *Fracture Mechanics: Perspectives and Directions*, ASTM STP 1020, (West Conshohocken, PA, ASTM International, 1989, p. 233-264).
11. T. Broom and A. Nicholson, Atmospheric Corrosion Fatigue of Age Hardenable Aluminum Alloys, *Journal of the Institute of Metals* 89 (1960-1961), 183-190.
12. R. P. Gangloff, Corrosion Fatigue Crack Propagation in Metals, R. P. Gangloff and M. B. Ives, Eds., *Environment Induced Cracking of Metals*, (Houston TX, NACE, 1989, p. 55-109).
13. R. P. Gangloff, Environment Sensitive Fatigue Crack Tip Processes and Propagation in Aerospace Aluminum Alloys, A. Blom, (Ed.), *Fatigue '02*, (West Midlands, UK, Engineering Materials Advisory Services, 2002, p. 3401-3433).
14. Y. Ro, S. R. Agnew, G. H. Bray and R. P. Gangloff, Environment-Exposure-Dependent Fatigue Crack Growth Kinetics for Al-Cu-Mg/Li, *Materials Science and Engineering: A*, 468-470 (2007), 88-97.
15. Y. J. Ro, "Characterization of Exposure Dependent Fatigue Crack Growth Kinetics and Damage Mechanisms for Aluminum Alloys" University of Virginia, (2008),
16. Y. J. Ro, S. R. Agnew and R. P. Gangloff, Environmental Exposure Dependence of Low Growth Rate Fatigue Crack Damage in Al-Cu-Li/Mg, J. E. Allison, J. Wayne Jones, J. M. Larsen and R. O. Ritchie, Eds., *Fourth International Very High Cycle Fatigue Conference*, (Warrendale, PA, TMS, 2007, p. 409-420).
17. Y. J. Ro, S. R. Agnew and R. P. Gangloff, Effect of Environment on Fatigue Crack Wake Dislocation Structure in Al-Cu-Mg, *Metallurgical and Materials Transactions A*, in review (2011).
18. R. P. Wei, P. S. Pao, R. G. Hart, T. W. Weir and G. W. Simmons, *Fracture Mechanics and Surface Chemistry Studies of Fatigue Crack Growth in an Aluminum Alloy*, *Metallurgical and Materials Transactions A*, 11A (1980), 151-158.
19. L. Corsetti and D. Duquette, The Effect of Mean Stress and Environment on Corrosion Fatigue Behavior of 7075-T6 Aluminum, *Metallurgical and Materials Transactions B*, 5 (1974), 1087-1093.
20. F. P. Ford, Corrosion Fatigue Crack Propagation in Aluminum-7% Magnesium Alloy, *Corrosion*, 35 (1979), 281-287.
21. A. D. B. Gingell and J. E. King, The Effect of Frequency and Microstructure on Corrosion Fatigue Crack Propagation in High Strength Aluminium Alloys, *Acta Materialia*, 45 (1997), 3855-3870.
22. N. J. H. Holroyd and D. Hardie, Factors Controlling Crack Velocity in 7000 Series Aluminium Alloys During Fatigue in an Aggressive Environment, *Corrosion Science*, 23 (1983), 527-531, 533-546.
23. M. Khobaib, C. T. Lynch and F. W. Vahldiek, Inhibition of Corrosion Fatigue in High Strength Aluminum Alloys, *Corrosion*, 37 (1981), 285-292.
24. Y. Nakai, A. Alavi and R. Wei, Effects of Frequency and Temperature on Short Fatigue Crack Growth in Aqueous Environments, *Metallurgical and Materials Transactions A*, 19 (1988), 543-548.
25. R. S. Piascik and R. P. Gangloff, Environmental Fatigue of an Al-Li-Cu Alloy: Part I. Intrinsic Crack Propagation Kinetics in Hydrogenous Environments, *Metallurgical and Materials Transactions A*, 22 (1991), 2415-2428.

26. R. E. Stoltz and R. M. Pelloux, Inhibition of Corrosion Fatigue in 7075 Aluminum Alloys, *Corrosion*, 29 (1973), 13-17.
27. S. P. Lynch, Mechanisms of Environmentally Assisted Cracking in Al-Zn-Mg Single Crystals, *Corrosion Science*, 22 (1982), 925-937.
28. E. U. Lee, A. K. Vasudevan and G. Glinka, Environmental Effects on Low Cycle Fatigue of 2024-T351 and 7075-T651 Aluminum Alloys, *International Journal of Fatigue*, 31 (2009), 1938-1942.
29. R. S. Piascik and R. P. Gangloff, Aqueous Environment Effects on Intrinsic Corrosion Fatigue Crack Propagation in an Al-Li-Cu Alloy, R. P. Gangloff and M. B. Ives, Eds., *Environment Induced Cracking of Metals*, (Houston, TX, NACE, 1989, p. 233-239).
30. P. S. Pao, M. A. Imam, L. A. Cooley and G. R. Yoder, Comparison of Corrosion-Fatigue Cracking of Aluminum-Lithium Alloy AA 2090-T8E41 and Alloy AA 7075-T651 in Salt Water, *Corrosion*, 45 (1989), 530-535.
31. A. M. Green and J. F. Knott, Effects of Environment and Frequency on the Long Fatigue Crack Growth of Aluminum Alloy 7475, K. Salama, (Ed.), *Advances in Fracture Research*, (New York, NY, Pergamon Press, 1989, p. 1747-1756).
32. J. S. Warner and R. P. Gangloff, Alloy Induced Inhibition of Fatigue Crack Growth in Age-hardenable Al-Cu alloys, *International Journal of Fatigue*, in press: doi: 10.1016/j.ijfatigue.2011.04.013 (2011).
33. J. S. Warner, S. Kim and R. P. Gangloff, Molybdate Inhibition of Environmental Fatigue Crack Propagation in Al-Zn-Mg-Cu, *International Journal of Fatigue*, 31 (2009), 1952-1965.
34. F. Lin and E. A. Starke, Mechanisms of Corrosion Fatigue Crack Propagation of 7XXX Aluminum Alloys in Aqueous Environments, I. M. Bernstein and A. W. Thompson, Eds., *Hydrogen Effects in Metals*, (Warendale, PA, TMS-AIME, 1980, p. 485-492).
35. R. Wanhill, Fractography of Fatigue Crack Propagation in 2024-T3 and 7075-T6 Aluminum Alloys in Air and Vacuum, *Metallurgical and Materials Transactions A*, 6 (1975), 1587-1596.
36. R. Carter, E. Lee, E. Starke and C. Beevers, The Effect of Microstructure and Environment on Fatigue Crack Closure of 7475 Aluminum Alloy, *Metallurgical and Materials Transactions A*, 15 (1984), 555-563.
37. F. J. Bradshaw and C. Wheeler, The Effect of Environment on Fatigue-Crack Growth in Aluminum and some Aluminum Alloys, *Applied Materials Research*, 5 (1966), 112-120.
38. Y. Ro, S. R. Agnew and R. P. Gangloff, Crystallography of Fatigue Crack Propagation in Precipitation-Hardened Al-Cu-Mg/Li, *Metallurgical and Materials Transactions A*, 38 (2007), 3042-3062.
39. Y. Ro, S. R. Agnew and R. P. Gangloff, Environmental Fatigue-Crack Surface Crystallography for Al-Zn-Cu-Mg-Mn/Zr, *Metallurgical and Materials Transactions A*, 39 (2008), 1449-1465.
40. P. S. Pao, M. Gao and R. P. Wei, Critical Assessment of the Model for Transport-Controlled Fatigue Crack Growth, R. P. Wei and R. P. Gangloff, Eds., vol. ASTM STP 924, *Basic Question in Fatigue*, (Philadelphia, ASTM, 1988, p. 182-195).
41. T. H. Shih and R. P. Wei, The Effects of Load Ratio on Environmentally Assisted Fatigue Crack Growth, *Engineering Fracture Mechanics*, 18 (1983), 827-837.
42. R. P. Wei, Environmental Considerations for Fatigue Cracking, *Fatigue Fract. Engng. Mater. Struct.*, 25 (2002), 845-854.
43. R. P. Wei, M. Gao and P. S. Pao, The Role of Magnesium in CF and SCC of 7000 Series Aluminum Alloys, *Scripta Metallurgica*, 18 (1984), 1195-1198.
44. K. R. Cooper, "Chemistry and Electrochemistry of Environment-Assisted Cracking of an Al-Zn-Mg-Cu Alloy" University of Virginia, (2001),



45. K. R. Cooper and R. G. Kelly, Using Capillary Electrophoresis to Study the Chemical Conditions within Cracks in Aluminum Alloys, *Journal of Chromatography A*, 850 (1999), 381-389.
46. K. R. Cooper and R. G. Kelly, Crack Tip Chemistry and Electrochemistry of Environmental Cracks in AA 7050, *Corrosion Science*, 49 (2007), 2636-2662.
47. J. S. Warner, "Inhibition of Environmental Fatigue Crack Propagation in Age-Hardenable Aluminum Alloys" University of Virginia, 2010),
48. F. P. Ford, Effect of Metallurgical and Mechanical Factors on Cracking in Ductile Alloy/Aqueous Environment Systems, R. P. Gangloff, (Ed.), *Embrittlement Localized Crack Environment*, (Warrendale, PA, Metallurgical Society AIME, 1984, p. 117-147).
49. F. P. Ford and P. L. Andresen, *Corrosion Fatigue of Pressure Boundary Materials*, K. Salema, (Ed.), *Advances in Fracture Research*, (Oxford, UK, Pergamon Press, 1989, p. 1571-1584).
50. F. P. Ford and P. L. Andresen, Electrochemical Effects on Environmentally-Assisted Cracking, S. M. Bruemmer, E. I. Meletis, R. H. Jones, W. W. Gerberich, F. P. Ford and R. W. Staehle, Eds., *Parkins Symposium on Fundamental Aspects of Stress Corrosion Cracking*, (Warrendale, PA, TMS, 1992, p. 43-67).
51. G. H. Bray, R. J. Bucci and R. L. Brazill, Lessons Neglected: Effects of Moist Air on Fatigue and Fatigue Crack Growth in Aluminum Alloys. , *Materials Science Forum*, 331-337 (2000), 1413-1426.
52. B. J. Finlayson-Pitts and J. N. Pitts, *Chemistry of the Upper and Lower Atmosphere*, (San Diego, CA: Academic Press, 2000),
53. C. Leygraf and T. Graedel, *Atmospheric Corrosion*, (New York, NY: Wiley-Interscience, John Wiley & Sons, 2000),
54. J. S. Warner and R. P. Gangloff, Molybdate Inhibition of Corrosion Fatigue Crack Propagation in Precipitation Hardened Al-Cu-Li, submitted to - *Corrosion Science*, (2011).
55. C. Giummarra, B. Thomas and R. J. Rioja, *New Aluminum Lithium Alloys for Aerospace Applications*, *Proceedings of the Light Metals Technology Conference*, 2007).
56. Y. J. Ro, "Fatigue Crack Surface Crystallography of Precipitation Hardened Aluminum Alloys" University of Virginia, 2004),
57. R. P. V. Cruz, A. Nishikata and T. Tsuru, AC impedance monitoring of pitting corrosion of stainless steel under a wet-dry cyclic condition in chloride-containing environment, *Corros Sci*, 38 (1996), 1397-1406.
58. J. F. Young, Humidity Control in the Laboratory Using Sat Solutions - A Review, *Journal of Applied Chemistry*, 17 (1967), 241-245.
59. H. Tada, P. C. Paris and G. R. Irwin, *The Stress Analysis of Cracks Handbook*, (St. Louis, MO: Paris Productions Inc., 1985), p. pp. 2.10-12.12.
60. R. P. Gangloff, D. C. Slavik, R. S. Piascik and R. H. Van Stone, Direct Current Electrical Potential Measurement of the Growth of Small Cracks, J. M. Larsen and J. E. Allison, Eds., *Small Crack Test Methods*, ASTM STP1149, (Philadelphia, PA, ASTM, 1992, p. 116-168).
61. J. K. Donald and J. Ruschau, Direct Current Potential Difference Fatigue Crack Growth Measurement Techniques, K. J. Marsh, R. A. Smith and R. O. Ritchie, Eds., *Fatigue Crack Measurement: Techniques and Applications*, (West Midland, UK, EMAS, 1991, p. 11-38).
62. Y. L. Cheng, Z. Zhang, F. H. Cao, J. F. Li, J. Q. Zhang, J. M. Wang and C. N. Cao, A study of the corrosion of aluminum alloy 2024-T3 under thin electrolyte layers, *Corros Sci*, 46 (2004), 1649-1667.

63. Z. Y. Chen, F. Cui and R. G. Kelly, An Analytical Modeling Method for Calculating the Current Delivery Capacity of a Thin-Film Cathode and the Stability of Localized Corrosion under Atmospheric Environments, *ECS Transactions*, 3 (2007), 443-457.
64. E. Schindelholz and R. G. Kelly, unpublished research. University of Virginia
65. W. Polini and L. Sorrentino, Improving the Wettability of 2024 Aluminium Alloy by Means of Cold Plasma Treatment, *Applied Surface Science*, 214 (2003), 232-242.
66. B. R. Strohmeier, The Effects of O<sub>2</sub> Plasma Treatments on the Surface Composition and Wettability of Cold-Rolled Aluminum Foil, *Journal of Vacuum Science & Technology A: Vacuum, Surfaces, and Films*, 7 (1989), 3238-3245.
67. B. R. Strohmeier, Improving the Wettability of Aluminum Foil with Oxygen Plasma Treatments, *Journal of Adhesion Science and Technology*, 6 (1992), 703-718.
68. B. R. Strohmeier, Testing and Improving the Wettability of Aluminum Foil. Part II., *Aluminium*, 68 (1992), 983-988.
69. B. R. Strohmeier, Testing and Improving the Wettability of Aluminum Foil. Part I., *Aluminium*, 68 (1992), 893-896.
70. J. S. Warner and R. P. Gangloff, Molybdate Inhibition of Corrosion Fatigue Crack Propagation in Precipitation Hardened Al-Cu-Li, *Corrosion Science*, 62 (2012), 11-21.
71. J. S. Warner and R. P. Gangloff, Alloy induced inhibition of fatigue crack growth in age-hardenable Al-Cu Alloys, *International Journal of Fatigue*, 42 (2012), 35-44.
72. M. Pourbaix, *Atlas of Electrochemical Equilibria in Aqueous Solutions*, (Houston, TX: NACE, 1974),
73. A. Nazarov and D. Thierry, Rate-determining reactions of atmospheric corrosion, *Electrochimica Acta*, 49 (2004), 2717-2724.
74. L. M. Young, "Microstructural Dependence of Aqueous-Environment Assisted Crack Growth and Hydrogen Uptake in AA 7050" University of Virginia, 1999),
75. S. Al-Ghamdi, "The Effect of Aqueous Phase Inhibitors on Mitigating Potential-Dependent Hydrogen Environment Assisted Cracking of an Ultra-High Strength Steel" University of Virginia, 2010),
76. K. R. Morasch and D. F. Bahr, Nanomechanical Testing for Fracture of Oxide Films, *Journal of Materials Research*, 20 (2005), 1490-1497.
77. M. Pang, D. E. Wilson and D. F. Bahr, The Strength and Fracture of Passive Oxide Films on Metals, *Materials Research Society Symposium Proceedings*, 594, p. 501-506, (MRS, 2000).
78. D. L. Davidson and J. Lankford, The Effects of Aluminum Alloy Microstructure on Fatigue Crack Growth, *Materials Science and Engineering*, 74 (1985), 189-199.
79. D. Williams, D. Davidson and J. Lankford, Fatigue-Crack-Tip Plastic Strains by the Stereoimaging Technique, *Experimental Mechanics*, 20 (1980), 134-139.
80. G. S. Frankel, C. V. Jahnes, V. Brusic and A. J. Davenport, Repassivation Transients Measured with the Breaking-Electrode Technique on Aluminum Thin-Film Samples, *Journal of the Electrochemical Society*, 142 (1995), 2290-2295.
81. F. P. Ford, G. T. Burstein and T. P. Hoar, Bare Surface Reaction Rates and their Relation to Environment Controlled Cracking of Aluminum Alloys. I. Bare Surface Reaction Rates on Aluminum-7 Weight Percent Magnesium in Aqueous Solutions, *Journal of the Electrochemical Society*, 127 (1980), 1325-1331.
82. L. Petry, D. W. Barrington and J. F. Dante, Evaluation of the Inhibitor Leaching Performance of Chromated Primers by Capillary Ion Analysis and Electrochemical Impedance Spectroscopy, *Tri-Service Conference on Corrosion*, (NACE, Houston, TX, 2003).

## 1.7 Blistering Phenomena in Early Generation Mg-Rich Primer Coatings on AA2024-T351 and the Effects of CO<sub>2</sub> (King, A. D. and Scully, J. R.)

### 1.7.1 Summary

Two different types of coating blistering on the coating system AA2024-T351/PreKote<sup>TM</sup>/MgRP/with or without Aerodur 5000 Topcoat occurred in early generations of MgRP exposed in ASTM B-117 laboratory tests but are not typically seen during exposures in the field at sites such as Daytona Beach, FL <sup>1-3</sup>. The most common type of blistering on AA2024-T351 was observed to occur proximate to scribe lines and is characterized by large blisters underneath the primer and topcoat layers of the coating system. The blisters are shown to form over thick, relatively uniform layers of aluminum corrosion product. This type of blistering is shown to be caused by anodic coating disbondment through an anodic undermining mechanism aided by H<sub>2</sub> generation and modest coating adhesion. A second type of blistering, or rupturing, was observed to occur more randomly over the coated surface and is characterized by small pinholes that penetrate deep into (or in some cases through) the AA2024-T351 substrate. This type of blistering or "rupturing" is shown to be caused by localized cathodic (or basic) corrosion of the AA2024-T351 substrate triggered by a local rise in solution pH. This rise in pH can be due to increased cathodic reaction rates on the surface of the Al substrate due to severe cathodic polarization of the AA2024-T351 and/or the formation of Mg(OH)<sub>2</sub> at sites of Mg pigment dissolution which when dissolved in an aqueous environment has an equilibrium pH of approximately 10.5.

The effect of increasing the CO<sub>2</sub> concentration, from ambient levels of 400 ppm to concentrations of 5000-6000 ppm, on the occurrence of each blistering phenomena was also studied. Elevated concentrations of CO<sub>2</sub> in the exposure environment suppress the occurrence of each type of blistering by different but related mechanisms. CO<sub>2</sub> does not substantially affect the depletion rate of the Mg pigment in the coating during an environmental exposure. The CO<sub>2</sub> effect does not explain the high severity of the ASTM B-117 lab exposure which is believed to be due to high time of wetness and chloride levels.

### 1.7.2 Introduction and Background

There has been significant interest in an organic coating system containing a Mg-pigmented organic primer (MgRP) on precipitation age hardened Al alloy 2024-T351 as well as others <sup>4-9</sup>. Other alloys of interest include AA7075-T6, AA2219-T87, and AA2024-Alclad <sup>1,2</sup>. One such AA2024-T351/Mg-rich coating system is comprised of AA2024-T351 sheet pretreated with Prekote® surface pretreatment, a 30-40 µm primer layer of magnesium rich primer with a Mg pigment volume concentration (PVC) of 45% and a 50-60 µm thick topcoat of high performance advanced life polyurethane coating. The Mg-rich primer consists of a 1-part epoxy matrix with Mg metal flake pigment with an average diameter of 20 µm. The high performance topcoat is a two-component polyurethane topcoat developed for military applications in a variety of exposure environments.

This system has been proposed as a candidate coating system to replace chromate type surface pretreatments as well as chromate pigmented primers <sup>4,10,11</sup>. One of the corrosion inhibition mechanisms, afforded by the MgRP, has been shown to be sacrificial anode based



cathodic protection of the aluminum alloy<sup>5-7, 12-15</sup>. The MgRP is designed to galvanically couple the metallic Mg pigment in the primer to the substrate and provide sacrificial anode based cathodic protection to the aluminum alloy (AA2024-T351). This concept has been successful in the design of zinc-rich primers for use on various steels which have been used for decades in the field<sup>12, 16-31</sup>. Protection by these Zn-rich primers is afforded primarily by sacrificial anode based cathodic protection and secondarily by precipitation of  $\text{Zn}(\text{OH})_2$  at bare sites after migration of  $\text{Zn}^{+2}$ <sup>25, 26</sup>. Zinc also has a low self-corrosion rate. In this case, magnesium is also less noble than almost all of the precipitation age hardened aluminum alloys it might be used to protect and is readily available and actively corrodes in most electrolytes<sup>6, 9, 32</sup>. Alclad<sup>TM</sup> also protects by sacrificial cathodic protection but pits locally and thus is an inefficient anode<sup>33-36</sup>. When coupled to the AA2024-T351 substrate, the Mg pigment becomes an electron donor, and mixed potential theory can be used to explain the galvanic couple potential of the system when exposed to full immersion. Results support the notion of mixed potential theory describing the galvanic coupling behavior of the primer and substrate<sup>3, 5-9, 12, 32, 37</sup>. Mediation of cathodic protection level is aided by resistive layers associated with pretreatments, epoxy resin or polymer type, PVC, and topcoat<sup>12</sup>.

In an effort to gauge performance in a short term test for this coating system, in terms of ability to afford protection, accelerated laboratory cabinet testing has been conducted<sup>3, 37-39</sup>. Interestingly, there are often differences in corrosion behavior of the MgRP between field and laboratory environmental exposures, at least in early generations of commercial products. For example, in ASTM B-117 exposures, scribes through topcoated MgRP systems, exposing AA2024-T351, exhibit noticeably more corrosion product when compared to the relatively clean scribes on samples exposed at Daytona Beach, FL and more benign environments. Moreover, blistering of the coating system is sometimes seen in ASTM B-117 laboratory tests but is typically not seen in field exposures such as at Daytona Beach or Kennedy Space Center<sup>1, 2</sup>. Therefore, it is important for us to understand this blistering phenomenon in order to predict whether it will be seen in any field environments as well as to reassess the relevancy of the ASTM B-117 test to field conditions.

In the lab, two, distinct types of blisters have been observed on the MgRP coating system; each is discussed in this publication. The most common type of blister is shown to be caused by a localized failure of the MgRP to provide adequate local sacrificial anodic protection of the underlying Al substrate. This may be due to a localized depletion of Mg in the primer or simply an area of delamination of the coating system proximate to a scribe line which can support cathodic reactions. This delamination is also aided by poor adhesion of the polymer organic coating. This lack of protection leads to anodic coating disbondment aided by  $\text{H}_2$  gas produced by Al dissolution, is more prevalent in MgRP lean or non-MgRP organic polymer coatings, and the formation of blisters along the defect or scribe<sup>40, 41</sup>. These blisters are characterized by large, round areas of delamination over top of thick, relatively uniform layers of aluminum corrosion product associated with shallow penetration.

A second, much less prevalent type of blister is shown to be caused by a local increase in solution pH due to the corrosion of the Mg pigment and/or increased cathodic reaction rates at sites of severe cathodic polarization of the Al substrate. The local rise in pH results in basic, or cathodic corrosion of the underlying Al substrate due to its amphoteric nature<sup>42-47</sup>. This type of attack is characterized by narrow, deep pinholes which penetrate into the AA2024-T31 substrate. The observation of these performance differences between exposure environments is



presumed to stem from fundamental differences in time of wetness, chloride concentration, and ambient CO<sub>2</sub> levels.

It has been shown in the past that CO<sub>2</sub> acts to reduce the cathodic reaction rates on aluminum alloys with Cu-rich secondary phases acting as cathode sites <sup>48</sup>. This is accomplished by minimizing Al dissolution such that a defect free Al oxide is formed without Cu-rich ligaments which could support cathodic reactions. This passivation of cathodic sites leads to more uniform corrosion of the aluminum alloy and a reduction in pitting. Moreover, the presence of high concentrations of CO<sub>2</sub> may also act to prevent cathodic corrosion of the aluminum alloy by moderating the pH at the surface of the alloy since the equilibrium pH of CO<sub>2</sub> sparged NaCl solution at 1 atm. partial pressure is 4 <sup>48</sup>. It has also been proposed that high CO<sub>2</sub> concentrations will result in the formation of dense magnesium carbonate as a corrosion product of Mg rather than porous magnesium hydroxide, arguing that it offers more effective barrier protection of the Al 2024-T351 substrate <sup>3</sup>.

This paper will characterize blisters observed in the field and in lab accelerated weathering exposures and identify similarities and differences. Two distinct types of blisters are distinguished. The fundamental processes that lead to the formation of each type of blister are outlined and reproduced experimentally in controlled laboratory experiments that simulate blisters and diagnostic electrochemical experiments. The performance of the MgRP coating system, with respect to Mg depletion and blister formation, in lab accelerated exposures (ASTM B-117) with ambient CO<sub>2</sub> and CO<sub>2</sub>-rich environments is also compared. Thermodynamic and kinetic information is used to interpret findings and mitigation strategies are discussed.

### 1.7.3 Lessons Learned

This report characterizes blisters observed in the field and in lab accelerated weathering exposures of early generation MgRP and identifies similarities and differences. Two distinct types of blisters are distinguished (referred to as Type 1 and Type 2). Type 1 Blisters are shown to be caused by disbondment of the organic polymer due to anodic undermining and H<sub>2</sub> gas production. In theory this could be improved by improving adhesion. Type 2 blisters are rare in field exposures and are shown to be ruptures caused by cathodic corrosion of precipitation age hardened Al substrate. The fundamental processes that lead to the formation of each type of blister are outlined and reproduced experimentally in controlled laboratory experiments that simulate blisters and diagnostic electrochemical experiments. The performance of the early generation MgRP coating system, with respect to Mg depletion and blister formation, in lab accelerated exposures (ASTM B-117) with ambient CO<sub>2</sub> and CO<sub>2</sub>-rich environments is also compared. Thermodynamic and kinetic information is used to interpret findings and mitigation strategies are discussed.

The effect of increasing the CO<sub>2</sub> concentration, from ambient levels of 400 ppm to concentrations of 5000-6000 ppm, on the occurrence of each blistering phenomena was also studied. Elevated concentrations of CO<sub>2</sub> in the exposure environment suppress the occurrence of each type of blistering by different but related mechanisms covered in this report. CO<sub>2</sub> was not found to passivate Mg pigment. The CO<sub>2</sub> effect buffers the pH below 10 and inhibits Al corrosion. CO<sub>2</sub> does not substantially affect the depletion rate of the Mg pigment in the coating during an environmental exposure. The CO<sub>2</sub> effect does not explain the high severity of the

ASTM B-117 lab exposure which already contains ambient CO<sub>2</sub> (~400 ppm). This lab blistering is believed to be due to high time of wetness and chloride levels.

#### 1.7.4 Technical Investigations

##### 1.7.4.1 Materials

1.6 mm thick AA2024-T351 sheet, 99.9% pure magnesium rod, 99.9% pure Mg powder with a flake geometry and an average diameter of 20 µm, as well as 1.6 mm thick AA2024-T351 panels coated with commercial Mg-rich primer (MgRP) were studied in these investigations. The Mg rod was 8.0 mm in diameter and about 2.50 cm long. The Mg rod and AA2024-T351 sheet were used as bare electrodes in full immersion electrochemical tests. The Mg rod had a measured purity of over 99.9% and was substantially similar to the powder used in the MgRP. Samples were mounted in epoxy resin, when necessary, in order to make clamping the sample to an electrochemical flat cell easier. The bare electrodes were used in electrochemical analysis and were prepared by alternating polishing with silicon-carbide paper and rinsing with 18.2 MΩ deionized water to a final polishing grit of 1200. The samples were then dried with lab tissue before use.

The MgRP-coated panels studied comprised of a 1.6 mm thick AA2024-T351 sheet with a 30 µm primer layer of magnesium rich primer of various pigment volume concentrations and a 50 µm thick topcoat of a commercial high performance advanced life polyurethane coating. The MgRP-coated AA2024 panels were pretreated with a non-toxic, non-corrosive, non-flammable, CFC free, ODS free, and chromate free surface pretreatment before the MgRp was applied. The pretreatment does not contain any corrosion inhibitors and is not a conversion coating; but promotes adhesion between the primer and substrate. The high performance advanced polymer topcoat is a two-component polyurethane topcoat developed for military applications in a variety of exposure environments. The magnesium rich primer consists of a 1-part epoxy matrix with Mg metal flake pigment mixed in at various volume concentrations (PVC). The Mg pigment itself has flake geometry with an average diameter of 20 µm. All of our coated panels were provided and painted by collaborators <sup>1,2</sup>.

##### 1.7.4.2 ASTM B-117 Salt Fog Exposure

Mg-rich primer-coated AA2024-T351 panels with Mg PVC ≥ 0% were exposed in a QFog Cyclic Corrosion Chamber according to ASTM B-117 <sup>38</sup>. ASTM B-117 covers the apparatus, procedure and conditions required to create and maintain the salt spray (fog) test environment. Ambient CO<sub>2</sub> concentration was monitored during the exposure in-situ with a CO<sub>2</sub> sensor with a sensing range of 0-10,000 ppm to be 425 ppm (Table 5).

During some salt fog exposures CO<sub>2</sub> was introduced into the exposure chamber via a regulated gas cylinder in order to increase the concentration of CO<sub>2</sub> in the exposure chamber to greater-than-ambient levels. During these exposures of increased CO<sub>2</sub> concentrations, a constant flow rate of CO<sub>2</sub> was utilized such that the concentration of CO<sub>2</sub> stabilized to approximately 6000 ppm (Table 5).

Table 5: Ambient Concentrations of CO<sub>2</sub> in Various Environments

Environment	[CO <sub>2</sub> ] (ppm)
Ambient Global Outdoors	400
Ambient Global Indoors	600
Ambient ASTM B-117 at Uva	425
CO <sub>2</sub> -rich ASTM B-117 at Uva	6000

#### 1.7.4.3 Field Exposures at Daytona Beach, FL

Natural weathering exposures of Mg-rich primer-coated AA2024-T351 panels with Mg PVC  $\geq$  0% were conducted at the Battelle Florida Materials Research Facility which is a marine atmospheric testing site located beach-front on the Atlantic Ocean. The Battelle Florida Materials Research Facility is located on the Ponce de Leon Peninsula, 10 miles south of the city of Daytona Beach, Florida, and is used primarily for the testing and evaluation of materials in a subtropical marine environment. During exposure, AA2024-T351 panels coated with MgRP with Mg PVC  $\geq$  0% and a topcoat of commercial high performance advanced life polyurethane coating were mounted on atmospheric test racks with full exposure to natural elements.

#### 1.7.4.4 Full Immersion Electrochemical Analysis

Potential control during electrochemical experiments was maintained using a potentiostat with computer interface software. Saturated Calomel reference electrodes (SCE) were used in full immersion testing. Particular potentiostat models were selected because they enable electrochemical impedance spectroscopy (EIS) measurements along with traditional electrochemical measurements.

#### 1.7.4.5 Anodic Potentiodynamic Scans

Anodic potentiodynamic scans were conducted on 99.9% pure, 8.0 mm diameter bare Mg electrodes as well as the prepared Mg-rich primer-coated AA2024-T351 panels with Mg PVC  $\geq$  25%. Both topcoated and non-topcoated panels were tested. The bare Mg electrodes were polished to 1200 grit silicon carbide paper until a mirror finish was obtained. The potentiodynamic scans were conducted after a 10 minute OCP. A typical anodic scan started at -0.2 V vs OCP up to +0.7 V vs. OCP and scanned at 0.1667 mV per second for bare electrodes and 2.0 mV per second for the coated panels.

#### 1.7.4.6 Cathodic Potentiodynamic Scans

Cathodic potentiodynamic scans were conducted on bare AA2024-T351 electrodes as well as Mg-rich primer coated AA2024-T351 panels with Mg PVC = 0%. Both topcoated and non-topcoated panels were tested. The bare AA2024-T351 electrodes were ground to 1200 grit silicon carbide paper until a mirror finish was obtained. The potentiodynamic scans were conducted after a 10 minute OCP. A typical cathodic scan started at +0.2 V vs OCP and scanned down to -1.0 V vs. OCP at 0.1667 mV per second.

#### 1.7.4.7 Electrochemical Impedance Spectroscopy (EIS)

EIS was conducted on bare Mg and AA2024-T351 electrodes as well as the prepared Mg-rich primer-coated AA2024-T351 panels. A typical EIS scan was acquired in sine sweep mode from 100 kHz to 0.01 Hz with 6 points per decade. Bare electrodes were scanned with an AC amplitude of 20 mV while coated panels were scanned with an AC amplitude of 60 or 80 mV to reduce noise. The bare Mg and AA2024-T351 electrodes were polished to 1200 grit silicon carbide paper until a mirror finish was obtained.

#### **1.7.4.8 Full Immersion, Electrochemical Testing Protocol (Cycle Test)**

A full immersion, electrochemical testing regimen was designed to monitor selected coating characteristics over time. This test included a 10 minute OCP followed by an EIS measurement to assess, nondestructively, the galvanic couple potential of the primer coated AA2024-T351 substrate in order to later interpret cathodic protection and the residual barrier properties of the coating. These were followed by a potentiostatic hold at -0.8 V vs. SCE to accelerate the Mg dissolution rate and measure the anodic charge supplied by the MgRP. The test always started and ended with a 10 minute OCP measurement followed by EIS. The cycle test was run under full immersion in 50 mM sodium chloride solution with ambient aeration and used a saturated calomel reference electrode. These three steps were repeated for a specified number of cycles. The cycles of exposure in full immersion cannot as yet be related to hours of exposure in natural environments.

#### **1.7.4.9 X-Ray Diffraction**

X-Ray diffraction was conducted on a powder diffractometer utilizing a Cu-K $\alpha$  source. The samples investigated included bare AA2024-T351 and the prepared, Mg-rich primer-coated AA2024-T351 panels of all PVC's. All samples were scanned continuously from 10 to 120 degrees. Scans were run at a scan rate of 1.0 degrees per minute on bare electrodes and non-topcoated coatings and 2.0 degrees per minute on topcoated coatings. Both fresh Mg-rich coated panels and panels exposed in full immersion were examined with XRD. XRD Spectra obtained from bare AA2024-T351 and AA2024-T351 coated with MgRP were normalized against the fcc Al <200>  $2\theta=44.7384^\circ$  peak. Samples of bare Mg electrodes were normalized against the Mg <101>  $2\theta=36.6190^\circ$  peak.

#### **1.7.4.10 Scanning Electron Microscopy and Energy Dispersive Spectroscopy**

Scanning electron microscopy and energy dispersive spectroscopy were used for coating characterization and post-mortem analysis. A field emission SEM with EDS analytical software was used to conduct these investigations. Various accelerating voltages and working distances were used depending on the samples and information being investigated. In general, for EDS, a working distance of 15 mm and an accelerating voltage of at least 3 times the energy of the maximum characteristic peak of interest were used. Signals for Mg and Al K $\alpha$  energies were obtained.

### **1.7.5 Experimental Results**

#### **1.7.5.1 Initial Characterization of MgRP Coating System**



SEM micrographs of two cross sectioned AA2024-T351 panels coated with MgRP are shown in Figure 58. EDS spot scans of the substrate show elemental Al. EDS spot scans conducted on magnesium pigment particles in the primer indicated low O levels which suggest the magnesium was largely unoxidized prior to weathering. The thickness of the primer layer was about 30  $\mu\text{m}$ . For topcoated samples, the topcoat was about 50  $\mu\text{m}$  thick. The total coating system thickness was about 80  $\mu\text{m}$ . X-Ray diffraction spectra of the as-received panels of AA2024-T351 coated with MgRP with and without topcoat, were discussed in a previous publication and also indicated the Mg pigment in the primer coating is largely unoxidized prior to weathering and showed that the polymer topcoat contains rutile as a pigment (unknown PVC) <sup>12</sup>.

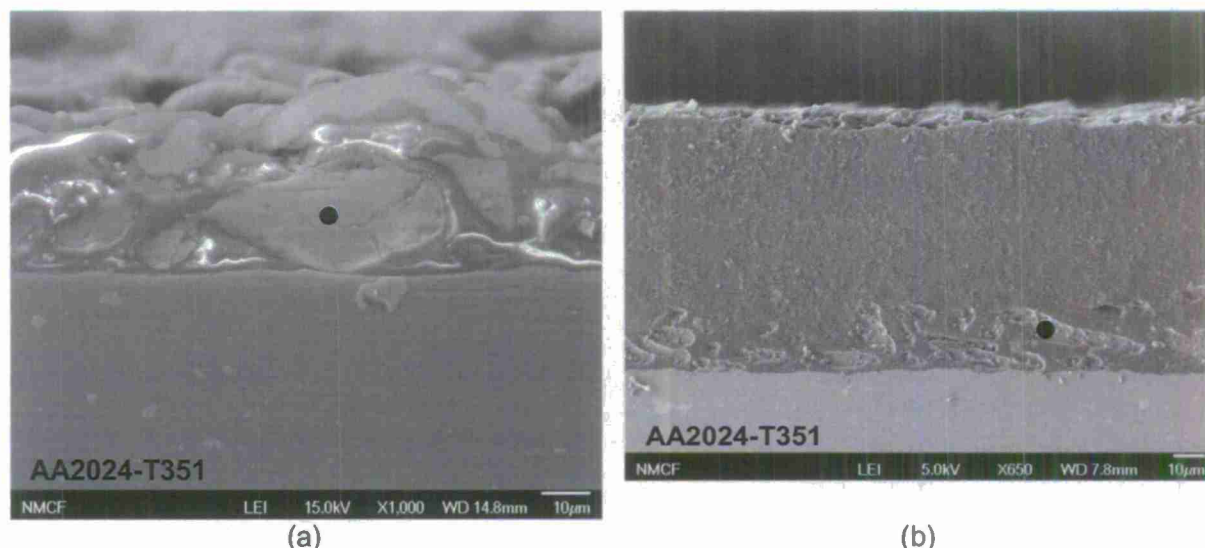


Figure 58. Scanning electron micrograph of cross sectioned AA2024-T351 coated with (a) MgRP Sample ID:493-039-A-P-P22 (b) MgRP + Topcoat Sample ID: T65f. Spot markers indicate approximate location of EDS analysis.

#### 1.7.5.2 Type 1 Blisters: Disbondment of the Organic Polymer Due to Anodic Undermining and H<sub>2</sub> Production

Panels of AA2024-T351 coated with MgRP (PVC = 0% and 45%) and a topcoat of high performance advanced life polyurethane coating were exposed in a salt fog chamber according to ASTM B-117 <sup>38</sup> under ambient aeration for 840 hours. The CO<sub>2</sub> levels inside the salt fog chamber during exposure were measured to be approximately 425 ppm. This does not vary significantly from accepted ambient concentrations globally (Table 5). After exposure the panels were compared to similar panels exposed outdoors at Daytona Beach for approximately 1 year (Figure 59). All panels exposed in the salt fog chamber according to ASTM B-117 exhibited large amounts of corrosion product within the scribe lines and exhibited coating blisters proximate-to, or along the scribe lines. Moreover, the panels without any Mg in the primer (Figure 59a) exhibited much larger blisters than panels with a PVC of Mg of 45% (Figure 59b). In contrast, panels exposed at Daytona Beach exhibited little-to-no corrosion product build-up within the scribe lines and appeared to be relatively defect free. Furthermore, the only panels from the field that exhibited visible blisters were panels without any Mg in the primer (Figure 59c). An interesting feature was the blisters' hemispherical or disc-like nature suggesting relatively uniform pressurization in addition to corrosion products.

Blistered areas along the scribes from each sample visible in Figure 59 were cross sectioned and examined in a field emission SEM with EDS capabilities (Figure 60 and Figure 61). EDS area scans were taken in three areas of each cross sectioned blister: 1) the substrate, 2) the corrosion product, and 3) the coating system and are indicated by the numbered boxes (1-3) in each micrograph in Figure 61. Figure 61d summarizes the results of the EDS measurements. There were striking similarities found between the blisters sectioned on each sample. They could be characterized by large areas of organic coating delamination over top of thick, relatively uniform layers of fractured corrosion product associated with shallow penetration. It was found that the corrosion product layer in each blister was located underneath both the primer and topcoat layers of the coating system, was approximately 50-80  $\mu\text{m}$  thick, and was relatively uniform. Each corrosion product layer appeared to follow the Al substrate morphology perfectly, suggesting that they grew from the substrate and that they have a Pilling-Bedworth ratio of approximately 1<sup>49</sup>. Furthermore, EDS analysis showed that the corrosion product layer in each blister consisted solely of Al and O. EDS analysis of the coating systems over top of each blister were also very similar, each exhibiting strong C, O, Al, Cl and Si peaks. Elemental Mg only appeared in the EDS area scans of the coating system which contained Mg pigment in the primer.

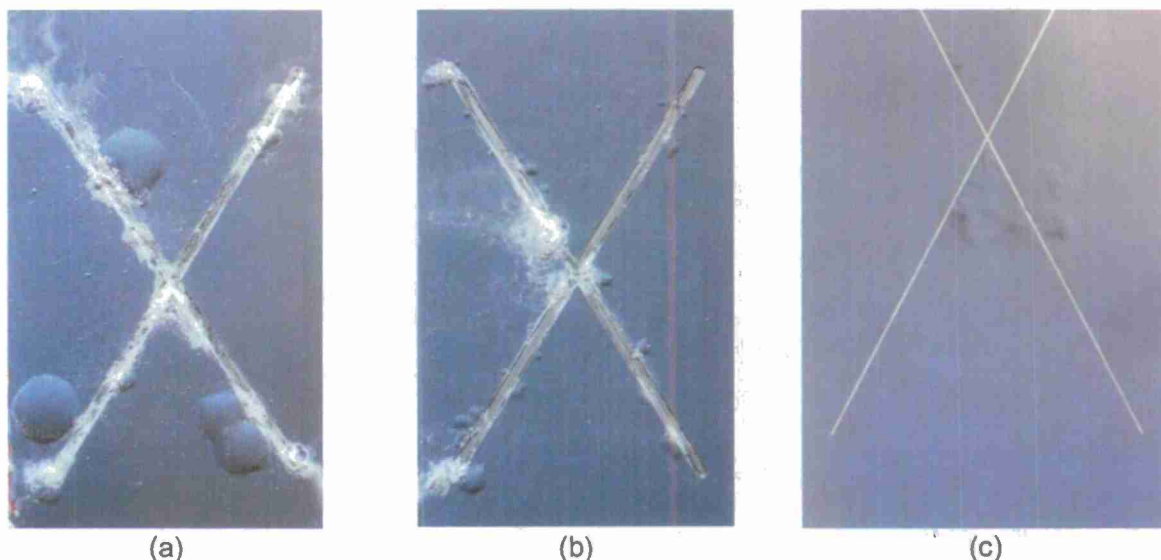


Figure 59. AA2024-T351 coated with (a) MgRP (PVC = 0%) and Aerodur 5000 Topcoat after 840 hrs in ASTM B-117 (b) MgRP (PVC = 45%) and Aerodur 5000 Topcoat after 840 hrs in ASTM B-117 (c) MgRP (PVC = 0%) and Aerodur 5000 Topcoat after 1 yr exposure at Daytona Beach, FL.  
(a) Sample ID:493-039-B-T-P22, (b) Sample ID:493-039-A-T-P22 and (c) Sample ID: unknown.

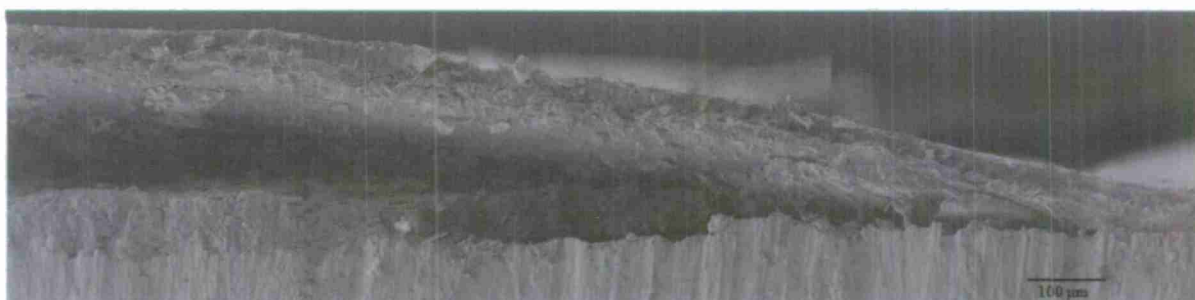
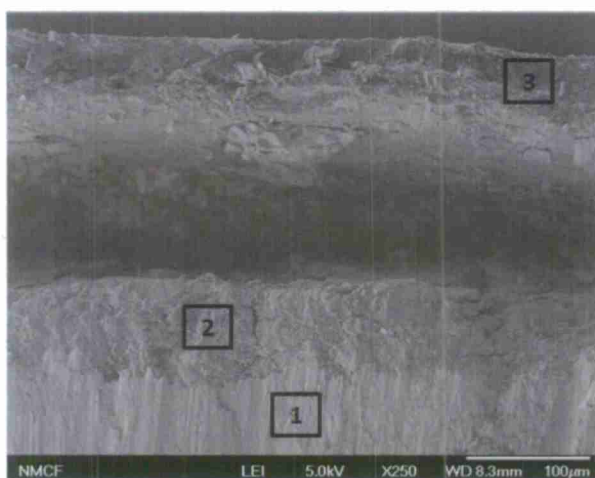
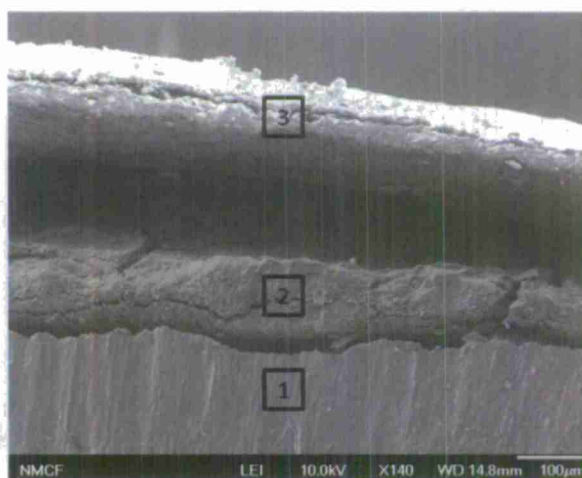


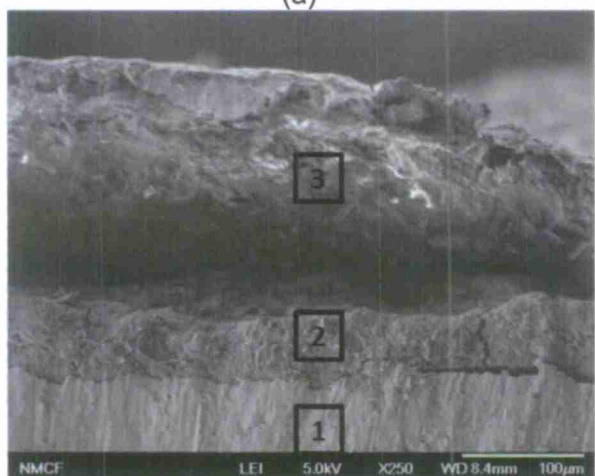
Figure 60. Montage of SEM cross-sections of blisters on AA2024-T351 coated with Akzo Nobel MgRP (PVC = 0%) and Aerodur 5000 Topcoat after environmental exposure at Dayton Beach, FL for 1 yr. Sample ID: unknown



(a)



(b)



(c)

Sample	PVC <sub>Mg</sub>	Environment	Species Present in EDS		
			1: Substrate	2: Corrosion Product	3: Coating System
a	0	Daytona	Al	Al, O, Cl	C, O, Al, Si, Cl
b	0	ASTM B-117	Al	Al, O, Cl	C, O, Al, Si, Cl
c	45	ASTM B-117	Al	Al, O, Cl	Mg, C, O, Al, Si, Cl

(d)

Figure 61. SEM cross-section and EDS analysis of blisters on AA2024-T351 coated with Akzo Nobel MgRP and Aerodur 5000 Topcoat after environmental exposure. EDS area scans conducted approximately over black outlined areas. (a) PVC<sub>Mg</sub> = 0% exposed



at Dayton Beach, FL for 1 yr. Sample ID: unknown (b)  $PVC_{Mg} = 0\%$  exposed in ASTM B-117 for 840 hrs Sample ID:493-039-B-T-P22 (c)  $PVC_{Mg} = 45\%$  exposed in ASTM B-117 for 840 hrs Sample ID:493-039-A-T-P22

### 1.7.5.3 Diagnostic Testing for Type I Blisters

Coupons of AA2024-T351 were coated with a model organic polymer epoxy coating which was clear in color and lacked any pigmentation. After curing, the samples were then scribed with a diamond tipped scribe and exposed to the ASTM B-117 test for 72 hours. After exposure the coupons exhibited coating blisters proximate-to, or along the scribe lines (Figure 62a). The model organic polymer epoxy coating was observed to change color from clear to white during exposure due to hydration. Universal pH indicator solution was injected via syringe into a blister immediately upon removing the coupons from the salt fog chamber. The indicator solution which seeped from the punctured blister was observed to be bright red in color indicating a pH of 4.0 or below (Figure 62b). In summary the blister could be characterized as an acidic site. Other regions on the unpainted back side of the coupon were blue, indicative of pH greater than or equal to 10.0.

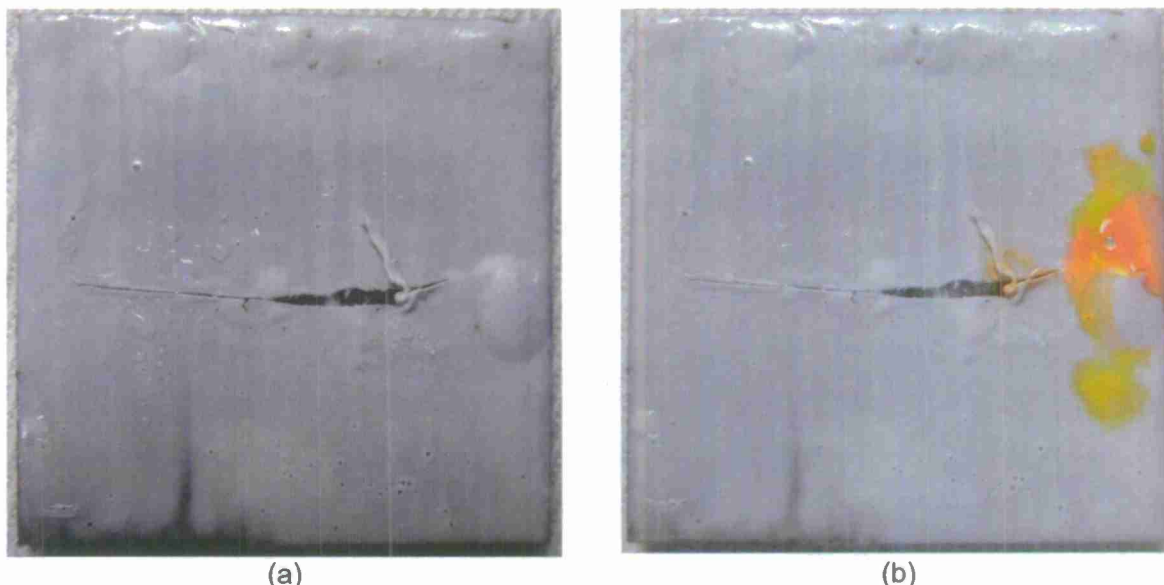


Figure 62. Optical images of AA2024-T351 coated with a model organic epoxy polymer coating after 72 hours exposure in ASTM B-117 with ambient aeration. (a) immediately after environmental exposure (b) universal pH indicator has been injected into a blister located at the base of the scribe.

### 1.7.5.4 Type 2 Blisters: Ruptures Caused by Cathodic Corrosion of Al

A second, much less prevalent type of blister (or rupture), which is characterized by narrow, deep pinholes in the aluminum substrate which can sometimes penetrate through the panel, has been reported in AA2024-T351 panels pretreated with prekote™ and coated with early generations of commercial MgRP ( $PVC = 45\%$ ) exposed to ASTM B-117 salt fog accelerated weathering by various researchers<sup>1,2</sup>. We have observed such a phenomenon under full



immersion testing of AA2024-T351 panels coated with MgRP without a topcoat. The exposure consisted of a full immersion electrochemical testing protocol in which an AA2024-T351 panel pretreated with prekote™ and coated with commercial MgRP (PVC = 45%) was immersed in aerated 50 mM NaCl and primarily subjected to a potentiostatic hold at -0.8 V vs. SCE with numerous cycles of nondestructive open circuit hold and electrochemical impedance measurements in order to track the coatings degradation<sup>12</sup>. It should be noted, however, that this test protocol did not change impedance barrier properties, i.e. did not damage the polymer away from the rupture site. After about 90 hours of total exposure to this cyclic test, the panels were cross sectioned and examined in a field emission SEM with EDS capabilities. Pinholes were observed to be forming in the AA2024-T351 substrate below areas that appear to be sites of Mg pigment dissolution (Figure 63). The coating was ruptured. EDS analysis showed evidence of Al, Mg and O in the pinhole and Mg, O, C, and Cl in the primer layer directly above the hole.

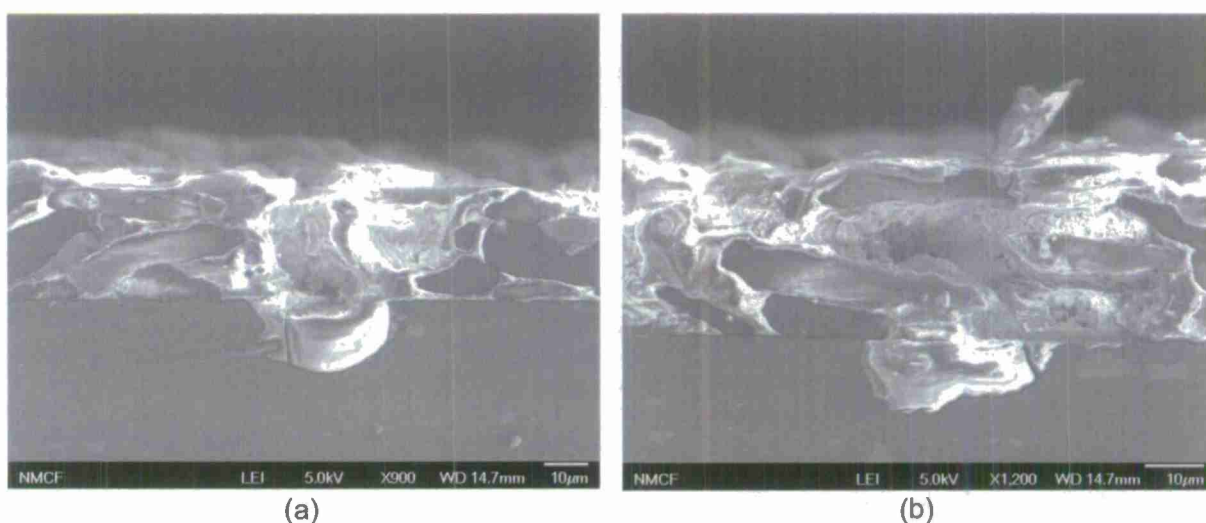


Figure 63. SEM cross-section and EDS analysis of AA2024-T351 coated with Akzo Nobel MgRP after potentiostatic hold at -0.8 V vs. SCE in 50 mM NaCl with ambient aeration for approximately 90 hours.

EDS spot scans inside pinhole show presence of Al, Mg, and O. Sample ID:493-039-A-P-P22

#### 1.7.5.5 Diagnostic Testing for Type 2 Ruptures

Cathodic, or basic, corrosion of the AA2024-T351 substrate has been suggested to be the mechanism for this type of blistering or rupturing. To test if cathodic, or basic, corrosion of AA2024-T351 is possible in chemical environments relevant to the AA2024-T351/MgRP system, 1" by 1" AA2024-T351 coupons were exposed in full immersion for 1 week to 200 mL of 50 mM NaCl along with 0.55 g of Mg shavings. The Mg shavings were observed to quickly dissolve within 24-48 hours and produce a fine white product which was shown to be primarily  $\text{Mg}(\text{OH})_2$  by X-ray diffraction. The pH of the solution was initially 5.6 but rose to 11 during the first 24 hours and declined to 10.6 over the rest of the exposure period. The AA2024-T351 coupon displayed a fairly thick layer of dark corrosion product (Figure 64) and after cleaning with nitric acid exhibited a mass loss of approximately 2%.

A similar experiment was conducted by placing a small pile (approximately 0.2 g) of Mg powder directly on a coupon of bare AA2024-T351. Then approximately 0.3 mL of 50 mM NaCl was applied to the surface and the sample was placed in a 100% relative humidity chamber for 24 hours to prevent evaporation of the electrolyte. After exposure, the pile of Mg was observed to have spread out over the entire surface of the AA2024-T351 coupon and the pH of the solution was measured by pH paper to be 10.0 or above. Severe corrosion of the Mg powder and the AA2024-T351 surface was observed. The coupon was rinsed with deionized water after exposure and is shown in Figure 65.

To investigate whether cathodic corrosion of AA2024-T351 is possible at potentials relevant to the Mg/Al galvanic couple system, a sample of bare AA2024-T351 polished to 1200 grit paper was potentiostatically held at -1.5 V vs. SCE for 1 hour in full immersion in 300 mL of aerated 50 mM NaCl. After exposure the sample showed significant corrosion (Figure 66a). Similarly a sample of bare AA2024-T351 was galvanically coupled to bare Mg in 300 mL of aerated 50 mM NaCl for 1 hour. The galvanic couple potential was measured to be fairly stable at -1.5 V vs SCE for the entirety of the test. This sample also showed significant AA2024-T351 corrosion after the exposure (Figure 66b).

Similar polarization tests were run on samples of AA2024-T351 with cross-sectional dimensions of 6.1 mm by 1.7 mm in approximately 0.3-0.4 mL of NaCl. The samples were constructed by mounting pieces of AA2024-T351 and Mg rod (with a cross sectional diameter of 8.0 mm) in epoxy resin utilizing a cylindrical mold with a diameter of 32 mm. Then, after polishing the samples to 1200 grit paper, the epoxy mold was used as a vertical, cylindrical cell in which approximately a 1-1.5 mm thick electrolyte layer was filled (Figure 67). The small volume and geometry of the cell allowed the pH of solution just above the AA2024-T351 electrode's surface to be measured with pH indicator paper during the electrochemical tests. A sample of bare AA2024-T351 was potentiostatically held at -1.5 V vs. SCE for 1 hour in full immersion in aerated 50 mM NaCl. During exposure, bubbles were observed emanating from the AA2024-T351 surface (Figure 67a) and the pH over the AA2024-T351 electrode was measured with pH indicator paper to be equal to or greater than 9.5 (Figure 67c). Similarly a sample of bare AA2024-T351 was galvanically coupled to bare Mg in full immersion in aerated 50 mM NaCl. The galvanic couple potential was measured to be relatively steady at -1.5 V vs. SCE for the length of the exposure period. During exposure, bubbles were observed emanating from the AA2024-T351 surface (Figure 67b) and the pH over the AA2024-T351 electrode was measured with pH indicator paper to be equal to or greater than 9.5 (Figure 67d). These results indicate that alkaline pH is the cause for dissolution of Al during exposure, not the presence of Mg.

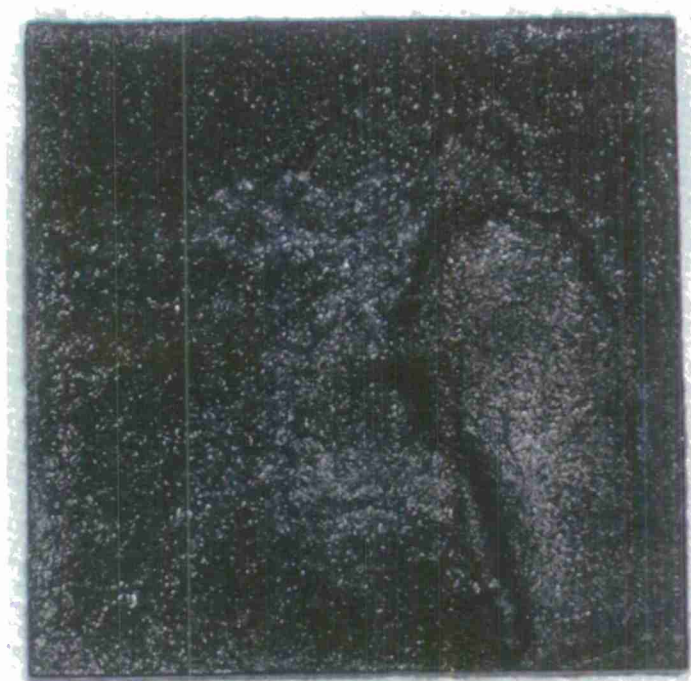


Figure 64. Optical images of AA2024-T351 after 1 week immersion in 50 mM NaCl with ambient aeration and Mg shavings.

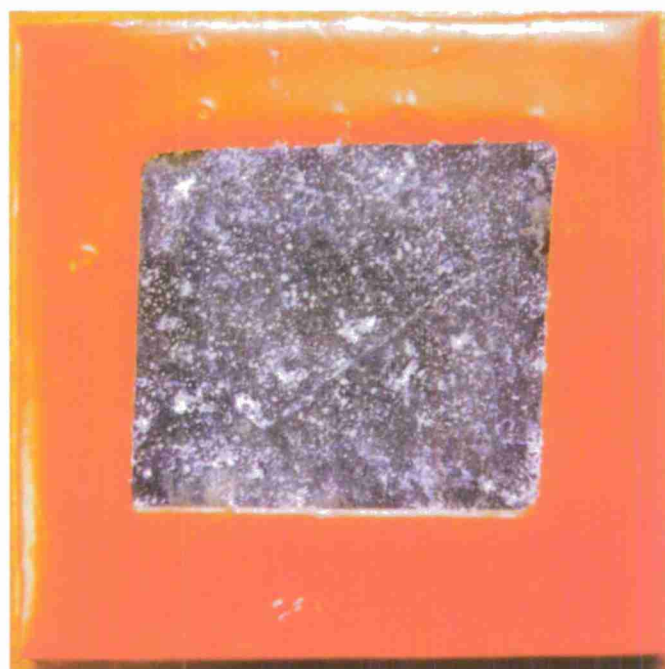
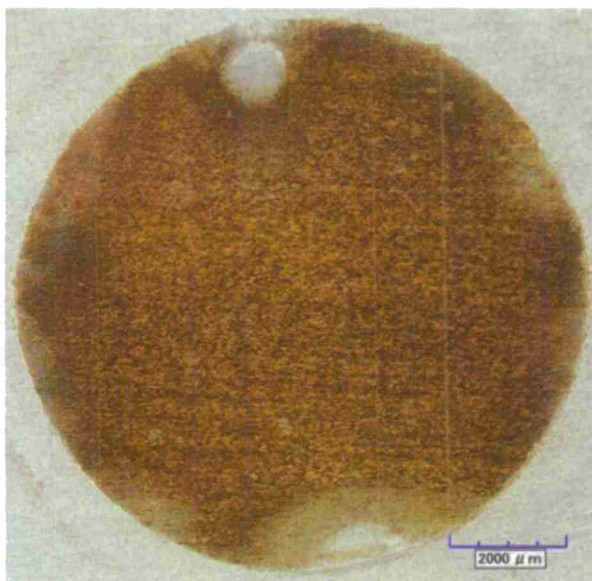


Figure 65. Optical images of AA2024-T351 after 72 hours immersion in 50 mM NaCl with ambient aeration and Mg powder.





(a)



(b)

Figure 66. Optical images of AA2024-T351 after (a) 1 hour potentiostatic hold at  $-1.5\text{ V vs. SCE}$  in  $50\text{ mM NaCl}$  with ambient aeration. (b) 1 hour galvanic couple with Mg in  $50\text{ mM NaCl}$  solution with ambient aeration



(a)



(b)



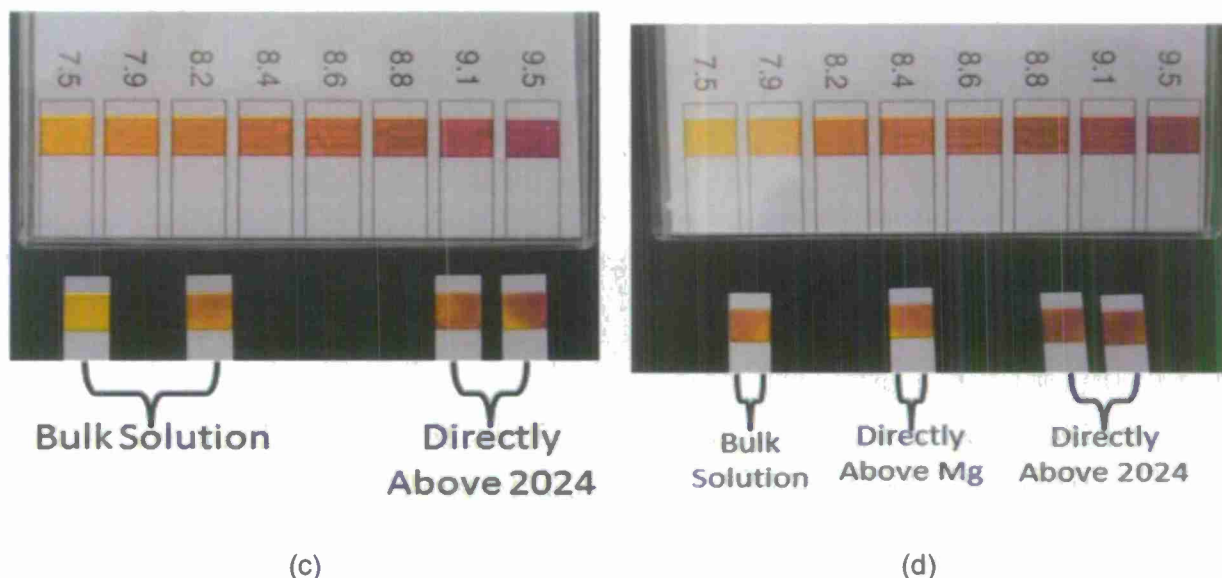


Figure 67. Small electrolyte cell setup. (a & b) schematic of sample setup (b & c) optical images of cell setup during experiment (e & f) pH indicator paper measurements, labels indicate location of measurement.

The effect of severe cathodic polarization is also experimentally shown in Figure 68. AA2024-T351 coated with an epoxy resin was galvanically coupled in aerated 50 mM NaCl to a piece of Mg coated with the same epoxy resin. The potential of the AA2024-T351 electrode with respect to a SCE reference electrode was measured throughout the experiment. With both electrodes coated the galvanic couple potential was approximately -1.0 V vs. SCE and no corrosion of the AA2024 surface was visible after 1 hour (Figure 68a). The coated AA2024-T351 was then scratched which produced a galvanic couple potential equal to that of bare AA2024-T351 (-0.55 V vs. SCE). After an hour of exposure while being galvanically coupled to the coated Mg electrode the scratch on the AA2024-T351 electrode showed no significant corrosion (Figure 68b). Finally when the coated Mg electrode was also scratched, the galvanic couple potential of the AA2024-T351 dropped to -1.5 V vs. SCE which slowly rose to -1.4 V vs. SCE by the end of an hour of exposure. After an hour of exposure while being coupled to the scratched Mg electrode, the scratch on the AA024-T351 electrode showed significant corrosion product (Figure 68c).

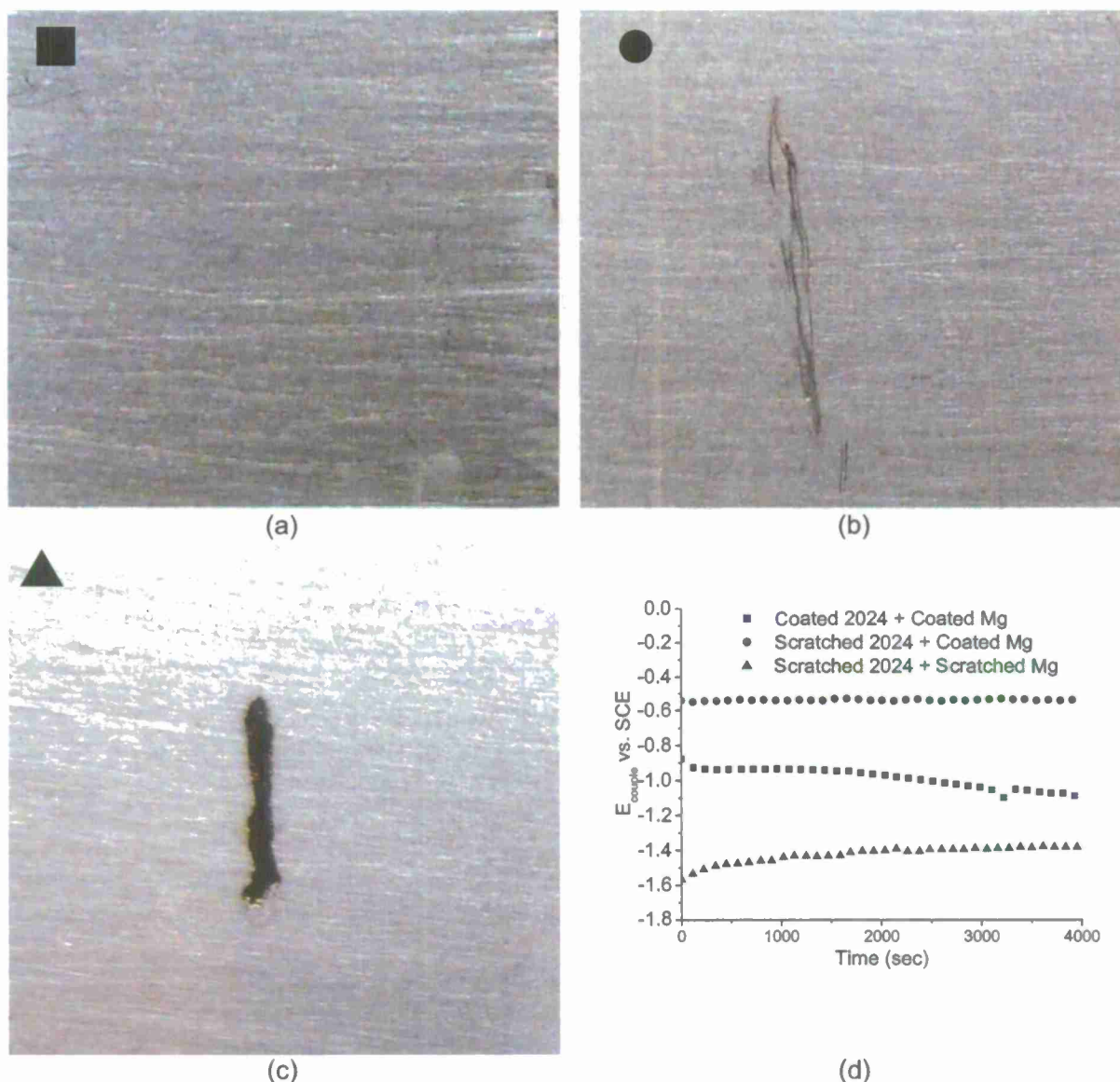


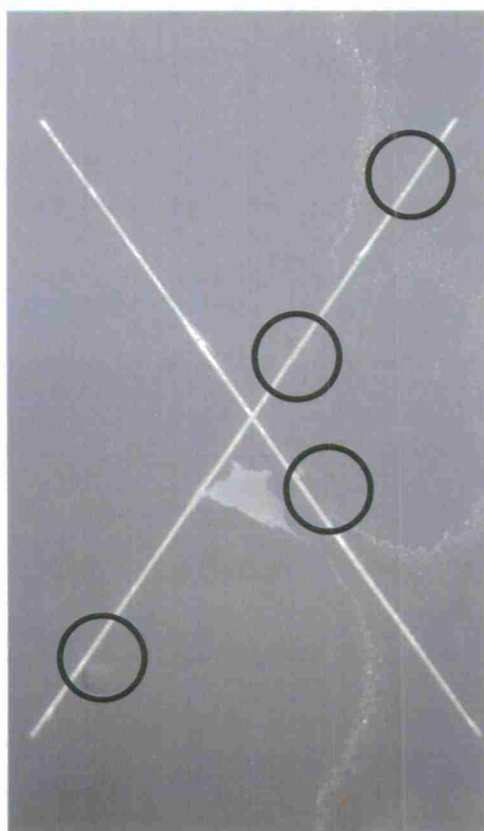
Figure 68.  $E_{\text{couple}}$  data and Optical images of AA2024-T351 after 1 hour galvanic couple between AA2024-T351 coated with Eponol and Mg coated with Eponol (a) both electrodes coated with Eponol (b) AA2024-T351 scratched (c) both electrodes scratched (d)  $E_{\text{couple}}$  for conditions a-c.

#### 1.7.5.6 The Mitigation of Type 1 and Type 2 Blisters by $\text{CO}_2$

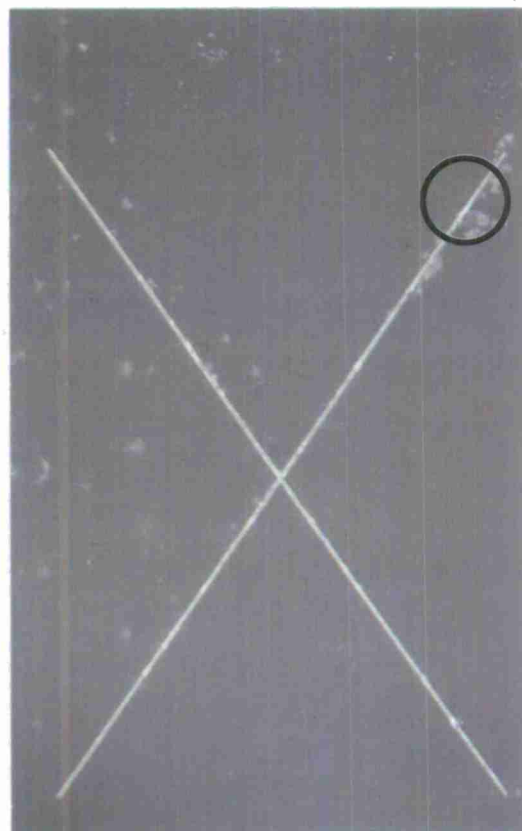
Two separate laboratory environmental exposures were conducted in a salt fog cabinet according to ASTM B-117 for approximately 800 hours. The exposures were conducted on two identical groups of panels of AA2024-T351 coated with MgRP. Panels with and without a topcoat of high performance advanced life polyurethane coating were included in each exposure. The first exposure was under ambient  $\text{CO}_2$  concentrations which were measured in the salt fog chamber by a  $\text{CO}_2$  sensor connected to a PC with data logging capabilities to be

approximately 400 ppm. During the second exposure  $\text{CO}_2$  was fed into the salt fog chamber at a constant flow rate from a regulated gas cylinder. During the second exposure the  $\text{CO}_2$  concentration in the salt fog chamber was observed to reach a steady state of approximately 6000 ppm. After exposure to salt fog according to ASTM B-117 under ambient  $\text{CO}_2$  concentrations (400 ppm) "type 1" blisters could be seen adjacent to the scribe lines on the topcoated samples (circled in Figure 69a). After exposure to salt fog according to ASTM B-117 under increased  $\text{CO}_2$  concentrations (6000 ppm) only one "type 1" blister could be seen adjacent to the scribe lines on the topcoated samples (circled in Figure 69a). This indicates that increasing the  $\text{CO}_2$  during the exposure resulted in a decreased occurrence of blistering phenomena. Non-topcoated panels were observed to show a general degradation of the coating but no blistering phenomena were observed after either exposure.

The Mg depletion rate in the MgRP was monitored throughout each exposure in the salt fog chamber with X-ray diffraction measurements (Figure 70 and Figure 71). The intensities of three prominent magnesium peaks were normalized against the Al  $\langle 111 \rangle$  peak which appeared in each spectrum due to the underlying AA2024-T351 substrate. The relative intensities of the Mg peaks decreased with increasing exposure time due to the depletion of Mg from the coating system. It was observed that the Mg peak intensities decreased at approximately equal rates in each exposure, suggesting that increasing the  $\text{CO}_2$  concentration during the exposure did not have a significant effect on the Mg depletion rates of non-topcoated or topcoated samples. For this reason it appears that increased concentrations of  $\text{CO}_2$  do not lead to increased barrier protection of the Mg pigment by the formation of  $\text{MgCO}_3$  or other compound.



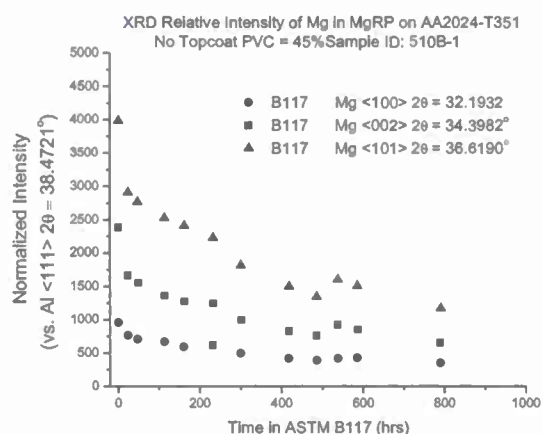
(a)



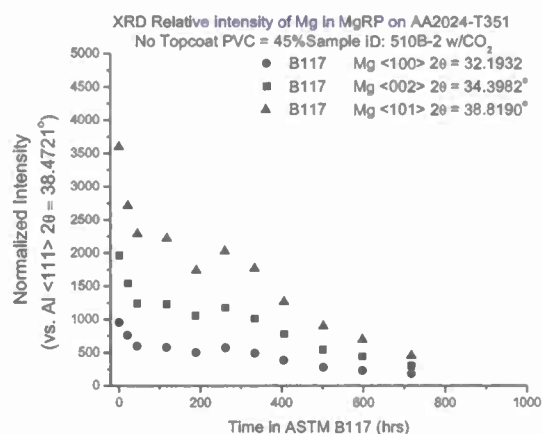
(b)

Figure 69. Optical images of panels of AA2024-T351 coated with MgRP and Aerodur 5000 Topcoat PVC = 45% after about 800 hours of environmental exposure in ASTM B-117. Blisters are circled. (a) in ambient  $\text{CO}_2$  environment 450 ppm Sample ID: 510A-1 (b) in  $\text{CO}_2$ -rich environment 6000 ppm Sample ID: 510A-2



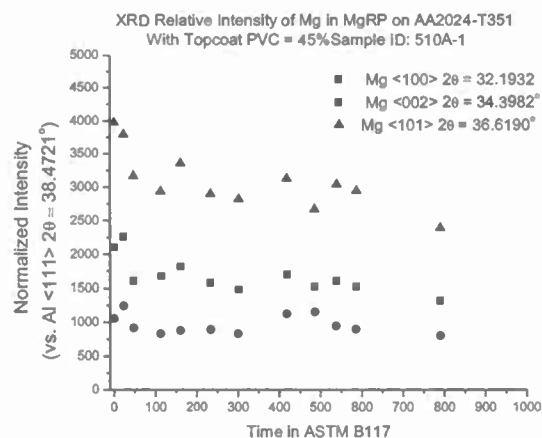


(a)

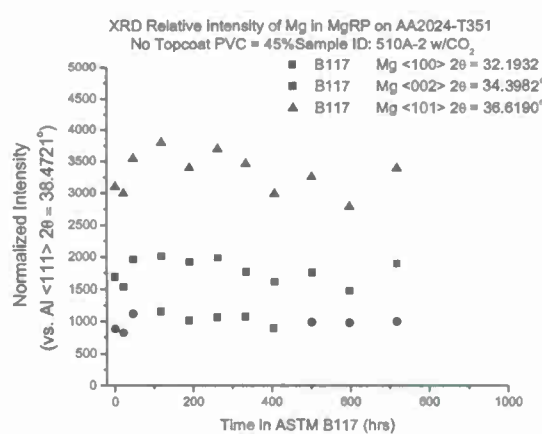


(b)

Figure 70. XRD Normalized Mg Peak Intensities vs. environmental exposure time in ASTM B-117 for panels of AA2024-T351 coated with MgRP PVC = 45% (a) in ambient CO<sub>2</sub> environment 450 ppm (b) in CO<sub>2</sub>-rich environment 6000 ppm



(a)



(b)

Figure 71. XRD Normalized Mg Peak Intensities vs. environmental exposure time in ASTM B-117 for panels of AA2024-T351 coated with MgRP and Aerodur 5000 Topcoat PVC = 45% (a) in ambient CO<sub>2</sub> environment 450 ppm (b) in CO<sub>2</sub>-rich environment 6000 ppm

The equilibrium concentrations of CO<sub>3</sub><sup>2-</sup> dissolved in solution according to various ambient partial pressures of CO<sub>2</sub> are shown in Table 6. The equilibrium concentrations of CO<sub>3</sub><sup>2-</sup> dissolved in solution were calculated utilizing Henry's Law with a Henry's Law coefficient of 0.034 for CO<sub>2</sub><sup>50, 51</sup>. The subsequent calculated E-pH diagrams of the Mg-CO<sub>2</sub>-H<sub>2</sub>O system (Figure 72) do not predict any stability of the MgCO<sub>3</sub> compound at concentrations of CO<sub>2</sub> relevant to ambient ( $P_{CO_2} = 0.0005$  atm) or CO<sub>2</sub>-rich ( $P_{CO_2} = 0.005$  atm) environments. However,

when an aqueous environment is sparged with  $\text{CO}_2$  ( $P_{\text{CO}_2} = 1.0 \text{ atm}$ ),  $\text{MgCO}_3$  becomes stable at a pH range of approximately 9 to 13 and above potentials of about -0.7 V vs. SCE.

Table 6: Equilibrium Concentrations of  $\text{CO}_3^{2-}$ , according to Henry's Law, in an Aqueous Environment under various partial pressures of  $\text{CO}_2$ .

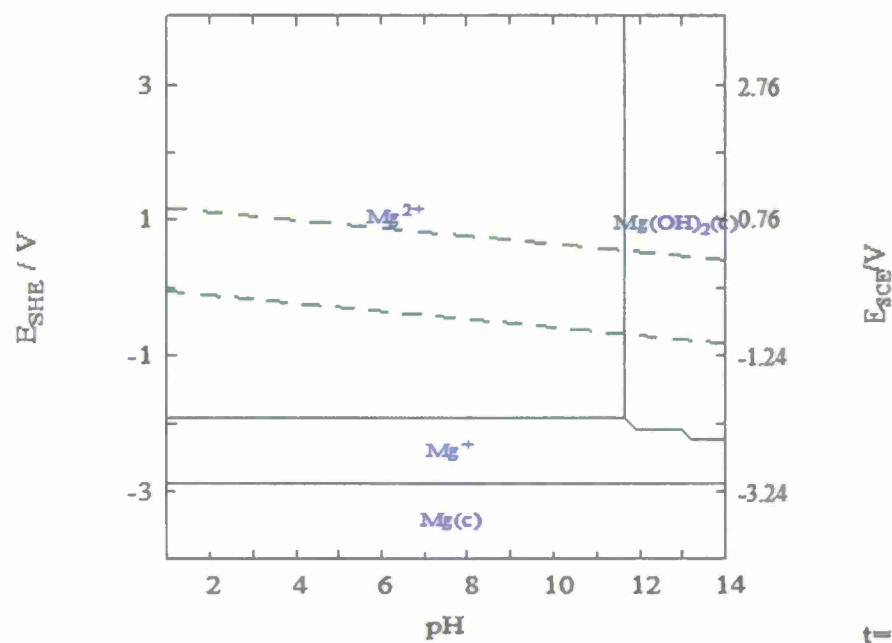
$P_{\text{CO}_2}$ atm	$[\text{CO}_2]$ vppm	$[\text{CO}_3^{2-}]$ mol/L
0.0005	500	0.000017
0.005	5000	0.00017
1	1000000	0.034

In an effort to understand the mechanisms by which  $\text{CO}_2$  may have mitigated blistering in topcoated systems during salt fog exposure, some model experiments were developed. pH measurements of various solutions of NaCl relevant to the AA2024-T351/MgRP system are shown in Figure 73. NaCl under ambient aeration was observed to have a pH of approximately 5.6. Aerated NaCl sparged with  $\text{CO}_2$  was observed to have a pH of 4.5. When 0.55 g of Mg shavings were dissolved in aerated NaCl the pH equilibrated to approximately 11 while the same solution sparged with  $\text{CO}_2$  equilibrated to a pH of approximately 7.

1" by 1" AA2024-T315 coupons were exposed in full immersion for 1 week to 200 mL of 50 mM NaCl along with 0.55 g of Mg shavings similar to the experiment conducted for Figure 64 however the solution was sparged with  $\text{CO}_2$  throughout the exposure. The Mg shavings were observed to quickly dissolve and produce a fine white product which was shown to be primarily  $\text{Mg}(\text{OH})_2$  by X-ray diffraction. The pH of the solution was initially 4.5 but rose to 7.2 during the first 24 hours and remained approximately 7 for the rest of the exposure period. After exposure the AA2024-T351 coupon displayed almost no corrosion product (Figure 74) and after cleaning with nitric acid exhibited a mass loss of less than 1%.

$[\text{Mg}^{2+}]_{\text{TOT}} = 1.00 \mu\text{M}$

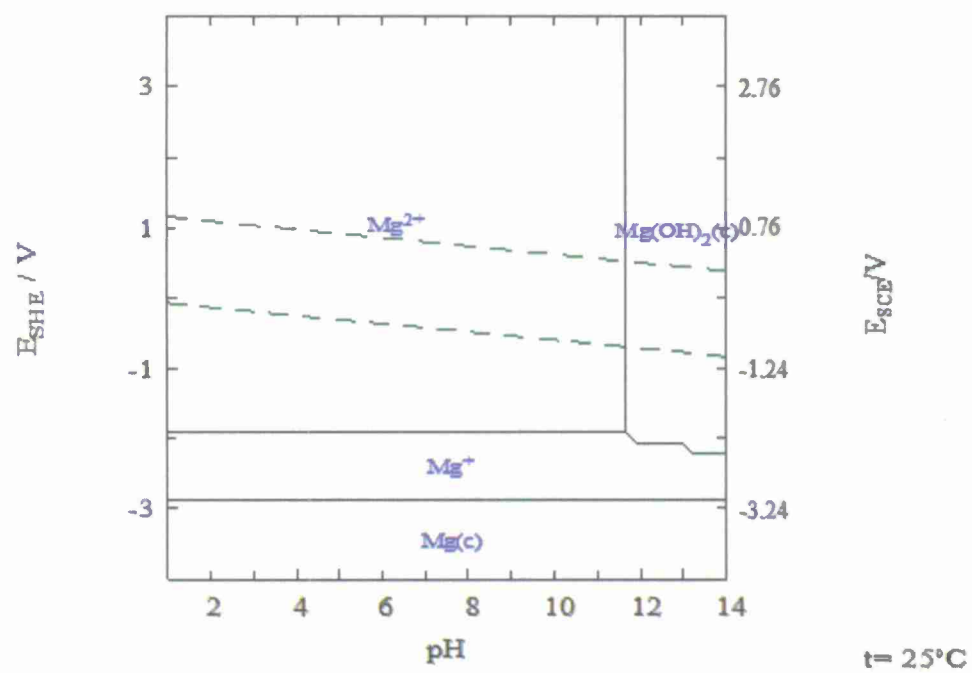
$[\text{CO}_3^{2-}]_{\text{TOT}} = 17.00 \mu\text{M}$



(a)

$[\text{Mg}^{2+}]_{\text{TOT}} = 1.00 \mu\text{M}$

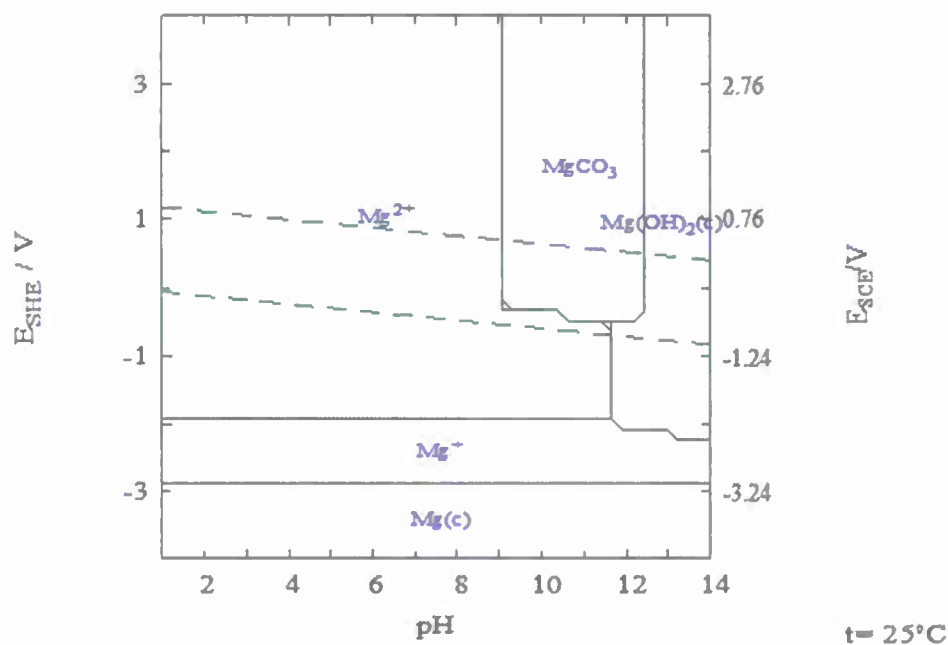
$[\text{CO}_3^{2-}]_{\text{TOT}} = 0.17 \text{ mM}$



(b)

$$[\text{Mg}^{2+}]_{\text{TOT}} = 1.00 \mu\text{M}$$

$$[\text{CO}_3^{2-}]_{\text{TOT}} = 34.00 \text{ mM}$$



(c)

Figure 72. The E-pH diagrams for carbonate with metal ion concentration of  $10^{-6} \text{ M}$  and 3 different partial pressures of atmospheric  $\text{CO}_2$ . (a)  $P_{\text{CO}_2} = 0.0005 \text{ atm}$  therefore  $[\text{CO}_3^{2-}] = 0.000017 \text{ M}$  (b)  $P_{\text{CO}_2} = .005 \text{ atm}$  therefore  $[\text{CO}_3^{2-}] = 0.00017 \text{ M}$  and (c)  $P_{\text{CO}_2} = 1 \text{ atm}$  therefore  $[\text{CO}_3^{2-}] = 0.034 \text{ M}$



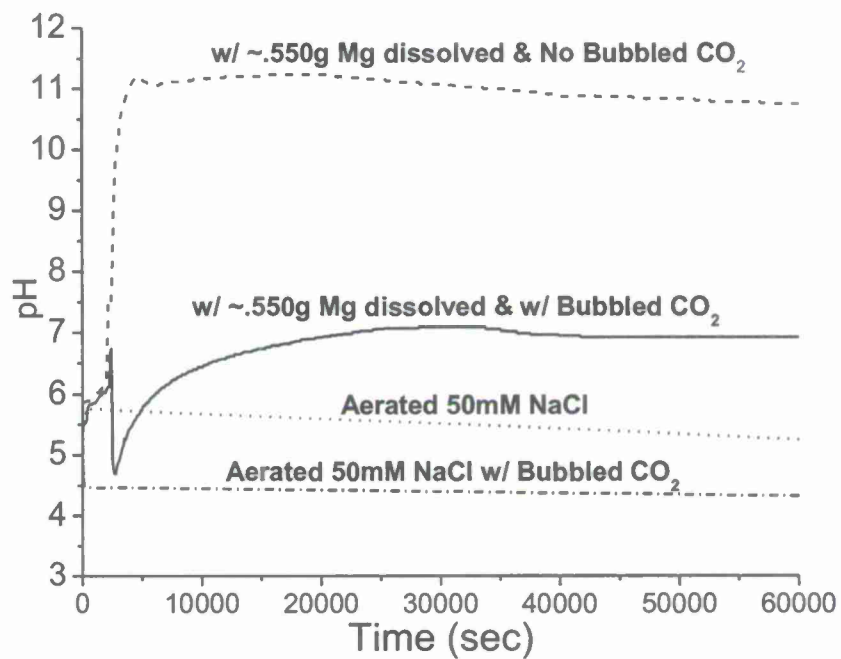


Figure 73. Solution pH of 50 mM NaCl with and without dissolved Mg and CO<sub>2</sub> sparging.



Figure 74. Optical images of AA2024-T351 after 1 week immersion in 50 mM NaCl with Mg shavings and bubbled CO<sub>2</sub>.

### 1.7.5.7 Electrochemical Diagnostics

Potentiodynamic scans of AA2024-T351 were conducted in various solutions of 50 mM NaCl and are shown in Figure 75. AA2024-T351 is shown to have an open circuit potential of approximately -0.55 V vs. SCE in aerated 50 mM NaCl and upon anodic polarization immediately pits. In aerated NaCl sparged with CO<sub>2</sub> AA2024-T351 is shown to have an open circuit potential of approximately -0.57 V vs. SCE with lower cathodic reaction rates (as compared to polarization in aerated 50 mM NaCl without CO<sub>2</sub> sparging) and slightly increased anodic dissolution rates with no change in pitting potential. In a basic solution (50 mM NaCl + 50 mM Na<sub>2</sub>CO<sub>3</sub>, pH = 11.3) AA2024-T351's open circuit potential is dramatically decreased to -1.2 V vs. SCE and the anodic dissolution of AA2024-T351 dramatically increases as compared to polarization in aerated 50 mM NaCl. When CO<sub>2</sub> is bubbled through the basic solution of 50 mM NaCl + 50 mM Na<sub>2</sub>CO<sub>3</sub> the pH is mediated to 6.7 and AA2024-T351 is shown to have an open circuit potential of -0.45 V vs. SCE.

A sample of bare AA2024-T351 polished to 1200 grit paper was potentiostatically held at -1.5 V vs. SCE for 1 hour in full immersion in aerated 50 mM NaCl similar to Figure 66a however the NaCl was sparged with CO<sub>2</sub> for the entirety of the exposure. After exposure the sample showed very little corrosion (Figure 76a). Similarly a sample of bare AA2024-T351 was galvanically coupled to bare Mg in aerated 50 mM NaCl sparged with CO<sub>2</sub> for 1 hour. The galvanic couple potential was measured to be fairly stable at -1.6 V vs SCE for the entirety of the test. This sample also showed significantly less corrosion after the exposure (Figure 76b) than in aerated NaCl which was shown earlier in Figure 66b.

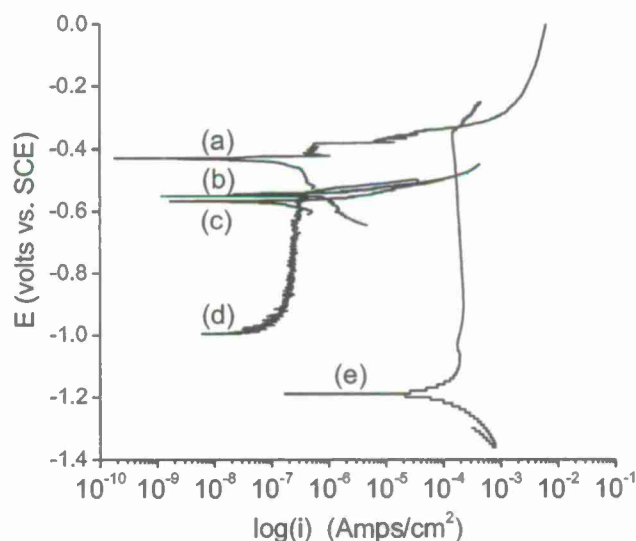


Figure 75. Anodic potentiodynamic scans of AA2024-T351 in various solutions. (a) aerated 50 mM NaCl solution + 50 mM Na<sub>2</sub>CO<sub>3</sub> + bubbled CO<sub>2</sub> pH = 6.7 (b)

aerated 50 mM NaCl solution pH = 5.6 (c) aerated 50 mM NaCl solution + bubbled  $\text{CO}_2$  pH = 4.3 (d) deaerated 50 mM NaCl solution (e) aerated 50 mM NaCl solution + 50 mM  $\text{Na}_2\text{CO}_3$  pH = 11.3

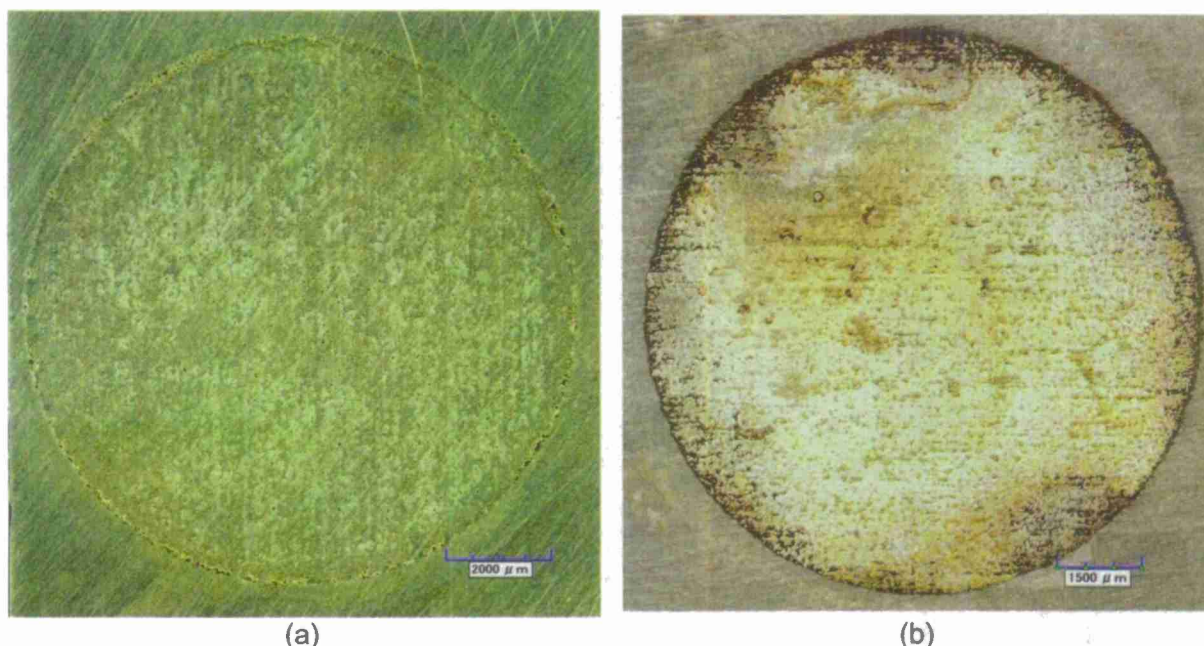


Figure 76. Optical images of AA2024-T351 after (a) 1 hour galvanic couple with Mg in 50 mM NaCl solution with bubbled  $\text{CO}_2$  (b) 1 hr potentiostatic hold at -1.5 V vs. SCE in 50 mM NaCl with bubbled  $\text{CO}_2$

### 1.7.6 Discussion

#### 1.7.6.1 Type 1 Blisters

Type 1 blisters are characterized by large areas of delamination over top of thick, relatively uniform layers of aluminum corrosion product with shallow penetration and occur solely along or proximate to scribe lines. Type 1 blisters were observed in coating systems with and without Mg pigment in the primer. The shape of the blister is consistent with osmotic blistering, in which de-adhesion is obtained by exceeding the adhesion strength of the coating with forces caused by osmotic pressurization. However a significant amount of corrosion product is seen inside the blister upon investigation with SEM. The corrosion product in these blisters was shown to consist solely of Al and O (Figure 61). Moreover, model diagnostics indicated an acidic pH at such sites (Figure 62). All of these observations strongly suggest that this phenomenon is not caused by osmotic blistering or the corrosion of Mg. It is proposed that Type 1 blisters are caused by a more classical mechanism, often associated with organic polymer coatings, involving anodic disbondment of the organic polymer<sup>40, 41</sup>. The primary mechanism for this phenomenon on aluminum alloys, particularly those containing Cu such as AA2024, has been proposed for years to be anodic coating disbondment through anodic undermining aided in this case by  $\text{H}_2$  production according to Equation 1 below<sup>41</sup>.





Equation 1

Figure 77 shows a schematic of the corrosion mechanism behind anodic disbondment. For this mechanism to be operative the Mg pigment surrounding a coating defect or scribe must be, for some reason, unable to locally prevent the dissolution of Al via cathodic polarization. This may be because the Mg pigment is simply absent from the primer (supported by PVC = 0%, Figure 61), depleted from the primer due to environmental exposure, or the primer coating is locally delaminated from the substrate at a site that lacks sufficient electrical or ionic conductivity to other Mg pigment particles in the primer. This theory is supported by the fact that the coating systems without any Mg in the primer coating exhibited much larger blisters of this type than samples which had Mg in the primer coating (Figure 59). The primary corrosion mechanism is the creation of a differential aeration cell within the defect, between the coating system and substrate, which leads to a galvanic couple between the more active, oxygen depleted head and the scribe<sup>40, 41</sup>. This galvanic couple is quickly exacerbated by an acidic shift in pH and an increase in Cl<sup>-</sup> concentration at the head of the blister (exhibited in Figure 62b) and a shift to high pH at the tail<sup>40, 41</sup>. The growth of the blister is due to the combination of anodic undercutting and hydrogen production at the outer edges of the blister where anodic dissolution of the AA2024-T351 substrate is taking place (Equation 1). The galvanic corrosion is eventually mediated by Ohmic resistances created by increased distance between anode and cathode and ionic resistances created by the deposition of corrosion product between the anode and cathode<sup>40</sup>.

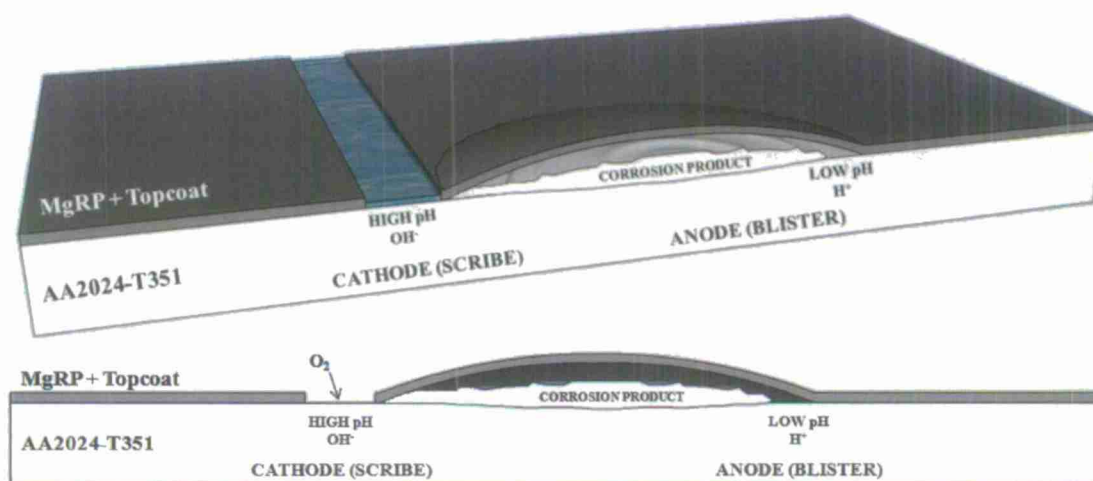


Figure 77. Schematic of proposed blistering mechanism: anodic disbondment through anodic undermining and hydrogen production.

#### 1.7.6.2 Type 2 Blisters

Type 2 blisters are characterized by narrow, deep pinholes which penetrate into the AA2024-T351 substrate. Observations of these blisters have been made on panels of AA2024-T351 coated with MgRP (PVC = 45%) without a topcoat exposed in laboratory salt fog exposures<sup>2</sup> and in laboratory full immersion exposures (Figure 63). The observation of Type 2 blisters after full immersion testing is particularly interesting because they occurred during an exposure where the panel was potentiostatically held at a potential below AA2024-T351's open circuit



potential of -0.55 V vs. SCE in 50 mM NaCl for the majority of the exposure period. Due to the fact that these blisters have been observed to form while AA2024-T351 was cathodically polarized, it has been suggested that the pinholes are caused by the cathodic, or basic, corrosion of Al which is possible due to Al's amphoteric nature<sup>43, 44, 47, 52-56</sup>. In aqueous environments the Al oxide layer is thermodynamically stable in only a narrow window of neutral pH ranges as shown by the E-pH diagram in Figure 78. For cathodic corrosion to be the mechanism to form a Type 2 blister, or rupture, there must be a local increase in solution pH at the surface of the AA2024-T351 substrate. There exist various scenarios in the AA2024-T351/MgRP system that could provide for this local pH rise. The rise in pH may be caused by the formation of Mg(OH)<sub>2</sub> at sites of Mg pigment dissolution which when dissolved in an aqueous environment at 25 °C has an equilibrium pH of approximately 10.45 (Equation 2).<sup>42</sup> Such an environment was shown experimentally to cause severe corrosion of AA2024-T351 (Figure 64).



Another possibility for localized pH increase is increased cathodic reaction rates at sites of severe cathodic polarization of the Al substrate which will lead to the cathodic dissolution of Al at such sites (Equation 3)<sup>42</sup>. In galvanic couples between Mg and AA2024-T351, there exists the possibility for the AA2024-T351 substrates to be polarized as negatively as -1.5 V vs. SCE as evidenced by the polarization scans of bare Mg and bare AA2024-T351 in Figure 79. Such severe cathodic polarization was shown experimentally to cause severe corrosion of AA2024-T351 (Figure 64).



However, it has been shown by King schematically (Figure 80) and with mixed potential modeling (Figure 81) that it is likely that such polarizations in atmospheric exposures are mediated by Ohmic resistances added by primer and topcoat polymers<sup>12</sup>. The primer and topcoat polymers act to add both ionic and electrical resistances between the Mg pigment and the AA2024-T351 substrate. The effect of such electrical resistances is demonstrated experimentally in Figure 82a by observing the galvanic couple potential between bare Mg and AA2024-T351 galvanically coupled in aerated 50 mM NaCl with a variable resistor in series between the two electrodes. When the electrical resistance in the galvanic couple is increased, the galvanic couple potential is mediated. Figure 82b shows the effect of adding ionic resistance by coating a bare AA2024-T351 exposed in full immersion to aerated 50 mM NaCl with an epoxy resin. This added ionic resistance also acts to mediate the galvanic potential. However, the possibility remains that there exists local sites of severe cathodic polarization at coating defects or scribe lines where there exists little or no ionic and electrical resistance between anode and cathode. The ASTM B-117 salt spray test is regarded to have a high time-of wetness (TOW) and NaCl concentration to trigger such attack.

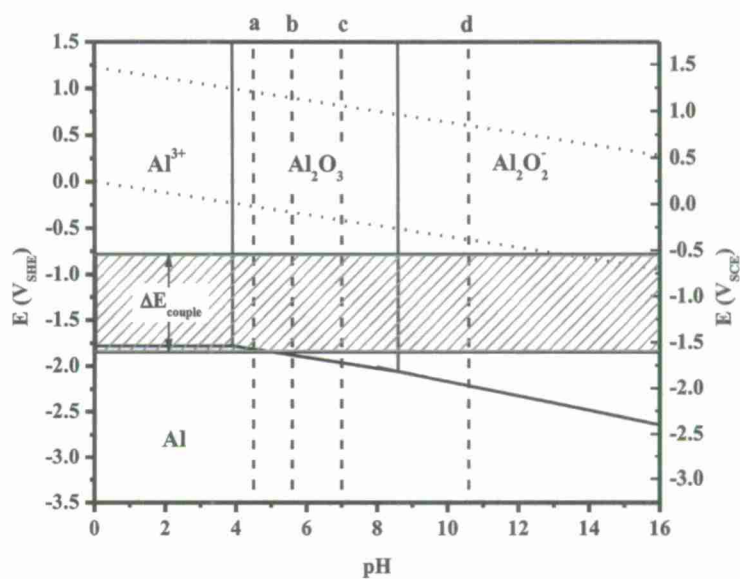


Figure 78. Potential-pH equilibrium diagram for Al-H<sub>2</sub>O system at 25°C assuming an ion concentration of  $10^{-6}$ . pH indications:  
 (a) pH = 4.5 Aerated 50 mM NaCl with CO<sub>2</sub> sparge (b) pH = 5.6 Aerated 50 mM NaCl (c) pH = 7.0 Aerated 50 mM NaCl with dissolved Mg shavings and CO<sub>2</sub> sparge (d) pH = 10.6 Aerated 50 mM NaCl with dissolved Mg shavings

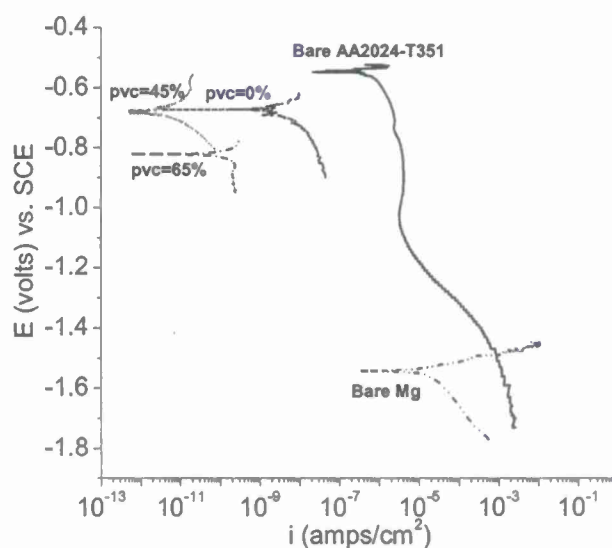


Figure 79. Potentiodynamic scans of bare electrodes and AA2024-T351 coated with Akzo Nobel MgRP + Aerodur 5000 topcoat exposed in 50 mM NaCl solution for 10 min, ambient aeration.

— = Bare AA2024-T351, - - - = Bare Mg Rod 99.9% Pure, · · · · = Topcoated MgRP PVC = 0% ID: 493-039-B-T-P22, · · · · = Topcoated MgRP PVC = 45% ID: T45F, - · - = Topcoated MgRP PVC = 65% ID: T65F.

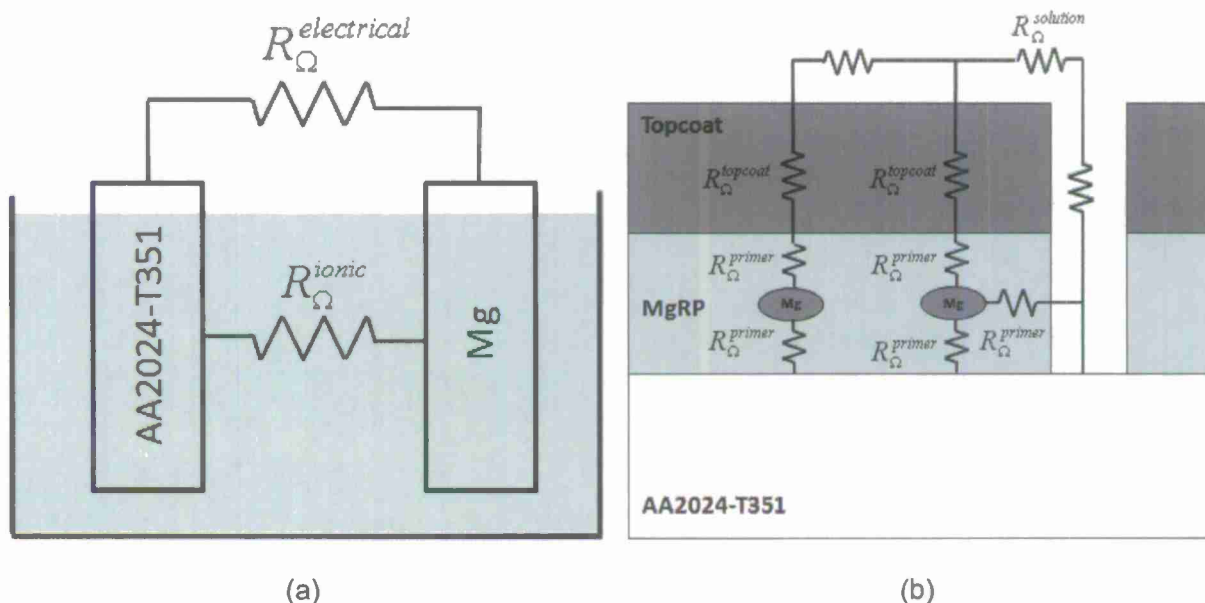


Figure 80. Schematic showing the Ohmic resistances that exist between the Mg pigment and the electrolyte (ionic) as well as between the Mg pigment and the substrate (electrical). (Interfacial resistances are omitted)

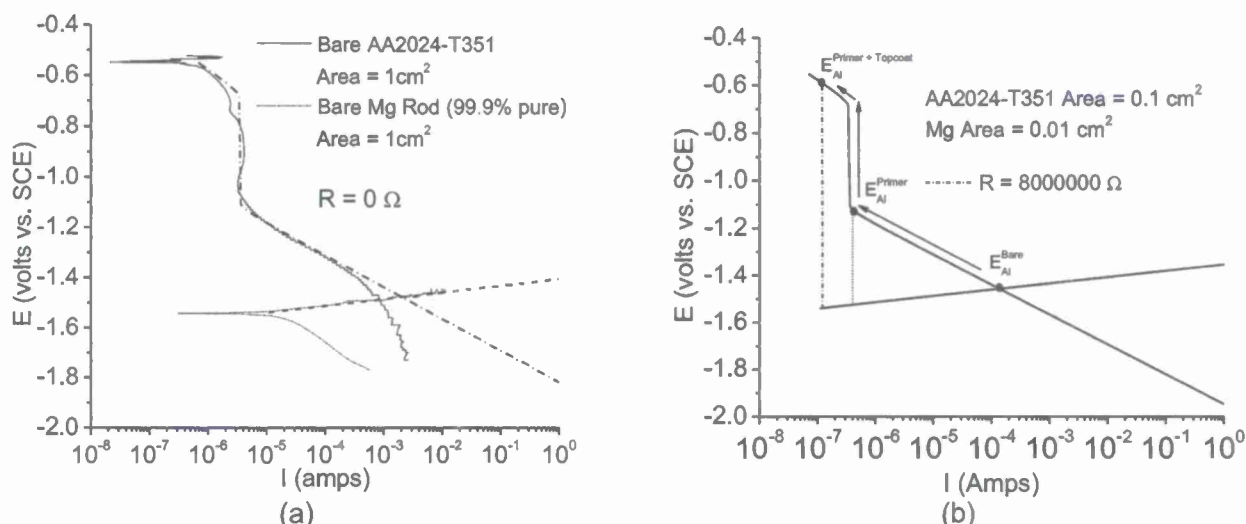


Figure 81. Mixed potential theory modeling based upon polarization scans of bare Mg and bare AA2024-T351.

(a) Polarization scans of bare AA2024-T351 and bare Mg with mixed potential model overlaid. (b) Hypothetically depicts the galvanic coupling of Mg pigment in the MgRP and the AA2024-T351 substrate, incorporating the potential drop due to ionic resistances through both the primer and topcoat polymers to the electrolyte and Ohmic resistances through the primer polymer to the AA2024-T351 substrate.

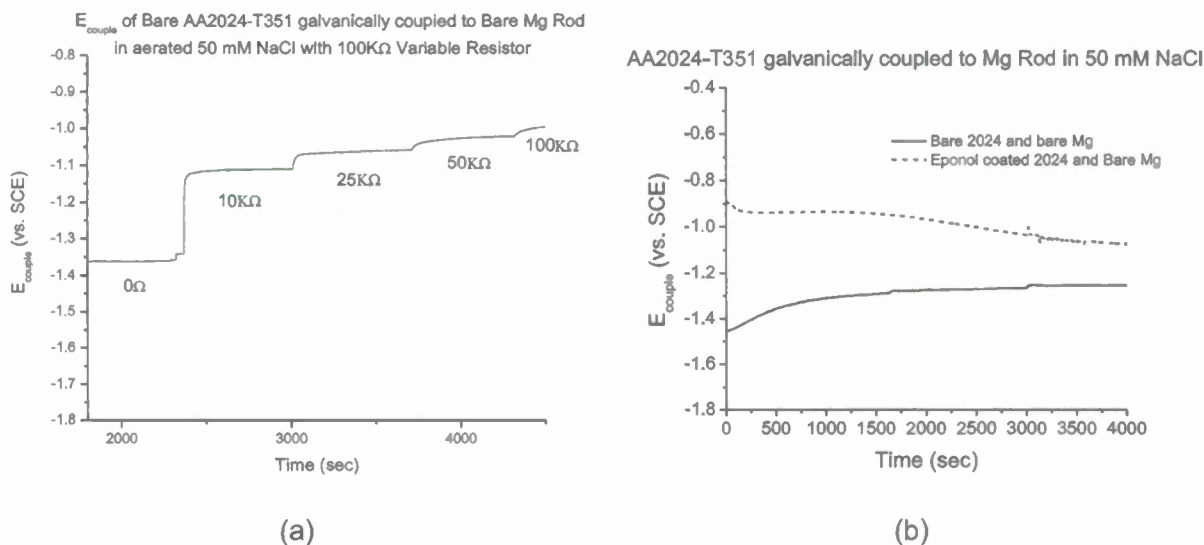


Figure 82. Galvanic couple potential ( $E_{\text{couple}}$ ) of bare AA2024 in a galvanic couple with bare Mg (a) Effect on  $E_{\text{couple}}$  by adding electrical resistance using a variable resistor. (b) Effect on  $E_{\text{couple}}$  by adding ionic resistance using an organic polymer coating of Eponol.

### 1.7.6.3 The Mitigation of Type 1 and Type 2 Blisters by $\text{CO}_2$



It has been reported <sup>1, 3, 57</sup> and shown experimentally that higher than ambient concentrations of CO<sub>2</sub> act to reduce the occurrence of Type 1 and Type 2 blisters during accelerated laboratory exposures. The addition of high concentrations of CO<sub>2</sub> to accelerated laboratory exposures of AA2024-T351 panels coated with MgRP has a two-fold effect: passivating the Cu-rich cathodic sites on the surface of the Al alloy at defect sites and moderating the pH of the aqueous exposure environment. However, due to the lack of stability of MgCO<sub>3</sub> in aqueous environments across the span of partial pressures of atmospheric CO<sub>2</sub> and negative potentials relevant to the various exposure environments utilized in this and similar works (as shown by the calculated E-pH diagrams of the Mg-CO<sub>2</sub>-H<sub>2</sub>O system in Figure 72) it is very unlikely that any realistic increase in atmospheric CO<sub>2</sub> concentration leads to an increased barrier protection brought about by the formation of Mg(CO)<sub>3</sub>. Furthermore, even under conditions of extremely high concentrations of atmospheric CO<sub>2</sub> (such as  $P_{CO_2} = 1$  atm) Mg(CO)<sub>3</sub> is not stable (Figure 72c ) at potentials relevant to Mg metal corroding in aqueous NaCl (Figure 79) or the pH of NaCl sparged with CO<sub>2</sub> with corroding Mg metal (Figure 73). Mg(OH)<sub>2</sub> which is electrically isolated from the MgRP may convert to MgCO<sub>3</sub>. However this process does not govern MgRP performance as XRD shows (Figure 70 and Figure 71).

Moreover there is a second mechanism of CO<sub>2</sub> operation. Scully and Frankenthal have shown that a high concentration of CO<sub>2</sub> acts to reduce the cathodic reaction rates on aluminum alloys with Cu-rich secondary phases acting as cathode sites <sup>48</sup>. This is accomplished by producing a thinner, more homogeneous, defect-free Al oxide film on the Cu-rich, second phase precipitates. This minimizes Al de-alloying in the alloy. As shown in Figure 73, high concentrations of CO<sub>2</sub> also mediate the pH of the aqueous environment such that the solubility of the Al oxide layer is minimized (Figure 83). For instance the pH of aerated 50 mM NaCl with CO<sub>2</sub> bubbling is 4.5 (Figure 73). This passivation of cathodic sites reduced ORR on intermetallic compounds and a reduction in the coupled anodic process or pitting. Type 1 blisters were shown to be caused by the creation of a differential aeration cell within the defect, between the coating system and substrate, which leads to a galvanic couple between the more active, oxygen depleted head and the scribe <sup>40</sup>. In high CO<sub>2</sub> environments, the Cu-rich cathodic sites in the scribe or defect become deaerated and passivated towards cathodic reactions, limiting the cathodic reaction rates in the defect. Limiting the cathodic reaction rates in the defect, in turn, limits the galvanic current between the blister and defect, reducing the anodic dissolution reactions of Al in the blister. Thus the driving forces for the growth of the blister, anodic undermining and hydrogen production, are reduced.

The presence of a high concentration of CO<sub>2</sub> also acts to moderate the pH of an aqueous environment in which Mg and AA2024-T351 are corroding by buffering (Figure 73). CO<sub>2</sub> dissolves in water and forms H<sub>2</sub>CO<sub>3</sub> which dissociates into HCO<sub>3</sub><sup>-</sup> and CO<sub>3</sub><sup>2-</sup> according to Equation 4 and Equation 5. <sup>3, 48</sup>



This acidification affect can prevent the formation of Type 2 blisters or ruptures which were shown to be caused by the cathodic, or basic, corrosion of the aluminum alloy. This effect is

evidenced by cathodic polarization and galvanic couple experiments reported earlier (Figure 74, Figure 75, Figure 76).

However Figure 75e indicates the adverse effect of alkalinity and NaCl on Al corrosion. The addition of  $\text{Na}_2\text{CO}_3$  shifts the pH of the electrolyte alkaline with the Na cation acting as a spectator via Equation 6 below.



Thus  $\text{Na}_2\text{CO}_3$  forms a solution with an approximate pH of 11.0 and results in significant corrosion of AA2024-T351.

#### 1.7.6.4 The ASTM B-117 Test

The ASTM B-117 test is quite severe. Speculatively, differences in corrosion behavior between field and ASTM B-117 exposures are believed to be associated with high TOW and high NaCl concentrations in the ASTM B-117 environment.  $\text{CO}_2$  level differences are not the cause as they were shown to be approximately equal in both environments. It should also be noted that high concentrations of  $\text{CO}_2$  can suppress both blister types but does not affect Mg pigment depletion nor passivate Mg as speculated elsewhere.<sup>3, 57</sup>

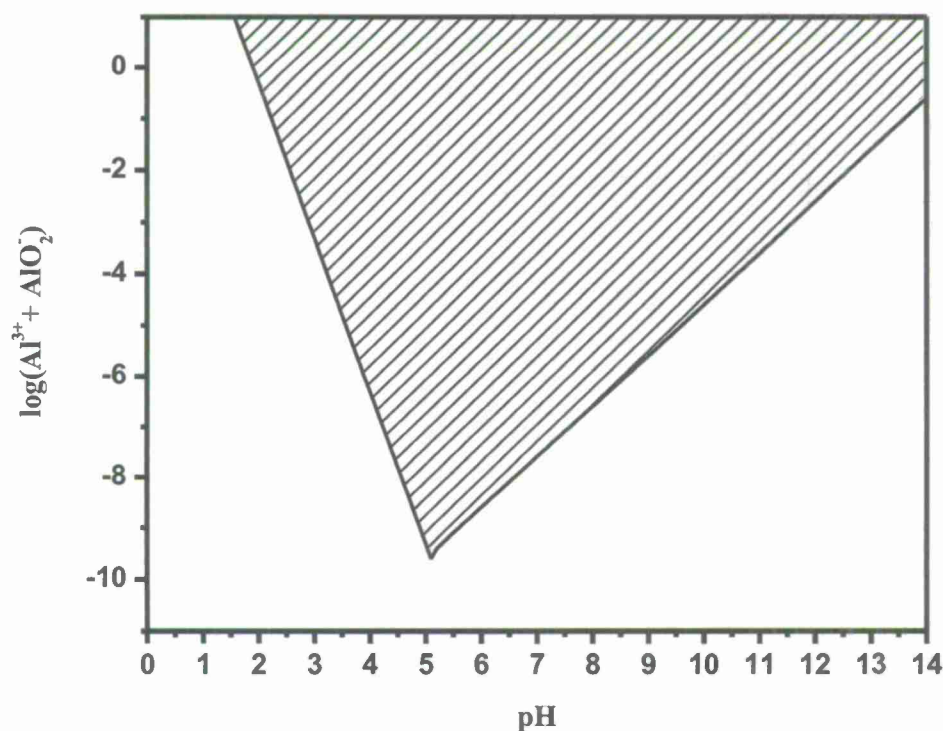


Figure 83. Al oxide stability diagram<sup>42</sup>

### 1.7.7 Economic Summary

This work further assesses and gains understanding of technological boundaries facing MgRP as an emerging technology to replace chromated corrosion inhibiting technology. It is the ultimate goal of this project to understand MgRP's current limitations such that the DoD and coating manufacturers can use the findings to improve the final product. The savings to components during the use of improved MgRP and MgRP/Topcoat systems is a little more difficult to assess. The maturation of an effective non-chromated corrosion inhibiting technology stands to save large sums in carcinogenic materials handling alone. If one single asset avoids an unscheduled repainting or repair due to proper coating degradation assessment or proper utilization of the MgRP, then several million dollars in savings is possible in each instance.

### 1.7.8 Implementation

In this report field lab discrepancies regarding blistering in early generation coatings in standard laboratory accelerated tests are examined. This report defines the role of atmospheric CO<sub>2</sub> and defines two kinds of blisters. This project does serve to provide some information on the degradation process of early generations of the commercial MgRP coating product in various, relevant, field and lab environments and helps to develop a foundation of knowledge that the DoD and coating manufacturers can use to effectively utilize the technology and/or improve the product. Should early generation MgRP be employed on other substrates, pretreatments or in a significantly different environment, variations in degradation (still yet unknown) may occur. This work makes no statement about the performance of more recent formulations of commercial MgRP coatings. Newer generation formulations are reported on in a follow up project.

### 1.7.9 Conclusion

- There are 2 distinct blistering phenomena observed in early generations of the commercial MgRP coating system on AA2024-T351:
  - Type 1 Blisters: Disbondment of the Organic Polymer Due to Anodic Undermining and H<sub>2</sub> Production
    - Have been observed on topcoated systems in ASTM B-117 and field sites at Daytona Beach (only on PVC<sub>Mg</sub> = 0% in field)
    - characterized by large areas of hemispherical delamination over top of thick, relatively uniform layers of aluminum corrosion product with shallow penetration and occur solely along or proximate to scribe lines.
    - observed in topcoated systems with and without Mg pigment in the primer.
    - caused by anodic coating disbondment through anodic undermining aided in this case by H<sub>2</sub> production
  - Type 2 Blisters: Ruptures Caused by Cathodic Corrosion of Al
    - Have been observed on non-topcoated systems in ASTM B-117
    - characterized by narrow, deep pinholes which penetrate into the AA2024-T31 substrate
    - observed on panels of AA2024-T351 coated with MgRP (PVC = 45%) exposed in laboratory salt fog exposures and in laboratory full immersion exposures where the AA2024-T351 is cathodically polarized

- due the cathodic, or basic, corrosion of Al caused by cathodic polarization of AA2024-T351 substrate and formation of  $\text{Mg}(\text{OH})_2$  at sites of Mg pigment dissolution.
- Increasing the concentration of  $\text{CO}_2$  to levels of 6000 ppm or higher (by sparging for example) during full immersion testing or accelerated lab exposures:
  - Reduces the occurrence of Type 1 blisters by passivating the Cu-rich cathodic sites on the surface of the Al alloy at defect sites limiting the galvanic current between cathodic defect sites and anodic sites of coating disbondment.
  - Reduces the occurrence of Type 2 ruptures by moderating the pH of the aqueous exposure environment preventing the cathodic corrosion of the AA2024-T351 substrate.
  - Does not have a significant effect on the Mg depletion rates of non-topcoated or topcoated samples. For this reason it appears that increased concentrations of  $\text{CO}_2$  do not lead to increased barrier protection of the Mg pigment by  $\text{MgCO}_3$  or otherwise.
  - Is not responsible for the difference in corrosion behavior between ASTM B-117 and field exposures.

#### 1.7.10 Appendices

#### 1.7.11 Bibliography

1. W. H. Abbott, personal correspondence with Dr. William Abbott of Battelle Memorial Institute, (2009).
2. C. Matzdorf, personal correspondence with Dr. Craig Matzdorf of NAVAIR, (2009).
3. S. S. Pathak, M. D. Blanton, S. K. Mendon and J. W. Rawlins, Investigation on dual corrosion performance of magnesium-rich primer for aluminum alloys under salt spray test (ASTM B117) and natural exposure, *Corros Sci*, 52 (2010), 1453-1463.
4. G. P. Bierwagen, D. E. Tallman, M. Nanna, D. Battocchi, A. Stamness and V. J. Gelling, New developments in Cr-free primers for aerospace alloys., *Abstr Pap Am Chem S*, 228 (2004), U360-U360.
5. D. Battocchi, A. M. Simoes, D. E. Tallman and G. P. Bierwagen, Comparison of testing solutions on the protection of Al-alloys using a Mg-rich primer, *Corros Sci*, 48 (2006), 2226-2240.
6. D. Battocchi, A. M. Simoes, D. E. Tallman and G. P. Bierwagen, Electrochemical behaviour of a Mg-rich primer in the protection of Al alloys, *Corros Sci*, 48 (2006), 1292-1306.
7. G. Bierwagen, D. Battocchi, A. Simoes, A. Stamness and D. Tallman, The use of multiple electrochemical techniques to characterize Mg-rich primers for Al alloys, *Prog Org Coat*, 59 (2007), 172-178.
8. A. Simoes, D. Battocchi, D. Tallman and G. Bierwagen, Assessment of the corrosion protection of aluminium substrates by a Mg-rich primer: EIS, SVET and SECM study, *Prog Org Coat*, 63 (2008), 260-266.
9. H. Xu, D. Battocchi, D. E. Tallman and G. P. Bierwagen, Use of Magnesium Alloys as Pigments in Magnesium-Rich Primers for Protecting Aluminum Alloys, *Corrosion*, 65 (2009), 318-325.
10. Report on Carcinogens, 11th Edition, U.S. Department of Health and Human Services, Public Health Services, National Toxicology Program,



11. R. G. Buchheit, Chromate and Chromate-Free Conversion Coatings, vol. 13A, ASM Handbook Volume 13A, Corrosion: Fundamentals, Testing, and Protection (ASM International), (Materials Park, Ohio, ASM International, 2003,
12. A. D. King and J. Scully, Sacrificial Anode based Galvanic and Barrier Corrosion Protection of AA2024-T351 by a Mg-Rich Primer and Development of Test Methods for Remaining Life Assessment Corrosion, 67 (2011), 055004.
13. K. N. Allahar, D. Battocchi, G. P. Bierwagen and D. E. Tallman, Transmission Line Modeling of EIS Data for a Mg-Rich Primer on AA 2024-T3, J Electrochem Soc, 157 (2010), C95-C101.
14. K. N. Allahar, D. Battocchi, M. E. Orazem, G. P. Bierwagen and D. E. Tallman, Modeling of electrochemical impedance data of a magnesium-rich primer, J Electrochem Soc, 155 (2008), E143-E149.
15. K. N. Allahar, D. Wang, D. Battocchi, G. P. Bierwagen and S. Balbyshev, Real-Time Monitoring of a United States Air Force Topcoat/Mg-Rich Primer System in ASTM B117 Exposure by Embedded Electrodes, Corrosion, 66 (2010), -.
16. S. Feliu, R. Barajas, J. M. Bastidas and M. Morcillo, Ac Impedance Study About the Protection Mechanisms of Zinc-Rich Primers, Abstr Pap Am Chem S, 195 (1988), 58-Pmse.
17. D. Pereira, J. D. Scantlebury, M. G. S. Ferreira and M. E. Almeida, The Application of Electrochemical Measurements to the Study and Behavior of Zinc-Rich Coatings, Corros Sci, 30 (1990), 1135-1147.
18. S. Feliu, M. Morcillo and S. Feliu, Deterioration of cathodic protection action of zinc-rich paint coatings in atmospheric exposure, Corrosion, 57 (2001), 591-597.
19. V. M. Rudoi, O. V. Yaroslavtseva, T. N. Ostanina, L. P. Yurkina and O. Y. Subbotina, Electrochemical behavior of protective anodic primers, Protection of Metals, 35 (1999), 277-281.
20. H. Marchebois, C. Savall, J. Bernard and S. Touzain, Electrochemical behavior of zinc-rich powder coatings in artificial sea water, Electrochim Acta, 49 (2004), 2945-2954.
21. C. M. Abreu, M. Izquierdo, M. Keddam, X. R. Novoa and H. Takenouti, Electrochemical behaviour of zinc-rich epoxy paints in 3% NaCl solution, Electrochim Acta, 41 (1996), 2405-2415.
22. S. G. Real, A. C. Elias, J. R. Vilche, C. A. Gervasi and A. Disarli, An Electrochemical Impedance Spectroscopy Study of Zinc Rich Paints on Steels in Artificial Sea-Water by a Transmission-Line Model, Electrochim Acta, 38 (1993), 2029-2035.
23. C. M. Abreu, M. Izquierdo, X. R. Novoa, C. Perez and A. Sanchez, Influence of different aggressive media on the protective behaviour of zinc rich paints, Rev Metal Madrid, 35 (1999), 182-189.
24. N. V. Kondrashova, S. A. Nesterenko, O. V. Naumenko and L. I. Antropov, Influence of Zinc and Magnesium Cations on the Electrochemical-Behavior of Steel with a Polymer Primer, Protection of Metals, 25 (1989), 73-75.
25. S. Feliu, R. Barajas, J. M. Bastidas and M. Morcillo, Mechanism of Cathodic Protection of Zinc-Rich Paints by Electrochemical Impedance Spectroscopy .1. Galvanic Stage, J Coating Technol, 61 (1989), 63-69.
26. S. Feliu, R. Barajas, J. M. Bastidas and M. Morcillo, Mechanism of Cathodic Protection of Zinc-Rich Paints by Electrochemical Impedance Spectroscopy .2. Barrier Stage, J Coating Technol, 61 (1989), 71-76.
27. C. M. Abreu, M. Izquierdo, P. Merino, X. R. Novoa and C. Perez, A new approach to the determination of the cathodic protection period in zinc-rich paints, Corrosion, 55 (1999), 1173-1181.

28. M. Morcillo, R. Barajas, S. Feliu and J. M. Bastidas, A-Sem Study on the Galvanic Protection of Zinc-Rich Paints, *J Mater Sci*, 25 (1990), 2441-2446.
29. R. A. Armas, C. A. Gervasi, A. Disarli, S. G. Real and J. R. Vilche, Zinc-Rich Paints on Steels in Artificial Seawater by Electrochemical Impedance Spectroscopy, *Corrosion*, 48 (1992), 379-383.
30. H. Marchebois, M. Keddam, C. Savall, J. Bernard and S. Touzain, Zinc-rich powder coatings characterisation in artificial sea water - EIS analysis of the galvanic action, *Electrochim Acta*, 49 (2004), 1719-1729.
31. O. O. Knudsen, U. Steinsmo and M. Bjordal, Zinc-rich primers - Test performance and electrochemical properties, *Prog Org Coat*, 54 (2005), 224-229.
32. M. E. Nanna and G. P. Bierwagen, Mg-rich coatings: A new paradigm for Cr-free corrosion protection of al aerospace alloys, *Jct Research*, 1 (2004), 69-80.
33. J. R. Scully, F. Presuel-Moreno, M. Goldman, R. G. Kelly and N. Talleart, User-selectable barrier, sacrificial anode, and active corrosion inhibiting properties of Al-Co-Ce alloys for coating applications, *Corrosion*, 64 (2008), 210-229.
34. F. J. Presuel-Moreno, M. E. Goldman, R. G. Kelly and J. R. Scully, Electrochemical sacrificial cathodic prevention provided by an Al-Co-Ce metal coating coupled to AA2024-T3, *J Electrochem Soc*, 152 (2005), B302-B310.
35. F. J. Presuel-Moreno, H. Wang, M. A. Jakab, R. G. Kelly and J. R. Scully, Computational modeling of active corrosion inhibitor release from an Al-Co-Ce metallic coating - Protection of exposed AA2024-T3, *J Electrochem Soc*, 153 (2006), B486-B498.
36. F. Presuel-Moreno, M. A. Jakab, N. Talleart, M. Goldman and J. R. Scully, Corrosion-resistant metallic coatings, *Mater Today*, 11 (2008), 14-23.
37. D. H. Wang, D. Battocchi, K. N. Allahar, S. Balbyshev and G. P. Bierwagen, In situ monitoring of a Mg-rich primer beneath a topcoat exposed to Prohesion conditions, *Corros Sci*, 52 (2010), 441-448.
38. ASTM, Standard Practice for Operating Salt Spray (Fog) Apparatus, ASTM B117 - 09. ASTM International, West Conshohocken, PA, 2009
39. G. P. Bierwagen, C. S. Jeffcoate, J. P. Li, S. Balbyshev, D. E. Tallman and D. J. Mills, The use of electrochemical noise methods (ENM) to study thick, high impedance coatings, *Prog Org Coat*, 29 (1996), 21-29.
40. D. A. Little, M. A. Jakab and J. R. Scully, Effect of surface pretreatment on the underpaint corrosion of AA2024-T3 at various temperatures, *Corrosion*, 62 (2006), 300-315.
41. E. L. Koehler, U. R. Evans, B. F. Brown, J. Kruger, R. W. Staehle and National Association of Corrosion Engineers. Research Committee., *Corrosion Under Organic Coatings, Localized Corrosion*, (Houston, Tex., National Association of Corrosion Engineers, 1974, p. 117-133).
42. M. Pourbaix, *Atlas of electrochemical equilibria in aqueous solutions*, 2d English, (Houston, Tex.: National Association of Corrosion Engineers, 1974), p. 644 p.
43. G. S. Frankel and Y. Baek, Electrochemical quartz crystal microbalance study of corrosion of phases in AA2024, *J Electrochem Soc*, 150 (2003), B1-B9.
44. H. Kaesche, Studies on the Corrosion of Aluminum, *Zeitschrift für physikalische Chemie*, 14 (1963), 557-566.
45. A. R. Despic, J. Radosevic, P. Dabic and M. Kliskic, Abnormal Yields of Hydrogen and the Mechanism of Its Evolution during Cathodic Polarization of Aluminum, *Electrochim Acta*, 35 (1990), 1743-1746.
46. E. P. G. T. Vandeven and H. Koelmans, Cathodic Corrosion of Aluminum, *J Electrochem Soc*, 123 (1976), 143-144.

47. S. M. Moon and S. I. Pyun, The corrosion of pure aluminium during cathodic polarization in aqueous solutions, *Corros Sci*, 39 (1997), 399-408.
48. J. R. Scully, R. P. Frankenthal, K. J. Hanson, D. J. Siconolfi and J. D. Sinclair, Localized Corrosion of Sputtered Aluminum and Al-0.5-Percent Cu Alloy Thin-Films in Aqueous Hf Solution .2. Inhibition by CO<sub>2</sub>, *J Electrochem Soc*, 137 (1990), 1373-1377.
49. N. B. Pilling and R. E. Bedworth, The Oxidation of Metals at High Temperatures, *Journal Institute of Metals*, 29 (1923), 529-591.
50. I. S. Cole, N. S. Azmat, A. Kanta and M. Venkatraman, What really controls the atmospheric corrosion of zinc? Effect of marine aerosols on atmospheric corrosion of zinc, *Int Mater Rev*, 54 (2009), 117-133.
51. C. Leygraf and T. E. Graedel, Atmospheric corrosion, The Electrochemical Society series, (New York: Wiley-Interscience, 2000), p. xii, 354 p.
52. S. I. Pyun and S. M. Moon, Corrosion mechanism of pure aluminium in aqueous alkaline solution, *J Solid State Electr*, 4 (2000), 267-272.
53. M. Mokaddem, P. Volovitch, F. Rechou, R. Oltra and K. Ogle, The anodic and cathodic dissolution of Al and Al-Cu-Mg alloy, *Electrochim Acta*, 55 (2010), 3779-3786.
54. H. Kaesche, *Zeitschrift für physikalische Chemie*, 34 (1962), 87-108.
55. R. D. Armstrong and V. J. Braham, The mechanism of aluminium corrosion in alkaline solutions, *Corros Sci*, 38 (1996), 1463-1471.
56. J. S. Zhang, M. Klasky and B. C. Letellier, The aluminum chemistry and corrosion in alkaline solutions, *J Nucl Mater*, 384 (2009), 175-189.
57. S. S. Pathak, M. D. Blanton, S. K. Mendon and J. W. Rawlins, Carbonation of Mg powder to enhance the corrosion resistance of Mg-rich primers, *Corros Sci*, 52 (2010), 3782-3792.

## 1.8 Environmental Degradation of a Mg-Rich Primer: Comparison of Selected Field Environments with Laboratory Exposures (King, A. D., Kannan, B. and Scully, J. R.)

### 1.8.1 Summary

Magnesium rich primer (Akzo Nobel Aerodur 2100 Product #: 2100P003 Lot #: 493-190 MFG: 03/2009), in a non-topcoated, scribed condition, was utilized for the corrosion protection of an AA2024-T351 substrate pretreated with PreKote™ surface pretreatment. Exposures were conducted in the field at a coastal marine site Kennedy Space Center, FL (KSC), at an inland rural site at Birdwood Golf Course in Charlottesville, VA, in ASTM B-117 with 5% NaCl and the same standard test modified with ASTM Sea Water as well as in full immersion in ambiently aerated 5% NaCl solution. Mg pigment depletion rate, galvanic protection potential and coating barrier properties were tracked throughout exposure periods in both field and laboratory environments. Analysis near and far from the scribe was performed. Post-mortem characterization with SEM/EDS was conducted to elucidate coating and scribe morphology, corrosion products present, corrosion of the AA2024-T351 substrate, as well as in an attempt to interrogate the throwing power of the coating system. No blistering or similar macroscopic coating failure phenomena were observed in the MgRP or along the scribe lines after exposure in any of the studied environments. Additionally, in contrast to similar environmental exposures of earlier generation commercial products in the past<sup>1,2</sup>, no indications of cathodic corrosion, as evidenced by narrow pinholes, or underpaint corrosion or anodic undermining, as evidenced by large areas of coating delamination above regions of Al corrosion, are visible at the coating/metal interface when viewed in SEM cross-section after environmental exposure in these field and laboratory environments. Full immersion in ambiently aerated 5% NaCl solution, ASTM B-117 in 5% NaCl and ASTM B-117 in ASTM artificial sea water all depleted the MgRP of metallic Mg pigment far from the scribe at various rates, with significant depletion (less than 5% by volume as detectable by XRD<sup>3</sup>) occurring after approximately 1000 hrs of exposure in all cases. Field exposures in Charlottesville, VA and Kennedy Space Center, FL resulted in depletion of metallic Mg pigment far from the scribe after 2000 and 4000 hrs of exposure, respectively. Hence, the general qualitative aspects of galvanic protection and Mg depletion were similar in all environments studied. As a result of remote pigment depletion, the global galvanic protection potential of the coating system, with respect to remote scratches, increases with exposure time in each environment, from values approximately equal to that of bare Mg (-1.6 V vs. SCE) to those approximately equal to that of bare AA2024-T351 (-0.55 V vs. SCE). Barrier properties of the MgRP primer coating also degrade with time in each environment. However, acceleration factors are hard to determine due to inherent scatter in the EIS data due to the random occurrence of defects in the coating. The primer affords little barrier protection after Mg depletion but corrosion of the AA2024-T351 substrate under the coating is not observed. Post-mortem SEM/EDS characterization after 1000 hrs of salt fog exposure indicate a throwing power that extended the entire half-width ( $\approx 350 \mu\text{m}$ ) of the scribe in both standard and modified ASTM B-117 exposures with thin-layer electrolyte geometries and continuous wetting. Post-mortem SEM/EDS characterization after 24 weeks of exposure in the field at Kennedy Space Center, FL indicates a throwing power that extends approximately 200 - 300  $\mu\text{m}$  in the scribe from the coating edge. Post-mortem SEM/EDS characterization after 24 weeks of exposure in the field at Charlottesville, VA was inconclusive due to the high self-corrosion rate of the MgRP coating and subsequent chemical dissolution of Mg-based corrosion products by high TOW and low pH rain ( $\text{pH} \approx 5$ ). The differences in rate-of-change of Mg depletion from the coating upon environmental exposure are presumed to stem from differences in time-of-wetness



and in rates of polymer degradation, specifically resistivity, due to UV exposure. Differences in throwing power in lab and field environments are presumed to stem from differences in electrolyte geometries; continuous thin-layer in salt fog cabinet exposures compared to isolated droplets which do not form a connected path in field exposures. Future studies examine the performance of a MgRP in a topcoated, scribed condition.

### 1.8.2 Introduction

Many field and laboratory studies conducted over the past few years have shown very promising corrosion mitigation results for an organic coating system containing a metallic Mg-pigmented organic primer (MgRP) used for the corrosion protection of the precipitation age hardened aluminum alloy 2024-T351.<sup>1, 2, 4-12</sup> MgRP is a primary candidate coating system to replace chromate type surface pretreatments and chromate pigmented primers which are known for their toxicity and carcinogenic properties.<sup>5, 13, 14</sup> Chromate pigmented organic primers not only provide a physical barrier to corrosion but also possess the ability to supply soluble chromate corrosion inhibitors to remote scratches and coating defects. Such coatings also possess the important ability to control and inhibit corrosion at the wetted coating/metal interface should bulk water layers be formed there.<sup>15-17</sup> The protection mechanisms provided by the MgRP are distinctly different than those offered by chromate pigmented organic primers based on ionic inhibitor release. While barrier protection of the aluminum alloy is also afforded by the MgRP, the MgRP has been designed and shown to provide sacrificial anode based cathodic protection to the aluminum alloy by galvanically coupling the metallic Mg pigment in the MgRP to the AA2024-T351 substrate.<sup>2, 4, 8, 10, 11</sup>

Barrier protection is afforded to the AA2024-T351 substrate by the continuous physical barrier consisting of the organic epoxy polymer matrix of the MgRP, the Mg pigment particles, and any other insoluble pigments in the primer or corrosion products which may have formed within defects in the coating. Also, an organic polyurethane polymer topcoat is often applied to add additional barrier protection and greatly decreases the coating system's susceptibility to UV degradation.<sup>18</sup> In general, barrier protection schemes rely mainly on lowering the ionic conductivity of the electrolyte film above the metal surface and at the coating metal interface through the low ionic transport properties of the organic coating itself in addition to the wet adhesion properties of the coating.<sup>19</sup> As a result, anodes and cathodes that are separated by short distances cannot operate to support corrosive half-cell reactions at metal sites under the coating because one of the four requirements for corrosion is severely suppressed (corrosion requires an anode, cathode, electrical contact, and ionic contact). Secondly, the coating can serve as a transport barrier to resist corrodant ingress such as Cl<sup>-</sup>. Ingress is often controlled by pigmentation with insoluble species at an appropriate pigment volume fraction and/or by cross-linking and vulcanization in the polymer matrix that serves as the binder for the pigment.<sup>20</sup> These properties of the polymer coating system are degraded by a host of "stresses" including UV photonic radiation, chemical reaction of the coating with the environment whether by hydrolysis or saponification or by mechanical forces which destroy adhesion.<sup>20, 21</sup> The latter includes osmotic blistering, corrosion product wedging, hydroxyl ion production and reductive dissolution of oxides that destroy wet adhesion. Such degradation is considered inevitable and is also the reason for including in the design of the coating system an additional primary protection mechanism, such as sacrificial cathodic protection, that remains operative should the barrier protection mechanism be damaged or destroyed.

The MgRP is designed to galvanically couple the active, metallic Mg pigment in the primer to the more noble AA2024-T351 substrate and provide sacrificial anode based cathodic protection to the aluminum alloy. This approach is well established in the design of zinc-rich primers for use on various steels and has been well documented.<sup>22-37</sup> Protection of steel by these Zn-rich primers is afforded primarily by sacrificial anode based cathodic protection and secondarily by precipitation of  $Zn(OH)_2$  at bare sites after migration of  $Zn^{+2}$ .<sup>31, 32</sup> A conductive, sacrificial metallic zinc matrix is formed throughout the primer layer by incorporating an appropriate volume fraction of zinc pigmentation in the primer. Zinc also has a low self-corrosion rate which facilitates a realistic protection lifetime. In this case, magnesium is less noble than the precipitation age hardened aluminum alloys it might be used to protect and is readily available and actively corrodes in most electrolytes.<sup>8, 9, 38</sup> When coupled to the AA2024-T351 substrate, the galvanically coupled Mg pigment becomes an electron donor, and mixed potential theory can be used to explain the open circuit of the system when exposed to full immersion. Therefore, this protection mechanism has been verified to be operative with open circuit and anodic polarization measurements of AA2024-T351 coated with experimental formulations of MgRP which all show the AA2024-T351 to be cathodically polarized in full immersion in ambiently aerated NaCl.<sup>2, 8, 11</sup>

In order for magnesium to be available for sacrificial cathodic protection of the AA2024-T351 substrate it must be both electrically and ionically "well connected" to the AA2024-T351 substrate. Both electrical and ionic conduction is required between metallic phases comprising anodes and cathodes. During environmental exposure, electrical conduction is obtained through the AA2024-T351 substrate's physical contact with the conductive Mg pigment matrix in the primer while ionic conduction is achieved between the substrate and Mg pigment through the electrolyte. When galvanic current flows, several ohmic voltage drops exist between the Mg pigment and the electrolyte (ionic) and also between the Mg pigment and the substrate (electrical) which result from resistive layers associated with substrate pretreatments, epoxy resin or polymer type, and Mg pigment volume concentration (MgPVC). King and Scully showed the MgPVC of the Mg-rich primer plays an important role in determining the sacrificial cathodic protection capabilities of the coating and can be assessed nondestructively with XRD.<sup>2</sup> The PVC not only determines the total supply of Mg sacrificial anode material available in the primer but also is a determining factor controlling the effective conductance of the primer layer and resulting cathodic protection afforded to the AA2024-T351 by the Mg pigment in the primer. Primer formulations with high MgPVC not only have a larger total supply of Mg but also have a higher conductance through the coating, allowing a larger percent of the distributed Mg pigment to be utilized to protect remote defects. Primer formulations with moderate MgPVC have a lower conductance through the coating. This is a result of a smaller amount of electrically connected Mg throughout the polymer. For this reason, a smaller amount of Mg is electrochemically sensed by a remote counter electrode and available for protection of remote defects in the coating. The application of a topcoat to the coating system also drastically increases the ohmic ionic resistance between the buried Mg pigment and the electrolyte.

Past lab and field exposure studies were conducted by collaborating organizations in hopes of determining an optimal primer formulation with respect to Mg pigment volume concentration along with optimal coating system stack-ups.<sup>18, 39, 40</sup> Most of these studies have pointed to an optimal Mg pigment volume concentration of approximately 45% which is at or just below the calculated theoretical critical pigment concentration.<sup>4, 9, 12, 38, 41-44</sup> King and Scully showed that this formulation provides a balance of moderated sacrificial cathodic protection, good long-term barrier protection and the beneficial characteristic of preserved, isolated clusters of Mg pigment available for the protection of future defects as they occur throughout a coating's lifetime in a

given exposure environment.<sup>1, 2, 38</sup> Thus, two possible modes of protection are described by King and Scully; long range protection of remote defects by the global galvanic protection potential afforded to the substrate and local or short range Mg pigment-based protection of local and buried defects. Both modes of protection are mediated by the high ionic and electrical resistance of the coating system as a function of MgRP PVC, substrate pretreatments, primer polymer and topcoat properties.<sup>1, 2</sup> The mediation of the cathodic protection abilities is important in the application of MgRP. It is important for the coating system to provide adequate cathodic protection to the AA2024-T351 substrate but to also avoid the detrimental effects of cathodic corrosion of the amphoteric AA2024-T351 substrate which can be caused by increased localized pH due to severe cathodic polarization and/or excessive Mg pigment dissolution.<sup>1, 2, 45-51</sup>

The period of protection provided by a coating system depends critically on the severity of the environment of exposure, the relevant alloy, surface finish, and electrochemical driving forces such as galvanic coupling. The outdoor corrosion of bare and coated metal alloys is controlled by several factors; including corrodant deposition rate, type of corrodant, time of wetness by rain or condensation, dew point, UV light, wet/dry cycling, relative humidity, temperature and temperature cycling. Some of these factors can act synergistically. Corrosivity of Al and steel in natural environments is typically a function of metrological parameters such as time of wetness, time above a certain relative humidity (e.g., 35% RH), Cl<sup>-</sup>, SO<sub>x</sub> and NO<sub>x</sub> deposition rates.<sup>52, 53</sup> Polymer coating degradation likely depends on UV wavelength, the cumulative dosage of UV light, time of wetness and corrodant concentration. In the past, several empirical environmental severity indexes have been proposed that rank the corrosivity of various environments towards bare, finished and/or coated metals.<sup>52, 54, 55</sup> A critical need resolved in this study of MgRP for the use of corrosion protection of aluminum alloys is to understand MgRP's degradation rate and characteristics in various relevant exposure environments in hopes of identifying environmental factors that are significant to MgRP's degradation which can then form the focus of future studies. The first step involves studying the degradation characteristics of the MgRP system without a topcoat.

Much of the previous work attempting to determine detailed, long term performance characteristics of a representative MgRP coating system have utilized laboratory accelerated life testing (LALT), primarily ASTM B-117 salt fog cabinet testing.<sup>4, 5, 38-40, 44, 56-58</sup> However, this testing environment was designed to be used for qualification testing (MIL-A-8625F Military Specification for Anodic Coatings for Al and Al Alloys, MIL-C-5541E Military Specification for Chemical Conversion Coatings on AL and Al Alloys, MIL-PRF-23377 Military Specification for Epoxy, High Solids Primers, and MIL-PRF-32239 Military Performance Specification for Advanced Performance Coating Systems for Aerospace Applications), not lifetime assessment, and the qualification standards of which were determined utilizing completely different coating technologies. The validity of the ASTM B-117 exposure environment has largely been questioned, particularly because the ASTM B-117 exposure environment makes no effort to realistically reproduce field exposure environments with respect to many factors commonly accepted to be relevant to environmental severity, such as electrolyte chemistry, atmosphere composition, time of wetness (TOW), relative humidity, cycling, or UV intensity. Additionally, unique macroscopic failure modes (i.e. blisters, scribe creep, etc) of early generations of the MgRP coating system were observed in the ASTM B-117 environment that are not typically seen in the field.<sup>4, 39, 40, 44</sup> The discrepancies in MgRP degradation phenomena between the lab and field eliminated the chance to estimate lab vs. field acceleration factors from standard laboratory lifetime tests. However, newer, optimized generations of the coating system do not typically display unique failure modes in field or LALT environments when applied to AA2024-



T351.<sup>39, 40</sup> Therefore, assuming a similarity of corrosion modes in the absence of any blistering phenomena in these accelerated environments, the determination of acceleration factors with respect to specific, measurable coating properties is a worthy goal.

The objective of this study is to track the degradation of a representative MgRP coating formulation (Akzo Nobel Aerodur 2100 Lot# 493-190 MFG 03/2009) and coating system stack-up throughout its lifetime in various environments. A working understanding of the coating system's degradation in relevant lab and field environments will be developed by measuring Mg pigment depletion rate far away from and proximate to a scribe (as measured by XRD and SEM/EDS), galvanic protection potential and coating barrier properties throughout each exposure. These measurements, in conjunction with post-mortem characterization, diagnostic electrochemical experiments, and mixed potential modeling, will provide insight into the significant factors controlling environmental severity in the context of the MgRP.

### 1.8.3 Lessons Learned

Regarding testing techniques, it was further shown that XRD is an excellent technique to quantify the remaining metallic Mg pigment in the MgRP and was capable of distinguishing metallic, hexagonal close packed Mg from  $\text{Mg}(\text{OH})_2$  or other forms of Mg such as  $\text{MgCO}_3$  and is capable of detecting polymer-encapsulated Mg, preserved and available for protection of future, local defects. Conventional OCP measurements were useful tools in assessing the global sacrificial anode capacity (ability to protect remote defects) available to remote scratches and whether the sacrificial galvanic function was operable in non-top coated formulations. EIS was a useful and valid tool for assessing the residual barrier properties of the depleted MgRP coating and clear trends with respect to barrier properties could be observed with environmental exposure. Additionally, a clear decrease in barrier properties of the coating was associated with a decrease in quantity of Mg pigment in the coating and an increase in galvanic protection potential throughout all exposure environments. However, EIS was not a useful tool to assess the sacrificial anode capacity or galvanic function. The XRD technique is ready for further development towards field implementation as a non-destructive tool for the assessment of metallic Mg pigment depletion in field exposed MgRP.

There is no evidence that the results of this project, with respect to characteristics of MgRP degradation, can be applied directly to other alloys. However, the conceptual idea of sacrificial cathodic protection by both well-connected and a buried or encapsulated sources of Mg pigment as well as approximated field vs. lab acceleration factors with regards to pigment depletion rate, global galvanic protection potential and coating barrier properties likely apply broadly and can be transferred knowledge. The assessment techniques themselves (XRD, OCP, EIS, etc.) are directly transferrable to all applications of MgRP on similar aerospace or structural alloys and can each be used as a field deployable suite of assessment tools. In this and previous reports, these techniques are used qualitatively, with respect to their initial values measured at time = 0 of exposure. In order to use these tools more quantitatively, on materials that have been field exposed and for which no "virgin", or pristine samples remain, a database of measurements must be compiled to include variations in coating pigment loading and coating thickness. This work is viewed to be outside of the scope of this project as the particular substrate alloys and coating parameters used the bounds for the database must be determined by the end-user. With respect to field and lab exposure environments, no significant variations in the overall degradation mechanism of the more-recent generation MgRP coating (Akzo Nobel Aerodur 2100 Lot# 493-190 MFG 03/2009) or alarming failure phenomena were observed in exposures in ASTM B117 with neutral 5% NaCl or ASTM artificial sea water or in field exposures at



Charlottesville, VA or Kennedy Space Center, FL. In fact, the general aspects of galvanic protection and Mg depletion were similar in all environments studied. In all environments studied, electrochemically available, connected Mg pigment is depleted and a small amount of encapsulated Mg pigment is preserved as long as the primer polymer can withstand UV degradation or water and corrodant ingress. The differences in rate-of-change of Mg depletion from the coating are presumed to stem from differences in time-of-wetness and in rates of polymer degradation, specifically resistivity, due to UV exposure. Differences in throwing power in lab and field environments are presumed to stem from differences in electrolyte covering geometries; continuous thin-layer in salt fog cabinet exposures and isolated droplet geometries in field exposures.

#### 1.8.4 Technical Investigations

##### 1.8.4.1 Materials

The MgRP-coated AA2024-T351 samples studied were comprised of AA2024-T351 sheet, pretreated with Prekote surface pretreatment, and primed with a  $30 \pm 10 \mu\text{m}$  thick layer of magnesium rich primer, "MgRP" (Akzo Nobel Aerodur 2100 Product# 2100P003 Lot# 493-190 MFG 03/2009). Before the MgRP was applied, the AA2024-T351 panels were pretreated with Prekote™, a non-toxic, non-corrosive, non-flammable, CFC free, ODS free, and chromate free surface pretreatment. The pretreatment does not contain any corrosion inhibitors and is not a conversion coating, but promotes adhesion between the primer and substrate. The magnesium rich primer consists of a 1-part epoxy matrix pigmented with Mg metal flake powder with a loading of approximately 45% volume fraction. The metallic Mg pigment in the primer has flake geometry with an average diameter of  $20 \mu\text{m}$ . All tested panels were provided and painted by collaborators at NAVAIR.<sup>39, 40</sup> After curing for approximately 4 weeks in a dry box, a 50.8 mm (2") by 101.6 mm (4") "X" with a width of approximately 0.7 mm was machine scribed through the coating layers of the panel, exposing bare AA2024-T351, to simulate a scratch prior to environmental exposure. In general, the scribe penetrated 20 to  $50 \mu\text{m}$  into the substrate. A schematic and optical micrograph of the MgRP coated AA2024-T351 panels investigated in this study are shown in Figure 84 and Figure 85, respectively. A cross-section schematic of the scribed region is shown in Figure 84b.

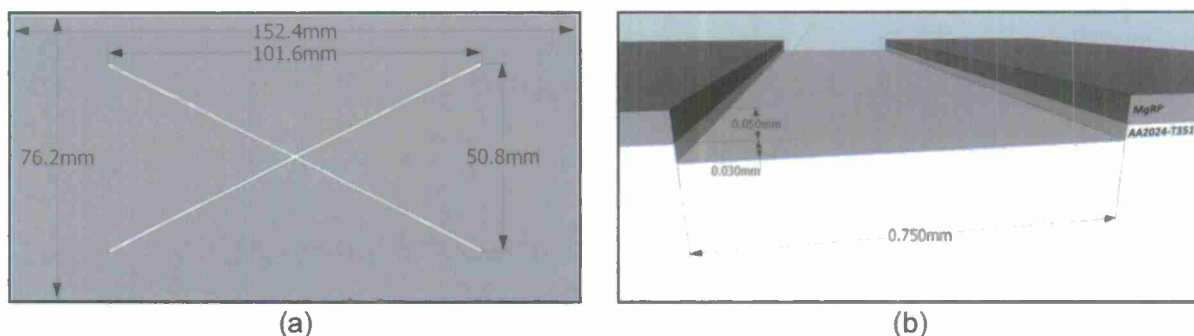
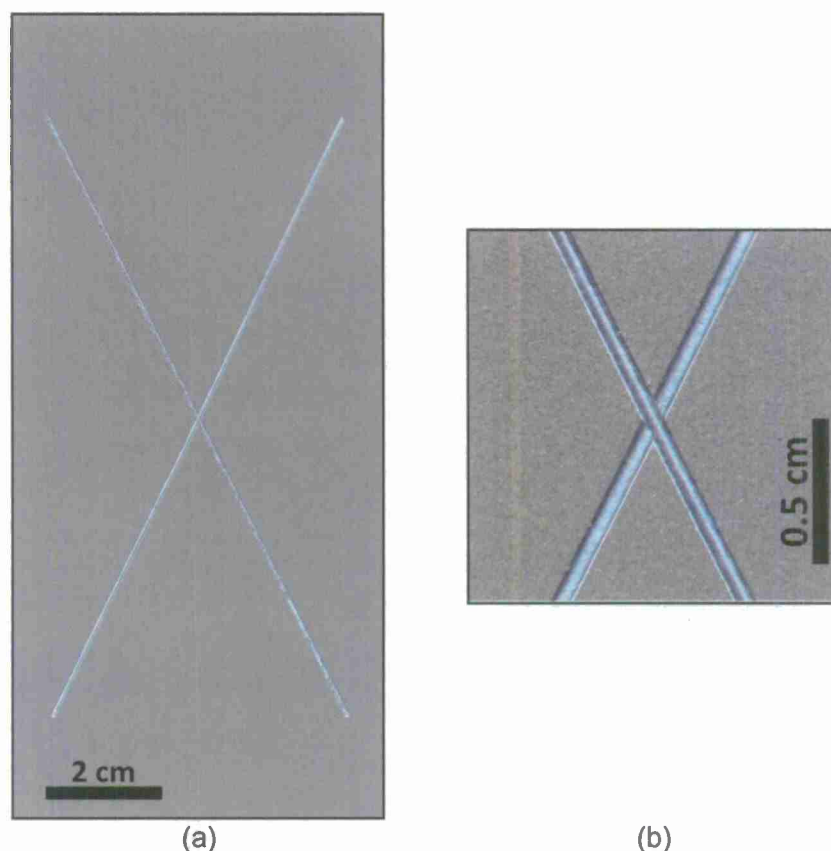


Figure 84. Schematic of AA2024-T351 panels coated with Mg-rich primer coating.



(a) (b)  
Figure 85. Optical micrograph of AA2024-T351 panels coated with MgRP that have not been environmentally exposed.

A planar SEM micrograph of a scribed MgRP-coated AA2024-T351 panel, before the sample has been exposed to any weathering environment, is shown in Figure 86a. EDS spot scans were taken at points labeled 1 and 2 in Figure 86a and are shown in Figure 86b. EDS of the MgRP coating shows strong Mg and C intensities and low O levels which suggests the as-applied MgRP to contain unoxidized Mg pigment encapsulated in the carbon-rich epoxy polymer matrix.

Figure 87 shows two SEM micrographs of cross-sectioned MgRP on AA2024-T351, before the sample has been exposed to any weathering environment, (a) far away from and (b) proximate to the scribe. The thickness of the primer layer is approximately 30  $\mu\text{m}$  and the scribe can be seen to penetrate into the substrate approximately 30-50  $\mu\text{m}$ . Mg pigment particles have an approximate diameter of 20  $\mu\text{m}$ . EDS spot scans conducted on the Mg particles (Figure 87c) in the cross-sectioned MgRP also indicated low O levels, which suggest the Mg is largely unoxidized prior to weathering.

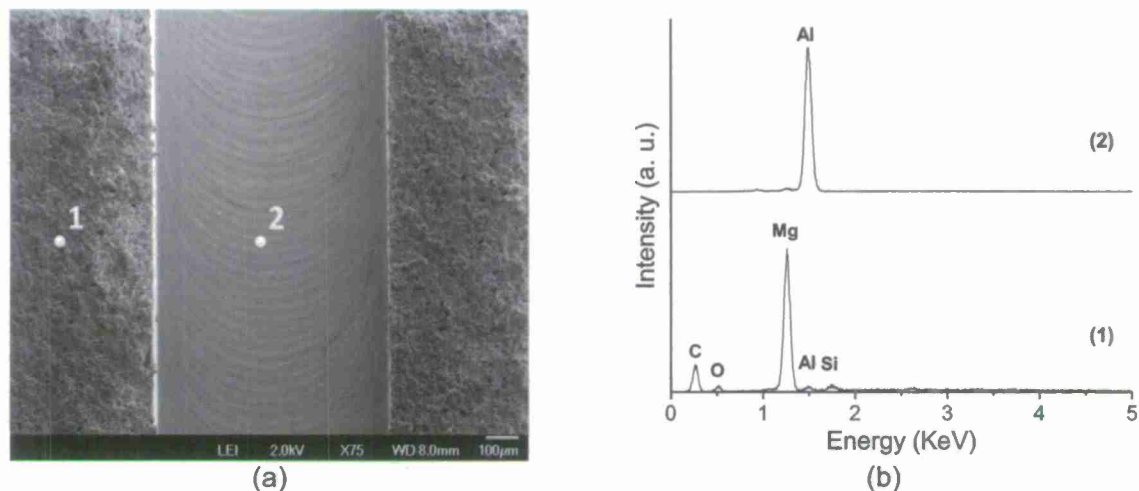


Figure 86. Scanning electron micrograph (a) and EDS (b) of AA2024-T351 pretreated with Prekote and coated with MgRP (MgPVC = 45%) as applied before environmental exposure. Spot markers indicate approximate location of EDS analysis.

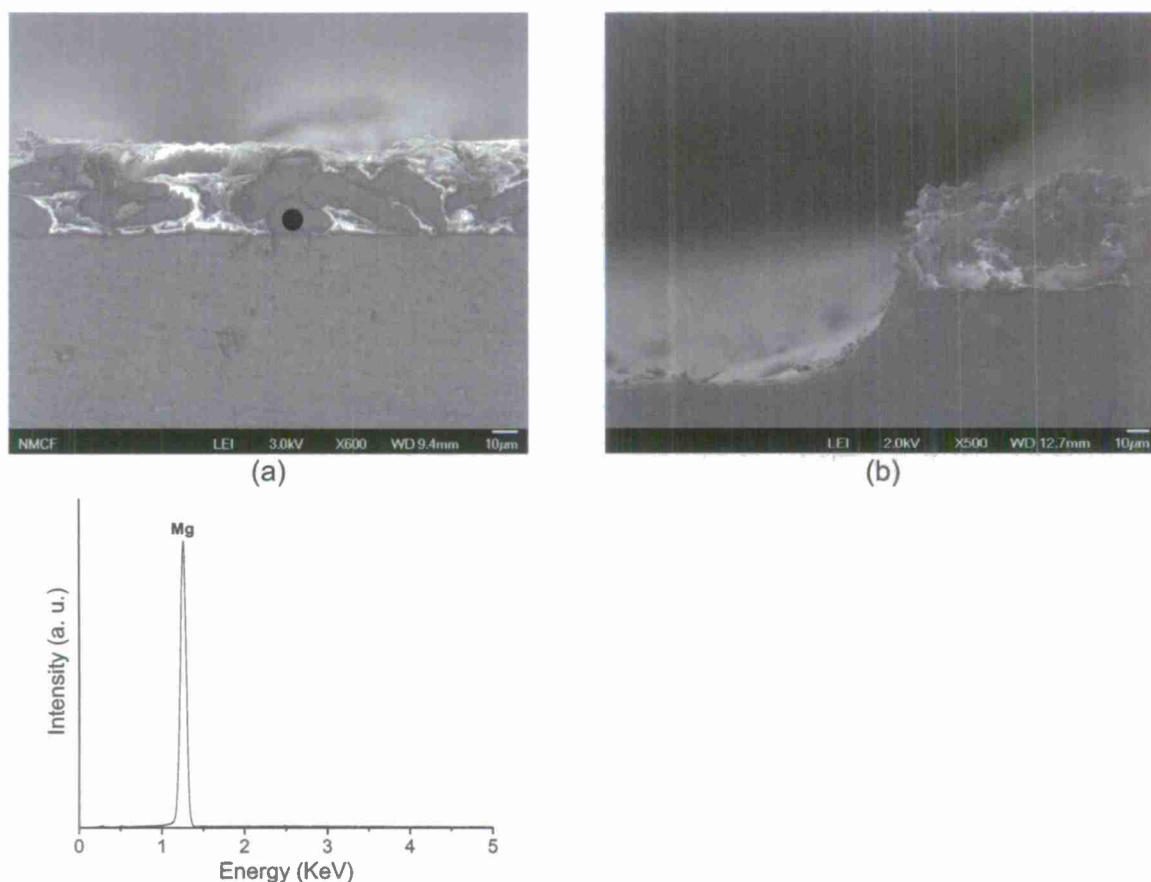


Figure 87. SEM micrograph (a) far away from and (b) near the scribe and (c) EDS of cross-sectioned MgRP (initial MgPVC = 45%) on AA2024-T351 pretreated with Prekote. Spot markers indicate approximate location of EDS analysis in (a).

#### 1.8.4.2 ASTM B-117 and Modified ASTM B-117 Salt Fog Exposure

Mg-rich primer-coated AA2024-T351 panels were exposed to salt spray in a QFog Cyclic Corrosion Tester (QFog model CCT 1100) according to ASTM B-117 "Standard Practice for Operating Salt Spray (Fog) Apparatus" with neutral 5% NaCl solution ( $\text{pH} = 6.9 \pm 0.4$ ) as the electrolyte for at least 1000 hours.<sup>57</sup> During a second exposure, the standard ASTM B-117 salt fog environment was altered such that the standard 5% NaCl solution electrolyte was replaced with ASTM artificial sea water ( $\text{pH} = 8.2 \pm 0.3$ ).<sup>59</sup> In all salt fog exposures reported on in this report, ambient air was supplied to the chamber and to the atomizer for fog production. Ambient concentrations of atmospheric gases such as  $\text{CO}_2$  are assumed. In previous work, the ambient concentration of  $\text{CO}_2$  inside the salt spray chamber was measured in-situ to be approximately 425 ppm.<sup>1</sup> Other ambient gas concentrations were not measured.

The QFog Cyclic Corrosion Test cabinet used for exposure of MgRP-coated AA2024-T351 to ASTM B-117 Salt Spray testing is shown in Figure 88a. The samples were mounted in the chamber according to ASTM B-117 (Figure 88b).<sup>57</sup> Panels were removed from exposure at a front-weighted removal schedule for imaging, electrochemical interrogation and post-mortem characterization. Typical removal times for salt spray exposures were 24, 48, 96, 192, 408, 696, and 1008 hours. Pertinent environmental parameters for the ASTM B-117 environment such as mean temperature, mean relative humidity, mean dew point, mean precipitation rate, precipitation pH and chloride deposition rate are shown in Table 7.

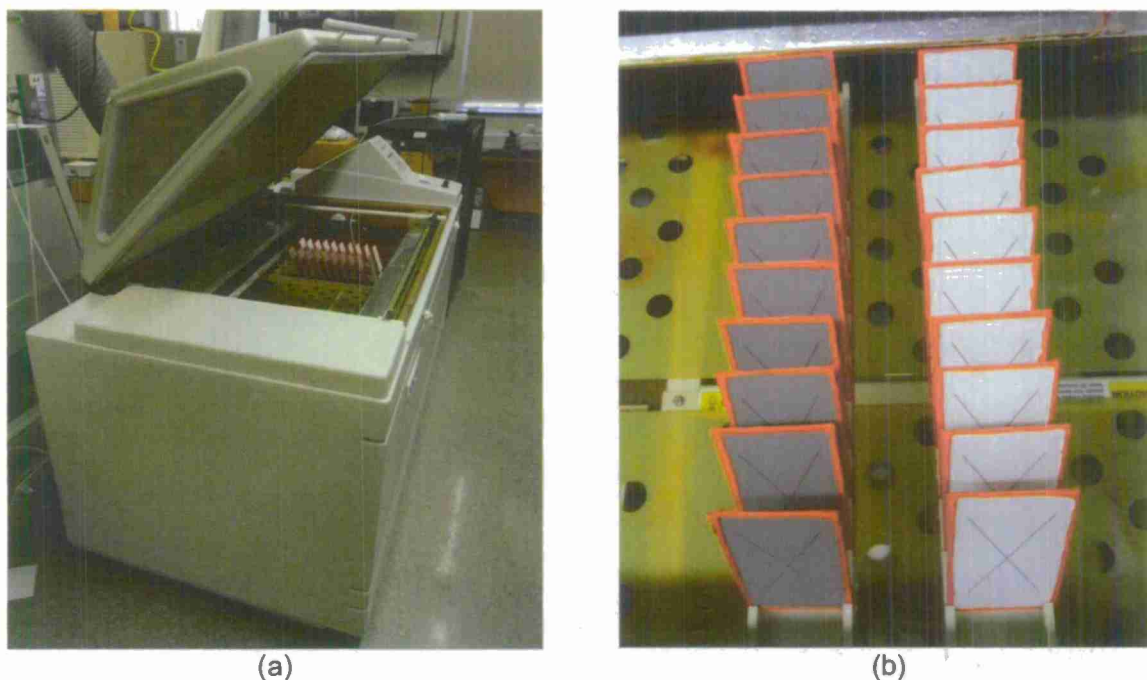


Figure 88. Picture of (a) QFog Cyclic Corrosion Tester Model: CCT 1100 (b) MgRP-coated AA2024-T351 samples mounted for exposure in the QFog Cyclic Corrosion Tester at  $t = 0$  hrs.



Table 7. Exposure conditions in field and lab accelerated life testing environments.

Environment	Mean Temp (°C)				Mean RH (%)				Mean Dew Point (°C)			
	Win.	Spr.	Sum.	Fall	Win.	Spr.	Sum.	Fall	Win.	Spr.	Sum.	Fall
KSC	18.7	23.3	28.2	24.2	71.7	69.7	74	72.7	13.5	17.4	23.1	19
Birdwood	8.1	19.9	24	10.2	59.3	58.3	75.2	65.5	0.6	11	19.3	4
B117	35				95				34			
B117 w/ ASW	35				95				34			

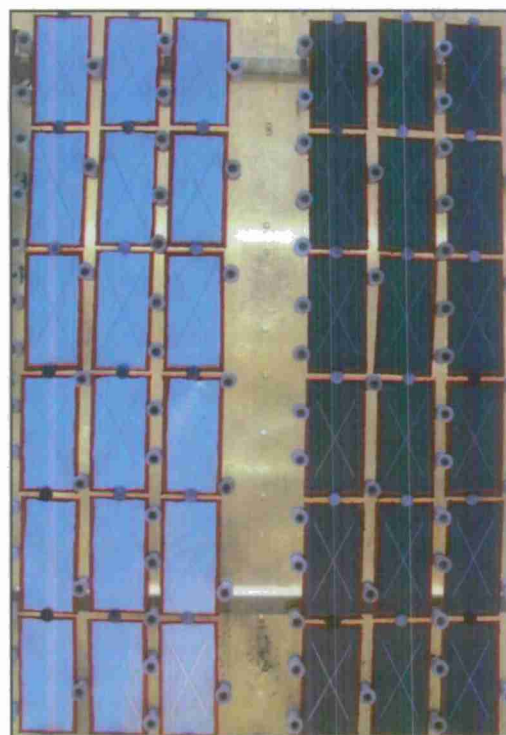
Environment	Mean Precipitation (mm/hr)				Precip. pH	Mean Cl <sup>-</sup> (µg/cm <sup>2</sup> /hr)
	Win.	Spr.	Sum.	Fall		
KSC	0.066	0.154	0.245	0.184	5.4 ± 0.4	0.8
Birdwood	0.102	0.102	0.135	0.139	4.9 ± 0.3	0.002
B117	0.190				6.9 ± 0.4	600
B117 w/ ASW	0.190				8.2 ± 0.3	390

#### 1.8.4.3 Field Exposures at Kennedy Space Center Titusville, FL

Natural weathering exposures of Mg-rich primer-coated AA2024-T351 panels were conducted at the Kennedy Space Center Corrosion Technology Lab (28.59406°N, 80.58283°W, elevation = 0 m). This is a marine atmospheric testing site located on the eastern shore of the state of Florida, approximately 30 m from the median high tide line of the Atlantic Ocean. The sample test racks face the water and are shown in Figure 89. The site has been documented as having some of the highest natural corrosion rates in the country.<sup>60</sup> During exposure, panels were mounted on unsheltered atmospheric test racks with full exposure to natural elements according to ASTM G-4 and G-50.<sup>61, 62</sup> Panels were removed at a front-weighted removal schedule for imaging, XRD analysis, electrochemical interrogation and post-mortem characterization initially in two week intervals and, after 8 weeks of exposure, in 4 week intervals. Pertinent environmental parameters for Kennedy Space Center, FL 30 m lot such as mean temperature, mean relative humidity, mean dew point, mean precipitation rate, precipitation pH and chloride deposition rate are shown in Table 7.



(a)



(b)

Figure 89. Picture of (a) test rack and (b) MgRP-coated AA2024-T351 samples on exposure at Kennedy Space Center, FL 30 m site at  $t = 0$  hrs. (28.59406°N, 80.58283°W, elevation = 0 m)

#### 1.8.4.4 Field Exposures at Birdwood Golf Course Charlottesville, VA

Natural weathering exposures of Mg-rich primer-coated AA2024-T351 panels were conducted at Birdwood Golf Course in Charlottesville, VA (38.0402°N, 78.54.27°W, elevation = 172 m) which is an atmospheric exposure site maintained by the UVA Department of Environmental Sciences. This is an inland, rural atmospheric testing site located in Central Virginia's Albemarle County. During exposure, panels were mounted on atmospheric test racks (shown in Figure 90) with full exposure to natural elements according to ASTM G4 and G50.<sup>61, 62</sup> Panels were removed at a front-weighted removal schedule for imaging, XRD analysis, electrochemical interrogation and post-mortem characterization initially in two week intervals and, after 2 weeks of exposure, in 4 week intervals. Pertinent environmental parameters for Birdwood Golf Course in Charlottesville, VA such as mean temperature, mean relative humidity, mean dew point, mean precipitation rate, precipitation pH and chloride deposition rate are shown in Table 7.



(a) (b)  
Figure 90. Picture of (a) test rack and (b) MgRP-coated AA2024-T351 samples on exposure at Birdwood GC in Charlottesville, VA at  $t = 0$  hrs. (38.0402°N, 78.54.27°W, elevation = 172 m)

#### 1.8.4.5 Full Immersion Electrochemical Analysis

Potential control during electrochemical experiments was maintained using a potentiostat with computer interface software. Saturated calomel reference electrodes (SCE) were used in all 3-electrode full immersion testing. The potentiostat models used were a Gamry Reference 600 as well as a Solartron model 1286 potentiostat with a model 1250 FRA. These models were chosen because they enable electrochemical impedance spectroscopy (EIS) measurements along with traditional electrochemical measurements. The electrolyte used for full-immersion exposure as well as post-mortem analysis after field and salt fog exposures was ambiently aerated 5% NaCl solution. Ambient concentrations of atmospheric gases such as  $\text{CO}_2$  are assumed. Full immersion measurements were made by clamping the environmentally exposed, MgRP-coated AA2024-T351 panel to a flat cell with a defined  $1 \text{ cm}^2$  area circular window sealed around the edges by a Teflon knife-edge washer to prevent crevice corrosion (shown in Figure 91). The area tested is far away ( $\geq 2 \text{ cm}$  away) from any edge or scribe and the entire cell/sample assembly is placed in a Faraday cage to prevent interference from outside sources during measurement.

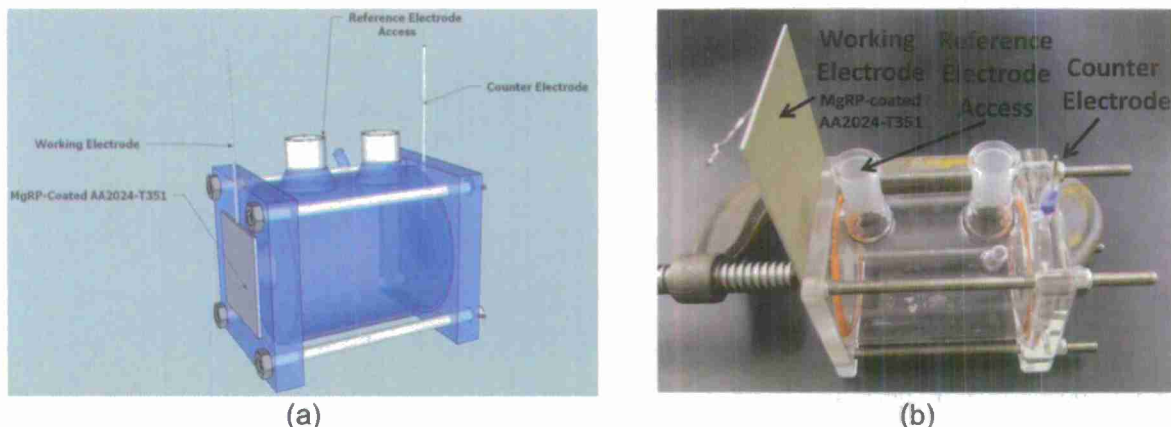


Figure 91. Labeled (a) schematic and (b) picture of electrochemical flat cell with 1 cm<sup>2</sup> window used for full immersion exposure and post-mortem characterization.

#### 1.8.4.6 Electrochemical Impedance Spectroscopy (EIS)

EIS was conducted on Mg-rich primer coated AA2024-T351 panels before, during and after environmental exposure in ambiently aerated 5% NaCl solution. Ambient concentrations of atmospheric gases such as CO<sub>2</sub> are assumed. A typical EIS scan was acquired in sine sweep mode from 100 kHz to 0.01 Hz with 6 points per decade. Coated panels were scanned with an AC amplitude of 50 - 80 mV to overcome the voltage drop through the polymer and to reduce noise. The tests were run in 5% NaCl solution with ambient aeration and used a saturated calomel reference electrode. An equivalent circuit, automated fitting routine module built into Scribner Associate's ZView 3.1c was used for circuit fitting of raw EIS data. An equivalent circuit consisting of a nested Randle's circuit was used as the conceptual model for fitting.<sup>63-66</sup>

#### 1.8.4.7 X-Ray Diffraction

X-Ray diffraction was conducted on a PANalytical X'pert powder X-Ray diffractometer utilizing a Cu-K $\alpha$  source. The samples investigated included MgRP-coated AA2024-T351 panels before and after environmental exposure. XRD measurements of pristine and environmentally exposed samples were made at areas far away ( $\geq 2$  cm away) from any edge or scribe, presumed to be representative of global coating degradation. All samples were scanned, continuously, from 10 to 120 degrees with a step size of 0.02 degrees. XRD Spectra obtained from bare AA2024-T351 and AA2024-T351 coated with MgRP were normalized against the fcc Al  $\langle 111 \rangle$   $2\theta = 38.4721^\circ$  peak for comparison. Peak normalization and integration was performed with Origin Lab 7.5 software. First-order approximation of XRD penetration depth as a function of  $2\theta$  in pure Al and pure Mg are shown in Figure 92.<sup>3, 67, 68</sup> The penetration depths responsible for 99% of the diffracted intensity vary by material and with incident beam angle but range from 40 to 125  $\mu\text{m}$  in the principle ranges of  $2\theta$  studied ( $2\theta \approx 30^\circ - 50^\circ$ ) in pure Al and Mg and for this reason is commonly considered to be a bulk characterization technique. It is important to note that the detection limit of bulk Bragg-Brentano X-ray diffraction for mixed or composite materials containing several crystalline phases is approximately 3 - 5% of the sample by volume.<sup>3</sup> Below these levels, it is unlikely that a crystalline phase will be detected in the XRD spectra. This estimate of the lower-bound of detection is supported by XRD measurements, shown in a



previous work<sup>2</sup>, performed on pristine samples of MgRP-coated AA2024-T351 panels coated with MgRP of varying PVC.

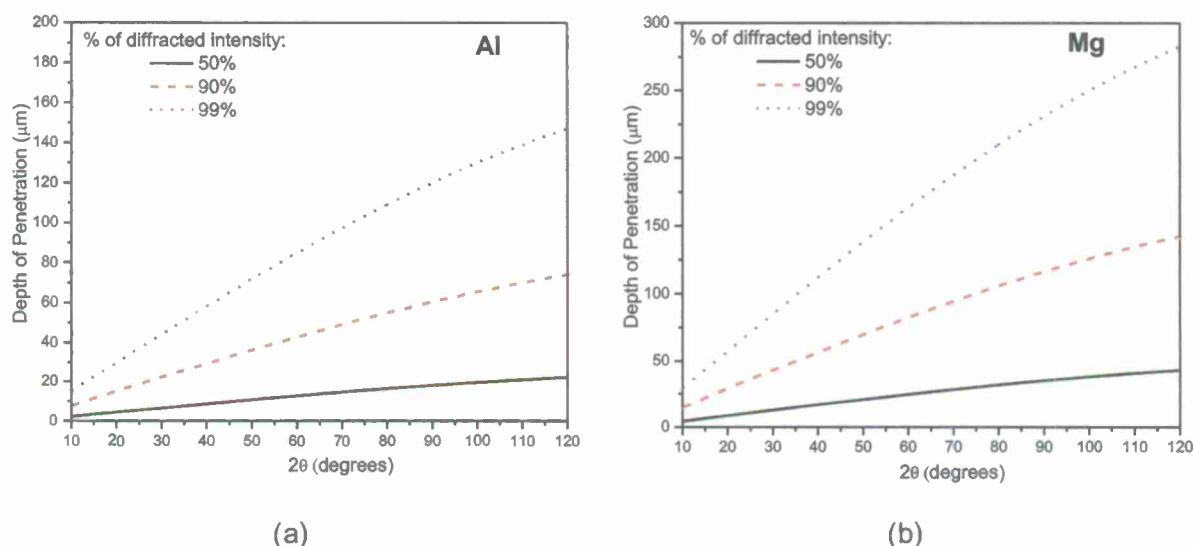
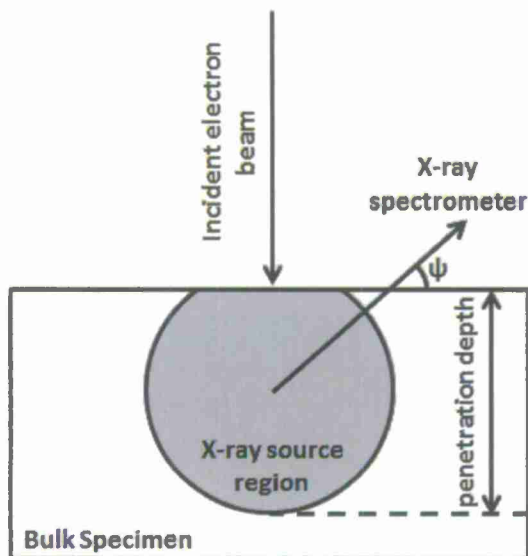


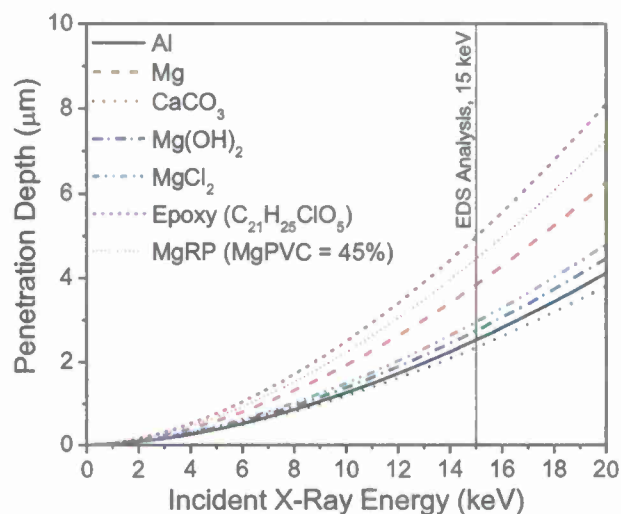
Figure 92. First-order approximation of XRD penetration depth as a function of  $2\theta$  in (a) pure Al and (b) pure Mg. The penetration depths responsible for 50%, 90%, and 99% of the diffracted intensity are shown.

#### 1.8.4.8 Scanning Electron Microscopy and Energy Dispersive Spectroscopy

Scanning electron microscopy and energy dispersive spectroscopy were used for coating characterization and post-mortem analysis. A JEOL 6700f field emission SEM with Spirit™ Energy dispersive X-ray spectroscopy (EDS) analytical software was used to conduct these investigations. An accelerating voltage of 2 – 5 kV was used for imaging to reduce charging of the polymer coating. For EDS, a working distance of 15 mm and an accelerating voltage of at least 3 times the energy of the maximum characteristic peak of interest were used (typically 15 kV). The first-order approximation of penetration depth<sup>69</sup> with respect to accelerating voltage in various materials of interest is plotted in Figure 93. At an accelerating voltage of 15 kV and in materials investigated in this study, EDS has a penetration depth of roughly 2 to 5 μm, making the technique suitable to investigate the composition of surface products on the MgRP-coated AA2024-T351 before and after environmental exposure. Additionally, model EDS spectra of bulk and layered materials can be accurately produced utilizing readily available software. Simulated EDS spectra for bulk samples of various materials relevant to the environmentally exposed MgRP-coated AA2024-T351 system are shown in Figure 94. The simulated EDS spectra in Figure 94 and Figure 95 were produced with DTSA-II software. DTSA-II is a multiplatform software package for quantitative x-ray microanalysis.<sup>70</sup> These data show the type of EDS fingerprint expected for each form of Mg possibly present.



(a)



(b)

Figure 93. Schematic of EDS penetration depth (a) and plot of first-order approximation<sup>69</sup> of EDS penetration depth in various materials (b).

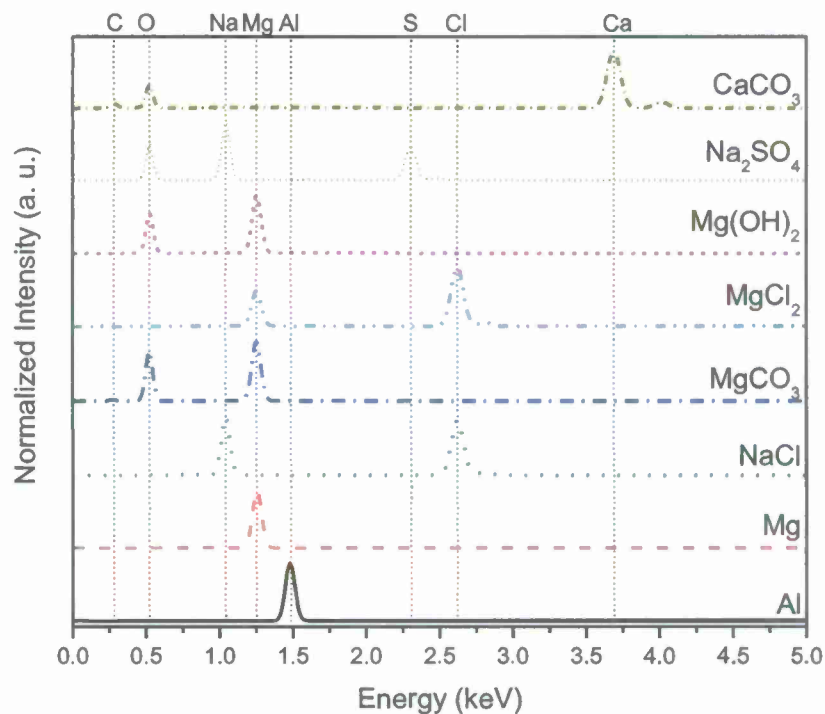


Figure 94. Simulated Energy dispersive X-ray (EDS) spectra for bulk samples of various relevant to the MgRP/AA2024-T351 system and environmental exposure.<sup>70</sup>

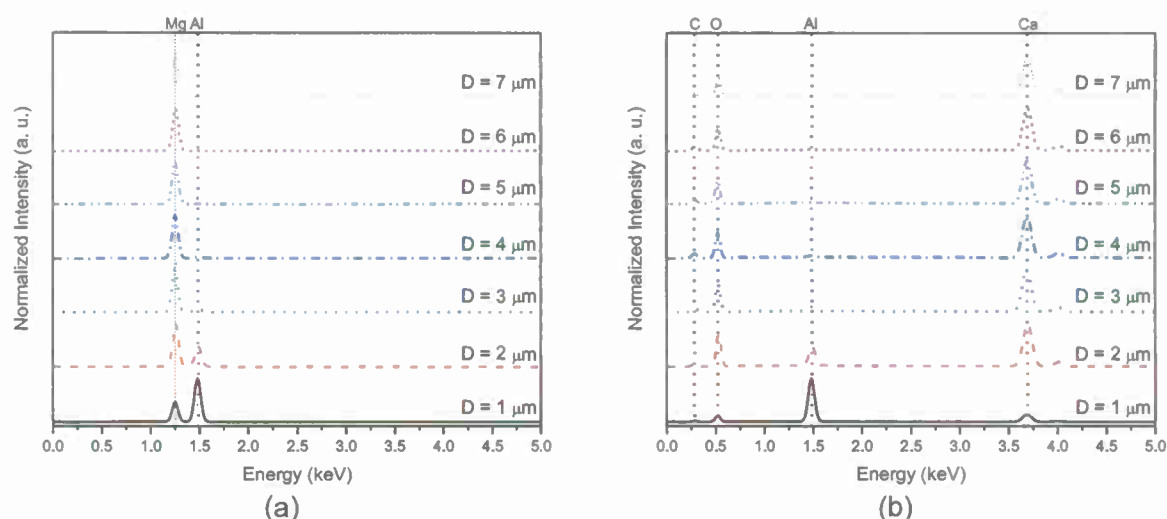


Figure 95. Simulated Energy dispersive X-ray (EDS) spectra for a sphere of (a) metallic Mg and (b) CaCO<sub>3</sub> with various diameter, D, on top of a bulk substrate of Al.<sup>70</sup>

### 1.8.5 Experimental Results

#### 1.8.5.1 Behavior During and After Exposure at Kennedy Space Center:

Optical micrographs of MgRP coated AA2024-T351 panels that have been exposed at Kennedy Space Center 30 m lot for 0, 12, and 24 weeks are shown in Figure 96 and Figure 97. In general, the coating was observed to turn ivory white in color and have a chalky texture with increased exposure time, presumably due to the accumulation of corrosion products (such as Mg(OH)<sub>2</sub>) and deposited calcareous salts and the degradation of the polymer matrix. At moderate exposure times (T > 20 weeks), small areas of the shiny Al substrate can begin to be seen beneath the MgRP coating layer. The scribe appears, at low magnification, to be relatively clean and without significant damage. It is important to note that no blistering or similar macroscopic coating failure phenomena are observed in the MgRP or along the scribe lines after exposure for 24 weeks at Kennedy Space Center, FL 30 m lot. Upon closer investigation with the SEM (Figure 98, Figure 99 and Figure 100), after 12 and 24 weeks of exposure, two apparent regions or zones can be viewed in the scribe (outlined by dashed lines in Figure 98b, Figure 99b and Figure 100b). Near the edges of the scribe there appears to be corrosion product deposits whereas the center of the scribe appears to be mostly bare.

To further investigate the composition of the deposits in the scribe, and of the MgRP proximate to the scribe, 16 consecutive EDS spot scans were obtained across the width of the scribe and coating interface (labeled 1-16 in Figure 101). The spacing between scans was approximately 65 μm. The basic EDS spectra obtained across the scribe and coating interface show combinations of peaks indicative of C, O, Mg, Al, Si, and Ca. The EDS spot scans proximate to the edge of the scribe, labeled 1, 2, 3, 10, 11, and 12 show the presence of Mg(OH)<sub>2</sub> or MgO indicated by Mg and O peaks (compared with simulated EDS spectra in Figure 94) as well as the presence of calcareous deposits. Calcareous deposits primarily consist of CaCO<sub>3</sub> and, along with Mg deposits, are indicative of regions of cathodic protection afforded to the AA2024-T351 by the MgRP.<sup>71-78</sup> The presence of these species 200 – 300 μm into the scribe suggest a

throwing power of the same dimensions can be observed upon environmental exposure at Kennedy Space Center, FL. The significant Al peaks present in the EDS spectra obtained at positions 13, 14, 15 and 16, in the once-MgRP coated region, further corroborate that most of the coating has been washed or dissolved away during exposure. The first-order approximation of the penetration depth of the EDS measurements at 15 keV (Figure 93) are estimated to be no more than 5  $\mu\text{m}$ .<sup>69</sup> As well, the simulated EDS spectra of a sphere of Mg with a diameter of 5  $\mu\text{m}$  on an infinitely thick, pure Al substrate (Figure 95a) does not contain an Al peak. This indicates that the remaining coating layer and any residual corrosion products present are likely no more than 5  $\mu\text{m}$  thick at the locations of the EDS measurements. If the remaining coating layer and any residual corrosion products were more than 5  $\mu\text{m}$  thick at the locations of the EDS measurements, the Al peak would be suppressed as in the pristine condition shown in Figure 86 spot 1.

SEM micrographs of cross-sectioned MgRP on AA2024-T351 far away from the scribe after (a) 12 and (b) 24 weeks of exposure in the field at Kennedy Space Center, FL 30 m lot are shown in Figure 102. Multiple EDS spot scans were obtained on the coating layer after 12 and 24 weeks of exposure at Kennedy Space Center, FL. Representative spectra are shown in Figure 102b and d. The EDS spectra indicate the presence of some metallic, unoxidized Mg in the coating after 12 weeks of exposure and the presence of a prominent O peak in the EDS spectrum obtained after 24 weeks of exposure suggests oxidation and depletion of a significant amount of the metallic Mg pigment. SEM micrographs of cross-sectioned MgRP on AA2024-T351 proximate to the scribe after (a) 12 and (b) 24 weeks of exposure in the field at Kennedy Space Center 30 m lot are shown in Figure 103 for visual inspection. Overall, the edges and walls of the scribes appear relatively clean and without significant damage and an overall dissipation of the MgRP coating can be observed. In contrast to similar environmental exposures of earlier generation commercial products in the past<sup>1</sup>, no indications of cathodic corrosion, as evidenced by narrow pinholes, or underpaint corrosion or anodic undermining, as evidenced by areas of coating delamination above regions of Al corrosion, are visible at the coating/metal interface when viewed in cross-section.

X-Ray Diffraction (XRD) spectra of MgRP coated AA2024-T351 (initial MgPVC = 45%) were obtained at each removal interval of environmental exposure in an attempt to track the depletion rate of the metallic Mg pigment in the MgRP throughout environmental exposure. XRD measurements of environmentally exposed samples were made over areas far away from the scribe, such that none of the interaction area of the incident X-rays interacted with the scribed region of the samples. The areas far away from the scribe were presumed to be areas representative of global coating degradation. XRD spectra of MgRP coated AA2024-T351 after 0, 12 and 24 weeks of exposure in the field at Kennedy Space Center, FL 30 m lot are shown in Figure 104. Three prominent Mg hexagonal close packed peaks ( $\langle 100 \rangle$ ,  $\langle 200 \rangle$ , and  $\langle 101 \rangle$ ) were normalized against the Al  $\langle 101 \rangle$  peak which appeared in each spectrum as a result of the underlying AA2024-T351 substrate. The relative intensities of the Mg peaks shown in Figure 104 decrease with increasing exposure time in the field at Kennedy Space Center, FL which indicates a depletion of metallic Mg pigment from the coating system to below the detection limit of bulk XRD ( $\leq 5\%$  by volume<sup>3</sup>) after 24 weeks. Principle XRD peaks of relevant Mg or Al corrosion products are labeled a, b, c, and d in Figure 104. Detectable surface products were not present in the XRD spectra of MgRP coated AA2024-T351 after 12 and 24 weeks of exposure in the field at Kennedy Space Center, FL 30 m lot.

Electrochemical impedance spectroscopy (EIS) measurements of MgRP coated AA2024-T351 (initial MgPVC = 45%) were also taken at each removal interval of environmental exposure in an



attempt to track the evolution of the coating barrier properties of the MgRP throughout environmental exposure. An automated fitting routine was used to fit the measured EIS spectra to a nested Randle's circuit, a schematic of which is shown in Figure 105. The nested Randle's circuit is an accepted solid state representation of polymer coated metals.<sup>65</sup> EIS measurements of MgRP coated AA2024-T351 (initial MgPVC = 45%) taken after 0, 2, 6, 12, and 24 weeks of exposure in the field at Kennedy Space Center, FL (scatter plot) and the results of the automated fitting analysis (lines) are shown in Figure 106. The values of each representative circuit component produced by the automated fitting routine for selected exposure times at Kennedy Space Center, FL 30 m lot are tabulated in Table 8. The MgRP coated AA2024-T351 displayed a decrease of four orders of magnitude of the low frequency (at 0.01 Hz) impedance as well as a shift towards high frequencies in the break point frequency of the Bode phase angle throughout environmental exposure at Kennedy Space Center, FL. Both phenomena indicate a significant loss of barrier protection capability throughout the duration of the exposure.<sup>63, 64</sup>

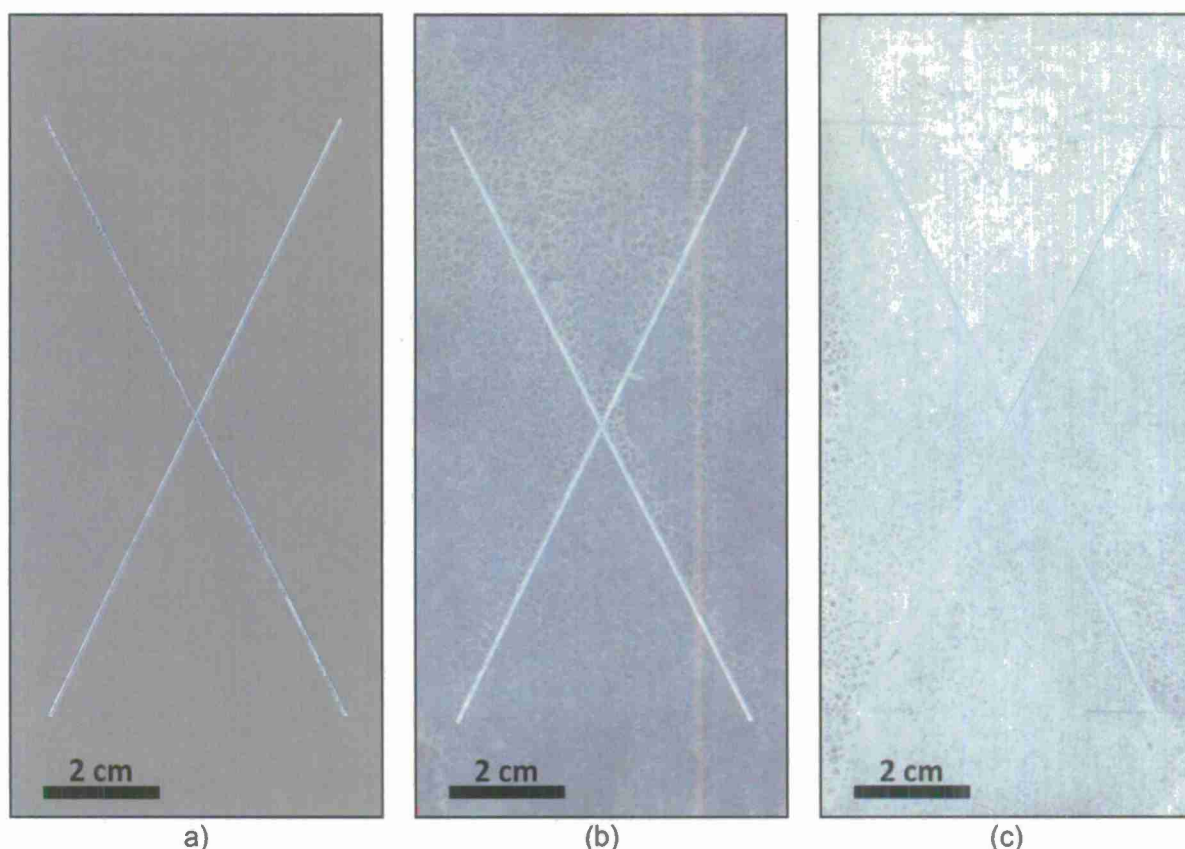


Figure 96. Optical micrograph of AA2024-T351 panels coated with MgRP (initial MgPVC = 45%) that have been exposed at Kennedy Space Center at 30 m lot for (a) 0 weeks (b) 12 weeks (c) 24 weeks

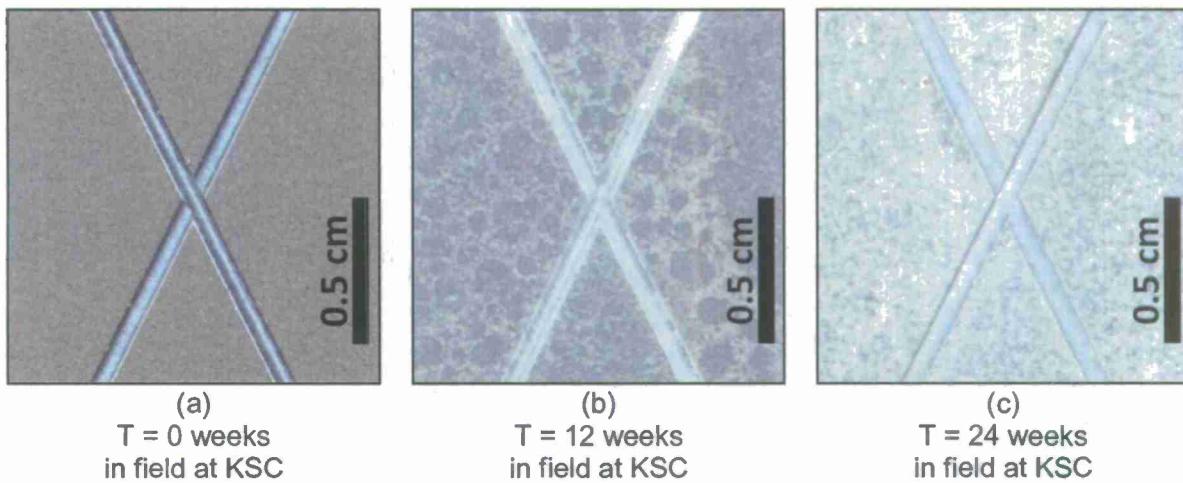


Figure 97. Optical micrograph of AA2024-T351 panels coated with MgRP (initial MgPVC = 45%) that have been exposed at Kennedy Space Center at 30 m lot for (a) 0 weeks (b) 12 weeks (c) 24 weeks

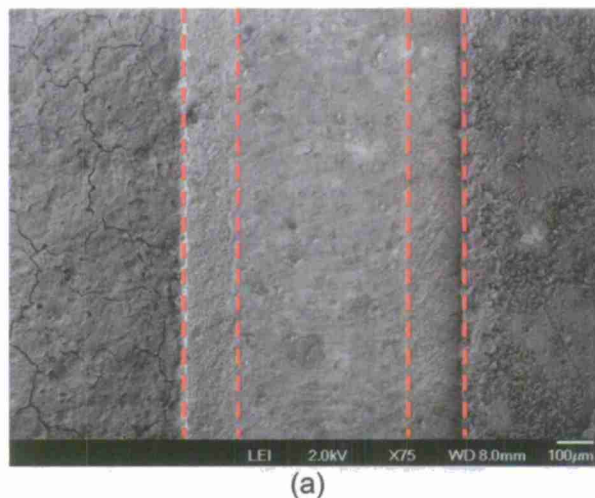
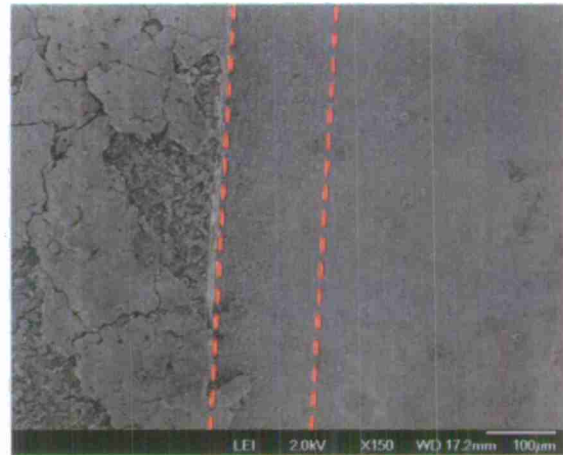


Figure 98. Scanning electron micrograph of AA2024-T351 pretreated with Prekote and coated with MgRP (initial MgPVC = 45%) after environmental exposure in the field at KSC for 24 weeks.



(a)

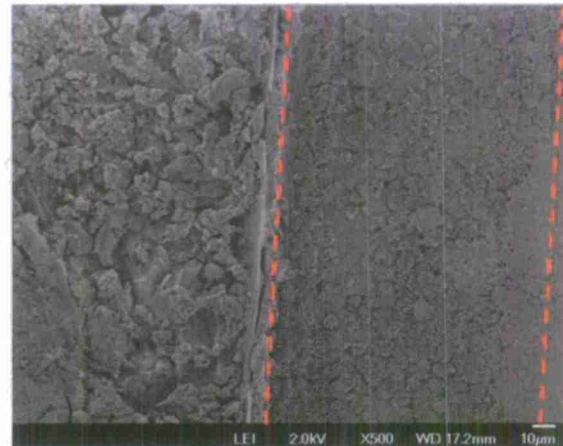


(b)

Figure 99. Scanning electron micrograph of AA2024-T351 pretreated with Prekote and coated with MgRP (initial MgPVC = 45%) after environmental exposure in the field at KSC for (a) 12 weeks and (b) 24 weeks.

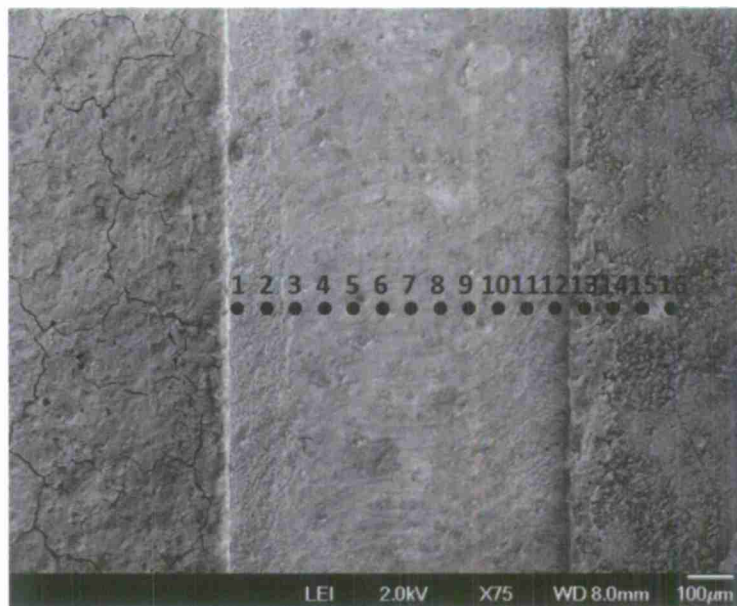


(a)

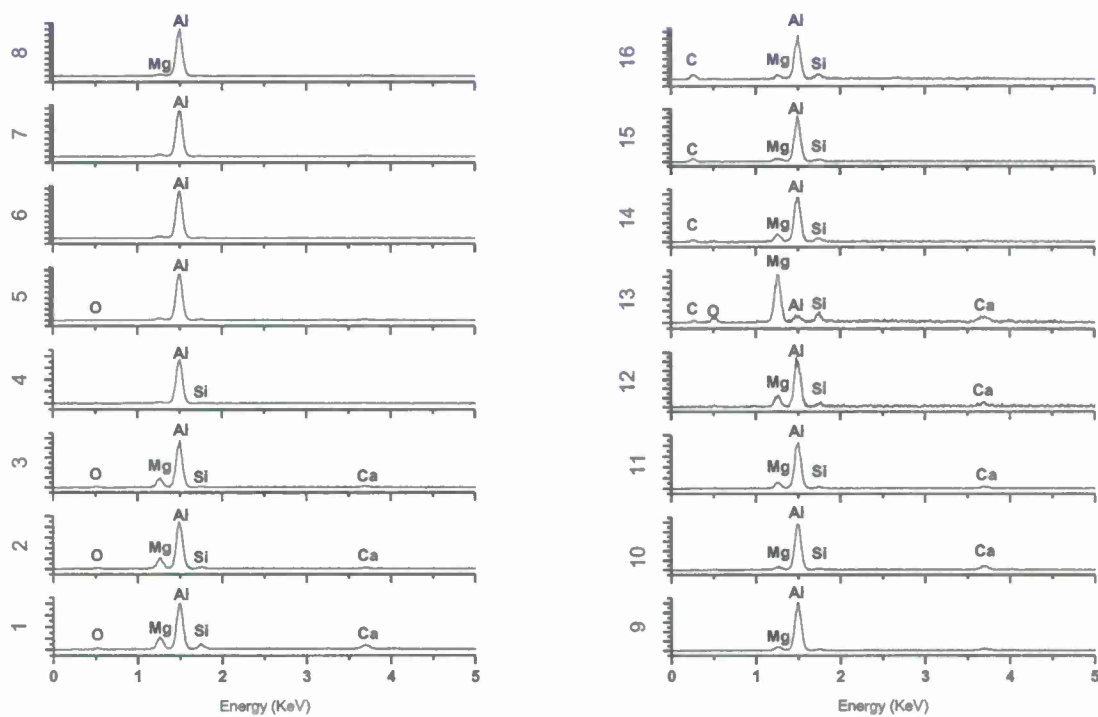


(b)

Figure 100. Higher magnification scanning electron micrograph (planar view) of scribed AA2024-T351 pretreated with Prekote and coated with MgRP (initial MgPVC = 45%) after field exposure at Kennedy Space Center 30 m lot for (a) 12 weeks and (b) 24 weeks.



(a)



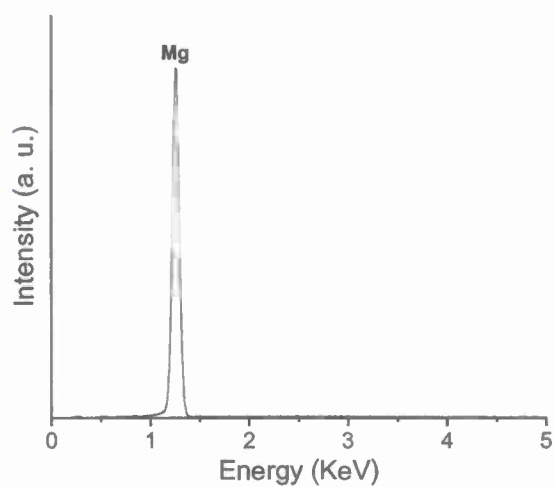
(b)

Figure 101. SEM micrograph (planar view) of scribed AA2024-T351 pretreated with Prekote and coated with MgRP (initial MgPVC = 45%) after field exposure in the field at KSC for 24 weeks. Spot markers indicate approximate location of EDS analysis shown in (b).





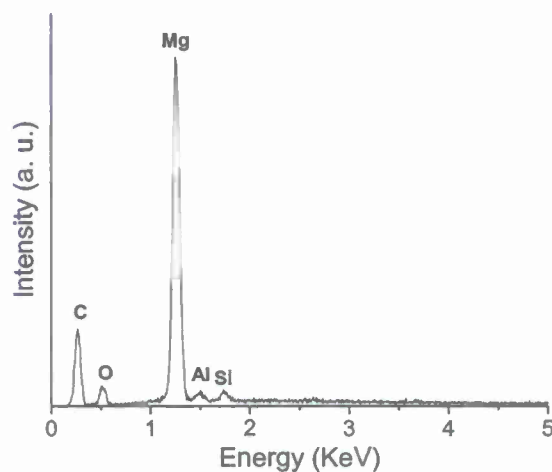
(a)



(b)



(c)



(d)

Figure 102. Scanning electron micrograph of cross sectioned AA2024-T351 pretreated with Prekote and coated with MgRP (initial MgPVC = 45%) after field exposure at Kennedy Space Center for (a,b) 12 weeks and (c,d) 24 weeks. Spot markers indicate approximate location of EDS analysis shown in (b) and (d).

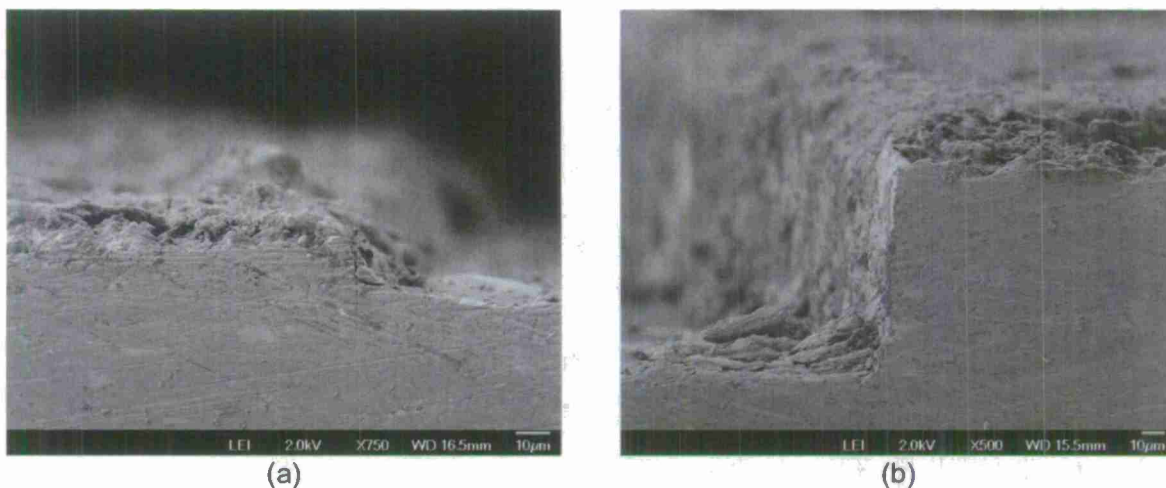


Figure 103. Scanning electron micrograph of cross sectioned AA2024-T351 pretreated with Prekote and coated with MgRP (initial MgPVC = 45%) after environmental exposure in the field at KSC for (a) 12 weeks and (b) 24 weeks.

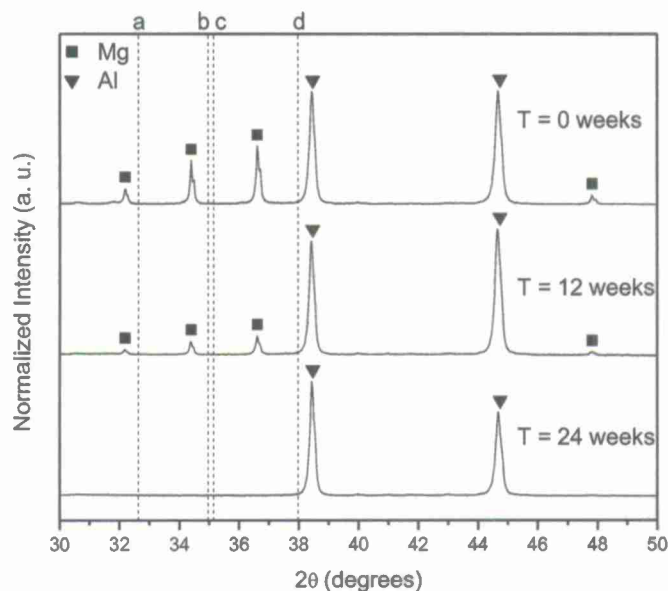


Figure 104. X-Ray diffraction spectra of AA2024-T351 panels coated with MgRP (initial MgPVC = 45%) after field exposure at Kennedy Space Center 30 m lot for 0, 12, and 24 weeks. Dotted lines indicate the position of the most intense diffraction peak for (a)  $\text{MgCO}_3$  (b)  $\text{MgCl}_2$  (c)  $\text{Al}_2\text{O}_3$  and (d)  $\text{Mg(OH)}_2$ .

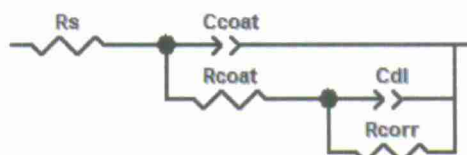


Figure 105. EIS equivalent circuit for a polymer coated metal used for fitting analysis.

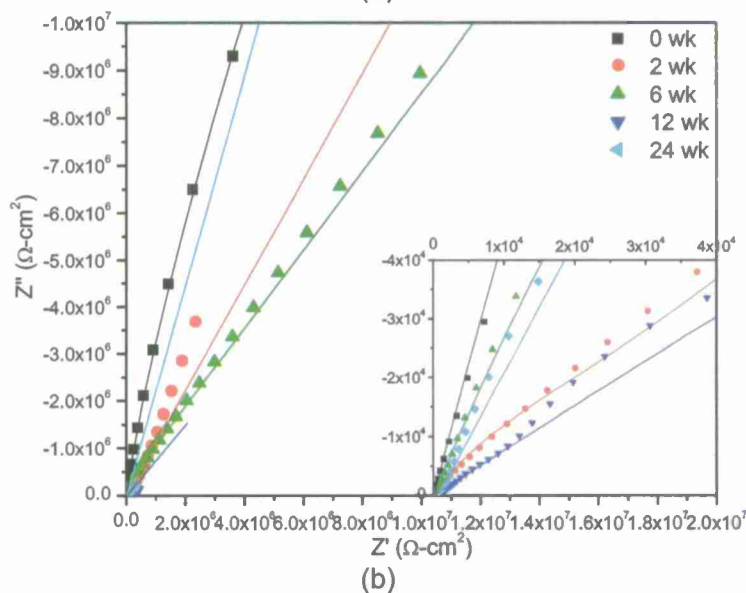
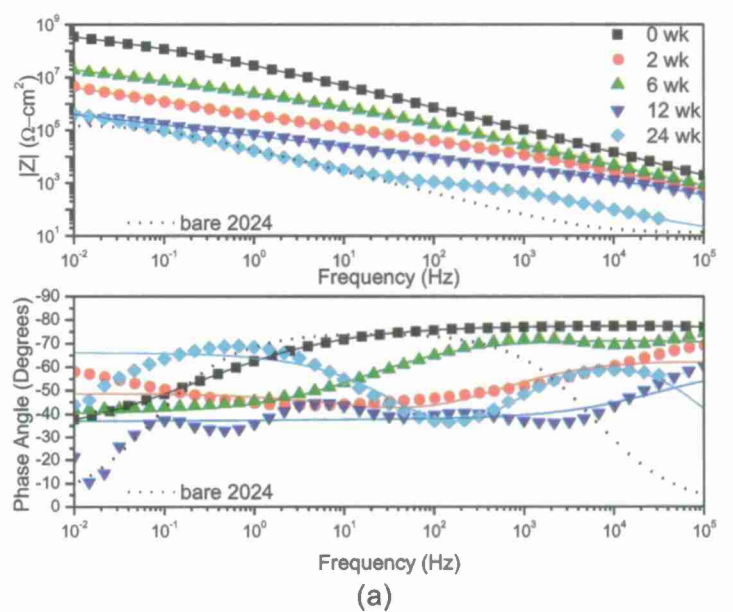


Figure 106. (a) Bode and (b) Nyquist plots of EIS of AA2024-T351 panels coated with MgRP (initial MgPVC = 45%) after field exposure at Kennedy Space Center 30 m lot for 0, 2, 6, 12, and 24 weeks. Tested in ambiently aerated 5% NaCl Solution. Fit results in Table 8.

Table 8. Fitting results of EIS measured on AA2024-T351 panels coated with MgRP (MgPVC = 45%) after field exposure at Kennedy Space Center 30 m lot for 0, 2, 6, 12, and 24 weeks. Tested in ambiently aerated 5% NaCl Solution. Equivalent electric circuit model used shown in Figure 105.

	units	0 wk	2 wk	6 wk	12 wk	24 wk
$R_s$	( $\Omega\text{-cm}^2$ )	10.000	10.000	10.000	10.000	10.000
$C_{\text{coat}}^{\text{Y}^0}$	( $\mu\text{F/cm}^2$ )	0.007	0.172	0.037	0.168	2.200
$C_{\text{coat}}^{\text{n}}$	-	0.357	0.703	0.790	0.723	0.774
$R_{\text{coat}}$	( $\text{k}\Omega\text{-cm}^2$ )	0.003	44.250	869.900	0.992	0.918
$C_{\text{dl}}^{\text{Y}^0}$	( $\mu\text{F/cm}^2$ )	0.005	0.969	0.167	7.790	14.820
$C_{\text{dl}}^{\text{n}}$	-	0.863	0.524	0.435	0.407	0.726
$R_{\text{corr}}$	( $\text{G}\Omega\text{-cm}^2$ )	10.000	10.000	10.000	10.000	10.000
$F_{45}$	(Hz)	0.04	21.31	0.68	10078.13	676.08
$F_{\text{saddle}}$	(Hz)	0.01	4.68	0.02	2159.93	$\geq 100000$

#### 1.8.5.2 Behavior During and After Exposure at Charlottesville, VA:

Optical micrographs of MgRP-coated AA2024-T351 panels that have been exposed at Birdwood Golf Course in Charlottesville, VA for 0, 12, and 24 weeks are shown in Figure 107 and Figure 108. In general, the coating was observed to turn chalky and opaque taupe in color and eventually lose mass with increased exposure time, presumably due to UV degradation of the epoxy polymer, dissolution of the Mg pigment and subsequent washing away by acidic rain precipitation (Table 7). Even at low exposure times ( $T > 16$  weeks), the shiny Al substrate can begin to be seen beneath the MgRP coating layer. The scribe appears, at low magnification, to be relatively clean and without significant damage. It is important to note that no blistering or similar macroscopic coating failure phenomena are observed in the MgRP or along the scribe lines after exposure for 24 weeks at Birdwood Golf Course in Charlottesville, VA. Upon closer investigation with the SEM (Figure 109, Figure 110, and Figure 111), after 12 and 24 weeks of exposure the scribes appear extremely clean and largely damage free.

To further investigate the composition of any deposits in the scribe, and of the MgRP proximate to the scribe, 16 consecutive EDS spot scans were obtained across the width of the scribe and coating interface (labeled 1-16 in Figure 112). The spacing between scans was approximately 65  $\mu\text{m}$ . The basic EDS spectra obtained across the scribe and coating interface shows combinations of peaks indicative of O, Mg, Al, and Si. The EDS spot scans throughout the width of the scribe, labeled 1 - 12 show very little indication of Mg or Ca deposits. It does not appear that a throwing power can be observed with EDS upon environmental exposure at Birdwood Golf Course in Charlottesville, VA after 24 weeks. The presence of the Al peak in the EDS spectra obtained at positions 13, 14, 15 and 16, in the once-MgRP coated region, further corroborate that most of the coating has been damaged during exposure. The first-order approximation of the penetration depth of the EDS measurements at 15 keV (Figure 93) are estimated to be no more than 5  $\mu\text{m}$ .<sup>69</sup> Moreover, the simulated EDS spectra of a sphere of Mg with a diameter of 5  $\mu\text{m}$  on an infinitely thick, pure Al substrate (Figure 95a) does not contain an Al peak. If the remaining coating layer and any residual corrosion products were more than 5



$\mu\text{m}$  thick at the locations of the EDS measurements the Al peak would be suppressed as in the pristine condition shown in Figure 86 spot 1.

SEM micrographs of cross-sectioned MgRP on AA2024-T351 far away from the scribe after (a) 12 and (b) 24 weeks of exposure in the field at Birdwood Golf Course in Charlottesville, VA are shown in Figure 113. After only 12 weeks of exposure, the remaining MgRP coating layer is observed to be much thinner as compared to the as-applied  $30\ \mu\text{m}$  thickness (Figure 87). Multiple EDS spot scans were obtained on the coating layer after 12 and 24 weeks of exposure at Birdwood Golf Course in Charlottesville, VA. Representative spectra are shown in Figure 113b and d. The EDS spectra show the presence of primarily Al which indicates the depletion of a large percentage of the polymer and metallic, unoxidized Mg pigment. SEM micrographs of cross-sectioned MgRP on AA2024-T351 proximate to the scribe after (a) 12 and (b) 24 weeks of exposure in the field at Kennedy Space Center 30 m lot are shown in Figure 114 for visual inspection. Overall, the edges and walls of the scribes appear relatively clean and without significant damage and an overall dissipation of the MgRP coating can be observed such that a MgRP coating thickness of less than  $5\ \mu\text{m}$  is remaining. In contrast to similar environmental exposures of earlier generation commercial products in the past<sup>1</sup>, no indications of cathodic corrosion, as evidenced by narrow pinholes, or underpaint corrosion or anodic undermining, as evidenced by areas of coating delamination above regions of Al corrosion, are visible at the coating/metal interface when viewed in cross-section.

XRD spectra of MgRP (initial MgPVC = 45%) coated AA2024-T351 after 0, 12 and 24 weeks of exposure in the field at Birdwood Golf Course in Charlottesville, VA are shown in Figure 115. The relative intensities of the Mg peaks shown in Figure 115 decrease with increasing exposure time in the field at Kennedy Space Center, FL which indicates a depletion of metallic Mg pigment from the coating system to below the detection limit of bulk XRD ( $\leq 5\%$  by volume<sup>3</sup>) after only 12 weeks of exposure. Principle XRD peaks of relevant Mg or Al corrosion products are labeled a, b, c, and d in Figure 115. Detectable surface products were not present in the XRD spectra of MgRP coated AA2024-T351 after 12 or 24 weeks of exposure at Birdwood Golf Course in Charlottesville, VA which, combined with a lack of significant corrosion product build-up on the sample as viewed in SEM, suggests most of such corrosion products were washed away by acidic precipitation during exposure.

EIS measurements of MgRP-coated AA2024-T351 (initial MgPVC = 45%) taken after 0, 2, 6, 12, and 24 weeks of exposure at Birdwood Golf Course in Charlottesville, VA (scatter plot) and the results of the automated fitting analysis (lines) are shown in Figure 116. The values of each representative circuit component produced by the automated fitting routine for selected exposure times at Birdwood Golf Course in Charlottesville, VA are tabulated in Table 9. The MgRP coated AA2024-T351 displayed a decrease of four orders of magnitude of the low frequency (at 0.01 Hz) impedance as well as a shift towards high frequencies in the break point frequency of the Bode phase angle in as little as 12 weeks of environmental exposure at Birdwood Golf Course in Charlottesville, VA. Both phenomena indicate a significant loss of barrier protection capability throughout the duration of the exposure.<sup>63, 64</sup>

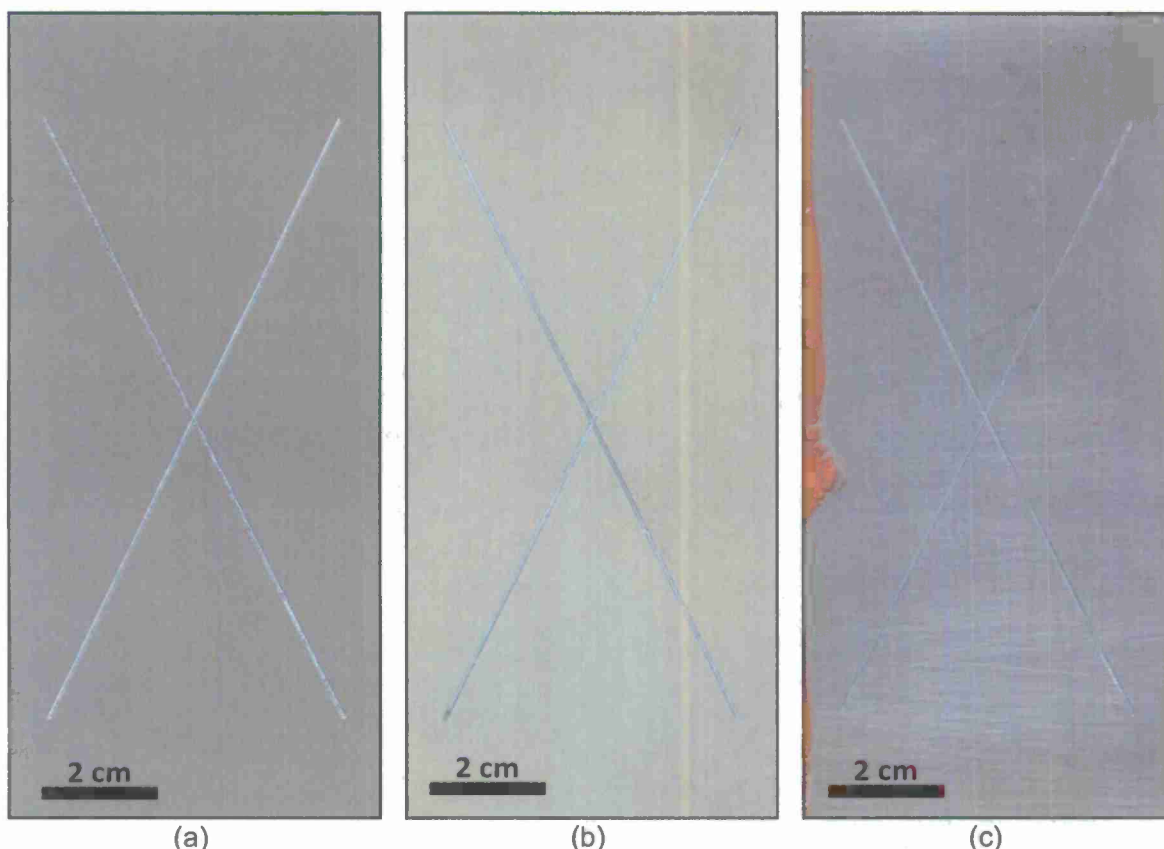


Figure 107. Optical micrograph of AA2024-T351 panels coated with MgRP (initial MgPVC = 45%) that have been exposed at Charlottesville, VA for (a) 0 weeks (b) 12 weeks and (c) 24 weeks.

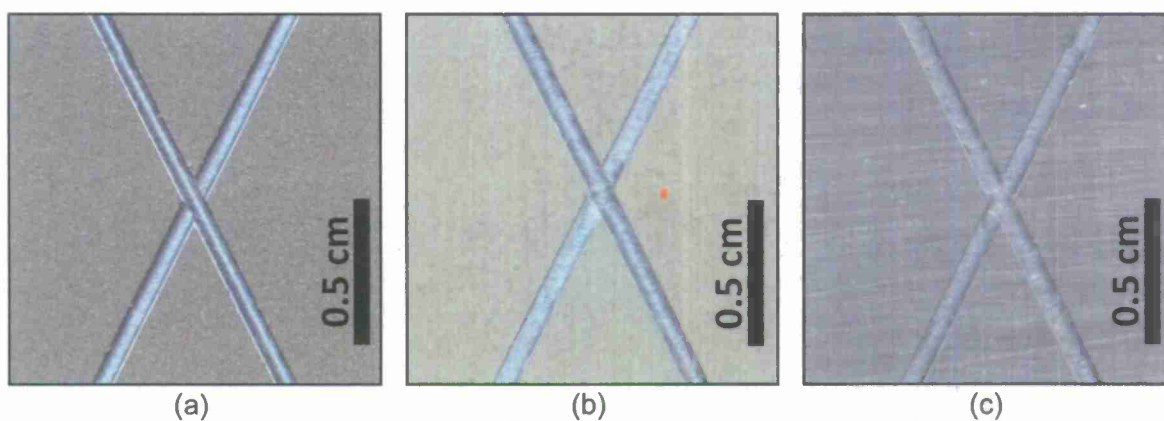


Figure 108. Optical micrograph of AA2024-T351 panels coated with MgRP (initial MgPVC = 45%) that have been exposed at Charlottesville, VA for (a) 0 weeks (b) 12 weeks and (c) 24 weeks.



(a)



(b)

Figure 109. Scanning electron micrograph of AA2024-T351 pretreated with Prekote and coated with MgRP (initial MgPVC = 45%) after environmental exposure in the field at Charlottesville, VA for (a) 12 weeks and (b) 24 weeks.



(a)



(b)

Figure 110. Scanning electron micrograph of AA2024-T351 pretreated with Prekote and coated with MgRP (initial MgPVC = 45%) after environmental exposure in the field at Charlottesville, VA for (a) 12 weeks and (b) 24 weeks.



(a)



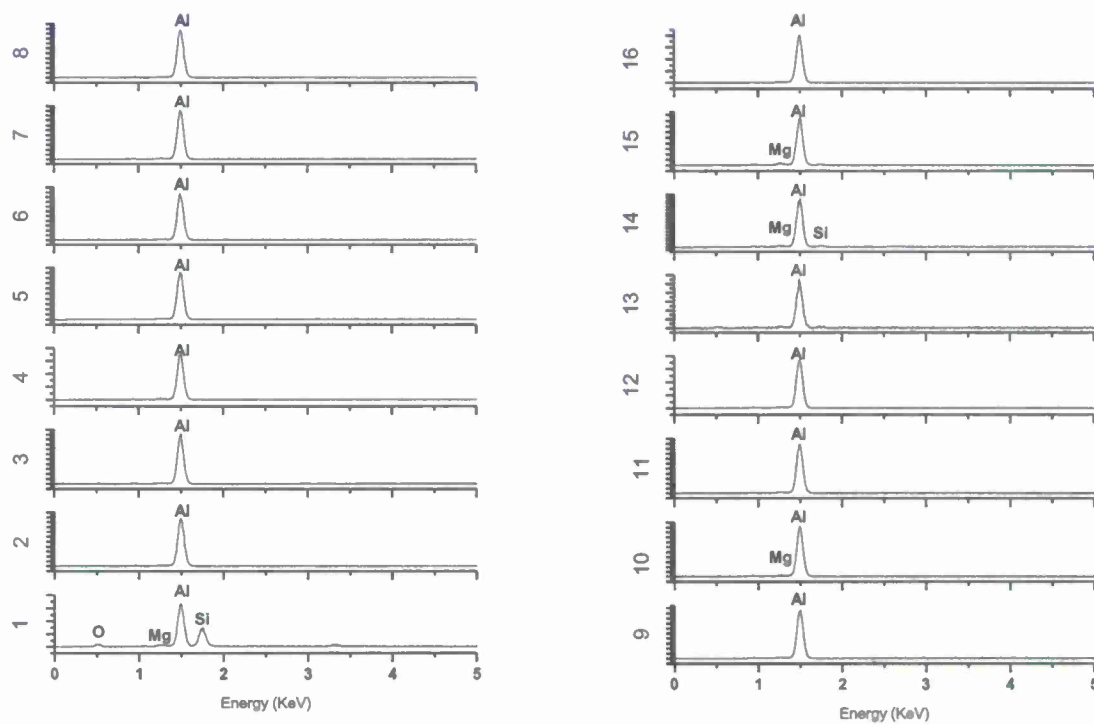
(b)

Figure 111. Higher magnification scanning electron micrograph (planar view) of scribed AA2024-T351 pretreated with Prekote and coated with MgRP (initial MgPVC = 45%) after field exposure at Charlottesville, VA for (a) 12 weeks and (b) 24 weeks.





(a)

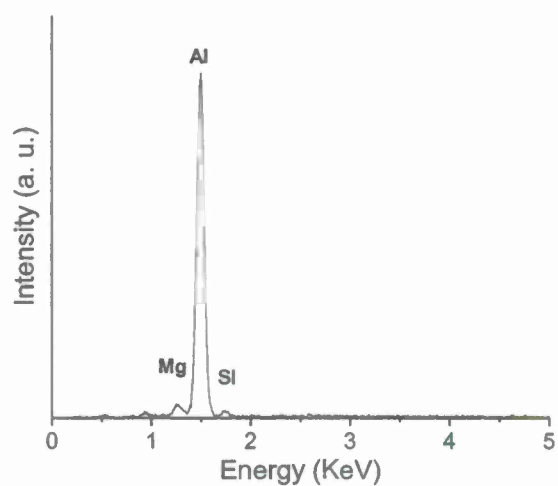


(b)

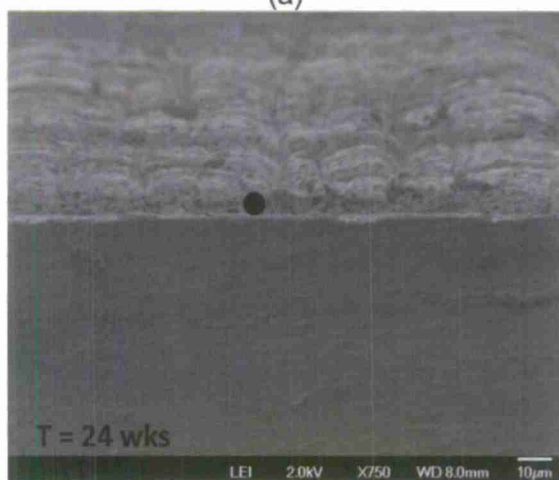
Figure 112. SEM micrograph (planar view) of scribed AA2024-T351 pretreated with Prekote and coated with MgRP (initial MgPVC = 45%) after field exposure at Charlottesville, VA for 24 weeks. Spot markers indicate approximate location of EDS analysis shown in (b).



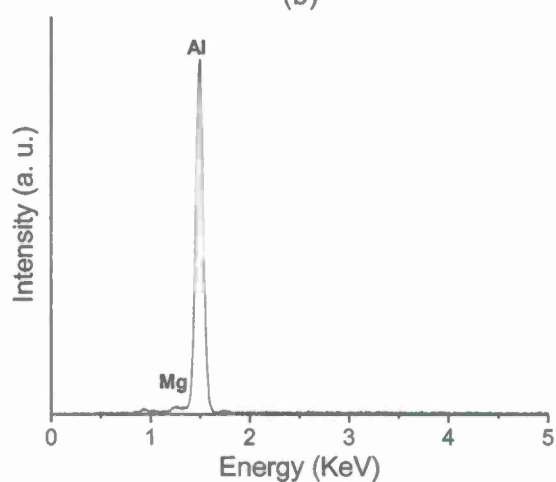
(a)



(b)



(c)



(d)

Figure 113. Scanning electron micrograph of cross sectioned AA2024-T351 pretreated with Prekote and coated with MgRP (initial MgPVC = 45%) after field exposure at Charlottesville, VA for (a,b) 12 weeks and (c,d) 24 weeks. Spot markers indicate approximate location of EDS analysis shown in (b) and (d).

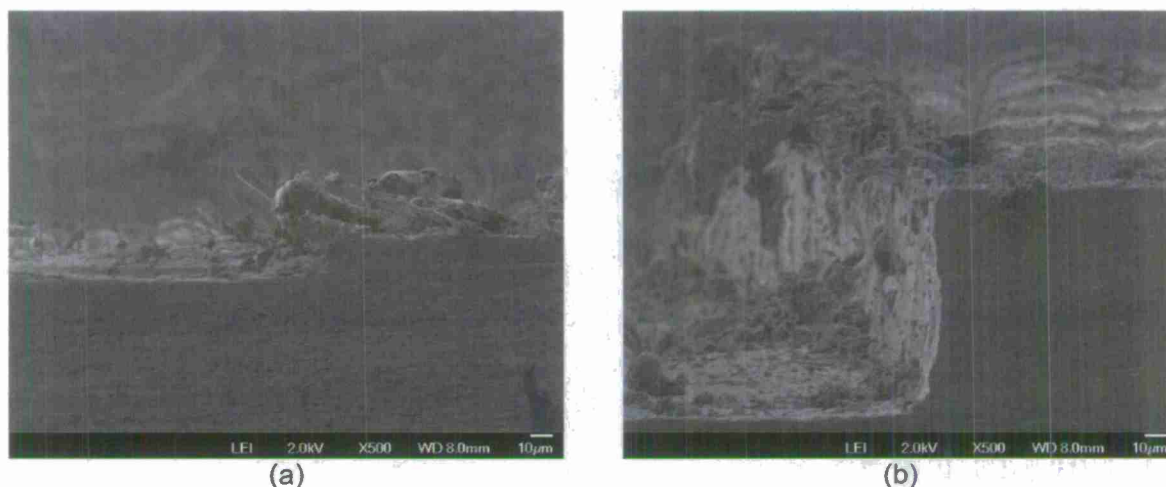


Figure 114. Scanning electron micrograph of cross sectioned AA2024-T351 pretreated with Prekote and coated with MgRP (initial MgPVC = 45%) after environmental exposure in the field at Charlottesville, VA for (a) 12 weeks and (b) 24 weeks.

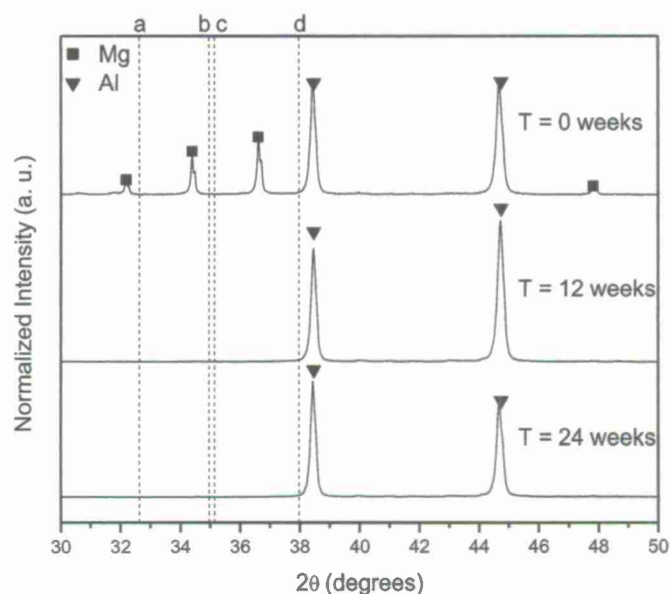


Figure 115. X-Ray diffraction spectra of AA2024-T351 panels coated with MgRP (initial MgPVC = 45%) after field exposure at Charlottesville, VA for 0, 12, and 24 weeks. Dotted lines indicate the position of the most intense diffraction peak for (a)  $\text{MgCO}_3$  (b)  $\text{MgCl}_2$  (c)  $\text{Al}_2\text{O}_3$  and (d)  $\text{Mg(OH)}_2$ .

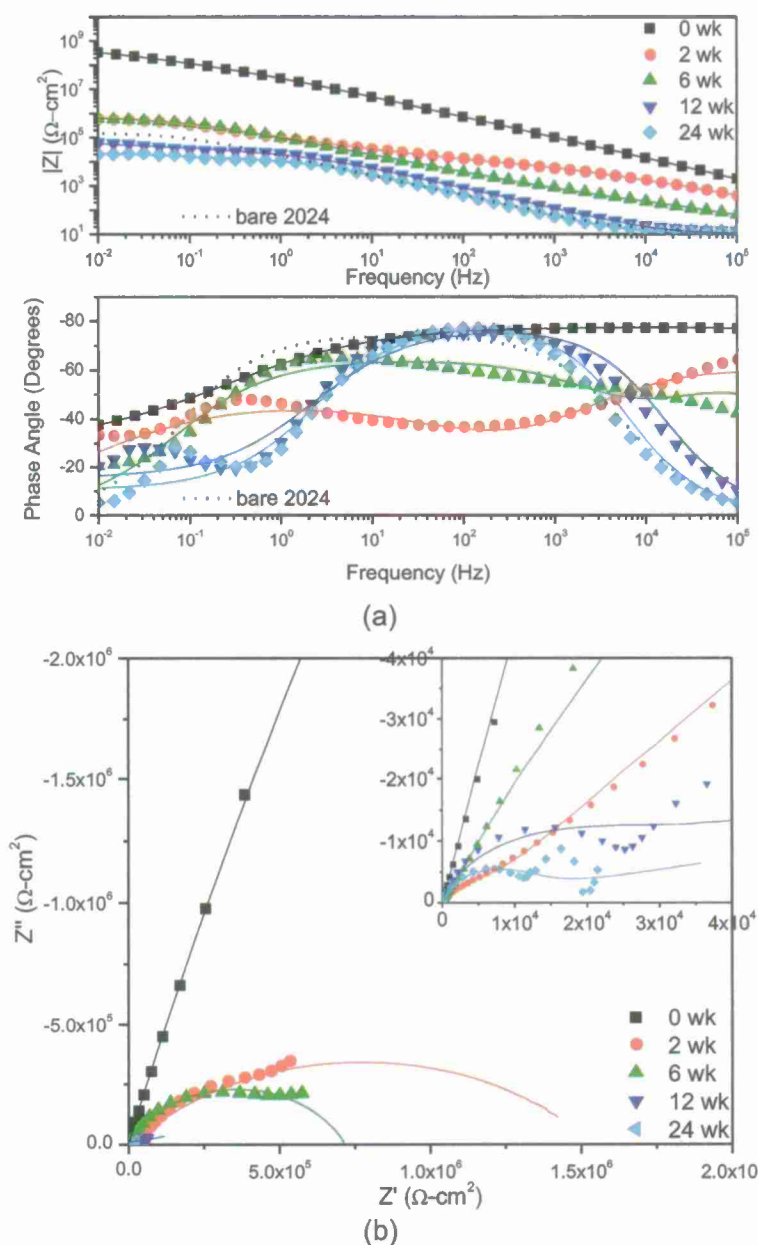


Figure 116. (a) Bode and (b) Nyquist plots of EIS of AA2024-T351 panels coated with MgRP (initial MgPVC = 45%) after field exposure at Charlottesville, VA for 0, 2, 6, 12, and 24 weeks. Tested in ambiently aerated 5% NaCl Solution. Fit results in Table 9.



Table 9. Fitting results of EIS measured on AA2024-T351 panels coated with MgRP (MgPVC = 45%) after field exposure at Charlottesville, VA for 0, 2, 6, 12, and 24 weeks. Tested in ambiently aerated 5% NaCl Solution. Equivalent electric circuit model used shown in Figure 105.

	units	0 wk	2 wk	6 wk	12 wk	24 wk
$R_s$	( $\Omega\text{-cm}^2$ )	10.000	10.000	10.000	10.000	10.000
$C_{\text{coat}}^-$ $Y^0$	( $\mu\text{F/cm}^2$ )	0.007	0.257	1.328	4.361	7.932
$C_{\text{coat}}^-$ $n$	-	0.357	0.689	0.708	0.870	0.888
$R_{\text{coat}}$	( $\text{k}\Omega\text{-cm}^2$ )	0.003	8.917	0.450	0.017	0.033
$C_{\text{dl}}^-$ $Y^0$	( $\mu\text{F/cm}^2$ )	0.005	3.272	1.321	28.020	63.440
$C_{\text{dl}}^-$ $n$	-	0.863	0.521	0.725	0.166	0.113
$R_{\text{corr}}$	( $\text{G}\Omega\text{-cm}^2$ )	10.000	0.002	0.001	0.065	0.083
$F_{45}$	(Hz)	0.04	2159.93	$\geq 100000$	$\geq 100000$	$\geq 100000$
$F_{\text{saddle}}$	(Hz)	0.01	158.49	$\geq 100000$	$\geq 100000$	$\geq 100000$

### 1.8.5.3 Behavior During and After Exposure in ASTM B-117 with 5% NaCl

Optical micrographs of MgRP coated AA2024-T351 panels that have been exposed in ASTM B-117 with 5% NaCl solution for 0, 384, and 984 hours are shown in Figure 117 and Figure 118. In general, the coating was observed to turn bright white in color with increased exposure time, presumably due to conversion of the metallic Mg pigment to  $\text{Mg}(\text{OH})_2$  corrosion product which has limited solubility in solutions of  $\text{pH} \geq 8$ . After 984 hours of exposure in ASTM B-117 with 5% NaCl solution the scribe appears, at low magnification, to be moderately clean and without significant damage. It is important to note that no blistering or similar macroscopic coating failure phenomena are observed in the MgRP or along the scribe lines after exposure for 984 hours in ASTM B-117 with 5% NaCl solution. Upon closer investigation with the SEM (Figure 119, Figure 120, and Figure 121), after 384 hours of exposure the MgRP-coated region appears to be very rough in texture; covered in lamellar flowers typically associated with  $\text{Mg}(\text{OH})_2$ .<sup>44, 51</sup> Metallic Mg is known to be readily converted to  $\text{Mg}(\text{OH})_2$  in most ambient aqueous environments. A moderate amount of  $\text{Mg}(\text{OH})_2$  precipitates are also present in the scribed region (particularly visible in Figure 120a and Figure 121a). Much of the lamellar structure appears to dissipate upon further exposure in ASTM B-117 with 5% NaCl solution up to 984 hours.

To further investigate the composition of any deposits in the scribe, and of the MgRP proximate to the scribe, 16 consecutive EDS spot scans were obtained across the width of the scribe and coating interface (labeled 1-16 in Figure 122). The spacing between scans was approximately 65  $\mu\text{m}$ . The basic EDS spectra obtained across the scribe and coating interface shows combinations of peaks indicative of C, O, Mg, Al, Si, and Cl. The EDS spot scans obtained throughout the width of the scribe, labeled 1 – 12, all show detectable amounts of Mg species present in the scribe suggesting that the whole scribe was subjected to cathodic protection in the ASTM B-117 with 5% NaCl solution environment. Increased Mg intensities along with significant amounts of Cl are detected at locations more proximate to the scribe edges (positions 1, 2, 3, 11, and 12), possibly indicating increased cathodic protection in these regions

compared with regions in the middle of the scribe (positions 4 – 10). Significant Mg, O and Cl peaks are present in the EDS spectra obtained over the MgRP coating at positions 13, 14, 15 and 16. The significant Mg, O and Cl peaks present at positions 13, 14, 15 and 16 appear very similar to the modeled EDS spectra of  $\text{Mg}(\text{OH})_2$  and  $\text{MgCl}_2$  in Figure 93. This similarity suggests the surface of the coating consists of a layer of residual  $\text{Mg}(\text{OH})_2$  and  $\text{MgCl}_2$ . Based on first order approximations of EDS penetration depth (Figure 94) the coating/product layer is at least 2 - 5  $\mu\text{m}$  thick.<sup>69</sup>

SEM micrographs of cross-sectioned MgRP on AA2024-T351 far away from the scribe after (a) 384 and (b) 984 hours of exposure in ASTM B-117 with 5% NaCl solution are shown in Figure 123. After 384 and 984 hours of exposure, the remaining MgRP coating layer is observed to be approximately 20 - 40  $\mu\text{m}$  thick. Multiple EDS spot scans were obtained in the coating layer after 384 and 984 hours of exposure in ASTM B-117 with 5% NaCl. Representative EDS spectra are shown in Figure 123b and d. EDS spot scans obtained on the coating layer after 384 hours of exposure in ASTM B-117 with 5% NaCl solution indicate the presence of a significant amount of metallic, unoxidized Mg in the coating. Similar EDS measurements obtained on the coating layer after 984 hours of exposure indicate the presence of Mg, O, and Cl in the coating. It is unclear from EDS analysis whether all of the Mg present in the coating layer is oxidized after 984 hours of exposure in ASTM B-117 with 5% NaCl solution. SEM micrographs of cross-sectioned MgRP on AA2024-T351 proximate to the scribe after (a) 384 and (b) 984 hours of exposure in ASTM B-117 with 5% NaCl solution are shown in Figure 124 for visual inspection. The MgRP coating layer is approximately 20 – 30  $\mu\text{m}$  thick. Overall, the edges and walls of the scribes appear to have moderate amounts of corrosion product deposited on them. In contrast to similar environmental exposures of earlier generation commercial products in the past<sup>1</sup>, no indications of cathodic corrosion, as evidenced by narrow pinholes, or underpaint corrosion or anodic undermining, as evidenced by areas of coating delamination above regions of Al corrosion, are visible at the coating/metal interface when viewed in cross-section.

XRD spectra of MgRP (initial MgPVC = 45%) coated AA2024-T351 after 0, 384 and 984 hours of exposure in ASTM B-117 with 5% NaCl solution are shown in Figure 125. The relative intensities of the Mg peaks shown in Figure 125 decrease to zero with increasing exposure time in ASTM B-117 with 5% NaCl solution which indicates a depletion of metallic Mg pigment from the coating system to below the detection limit of bulk XRD ( $\leq 5\%$  by volume<sup>3</sup>) after 984 hours of exposure. Principle XRD peaks of relevant Mg or Al corrosion products are labeled a, b, c, and d in Figure 125. No relevant Mg or Al corrosion products were observed with XRD after 384 or 984 hours of exposure in ASTM B-117 with 5% NaCl solution. It is likely that the corrosion products formed are either not voluminous enough to be detected by XRD or are of an amorphous crystal structure rendering them undetectable by XRD. With increasing exposure time, NaCl became prevalent in the XRD spectra as a result of the high deposition rate and continuous wetting characteristics of the salt fog environment.

EIS measurements of MgRP-coated AA2024-T351 (initial MgPVC = 45%) taken after 0, 168, 384, 744 and 984 hours of exposure in ASTM B-117 with 5% NaCl solution (scatter plot) and the results of the automated fitting analysis (lines) are shown in Figure 126. The values of each representative circuit component produced by the automated fitting routine for selected exposure times in ASTM B-117 with 5% NaCl solution are tabulated in Table 10. The MgRP coated AA2024-T351 displayed a decrease of three orders of magnitude of the low frequency (at 0.01 Hz) impedance as well as a shift towards high frequencies in the break point frequency of the Bode phase angle in as little as 168 hours of environmental exposure in ASTM B-117 with

5% NaCl solution. Both phenomena indicate a significant loss of barrier protection capability throughout the duration of the exposure.<sup>63, 64</sup>

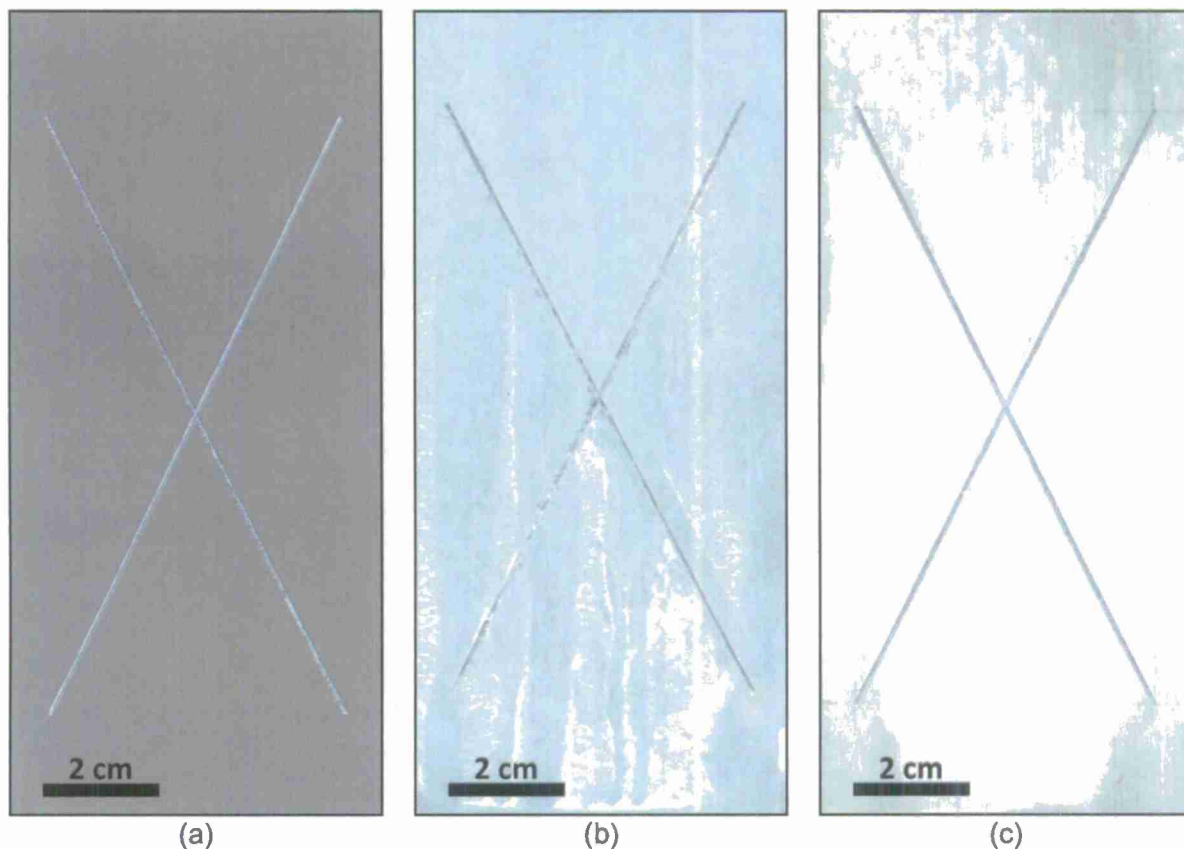


Figure 117. Optical micrograph of AA2024-T351 panels coated with MgRP (initial MgPVC = 45%) after lab accelerated life testing in ASTM B117 for (a) T = 0 hrs (b) T = 384 hrs (c) T = 984 hrs

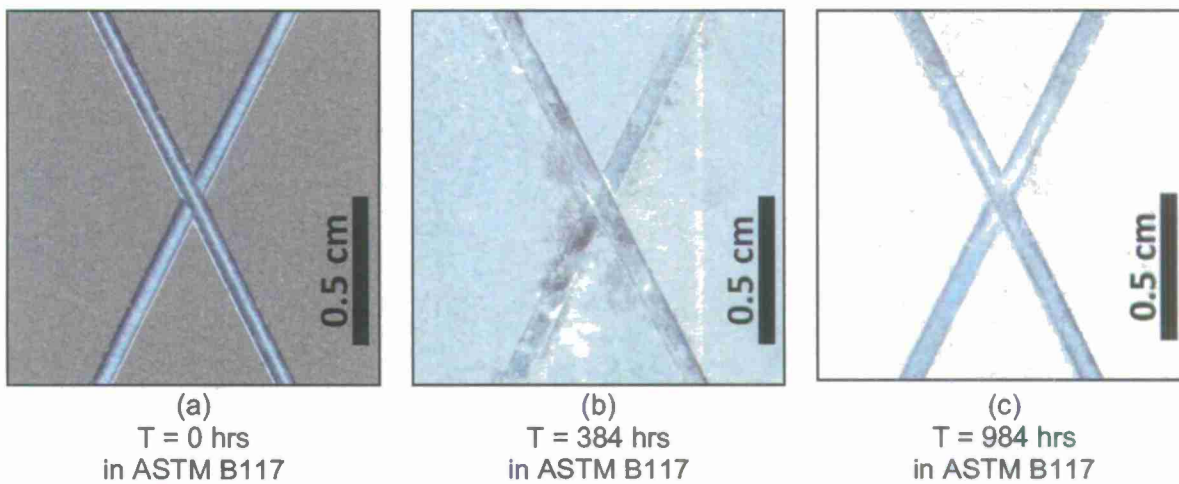


Figure 118. Optical micrograph of AA2024-T351 panels coated with MgRP (initial MgPVC = 45%) after lab accelerated life testing in ASTM B117 for (a) T = 0 hrs (b) T = 384 hrs (c) T = 984 hrs

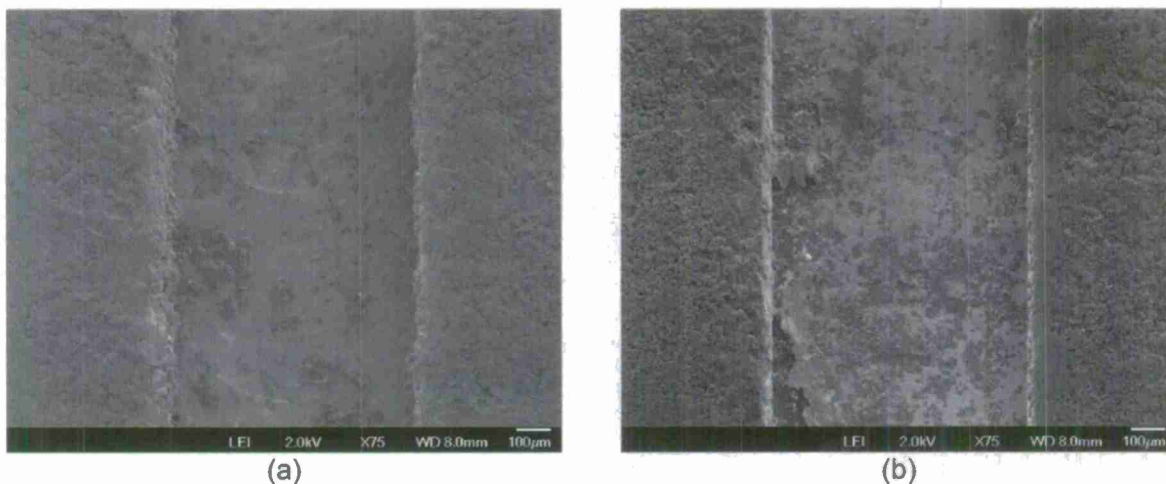
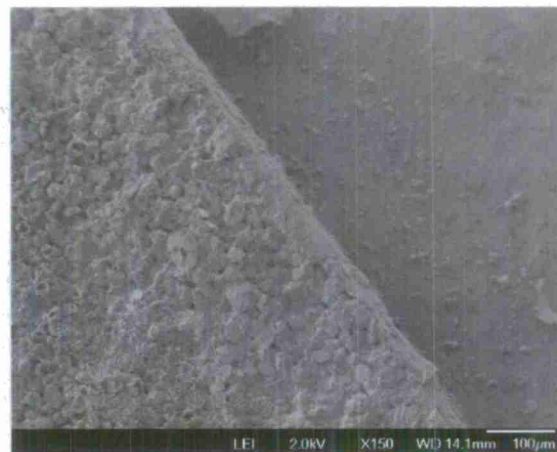


Figure 119. Scanning electron micrograph (planar view) of scribed AA2024-T351 pretreated with Prekote and coated with MgRP (initial MgPVC = 45%) after lab accelerated life testing in ASTM B117 for (a) 384 hrs and (b) 984 hrs.





(a)

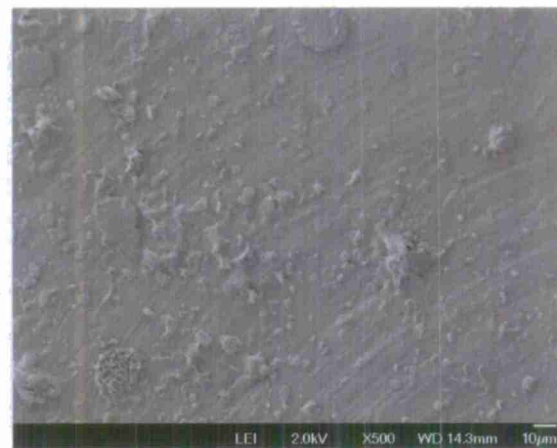


(b)

Figure 120. Scanning electron micrograph (planar view) of scribed AA2024-T351 pretreated with Prekote and coated with MgRP (initial MgPVC = 45%) after lab accelerated life testing in ASTM B117 for (a) 384 hrs and (b) 984 hrs.



(a)

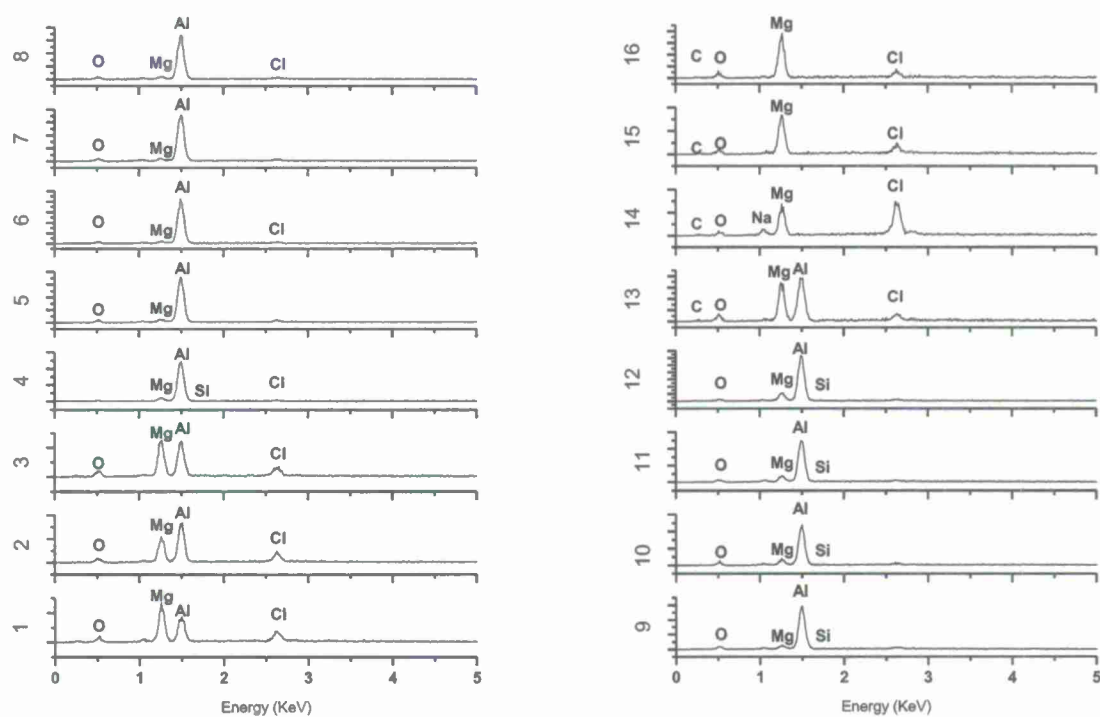


(b)

Figure 121. Scanning electron micrograph (planar view) of scribed AA2024-T351 pretreated with Prekote and coated with MgRP (initial MgPVC = 45%) after lab accelerated life testing in ASTM B117 for (a) 384 hrs and (b) 984 hrs.



(a)

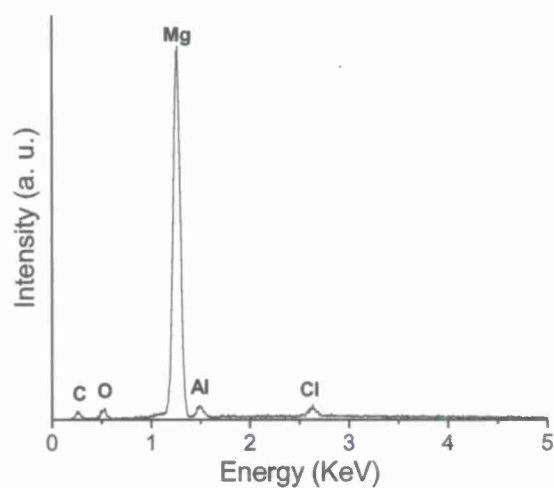


(b)

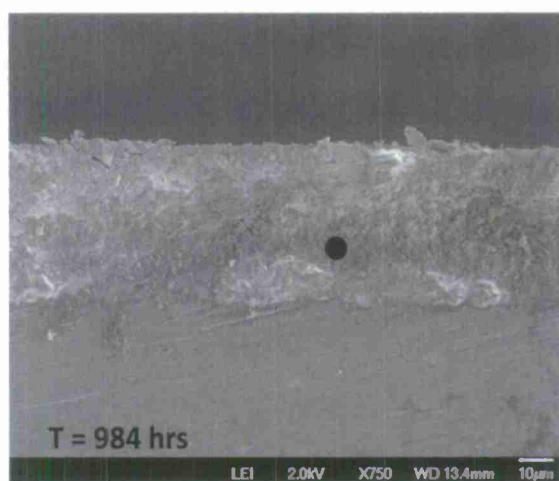
Figure 122. SEM micrograph (planar view) of scribed AA2024-T351 pretreated with Prekote and coated with MgRP (initial MgPVC = 45%) after lab accelerated life testing in ASTM B117 for 984 hrs. Spot markers indicate approximate location of EDS analysis shown in (b).



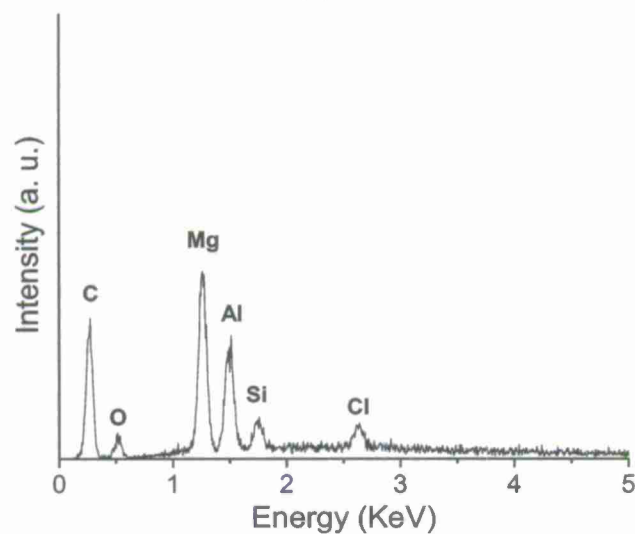
(a)



(b)



(c)



(d)

Figure 123. Scanning electron micrograph of cross sectioned AA2024-T351 pretreated with Prekote and coated with MgRP (initial MgPVC = 45%) after lab accelerated life testing in ASTM B117 for (a,b) 384 hrs and (c,d) 984 hrs. Spot markers indicate approximate location of EDS analysis shown in (b) and (d).

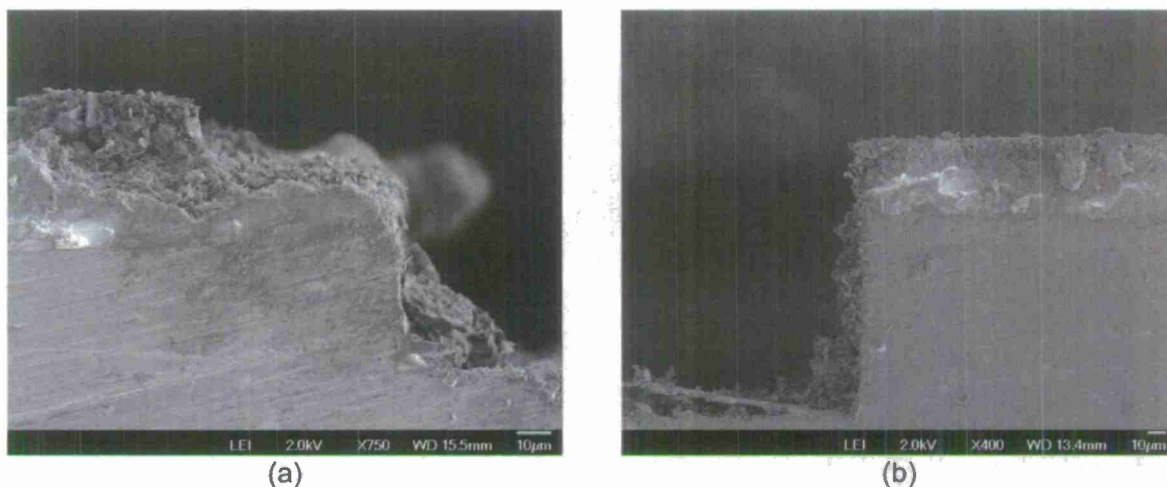


Figure 124. Scanning electron micrograph of cross sectioned AA2024-T351 pretreated with Prekote and coated with MgRP (initial MgPVC = 45%) after lab accelerated life testing in ASTM B117 for (a) 384 hrs and (b) 984 hrs.

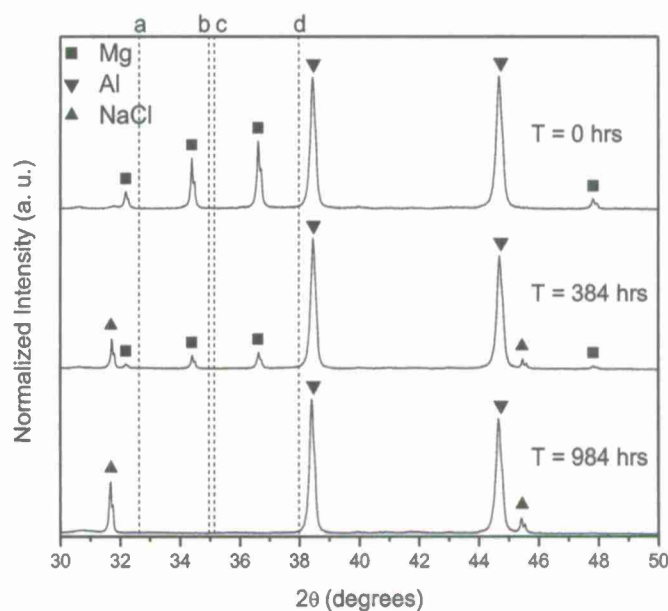


Figure 125. X-Ray diffraction spectra of AA2024-T351 panels coated with MgRP (initial MgPVC = 45%) that have been environmentally exposed in ASTM B117 for 0, 384 and 984 hours. Dotted lines indicate the position of the most intense diffraction peak for (a)  $\text{MgCO}_3$  (b)  $\text{MgCl}_2$  (c)  $\text{Al}_2\text{O}_3$  and (d)  $\text{Mg}(\text{OH})_2$ .



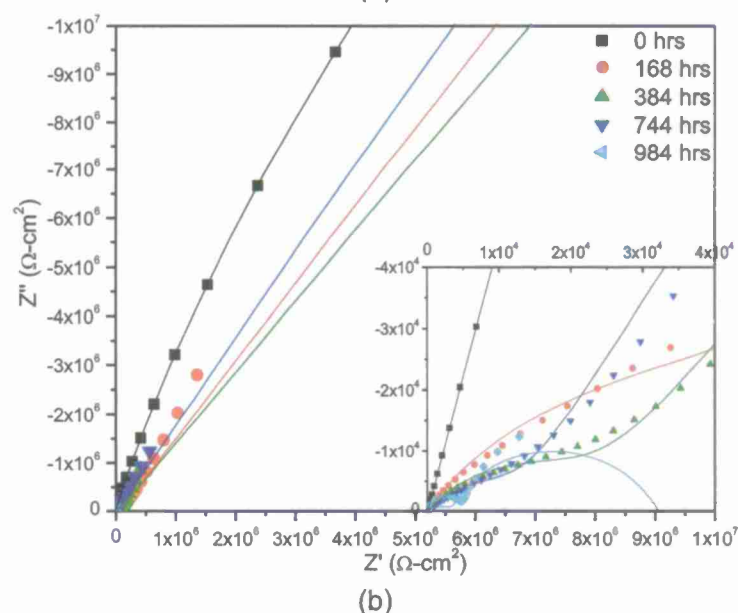
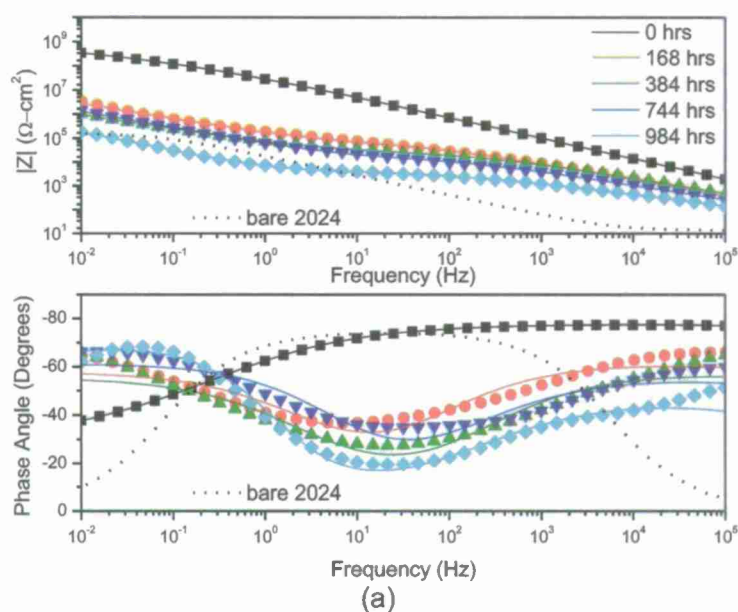


Figure 126. (a) Bode and (b) Nyquist plots of EIS of AA2024-T351 panels coated with MgRP (initial MgPVC = 45%) that have been environmentally exposed in ASTM B117 for 0, 168, 384, 744, and 984 hours. Tested in ambiently aerated 5% NaCl Solution. Fit results shown in Table 10.

Table 10. Fitting results of EIS measured on AA2024-T351 panels coated with MgRP (MgPVC = 45%) after LALT in ASTM B117 for 0, 168, 384, 744, and 984 hours. Tested in ambiently aerated 5% NaCl Solution. Equivalent electric circuit model used shown in Figure 105.

	units	0 hrs	168 hrs	384 hrs	744 hrs	984 hrs
$R_s$	( $\Omega\text{-cm}^2$ )	10.000	10.000	10.000	10.000	16.920
$C_{\text{coat}}^{\text{Y}^0}$	( $\mu\text{F/cm}^2$ )	0.007	0.318	0.451	1.087	6.856
$C_{\text{coat}}^{\text{Y}^0}$	-	0.357	0.680	0.638	0.617	0.531
$R_{\text{coat}}$	( $\text{k}\Omega\text{-cm}^2$ )	0.003	67.070	26.460	17.280	4.038
$C_{\text{dl}}^{\text{Y}^0}$	( $\mu\text{F/cm}^2$ )	0.005	1.971	5.700	4.162	44.390
$C_{\text{dl}}^{\text{Y}^0}$	-	0.863	0.638	0.614	0.698	0.817
$R_{\text{corr}}$	( $\text{G}\Omega\text{-cm}^2$ )	10.000	10.000	10.000	10.000	0.000
$F_{45}$	(Hz)	0.04	217.01	1459.32	1459.32	21609.38
$F_{\text{saddle}}$	(Hz)	0.01	9.93	21.31	31.62	21.31

#### 1.8.5.4 Behavior During and After Exposure in ASTM B-117 Modified with ASTM Sea Water:

Optical micrographs of MgRP coated AA2024-T351 panels that have been exposed in ASTM B-117 modified with ASTM artificial sea water solution for 0, 408, and 1000 hours are shown in Figure 127 and Figure 128. In general, with increased exposure time, the coating developed a dense, ivory colored film covering the whole sample. The film is presumably due to the conversion of Mg to a corrosion product or the deposition of a salt present in the ASTM artificial sea water which has limited solubility in solutions of  $\text{pH} \geq 8$ . After 1000 hours of exposure in the ASTM B-117 environment modified with ASTM artificial sea water the scribe appears, at low magnification, to be full of corrosion product or deposit. It is important to note that no blistering or similar macroscopic coating failure phenomena are observed in the MgRP or along the scribe lines after exposure for 1000 hours in the ASTM B-117 environment modified with ASTM artificial sea. Upon closer investigation with the SEM (Figure 129, Figure 130, and Figure 131), after 408 hours of exposure the scribe and MgRP-coated region appear to be very rough in texture and covered in spherical groupings of needle-like precipitates. The precipitates can be easily seen in Figure 131.

To further investigate the composition of the deposits on the coating and in the scribe 16 consecutive EDS spot scans were obtained across the width of the scribe and coating interface (labeled 1-16 in Figure 132). The spacing between scans was approximately 65  $\mu\text{m}$ . Two basic EDS spectra, one consisting solely of Ca, and a second consisting of both Mg and Al, were observed across the scribe and coating interface. The EDS spot scans throughout almost the entire width of the scribe (positions labeled 1 – 11) as well as over the MgRP coating (positions labeled 14, 15, and 16) solely show significant amounts of Ca species present. Calcareous deposits primarily consist of  $\text{CaCO}_3$  and are indicative of regions of cathodic protection afforded to the AA2024-T351 by the MgRP.<sup>71-78</sup> The deposition of Ca species throughout most of the

scribe suggests that the whole scribe may have been subject to cathodic protection in the ASTM B-117 environment modified with ASTM artificial sea water. The lack of Al peaks at positions 1 – 11 and 14-16 indicate that the layer of calcareous deposits is thicker than 3  $\mu\text{m}$ . The simulated EDS spectrum of a sphere of  $\text{CaCO}_3$  with a diameter of 3  $\mu\text{m}$  on an infinitely thick, pure Al substrate, shown in Figure 95b, does not contain an Al peak. If the layer of calcareous was less than 3  $\mu\text{m}$  thick at the locations of the EDS measurements the Al peak would not be suppressed. Positions 12 and 13, which are directly proximate to the edge of the MgRP coating on one side of the scribe show Al and Mg peaks from the substrate and MgRP coating. This is likely the side of the scribe that is positioned towards the top of the panel during exposure, resulting in a thinner electrolyte layer at this position and subsequently less deposition of the Ca-containing precipitate.

SEM micrographs of cross-sectioned MgRP on AA2024-T351 far away from the scribe after (a) 408 and (b) 1000 hours of exposure in ASTM B-117 environment modified with ASTM artificial sea water are shown in Figure 133. After 408 and 1000 hours of exposure, the remaining MgRP coating layer is observed to be approximately 20 - 30  $\mu\text{m}$  thick. Multiple EDS spot scans were obtained in the coating layer after 408 and 1000 hours of exposure in ASTM B-117 with ASTM artificial sea water. Representative EDS spectra are shown in Figure 133b and d. EDS spot scans obtained on the coating layer after 408 hours of exposure in the ASTM B-117 environment modified with ASTM artificial sea water indicate the presence of a significant amount of Mg in the coating as well as Cl and significant amounts of Ca. It is unclear from EDS analysis whether all of the Mg present in the coating layer is oxidized after 408 hours of exposure in ASTM B-117 environment modified with ASTM artificial sea water. Similar EDS measurements obtained on the coating layer after 1000 hours of exposure indicate the presence of Ca, C, and O suggesting the Ca-rich deposit covering the sample is a calcareous deposit. SEM micrographs of cross-sectioned MgRP on AA2024-T351 proximate to the scribe after (a) 408 and (b) 1000 hours of exposure in the ASTM B-117 environment modified with ASTM artificial sea water are shown in Figure 134 for visual inspection. The MgRP coating layer is approximately 20 – 30  $\mu\text{m}$  thick. Overall, the edges and walls of the scribes appear to have corrosion product deposited on them. In contrast to similar environmental exposures of earlier generation commercial products in the past<sup>1</sup>, no indications of cathodic corrosion, as evidenced by narrow pinholes, or underpaint corrosion or anodic undermining, as evidenced by areas of coating delamination above regions of Al corrosion, are visible at the coating/metal interface when viewed in cross-section.

XRD spectra of MgRP (initial MgPVC = 45%) coated AA2024-T351 after 0, 408 and 1000 hours of exposure in the ASTM B-117 environment modified with ASTM artificial sea water are shown in Figure 135. The relative intensities of the Mg peaks shown in Figure 135 decrease with increasing exposure time in the ASTM B-117 environment modified with ASTM artificial sea water which indicates a depletion of metallic Mg pigment from the coating system to below the detection limit of bulk XRD ( $\leq 5\%$  by volume<sup>3</sup>) after 1000 hours of exposure. Principle XRD peaks of relevant Mg or Al corrosion products are labeled a, b, c, and d in Figure 125. No relevant Mg or Al corrosion products were observed with XRD after 408 or 1000 hours of exposure in the ASTM B-117 environment modified with ASTM artificial sea water. With increasing exposure time,  $\text{CaCO}_3$  became prevalent in the XRD spectra and is shown to be the predominant calcareous deposit covering the samples.

EIS measurements of MgRP-coated AA2024-T351 (initial MgPVC = 45%) taken after 0, 192, 408, 698, and 1000 hours of exposure in the ASTM B-117 environment modified with ASTM artificial sea water (scatter plot) and the results of the automated fitting analysis (lines) are

shown in Figure 136. The values of each representative circuit component produced by the automated fitting routine for selected exposure times at Birdwood Golf Course in Charlottesville, VA are tabulated in Table 11. The MgRP coated AA2024-T351 displayed a decrease of three orders of magnitude of the low frequency (at 0.01 Hz) impedance as well as a shift towards high frequencies in the break point frequency of the Bode phase angle in as little as 192 hours of environmental exposure at Birdwood Golf Course in Charlottesville, VA. Both phenomena indicate a significant loss of barrier protection capability throughout the duration of the exposure.<sup>63, 64</sup>

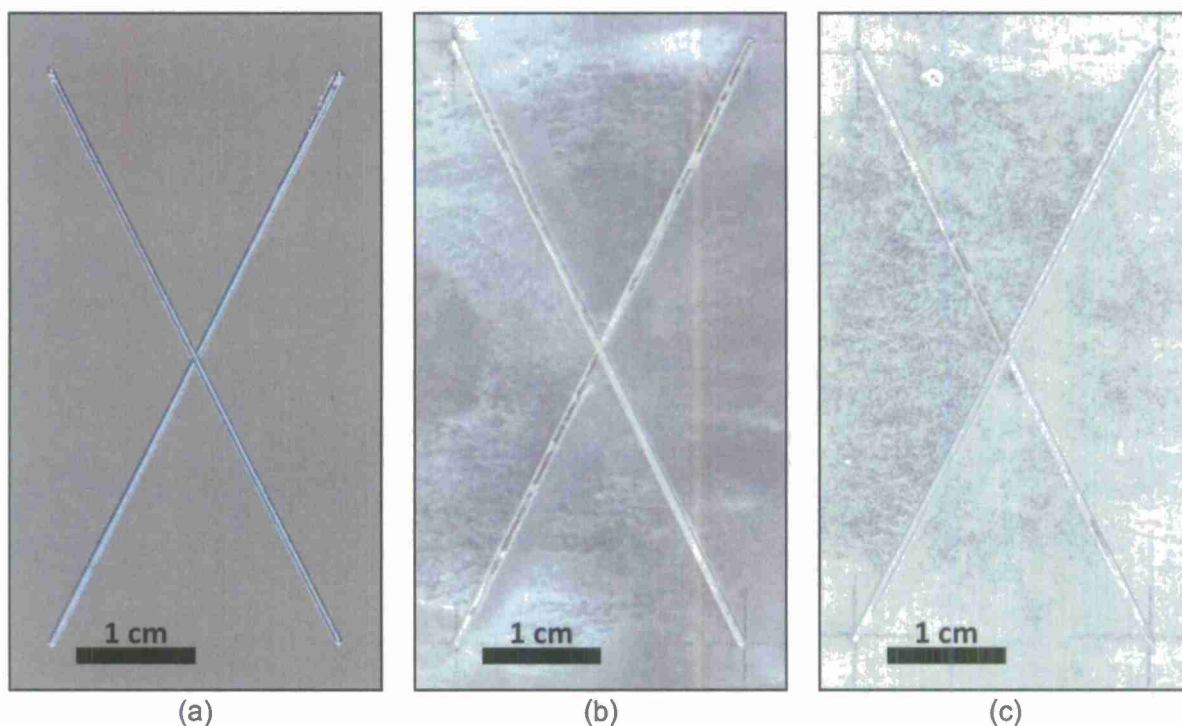


Figure 127. Optical micrograph of AA2024-T351 panels coated with MgRP (initial MgPVC = 45%) after lab accelerated life testing in ASTM B117 modified with artificial sea water. (a) T = 0 hrs (b) T = 408 hrs (c) T = 1000 hrs



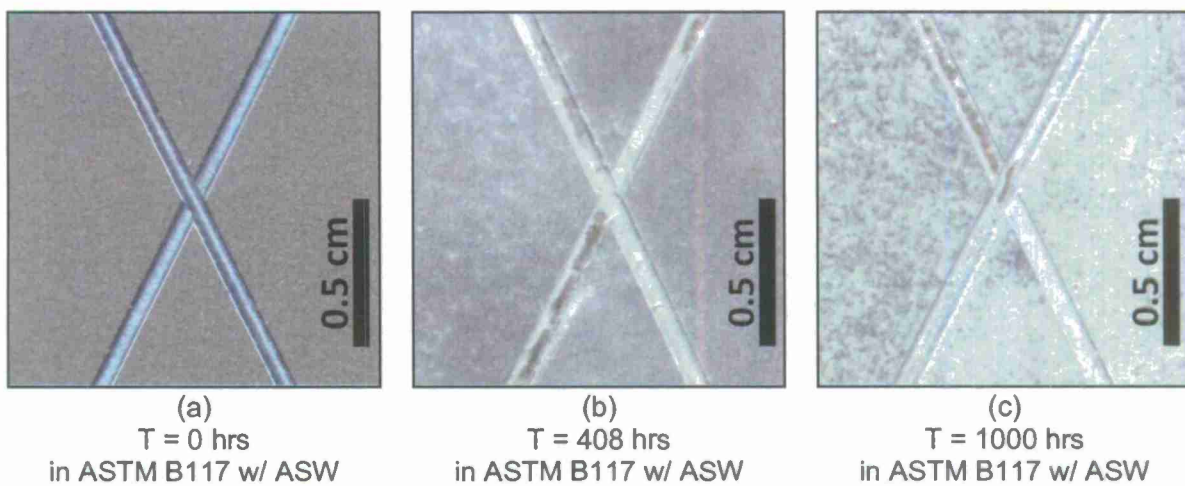


Figure 128. Optical micrograph of AA2024-T351 panels coated with MgRP (initial MgPVC = 45%) after lab accelerated life testing in ASTM B117 modified with artificial sea water. (a) T = 0 hrs (b) T = 408 hrs (c) T = 1000 hrs

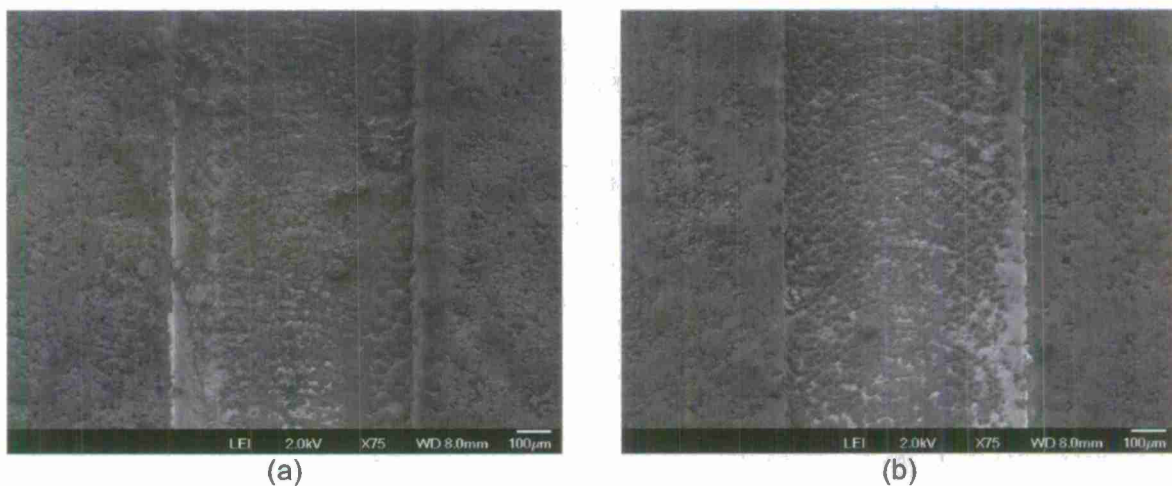


Figure 129. Scanning electron micrograph (planar view) of scribed AA2024-T351 pretreated with Prekote and coated with MgRP (initial MgPVC = 45%) after lab accelerated life testing in ASTM B117 modified with artificial sea water for (a) 408 hrs and (b) 1000 hrs.

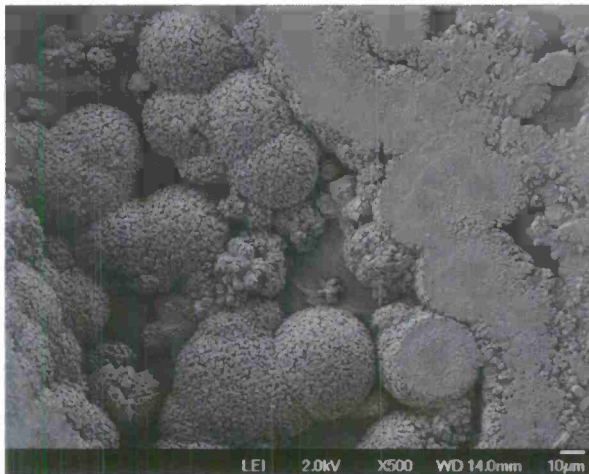


(a)



(b)

Figure 130. Scanning electron micrograph (planar view) of scribed AA2024-T351 pretreated with Prekote and coated with MgRP (initial MgPVC = 45%) after lab accelerated life testing in ASTM B117 modified with artificial sea water for (a) 408 hrs and (b) 1000 hrs.



(a)

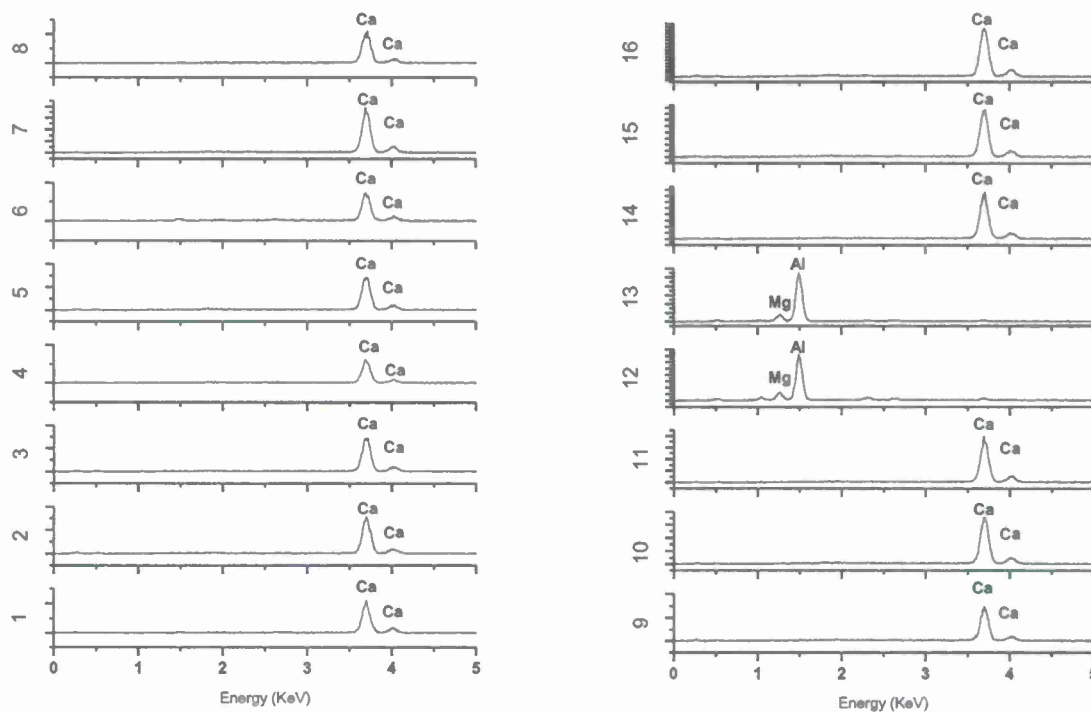


(b)

Figure 131. Higher magnification scanning electron micrograph (planar view) of scribed AA2024-T351 pretreated with Prekote and coated with MgRP (initial MgPVC = 45%) after lab accelerated life testing in ASTM B117 modified with artificial sea water for (a) 408 hrs and (b) 1000 hrs.



(a)

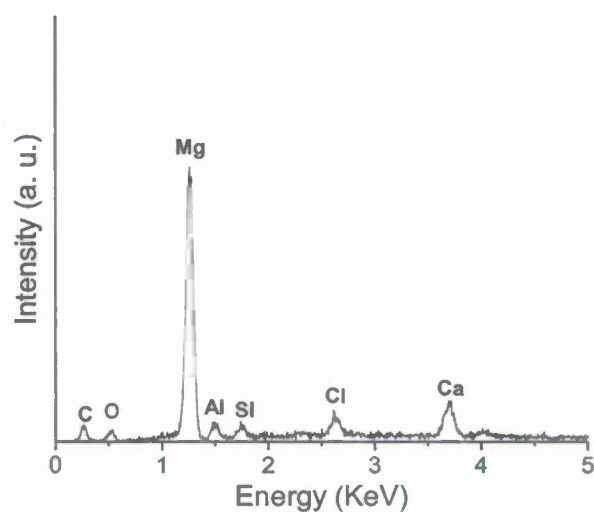


(b)

Figure 132. SEM micrograph (planar view) of scribed AA2024-T351 pretreated with Prekote and coated with MgRP (initial MgPVC = 45%) after after lab accelerated life testing in ASTM B117 modified with artificial sea water for 1000 hrs. Spot markers indicate approximate location of EDS analysis shown in (b).



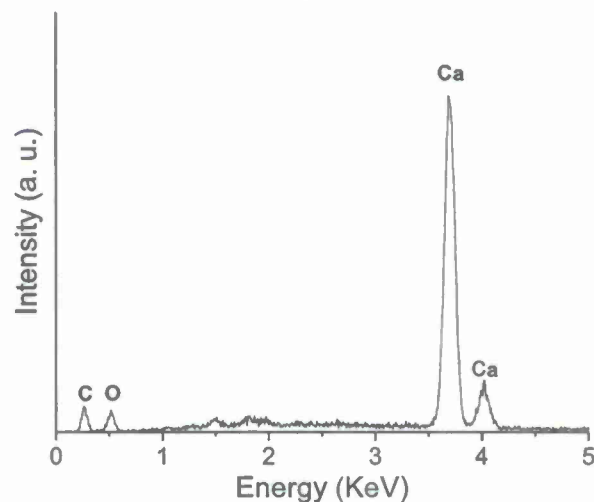
(a)



(b)



(c)



(d)

Figure 133. Scanning electron micrograph of cross sectioned AA2024-T351 pretreated with Prekote and coated with MgRP (initial MgPVC = 45%) after lab accelerated life testing in ASTM B117 modified with artificial sea water for (a,b) 408 hrs and (c,d) 1000 hrs. Spot markers indicate approximate location of EDS analysis shown in (b) and (d).



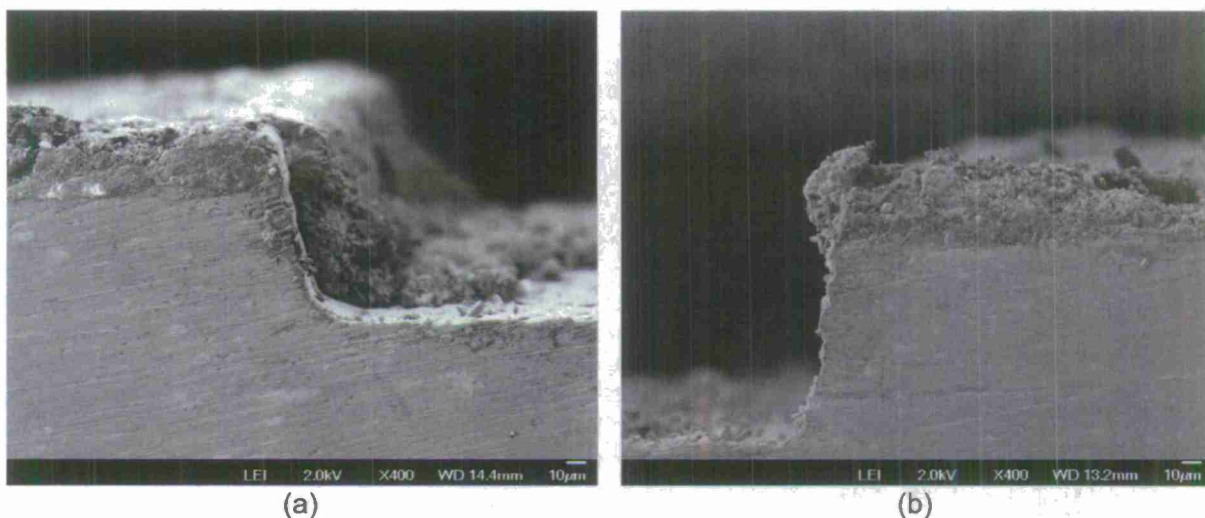


Figure 134. Scanning electron micrograph of cross sectioned AA2024-T351 pretreated with Prekote and coated with MgRP (initial MgPVC = 45%) after lab accelerated life testing in ASTM B117 modified with artificial sea water for (a) 408 hrs (b) 1000 hrs.

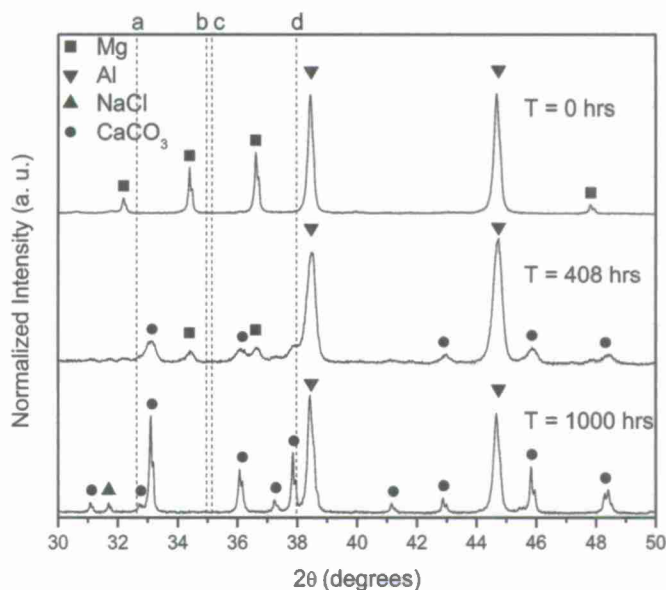
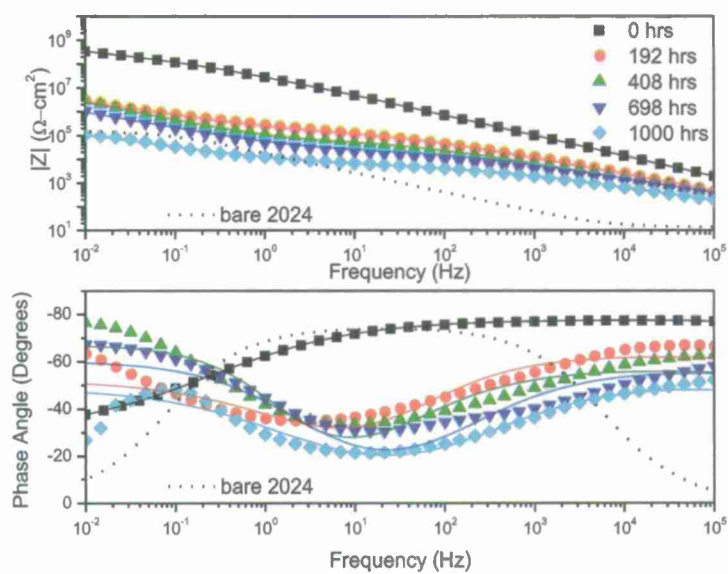
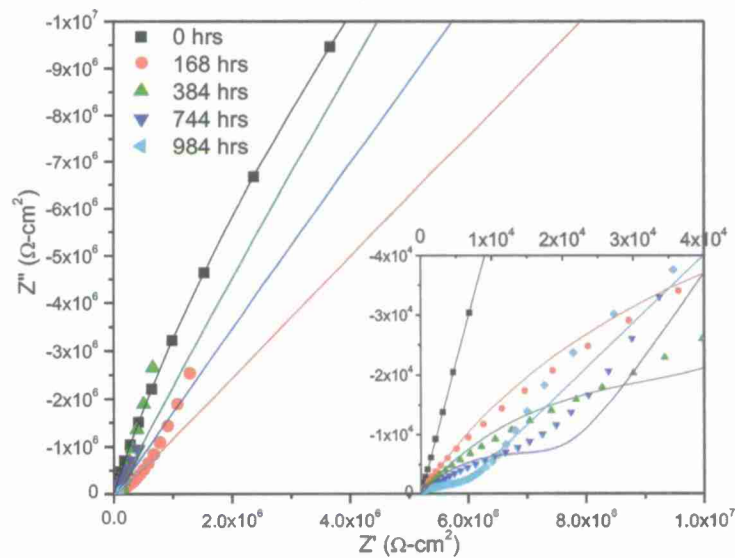


Figure 135. X-Ray diffraction spectra of AA2024-T351 panels coated with MgRP (initial MgPVC = 45%) after lab accelerated life testing in ASTM B117 modified with artificial sea water for 0, 408 and 1000 hours. Dotted lines indicate the position of the most intense diffraction peak for (a)  $\text{MgCO}_3$  (b)  $\text{MgCl}_2$  (c)  $\text{Al}_2\text{O}_3$  and (d)  $\text{Mg(OH)}_2$ .



(a)



(b)

Figure 136. (a) Bode and (b) Nyquist plots of EIS of AA2024-T351 panels coated with MgRP (initial MgPVC = 45%) after lab accelerated life testing in ASTM B117 modified with artificial sea water for 0, 192, 408, 698 and 1000 hours. Tested in ambiently aerated 5% NaCl Solution. Fit results shown in Table 11.

Table 11. Fitting results of EIS measured on AA2024-T351 panels coated with MgRP (MgPVC = 45%) after LALT in ASTM B117 modified with artificial sea water for 0, 192, 408, 698 and 1000 hours. Tested in ambiently aerated 5% NaCl Solution. Equivalent electric circuit model used shown in Figure 105.

	units	0 hrs	192 hrs	408 hrs	698 hrs	1000 hrs
$R_s$	( $\Omega\text{-cm}^2$ )	10.000	10.000	10.000	10.000	10.000
$C_{\text{coat}}^- Y^0$	( $\mu\text{F/cm}^2$ )	0.007	0.198	0.617	0.608	2.848
$C_{\text{coat}}^- n$	-	0.357	0.696	0.630	0.629	0.572
$R_{\text{coat}}$	( $\text{k}\Omega\text{-cm}^2$ )	0.003	122.000	63.400	23.070	5.517
$C_{\text{dl}}^- Y^0$	( $\mu\text{F/cm}^2$ )	0.005	1.730	2.691	6.294	42.560
$C_{\text{dl}}^- n$	-	0.863	0.570	0.783	0.674	0.540
$R_{\text{corr}}$	( $\text{G}\Omega\text{-cm}^2$ )	10.000	10.000	10.000	10.000	10.000
$F_{45}$	(Hz)	0.04	100.45	315.50	3170.96	4641.54
$F_{\text{saddle}}$	(Hz)	0.01	2.15	10.00	14.74	14.74

#### 1.8.5.5 Tracking MgRP Degradation throughout Environmental Exposure:

The integrated normalized XRD Mg <200> peak intensity is plotted versus exposure time in each environment in Figure 137. In each exposure environment investigated in this study, the integrated normalized intensity of metallic Mg was observed to decrease with increased exposure time. It was found that full immersion in ambiently aerated 5% NaCl solution, ASTM B-117 in 5% NaCl and ASTM B-117 in ASTM artificial sea water deplete the MgRP of metallic Mg pigment at approximately equal rates, with depletion (less than 5% by volume as detectable by XRD<sup>3</sup>) occurring after approximately 1000 hrs of exposure. Field exposures in Charlottesville, VA and Kennedy Space Center, FL resulted in depletion of metallic Mg pigment after 2000 and 4000 hrs of exposure respectively. The acceleration factors, with respect to Mg depletion rate, observed for field exposure versus the full immersion and salt fog cabinet exposures were approximately 2:1 and 4:1. It is important to note that even though metallic Mg pigment is not detectable after extended exposure times in each environment, it is likely that there still exists a small amount (less than 5% PVC) of encapsulated metallic Mg pigment dispersed through any residual polymer coating that remains. This is particularly likely in samples that were not exposed to environments without significant UV, such as in ASTM B-117 salt spray testing, as the polymer does not degrade as readily in these environments.

As a result of pigment depletion in all environments, the global<sup>1</sup> galvanic protection potential of the coating system (as measured in ambiently aerated 5% NaCl solution) increases with exposure in each environment, from values approximately equal to that of bare Mg (-1.6 V vs. SCE) to those approximately equal to that of bare AA2024-T351 (-0.55 V vs. SCE). In an

<sup>1</sup> "Global" refers to the capability to protect a remote, bare area of AA2024-T351 as long as it is electrically and ionically connected to the coating.

attempt to develop acceleration factors with respect to galvanic protection potential in each exposure environment the open circuit potential of the MgRP-coated AA2024-T351 panel in ambiently aerated 5% NaCl solution is plotted versus exposure time in each environment in Figure 138. It was found that global galvanic protection potential increases to approximately equal to that of bare AA2024-T351 (-0.6 V vs. SCE) at approximately equal rates (after approximately 300 hours of exposure ) in full immersion in ambiently aerated 5% NaCl solution, ASTM B-117 in 5% NaCl and in ASTM B-117 with ASTM artificial sea water. Field exposures in Charlottesville, VA and Kennedy Space Center, FL both resulted in an increases in global galvanic protection potential to approximately equal to that of bare AA2024-T351 (-0.6 V vs. SCE) after approximately 1000 hours of exposure. The acceleration factors, with respect to global galvanic protection potential, observed for field exposure versus the full immersion and salt fog cabinet exposures were approximately 3:1 for non-topcoated MgRP systems. The correlation between global galvanic protection potential afforded to the AA2024-T351 substrate and metallic Mg pigment remaining in the coating is presented in Figure 139. In general, in all environments studied, the galvanic protection potential of the coating system (as measured in ambiently aerated 5% NaCl solution) increases with exposure in each environment, as a result of Mg pigment depletion.

Coating barrier properties in each exposure environment the low frequency impedance (at 0.01 Hz) and the breakpoint frequency of the MgRP-coated AA2024-T351 panel in ambiently aerated 5% NaCl solution are plotted versus exposure time in each environment in Figure 140 and Figure 141, respectively. In general, for all environments a significant decrease in barrier properties of MgRP-coated AA2024-T351 is observed with increased environmental exposure time but acceleration factors are hard to determine due to inherent scatter in the EIS data due to the near random occurrence of defects in the coating.

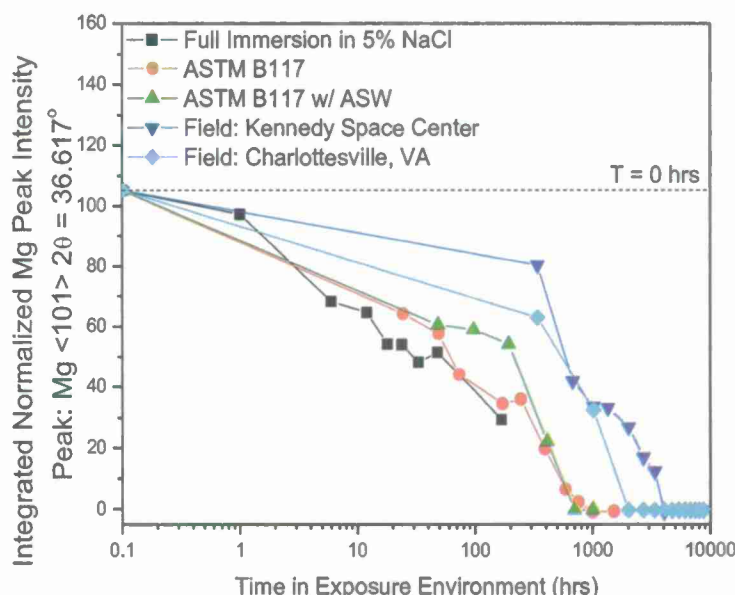


Figure 137. Integrated Mg peak ( $\text{Mg} <200> 2\theta = 36.617^\circ$ ) intensity vs. environmental exposure time in various lab and field exposure environments for panels of AA2024-T351 coated with MgRP (initial MgPVC = 45%). Dotted line indicates initial integrated Mg peak intensity of an unexposed panel. XRD Detection limit is estimated to be 3 – 5% of samples by volume.<sup>3</sup>



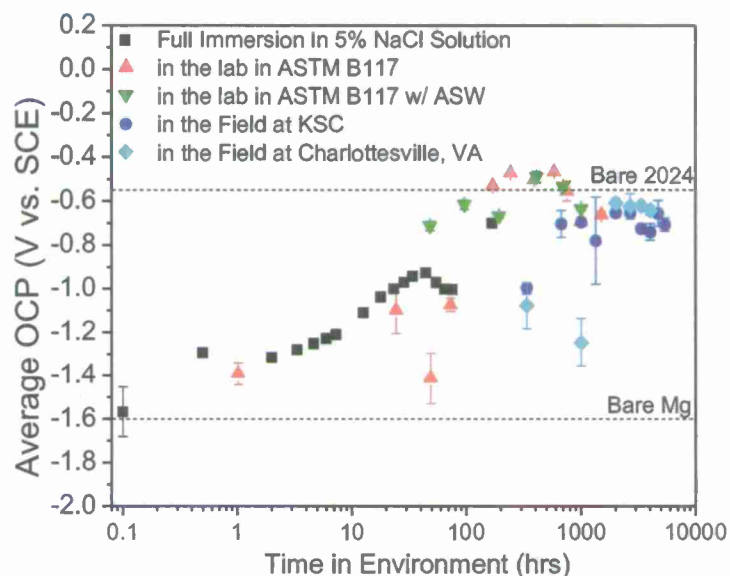


Figure 138. Galvanic protection potential of AA2024-T351 coated with MgRP (initial MgPVC = 45%) in ambiently aerated 5% NaCl solution vs. environmental exposure time in various lab and field exposure environments.

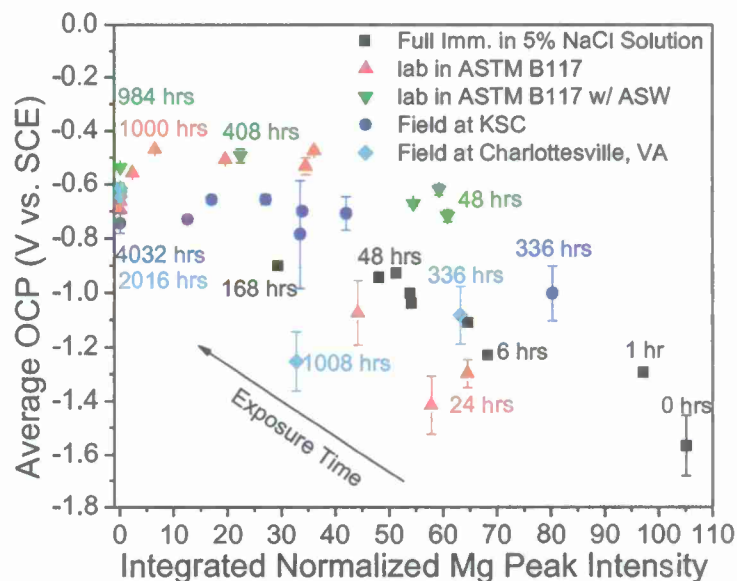


Figure 139. Correlation between integrated Mg peak ( $\text{Mg } \langle 200 \rangle$   $2\theta = 36.6170^\circ$ ) intensity vs. galvanic protection potential of AA2024-T351 coated with MgRP (initial MgPVC = 45%) in ambiently aerated 5% NaCl solution after exposure in various environments.

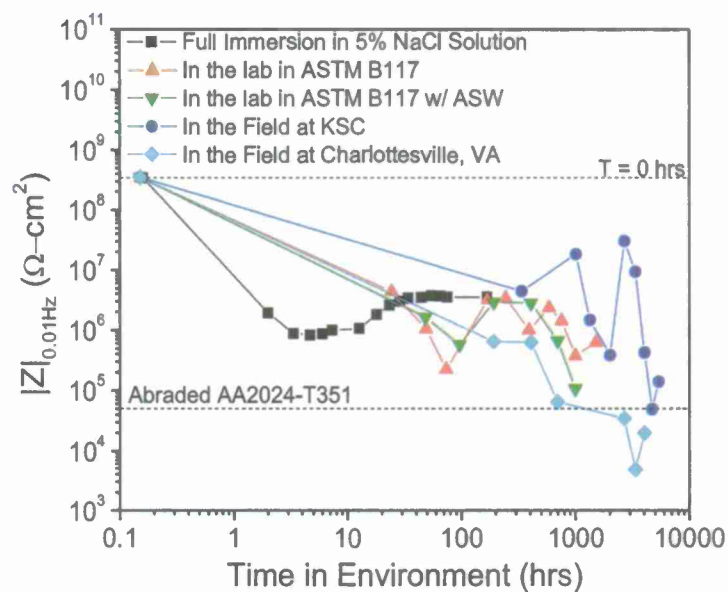


Figure 140. Magnitude of electrochemical impedance at 0.01 Hz in ambiently aerated 5% NaCl solution vs. environmental exposure time in various exposure environments for panels of AA2024-T351 coated with MgRP (initial MgPVC = 45%).

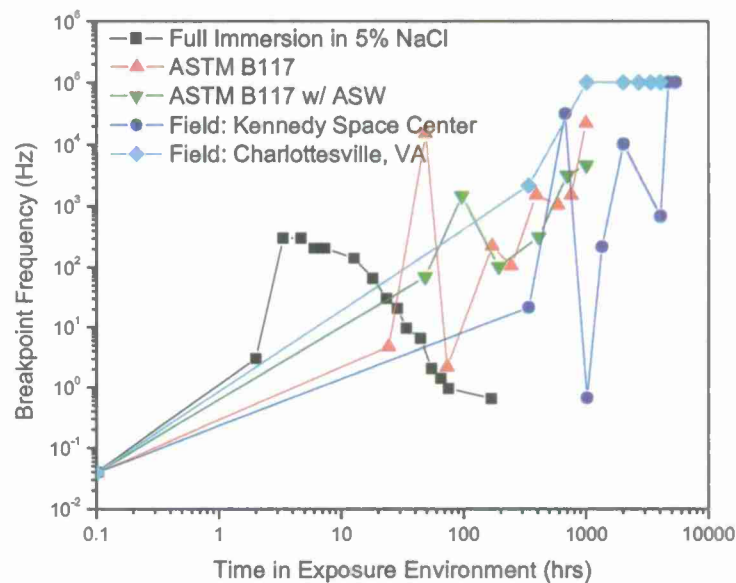


Figure 141. Breakpoint frequency in ambiently aerated 5% NaCl solution vs. environmental exposure time in various exposure environments for panels of AA2024-T351 coated with MgRP (initial MgPVC = 45%).

## 1.8.6 Discussion

### 1.8.6.1 Throwing Power

One purpose of this study was to try and determine the "throwing power" of the MgRP primer coating on AA2024-T351 in various lab and field environments. The "throwing power" pertains to the distance over which the MgRP coating system can protect bare AA2024-T351 by sacrificial anode based cathodic protection. Predicting the throwing power is quite complicated because the scribe size, coating formulation, electrolyte composition, electrolyte geometry, and bare/coated area ratios can all be limiting factors when considering protection ability or throwing power of a coating that protects by sacrificial anode based galvanic protection. A large source of variation between performance of the coating in the salt fog and field exposure environments, with regards to throwing power, is the electrolyte geometry in each environment. A sacrificial coating can only protect defects (or bare substrate at scratches) which it is both electrically and ionically connected to. In an artificial environment like ASTM B-117 salt fog, in a rainstorm with large drops, or during a dewing event, the whole panel might be wet with a continuous electrolyte layer and the "throwing power/ability" of the MgRP that is measured or observed will be limited electrochemically based in the secondary or tertiary current distribution based on mixed potential theory (showed schematically in Figure 142 and Figure 143). In these cases the throwing power will spread across the scratch. However if the environment is such that the electrolyte layer is tortuous and individual droplets start to form, a limitation in throwing power brought about by a tortuous electrolyte (ionic path), will be observed (showed schematically in Figure 144). If a droplet is not in contact with the MgRP and instead exists only above bare AA2024-T351 substrate, there can be no sacrificial protection due to a remote coating within the area covered by that droplet. Under these conditions of a tortuous electrolyte path an environmental limitation rather than an electrochemical limitation is placed on the throwing power of the coating system. For these reasons it is understandable why the throwing power is observed with EDS in the field at Kennedy Space Center (Figure 101) to be approximately 200 – 300  $\mu\text{m}$  and in the salt fog environment (Figure 122 and Figure 132) to cover the full half-width of the scribe ( $\geq 350 \mu\text{m}$ ). It should be noted that during a given episodic drying or wetting event, throwing power may be temporarily increased or diminished.

Additional factors which complicate the determination of a throwing power result from the chemical dissolution of chemical species used as markers indicative of zones of cathodic protection as well as difficulties in distinguishing between definitive regions of protection and of substrate corrosion in defect areas. Chemical dissolution of the precipitates that are common to zones of cathodic protection is likely in acidic, high TOW environments like that of Birdwood Golf Course in Charlottesville, VA which is subject to regular acidic precipitation (Table 7). EDS spot scans obtained throughout the width of the scribe after 24 weeks of exposure at Birdwood Golf Course in Charlottesville, VA, (Figure 112) showed very little indication of Mg or Ca deposits common to regions of cathodic protection, making evidence and observation for throwing power in this environment difficult. Moreover, it is likely that the throwing power of the MgRP could be detected in EDS spot scans obtained throughout the width of the scribe after exposure at Kennedy Space Center, FL (Figure 101) due to the more alkaline exposure conditions. Not only is the rain precipitation at Kennedy Space Center, FL slightly alkaline as compared to Charlottesville, VA (Table 7) but the proximity of the test racks to the ocean make the samples susceptible to spray from the ocean surf which has a pH of roughly 8.2.<sup>59</sup> This alkaline pH suppresses the chemical dissolution of species used to identify zones of cathodic protection. Additionally, in most exposure environments and moderate pH ranges, aluminum is

well known to form a barrier oxide film that reforms quickly when damaged, leaving the primary form of attack observed after exposure in most service environments to be non-uniform pitting corrosion.<sup>79</sup> For this reason, in all environments studied in this report, definitive zones of significant Al corrosion in the scribes could not be identified due to low pit densities.

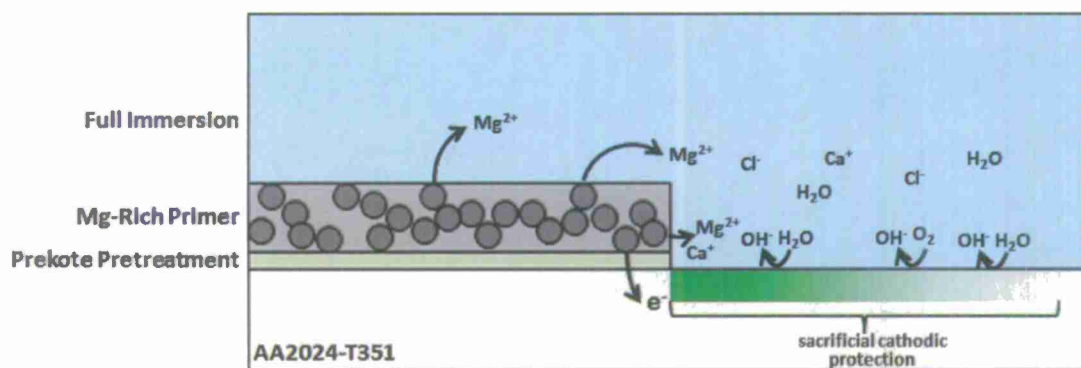


Figure 142. Schematic of AA2024-T351 coated with MgRP depicting MgRP sacrificial cathodic protection function under full immersion.

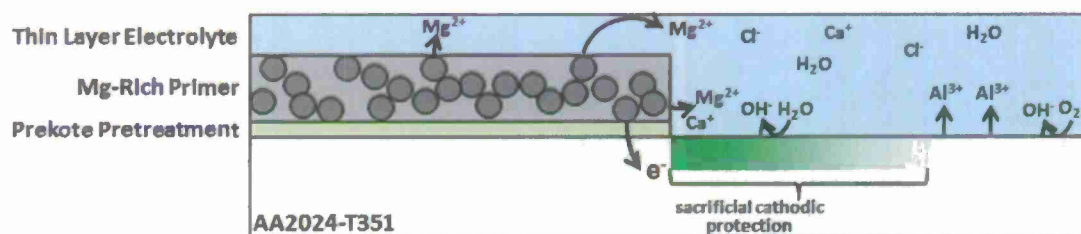


Figure 143. Schematic of AA2024-T351 coated with MgRP depicting MgRP sacrificial cathodic protection function under thin-layer electrolyte conditions found in high TOW exposure environments such as ASTM B-117 or during specific situations in the field such as during heavy precipitation, immersion or dewing.

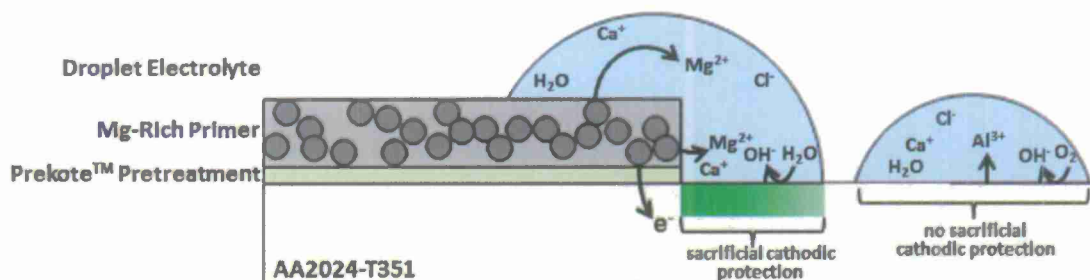


Figure 144. Schematic of AA2024-T351 coated with MgRP depicting MgRP sacrificial cathodic protection function under droplet electrolyte geometry conditions likely found in the lab in RH cabinet exposures and in the field during light precipitation or deliquescence of deposited salts due to moderate RH.



### 1.8.6.2 Residual Protection After Mg Pigment Depletion

Variations in MgRP polymer degradation were also observed between laboratory salt fog and field exposure environments. In the field, the polymer exhibited severe damage and dissolution as evidenced by EDS (Figure 101 and Figure 112) and SEM cross-section (Figure 102 and Figure 113). In the lab, a significant amount of the MgRP polymer was observed to remain after prolonged exposures in ASTM B-117 with 5% NaCl (Figure 122 and Figure 123) and with ASTM artificial sea water (Figure 132 and Figure 133). This variation in performance in the field is presumed to be due to UV degradation. The mean hourly solar radiation at Kennedy Space Center, FL over the dates of exposure is shown in Figure 145 and is known to be a severe site of UV exposure.<sup>60</sup> UV radiation is known to severely degrade epoxy organic polymers that are used in the Mg-rich primer.<sup>18, 20, 21, 40</sup> The degradation process is very common and is referred to "chalking" due to the continuous breakdown of the polymeric backbone and subsequent formation of a chalky mixture of polymer and pigment fragments on the coating's surface. The chalky mixture is then easily removed by wind and precipitation. This chalking behavior was observed on MgRP-coated AA2024-T351 panels exposed in the field at Kennedy Space Center, FL (Figure 96 and Figure 97) and at Birdwood Golf Course in Charlottesville, VA (Figure 107 and Figure 108) but not in laboratory ASTM B-117 exposures where UV exposure is extremely low. Polyurethane organic polymers undergo far less degradation as a result of UV exposure. For this reason Polyurethane polymers with UV absorbing pigments, like the one used in the Aerodur 5000 Topcoat, are primarily used as topcoat polymers.<sup>18, 21</sup> It is recognized that primer only systems may not be deployed in service. However, this is an initial step necessary to understand performance in this system.

It is apparent that modest corrosion protection is still afforded to the AA2024-T351 substrate by the MgRP polymer after the Mg pigment is largely depleted (to less than 5% by volume as evidenced by XRD in Figure 137), particularly after exposure in low UV environments where significant chalking is avoided. Evidence of residual barrier protection afforded to the AA2024-T351 substrate by the MgRP primer polymer after 1000 hours of exposure in ASTM B-117 with 5% NaCl and in ASTM B-117 with ASTM artificial sea water is provided by elevated low-frequency Bode electrochemical impedance (at 0.01 Hz) shown in Figure 140 as compared to that of bare abraded AA2024-T351. Moreover, interface corrosion under the MgRP is not seen in SEM cross-section (Figure 102, Figure 103, Figure 113, Figure 114, Figure 123, Figure 124, Figure 133, and Figure 134). Additionally, any unoxidized Mg pigment that remains in the MgRP after the MgRP has been largely depleted of Mg pigment and has lost most of its remote protection capability (as evidenced by XRD in Figure 137 and an increase in global galvanic protection potential shown in Figure 138) is likely available for the protection of future localized defects

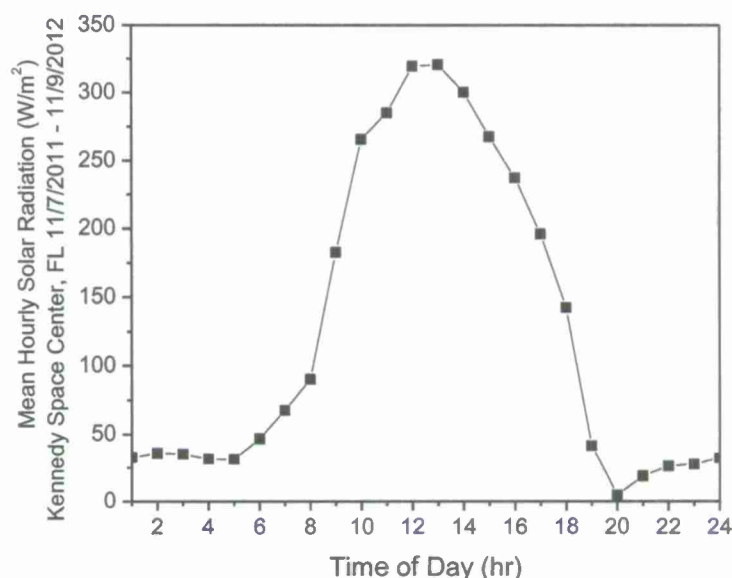


Figure 145. Mean hourly solar radiation at Kennedy Space Center, FL over the dates 11/7/2012 – 11/9/2012.

#### 1.8.6.3 Anodic Undermining and Cathodic Corrosion

It is important for the MgRP coating system to provide adequate cathodic protection to the AA2024-T351 substrate but to also avoid the detrimental effects of cathodic corrosion of the amphoteric AA2024-T351 substrate and of anodic undermining (or scribe creep) of the coating polymer at coating defect sites. In the case of early generation MgRP-coated AA2024-T351 studied in the past, cathodic corrosion of the AA2024-T351 substrate was caused by increased localized pH due to severe cathodic polarization and/or excessive Mg pigment dissolution.<sup>1, 2, 45-</sup>

<sup>51</sup> Anodic undermining of early generation MgRP-coated AA2024-T351 studied in the past was observed and proposed to be caused by a classical mechanism, often associated with organic polymer coatings, involving anodic disbondment of the organic polymer<sup>80, 81</sup>. The primary mechanism for this phenomenon on aluminum alloys, particularly those containing Cu such as AA2024, has been proposed for years to be anodic coating disbondment through anodic undermining aided in this case by H<sub>2</sub> production.

A summary of observations made after environmental exposure of MgRP-coated AA2024-T351 in various environments is shown in Table 12. In this study of a more recent formulation of a commercial MgRP product (AkzoNobel Aerodur 2100 Product #: 2100P003 Lot #: 493-190 MFG: 03/2009) no indications of cathodic corrosion or anodic undermining were observed at the coating/metal interface when viewed in SEM cross-section after environmental exposure in these field and laboratory environments (Figure 102, Figure 103, Figure 113, Figure 114, Figure 123, Figure 124, Figure 133, and Figure 134). This is a major improvement over early generations of the commercial Mg-rich primer coating product which frequently exhibited unique macroscopic failure modes (i.e. blisters, scribe creep, etc) in the ASTM B-117 environment.<sup>1, 4, 39, 40, 44</sup> The mediation of the cathodic protection abilities is important in the application of MgRP. Improvements in the MgRP's performance is presumed to be due to improvements in the organic epoxy comprising the polymer matrix of the primer by improving adhesion or adding

increased ohmic resistance between Mg pigment particles. Electrochemical measurements did not show significant differences in electrochemical properties of the coating from past formulations. It is unknown what specific improvements were made.

Table 12. Summary of observations made after environmental exposure in various environments.

Environment	UV?	Macroscopic Blistering	Underpaint Corrosion	Cathodic Corrosion	Throwing Power
Kennedy Space Center, FL	YES	NO	NO	NO	200 - 300 $\mu\text{m}$
Charlottesville, VA	YES	NO	NO	NO	n/a
ASTM B-117 w/ 5% NaCl	NO	NO	NO	NO	$\geq 350 \mu\text{m}$
ASTM B-117 w/ ASW	NO	NO	NO	NO	$\geq 350 \mu\text{m}$
Full Immersion in ambiently aerated 5% NaCl	NO	NO	NO	NO	No scribe*

\*a non-scribed area of MgRP-coated AA2024-T351 was exposed in a flat cell to 5% NaCl to study the representative global degradation of the coating. Follow up experiments include the same exposure and include variations in the area of bare AA2024-T351.

#### 1.8.6.4 Future Work

A forthcoming report will summarize findings made during identical exposures of a topcoated variation of MgRP-coated AA2024-T351. In light of the findings in this report, additional modifications to the ASTM environment will be studied including an acidified electrolyte and the inclusion of UV light in the test chamber. Future studies will also include diagnostic full immersion and droplet experiments aimed at studying the effects of environmental factors pertinent to environmental severity such as electrolyte chemistry, atmospheric chemistry, and UV exposure.

#### 1.8.7 Economic Summary

This project has further illuminated and verified test methods to assess MgRP that could be used in the laboratory and in the field and could be applied to the characterization and performance on other substrates. Since the test methods should be transferable and applicable to other materials, substrates, pretreatments, etc. the cost of unique test development for each and every case where a MgRP must be tested and might be deployed can be avoided. Assuming the cost of several scientist person years, this should save several hundred thousand dollars. Trial and error, guess-based development of field deployable test methods that may or may not work satisfactorily has also been avoided. This should save an additional several hundred thousand dollars in test development costs for a field deployable MgRP assessment tool.

This work further validates MgRP as an emerging, promising technology to replace chromated corrosion inhibiting technology. The savings to components during the use of MgRP and MgRP/Topcoat systems is a little more difficult to assess. The maturation of an effective non-

chromated corrosion inhibiting technology stands to save financial resources dedicated to carcinogenic materials handling alone. If one single asset avoids an unscheduled repainting or repair due to proper coating degradation assessment or proper utilization of the MgRP, then several million dollars in savings is possible in each instance.

#### 1.8.8 Implementation

This project does serve to provide some information on the degradation process of the MgRP coating in various, relevant, field and lab environments and further shows that newer generation MgRP formulations tend to degrade predictably and reliably in the environments investigated in this study when used to protect Prekote pretreated AA2024-T351. Should MgRP be employed on other substrates, pretreatments or in a significantly different environment, variations in degradation (still yet unknown) may occur.

However, this project demonstrates a suite of field deployable electrochemical and characterization techniques can be used to track coating degradation with respect to Mg pigment depletion rate, global galvanic protection potential and coating barrier properties throughout exposure periods in both field and laboratory environments. Should the decision be made to deploy a MgRP coating system on a DoD asset based on other information such as more extensive field exposures, a field deployable XRD method for remaining Mg pigment assessment and field deployable electrochemical assessment tools should be deployed and would be ready to pursue in a follow-on program with the goal of deployment of a portable unit. Commercial available XRD units are available mainly for residual stress measurement. Professor Brewer at Naval Post Graduate School has been approached about making a trial field measurement of residual Mg in a MgRP. The DoD should consider the pursuit of a field deployable device made available to repair depo facilities. The resources were not provided within this project to pursue such goals. One way to accomplish this goal would be through issuance of an SBIR program to build, or otherwise acquire and demonstrate a field deployable instrument. After this is done, we recommend conducting remaining lifetime assessments of MgRP exposed in the field, corroborate the residual MgRP assayed by other means and develop calibration standards that can be used to accompany field measurements. Calibration standards would be necessary for quantitative measurements.

#### 1.8.9 Conclusion

- Magnesium rich primer (Akzo Nobel Aerodur 2100 Product #: 2100P003 Lot #: 493-190 MFG: 03/2009), in a non-topcoated, scribed condition, was utilized for the corrosion protection of a 2024-T351 substrate pretreated with PreKote™ surface pretreatment.
- Exposures were conducted in the field at Kennedy Space Center, FL (coastal marine), at Birdwood Golf Course in Charlottesville, VA (rural), in ASTM B-117 with 5% NaCl and modified with ASTM Sea Water as well as in full immersion in ambiently aerated 5% NaCl solution. Ambient concentrations of atmospheric gases such as CO<sub>2</sub> are assumed in the field and lab exposures. A summary of observations made after environmental exposure in various environments is shown in Table 12. No blistering or similar macroscopic coating failure phenomena were observed at low magnification in the MgRP or along the scribe lines after exposure in any of the studied environments.
- A suite of field deployable electrochemical and X-ray diffraction techniques was used to track coating degradation with respect to Mg pigment depletion rate, galvanic protection



potential and coating barrier properties throughout environmental exposure and was successfully demonstrated. It was found that:

- full immersion in ambiently aerated 5% NaCl solution, ASTM B-117 in 5% NaCl and ASTM B-117 in ASTM artificial sea water deplete the MgRP of metallic Mg pigment at approximately equal rates, with significant depletion of Mg pigment occurring after approximately 1000 hrs of exposure. Field exposures in Charlottesville, VA and Kennedy Space Center, FL resulted in significant depletion of metallic Mg pigment after 2000 and 4000 hrs of exposure respectively indicating acceleration factors of approximately 2 and 4.
  - As a result of pigment depletion, the global galvanic protection potential of the coating system, with respect to remote scratches, increases with exposure time in each environment, from values approximately equal to that of bare Mg (-1.6 V vs. SCE) to those approximately equal to that of bare AA2024-T351 (-0.55 V vs. SCE). It was found that this increase took approximately 300 hours in full immersion in ambiently aerated 5% NaCl solution, ASTM B-117 in 5% NaCl and in ASTM B-117 with ASTM artificial sea water. Field exposures in Charlottesville, VA and Kennedy Space Center, FL both resulted in an increases in global galvanic protection potential to approximately equal to that of bare AA2024-T351 (-0.6 V vs. SCE) after approximately 1000 hours of exposure. The acceleration factors, with respect to global galvanic protection potential, observed for field exposure versus the full immersion and salt fog cabinet exposures were approximately 3:1.
  - Barrier properties of the MgRP coating system also degrade with time in each environment. However, corrosion under residual coating polymer was not observed.
- Post-mortem characterization with SEM/EDS was conducted to elucidate coating and scribe morphology, corrosion products present and in an attempt to interrogate the throwing power of the coating system.
    - Post-mortem SEM/EDS characterization after 1000 hrs of salt fog exposure indicate a throwing power that extended the entire half-width of the scribe in both standard and modified ASTM B-117 exposures with thin-layer electrolyte geometries and continuous wetting. A significant thickness of primer polymer was shown to remain after 1000 hours in both environments.
    - Post-mortem SEM/EDS characterization after 24 weeks of exposure in the field at Kennedy Space Center, FL indicates a throwing power that extends approximately 200 - 300  $\mu\text{m}$  in the scribe from the coating edge. A significant thickness of primer polymer was shown to be damaged after 24 weeks of exposure at Kennedy Space Center, FL.
    - Post-mortem SEM/EDS characterization after 24 weeks of exposure in the field at Charlottesville, VA was inconclusive due to the likely dissolution of the MgRP coating and subsequent corrosion products by high TOW and low pH rain ( $\text{pH} \approx 5$ , Table 7). A significant thickness of primer polymer was shown to be damaged after 24 weeks of exposure at Birdwood Golf Course in Charlottesville, VA.
    - It is likely that there still exists a small amount (less than 5% PVC) of encapsulated metallic Mg pigment dispersed through any residual polymer coating that remains after environmental exposure. This is particularly likely in samples that are not exposed to environments without significant UV, such as in

ASTM B-117 salt spray testing, where it was observed that the polymer does not degrade as readily.

- no indications of cathodic corrosion, as evidenced by narrow pinholes, or underpaint corrosion or anodic undermining, as evidenced by large areas of coating delamination above regions of Al corrosion, were visible at the coating/metal interface when viewed in SEM cross-section after environmental exposure in these field and laboratory environments.
- The differences in rate-of-change of Mg depletion from the coating are presumed to stem from differences in time-of-wetness and in rates of polymer degradation, specifically resistivity, due to UV exposure. Differences in throwing power in lab and field environments are presumed to stem from differences in electrolyte geometries; continuous thin-layer in salt fog cabinet exposures and droplet geometries in field exposures. Future studies examine the performance of a MgRP in a topcoated, scribed condition.

#### **1.8.9.1 Acknowledgements**

This work was supported by the Office of the Undersecretary of Defense Corrosion University Pilot Program under the direction of Mr. Daniel Dunmire. Members of NAVAIR<sup>1</sup> and Battelle Memorial Institute<sup>2</sup> are acknowledged for graciously conducting field exposures at Kennedy Space Center, FL and for the generous supply and preparation of MgRP-coated AA2024-T351 panels specifically: Dr. Craig Matzdorf<sup>1</sup>, Mr. Frank Pepe<sup>1</sup>, Mr. Jerry Curran<sup>1</sup> and Mr. William Abbott<sup>2</sup>.

#### **1.8.10 Bibliography**

1. A. D. King and J. R. Scully, Blistering Phenomena in Early Generation Mg-Rich Primer Coatings on AA2024-T351 and the Effects of CO<sub>2</sub>, NACE DoD 2011 Conference Proceedings, (Palm Springs, CA, 2011).
2. A. D. King and J. R. Scully, Sacrificial Anode-Based Galvanic and Barrier Corrosion Protection of 2024-T351 by a Mg-Rich Primer and Development of Test Methods for Remaining Life Assessment, Corrosion, 67 (2011).
3. V. K. Pecharsky and P. Y. Zavalij, Fundamentals of powder diffraction and structural characterization of materials, 2nd, (New York: Springer, 2009), p. xxiii, 741 p.
4. S. S. Pathak, M. D. Blanton, S. K. Mendon and J. W. Rawlins, Investigation on dual corrosion performance of magnesium-rich primer for aluminum alloys under salt spray test (ASTM B117) and natural exposure, Corros Sci, 52 (2010), 1453-1463.
5. G. P. Bierwagen, D. E. Tallman, M. Nanna, D. Battocchi, A. Stamness and V. J. Gelling, New developments in Cr-free primers for aerospace alloys., Abstr Pap Am Chem S, 228 (2004), U360-U360.
6. A. Simoes, D. Battocchi, D. Tallman and G. Bierwagen, Assessment of the corrosion protection of aluminium substrates by a Mg-rich primer: EIS, SVET and SECM study, Prog Org Coat, 63 (2008), 260-266.
7. D. Battocchi, A. M. Simoes, D. E. Tallman and G. P. Bierwagen, Comparison of testing solutions on the protection of Al-alloys using a Mg-rich primer, Corros Sci, 48 (2006), 2226-2240.

8. D. Battocchi, A. M. Simoes, D. E. Tallman and G. P. Bierwagen, Electrochemical behaviour of a Mg-rich primer in the protection of Al alloys, *Corros Sci*, 48 (2006), 1292-1306.
9. H. Xu, D. Battocchi, D. E. Tallman and G. P. Bierwagen, Use of Magnesium Alloys as Pigments in Magnesium-Rich Primers for Protecting Aluminum Alloys, *Corrosion*, 65 (2009), 318-325.
10. G. Bierwagen, D. Battocchi, A. Simoes, A. Stanness and D. Tallman, The use of multiple electrochemical techniques to characterize Mg-rich primers for Al alloys, *Prog Org Coat*, 59 (2007), 172-178.
11. B. Maier and G. S. Frankel, Behavior of Magnesium-Rich Primers on AA2024-T3, *Corrosion*, 67 (2011), 055001.
12. J. Nie, M. C. Yan, J. Wang, D. E. Tallman, D. Battocchi and G. P. Bierwagen, Cathodic Corrosion Protection Performance of Mg-Rich Primers: Effect of Pigment Shape and Pigment Volume Concentration, *ECS Transactions*, 24 (2010), 261-275.
13. Report on Carcinogens, 11th Edition, U.S. Department of Health and Human Services, Public Health Services, National Toxicology Program,
14. R. G. Buchheit, Chromate and Chromate-Free Conversion Coatings, vol. 13A, *ASM Handbook Volume 13A, Corrosion: Fundamentals, Testing, and Protection* (ASM International), (Materials Park, Ohio, ASM International, 2003,
15. I. M. Zin, R. L. Howard, S. J. Badger, J. D. Scantlebury and S. B. Lyon, The mode of action of chromate inhibitor in epoxy primer on galvanized steel, *Prog Org Coat*, 33 (1998), 203-210.
16. J. Sinko, Challenges of chromate inhibitor pigments replacement in organic coatings, *Prog Org Coat*, 42 (2001), 267-282.
17. B. S. Skerry, G. E. Thompson, G. C. Wood, V. Ashworth, J. B. Johnson, J. D. Scantlebury and V. C. R. Mc Loughlin, Inhibition of Corrosion of Aluminum and its Alloys in the Presence of Paint Films Containing Inhibitive Pigments, *Proceedings of the 6th European Symposium on Corrosion Inhibitors*, p. 521, (Ferrara, Italy, 1985).
18. P. J. Adams, Personal correspondence with Dr. Pat J. Adams of AkzoNobel Aerospace Coatings Inc., (2011).
19. W. Funke, Mechanisms of Protecting Metals by Organic Coatings against Corrosion, *J Electrochem Soc*, 133 (1986), C304-C304.
20. Z. W. Wicks, *Organic coatings : science and technology*, 3rd, (Hoboken, N.J.: Wiley-Interscience, 2007), p. xxiii, 722 p.
21. A. Forsgren, Corrosion control through organic coatings, *Corrosion technology*, (Boca Raton, FL: CRC/Taylor & Francis, 2006), p. 161 p.
22. S. Feliu, R. Barajas, J. M. Bastidas and M. Morcillo, Ac Impedance Study About the Protection Mechanisms of Zinc-Rich Primers, *Abstr Pap Am Chem S*, 195 (1988), 58-Pmse.
23. D. Pereira, J. D. Scantlebury, M. G. S. Ferreira and M. E. Almeida, The Application of Electrochemical Measurements to the Study and Behavior of Zinc-Rich Coatings, *Corros Sci*, 30 (1990), 1135-1147.
24. S. Feliu, M. Morcillo and S. Feliu, Deterioration of cathodic protection action of zinc-rich paint coatings in atmospheric exposure, *Corrosion*, 57 (2001), 591-597.
25. V. M. Rudoï, O. V. Yaroslavl'tseva, T. N. Ostanina, L. P. Yurkina and O. Y. Subbotina, Electrochemical behavior of protective anodic primers, *Protection of Metals*, 35 (1999), 277-281.
26. H. Marchebois, C. Savall, J. Bernard and S. Touzain, Electrochemical behavior of zinc-rich powder coatings in artificial sea water, *Electrochim Acta*, 49 (2004), 2945-2954.

27. C. M. Abreu, M. Izquierdo, M. Keddam, X. R. Novoa and H. Takenouti, Electrochemical behaviour of zinc-rich epoxy paints in 3% NaCl solution, *Electrochim Acta*, 41 (1996), 2405-2415.
28. S. G. Real, A. C. Elias, J. R. Vilche, C. A. Gervasi and A. Disarli, An Electrochemical Impedance Spectroscopy Study of Zinc Rich Paints on Steels in Artificial Sea-Water by a Transmission-Line Model, *Electrochim Acta*, 38 (1993), 2029-2035.
29. C. M. Abreu, M. Izquierdo, X. R. Novoa, C. Perez and A. Sanchez, Influence of different aggressive media on the protective behaviour of zinc rich paints, *Rev Metal Madrid*, 35 (1999), 182-189.
30. N. V. Kondrashova, S. A. Nesterenko, O. V. Naumenko and L. I. Antropov, Influence of Zinc and Magnesium Cations on the Electrochemical-Behavior of Steel with a Polymer Primer, *Protection of Metals*, 25 (1989), 73-75.
31. S. Feliu, R. Barajas, J. M. Bastidas and M. Morcillo, Mechanism of Cathodic Protection of Zinc-Rich Paints by Electrochemical Impedance Spectroscopy .1. Galvanic Stage, *J Coating Technol*, 61 (1989), 63-69.
32. S. Feliu, R. Barajas, J. M. Bastidas and M. Morcillo, Mechanism of Cathodic Protection of Zinc-Rich Paints by Electrochemical Impedance Spectroscopy .2. Barrier Stage, *J Coating Technol*, 61 (1989), 71-76.
33. C. M. Abreu, M. Izquierdo, P. Merino, X. R. Novoa and C. Perez, A new approach to the determination of the cathodic protection period in zinc-rich paints, *Corrosion*, 55 (1999), 1173-1181.
34. M. Morcillo, R. Barajas, S. Feliu and J. M. Bastidas, A-Sem Study on the Galvanic Protection of Zinc-Rich Paints, *J Mater Sci*, 25 (1990), 2441-2446.
35. R. A. Armas, C. A. Gervasi, A. Disarli, S. G. Real and J. R. Vilche, Zinc-Rich Paints on Steels in Artificial Seawater by Electrochemical Impedance Spectroscopy, *Corrosion*, 48 (1992), 379-383.
36. H. Marchebois, M. Keddam, C. Savall, J. Bernard and S. Touzain, Zinc-rich powder coatings characterisation in artificial sea water - EIS analysis of the galvanic action, *Electrochim Acta*, 49 (2004), 1719-1729.
37. O. O. Knudsen, U. Steinsmo and M. Bjordal, Zinc-rich primers - Test performance and electrochemical properties, *Prog Org Coat*, 54 (2005), 224-229.
38. M. E. Nanna and G. P. Bierwagen, Mg-rich coatings: A new paradigm for Cr-free corrosion protection of al aerospace alloys, *Jct Research*, 1 (2004), 69-80.
39. W. H. Abbott, personal correspondence with Dr. William Abbott of Battelle Memorial Institute, (2009).
40. C. Matzdorf, personal correspondence with Dr. Craig Matzdorf of NAVAIR, (2009).
41. G. Bierwagen, R. Fishman, T. Storsved and J. Johnson, Recent studies of particle packing in organic coatings, *Prog Org Coat*, 35 (1999), 1-9.
42. G. P. Bierwagen, A Reexamination of Cpvc as a Transition Point in Coatings Properties, *Abstr Pap Am Chem S*, 200 (1990), 41-Pmse.
43. G. P. Bierwagen, Critical Pigment Volume Concentration (Cpvc) as a Transition Point in the Properties of Coatings, *J Coating Technol*, 64 (1992), 71-75.
44. S. S. Pathak, M. D. Blanton, S. K. Mendon and J. W. Rawlins, Carbonation of Mg powder to enhance the corrosion resistance of Mg-rich primers, *Corros Sci*, 52 (2010), 3782-3792.
45. M. Mokaddem, P. Volovitch, F. Rechou, R. Oltra and K. Ogle, The anodic and cathodic dissolution of Al and Al-Cu-Mg alloy, *Electrochim Acta*, 55 (2010), 3779-3786.
46. S. M. Moon and S. I. Pyun, The corrosion of pure aluminium during cathodic polarization in aqueous solutions, *Corros Sci*, 39 (1997), 399-408.



47. S. I. Pyun and S. M. Moon, Corrosion mechanism of pure aluminium in aqueous alkaline solution, *J Solid State Electr*, 4 (2000), 267-272.
48. H. Kaesche, Studies on the Corrosion of Aluminum, *Zeitschrift für physikalische Chemie*, 14 (1963), 557-566.
49. H. Kaesche, *Zeitschrift für physikalische Chemie*, 34 (1962), 87-108.
50. R. D. Armstrong and V. J. Braham, The mechanism of aluminium corrosion in alkaline solutions, *Corros Sci*, 38 (1996), 1463-1471.
51. M. Pourbaix, Atlas of electrochemical equilibria in aqueous solutions, 2d English, (Houston, Tex.: National Association of Corrosion Engineers, 1974), p. 644 p.
52. D. Knotkova and K. Barton, Effects of Acid Deposition on Corrosion of Metals, *Atmos Environ a-Gen*, 26 (1992), 3169-3177.
53. W. W. Kirk, H. H. Lawson and American Society for Testing and Materials., Atmospheric corrosion, Stp, (Philadelphia, PA: ASTM, 1995), p. vii, 280 p.
54. S. Feliu, M. Morcillo and S. Feliu, The Prediction of Atmospheric Corrosion from Meteorological and Pollution Parameters .1. Annual Corrosion, *Corros Sci*, 34 (1993), 403-414.
55. S. Feliu, M. Morcillo and S. Feliu, The Prediction of Atmospheric Corrosion from Meteorological and Pollution Parameters .2. Long-Term Forecasts, *Corros Sci*, 34 (1993), 415-422.
56. K. N. Allahar, D. Wang, D. Battocchi, G. P. Bierwagen and S. Balbyshev, Real-Time Monitoring of a United States Air Force Topcoat/Mg-Rich Primer System in ASTM B117 Exposure by Embedded Electrodes, *Corrosion*, 66 (2010), -.
57. ASTM, Standard Practice for Operating Salt Spray (Fog) Apparatus, ASTM B117 - 09. ASTM International, West Conshohocken, PA, 2009
58. J. Li, J. He, B. J. Chisholm, M. Stafslie, D. Battocchi and G. P. Bierwagen, An investigation of the effects of polymer binder compositional variables on the corrosion control of aluminum alloys using magnesium-rich primers, *J Coat Technol Res*, 7 (2010), 757-764.
59. ASTM, Standard Practice for the Preparation of Substitute Ocean Water, ASTM D1141 - 98. ASTM International, West Conshohocken, PA, 1998
60. J. D. Morrison, Report on Relative Corrosivity of Atmospheres at Various Distances from the Seacoast, 1980.
61. ASTM, Standard Practice for Conducting Atmospheric Corrosion Tests on Metals, ASTM G50 - 76. ASTM International, West Conshohocken, PA, 2003
62. ASTM, Standard Guide for Conducting Corrosion Tests in Field Applications, ASTM G4 - 01. ASTM International, West Conshohocken, PA, 2001
63. H. P. Hack and J. R. Scully, Defect Area Determination of Organic Coated Steels in Seawater Using the Breakpoint Frequency Method, *J Electrochem Soc*, 138 (1991), 33-40.
64. F. Mansfeld, Determination of the Reactive Area of Organic Coated Metals - Physical Meaning and Limits of the Break-Point Method - Discussion, *Electrochim Acta*, 39 (1994), 1451-1452.
65. A. Amirudin and D. Thierry, Application of electrochemical impedance spectroscopy to study the degradation of polymer-coated metals, *Prog Org Coat*, 26 (1995), 1-28.
66. J. E. B. Randles, Kinetics of rapid electrode reactions, *Discussions of the Faraday Society*, 1 (1947), 11-19.
67. B. D. Cullity, Elements of x-ray diffraction, Addison-Wesley series in metallurgy and materials, 2d, (Reading, Mass.: Addison-Wesley Pub. Co., 1978), p. xii, 555 p.
68. J. H. Hubbell and S. M. Seltzer, Tables of X-Ray Mass Attenuation Coefficients and Mass Energy-Absorption Coefficients from 1 keV to 20 MeV for Elements Z = 1 to 92

- and 48 Additional Substances of Dosimetric Interest, NIST Standard Reference Database 126. NIST Chemistry WebBook, 2004
69. R. Castaing, Electron Probe Microanalysis, L. Marton and M. Claire, Eds., vol. Volume 13, Advances in Electronics and Electron Physics, Academic Press, 1960, p. 317-386).
  70. N. W. M. Ritchie, DTSA-II Desktop Spectrum Analyzer Quantitative X-ray Microanalysis Software. National Institute of Standards and Technology, 2012
  71. C. Deslouis, A. Doncescu, D. Festy, O. Gil, V. Maillot, S. Touzain and B. Tribollet, Kinetics and characterisation of calcareous deposits under cathodic protection in natural sea water, Electrochemical Methods in Corrosion Research Vi, Pts 1 and 2, 289-2 (1998), 1163-1180.
  72. C. Deslouis, D. Festy, O. Gil, G. Rius, S. Touzain and B. Tribollet, Characterization of calcareous deposits in artificial sea water by impedance techniques - I. Deposit of  $\text{CaCO}_3$  without  $\text{Mg(OH)}_2$ , Electrochim Acta, 43 (1998), 1891-1901.
  73. R. A. Humble, Cathodic protection of steel in seawater with magnesium anodes, Corrosion, 4 (1948), 358-370.
  74. R. U. Lee and J. R. Ambrose, Influence of Cathodic Protection Parameters on Calcareous Deposit Formation, Corrosion, 44 (1988), 887-891.
  75. F. G. Liu, S. R. Wu and C. S. Lu, Characterisation of calcareous deposits on freely corroding low carbon steel in artificial sea water, Corros Eng Sci Techn, 46 (2011), 611-617.
  76. C. Rousseau, F. Baraud, L. Leleyter, M. Jeannin and O. Gil, Calcareous deposit formed under cathodic protection in the presence of natural marine sediments: A 12 month experiment, Corros Sci, 52 (2010), 2206-2218.
  77. C. Barchiche, C. Deslouis, D. Festy, O. Gil, P. Refait, S. Touzain and B. Tribollet, Characterization of calcareous deposits in artificial seawater by impedance techniques 3 - Deposit of  $\text{CaCO}_3$  in the presence of  $\text{Mg(II)}$ , Electrochim Acta, 48 (2003), 1645-1654.
  78. C. Deslouis, D. Festy, O. Gil, V. Maillot, S. Touzain and B. Tribollet, Characterization of calcareous deposits in artificial sea water by impedances techniques: 2-deposit of  $\text{Mg(OH)}_2$  without  $\text{CaCO}_3$ , Electrochim Acta, 45 (2000), 1837-1845.
  79. J. G. Kaufman, Corrosion of Aluminum and Aluminum Alloys, vol. 13B, ASM Handbook Volume 13B, Corrosion: Materials (ASM International), (Materials Park, Ohio, ASM International, 2003, p. 95-124).
  80. D. A. Little, M. A. Jakab and J. R. Scully, Effect of surface pretreatment on the underpaint corrosion of AA2024-T3 at various temperatures, Corrosion, 62 (2006), 300-315.
  81. E. L. Koehler, U. R. Evans, B. F. Brown, J. Kruger, R. W. Staehle and National Association of Corrosion Engineers. Research Committee., Corrosion Under Organic Coatings, Localized Corrosion, (Houston, Tex., National Association of Corrosion Engineers, 1974, p. 117-133).

## **1.9 Underpaint Corrosion on Chromate –Free Organic- Coated AA2024-T351 as a Function of Accelerated Testing Variables Compared with Natural Exposures (Tayler, M.L. and Scully, J.R.)**

### **1.9.1 Summary**

The discrepancy between lab accelerated life tests (LALTs) and field tests of organically coated aerospace alloys is a well-known problem. For example, a NAVAIR study with aluminum alloys showed that B-117 paired with a cyclic LALT, like GM9540P, correlated better with beachfront results than did B-117 alone <sup>1</sup>. Currently, it is not well understood how and which environmental factors cause such discrepancies. This research seeks to increase understanding of the influence of environmental stresses and subsequent changes in the mechanisms and rates of underpaint corrosion.

In this report, we compare results from standard LALTs, such as ASTM B-117, ASTM G-85 Annex 3 and Annex 5, ASTM D-4587 and ASTM D-5894, to field sites to elucidate similarities and differences between certain LALT results and field results. The materials used in all tasks are chromate-free bare and Eponol coated AA2024-T351. The comparisons between LALT and field were made using a suite high level surveillance methods: electrochemical impedance spectroscopy (EIS), confocal laser scanning microscopy (CLSM), scanning electron microscopy (SEM), 3D optical microscopy and Fourier Transform Infrared Spectroscopy (FTIR). These methods maximize our ability to detect corrosive change, improve our ability make comparisons between LALT, FI and field tests, and demonstrate a methodological improvement upon previous studies based on visual or low magnification analysis. All tests were conducted according to the LALT standards but during exposure were interrogated with the above listed high level surveillance methods numerous times during a total test time of 15 days. Field test exposure time varied by location, and was from 1 to 2 years. By elucidating discrepancies of scribe creep mechanisms and corrosion products between field results and LALTs, and by identifying environmental severity factors critical to underpaint corrosion, the current study ultimately provides guidance that will enable the development of LALT methods that better simulate field chemistry and environmental conditions.

Results from this work demonstrate the need for the inclusion of UV in any LALT designed to examine field exposure of organic-coated precipitation age hardened AA2024-T351. Acceleration factors based on EIS parameters and scribe creep rate were calculated for field sites and LALTs and are presented in detail in this work. ESFs that have an apparent effect on the corrosion of organic coated AA2024-T351 are UV light, chloride and cycling. FTIR analysis of Eponol films exposed on inert substrates shows that organic coating damage is primarily caused by ESFs that attack the coating specifically, like UV and ozone.

Finally, we do not recommend using the ASTM B-117 method for life prediction testing of organic barrier coatings on chromate-free high strength aluminum alloys subjected to field exposure in natural environments such as marine, coastal and inland rural. We recommend an LALT that incorporates UV irradiation, wet/dry cycling, and an ESF that promotes corrosion of the substrate alloy, such as chloride, as seen in the field. Moreover, it should be noted that many standard LALTs do not cause direct damage to coating over short time scales; rather the

damage to the coating occurs only when substrate corrosion proceeds and triggers underpaint corrosion. This, along with ESFs that may be specific to the operating environment of the coating system, must be taken into account by the user when considering LALTs for life prediction of coated metals. High level surveillance methods must also be recommended and should be incorporated into coating system analysis, especially if damage to the coating specifically is important to the user.

### 1.9.2 Introduction: Necessary Development of LALTs for Chromate Free Coatings

Chromate conversion coatings (CCCs) have been used since the early 1900's to protect metal alloys from corrosion<sup>2</sup>. CCCs increase the corrosion resistance of steel and 2xxx series aluminum alloys, among others. Hexavalent chromium ( $\text{Cr}^{6+}$ ) is the main protective component in CCCs. However, it has been found to be a carcinogen<sup>3</sup> and has become a highly regulated substance. The US Department of Labor recently issued a new regulation that limits the amount of  $\text{Cr}^{6+}$  exposure for workers, cutting the permissible limit from  $100 \mu\text{g}/\text{m}^3$  of air to  $5 \mu\text{g}/\text{m}^3$  of air<sup>4</sup>. In addition, the EPA has set the permissible amount of  $\text{Cr}^{6+}$  in drinking water at 100 ppb<sup>5</sup>, and has established guidelines for enhanced monitoring of  $\text{Cr}^{6+}$  levels<sup>6</sup>. Finally, the Undersecretary of Defense has issued a memorandum which instructs the military to reduce its use of hexavalent chromium and find alternatives to CCCs<sup>7</sup>.

The drive to move away from pretreatments containing hexavalent chromium has led to an increase in the diversity of pretreatments and coating primers for corrosion protection on aerospace alloys. Chromate free pretreatments that promote adhesion of paint to the metal surface<sup>8</sup> and Mg rich primers<sup>9</sup> are just two examples. New chromate free pretreatments must still protect against scribe creep on aluminum alloys over their service lives. Therefore, the service lifetimes of these new coating systems must be established. However, field exposures take many years to complete. As a result, the development of new priming and coating schemes has relied on the use of accelerated life corrosion tests (LALTs).

Accelerated testing saves time and reduces cost<sup>10</sup>. By understanding the limits of materials and products, companies can accurately gauge warranty and production costs<sup>10</sup>. There are two types of LALTs; quality assurance tests and developmental tests<sup>10</sup>. Quality assurance tests are used ensure that the production process is up to specifications (i.e., passing X number of hours in the test assumes good service for many years in the field). Developmental tests are used to evaluate and improve the performance of new coating/substrate systems by providing valuable data on how a new system will react to anticipated environmental variables in the field<sup>10</sup>. However, current LALTs do not accurately predict the service lifetimes of many new priming and coating schemes under development<sup>11</sup>. For example, the ASTM B-117 is a quality assurance test but has often been misapplied as a developmental test, despite warnings provided in the test method<sup>12</sup>. Until a LALT that correlates well with long term field results can be designed, accelerated testing is not exact and is only "...a balance between science and judgment"<sup>10</sup>. It is therefore of high interest to develop better LALTs that more accurately mimic and predict service life. It is essential to mimic scribe creep at intentional defects, degradation at latent coating defects and degradation of the coating. The mechanism of scribe creep on aluminum should be reviewed in order to gain insight on environmental factors that could affect field performance when this mode of corrosion occurs.

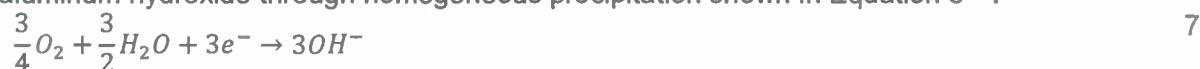


### 1.9.2.1 Scribe Creep Mechanisms for Aluminum

Cathodic delamination does not often occur in aluminum alloys because of a lack of electronic conductivity of the surface oxides, the slow rates of cathodic electron transfer reactions, and a lack of global  $\text{OH}^-$  production under the coating<sup>13</sup>. Filiform Corrosion (FFC) is a form of surface corrosion that forms long, thin filaments of corrosion under a coating and delaminates and detaches the coating<sup>13,14</sup>. The filament has an anodic head and a cathodic tail and starts growing from a defect in the coating, like a scratch. The electrochemical reactions that take place are Equation 5, the anodic reaction at the head of the filament, and Equation 6, which is a secondary reaction near the head upon hydrolytic acidification<sup>13</sup>.



Equation 7 is the cathodic reaction in the tail of the filament. Then  $\text{OH}^-$  ions form a gelatinous aluminum hydroxide through homogeneous precipitation shown in Equation 8<sup>13</sup>.



The anodic head of the filament is very acidic ( $\text{pH}=1-3$ ) and the evolution of hydrogen gas (Equation 6) occurs in the same area as the anodic dissolution of aluminum<sup>14</sup>. The tail of the filaments is very basic and  $\text{Al}(\text{OH})_3$  is precipitated in the path of the tail (Equation 8)<sup>13</sup>. The propagation of the filaments has been proposed to be due to anodic undercutting caused by differential oxygen concentration between the front and the back of the head of the filament<sup>14-16</sup>. Figure 146 shows a schematic of filiform corrosion on an aluminum alloy<sup>17</sup>. While some water and oxygen can diffuse through the coating in order for Equation 7 to occur<sup>13</sup>, most of the oxygen and water diffuse through the tail of the filament<sup>18</sup>. Even when an oxygen impermeable metal film was placed over the head and tail of the filament, leaving only the scratch in the coating where the filament originated exposed to air, FFC continued unabated<sup>18</sup>. It has been calculated that the rate of diffusion through the tail of the filament can be up to ten times greater than diffusion vertically through the coating<sup>18</sup>. It has been suggested that coating adhesion to the metal substrate determines the corrosion protection of the coating better than the barrier properties of the coating when this mechanism prevails<sup>15,16</sup>. Often, blisters in the coating of AA2024-T351 are just a cluster of filaments<sup>13</sup>.

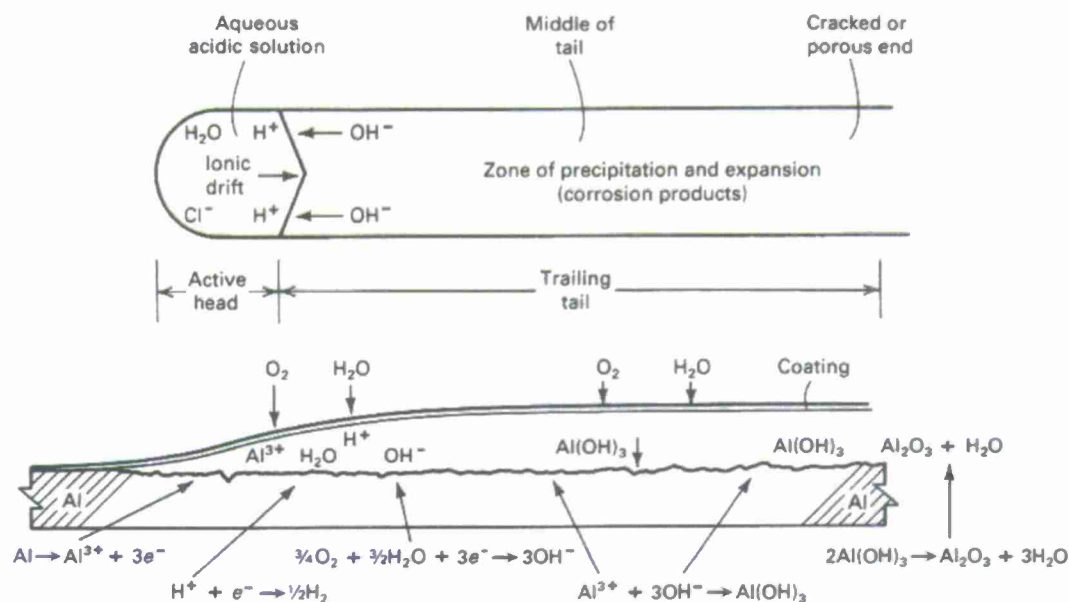


Figure 146. Schematic of filiform corrosion on an aluminum alloy <sup>17</sup>.

Certain factors have been shown to affect the growth rate of FCC and scribe creep on coated aluminum alloys. Increasing temperature has been shown to increase scribe creep length on AA2024-T351 <sup>13, 19</sup>. Scribe creep on AA2024-T351 has been approximated to be an Arrhenius-type thermally activated behavior that decreases over time. Scribe creep length also decreases over time, and it has been shown that the scribe creep length is proportional to time to the one half power <sup>19</sup>. Increasing relative humidity (%RH) has been shown to proportionally increase the width of the filaments in FCC <sup>14</sup>. Filiform corrosion rate is also increased by application of HCl solution at the scratch <sup>13</sup>. The HCl solution promotes anodic undercutting and helps to initiate FCC <sup>13</sup>. Aluminum alloys that contain copper have been shown to support enhanced rates of FCC over copper free alloys <sup>13</sup>. Copper rich inter-metallic particles (IMCs) are cathodic to the aluminum matrix, and re-plated copper has been shown to enhance the overall rate of the oxygen reduction reaction (ORR) on bare AA2024-T351 <sup>13, 20</sup>. Additionally, rates of scribe creep on AA2024-T351 have been shown to be accelerated with higher surface coverage of copper because the ORR occurs preferentially on the Cu-bearing particles <sup>13, 19</sup>. Studies have shown that by limiting the amount of copper available at the surface, either by passivating the Cu bearing IMCs with pretreatments or by decreasing the amount of Cu in the IMCs by keeping the copper in solid solution, will cause a decrease in the scribe creep rate <sup>13, 19</sup>. Studies in the Automotive industry have found that increasing salt levels in LALTs showed no noticeable increase in the corrosion of aluminum alloys <sup>21</sup>.

### 1.9.2.2 Environmental Severity Factors

Literature on the corrosion of coated metal systems and LALTs has provided a number of environmental severity factors (ESF) that affect corrosion of bare metals and underpaint corrosion. However, the singular effects of isolated corrosion drivers on coated metal systems are poorly understood. To address this issue, the current study has investigated the following ESFs individually and in combinations. A brief review is presented regarding the possible impact of the ESFs examined for this study.

### UV Radiation

UV irradiation was not considered in the SAE J2334 test, and is absent from many LALTs for organic-coated metals; the ASTM B-117, ASTM G-85 annex 3, ASTM G-85 Annex 5, and the GM 9540P are notable examples. However, it has been found to be an important factor for organic-coated metals that are exposed to UV irradiation in the field<sup>22-25</sup>. Photo-oxidation of polymer coatings begins at the surface and progresses downward into the coating<sup>24</sup>. Oxidation of a polymer coating can increase the amount of water absorbed into the coating<sup>25</sup>. Studies of coated systems exposed to UV revealed that coatings that show very good resistance to blistering in ASTM B-117 are far less protective after exposure to UV radiation<sup>22</sup>. The photo-oxidation of the coating by UV radiation reduces the coatings barrier effect in relation to moisture and ionic species allowing the formation of the blisters<sup>22</sup>. Reduction in coating barrier properties has been demonstrated in previous work examining melamine ( $C_3H_6N_6$ ) bridges that form between polymer chains as polyester resins harden<sup>22</sup>. By monitoring the change in melamine quantity with FTIR as the coating is photo-oxidized, the degradation of the coating can be monitored. When these melamine bridges are oxidized and break down, the ability of the coating to keep water from permeating becomes compromised<sup>22</sup>. Other work demonstrates that defect area in organic-coated metals, coating permeability and water uptake amount and kinetics, increase with increasing exposure to UV irradiation<sup>26</sup>. A study on galvanized and phosphated steel, coated with a polyester resin used EIS to measure the change in pore resistance as a function of exposure to UV radiation<sup>27</sup>. Pore resistance has been shown to be a measure of the defect area of the coating (a lower pore resistance corresponds to a higher defect area) and can be found by modeling the surface as an equivalent circuit<sup>28, 29</sup>. Using this method established by earlier groups, Deflorian et al. were able to find the pore resistance<sup>26, 28</sup>. Figure 147 shows the change in pore resistance over time for samples immersed in 5% sodium chloride solution for three different UV irradiation times. The defect area of the coating increases with increasing exposure to UV irradiation (Figure 147). This is attributed to the photo-oxidation of the coating polymer causing defects where corrosion can initiate<sup>27</sup>.

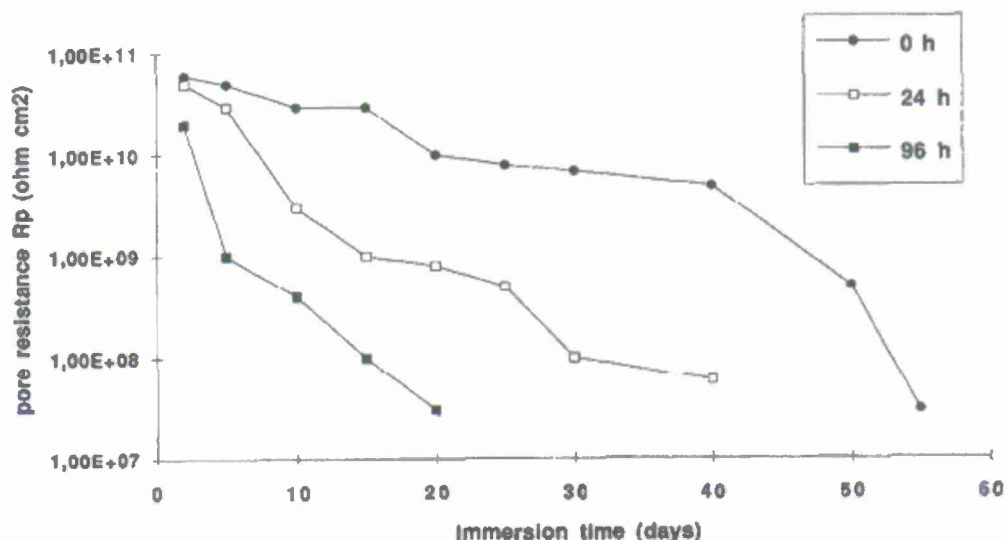


Figure 147. The pore resistance for polyester resin coated galvanized and phosphated steel as a function of immersion time. Three different UV irradiation times are shown. The samples were immersed in 5% sodium chloride solution<sup>27</sup>.

## Ozone

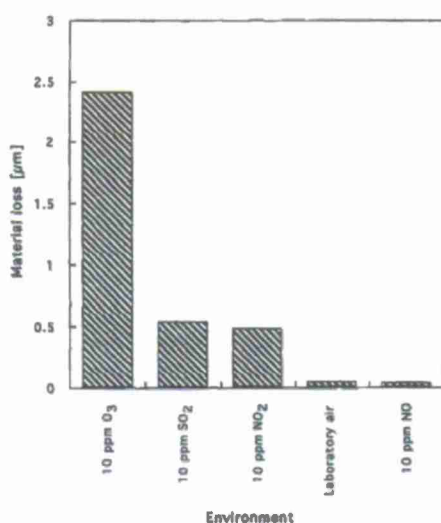
As a strong oxidizer, ozone can accelerate the corrosion of bare unalloyed carbon steel and bare aluminum by itself<sup>30, 31</sup>. It has also been shown to increase corrosion rates on bare steel by turning nitrogen dioxide (NO<sub>2</sub>), a gaseous pollutant in the atmosphere, into nitric acid (HNO<sub>3</sub>) via the following sequence of reactions (Equations 9, 10, and 11)<sup>30</sup>.



The oxidation of NO<sub>2</sub> to NO<sub>3</sub> by ozone occurs in the gas phase (Equation 9), as does the reaction of NO<sub>3</sub> with NO<sub>2</sub> to form N<sub>2</sub>O<sub>5</sub> (Equation 10). N<sub>2</sub>O<sub>5</sub> is a relatively unstable molecule and reacts quickly with H<sub>2</sub>O in the air or in the aqueous film on the surface of the metal to create nitric acid<sup>30</sup>. Ozone can also react with sulfite ions (formed when sulfur dioxide reacts with water) in the water film to create sulfate ions, a known corrosion driver, in a sequence of two reactions (Equations 12 and 13)<sup>30</sup>.



Ozone was also found to concentrate nitrogen and sulfur based corrosion species on the surface of steel<sup>30</sup>, even when the concentration of these species in lab air was 10 ppb and 0.6 ppb, respectively. On aluminum, 10 ppm ozone caused more material loss and a lower surface water film pH than sulfur and nitrogen based pollutants at equal amounts (Figure 148)<sup>31</sup>. The lower surface water film pH is believed to be caused by the fast oxidation of NO<sub>2</sub> by ozone.



Environment	pH
10 ppm O <sub>3</sub>	4.1
10 ppm SO <sub>2</sub>	4.5
10 ppm NO <sub>2</sub>	4.8
10 ppm NO	5.9
laboratory air	5.9
0.5 ppm SO <sub>2</sub>	6.2

Figure 148. Graph showing the relative material loss of pure aluminum exposed to different pollutant gases (left), and a table showing the pH of the surface water films produced in each exposure environment (right) after 4 weeks of exposure<sup>31</sup>.



Although no studies of the effects of ozone on the corrosion of organically coated steel or aluminum have been completed to date, there is literature on the effect of ozone on polymers. Ozone preferentially attacks double bonds found in many polymers<sup>32-34</sup>. The oxidation of the double bonds in the base resins and the binders in organic coatings causes a weakening of the elasticity of the coating<sup>34</sup>. Additionally, ozone has been determined to initiate chain oxidations, i.e., the reaction of ozone with polymers produces peroxyradicals that further oxidize the base resin and binders<sup>33</sup>. This damage to the coating creates defects where water and other ESFs can come into contact with the metal substrate and initiate corrosion.

### Chloride

The addition of chloride ions has long been used in LALTs for aluminum alloys. Chlorides are used for many reasons. Chlorides are one of the principle pollutants in atmospheric corrosion, and can accelerate the corrosion rate of metals by several orders of magnitude<sup>35</sup>. They are found in abundance in marine and coastal regions in the form of aerosol particles from the ocean, as well as in industrial areas from pollutant gases<sup>35</sup>. In temperate climates, chlorides come from de-icing salts used on roadways in urban areas. Chloride salts often dissociate in water films that form on the surface of metals exposed to the atmosphere creating an electrolyte solution, which is needed for corrosion to take place<sup>35</sup>. Chloride ions are aggressive and can break down the passive oxide on aluminum alloys and cause pitting corrosion<sup>36</sup>. Chloride ions are small, have a high diffusivity, and also interfere with passivation<sup>36</sup>.

There is some literature on the effects of ions on polymer coatings<sup>37-41</sup>. However, these works mainly look at the effect of positive ions on the coating. One study showed that sodium ions (from NaCl) degrade polybutadiene coatings by either ion exchange reactions in the coating or by breaking the bonds at the polymer/metal interface<sup>38</sup>. When the polymer was exposed to BaCl<sub>2</sub> the same effects were not seen, ruling out the Cl<sup>-</sup> ions as the cause of the coating degradation<sup>38</sup>. Other work showed that when mild steel coated with polybutadiene was polarized to -0.8 V vs. Ag/AgCl not only was the rate of cation migration through the coating increased, but the rate of Cl<sup>-</sup> ion migration increased as well<sup>39</sup>. The authors proposed three possible explanations: 1) the accumulation of positive charge at the coating/metal interface attracted the Cl<sup>-</sup> anions, 2) the applied potential may enlarge minute pores in the coating allowing for greater diffusion rates, or 3) applied cathodic potential has been shown to increase the rate of water through the coating and perhaps the solvated Cl<sup>-</sup> anions diffused with the water<sup>39</sup>. Lastly, a study of PMMA polymer for slow-release medicine applications showed that 0.1 M Cl<sup>-</sup> slowed the diffusion rate of water through the coating, though no explanation was given<sup>42</sup>.

### Time of Wetness and Relative Humidity

Electrochemical corrosion cannot occur without an electrolyte<sup>43-45</sup>. The usual electrolyte is composed of thin films of water with impurities on the surface of the metal<sup>45</sup>. In regards to atmospheric corrosion, it is then important to know how often the surface of a metal is wet. Surfaces can be wetted by rain or dew. Water films can also form on the surfaces of metals due to humidity in the atmosphere<sup>44</sup>. This has led to the concept of Time of Wetness (ToW). ToW is defined many different ways, but perhaps it is best defined by Leygraf et al. as "time during which a corrosion stimulating film exists on the surface"<sup>44</sup>. Many aerosol particles that accumulate on metal surfaces are hygroscopic and absorb water from the atmosphere. Called deliquescence, this phenomenon can cause the surface of the metal to wet at a lower relative

humidity than would be expected for a clean, bare metal surface<sup>45</sup>. The deliquescence of hygroscopic species on a metal surface can cause corrosion at relatively low relative humidity. The study of the effects of relative humidity and of deliquescence led to the development of the concept of critical relative humidity (%RH<sub>crit</sub>). Vernon first observed the existence of critical relative humidity in studies of bare copper exposed to varying levels of humidity and sulfur dioxide (SO<sub>2</sub>), a common pollutant<sup>46,47</sup>. Samples were exposed at five different %RH levels, 50%, 63%, 75%, 99% and 100%. A "profound" difference in corrosion rate was found between 63% RH and 75% when sulfur dioxide was added to exposure atmosphere. This was true for all levels of sulfur dioxide tested. The %RH level at which corrosion rate sharply increases is called the critical humidity. This critical humidity is the humidity level at which hygroscopic particles begin to absorb water from the air. With such particles, a metal surface can experience corrosion attack at lower humidity levels than would be expected for a clean metal surface with an atmosphere free of pollutants and particulates<sup>46,47</sup>.

### Cycling

Materials exposed to the environment experience many natural cycles. Day and night leads to a cycling of UV irradiation, as well as temperature and humidity. Cycling in LALTs has shown to provide results that are closer than non-cycling LALTs to field as demonstrated in the following examples. An Alcoa study on various coated aluminum alloys showed that an LALT consisting of repeated cycles of dipping in an HCl solution and exposure to high humidity (85% RH) and temperature (40°C) correlated better with a 6 month coastal exposure than did ASTM B-117 for scribe creep<sup>1</sup>. This test was cyclic in that the samples were removed from high humidity to a lower humidity environment for the reapplication of the HCl solution. Additionally, recent work by NAVAIR compared 24 month exposures on the Florida coast to various industry standard LALTs<sup>48</sup>. The comparison showed that for AA2024-T351 pretreated with a Chromate Conversion Coating and coated, ASTM B-117 used in combination with a cyclic LALT like GM 9540P correlated better with beachfront exposure than ASTM B-117 alone.

Wet/dry cycling has also been shown to increase the corrosion rate of bare metals<sup>49-51</sup>. Using a Scanning Kelvin Probe (SKP), Stratmann et al. were able to show that the corrosion rate of pure iron increases as the metal surface dries<sup>50</sup>. As the surface electrolyte layer becomes thinner, oxygen diffusion through the electrolyte becomes faster and allows for an increased corrosion rate<sup>50</sup>.

When discussing the quantification of ESFs it is important to note that cycling is a different type of corrosion driver. ESFs like chloride levels and UV exposure can be easily and accurately quantified. However, cycling is an action and must be expressed in terms of other quantities. For example, if we were to quantify running, we would do it in terms of distance covered or time spent running, but to directly quantify running in terms of itself has no actual meaning. Therefore, it is important that cycling is clearly defined in this work and is directly comparable to field exposure. As has been shown previously, the cycling of many different ESFs can play a role in the scribe creep of coated metal systems. To cycle every ESF that may have an effect on scribe creep rate and then quantify the effects would be a large task and is not in the scope of the current work. Wet/dry cycling and temperature are probably the most encountered forms of cycling in the field. In this work cycling will be quantified by the effect of wet/dry cycling on scribe creep rate.

### 1.9.2.3 Overall Critical Unresolved Issues

To date, there has been little systematic evaluation and quantification of corrosion drivers in the field or lab. Although a few examples of individual corrosion drivers can be found in the literature, overall, widespread systematic studies have not been performed. Often, all the drivers that may affect a system are "lumped together" in some combination which comprises the LALT. As a result, LALTs are often much more severe than field environments. The conventional notion has been that good coating performance in the severe LALTs will mean good performance in the comparatively benign field, even if the drivers differ. In addition to obfuscating the impact of individual corrosion drivers on the substrate, lumping all drivers together has impaired our understanding of the effects of individual corrosion drivers on the degradation of the coating itself, as well as the interactions between the coating and the substrate during the degradation of the system.

To accurately mimic field environments and to systematically study the effects of isolated and combined corrosion drivers, a controlled cycling of the corrosion drivers is needed. There is no one lab exposure device that can cycle humidity, UV, condensation, time of wetness, chloride deposition and concentration of gases (e.g. ozone). Existing exposure systems must be modified and perhaps new systems made to accurately control and cycle the corrosion drivers needed for this study.

In a coated system, the effects of corrosion drivers on the degradation of the coating itself must also be studied. Factors such as UV, may that have a much greater effect on the degradation of the coating than on the corrosion of the metal substrate. Effects of underpaint corrosion and scribe creep on the resulting chemistry under the coating are also important aspects of the overall degradation of the coated metal system. Other factors affecting the coating are corrosion product wedging and physical damage to the coating caused by growth of corrosion product upwards into the coating. Many of these factors are poorly understood presently, and insight must be gained as to how they affect the degradation of the coating to the degree that quantitative laws describing scribe creep or impedance drop can be developed.

The following important issues must be resolved in order to properly construct LALTs from the bottom up:

1. One must determine the effects of individual corrosion drivers on underpaint corrosion and scribe creep and coating polymer degradation using high level surveillance in order to understand their role and quantitative impact on each individually.
2. An understanding of the combined effects of key corrosion drivers on underpaint corrosion using high level surveillance must be gained. To do this, the effects of corrosion drivers on the metal, the polymer coating and the system as a whole interact to cause scribe creep and underpaint corrosion must also be understood.
3. One must determine the extent of degradation of the organic coating itself, triggered by the environment, versus degradation triggered by conditions developing at the coating/metal interface (i.e., caused by underpaint corrosion).



4. Scribe creep or EIS parameter degradation models for organically coated aluminum alloys based input of coating system and on quantified corrosion drivers must be developed.

Previous comparisons of LALTs vs. field studies of coated metals have relied heavily on visual examination of corrosion and coating appearance, such as gloss measurements (ASTM D523-08)<sup>52</sup>, a count of the number of blisters of a certain size (ASTM D714-02)<sup>53</sup> or the extent of visible rust (ASTM D610-08)<sup>54</sup>. However, these approaches are only visual or at best low magnification microscopic methods, and may not identify potential differences in corrosion mechanisms or corrosion product identity in LALT compared to field exposures. For example, a recent NAVAIR study for the DoD addressed problems using visible test methods and ASTM B-117 to evaluate the corrosion inhibition of coatings on aluminum alloys<sup>1</sup>. The report was commissioned to address the issue of poor correlation between lab and field results when using ASTM B-117. This poor correlation manifested itself in the form of distributions in the data, i.e., variable coating degradation from sample to sample leading to erroneous passing or failure of coated samples that were exposed in ASTM B-117. These samples were evaluated using the ASTM D-1654 Procedure A test method which involves removing the coating by compressed air or mechanical scraping and then visually rating the extent of corrosion. The report supplied two conclusions in order to reduce the spread in the data. The first is that when using the ASTM D-1654 test method, a great number of samples need to be tested to establish trends in order to overcome specimen variability or distributions in the results. The report suggests using two to four different alloy substrates with 12 replicates per substrate for each coating system to be evaluated. In fact, the study shows that using four different alloy substrates instead of one can increase the overall correlation between lab and field by as much as 15%. The second conclusion was that exposing samples to least two different LALTs, for example ASTM B-117 and GM9540P, would give more robust correlations with field results than would exposing the samples to just one standard LALT that might have discrepancies with field behavior. These are brute force approaches to developing LALTs that correlate with field performance. The man-hours involved in determining coating performance using ASTM B-117/GM9540P and visual corrosion evaluation is extensive. As an example, if one wanted to evaluate three competing coating schemes and used the recommended four substrates, the consequence would be that 144 samples would be prepared, exposed and evaluated.

Therefore, high level surveillance methods of coating/metal system analysis are needed to move beyond visual examination and more accurately compare the mechanisms and morphologies of corrosion between lab and field. Then, an LALT that correlates the best with field behavior could be selected. However, detailed high surveillance analysis of field samples is largely lacking in previous work<sup>21, 27, 55-57</sup>. There are several reasons for this: (1) opaque pigments in the coating make it difficult to determine the corrosion mechanisms and analyze the corrosion products during underpaint corrosion, (2) non-destructive methods to monitor underpaint corrosion are limited, and (3) instruments that analyze the coating are not useful in analysis of the substrate, requiring a suite of many different techniques to analyze the entire coated metal system (properties of the coating, underpaint corrosion, scribe behavior, corrosion product identities, etc). A fourth issue is the challenge of variability or distributions in behavior which challenge every technique.

The opportunity exists to improve the understanding of lab/field correlations by using high level surveillance techniques to better understand the mechanisms and morphologies of corrosion in



lab and field exposures. Isolation of identified corrosion drivers can then be used to more fully understand the effects of separate drivers on corrosion and coating degradation. This knowledge can then be used to build more accurate LALTs that correlate with field environments. The first step is to compare field results to standard LALTs.

#### 1.9.2.4 Overall Problem Statement

Field tests and LALTs to determine the service life of coated metals do not always produce the same mechanism of corrosion; specifically, field tests usually have no agreement with the ASTM B-117 method. Additionally, acceleration factors for many systems are unknown, even when the mode and mechanism of field and lab attack are similar. As a first step, a fundamental understanding of the effects of corrosion drivers in terms of standard LALTs compared to field are evaluated in this report. This report focuses on this issue on chromate-free Eponol coated AA2024-T351.

#### 1.9.2.5 Objective

The objective of this work is to compare and contrast the corrosion processes associated with underpaint corrosion and scribe creep produced by the combination of corrosion drivers present in existing standard LALTs (like ASTM b-117, ASTM G-85 Annex 5, AATM G-85 Annex 3 and ASTM D-5894) compared to field exposures on chromate-free Eponol coated AA2024-T351. This will be accomplished using our suite of high level surveillance techniques named previously.

#### 1.9.2.6 General Approach

In collaboration with USM, a clear epoxy resin (Poly(Bisphenol A-co-epichlorohydrin) glycidyl end-capped ( $C_{18}H_{22}O_3$ ) $_n \cdot C_{22}H_{26}O_4$ ; Trade name Eponol. See Figure 149) was chosen for use in coating aluminum samples. The chosen epoxy resin is a high molecular weight resin used primarily as a constituent of paint coatings. The coating was applied to be 30 microns thick and has a high initial impedance of around  $10^{11} \Omega \cdot \text{cm}^2$  when physical defects are minimized. The choice of this clear resin as a coating for samples in field tests and LALTs allows the underpaint corrosion to be seen. It also enables interrogation of the underpaint environment by 3D optical microscopy.

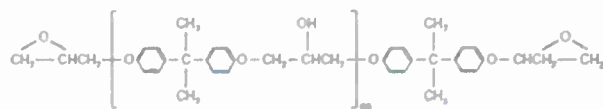


Figure 149. Molecular structure of Eponol

The surface of the metal samples were ground with 180, 240, 300, and 600 grit silicon carbide paper to remove any surface oxide, even out any imperfections and create a clean bare surface for the application of the coating. The samples were then blown with compressed air to remove any large debris from the grinding. The samples were washed with water and Alconox detergent soap and rinsed with Millipore water. After washing, the samples are immediately blown dry with compressed air. The Eponol was applied to AA2024-T351 samples by spin coating (early work) and by draw down bar (later work) to a thickness of  $30 \pm 5$  microns. The latter method provides a much more uniform coating thickness and tends to avoid physical defects. The metal samples were cured for five days in lab air and then cured at  $60^\circ\text{C}$  for 24

hours. After curing, the samples were cut to 2.5 x 2.5 cm dimensions and then scribed by hand with a diamond scribe tool through the organic coating to expose the AA2024-T351 underneath. Figure 150 shows a top down schematic of the coated and scribed sample, while Figure 151 shows the sample and scribe in cross-section.

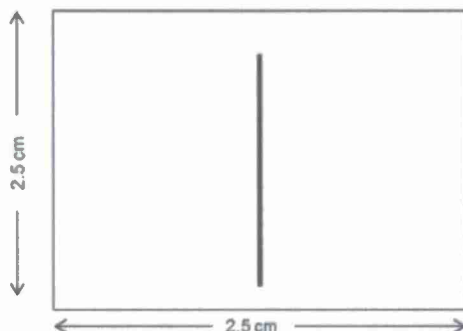


Figure 150. Schematic of Eponol coated and scribed AA2024-T351 sample. The sample is a square that is 2.5 cm on a side.

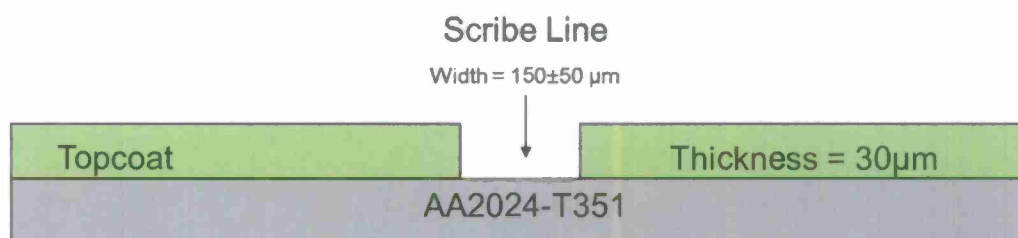


Figure 151. Schematic of Eponol coated and scribed AA2024-T351 sample. The substrate is roughly 1 mm thick and the Eponol topcoat is  $30 \pm 5 \mu\text{m}$ . The scribe line is  $150 \pm 50 \mu\text{m}$  in width.

High surveillance analysis methods have been chosen. X-Ray Diffraction (XRD) provides an analysis of the crystal structure of bulk crystalline corrosion products. 3D optical microscopy (Hirox) enables the tracking and quantification of scribe creep and corroded area over time based on color change. The 3D system has a vertical resolution of  $1 \mu\text{m}$ . Confocal Scanning Laser Microscopy (CSLM) gives detailed 3D topography information at higher resolutions than can be achieved with the optical 3D system. Cross-sectioning of samples was also done to enable imaging of the metal/coating, metal/corrosion product, and corrosion product/coating interfaces. Scanning Electron Microscopy (SEM) and Energy Dispersive Spectroscopy (EDS) were also used to identify the chemical elements present in cross-sectioned samples. Lastly, EIS was used to measure the change in the electrical properties of the coating over time. EIS was performed at locations near to and far from the scribe (Figure 152). This was done to more accurately determine the rate at which the scribe creep front moved away from the scribe and to determine the effects of the scribe and ESFs on the electrical characteristics of the coating.

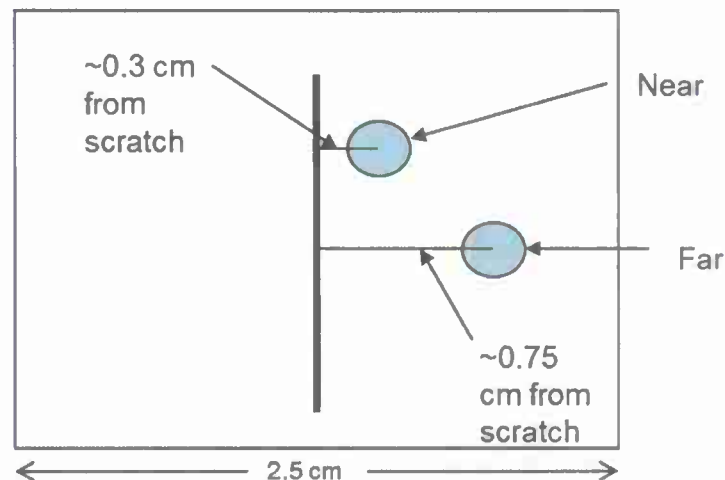


Figure 152. Schematic showing locations where EIS was performed on coated and scribed samples.

The suite of LALT exposure chambers includes a humidity chamber, a QUV cyclic condensation (CC/UV) chamber and a salt fog chamber. The salt fog chamber was modified by Ye Wan to include UV lights and an input for gases <sup>58</sup>. The QUV allows the use of elevated temperatures, humidity and condensation cycling, and UV exposure in LALTs <sup>59</sup>. It was also modified to enable the input of additional gases. These chambers can be used to perform standard LALTs like ASTM B-117 and ASTM D5894, and also allow for modified versions of standard LALTs.

AA2024-T351 samples were prepared and deployed to field sites around the country. Point Judith RI (PJ) is a harsh marine site that experiences large variations of temperature and UV irradiation through the year. Coconut Island HI (HI) is a marine site that has relatively constant conditions all year long. Los Angeles CA (LA) is a moderate industrial area about three miles from the ocean. Table 15 reports environmental severity factors for all field sites. EIS measurements on aluminum samples deployed at the field sites have been made. Aluminum samples have been sent to Kennedy Space Center (KSC), a harsh marine environment, for a one year deployment and are being returned every three months for high level surveillance analysis. Samples have also been deployed to Birdwood Golf Course in Charlottesville Va, and are being returned every 3 months for a year.

### 1.9.3 Lessons Learned

#### 1.9.3.1 Applicability of information across coating types

Organic coatings on metals for corrosion control can operate in a variety of ways. This work shows that ESFs interact differently with different parts of the coating system. The lessons learned and implementation procedures apply only to organic coatings on precipitation age hardened aluminum alloys and are not necessarily applicable to other coating types, i.e., sacrificial pigments in primers, conversion coatings or metallic coatings.

### 1.9.3.2 Coating performance assessment methods

It was found that a combination of high surveillance test methods was required to accurately assess the degradation of the coating and the metal. Field exposed and LALT samples should not be assessed visually, or by only one test method. As an example, a previous study compared steel with a polyester coating exposed either to UV followed by B-117 or to B-117 alone. Large differences in blister counts were seen between the two sets of samples, but were not accompanied by changes in gloss<sup>22</sup>. Gloss measurements from sample to sample were so similar that they did not provide any information on the degradation of the barrier properties of the coatings, let alone underpaint corrosion processes<sup>22</sup>. Additionally, many coatings exposed to UV cycles showed no visual differences upon changes in irradiation time. Thus, the limited data that could be obtained through visual inspection methods and methods that focus on coating evaluation only make accurate comparisons between lab and field exposures difficult. However, it is worth noting that the authors of this study<sup>22</sup> were able to detect changes in the coating through EIS and FTIR that were undetectable by gloss measurements or other visual inspection methods. Similarly, post-mortem analysis of substrate corrosion after coating removal obviously provides no information on the coating. This shows the benefits of using a suite of high surveillance test methods in contrast to just using visual inspection of coated systems.

### 1.9.3.3 Laboratory accelerated tests

The ASTM B-117 test method is not recommended if correlation of degradation mechanisms with field exposures is sought. The ASTM B-117 test method's lack of UV or cycling and constant immersion in 5% NaCl solution make it particularly ineffective at predicting real world performance of organically coated aluminum alloys from both a coating degradation and a corrosion perspective. Finally, the corrosion morphology and mode of scribe creep induced by corrosion appears to differ from that in field exposures.

## 1.9.4 Technical Investigations

### 1.9.4.1 Sample Preparation for Bare and Coated Samples

Samples of AA2024-T351 plate measuring 7.62 by 12.7 by 0.3175 cm (3 x 5 x 1/8<sup>th</sup> inch) were ground with 180, 240, 300, and 600 grit silicon carbide papers to remove any surface oxide, even out any imperfections and create a clean bare surface. The sample was then blown with compressed air to remove any large debris from the grinding. The sample was washed with water and Alconox detergent soap and rinsed with Millipore water. After washing, the sample was immediately blown dry with compressed air. Bare samples were then placed in a desiccator until they were exposed. The samples to be coated were placed in a fume hood. The Eponol (Poly(Bisphenol A-co-epichlorohydrin) glycidyl end-capped, CAS registry number: 25036-25-3. molecular formula:  $(C_{18}H_{22}O_3)_n \cdot C_{22}H_{26}O_4$ ) coating solution was applied to the top of the plate and a Gardco 8 path wet film applicator was used apply the coating to the sample. The 8 path wet film applicator was pulled by hand over the plate. The sample was allowed to cure for 5 days in air and then put into a 60°C oven for 24 hours to finish curing. The wet film thickness was roughly 75 microns (3 mils). The dry film thickness was 30±5 microns (1 mil). After curing, the plate was cut into 2.5 x 2.5 cm (1 x 1 inch) pieces with a band saw. The samples were then scratched by hand with a diamond scribe to give a scribe of 150±50 microns in width, 18±3 mm in length and 10±4 microns in depth into the metal substrate. A schematic of a finished sample in cross section is shown in Figure 151. It should be noted that the data for all LALTs is for un-pretreated and coated aluminum samples, while the data from the HI, PJ,



and LA field sites is for sample pretreated with Pre-Kote and then coated. The samples exposed to the KSC and BRD field sites were not pretreated before coating.

#### **1.9.4.2 EIS Implementation Procedure**

EIS was conducted on coated AA2024-T351 samples that had been exposed to various environments in order to examine the electrical properties of the coatings and detect the evolution of coating defects. The testing was done on a Princeton Applied Research Versastat 4 using the VersaStudio software. A five minute OCP test was run before EIS. A typical EIS scan was acquired in sine mode from 100 kHz to 0.05 Hz with 6 points per decade. Samples were scanned with an AC amplitude of 60 mV to reduce noise. The tests were run in a flat cell containing 50 mM sodium sulfate solution with ambient aeration. The area of the sample tested was a circle with an area of 1 cm<sup>2</sup>. The samples were tested at locations 0.3 cm and 0.75 cm away from the scribe. The reference electrode used was saturated calomel reference electrode, the samples were the working electrode, and a platinum mesh was used as the counter electrode.

#### **1.9.4.3 FTIR Analysis Procedure**

FTIR analysis of Eponol films was conducted to better understand the effects of ESFs on coating degradation in the form of polymer bond breaking. FTIR analysis enables the detection of degradation of Eponol films exposed on inert substrates to determine the effects of ESFs on the coating itself without any effects due to the substrate. FTIR analysis was performed on Eponol films that had been cast on inert polypropylene substrates and then exposed. For samples analyzed at UVA, the films were removed from the substrate after exposure and placed into a ScienceTech benchtop FTIR spectrometer for analysis. For samples analyzed at USM, coatings were left on the substrate and spectra were taken from three different locations on the eponol film by securing them to a Smart iTR attachment. The spectra were obtained using a Nicolet 6700 FTIR from Thermo Scientific running Omnic software, in 4000-650 cm<sup>-1</sup> range. The spectrophotometer was operated in transmission mode. The spectra were recorded at a resolution of 2 cm<sup>-1</sup> and 32 scans were conducted per location.

#### **1.9.4.4 Differential Scanning Calorimetry (DSC)**

DWSC was used to measure the change in the glass transition temperature ( $T_g$ ) of the Eponol film to gain insight into how different ESFs affected the nature of the Eponol polymer over time. DSC and MDSC measure the amount of heat required to increase the temperature of a sample. For polymers, it is used to measure the change in glass transition temperature ( $T_g$ ), or the temperature at which the polymer changes from an amorphous solid to a crystalline solid. The glass transition temperature is important because the properties of the polymer change as it moves from above the  $T_g$  to below. For example, above the transition temperature, polymers are amorphous and are generally more flexible and rubbery, while below the  $T_g$  they are crystalline and are generally more brittle<sup>60</sup>. Shorter polymer chains, limited crosslinking, and incorporation of plasticizers or residual solvent can lower the  $T_g$ , while longer chains, extensive crosslinking and large side groups raise the  $T_g$ <sup>60</sup>. Environmental factors can affect the  $T_g$ . For example, higher temperatures would cause more residual solvent to evaporate leading to higher  $T_g$ , while factors that break the crosslinking or the backbone of the chains themselves, like UV or ozone, would cause  $T_g$  to lower<sup>60</sup>. DSC was performed on unexposed and exposed (ASTM D4587, B117, and G85 A3) Eponol 53-BH-35 films on polypropylene. The samples were

prepared by using a hollow punch of 6 mm on each of the respective films once they were removed from the substrate. Two to three punches of each sample were loaded in to standard Al DSC pans. A Heat/cool/heat cycle was carried out between -25 ° C and 130 °C with a heating rate of 10 °C/min, under a nitrogen atmosphere (flow rate = 50 mL/min); with a TA Instruments DSC Q2000T calorimeter.

Modulated DSC was also performed on the same samples as above following the same procedure of sample preparation but they were loaded into T-zero Al hermetic pans. The conventional modulated DSC run was carried out between -25 ° C and 130 °C with a heating rate of 2 °C/min, modulating 60 seconds, under a nitrogen atmosphere (flow rate = 50 mL/min); with a TA instruments DSC Q2000 calorimeter.

#### **1.9.4.5 Thermogravimetric Analysis (TGA)**

TGA was performed on unexposed and exposed samples of Eponol 53-BH-35 on polypropylene. TGA involves heating the sample in a controlled setting and constantly measuring the changing weight. It has been used to measure the amount of residual solvent and the amount of organic content in the polymer. The remaining material after the sample has been heated to the point of complete polymer degradation is inorganic material. The samples were removed from the substrate and then using a hollow punch of 8 mm disks were punched out and two disks were loaded into the sample pan for each run. The sample pan was platinum and the runs were high resolution dynamic and were carried out from room temperature to 500 °C with a ramp rate of 10 °C/min, sensitivity of 1 and resolution of 4°C under a nitrogen atmosphere with a TA instruments TGA Q500 thermogravimetric analyzer.

#### **1.9.4.6 Hirox Imaging Procedure**

The bare and coated AA2024 aluminum samples were imaged with a Hirox KH-7700 digital microscope in order to examine corrosion morphology. The samples were first imaged with a macro lens to get one image of the entire sample surface. The coated samples then had a 2D tiled image taken at 50x that extended the length of the scratch using the MXG-4050RZ lens. The coated samples then have 3D tiled images taken at 350x that start at the scratch and run perpendicular out from the scratch using the MXG-10C lens with the OL 350 II lens attachment. These 3d tiled images were taken at the same place every time to monitor the progress of the corrosion from the scratch. Higher resolution images (+400x) were taken at various interesting spots on the samples. The 3D images were processed using Mitiani Corporation 3DMeasurement software and with Mountains Map software<sup>61</sup>.

#### **1.9.4.7 Scanning Electron Microscope Imaging Procedure**

Scanning electron microscopy (SEM) was conducted on a Jeol 6700F scanning electron microscope. Energy dispersive analysis (EDS) was performed using the same instrument and analyzed using PGT Spirit software.

#### **1.9.4.8 Scribe Creep Measurement Procedure**

Scribe creep was measured using optical images such as those found in Figure 156. The images were analyzed using ImageJ software<sup>62</sup>. The images were opened in ImageJ and the distance/pixel ratio was determined using the scale bar in the images. Ten points were then selected at random along the scribe. The scribe creep was then measured in both directions

from each of these ten points by drawing lines and then measuring the lengths of each line. The distances were then averaged together to give an average scribe creep length value.

#### **1.9.4.9 Nitric Acid Sample Cleaning Procedure**

The one bare AA2024-T351 sample exposed to CC+O<sub>3</sub> (10-25 ppm) were cleaned with a nitric acid solution after detailed analysis. This was done to remove the surface oxide in order to conduct further analysis on these samples. The sample was cleaned with a 50% nitric acid solution for 30 seconds. The sample was then rinsed in DI water and blown dry with compressed air. The sample was then taken immediately to the SEM for analysis.

#### **1.9.4.10 Image Analysis of Pitting on Bare AA2024-T351 Procedure**

Images taken with the Hirox were analyzed using ImageJ software<sup>62</sup>. The images were imported into ImageJ and converted into 8-bit greyscale images. The image was then converted to binary with the threshold selected to show all the pits as black areas and everything else as white areas. The Count Particles command was then used and the lower threshold for particle size was 20  $\mu\text{m}^2$ . The data returned was average particle area, area fraction of particles and particle density.

#### **1.9.4.11 Field and LALT Exposure Protocols**

Coated and scribed AA2024 samples were tested in standard LALTs, such as ASTM B-117, ASTM D-5894 and ASTM D-4587. A full list summarizing the key attributes and reference sources of standard LALTs conducted can be found in Table 13. The samples were then compared to the field samples using our suite of high surveillance instruments (Raman, XRD, EIS, CLSM, and 3D optical microscopy) to determine corrosion modes, mechanisms, rates and corrosion products at various stages of degradation. Samples were also exposed in non-standard LALTs. These were conducted in a QUV cyclic UV exposure chamber that had been modified to allow for the input of ozone gas. The exposure conditions were cyclic condensation (CC) consisting of two hours of condensation at 50°C followed by one hour of dry out also at 50°C, CC+UV (UV added to the one hour dry out during the CC cycling, done at 50°C, all UV exposures were done at an irradiance of 0.68 W/m<sup>2</sup> centered around 340 nm wavelength), CC+O<sub>3</sub> (0.7-2.5 ppm), CC+O<sub>3</sub> (10-25 ppm), and CC+UV+O<sub>3</sub> (0.7-2.5 ppm). Variations in the ozone levels were caused by the UV light that decomposes ozone, as well as the cooling fans that come on during the dry out phase to cool the UV bulbs.

Table 13. List of all standard LALTs used in this study.

Standard LALT	Conditions and Notes	Chloride	UV	Cycling
ASTM B-117	Standard Practice for operating salt spray (fog) apparatus. 5% NaCl solution, continuous spray <sup>12</sup> . ASTM B-117 SW used ASTM synthetic sea water solution in place of the 5% NaCl solution. ToW 75 100%	✓		
ASTM G-85 A3	Seawater acidified test, cyclic. Solution is 42 g of synthetic sea salt and 10 mL glacial acetic acid per liter of solution. $2.8 \leq \text{pH} \leq 3.0$ . Test cycle is 0.5 hours spray of this solution followed by 1.5 hours soak at or above 98% RH <sup>63</sup> .	✓		✓
ASTM G-85 A5	Dilute electrolyte cyclic fog dry test. Test consists of two step cycles of 1 hour spray at room temperature and 1 hour dry off at 35°C. Solution of 0.05% sodium chloride and 0.35% ammonium sulfate <sup>63</sup> .	✓		✓
ASTM D-4587	Standard Practice for Fluorescent UV-Condensation Exposures of Paint and Related Coatings. 4 hours of UV (340 nm) at 0.89 W/m <sup>2</sup> at 60°C followed by 4 hours of condensation (dark) at 50°C <sup>64</sup> . Condensation comes from the heating of water in a tray below the samples.		✓	✓
ASTM D-5894	Standard Practice for Cyclic Salt Fog/UV Exposure of Painted Metal (Alternating Exposures in a Fog/Dry Cabinet and a UV/Condensation Cabinet). A combination of ASTM G-85 Annex 5 and ASTM D-4587 Cycle 2. One week of ASTM D-4587 (4 hours of UV (340 nm) at 0.89 W/m <sup>2</sup> at 60°C followed by 4 hours of condensation (dark) at 50°C.) followed by one week of ASTM G-85 Annex 5 <sup>65</sup> .	✓	✓	✓

Table 14. List of all non-standard LALTs used in this study.

LALT designation	CC (2 hour condensation + 1 hour dry out)	UV (irradiated during dry out. Wavelength is centered at 340 nm with an intensity of 0.68 W/m <sup>2</sup> )	O <sub>3</sub> (pumped into the chamber continuously)
CC	✓	none	none
CC+UV	✓	✓	none
CC+O <sub>3</sub>	✓	none	0.7-2.5 ppm
CC+O <sub>3</sub>	✓	none	10.25 ppm
CC+UV+O <sub>3</sub>	✓	✓	0.7-2.5 ppm

Samples have also been deployed at various sites around the country for comparison to standard LALTs. A list of these sites and the site characterization data can be found in Table 15.



Table 15. Environmental severity factors for field sites.

Site Location	Mean Temp °C	% ToW	Mean RH (%)	Mean O <sub>3</sub> Concentration (ppb)	Mean UV (W/m <sup>2</sup> )	Mean Cl <sup>-</sup> dep rate (µg/cm <sup>2</sup> /hr)	Mean Cl <sup>-</sup> dep rate (mg/m <sup>2</sup> /day)
Coconut Island, HI	26.2	14	75.5	-	10.11	0.30	71.18
Los Angeles, CA	17.5	-	70.3	70*	-	-	-
Point Judith, RI	10	-	77.9	72.5	-	0.051	12.2
Charlottesville, VA	15.6	-	64.6	47*	-	0.002	0.48
Kennedy Space Center, FL	23.6	-	72.0	75.3*	-	0.8	192

Note: "-" indicates that the data is not available. "\*" indicates that data was taken from nearby NOAA site, not taken directly at exposure site.

### 1.9.5 Experimental Results

#### 1.9.5.1 Scribe creep results on aluminum

Image analysis was also performed in order to determine the scribe creep length over time for Eponol coated AA2024-T351 samples. Figure 153 shows an example of how scribe creep over time is tracked visually. Figure 153 shows the progression of scribe creep during exposure at KSC. Figure 154 shows scribe creep behavior for BRD. Figure 155 is of samples exposed in the ASTM B-117. Figure 156 and Figure 157 show the behavior for ASTM G-85 Annex 3 and Annex 5, respectively. Figure 158 shows the scribe creep behavior of samples exposed in ASTM D-5894. Figure 159 shows the behavior of samples exposed in the non-standard LALT CC+UV+O<sub>3</sub> (0.7-2.5 ppm). Figure 160 shows a visual comparison of scribe creep for all LALTs and Figure 161 shows a visual comparison for field sites. The results are shown in graphical form (Figure 162). It can be seen from these figures that ASTM D-5894 and ASTM G-85 Annex 5 best match with KSC for appearance of corrosion at and around the scribe. The lack of scribe creep seen for samples exposed at BRD is most likely due to the mild rural/suburban nature of the site. The samples exposed at PJ, HI and LA were so degraded that it was impossible to get accurate scribe creep data.

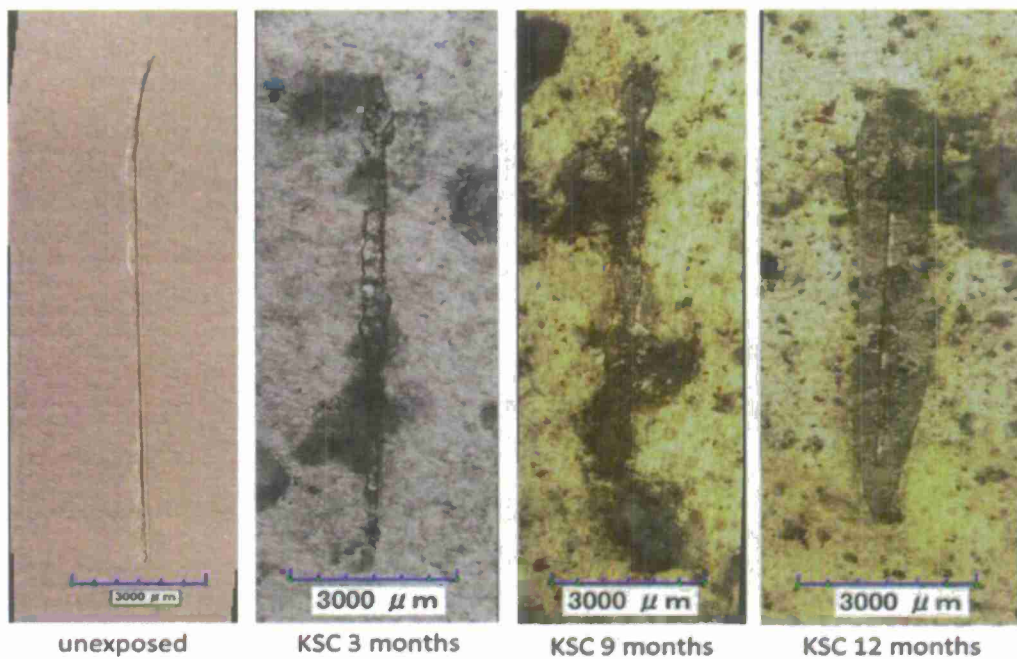


Figure 153. Optical Images of scribe creep over time for Eponol coated AA2024-T351 exposed at KSC.

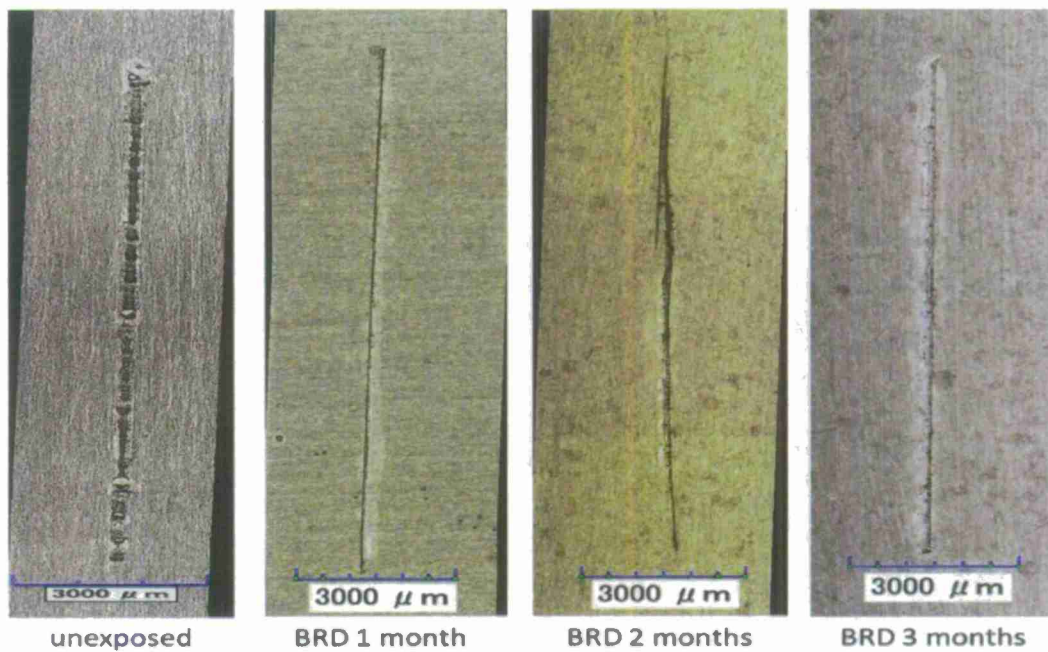


Figure 154. Optical Images of scribe creep over time for Eponol coated AA2024-T351 exposed at BRD.

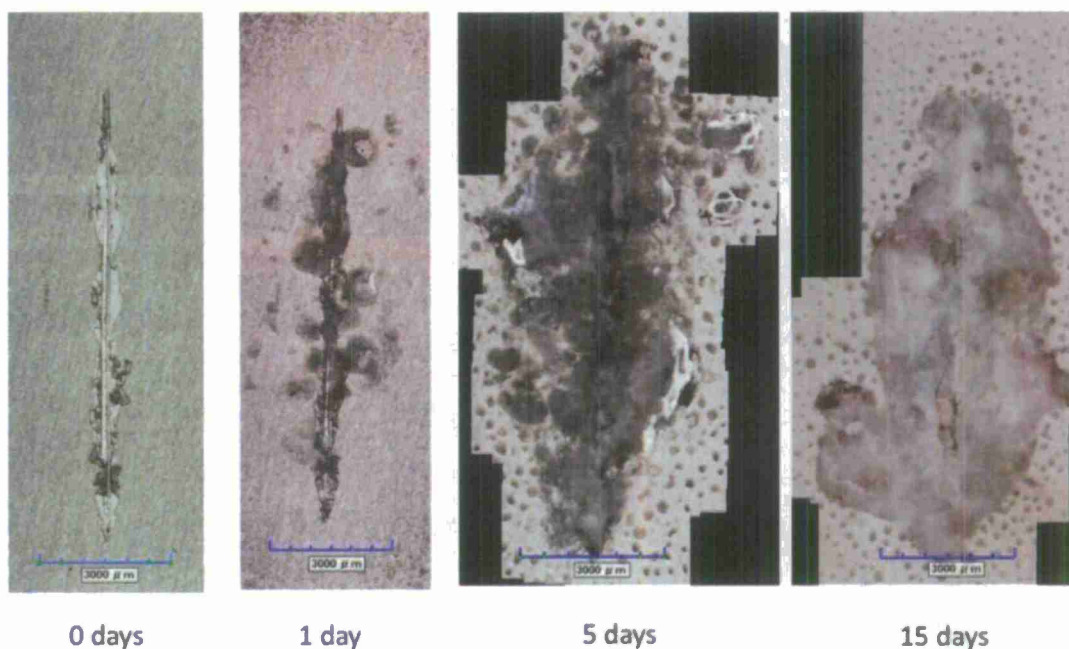


Figure 155. Optical images of Eponol coated AA2024-T351 exposed in ASTM B-117.

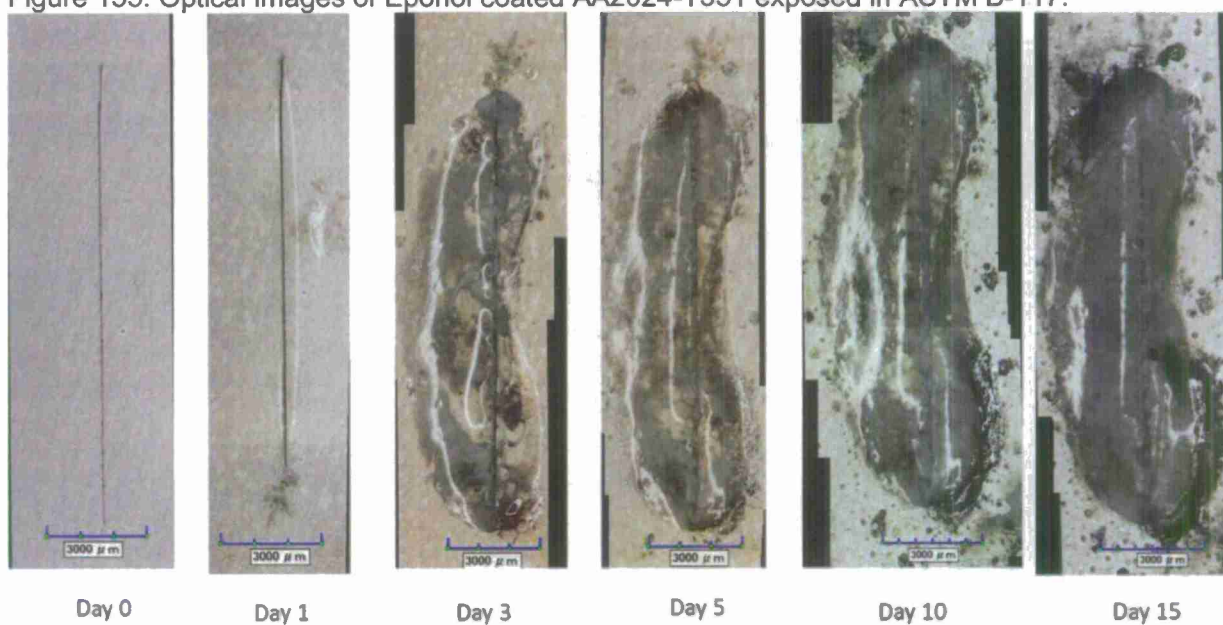


Figure 156. Optical Images of scribe creep over time for Eponol coated AA2024-T351 exposed to ASTM G-85 Annex 3.



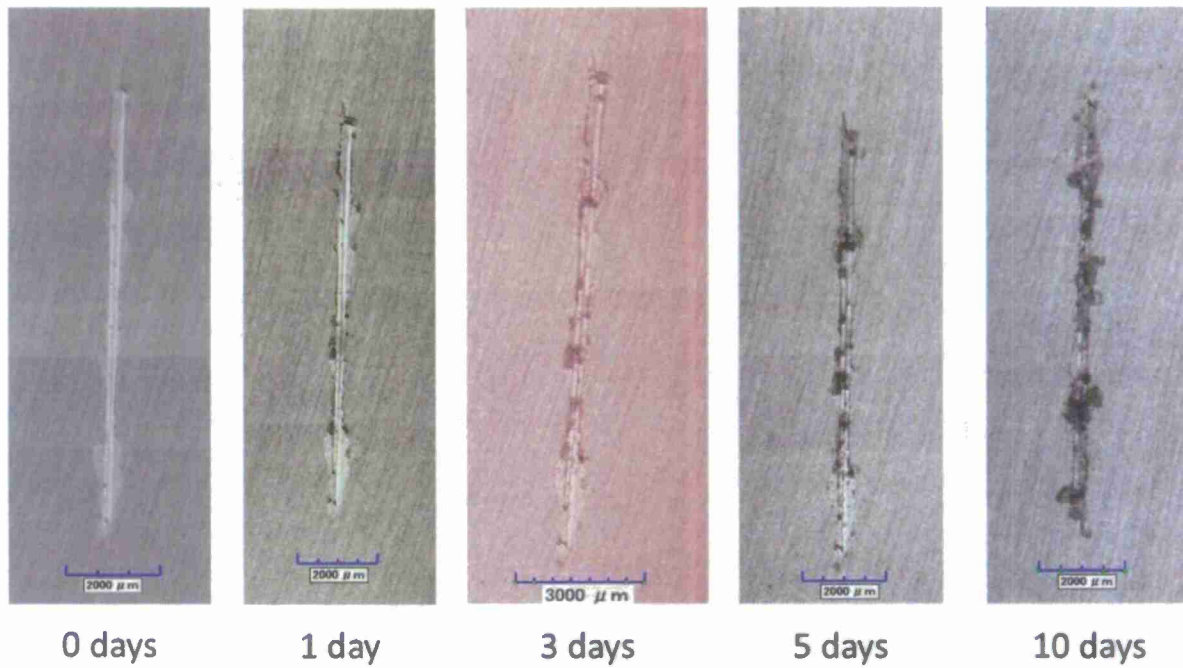


Figure 157. Optical images of the scribe on Eponol coated AA2024-T351 exposed to ASTM G-85 Annex 5.

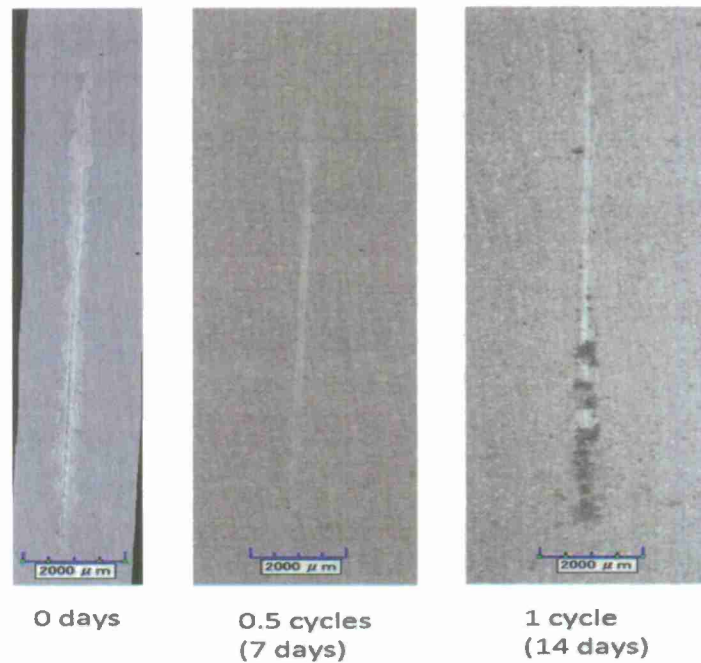


Figure 158. Optical images of the scribe on Eponol coated AA2024-T351 exposed to ASTM D-5894.



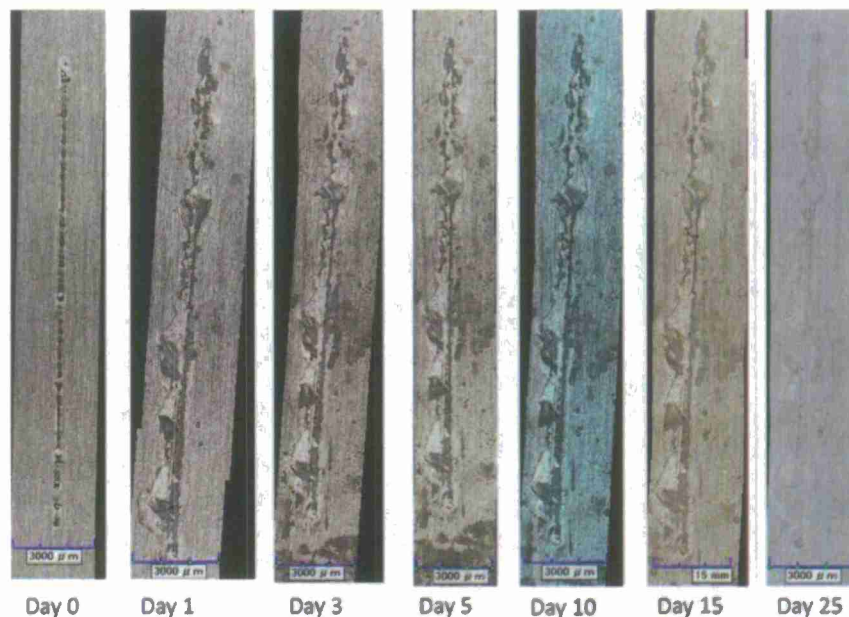


Figure 159. Optical images of the scribe on Eponol coated AA2024-T351 exposed to CC+O<sub>3</sub> (0.7-2.5 ppm).

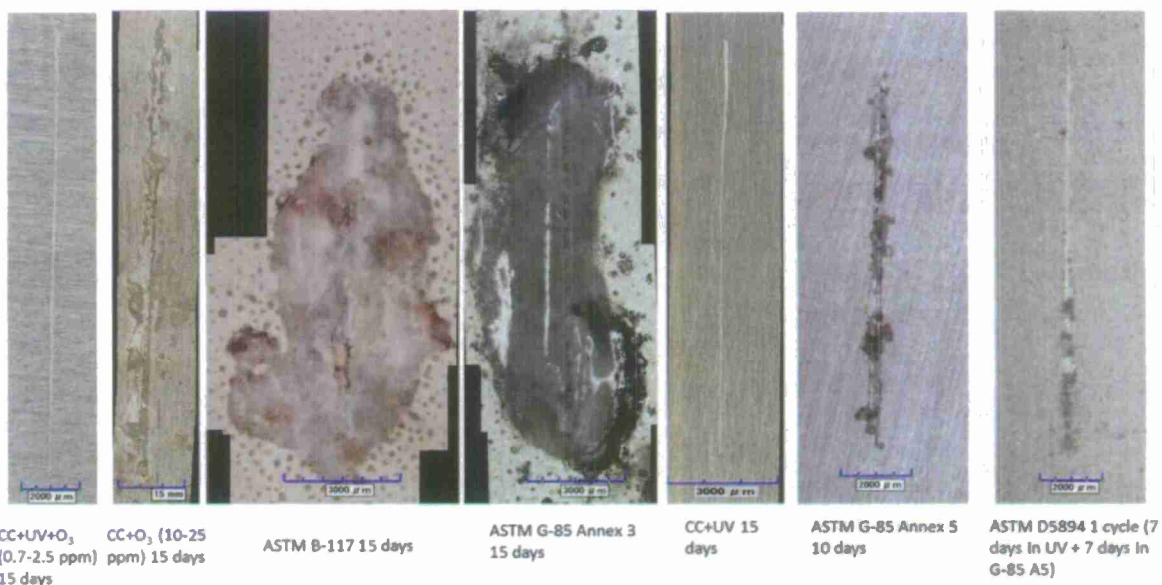


Figure 160. Optical images of eponol coated AA2024-T351 exposed in various LALTs showing the extent of scribe creep after 15 days.

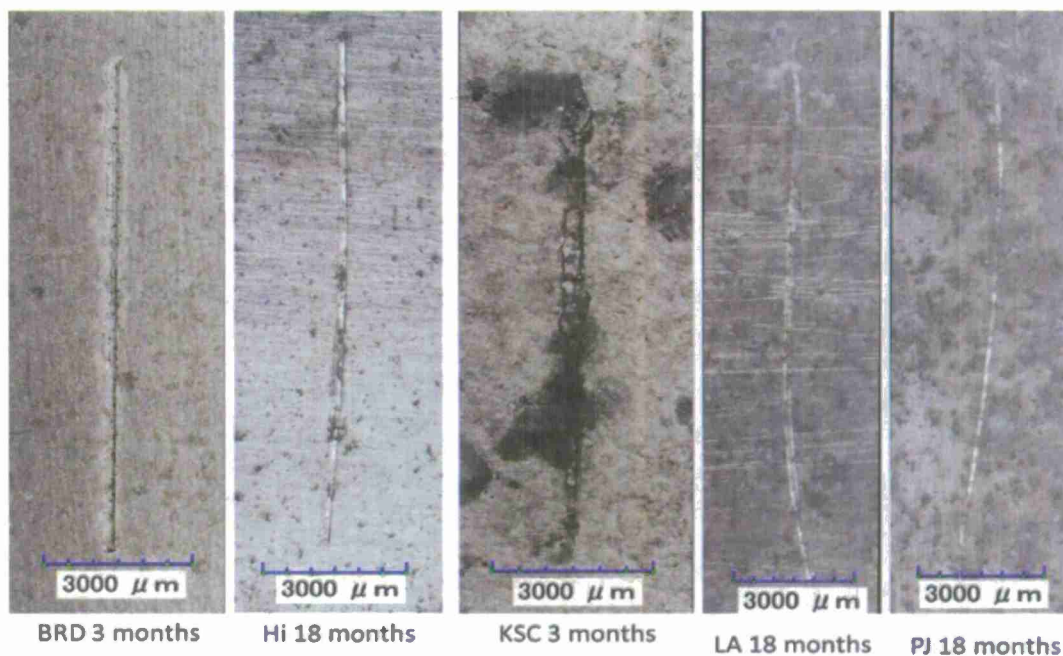


Figure 161. Optical images of eponol coated AA2024-T351 exposed at various field sites showing the extent of corrosion and scribe creep over time.

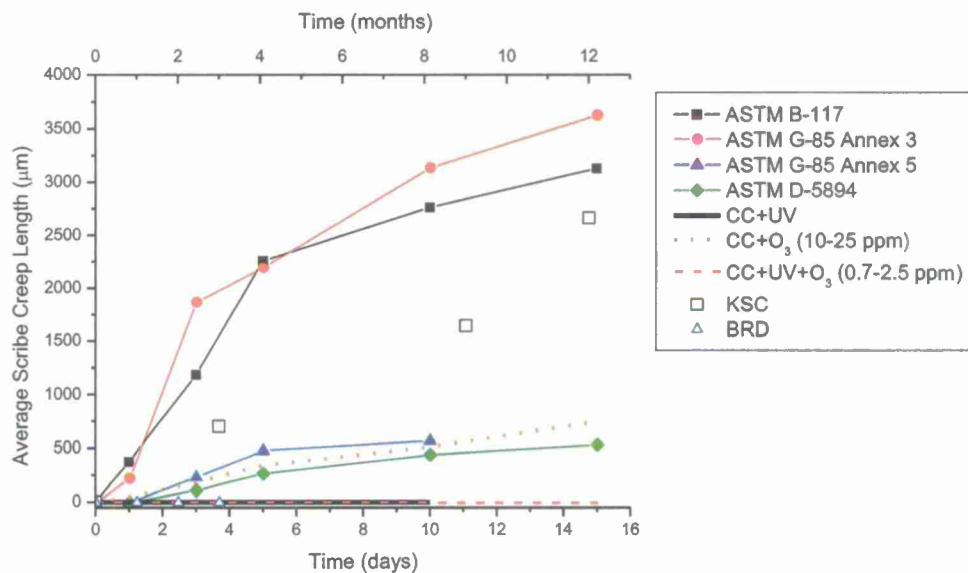


Figure 162. Scribe creep length over time for eponol coated AA2024-T351 for all LALTs and field sites. The KSC and BRD data points correspond to the upper X axis, as indicated by the arrows.

From the scribe creep data obtained, acceleration factors were calculated and are presented in Table 16. Acceleration factors were calculated based upon the time taken to reach a scribe creep length of 3000  $\mu\text{m}$ . It should be noted that some LALTs produced no noticeable scribe

creep and were therefore omitted from the table. The LALTs that produced no noticeable scribe creep obviously do not behave like KSC in that manner. Additionally, no noticeable scribe creep was seen on samples exposed at BRD, so acceleration factors with respect to BRD were not calculated. The other field sites (Hi, LA, PJ) were omitted because the overall high degradation of the coating made it difficult to determine if scribe creep had occurred.

Table 16. Acceleration factors for LALTs with respect to KSC based on scribe creep length.

Environment	AF wrt KSC
CC+O <sub>3</sub> (10-25ppm)	3.3
G-85 A3	21
G-85 A5	3.5
B-117	14
D-5894	1.9

#### 1.9.5.2 Image Analysis of Pitting on Bare AA2024-T351

Optical, CLSM and Hirox imaging of bare AA2024-T351 exposed to different environments indicated different pit morphologies as a function of standard lab and field environments. All samples were rinsed in DI water and dried before imaging. Samples exposed in high ozone environments had a high density of small pits, i.e., samples exposed in CC+O<sub>3</sub> (10-25 ppm) for 5 days had a pit density of  $7.9 \times 10^3$  pits/cm<sup>2</sup> but an average pit area of only 165  $\mu\text{m}^2$ . (Figure 163, Figure 164 and Table 17), while samples exposed at field sites shows a small number of large deep pits i.e., samples exposed at BRD had pit a pit density of 53.2 pits /cm<sup>2</sup> and an average pit area of 367  $\mu\text{m}^2$  (Figure 165 and Table 17). Image comparisons can be seen for samples exposed at field sites (Figure 166 and Figure 167) and for samples exposed in LALTs (Figure 168).

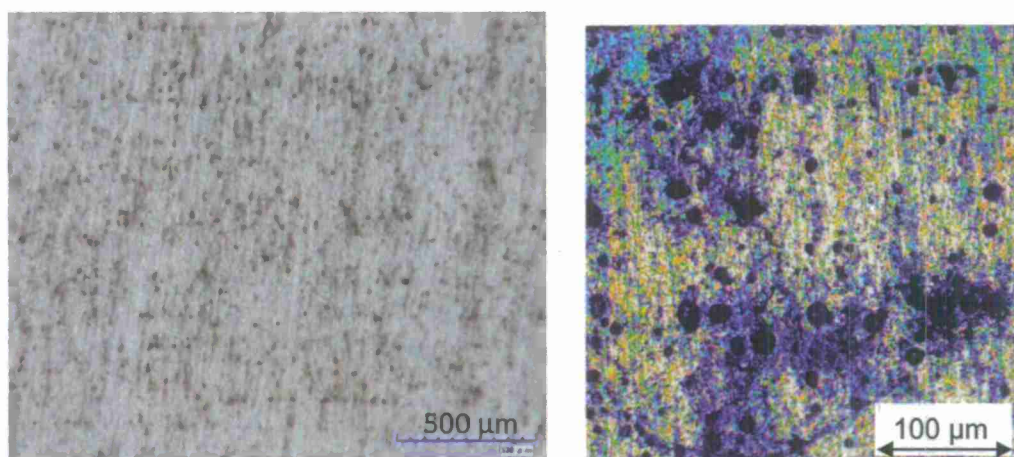


Figure 163. Optical image (left) and CSLM image (right) of pitting on bare AA2024 exposed to CC+O<sub>3</sub> (10-25 ppm) for 5 days. All samples rinsed in DI water before imaging.



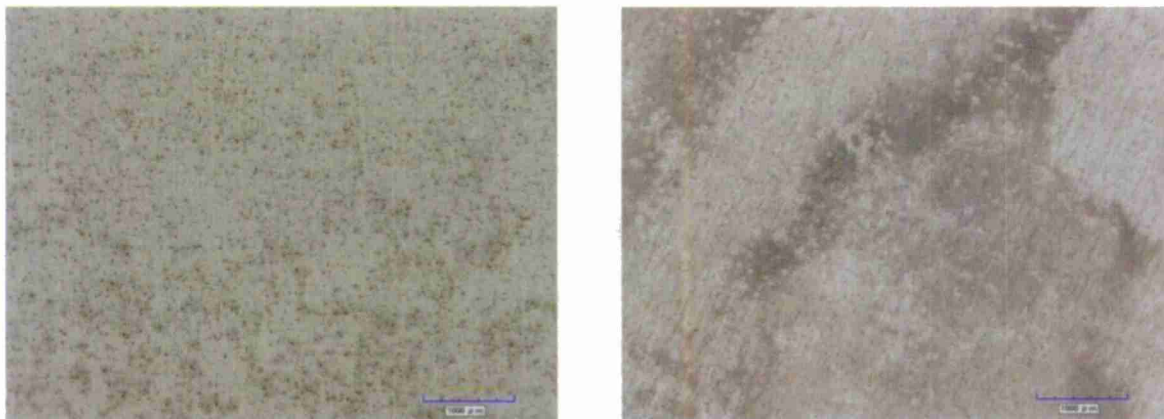


Figure 164. Optical images of pitting on bare AA2024-T351 exposed in CC+O<sub>3</sub> (0.7-2.5 ppm) for 15 days (left) and CC+O<sub>3</sub> (10-25 ppm) for 5 days (right). All samples rinsed in DI water before imaging.

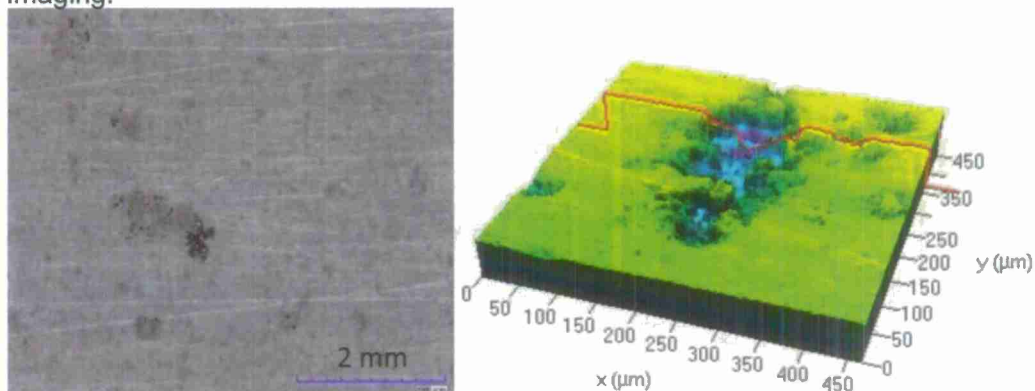


Figure 165. Optical image (left) and CLSM image (right) of pitting on bare AA2024 exposed at LA for 9 months. All samples rinsed in DI water before imaging.



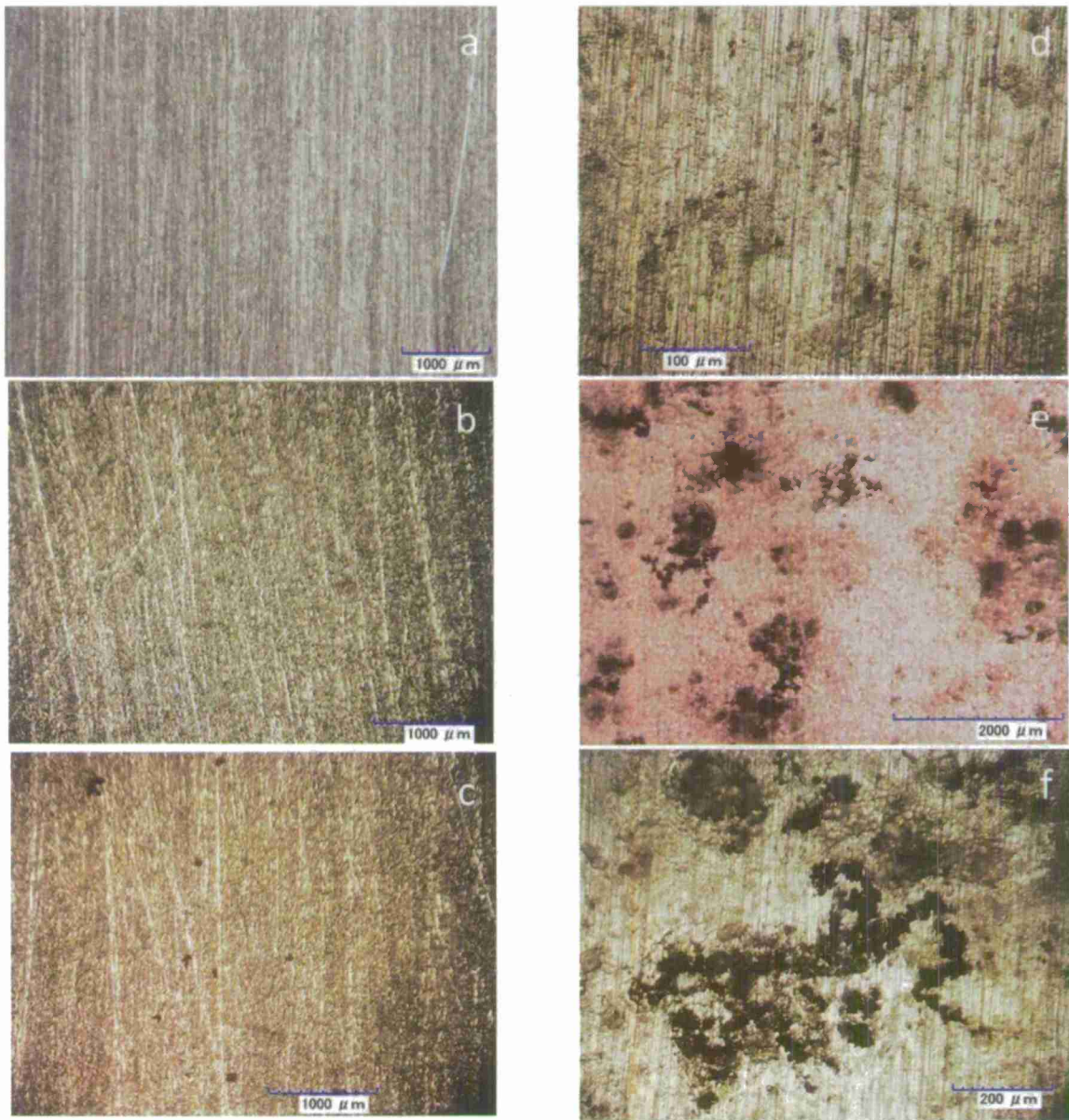


Figure 166. Optical images of pitting on bare AA2024-T351. a) unexposed sample, b) exposed at BRD for 1 month, c) Exposed at BRD for 3 months, d) Exposed at KSC for 1 month, e) exposed at KSC for 3 months, f) exposed at KSC for 3 months. All samples rinsed in DI water before imaging.

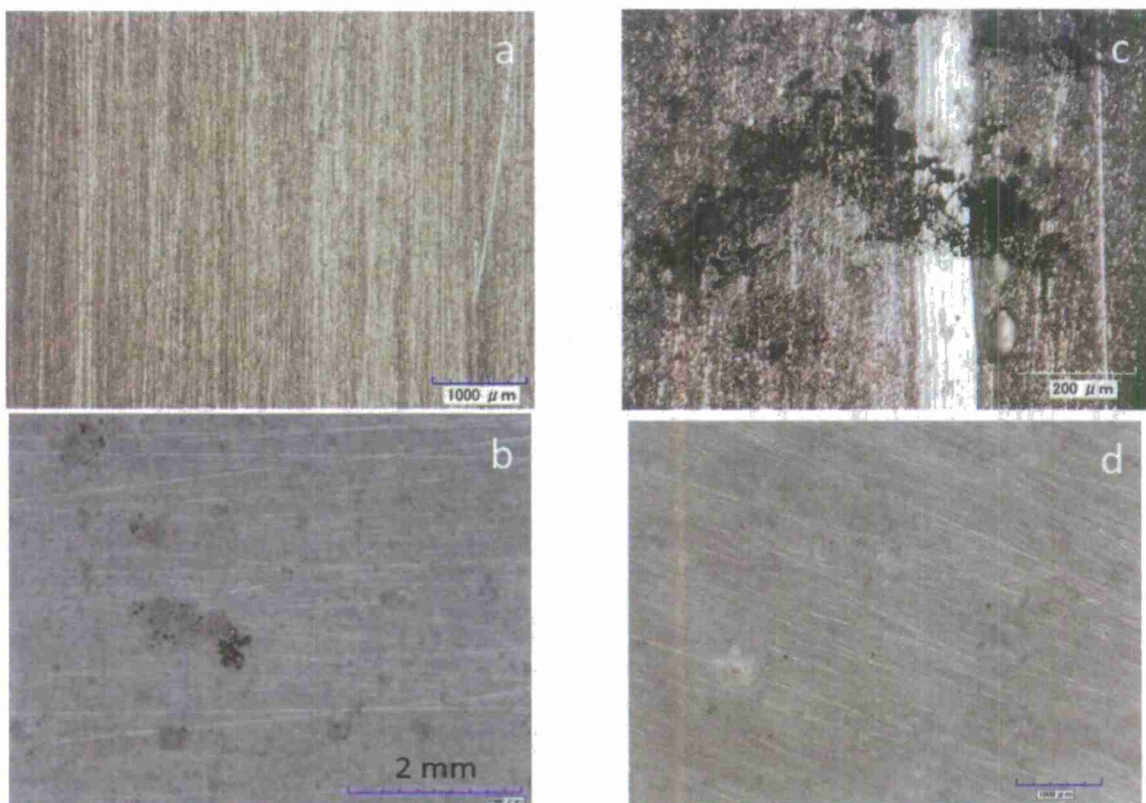


Figure 167. Optical images of pitting on bare AA2024-T351 a) unexposed, b) exposed at LA for 9 months, c) exposed at KSC for 3 months, d) exposed at PJ for 9 months. All samples rinsed in DI water before imaging.



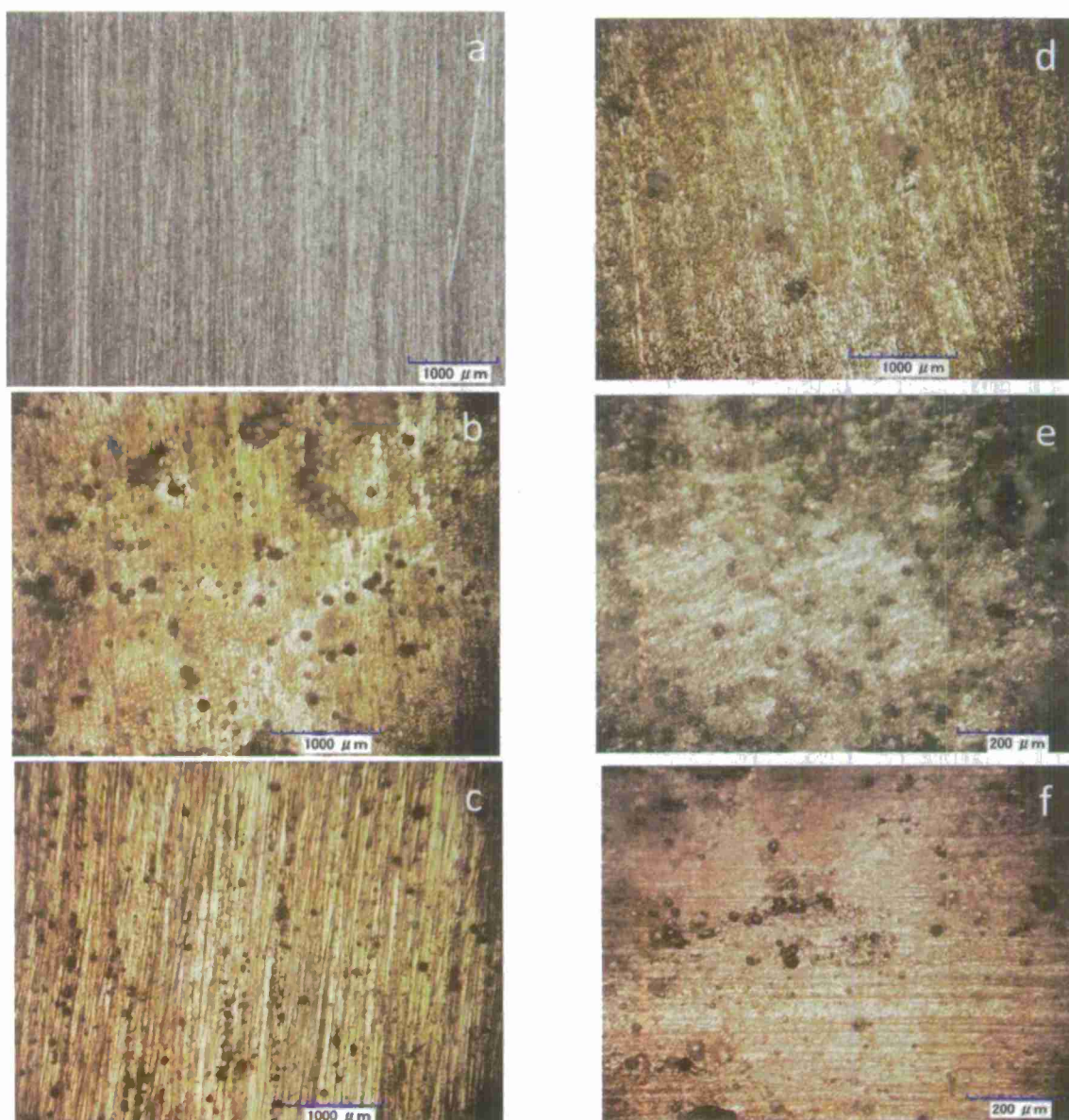


Figure 168. Optical images of pitting on bare AA2024-T351 a) unexposed, b) exposed in ASTM D-5894 for 1 cycle (14 days), c) exposed in ASTM D-4587 for 15 days, d) exposed in ASTM G-85 Annex 5 for 10 days, e) exposed in ASTM G-85 Annex 3 for 15 days, f) exposed in ASTM B-117 for 15 days. All samples rinsed in DI water before imaging.

In order to perform a quantitative measurement of pitting across the different exposure conditions, image analysis was performed using ImageJ software<sup>62</sup>. An optical image, like the one in Figure 169, was converted into a binary black and white image. The image was then processed to determine, total number of pits, total area of pits, average area per pit and the area fraction of pits. The results can be seen in Table 17. Using the results obtained from ImageJ, histograms were also constructed of the distribution of pit sizes. Due to the difference in the size of the pits the bins are not the same size for each graph. However, the general

trends can be seen. Namely, KSC and ASTM B-5894 both show large numbers of small pits but then have long tails in pit size distributions indicating a few pits that are much larger than the rest (Figure 170 and Figure 171). ASTM B-117 shows a much smaller tail in pit size distribution and a more normal distribution (Figure 172).

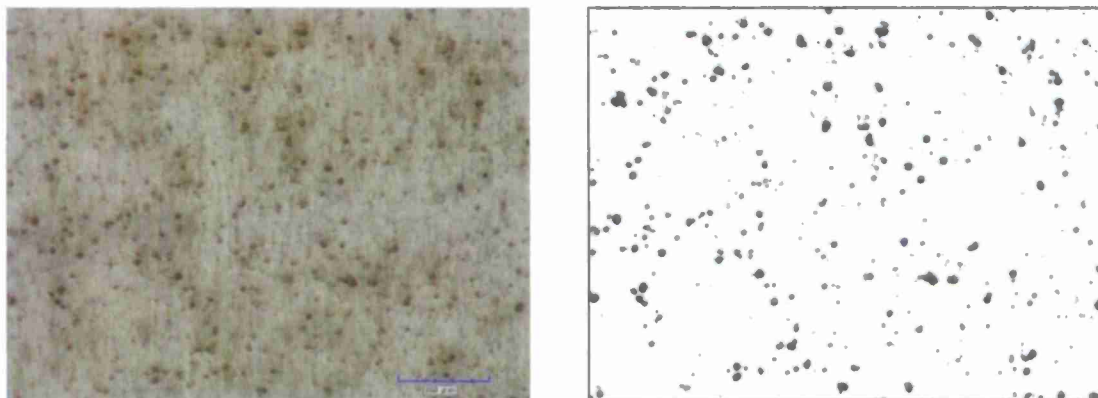


Figure 169. Optical image (left) and binary image (right) of pitting on bare AA2024-T351 exposed to CC+UV+O<sub>3</sub> (0.7-2.5 ppm) for 15 days. All samples rinsed in DI water before imaging.

Table 17. Summary of Image Analysis of Pitting on bare AA2024-T351

Exposure	Average Pit Area (μm <sup>2</sup> )	Area Fraction	Pit Density (pits/cm <sup>2</sup> )
CC+UV+O <sub>3</sub> (0.7-2.5 ppm) 15 days	289.5	5.8	2x10 <sup>4</sup>
CC+O <sub>3</sub> (10-25 ppm) 5 days	165	1.3	7.9x10 <sup>3</sup>
CC+UV 15 days	160.1	0.1	624.6
CC 15 days	90	0.3	3.3x10 <sup>3</sup>
ASTM G-85 Annex 5 15 days	331.5	0.6	1.8x10 <sup>3</sup>
ASTM D-5894 15 days	249.1	0.9	3.6x10 <sup>3</sup>
ASTM D-4587 15 days	99	0.3	3.0x10 <sup>3</sup>
ASTM B-117 15 days	102	1.3	1.3x10 <sup>4</sup>
KSC 3 months	954	10.2	1.1x10 <sup>4</sup>
BRD 1 month	0	0	0
BRD 3 months	376	0.02	53.2
PJ 3 months	228	0.8	3.5x10 <sup>3</sup>
LA 3 months	137	0.3	2.2x10 <sup>3</sup>
Hi 3 months	162	0.4	2.5x10 <sup>3</sup>

Note: Samples exposed in ASTM G-85 Annex 3 were too corroded to obtain any meaningful pitting data.



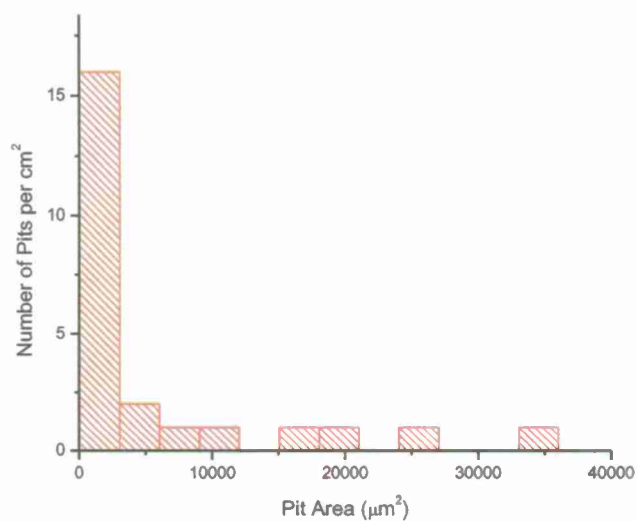


Figure 170. Histogram of pit area for bare AA2024-T351 exposed at KSC for 3 months.

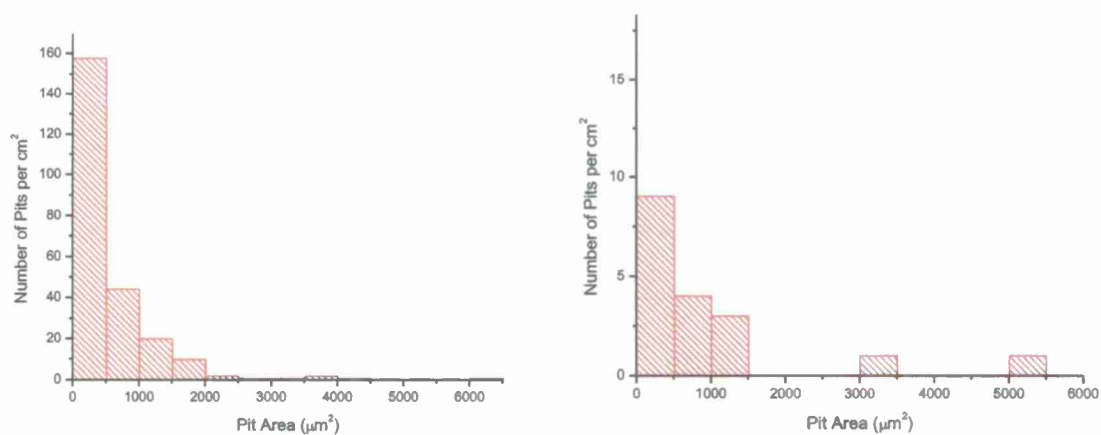


Figure 171. Histograms of pit area for bare AA2024-T351 exposed in ASTM D-5894 for 1 cycle (14 days) (left) and for samples exposed at KSC for 3 months (right). Note that the x axis scales are equal in this figure and that the x axis scales for samples exposed at KSC is different in this figure compared with Figure 170.

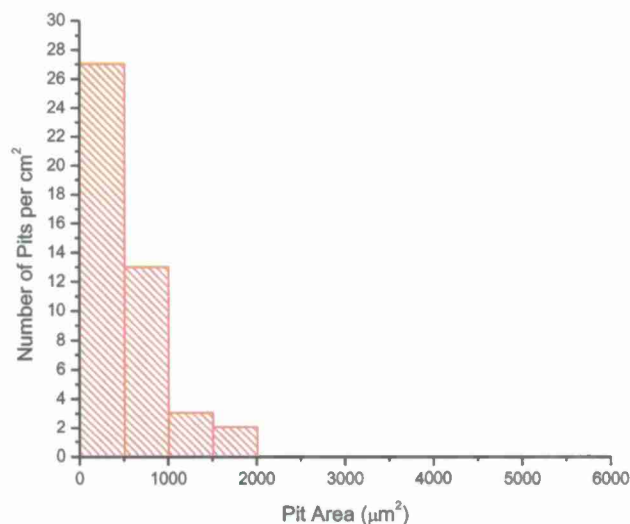


Figure 172. Histogram of pit area for bare AA2024-T351 exposed in ASTM B-117 for 15 days.

#### 1.9.5.3 SEM Analysis of Pits

During analysis of optical images, images from samples exposed in high ozone (10-25 ppm) showed different pit morphologies that were not seen in other exposures. As can be seen in Figure 173, there are gray spots that were not identified at first. This sample was cleaned for 30 seconds in a 50% nitric acid solution to remove the surface oxide for further analysis. SEM (Figure 174) and EDS (Figure 175) analysis later showed these to be pits that had been filled with oxide deposits.

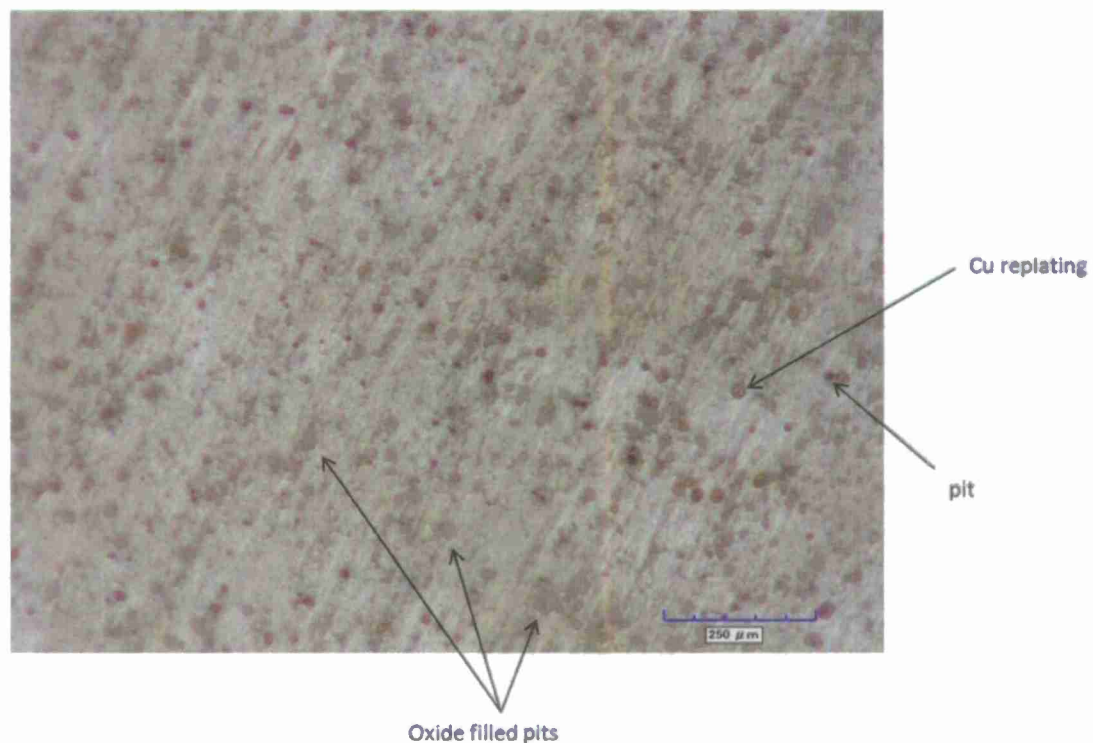


Figure 173. Optical image of AA2024-T351 exposed in CC+O<sub>3</sub> (10-25 ppm) for 5 days showing open pits, copper replating and oxide filled pits. Sample was rinsed with DI water before imaging.



Figure 174. SEM image of pit that is filled with oxide. Sample exposed in CC+O<sub>3</sub> (10-25 ppm) for 5 days. Sample was rinsed with DI water before imaging.

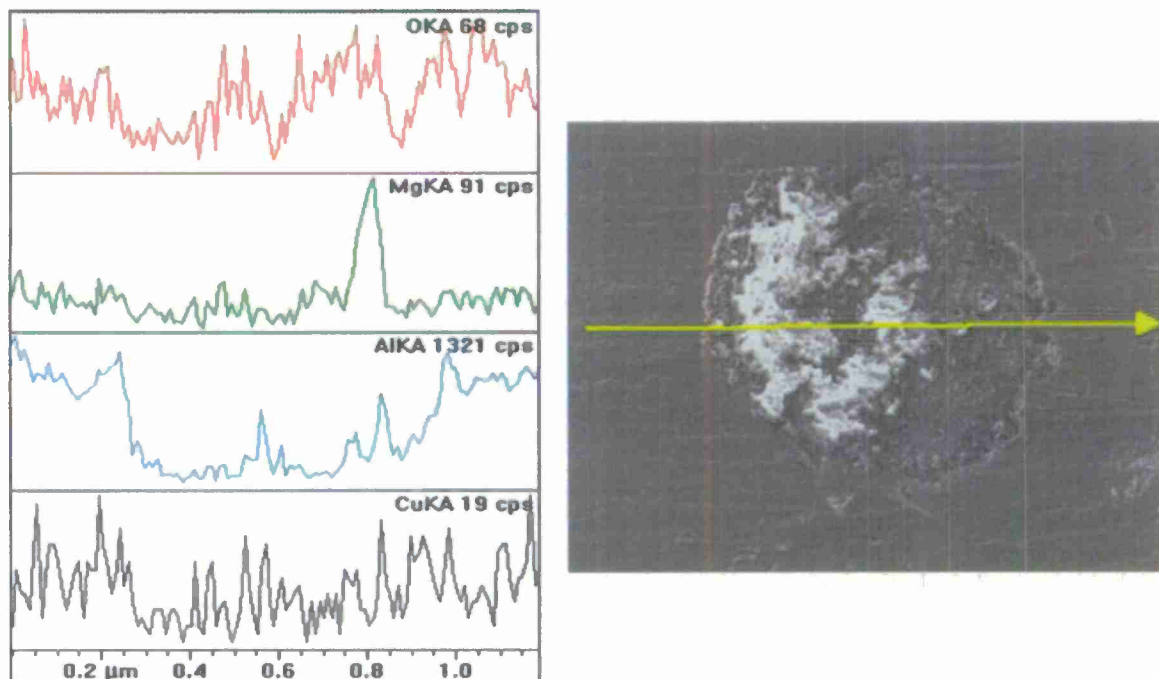


Figure 175. EDS linescan of oxide filled pit of sample exposed in  $\text{CC}+\text{O}_3$  (10-25 ppm) for 5 days. The spectra on the left show the relative abundances of oxygen, magnesium, aluminum and copper. The image on the right shows the length and direction of the scan. Sample was rinsed with DI water before imaging.

Pits exposed to high ozone (10-25 ppm) grow outward by undercutting the surface oxide layer. Figure 176 shows the pits that have grown down into the metal and have undercut the surface oxide which results in eventual collapse of the unsupported oxide. It is unclear at this time if this process creates the oxide filled pits.

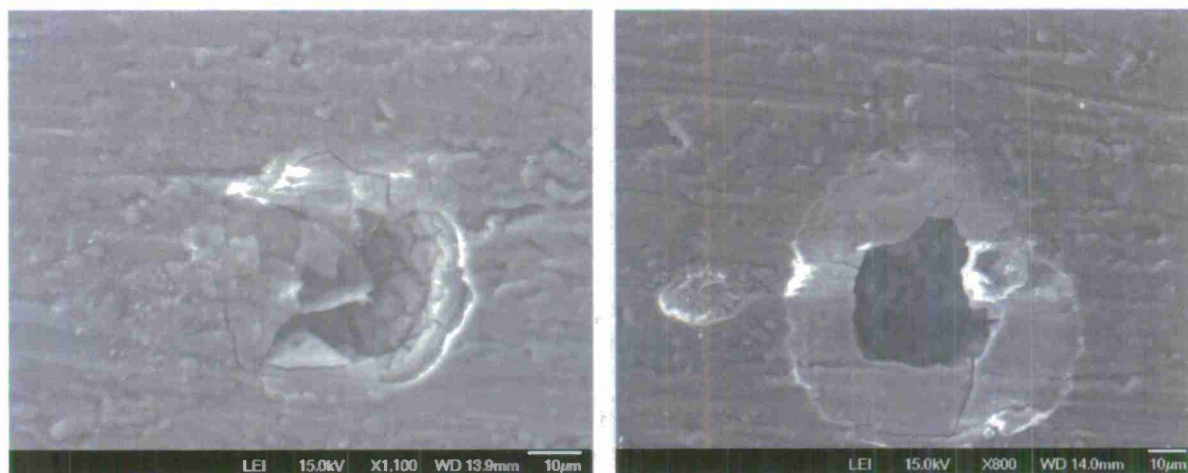


Figure 176. Images of small pits growing by undercutting the surface oxide layer on AA2024-T351 exposed to  $\text{CC}+\text{O}_3$  (10-25 ppm) for 5 days. Sample was rinsed with DI water before imaging.



Samples exposed to CC+O<sub>3</sub> (10-25 ppm) were immersed in a 60% nitric acid solution to remove the surface oxide. This was done to these samples to determine the nature of the filled pits and the material filling the pits. These samples were imaged in the SEM and the results can be seen in Figure 177. The images show both smooth pits and rough pits. The lower left image of Figure 177 shows pits growing underneath the surface oxide.

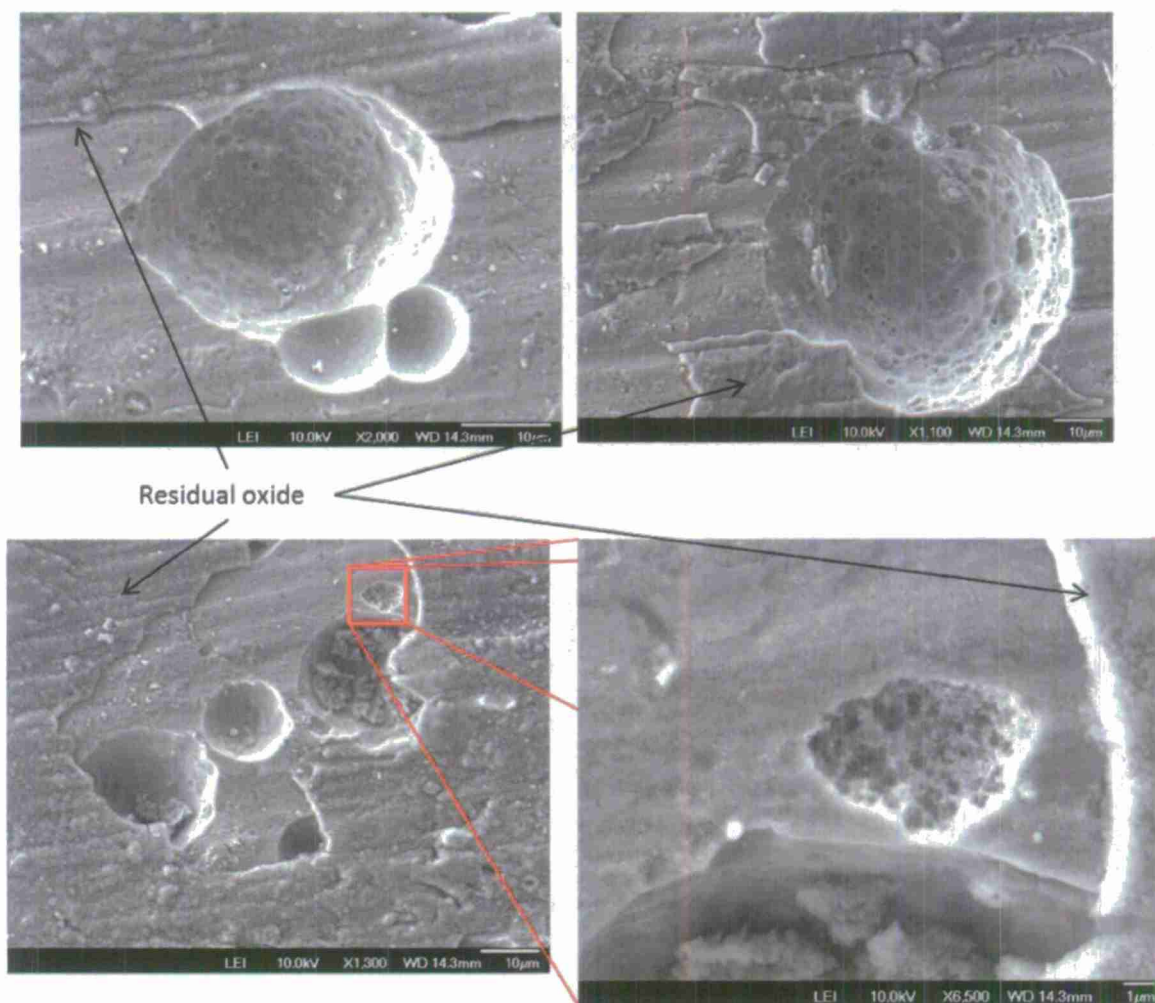


Figure 177. SEM images of AA2024-T351 exposed in CC+UV+O<sub>3</sub> (0.7-2.5 ppm) for 15 days and then immersed in 60% nitric acid solution to remove the surface oxide. Sample was rinsed with DI water before imaging.

SEM imaging of samples exposed in different conditions also showed the differences in pit morphology between differing exposure conditions. Samples exposed in high ozone showed a large number of small pits (Figure 163, Figure 176). Samples exposed in CC+UV+O<sub>3</sub> (0.7-2.5 ppm) showed fewer pits that were larger than the pits in the high ozone exposure (Figure 169, Table 17). These samples also showed many small surface oxide particles that were absent from the samples exposed to high ozone without UV (Figure 178). Samples exposed at field sites showed pits that were very different from the LALT exposed samples. Figure 179 shows the cracked and broken morphology that was commonly seen in samples exposed at field sites.

These pits were generally larger and farther apart than the pits in LALT exposed samples. Subsequent EDS analysis showed an abundance of sodium in the pit indicating the presence of sodium chloride.

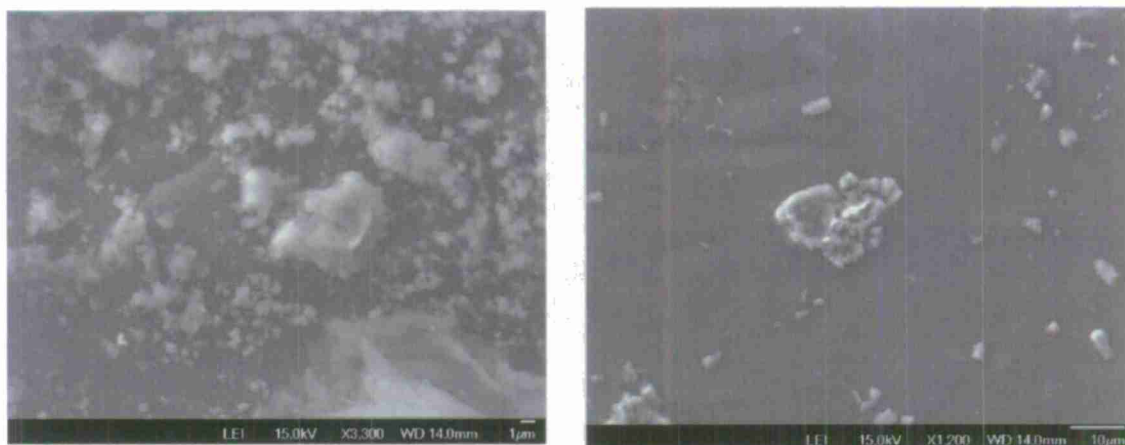
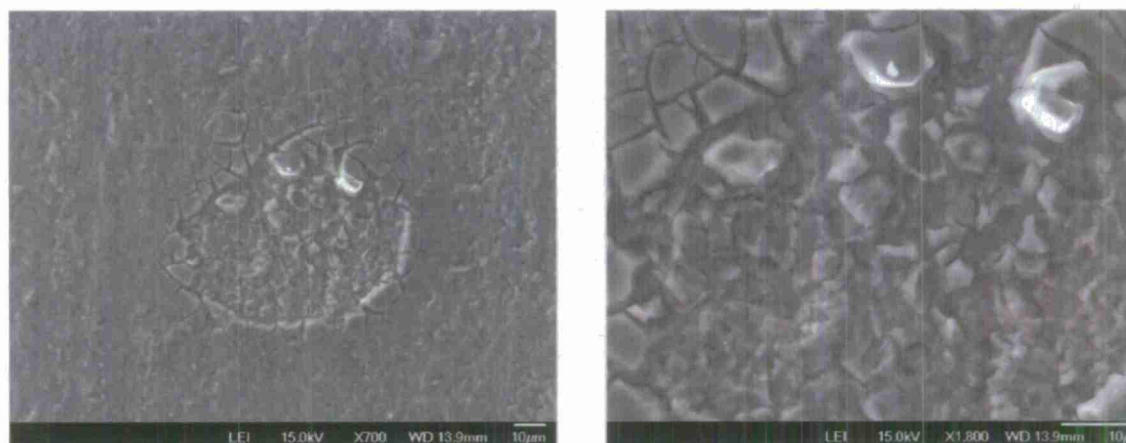


Figure 178. SEM images of AA2024-T351 exposed to CC+UV+O<sub>3</sub> (0.7-2.5 ppm) for 15 days showing oxide particles on the surface of the sample. The particles were absent from samples exposed in other conditions. Sample was rinsed with DI water before imaging.



1.9.5.4  
Figure 179. SEM images of AA2024-T351 exposed at LA for nine months showing pit morphology characteristic of samples exposed at field sites. Sample was rinsed with DI water before imaging.

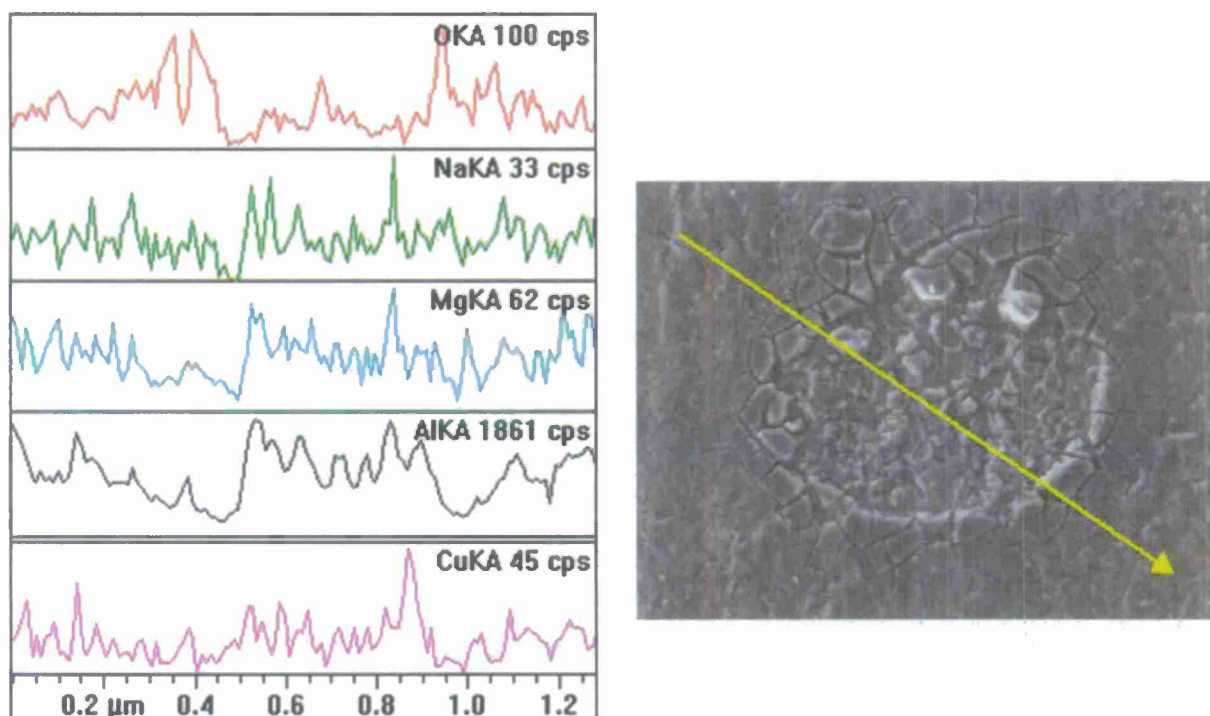


Figure 180. EDS spectra (right) of a pit on AA2024-T351 exposed at LA field site for 9 months. The image on the right shows the direction of the scan. Sample was rinsed with DI water before imaging.

#### 1.9.5.5 Analysis of coated samples by Electrochemical Impedance Spectroscopy (EIS)

AA2024-T351 samples exposed to various LALTs and field environments listed in Table 13 and Table 15 were examined by EIS. The EIS data has been obtained from the LALTs and the field sites over exposure times. EIS data was taken at two locations on the sample, near to the scribe and far from the scribe (see Figure 152). The EIS data is presented below, starting with KSC (Figure 181) and BRD (Figure 182). KSC shows degradation of the coating electrical properties nearly equally both near to and far from the scribe. This is indicative of an ESF that attacks the coating specifically and only moderate corrosion conditions that attack the bare metal at the scribe. LALTs that have no ESF that attacks the coating specifically, like ASTM B-117 and ASTM G-85 Annex 5, show more coating degradation near to the scribe where corrosion occurs than far from the scribe (Figure 183 and Figure 185). Thus, one significant difference is whether ESFs affect the coating or induce corrosion which is reflected by scribe creep and particularly a drop in EIS parameters near the scribe. Samples exposed in ASTM G-85 Annex 3 show nearly equal drop in EIS parameters near to and far from the scribe, this is most likely due to the acidic nature of the test. The non-standard LALTs show nearly equal degradation both near and far for all tests incorporating either UV or ozone (Figure 188 through Figure 190). Acceleration factors were calculated for the LALTs base on the low frequency impedance values ( $Z_{[0.01]}$ ). The acceleration factors are reported in Table 18.

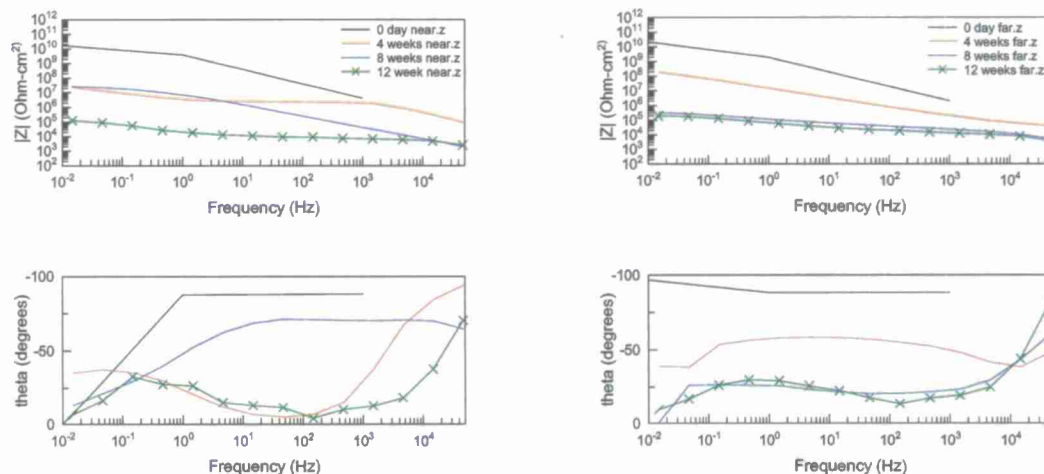


Figure 181. EIS data for coated AA2024 exposed at Kennedy Space Center, FL. Left is near and right is far.

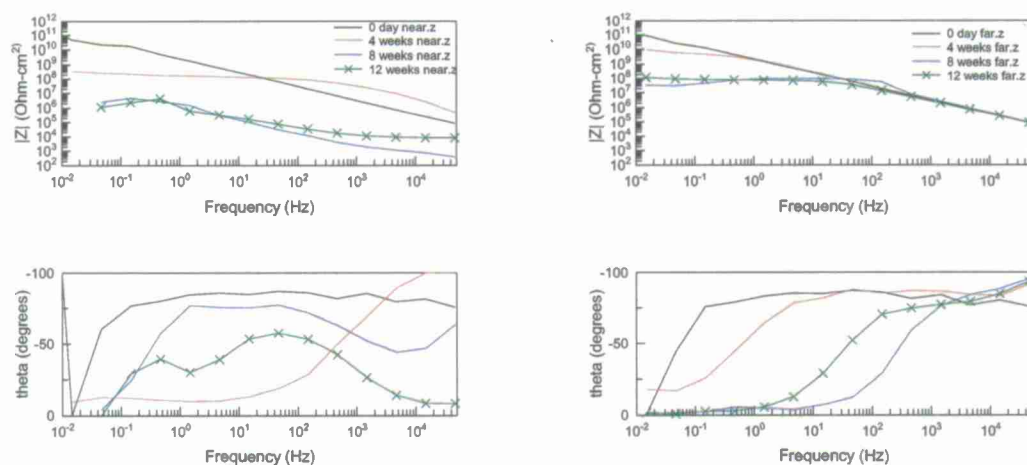


Figure 182. EIS data for coated AA2024 exposed at Birdwood Golf Course, Charlottesville VA (BRD). Left is near and right is far.



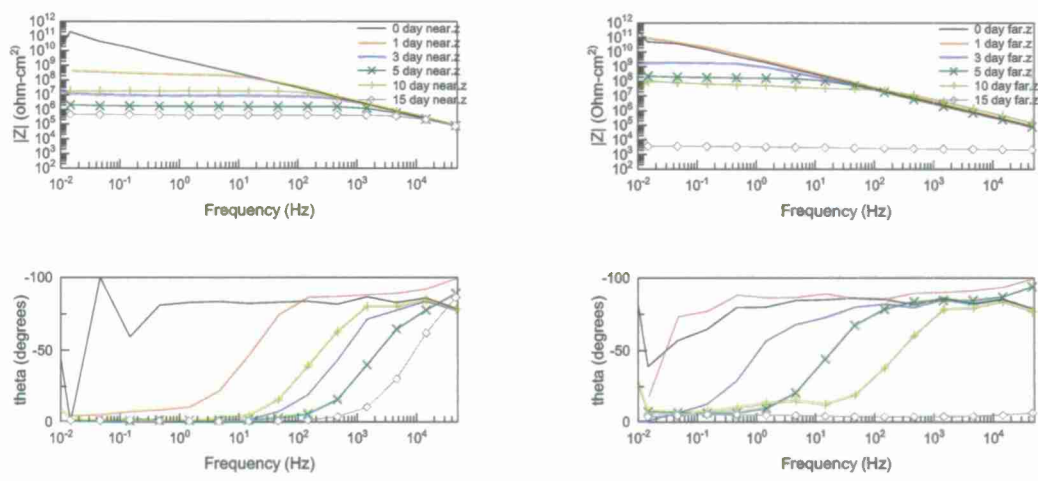


Figure 183. EIS data for coated AA2024 exposed to ASTM B-117. Left is near and right is far.

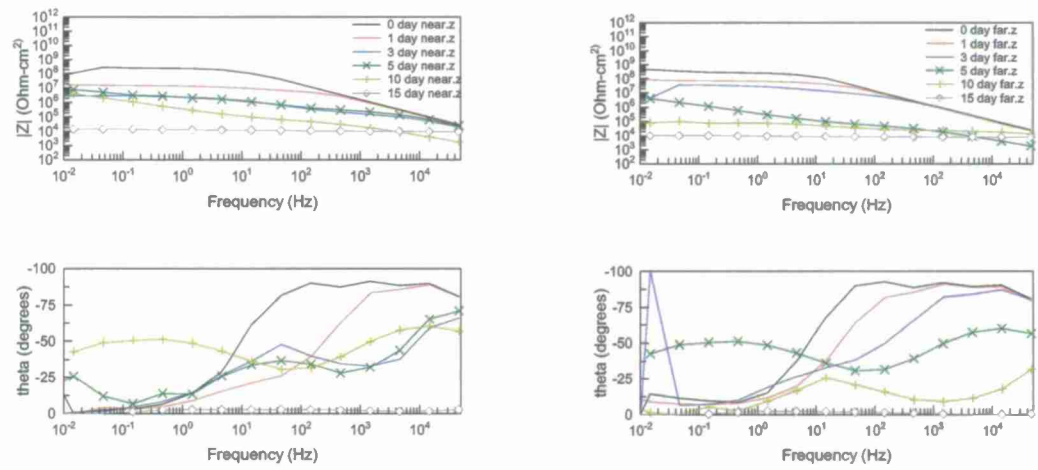


Figure 184. EIS data for coated AA2024 exposed to ASTM G-85 Annex 3. Left is near and right is far.

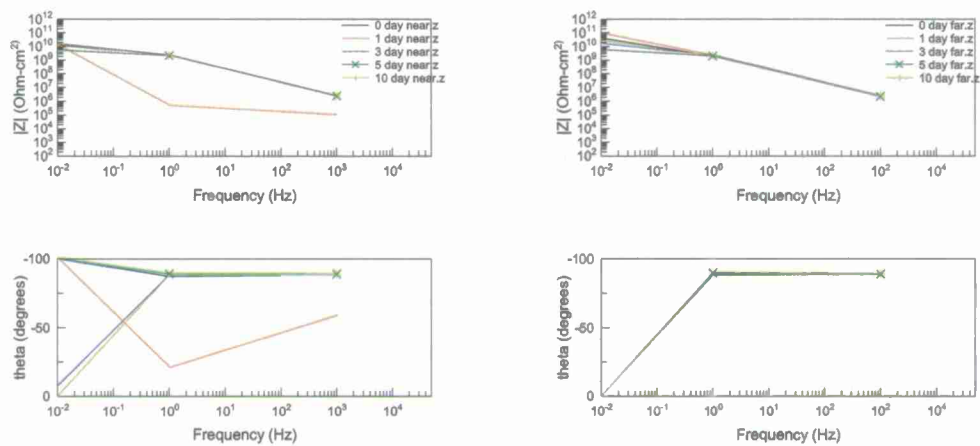


Figure 185. EIS data for coated AA2024 exposed to ASTM G-85 Annex 5. Left is near and right is far.

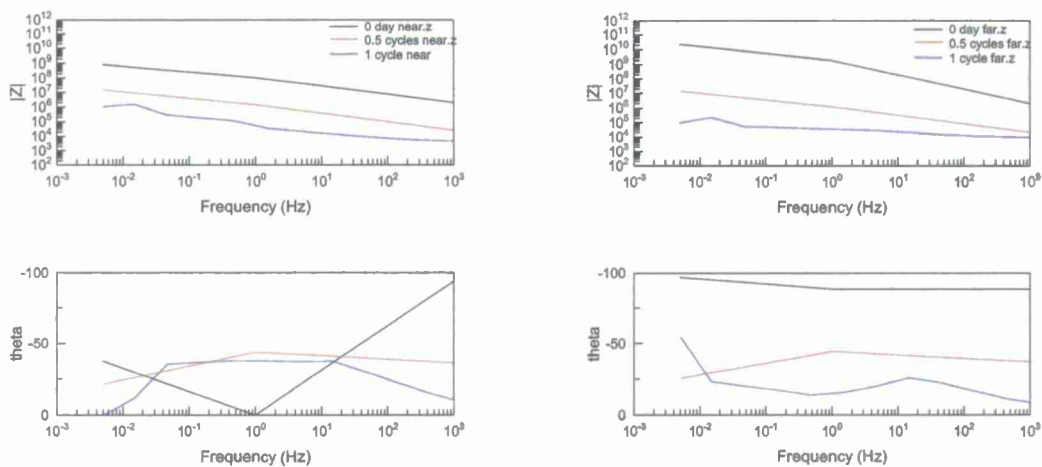


Figure 186. EIS data for coated AA2024 exposed in ASTM D-5894. Left is near and right is far.

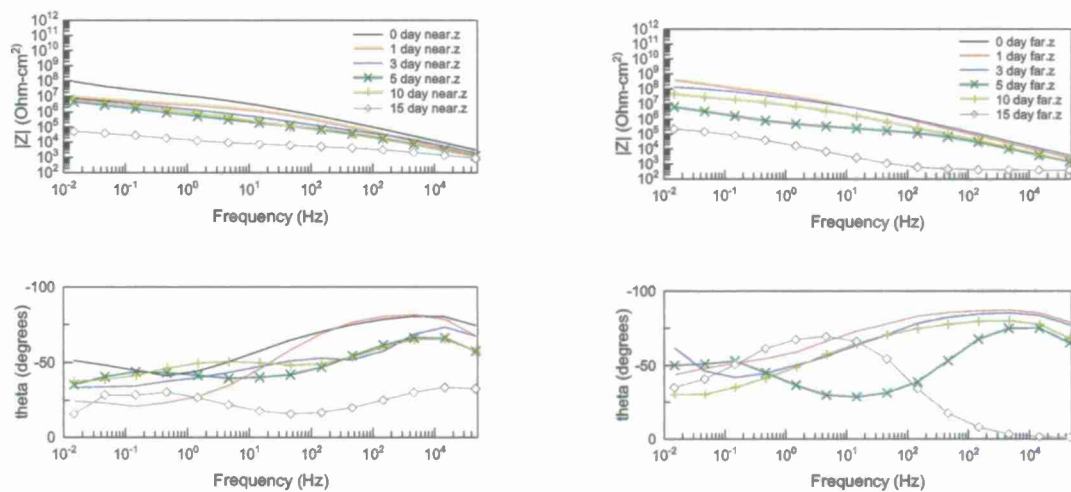


Figure 187. EIS data for coated AA2024 exposed to CC. Left is near and right is far.

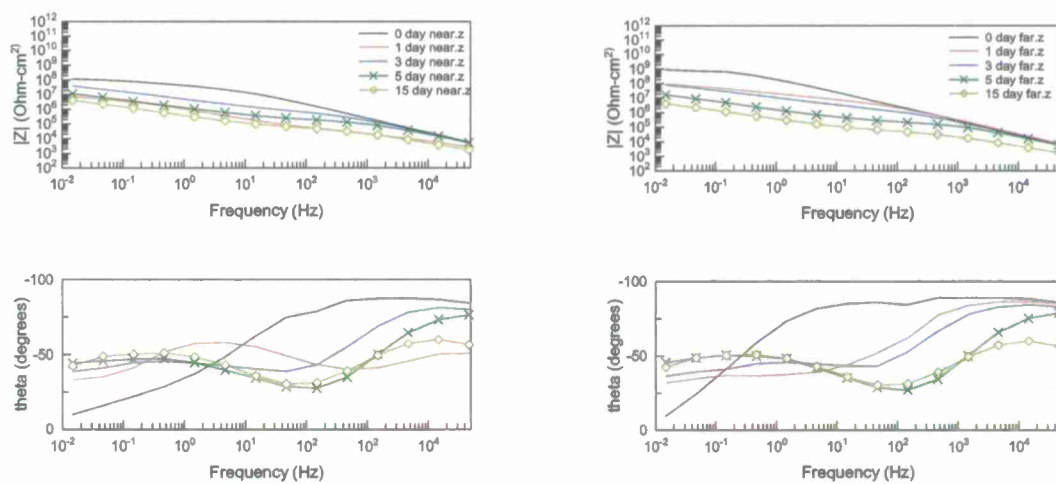


Figure 188. EIS data for coated AA2024 exposed to CC+UV. Left is near and right is far.

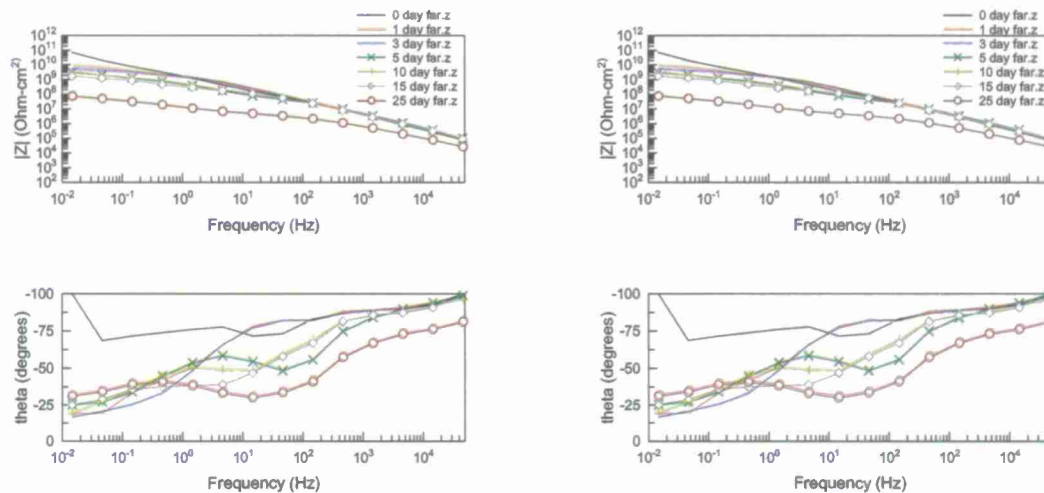


Figure 189. EIS data for coated AA2024 exposed to CC+O<sub>3</sub> (0.7-2.5ppm). Left is near and right is far.

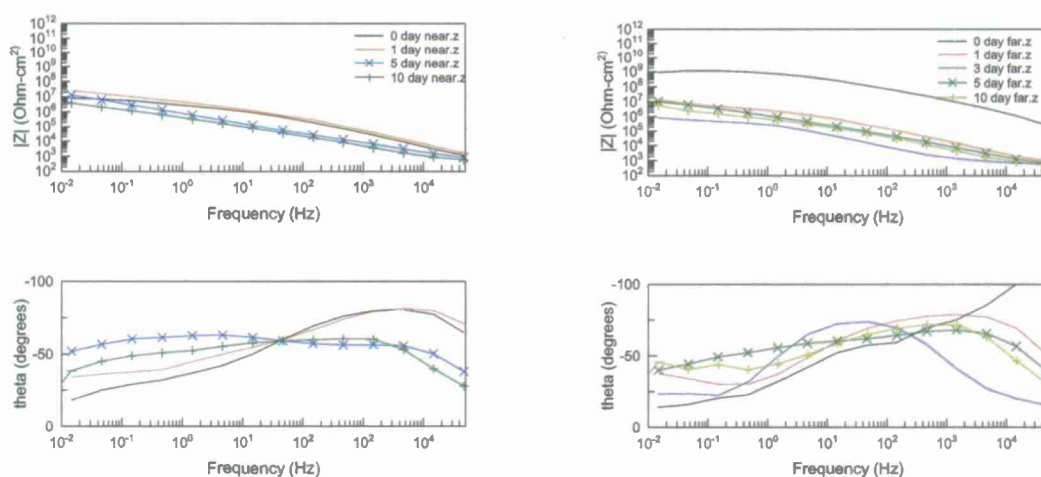


Figure 190. EIS data for coated AA2024 exposed to CC+UV+O<sub>3</sub> (0.7-2.5ppm). Left is near and right is far.



Table 18. Acceleration factors for AA2024-T351 based on low frequency impedance ( $Z_{0.01}$ ).

Test	AF wrt BRD	AF wrt KSC	AF wrt Hi	AF wrt LA	AF wrt PJ
CC+UV	5.6	2.8	3.27	3.83	2.13
CC+O3(10-25ppm)	16.8	8.4	9.8	11.5	6.4
CC+O3(0.7-2.5ppm)	3.36	1.68	1.96	2.3	1.28
CC+UV+O3(0.7-2.5ppm)	11.2	5.6	6.53	7.7	4.27
ASTM G-85 A3	16.8	6.3	9.8	11.5	6.4
ASTM G-85 A5	4.48	1.68	2.61	3.07	1.71
ASTM B-117	9.6	3.6	5.6	6.57	3.66
ASTM D-5894	12	4.5	7	8.2	4.6

EIS data can provide a wealth of information. In addition to the change in the electrical resistance of the coating over time (previous EIS plots), the saddle frequency method was used to determine the defect area of the coating<sup>28</sup>. The coated metal was modeled as an equivalent circuit (Figure 191). Constant Phase Elements (CPEs) were used instead of ideal capacitors because of the tendency for coatings to behave somewhere between a pure capacitor and a pure resistor<sup>66</sup>.  $R(\text{soln})$  is the solution resistance,  $R(\text{pore})$  and CPE2 are the pore resistance and coating capacitance respectively, and the  $R_{dl}$  and CPE1 are the resistance and capacitance of the solution double layer that forms at the solution/coating interface. Pore resistance is the electrical resistance of the pores in the coating<sup>28, 29</sup>. As the size and defective nature of the pores increases, the resistance of the pores decreases.

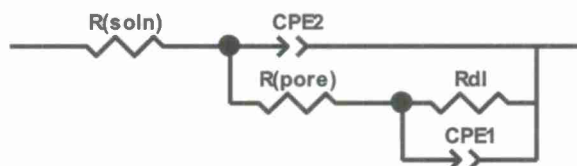


Figure 191. The equivalent circuit model for an organically coated metal.  $R(\text{soln})$  is the solution resistance,  $R(\text{pore})$  is the resistance of the pores in the coating,  $R_{dl}$  is the double layer resistance, CPE2 is the coating capacitance and CPE1 is the double layer capacitance.

Figure 192 shows the EIS results of a computer simulation of the circuit in Figure 191 with increasing pore area over time. From Figure 192, it can be seen that as the pore resistance of the coating decreases over time, the saddle frequency decreases as well. This indicates that the number, size, and defective nature of pores is increasing which corresponds to increase in the defect area of the coating.

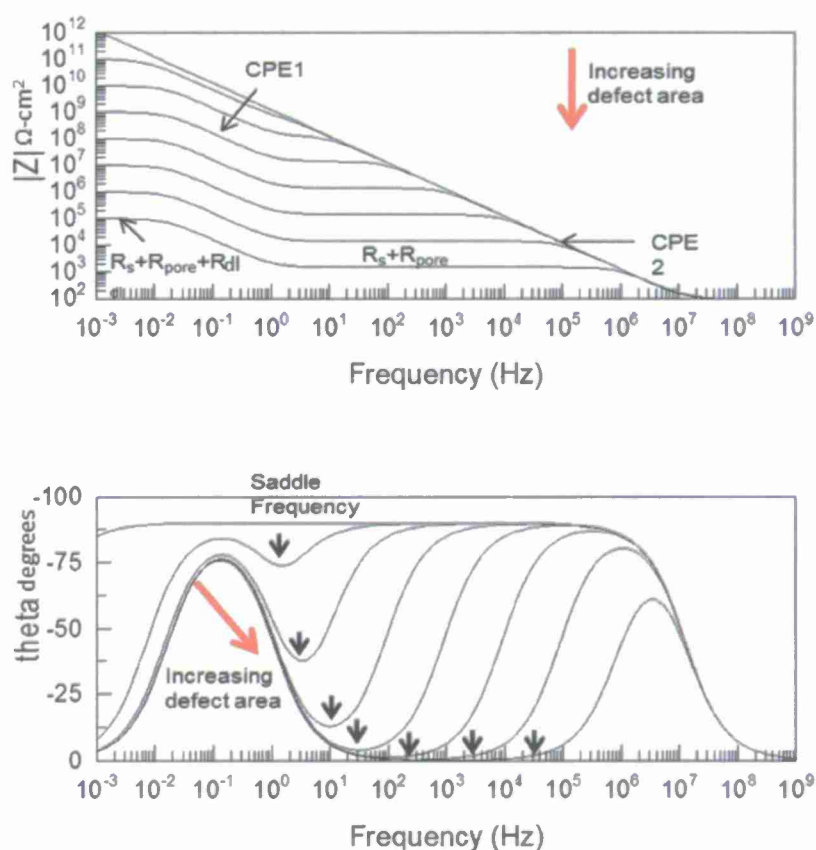


Figure 192. Example of the data that can be obtained from EIS. Saddle frequency decreases as  $R_{pore}$  decreases. For this simulation,  $R_s$  was  $10 \Omega\text{-cm}^2$ ,  $R_{pore}$  varied from  $10^{12}$  to  $10^3 \Omega\text{-cm}^2$ ,  $R_{dl}$  varied from  $10^8$  to  $10^4 \Omega\text{-cm}^2$ , and the total area was  $1 \text{ cm}^2$ .

From the phase angle plots (the lower plots on the EIS figures), the saddle frequency was determined. This data was graphed for LALT and field exposed samples and is presented in Figure 193. The change in saddle frequency over time shows an increase in pore area over time that is undetectable by visual methods. This data also enabled the calculation of acceleration factors by comparing the change in saddle frequency over time (Figure 193). Acceleration factors were calculated by comparing the time to reach a saddle frequency of 10 kHz for LALTs to field sites. This was done for each field site with respect to each LALT used and the results can be seen in

Table 19.

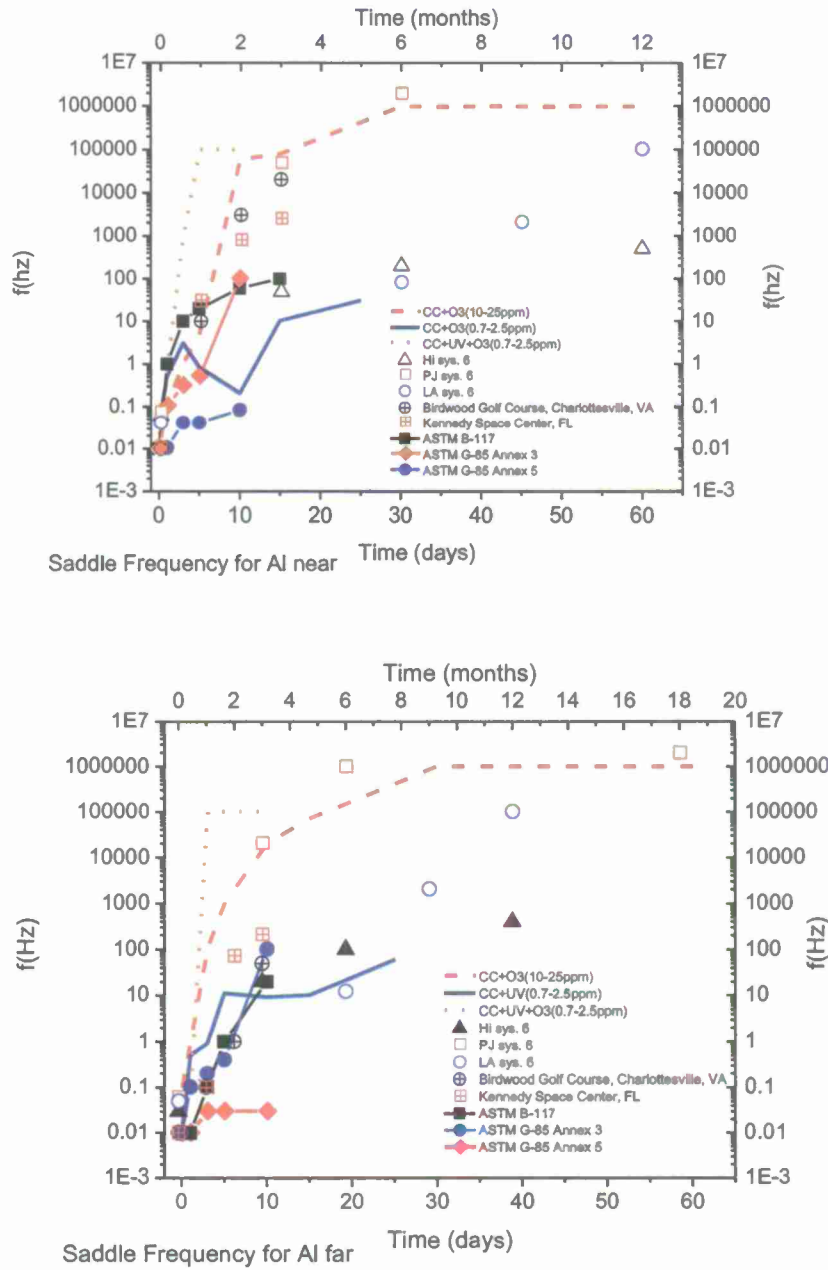


Figure 193. Saddle frequency plots for coated AA2024 exposed to various environments. The top plot is data taken from the Near location. The bottom plot is data taken from the Far location. Open symbols represent data for samples exposed at field sites; time is on the top axis for the field sites.

Table 19. Acceleration factors for AA2024-T351 based on saddle frequency.

Environment	AF wrt BRD	AF wrt KSC	AF wrt Hi	AF wrt LA	AF wrt PJ
CC+UV	6	5	16	10	3
CC+O3(10-25ppm)	18	15	29	30	7.83
CC+O3(0.7-2.5ppm)	9	7.5	24	15	4.5
CC+UV+O3(0.7-2.5ppm)	36	30	155	95	25
ASTM G-85 A3	6.4	5.36	17.14	10.7	3.21
ASTM G-85 A5	1	0.83	5.7	3.45	0.825
ASTM B-117	2.57	2.14	8	5	1.2
ASTM D-5894	12.8	10.7	34.2	21.4	6.4

By fitting the data from the samples to the equivalent circuit in Figure 191 using the parameters CPE1, CPE2,  $R_{\text{pore}}$  and  $R_{\text{dl}}$ , values for  $R_{\text{pore}}$  were calculated. The Z-view software package iteratively changes the parameters of the equivalent circuit until a fitting curve is found<sup>66</sup>. An example of such a fit is given in Figure 194.  $R_{\text{pore}}$  values were determined which shows the specific degradation of the electrical resistance of the coating over time (Figure 195).

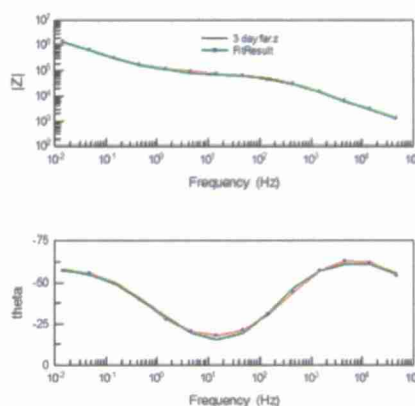


Figure 194. EIS data and equivalent circuit fit Eponol coated AA2024-T351 exposed to CC+O<sub>3</sub> (0.7-2.5 ppm) for 3 days. Data taken at the far location (see Figure 152).



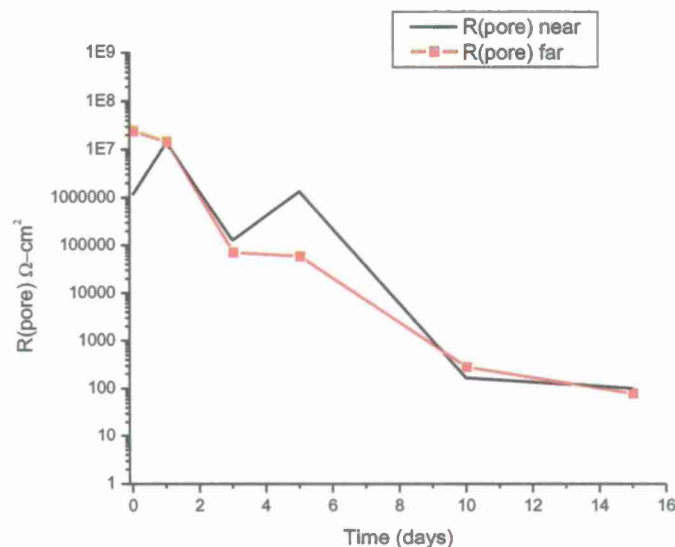


Figure 195.  $R_{\text{pore}}$  values for Eponol coated AA2024-T351 exposed in  $\text{CC}+\text{O}_3$  (0.7-2.5 ppm). EIS data was taken at near and far locations and then fit to an equivalent circuit to obtain  $R_{\text{pore}}$ . It was shown previously that the breakpoint frequency method<sup>28, 29</sup> and data fitting can be used to obtain  $R_{\text{pore}}$  values for the coated AA2024-T351. With  $R_{\text{pore}}$  the defect area of the coating can be calculated using Equation 14. Where  $A_d$  is the defect area,  $\rho$  is the intrinsic resistivity of the coating (assumed to be  $10^6 \Omega\text{-cm}$ ), and  $d$  is the thickness of the coating ( $30 \mu\text{m}$ ). Graphing Equation 14 shows the relationship between pore resistance and defect area of the coating (Figure 196). Figure 196 also demonstrates the ability of EIS to detect changes in  $R_{\text{pore}}$  and thus, defect area long before the defect area becomes large enough to be visible to the naked eye.

$$A_d = \frac{\rho \cdot d}{R_{\text{pore}}}$$

14

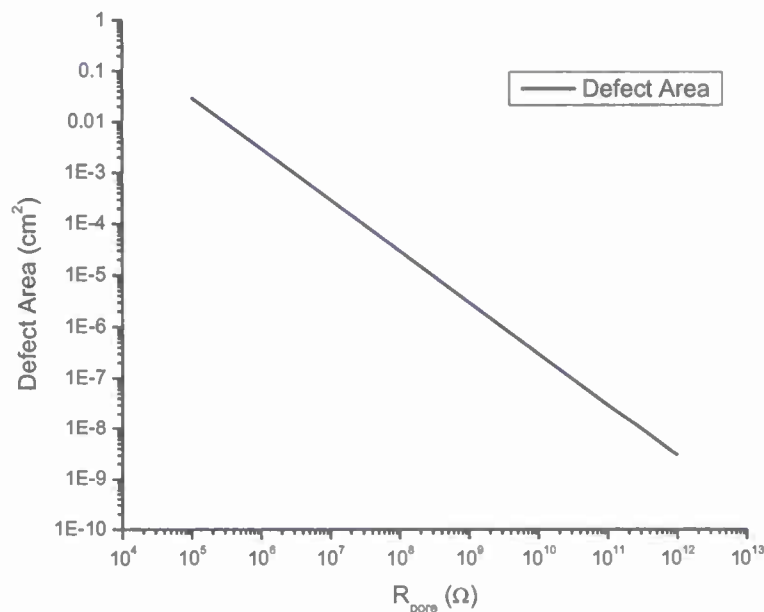


Figure 196. Graph of Equation 14 showing the increase in electrical defect area associated with the decrease of  $R_{\text{pore}}$ .

Additionally, the importance of saddle frequency can be seen in Figure 197. The relationship between saddle frequency and electrical defect area of the coating can be seen. There are also two other parameters,  $f_{45}$  (low) and  $f_{45}$  (high), also called the lower and higher breakpoint frequencies. These parameters are determined from the plot of Phase angle (the lower plot in Figure 192) where the curves cross a line drawn at  $-45$  degrees. The lower breakpoint frequency ( $f_{45}$  (low)) is dependent on defect area for very small defects when  $f_{45}$  (high) cannot be resolved, while  $f_{45}$  (high) is always dependent on defect area and becomes resolvable as the defect area increases<sup>28</sup>.

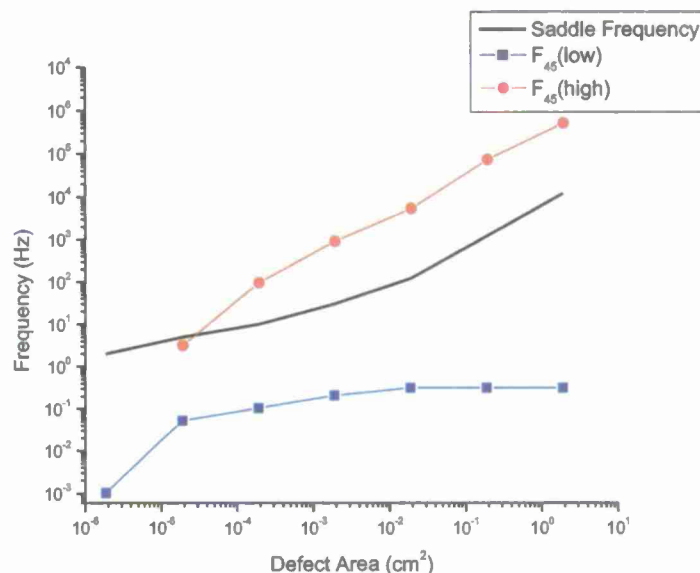


Figure 197. Plot of saddle frequency and high and low breakpoint frequency ( $f_{45}$ ) for the model presented in Figure 192. The parameters are identical;  $R_s$  was  $10 \Omega\text{-cm}^2$ ,  $R_{\text{pore}}$  varied from  $10^{12}$  to  $10^3 \Omega\text{-cm}^2$ ,  $R_{\text{dl}}$  varied from  $10^8$  to  $10^4 \Omega\text{-cm}^2$ , and the area was  $1 \text{ cm}^2$ .

#### 1.9.5.6 Polymer Coating Analysis

Fourier Transform Infrared Spectroscopy (FTIR) has been performed on  $30 \mu\text{m}$  thick Eponol coatings on polypropylene substrates exposed to various standard LALTs and at various field sites. The polypropylene substrate is inert in these tests and thus has no effect on the degradation of the coating. The results, shown in Figure 198, show that there is no degradation of the Eponol coating after 15 days of exposure in ASTM B-117 or ASTM G-85 Annex 5. Figure 199 shows ASTM B-117 and ASTM G-85 Annex 3, as well as two samples exposed at KSC for 2 and 5 months. There is a noticeable difference between the samples exposed at KSC and the other samples. In the KSC samples there is a decrease in intensity of the  $2963$  and  $2920 \text{ cm}^{-1}$  peaks, a new peak appears at  $1717 \text{ cm}^{-1}$ , the  $3362 \text{ cm}^{-1}$  peak broadens and a shoulder appears on the  $1609 \text{ cm}^{-1}$  peak.

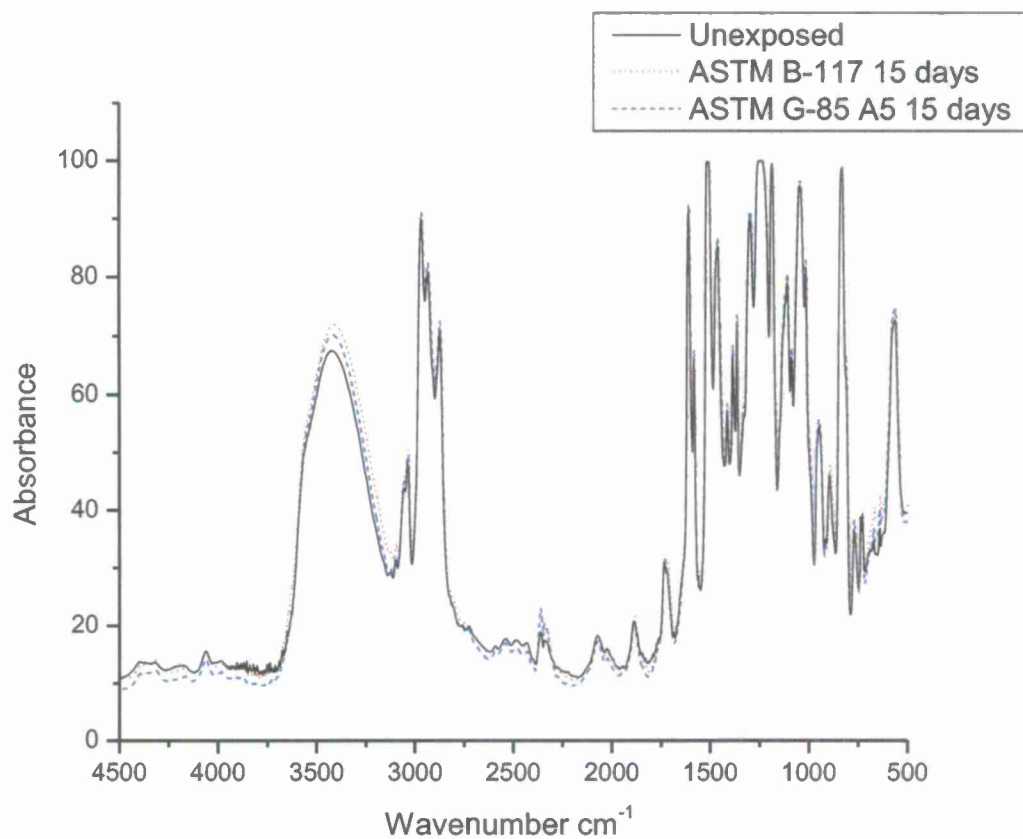


Figure 198. FTIR spectra of Eponol films exposed in ASTM B-117 and G-85 A5 for 15 days. Data taken at UVa.



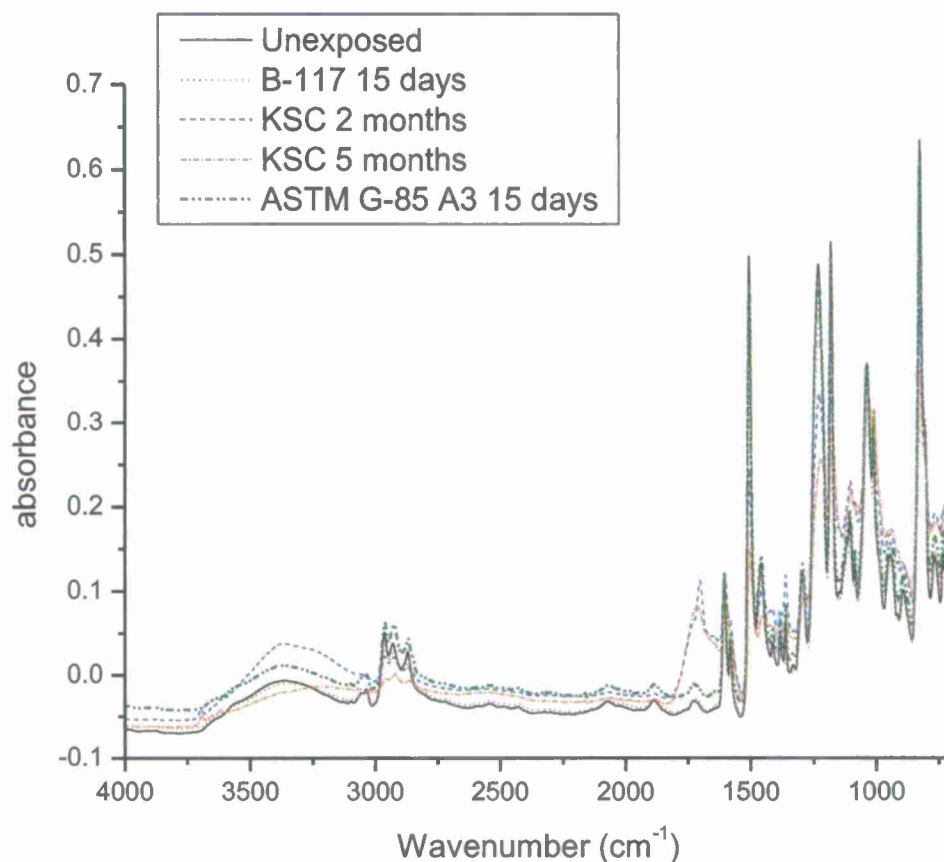


Figure 199. FTIR spectra of Eponol films exposed in various conditons. Data taken at USM.

USM has also performed Differential Scanning Calorimetry (DSC) and modified Differential Scanning Calorimetry (MDSC) on Eponol films exposed in various LALTs. DSC and MDSC measure the amount of heat required to increase the temperature of a sample. For polymers, it is used to measure the change in glass transition temperature ( $T_g$ ), or the temperature at which the polymer changes from an amorphous solid to a crystalline solid. The glass transition temperature is important because the properties of the polymer change as it moves from above the  $T_g$  to below. For example, above the transition temperature, polymers are amorphous and are generally more flexible and rubbery, while below the  $T_g$  they are crystalline and are generally more brittle<sup>60</sup>. Shorter polymer chains, limited crosslinking, and incorporation of plasticizers or residual solvent can lower the  $T_g$ , while longer chains, extensive crosslinking and large side groups raise the  $T_g$ <sup>60</sup>. Environmental factors can affect the  $T_g$ . For example, higher temperatures would cause more residual solvent to evaporate leading to higher  $T_g$ , while factors that break the crosslinking or the backbone of the chains themselves, like UV or ozone, would cause  $T_g$  to become lower<sup>60</sup>.

Table 20. DSC and MDSC results showing the glass transition temperature for eponol exposed to various conditions.

Sample	DSC			MDSC	
	Tg (°C)	Onset (°C)	Aging Peak Area (J/g)	Tg (°C)	Onset (°C)
Unexposed	72.63	69.16	117.7	62.41	55.76
ASTM B-117	73.33	69.58	96.22	60.19	58.56
ASTM D-4587	74.38	70.16	95.05	61.81	56.72
ASTM G-85 A3	71.28	66.78	72.64	57.26	52.57

USM has also run Thermogravimetric Analysis (TGA) on samples exposed in ASTM B-117, G-85 A3 and ASTM D-4587 as well as unexposed samples. TGA involves heating the sample in a controlled setting and constantly measuring the changing weight. Continuous heating of the sample eventually drives off all organic material. It has been used to measure the amount of residual solvent and the amount of organic content in the polymer. The remaining material is inorganic material. The data is shown in Table 21. The weight loss numbers in the table are total values i.e., for the ASTM G-85 A3, 76.3% of its weight after the residual solvent had been driven off was organic material and the remainder was non-organic. Generally, a higher amount of inorganic solids indicates that the coating was damaged and there was an ingress of inorganic matter, such as salts. However, it is unclear at this time if the large amount of inorganic material remaining in the samples exposed to ASTM G-85 Annex is due to high levels of salts that were in the polymer itself, or if the acidic nature of the test altered the polymer structure in some way.

Table 21. TGA results on Eponol films showing the amounts of residual solvents, organic material and inorganic material.

Sample	Weight Loss (from RT to 300°C)	Weight Loss (from 300°C to complete degradation and loss of organic material)
ASTM D-4587	6.6%	85.9%
Unexposed	8.9%	94.9%
ASTM B-117	7.0%	90.3%
ASTM G-85 A3	6.8%	76.3%

## 1.9.6 Discussion

### 1.9.6.1 Visual Analysis

From the visual data presented earlier in this section, it can be seen that the ASTM G-85 Annex 5 and the ASTM D-5894 best match with KSC (Figure 153, Figure 157, and Figure 158). The ASTM B-117 and ASTM G-85 Annex 3 appear to match with KSC for short time scales; but as time progresses scribe creep in the LALT's progress much more rapidly than is seen at KSC.

### 1.9.6.2 EIS analysis

EIS data shows that ASTM B-117 and ASTM G-85 Annex 5 cause very little environmental damage to the coating itself (Figure 183 and Figure 185). KSC shows that most of the damage detected by EIS is coming from the field environment and is not due to scribe creep or the degradation of the substrate (Figure 181). This is most similar to the ASTM D-5894 (Figure 186), the ASTM G-85 Annex 3 (Figure 184) and the non-standard LALTs that contain UV and ozone (Figure 188, Figure 189, Figure 190).

### 1.9.6.3 Importance of UV

Table 19 demonstrates the importance of UV as part of an accurate LALT. The ASTM D-5894 has cycles consisting of one week in ASTM G-85 Annex 5 and one week in ASTM D-4857 (one week of four hours of UV exposure (340 nm) at  $0.89\text{W/m}^2$  at  $60^\circ\text{C}$  and four hours of CC at  $50^\circ\text{C}$  in the dark). The major difference between the G-85 Annex 5 and the ASTM D-5894 is that samples exposed in the ASTM D-5894 are exposed to UV light. As can be seen in

Table 19, the addition of UV light increases the degradation of the coating roughly by a factor of five.

Figure 201 shows an example of damage that occurs when Eponol films are exposed to UV. The decrease in intensity of the  $2963$  and  $2920\text{ cm}^{-1}$  peaks show degradation of  $\text{CH}$ ,  $\text{CH}_2$ , and  $\text{CH}_3$  bonds in the coating<sup>67-71</sup>. The appearance and increase of a peak at  $1717\text{ cm}^{-1}$  is caused by the formation of carbonyls and aldehydes which are products of degradation of the aliphatic carbon bonds in the coating<sup>67-71</sup>. UV irradiation breaks bonds and allows water to enter the polymer where damage has occurred. The broadening of the peak at  $3362\text{ cm}^{-1}$  and the appearance of a shoulder at  $1609\text{ cm}^{-1}$  indicate an increase in OH bonds<sup>67-71</sup>. This is due to the increase in water in the coating due to degradation caused by UV exposure<sup>68</sup>.

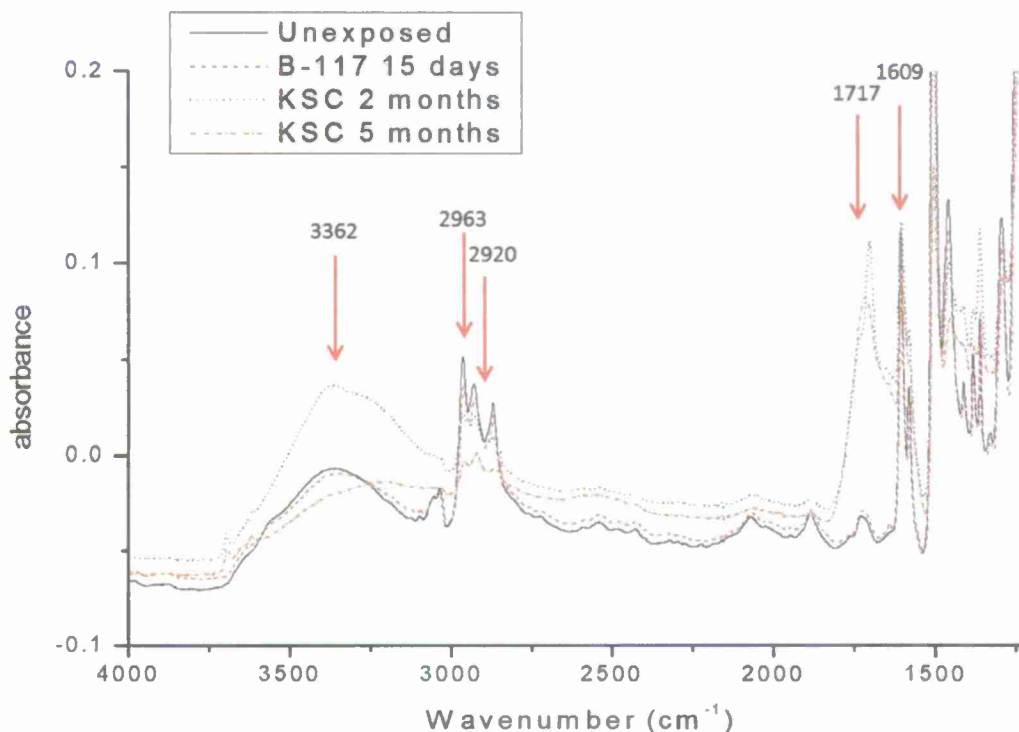


Figure 200. FTIR spectra of Eponol films on inert polypropylene substrates exposed in various conditions. Arrows indicate peaks that are expected to change with exposure to UV.

The DSC and MDSC data (Table 20) shows the changes in  $T_g$  that have occurred. Although the sample exposed to ASTM D-4587 was exposed to UV and would therefore be expected to have the lowest  $T_g$ , the samples exposed to B-117 and G-85 A3 have lower  $T_g$  numbers. This is believed to be because the B-117 and G-85 A3 samples have more entrapped water that plasticizes the polymer. D-4587 may be showing the net effect on  $T_g$  from two opposite factors. The high temperature of the D-4587 (60°C) is continuing to drive off solvent from the film which increases  $T_g$ . However, the UV light degrades the polymer which lowers the  $T_g$ .

The TGA data (Table 21) shows that the unexposed samples have the least amount of inorganic remnants, as would be expected. ASTM G-85 A3 has the most non-organic remnants. However, the reason behind this remains unclear. It may be due to the sample accumulating more salts than the others during exposure, but why that would happen is not clear.

#### 1.9.6.4 Role of Chloride

Comparing the visual images of KSC (Figure 153) to ASTM B-117 (Figure 155), it can be seen that the ASTM B-117 suffers from scribe creep to a larger extent than is seen for KSC. Noticeable scribe creep doesn't appear at KSC until 1 year of exposure. Accept for the ASTM G-85 Annex 3, which is acidified and thus not a one to one comparison, not other LALT suffers from visually noticeable scribe creep. Chloride, then, plays a role in scribe creep. Its effect is most likely due to the damage to the substrate in the form of corrosion caused by the chloride



leading to scribe creep. However, the noticeable differences in the scribe creep rates between KSC and ASTM B-117 suggest that the high level of chloride in the ASTM B-117 (5%) may be too severe and cause the scribe creep to dominate over other forms of corrosion. Scribe creep as the dominant form of corrosion is not what is seen in the field.

#### 1.9.6.5 Analysis of Corrosion on Bare AA2024-T351

The SEM analysis of corrosion/pitting morphology on bare aluminum samples shows a distinct difference between LALTs and field exposures. LALTs with high ozone and UV exposures showed a high number of small pits evenly spaced across the surface of the samples, while field exposed samples showed relatively few but very large pits. This can be seen in both Table 17 and in Figure 201 below. Samples with low ozone and UV showed little pitting. UV is a major ESF that field samples are exposed to, but these results show that UV alone cannot be causing the difference in morphology seen between LALT and field exposed samples from the standpoint of corrosion. No samples were exposed in LALTs that had UV, cycling and chloride in a manner that mimicked the field exposures. The ASTM D-5894 does have a period of time in exposed to chloride and a period of time exposed to UV. However, the UV exposure comes before the chloride exposure. Also, due to the very harsh nature of the UV in the ASTM D-5894, the samples were only exposed to UV once during the course of testing. This leads us to conclude that ESFs like chloride, cycling and UV may have confounding effects that cause the discrepancies between LALT and field exposed samples.

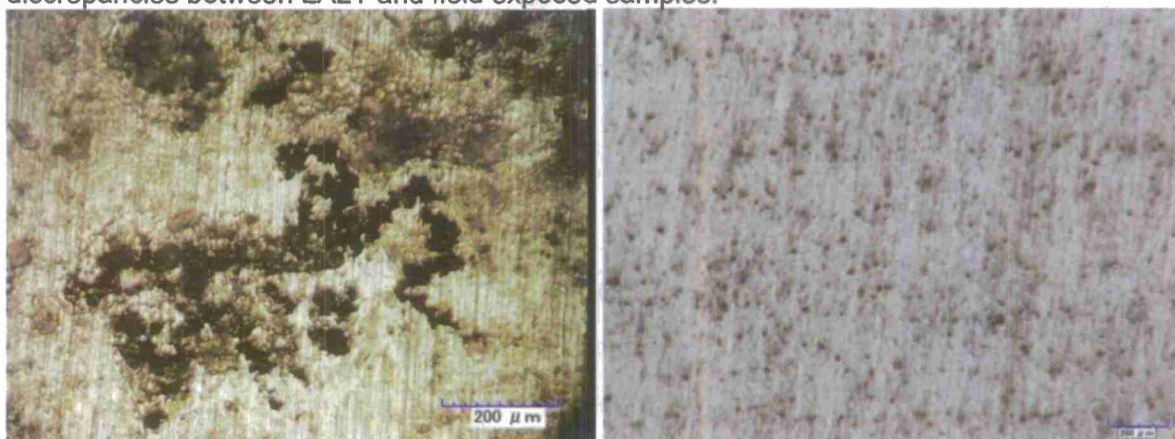


Figure 201. Optical images showing the comparison of pitting/corrosion morphology on bare AA2024-T351 exposed at KSC (left) and in CC+UV+O<sub>3</sub> (0.7-2.5 ppm) (right).

#### 1.9.6.6 Overall

The ASTM D-5894 best matches the degradation of the coating and substrate seen in the field. Visually, it appears similar to KSC (Figure 153 and Figure 157). Additionally, EIS shows degradation of the coating both near to and away from the scribe that mimics what is seen in samples exposed in the field. However, ASTM B-117 does not mimic the field results for Eponol coated AA2024-T351 (Figure 155). The coating was not damaged in the ASTM B-117 in the same way that is was in field results due to a lack of ESF (like UV) that attacks the coating specifically. The ASTM B-117 has a high level of chloride such that in general the scribe is attacked more than is seen in the field while the coating is attacked less. Field exposures are naturally subjected daily wet/dry cycles, and standard and non-standard tests with cycling appeared to mimic the field better than the ASTM B-117 which has no cycling.

### 1.9.7 Economic Summary

This project has studied lab accelerated life test (LALT) methods that are used to assess organically coated aluminum alloys that could be used in any laboratory and that also could be applied to the characterization and performance of other coatings on aluminum alloys. Although each organic coating is different, this study gives broad guidelines that should be applicable to other organic coatings on aluminum alloys. As such, the cost of unique test development for each and every case where organically coated aluminum alloys must be evaluated and might be deployed can be avoided. The ASTM B-117 test method is not recommended if correlation is sought with the degradation mechanisms in the field of service of coated aluminum alloys. EIS methods are viable for field testing of coatings and pursuit of field deployable devices should be continued. However, this single method, while better than visual evaluations, should not be used in isolation. Assuming the cost of several scientist person years to find a viable LALT exposure test that correlates with field exposures, if undertaken for each organic coating on aluminum alloy, is saved; such clarification of viable LALT conducted within this study should save several hundred thousand dollars in each instance such a LALT is sought. Trial and error, and educated guess-based development of lab surveillance methods that may or may not work satisfactorily can also be avoided. For instance, the LALT or field exposed coated panels should not be evaluated visually or only by isolated methods that address only the coating performance, i.e., the only evaluation is by gloss measurements. Multiple surveillance methods should be employed to evaluate the degradation of the coating and the substrate. Adherence to this recommendation should save an additional several hundred thousand dollars in unnecessary and not useful test development costs to find a useful suite of evaluation methods.

The savings to components during the use of organically coated systems is a little more difficult to forecast. If one single asset avoids an unscheduled repainting or repair due to the choice of a better standard LALT exposure selection that can better forecast field performance compared to ASTM B-117 and the choice of a suite of evaluation tools instead of a single measurement, like coating gloss, that then leads to better selection of a high performing organically coated aluminum alloy. The choice of the higher performing coating could possibly save several million dollars in each instance of avoided unscheduled repainting or repair. Another viable cost avoidance strategy would be to make better use of acceleration factors from the best correlating LALT. This could be used in an "anticipate and manage" strategy to schedule orderly repair and recoating. The cost avoidance in this case would be realized through better ability to anticipate and manage corrosion. Another way to achieve cost avoidance would be through the wise choice of LALT and surveillance methods when new coatings are tested to avoid incorrect or poor choices of high performing coating systems.

### 1.9.8 Implementation

This project mainly points toward characteristics of LALTs to consider and those to avoid for better correlation with field performance when seeking tests to evaluate organic coatings on precipitation age hardened aluminum alloys. Regarding laboratory LALT that correlate with field performance, it was found that LALT which have cycling of wet and dry periods, have some TOW but are not immersed, have some Cl<sup>-</sup> dosing and UV were all better laboratory test to mimic field exposure testing especially at Kennedy Space Flight Center and in a rural atmospheric setting. The ASTM B-117 tests does not include UV, includes 100% TOW in 5%NaCl solution and consequently does not match well with field results on organically coated aluminum alloys. It should be abandoned at this time as a test method for evaluation of field atmospheric testing of organic coatings on aluminum alloys. These recommendations can be implemented through future decisions and best-practices.

A new LALT is not ready for recommendation or implementation.

#### **1.9.9 Conclusions**

The long known problem of discrepancy between accelerated life testing and field exposures for organically coated metals is addressed in this work. Eponol coated AA2024-T351 samples were exposed in many standard LALTs including ASTM B-117, ASTM G-85 Annex 3, ASTM G-85 Annex 5, and ASTM D-5894, as well as field sites at Kennedy Space Center in Florida and at Charlottesville Virginia. The exposed samples were then interrogated using a suite of high level surveillance methods including EIS, CLSM, FTIR, 3D optical microscopy and XRD. These methods enabled the detection of differences in corrosion morphology for these different exposures, as well as degradation of the polymer coating. These methods also allowed for the determination of the effects of environmental severity factor that are important to understand in the use of accelerated life testing.

Therefore, we do not recommend using ASTM B-117 for life prediction testing to simulate field performance. We recommend an LALT that incorporates UV irradiation, time of wetness cycling (i.e., wet/dry cycles), and an ESF that is present in coastal environments and attacks the substrate, like chloride, but is not overly severe in its corrosive attack. Results indicated that the ASTM D-5894 was most similar to KSC and BRD. Many standard LALTs do not cause direct damage to coating over short time scales due to insufficient ESFs; rather the damage to the coating occurs as substrate damage proceeds. This, along with ESFs that may be specific to the operating environment of the coating system, must be taken into account by the user when considering LALTs for life prediction of coated metals. High level surveillance methods of both substrate and coating must also be incorporated into coating system analysis, especially if understanding damage to the coating specifically is important to the user.

#### **1.9.10 Appendices**

#### **1.9.11 Bibliography**

1. C. A. Matzdorf and C. W. Nickerson, Assessment of Accelerated Tests Compared to Beachfront Test and Proposed Evaluation Method, DoD Corrosion Conference, 2009).
2. R. G. Buchheit, Conversion Coating Science and Technology - is it Evolving or is it Stuck?, G. Frankel, J. R. Scully, H. S. Issacs and J. D. Sinclair, Eds., vol. 2002-13, Corrosion Science: a Retrospective and Current Status in Honor of Robert P. Frankenthal, (Pennington, New Jersey, Electrochemical Society, 2002, p. 430-437).
3. M. E. Nanna and G. P. Bierwagen, Mg-rich coatings: A new paradigm for Cr-free corrosion protection of al aerospace alloys, Jct Research, 1 (2004), 69-80.
4. Revising the Notification Requirements in the Exposure Determination Provisions of the Hexavalent Chromium Standards in D. o. Labor (Ed.). Federal Register, 2010, p. 27188-27189.
5. Chromium-6 in Drinking Water in U. E. P. Agency (Ed.). Office of Water, 2010
6. P. S. Silva, Guidance for Public Water Systems on Enhanced Monitoring for Chromium-6 (Hexavalent Chromium) in Drinking Water in U. E. P. Agency (Ed.). Office of Water, 2011
7. J. J. Young, Minimizing the Use of Hexavalent Chromium, 2009



8. M. Daniel E. Bullock, Memorandum for distribution, Subject: Adding PreKote SP to Technical Order (T.O.) 1-1-8. Department of the Air Force, 2004, p. 1.
9. J. R. S. Andrew King, Corrosion Protection of 2024-T351 by a Mg-Rich Primer: Discrepancies Between Field Versus Laboratory Exposures, NACE 2010, San Antonio Tx, 2011
10. B. Dodson and H. Schwab, Accelerated Testing - A Practitioner's Guide to Accelerated and Reliability Testing, SAE International, 2006),
11. C. E. Miller, COMPARISON OF ELECTROCHEMICAL IMPEDANCE SPECTROSCOPY (EIS) RESULTS FOR FOUR ACCELERATED EXPOSURES VERSUS OUTDOOR DoD Corrosion Conference, 2009).
12. ASTM B-117-07a: Standard Practice for Operating Salt Spray (Fog) Apparatus. ASTM International, West Conshohocken, PA, 2007
13. D. E. Little, "ROLE(S) OF PRETREATMENT, INHIBITORS, AND OTHER PROCESS STEPS THAT EFFECT SURFACE COMPOSITION ON THE UNDER-PAINT CORROSION OF AN Al-Cu-Mg ALLOY 2024-T3" University of Virginia, 2006),
14. A. Bautista, Filiform corrosion in polymer-coated metals, Progress in Organic Coatings, 28 (1996), 49-58.
15. G. Grundmeier, W. Schmidt and M. Stratmann, Corrosion protection by organic coatings: electrochemical mechanism and novel methods of investigation, Electrochimica Acta, 45 (2000), 2515-2533.
16. J. V. Kloet, W. Schmidt, A. W. Hassel and M. Stratmann, The role of chromate in filiform corrosion inhibition, Electrochimica Acta, 49 (2004), 1675-1685.
17. C. Hahin and R. G. Buchheit, Filiform Corrosion, S. D. Cramer and B. S. Covino Jr., Eds., vol. 13A, ASM Handbook - Corrosion: Fundamentals, Testing, and Protection, ASM, 2003, p. 248).
18. R. T. Ruggeri and T. R. Beck, An Analysis of Mass Transfer in Filiform Corrosion, NACE, 1983), p. 452-465.
19. D. A. Little, M. A. Jakab and J. R. Scully, Effect of surface pretreatment on the underpaint corrosion of AA2024-T3 at various temperatures, Corrosion, 62 (2006), 300-315.
20. G. O. Ilevbare and J. R. Scully, Mass-Transport-Limited Oxygen Reduction Reaction on AA2024-T3 and Selected Intermetallic Compounds in Chromate-Containing Solutions, Corrosion, 55 (2000), 134.
21. N. LeBozec and D. Thierry, Influence of climatic factors in cyclic accelerated corrosion test towards the development of a reliable and repeatable accelerated corrosion test for the automotive industry, Mater. Corros., 61 (2010), 845-851.
22. J. Mallegol, M. Poelman and M. G. Olivier, Influence of UV weathering on corrosion resistance of prepainted steel, Progress in Organic Coatings, 61 (2008), 126-135.
23. B. S. Skerry, ACCELERATED TEST METHOD FOR ASSESSING CORROSION AND WEATHERING OF PAINTS FOR ATMOSPHERIC CORROSION CONTROL, Corrosion, 49 (1993), 663-674.
24. J. Pospíšil, J. Pilar, N. C. Billingham, A. Marek, Z. Horák and S. Nespurek, Factors affecting accelerated testing of polymer photostability, Polymer Degradation and Stability, 91 (2006), 417-422.
25. B. R. Hinderliter, S. G. Croll, D. E. Tallman, Q. Su and G. P. Bierwagen, Interpretation of EIS data from accelerated exposure of coated metals based on modeling of coating physical properties, Electrochimica Acta, 51 (2006), 4505-4515.
26. F. Deflorian, L. Fedrizzi and S. Rossi, Electrochemical impedance spectroscopy and Fourier transform infrared spectroscopy of natural and accelerated weathering of organic coatings, Corrosion, 54 (1998), 598-605.



27. F. Deflorian, L. Fedrizzi and P. L. Bonora, INFLUENCE OF THE PHOTO-OXIDATIVE DEGRADATION ON THE WATER BARRIER AND CORROSION PROTECTION PROPERTIES OF POLYESTER PAINTS *Corrosion Science*, 38 (1996), 1697-1708.
28. H. P. Hack and J. R. Scully, Defect Area Determination of Organic Coated Steels in Seawater Using the Breakpoint Frequency Method, *J Electrochem Soc*, 138 (1991), 33-40.
29. F. Mansfeld and C. H. Tsai, Determination of Coating Deterioration with Eis .1. Basic Relationships, *Corrosion*, 47 (1991), 958-963.
30. S. Oesch, The effect of SO<sub>2</sub>, NO<sub>2</sub>, NO and O<sub>3</sub> on the corrosion of unalloyed carbon steel and weathering steel - The results of laboratory exposures, *Corrosion Science*, 38 (1996), 1357-1368.
31. S. Oesch and M. Faller, ENVIRONMENTAL EFFECTS ON MATERIALS: THE EFFECT OF THE AIR POLLUTANTS SO<sub>2</sub>, NO<sub>2</sub>, NO AND O<sub>3</sub> ON THE CORROSION OF COPPER, ZINC AND ALUMINIUM. A SHORT LITERATURE SURVEY AND RESULTS OF LABORATORY EXPOSURES *Corrosion Science*, 39 (1997), 1505-1530.
32. J. J. Robin, Overview of the Use of Ozone in the Synthesis of New Polymers and the Modification of Polymers *Advances in Polymer Science*, 167 (2004), 235.
33. S. D. Razumovskii, A. A. Kefeli and G. E. Zaikov, Degradation of polymers in reactive gases, *European Polymer Journal*, 7 (1971), 275-285.
34. R. D. Edwards, N. L. Lam, L. Zhang, M. A. Johnson and M. T. Kleinman, Nitrogen Dioxide and Ozone As Factors in the Availability of Lead from Lead-Based Paints, *Environmental Science & Technology*, 43 (2009), 8516-8521.
35. L. Veleva and R. D. Kane, *Atmospheric Corrosion Various*, (Ed.), vol. 13a, *Corrosion: Fundamentals, Testing and Protection*, (Materials Park, OH, ASM International, 2003, p. 196-209).
36. G. S. Frankel, *Pitting Corrosion Various*, (Ed.), vol. 13a, *Corrosion: Fundamentals, Testing and Protection*, (Materials Park, OH, ASM International, 2003, p. 236-241).
37. H. Leidheiser and P. D. Deck, Chemistry of the Metal-Polymer Interfacial Region, *Science*, 241 (1988), 1176-1181.
38. H. Leidheiser, R. D. Granata and R. Turoscy, Technical Note: Alkali Metal Ions as Aggressive Agents to Polymeric Corrosion Protective Coatings, *Corrosion*, 43 (1987), 296-297.
39. J. Parks and H. Leidheiser, Ionic migration through organic coatings and its consequences to corrosion, *Industrial & Engineering Chemistry Product Research and Development*, 25 (1986), 1-6.
40. R. Turoscy, J. Henry Leidheiser and J. E. Roberts, Solid-State Nuclear Magnetic Resonance Studies of Ions in Protective Coatings III: Sodium, Lithium, and Cesium Ions in Polyimide and Epoxy-Polyamide Coatings, *J. Electrochem. Soc.*, 140 (1993), 149-154.
41. R. Turoscy, J. Henry Leidheiser and J. E. Roberts, Solid-State NMR Studies of Sodium Ions in a Polybutadiene Matrix, *J. Electrochem. Soc.*, 137 (1990), 1785-1788.
42. K. Knop, Influence of buffer solution composition on drug release from pellets coated with neutral and quaternary acrylic polymers and on swelling of free polymer films, *European Journal of Pharmaceutical Sciences*, 4 (1996), 293-300.
43. M. Tullmin and P. R. Roberge, *Atmospheric Corrosion*, R. W. Revie, (Ed.), *Uhlig's Corrosion Handbook*, John Wiley & Sons, 2000,
44. C. Leygraf and T. E. Graedel, *Atmospheric Corrosion*, John Wiley & Sons, 2000),
45. E. Schindelholz and R. G. Kelly, *Wetting Phenomena and Time of Wetness in Atmospheric Corrosion*, Center for Electrochemical Science and Engineering

Univeristy of Virginia, 2010.

46. W. H. J. Vernon, A laboratory study of the atmospheric corrosion of metals. Part I.-The Corrosion of copper in certain synthetic atmospheres, with particular reference to the influence of sulphur dioxide in air of various relative humidities, Transactions of the Faraday Society, 27 (1931), 255-277.
47. W. H. J. Vernon, A laboratory study of the atmospheric corrosion of metals. Part II.-Iron: the primary oxide film. Part III.-The secondary product or rust (influence of sulphur dioxide, carbon dioxide, and suspended particles on the rusting of iron), Transactions of the Faraday Society, 31 (1935), 1668-1700.
48. L. Petry and J. F. Dante, SAE-G8 Round Robin Corrosion Test Method Comparison, 2003, p. Powerpoint Presentation.
49. M. Stratmann and H. Streckel, On the atmospheric corrosion of metals which are covered with thin electrolyte layers—I. Verification of the experimental technique, Corrosion Science, 30 (1990), 681-696.
50. M. Stratmann and H. Streckel, On the atmospheric corrosion of metals which are covered with thin electrolyte layers—II. Experimental results, Corrosion Science, 30 (1990), 697-714.
51. M. Stratmann, H. Streckel, K. T. Kim and S. Crockett, On the atmospheric corrosion of metals which are covered with thin electrolyte layers-iii. the measurement of polarisation curves on metal surfaces which are covered by thin electrolyte layers, Corrosion Science, 30 (1990), 715-734.
52. ASTM Standard D523-08 Standard Test Method for Specular Gloss. ASTM International, West Conshohocken, PA, 2008
53. W. H. Abbott, personal correspondence with Dr. William Abbott of Battelle Memorial Institute, (2009).
54. ASTM Standard D610-08 Standard Practice for Evaluating Degree of Rusting on Painted Steel Surfaces. ASTM International, West Conshohocken, PA, 2008
55. C. C. Lin and C. X. Wang, Correlation between accelerated corrosion tests and atmospheric corrosion tests on steel, Journal of Applied Electrochemistry, 35 (2005), 837-843.
56. O. Guseva, S. Brunner and P. Richner, Service life prediction for aircraft coatings, Polymer Degradation and Stability, 82 (2003).
57. R. A. Dickie, Paint adhesion, corrosion protection, and interfacial chemistry, Progress in Organic Coatings, 25 (1994), 3-22.
58. Y. Wan, E. Neiser and R. G. Kelly, Modification of ASTM Standard B117 Salt Spray Corrosion Test for Improved Correlation to Field Measurements, DoD Corrosion Conference, Plam Springs, Ca, 2011
59. QUV Accelerated Weathering Tester in Q-Lab (Ed.), 2006
60. R. Overney, C. Buenviaje, R. Luginbühl and F. Dinelli, Glass and Structural Transitions Measured at Polymer Surfaces on the Nanoscale, Journal of Thermal Analysis and Calorimetry, 59 (2000), 205-225.
61. MountainsMap. Digital Surf, Besancon, France, 2005-2012
62. W. S. Rasband, ImageJ. U.S. National Institutes of Health, Bethesda, Maryland, 1997-1212
63. ASTM Standard G-85, Standard Practice for Modified Salt Spray Testing. ASTM International, West Conshohocken, PA, 2002
64. B. Maier and G. S. Frankel, Behavior of Magnesium-Rich Primers on AA2024-T3, Corrosion, 67 (2011), 055001.

65. D5894-10 Standard Practice for Cyclic Salt Fog/UV Exposure of Painted Metal, (Alternating Exposures in a Fog/Dry Cabinet and a UV/Condensation Cabinet). ASTM International, West Conshohocken, PA, 2010
66. D. Johnson, Z-view. Scribner Associates, 1990-2012
67. P. Musto, G. Ragosta, M. Abbate and G. Scarinzi, Photo-oxidation of high performance epoxy networks: Correlation between the molecular mechanisms of degradation and the viscoelastic and mechanical response, *Macromolecules*, 41 (2008), 5729-5743.
68. C. Konecki, correspondence to M. Tayler, 2012.
69. M. Diepens and P. Gijsman, Photodegradation of bisphenol A polycarbonate, *Polymer Degradation and Stability*, 92 (2007), 397-406.
70. N. Nagai, H. Okumura, T. Imai and I. Nishiyama, Depth profile analysis of the photochemical degradation of polycarbonate by infrared spectroscopy, *Polymer Degradation and Stability*, 81 (2003), 491-496.
71. A. Rivaton, B. Mailhot, J. Soulestin, H. Varghese and J. L. Gardette, Comparison of the photochemical and thermal degradation of bisphenol-A polycarbonate and trimethylcyclohexane-polycarbonate, *Polymer Degradation and Stability*, 75 (2002), 17-33.

## 1.10 Molybdate Inhibition of Corrosion Fatigue Crack Propagation in Precipitation Hardened Al-Cu-Li (Warner, J.S. and Gangloff, R.P.)

### 1.10.1 Summary

Addition of molybdate ( $\text{MoO}_4^{2-}$ ) to aqueous chloride solution effectively inhibits environmental fatigue crack propagation (EFCP) in peak aged Al-2.6Cu-1.6Li (wt pct, C47A-T86) which also exhibits alloy-induced inhibition in pure chloride solution.  $\text{MoO}_4^{2-}$  inhibits EFCP at frequencies below an upper bound and eliminates the effect of environment at sufficiently low loading frequencies by yielding crack growth rates equivalent to those for fatigue in ultra-high vacuum. Ion assisted inhibition is attributed to  $\text{MoO}_4^{2-}$  stabilizing a crack tip passive film which reduces H production and uptake due to a diffusion barrier film, reduced crack acidification by hydrolysis, and buffered pH. Inhibition is governed by the balance between passive film rupture by crack tip strain and repassivation. As such, inhibition is promoted by reduced loading frequency and potentials at or anodic to free corrosion; each of which favors passivity over film rupture. Alloy-induced inhibition is destabilized by addition of molybdate. This is likely due to molybdate inhibiting localized corrosion of  $\text{Al}_2\text{CuLi}$  precipitates in the crack wake which otherwise leads to Cu enrichment required for alloy-induced EFCP inhibition in C47A-T86. The inhibiting effect of molybdate for this Al-Cu-Li alloy parallels chromate and molybdate inhibition of EFCP in 7075-T651, establishing molybdate as a viable chromate replacement inhibitor.

### 1.10.2 Introduction

Precipitation hardened aluminum alloys, including the Al-Cu-Li system used in aerospace structures, are susceptible to corrosion fatigue crack propagation or, as it is also known, environmental fatigue crack propagation (EFCP). Such cracking is explained in large part by the hydrogen environment embrittlement (HEE) mechanism<sup>1-17</sup>. This mechanism attributes EFCP damage in water vapor and many aqueous chloride solutions to the interaction between irreversible plastic deformation, tensile stress, and atomic hydrogen (H) produced by chemical or electrochemical reactions all highly localized at the crack tip. Basically, reaction product H absorbs on the crack tip surface and diffuses within the fatigue process zone (FPZ) where it interacts with local tensile stresses and dislocation structure from cyclic deformation to cause embrittlement, thereby enhancing fatigue crack propagation rate ( $da/dN$ ) relative to inert gas and vacuum<sup>1, 2, 5, 6, 8-10, 12, 13, 15-17</sup>.

The H concentration in the FPZ, and thereby EFCP by HEE, can be limited kinetically by one of the following steps: a) transport of hydrogen producing reaction species from the bulk environment to crack surface reaction sites, b) time for crack surface chemical or electrochemical reactions to produce H, and c) diffusion of atomic reaction product H within the metal to the FPZ<sup>2, 7, 10, 12, 13, 18</sup>. As such, the environmental driving force for cracking is quantified by: a) fatigue loading frequency ( $f$ ); b) water vapor pressure (for water vapor environments) or the overpotential for H production at the crack tip (for full immersion), which is a function of crack tip pH and potential; and c) passivity, as it reduces dissolution and H production, and can create a barrier to H uptake. For full immersion in aqueous chloride solutions, H is produced near to an oxygen depleted crack tip by cathodic water reduction



and/or dissolution introducing  $\text{Al}^{3+}$  which is hydrolyzed to  $\text{H}^+$  then subsequently cathodically reduced to atomic H<sup>12, 19-21</sup>. For aluminum alloys with no crack tip passive film to impede H production and uptake, chemical/electrochemical reaction rates are rapid and crack advance appears to be H-diffusion controlled<sup>13</sup>. Modeling predicts that  $da/dN$  increases with decreasing  $f$  due to increasing time for H to diffuse to the FPZ, then becomes  $f$  and time independent under moderate to low  $f$  loading where neither surface reaction nor H diffusion are rate limiting<sup>3, 4</sup>. This typical time -  $f$  dependence is observed in 7000-series (Al-Zn-Mg) Al alloys stressed in aqueous chloride solutions<sup>3, 4, 22, 23</sup>.

For Al-Cu-Mg and Al-Cu-Li alloys (2000-series), decreasing  $da/dN$  with decreasing  $f$  has been reported for EFCP in pure chloride solutions<sup>24-28</sup>. This  $f$  dependence, contrary to that predicted by H diffusion modeling, is attributed to alloy-induced inhibition where stabilization of a crack tip surface passive film results from: 1) crack flank Cu enrichment following dissolution of anodic Cu-containing GP zones or precipitates and 2) enhanced crack wake cathodic reaction kinetics on Cu enriched zones which increases crack solution pH to stabilize a native alumina crack tip passive film in the presence of chloride<sup>24, 28</sup>. This alloy-induced inhibition can be understood by the film rupture-H embrittlement mechanism<sup>12, 24, 28-31</sup> where crack tip passivity reduces production and uptake of embrittling H through reduced crack hydrolysis and a H-diffusion barrier crack tip film. The crack tip alumina passive film is destabilized mechanically and rendered incapable of EFCP protection when the per-cycle strain accumulated at the fatigue crack tip exceeds the strain required for film rupture. After one or more rupture events, inhibition can resume once the rupture site(s) repassivates. The observed decreasing  $da/dN$  with decreasing  $f$  behavior is determined by the interplay between the rates of film rupture, governed by crack tip strain rate, and repassivation, which is a material property for a given environment. Hence, inhibition is promoted by reduced loading frequency, and thus reduced crack tip strain rate, which favors repassivation over film rupture.

The peak aged Al-Zn-Mg-Cu alloy 7075-T651 does not exhibit alloy-induced inhibition because the predominant anodic phase does not provide a sufficient source for Cu surface enrichment in the peak aged condition<sup>24, 28, 32</sup>; but, research has shown that inhibition of EFCP is possible through addition of localized corrosion inhibitors like chromate<sup>3, 4</sup> and molybdate<sup>28, 33, 34</sup> to aqueous chloride solution. This ion-assisted inhibition parallels alloy-induced inhibition; and as such, is described by the film rupture-H embrittlement mechanism where molybdate ( $\text{MoO}_4^{2-}$ ) and chromate ( $\text{CrO}_4^{2-}$ ) stabilize a crack tip-surface passive film<sup>3, 4, 28, 34</sup>. As in alloy-induced inhibition, the frequency dependence of ion-assisted inhibition is determined by the interplay between rupture and repassivation of the  $\text{CrO}_4^{2-}$  or  $\text{MoO}_4^{2-}$  stabilized passive film.  $\text{MoO}_4^{2-}$  and  $\text{CrO}_4^{2-}$  each alter the pure NaCl crack propagation kinetics by decreasing  $da/dN$  with decreasing  $f$  below an upper bound critical  $f$  ( $f_{\text{critUB}}$ )<sup>28, 33, 34</sup>. Ion-assisted inhibition via  $\text{MoO}_4^{2-}$  and  $\text{CrO}_4^{2-}$  is promoted by reduced loading frequency, increased crack tip inhibitor concentration, reduced crack tip strain rate, and potentials at or anodic to free corrosion; all of which favor repassivation over film rupture<sup>3, 4, 28, 34</sup>. At relatively low loading frequencies, near a critical lower bound level ( $f_{\text{critLB}}$ ), ion-assisted inhibition via  $\text{MoO}_4^{2-}$  has the ability to further suppress H uptake by buffering crack tip pH to neutral or slightly alkaline levels<sup>28, 34</sup>. Together the  $\text{MoO}_4^{2-}$  stabilized crack tip passive film and crack tip buffering by  $\text{MoO}_4^{2-}$  sufficiently suppress H production and uptake to eliminate the environmental acceleration in fatigue crack propagation and yield  $da/dN$  equivalent to those measured in ultra high vacuum<sup>28, 34</sup>.

Because of the drive to replace  $\text{CrO}_4^{2-}$  in corrosion protection systems used in aerospace applications, and evidence showing the ability of chromate to inhibit both localized corrosion<sup>35-37</sup> and EFCP<sup>3, 4</sup>; it is important to establish the ability of possible replacement inhibitors to inhibit

EFCP. Given the data and mechanistic understanding above, which show that molybdate can eliminate the effect of environment on fatigue in 7075-T651<sup>28,34</sup>,  $\text{MoO}_4^{2-}$  is established from the fatigue perspective as a possible chromate replacement inhibitor. However, such assessment has not been reported for Al-Cu-X alloy systems, which are capable of alloy inhibition in pure chloride solution.

#### 1.10.2.1 Goal

The objective of this research is to understand if ion-assisted and alloy-induced inhibition are mutually exclusive or synergistically additive; more specifically, to assess if molybdate will enhance or destabilize alloy-induced inhibition in peak aged Al-Cu-Li alloys.

#### 1.10.3 Lessons Learned

Molybdate ( $\text{MoO}_4^{2-}$ ) presence in aqueous chloride solution effectively inhibits environmental fatigue crack propagation (EFCP) in peak aged Al-2.6Cu-1.6Li (wt pct, C47A-T86). This is a modern Al-Cu-based alloy aimed at airframe applications where the peak aged strength exceeds that of conventional 2024-type Al-Cu-Mg alloys.  $\text{MoO}_4^{2-}$  inhibits EFCP at frequencies below an upper bound and eliminates the effect of environment at sufficiently low loading frequencies by yielding crack growth rates equivalent to those for fatigue in ultra-high vacuum. Ion assisted inhibition is attributed to  $\text{MoO}_4^{2-}$  stabilizing a crack tip passive film which reduces H production and uptake due to a diffusion barrier film, reduced crack acidification by hydrolysis, and buffered pH. Inhibition is governed by the balance between passive film rupture by crack tip strain and repassivation. As such, inhibition is promoted by reduced loading frequency and potentials at or anodic to free corrosion; each of which favors passivity over film rupture. Alloy-induced inhibition is destabilized by addition of molybdate. This is likely due to molybdate inhibiting localized corrosion of  $\text{Al}_2\text{CuLi}$  precipitates in the crack wake which otherwise leads to Cu enrichment required for alloy-induced EFCP inhibition in C47A-T86. The inhibiting effect of molybdate for this Al-Cu-Li alloy parallels chromate and molybdate inhibition of EFCP in 7075-T651, establishing molybdate as a viable chromate replacement inhibitor.

#### 1.10.4 Experimental Procedures

The material studied is C47A-T86, which is the registered alloy 2199 designed for improved mechanical property isotropy<sup>38</sup>. The C47A used in this study has a composition of Al-2.6Cu-1.6Li-0.6Zn-0.3Mn-0.2Mg-0.06Zr (wt%) and was provided by Alcoa Technical Center as a 19 mm thick plate in the T36 temper. The as-received material has grain dimensions of 88  $\mu\text{m}$  in the thickness (S) direction and 896  $\mu\text{m}$  in the width (T) direction<sup>15</sup>, and was artificially aged at the University of Virginia for 36 h at 149°C in order to obtain the near-peak aged microstructure (T86). A detailed analysis of the microstructure and texture was performed previously<sup>15,39</sup>. The microstructure contains  $\text{Al}_2\text{LiCu}$  ( $T_1$ ),  $\text{Al}_2\text{Cu}$  ( $\theta$ ), and  $\text{Al}_3\text{Li}$  ( $\delta'$ ) precipitates, resulting in a tensile yield strength ( $\sigma_{ys}$ ) of 426 MPa.

Single edge micronotch tension (SENT) specimens were machined in the L-T orientation (L is the longitudinal or rolling direction) with a notch depth of 200  $\mu\text{m}$ , specimen width of 10.2 mm, and thickness of 2.5 mm. The notch was produced by electrical-discharge machining. The mid-portion of the specimen was sealed with O-rings into a Plexiglas cell so that the crack was always immersed in aqueous electrolyte. All experiments were performed under full immersion

in solutions of NaCl or NaCl + Na<sub>2</sub>MoO<sub>4</sub> and the solution was circulated from a 1 L basin at 20 mL/min. The specimen grips were positioned outside the Plexiglas cell to eliminate galvanic coupling. Specimen gripping enabled unhindered rotation necessary for the stress intensity solution that was employed<sup>40</sup>. Crack length was monitored continuously using the Direct Current Potential Difference (DCPD) method<sup>41, 42</sup> utilizing a constant current of 12.000 to 15.000 ± 0.005 A. Voltage readings, amplified up to 20,000 times, were only collected within 25% of the peak load during each load cycle in order to eliminate crack wake electrical shorting which may cause a false crack length measurement. For the constant current power supply, the DCPD potential resolution was ±0.13 μV and the associated resolvable average crack extension was 4 μm. The da/dN was determined by linear regression of crack length versus load cycles data which were generally linear for constant ΔK loading.

Fatigue experiments were conducted using a servo-hydraulic machine operated in load control with a constant amplitude sinusoidal waveform. All specimens were precracked in the test environment prior to EFCP experimentation under a constant ΔK of 7 MPa√m, R of 0.1 or 0.3, and *f* of 1 to 5 Hz to a total notch plus fatigue precrack length of 0.6 mm. This minimized net-section plastic deformation during initial loading and provided a sharpened fatigue crack for the EFCP experiments. All experiments were loaded with a constant stress intensity range (ΔK = K<sub>max</sub> - K<sub>min</sub>) of 7 MPa√m constant stress ratio (R = K<sub>min</sub>/K<sub>max</sub>) of 0.58, and varied *f* between 30 Hz and 0.06 Hz. Each *f* was maintained constant for at least 0.5 mm of crack extension. During loading, each specimen was polarized at either a potential near the freely corroding or open circuit (OCP) level (-500 mV<sub>SCE</sub>), anodically (up to OCP + 150 mV), or cathodically (as low as OCP - 100 mV). Scanning Electron Microscopy (SEM) was performed to characterize the fatigue crack surface morphology as a function of *f* and environment. Specimens were ultrasonically cleaned in acetone and methanol after removal from the test environment, and then preserved in vacuum.

### 1.10.5 Results

#### 1.10.5.1 EFCP

Addition of molybdate to pure chloride solution effectively inhibits EFCP at low *f* for C47A-T86 stressed at a constant ΔK of 7 MPa√m and R of 0.58 under near open circuit (OCP) polarization. The pure NaCl behavior for C47A-T86, which exhibits decreasing da/dN with decreasing *f* and is indicative of alloy-induced inhibition, is shown at several fixed applied potentials ranging from -500 to -750 mV<sub>SCE</sub> in Figure 202. For an applied polarization of -500 mV<sub>SCE</sub>, near OCP for 0.06M NaCl + 0.6M Na<sub>2</sub>MoO<sub>4</sub>, an addition of 0.6M Na<sub>2</sub>MoO<sub>4</sub> to 0.06M NaCl (■) somewhat promotes crack growth at frequencies of 6 Hz and greater; but critically, da/dN decreases to vacuum level as *f* decreases from 3 Hz to 0.1 Hz. *f*<sub>critUB</sub>, the frequency above which inhibition is no longer observed, is between 3 and 6 Hz. The rapid decrease in da/dN that occurs near *f*<sub>critUB</sub> will be addressed in the Discussion. An *f*<sub>critLB</sub> of 0.1 Hz, the frequency at which maximum inhibition is attained and *f*-independent behavior exists, is suggested by the data in Figure 202. Although *f* values lower than 0.1 Hz were not probed to ensure that a *f*-independent regime exists, this *f*<sub>critLB</sub> is assumed as da/dN at 0.1 Hz is equivalent to that measured for this alloy when stressed in ultra high vacuum (about 2.3x10<sup>-6</sup> mm/cyc)<sup>16</sup>. These results indicate that molybdate, at low *f*, is capable of completely eliminating the environmental contribution to EFCP, just as it did for 7075-T651<sup>28, 34</sup>.



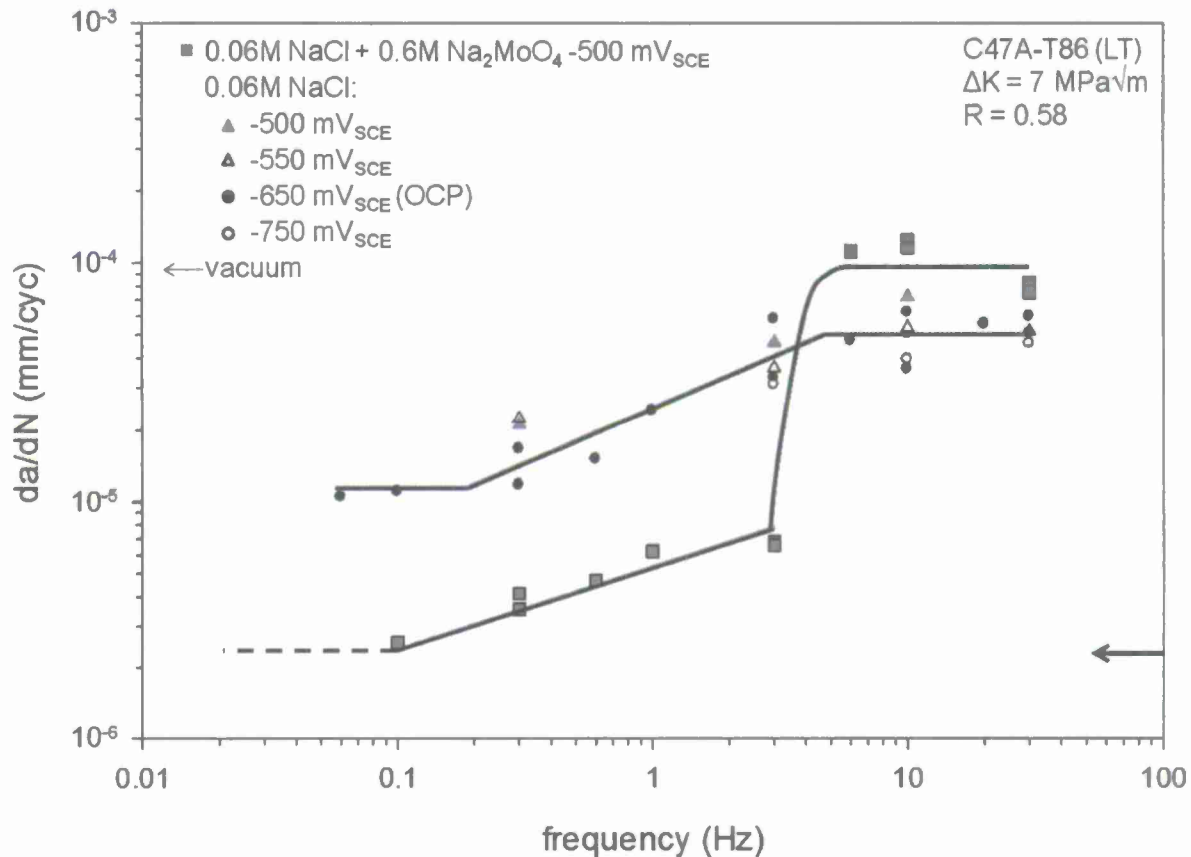


Figure 202. Loading frequency dependence of  $da/dN$  for C47A-T86 (L-T) stressed in aqueous solutions of chloride and chloride-molybdate at a constant  $\Delta K$  of 7 MPa $\sqrt{m}$  and  $R$  of 0.58.

The 0.06M NaCl data at 4-fixed potential levels were reported by Warner<sup>24, 28</sup>. The ultra-high vacuum  $da/dN$  level was reported by Ro et al.<sup>14-16</sup>.

The magnitude of ion-assisted inhibition of EFCP in C47A-T86 depends on applied potential. Figure 203 shows that for a  $f$  of 6 Hz and greater, where no inhibition was seen for -500 mV<sub>SCE</sub> (OCP polarization; Figure 202), there is no effect of applied polarization; both a 100 mV anodic (-400 mV<sub>SCE</sub>: $\blacklozenge$ ) and a 100 mV cathodic (-600 mV<sub>SCE</sub>: $\blacklozenge$ ) polarization produced  $da/dN$  greater than 0.06M NaCl at all polarizations and equal to that for 0.06M NaCl + 0.6M Na<sub>2</sub>MoO<sub>4</sub> under open circuit polarization. For  $f$  at and below 3 Hz, the effect of applied polarization is significant. At 3 Hz and 0.3 Hz, the -600 mV<sub>SCE</sub> (cathodic) polarization produced  $da/dN$  between that measured for pure chloride at all polarizations and chloride-molybdate solution at OCP polarization. At 3 Hz and the -400 mV<sub>SCE</sub> polarization,  $da/dN$  was initially between that for pure chloride and chloride-molybdate at OCP polarization ( $1.8 \times 10^{-5}$  mm/cyc) like the -600 mV<sub>SCE</sub> polarization result; but after 1.4 h into the 3 Hz loading segment,  $da/dN$  fell for 0.9 h until stabilizing at  $3.6 \times 10^{-6}$  mm/cyc. This shift in  $da/dN$  is indicated by the arrow in Figure 203 and highlighted by the crack length versus load-cycle data in Figure 204. (These results are typical of the high level of linearity observed for crack length versus load cycles measured at constant  $\Delta K$  and  $R$ , allowing for good resolution of differences in steady state  $da/dN$  due to changing  $f$



and transient effects of environment.) The  $-400 \text{ mV}_{\text{SCE}}$  polarization exhibits the largest inhibiting capacity by producing vacuum level  $da/dN$  at 0.3 Hz. This implies that the 100 mV anodic polarization increased  $f_{\text{critLB}}$  to at or above 0.3 Hz and increased the  $f$  range over which the environmental contribution to FCP can be eliminated.

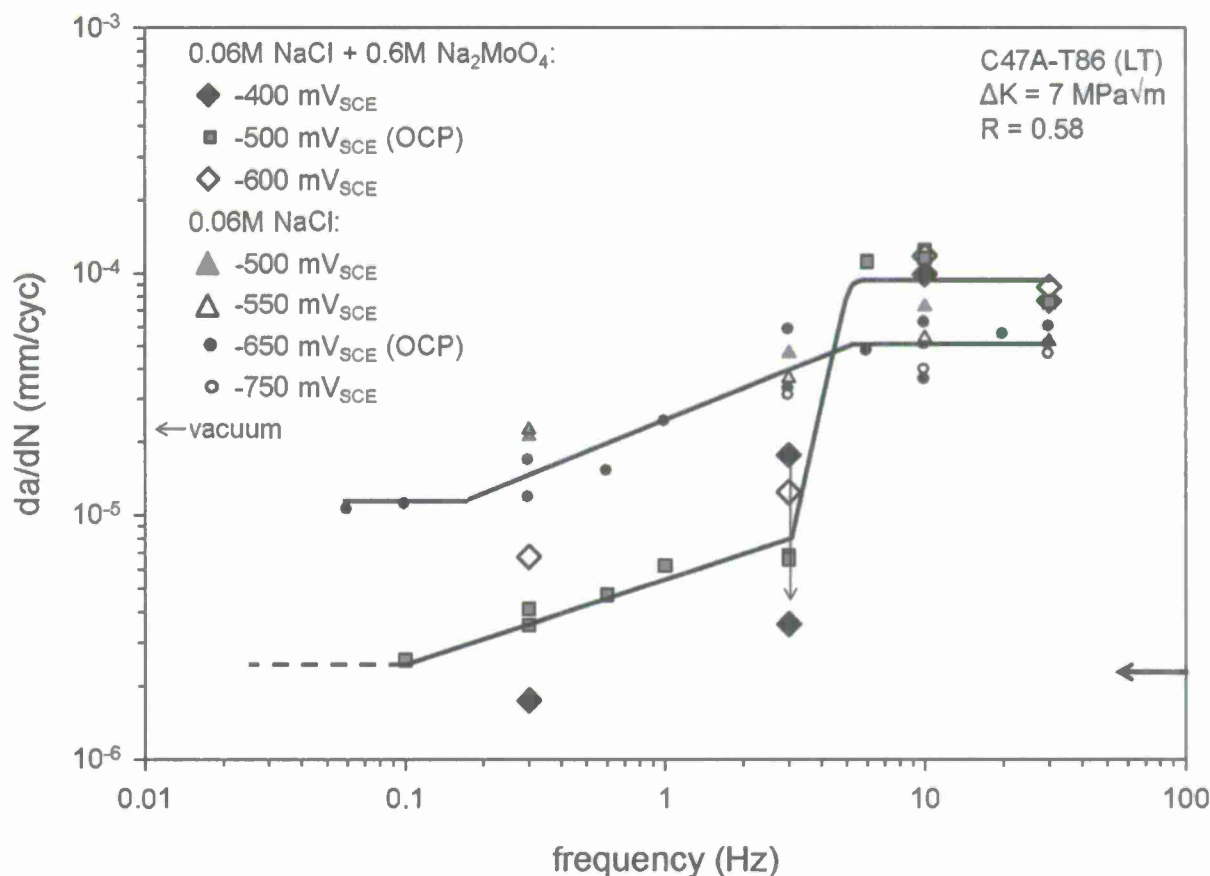


Figure 203. Loading frequency and applied potential dependencies of  $da/dN$  for C47A-T86 (L-T) stressed in aqueous chloride and chloride-molybdate solutions at constant  $\Delta K$  of  $7 \text{ MPa}\sqrt{\text{m}}$  and  $R$  of 0.58.

The 0.06M NaCl data were reported by Warner<sup>24, 28</sup>. The  $da/dN$  for the chloride-molybdate solution at  $-500 \text{ mV}_{\text{SCE}}$  is repeated from Figure 202. The diamonds represent results from loading in 0.6M  $\text{Na}_2\text{MoO}_4$  with applied polarization of either  $-400 \text{ mV}_{\text{SCE}}$  (filled) or  $-600 \text{ mV}_{\text{SCE}}$  (open). The arrow for  $-400 \text{ mV}_{\text{SCE}}$  and 3 Hz represents a  $da/dN$  change during loading which is expanded upon in Figure 204. The ultra-high vacuum  $da/dN$  level was reported by Ro et al.<sup>14-16</sup>

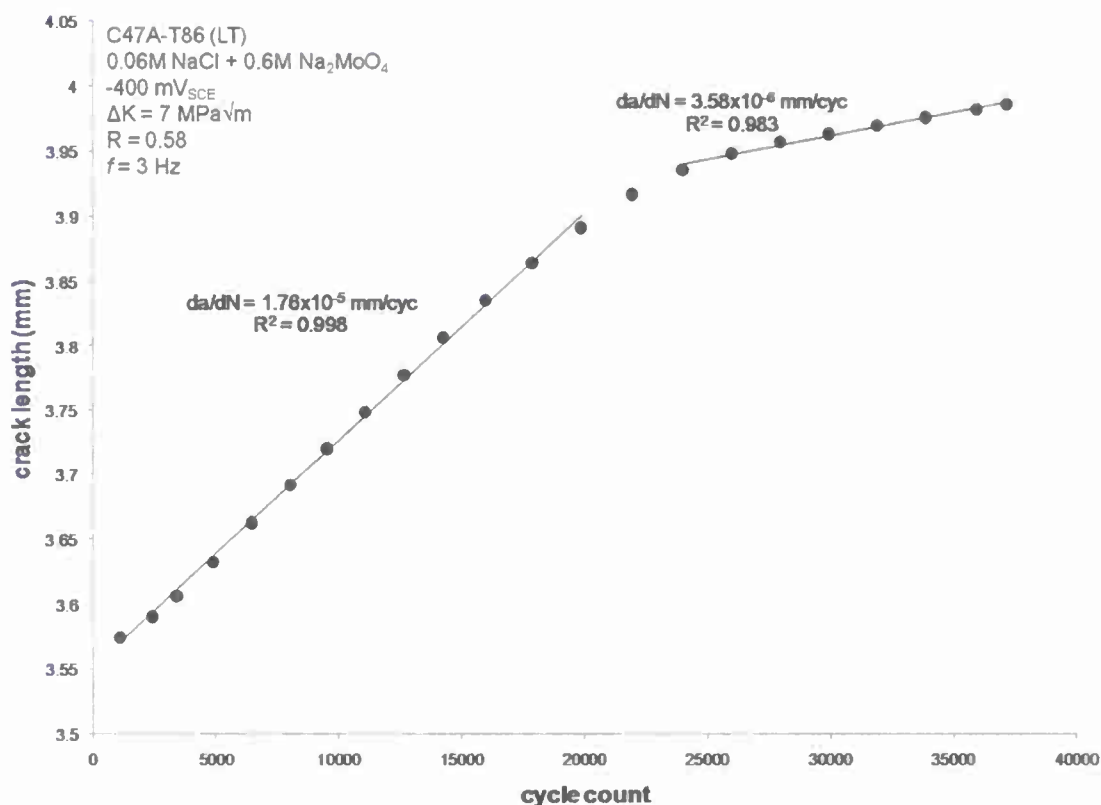


Figure 204. Crack length versus fatigue loading cycles for C47A-T86 (L-T) stressed in 0.06M NaCl + 0.6M Na<sub>2</sub>MoO<sub>4</sub> with polarization of -400 mV<sub>SCE</sub> at constant  $\Delta K$  of 7 MPa $\sqrt{\text{m}}$ ,  $R$  of 0.58, and  $f$  of 3 Hz.

#### 1.10.5.2 Fractography

Investigation of the crack surface morphology for C47A-T86 stressed under full immersion in chloride-molybdate solution is hindered by corrosion product and/or corrosion topography which likely resulted from crack wake corrosion not necessarily related to the crack tip processes that control EFCP and  $da/dN$ . An example of this corrosion product can be seen in Figure 205. This crack wake artifact is inevitable given the prolonged exposure time associated with the slower loading frequencies and multiple- $f$  segments for a single SENT specimen. Similar corrosion product was seen in the prior 7075 molybdate study when the SENT specimen was stressed for long times (4 weeks) in solution. Figure 206 shows that further into the fatigue experiment at longer crack lengths, the corrosion product on the crack wake is no longer present; but is replaced with a cracked surface oxide which also obscures the crack morphology. Qualitative EDS, as seen in Figure 207, shows a considerable Mo peak for the surface corrosion product (Figure 207a) and cracked surface oxide (Figure 207b). Alloy C47A does not contain Mo.

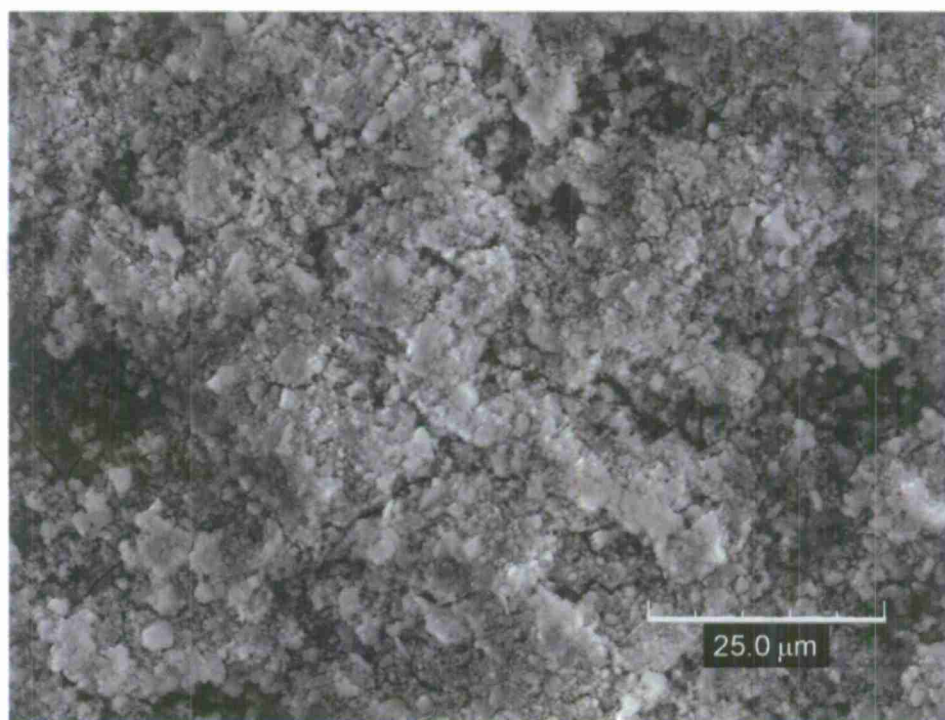


Figure 205. SEM image of the fatigue crack surface morphology for a specimen of C47A-T86 stressed in 0.06M NaCl + 0.6M Na<sub>2</sub>MoO<sub>4</sub> (near-OCP polarization of -500 mV<sub>SCE</sub>) at  $\Delta K$  of 7 MPa $\sqrt{m}$ , R of 0.58, and  $f$  of 3 Hz. The direction of crack growth is from bottom to top.

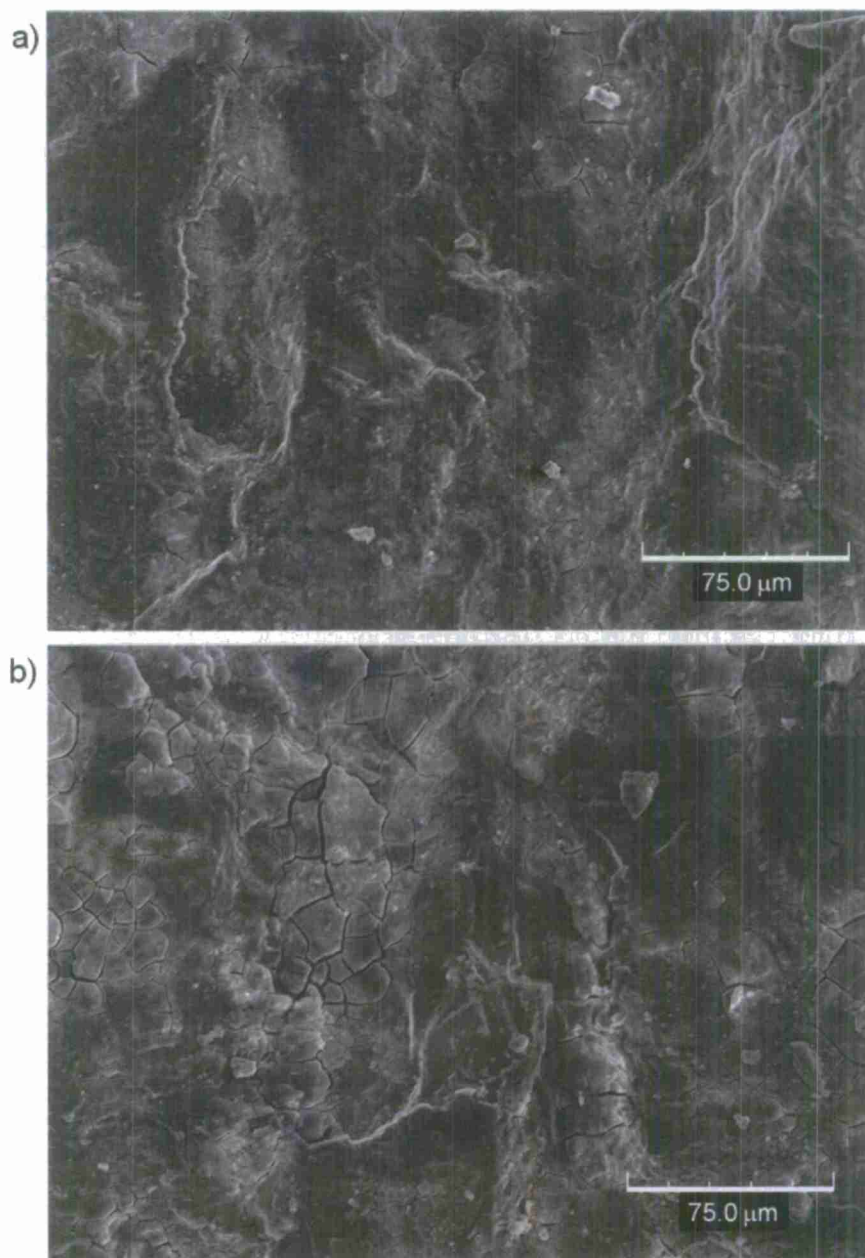


Figure 206. SEM images of the fatigue crack surface morphology for a specimen of C47A-T86 stressed in 0.06M NaCl + 0.6M Na<sub>2</sub>MoO<sub>4</sub> at  $\Delta K$  of 7 MPa $\sqrt{m}$ , R of 0.58, and 0.3 Hz. a) -500 mV<sub>SCE</sub> and b) -400 mV<sub>SCE</sub>. The direction of crack growth is from bottom to top.



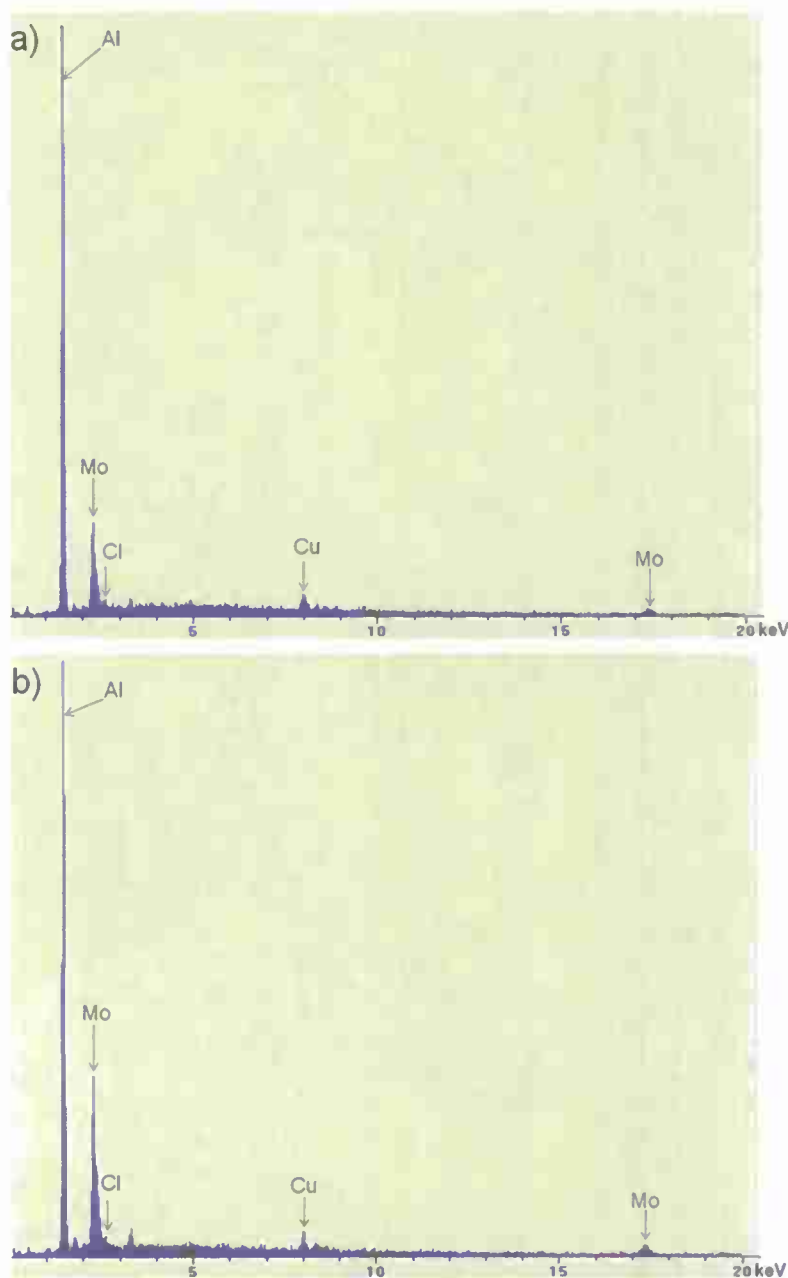


Figure 207. a) EDS spectrum of fatigue crack surface reaction product produced during stressing in 0.06M NaCl + 0.6M Na<sub>2</sub>MoO<sub>4</sub> ( $\Delta K = 7 \text{ MPa}\sqrt{\text{m}}$ ,  $R = 0.58$ ,  $f = 3 \text{ Hz}$ ) at near-OCP of  $-500 \text{ mV}_{\text{SCE}}$ .

The dead time while acquiring this spectrum was 21%. b) EDS spectrum of a cracked surface oxide found on the fatigue crack surface generated in 0.06M NaCl + 0.6M Na<sub>2</sub>MoO<sub>4</sub> just prior to removal from solution ( $\Delta K = 7 \text{ MPa}\sqrt{\text{m}}$ ,  $R = 0.58$ ,  $f = 0.3 \text{ Hz}$ ) while applying  $-400 \text{ mV}_{\text{SCE}}$ . The dead time while acquiring this spectrum was 19%.

Figure 208 shows the crack surface morphology for the EFCP segment conducted just before specimen removal from solution, which was generated while stressing at 0.3 Hz and  $-600 \text{ mV}_{\text{SCE}}$  in  $0.06\text{M NaCl} + 0.6\text{M Na}_2\text{MoO}_4$ . The crack surface is macroscopically flat transgranular mode I with two distinct regions of microscopic morphology which are shown in Figure 208b and c. This crack surface morphology is consistent with the complex facet-like features reported by Ro et al.<sup>15, 16, 39, 43, 44</sup> for the same material stressed in various pressures of pure water vapor, as detailed in the Discussion.

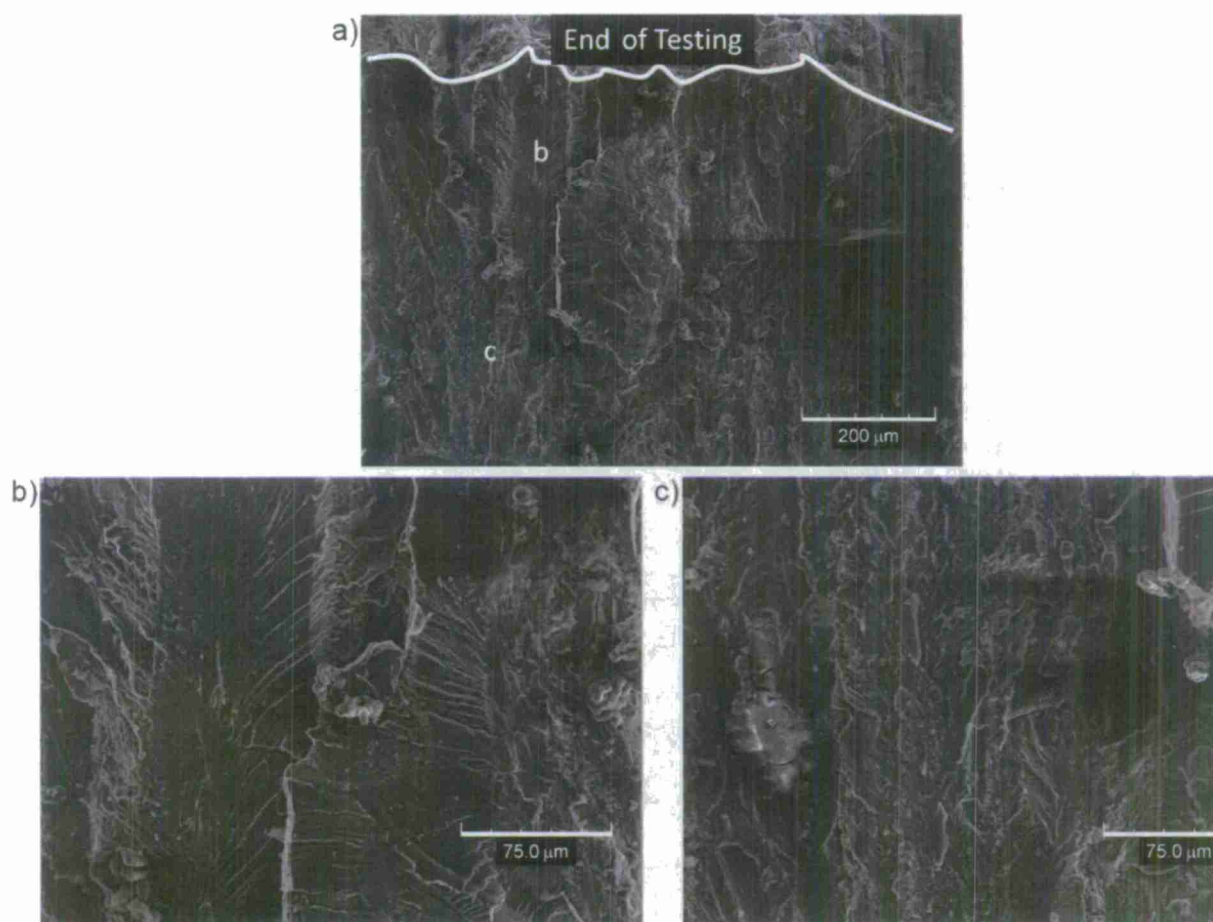


Figure 208. SEM images of the fatigue crack surface morphology for C47A-T86 stressed in  $0.06\text{M NaCl} + 0.6\text{M Na}_2\text{MoO}_4$  at  $\Delta K$  of  $7 \text{ MPa}\sqrt{\text{m}}$ ,  $R$  of 0.58,  $f$  of 0.3 Hz, and  $-600 \text{ mV}_{\text{SCE}}$ .

b) and c) show higher magnification images of the two distinct regions labeled in a). The direction of crack growth is from bottom to top.

### 1.10.6 Discussion

#### 1.10.6.1 Inhibition Mechanism

Results in Figure 202 show that ion-assisted inhibition by molybdate occurs in age-hardenable Al-Cu based alloys which also exhibit alloy-induced inhibition in pure chloride solutions. Furthermore,  $\text{MoO}_4^{2-}$  inhibition of C47A-T86 parallels  $\text{MoO}_4^{2-}$  and  $\text{CrO}_4^{2-}$  inhibition in 7075-T651 which is not typically capable of alloy-induced inhibition<sup>3, 4, 28, 34</sup>. The primary mechanism controlling  $\text{MoO}_4^{2-}$  EFCP inhibition and the  $f$  dependence, which was established for 7075-T651 stressed in chloride-chromate and chloride-molybdate solutions, is the film rupture-H embrittlement mechanism<sup>12, 28-31, 34</sup>. This mechanism attributes EFCP inhibition to  $\text{MoO}_4^{2-}$  (or  $\text{CrO}_4^{2-}$ ) stabilizing a crack tip passive film which reduces crack tip Al dissolution; and in turn, decreases H production/uptake and the environmental contribution to FCP by one or more of 3 H-based damage mechanisms: (a) reduced metal ion concentration and hydrolysis resulting in reduced crack acidification and thus a reduced overpotential for H production; (b) reduced exchange current density for cathodic water reduction, owing to the catalytic action of corroding Al and/or the effect of reduced acidification; and (c) acting as a barrier to H uptake.<sup>12, 28-31, 34</sup>

Crack closure from corrosion product build up is not believed to be a significant part of the mechanism for either alloy-induced inhibition<sup>24</sup> or molybdate ion-assisted inhibition of C47A-T86 stressed in the chloride solutions studied. Because crack closure is difficult to quantify experimentally, the current experiments were designed at relatively high stress ratio ( $R = 0.58$ ) and high  $\Delta K$  (7 MPa $\sqrt{\text{m}}$ ) to minimize this complicating effect. (The maximum and minimum crack tip opening displacements in this fatigue-load cycle are on the order of 2 to 0.5  $\mu\text{m}$ , and opening displacements increase substantially toward the crack mouth.) Moreover, experiments were conducted at constant  $\Delta K$  to detect crack closure which, if present, results in decreasing  $da/dN$  with increasing time in solution. When corrosion product closure is operative in aluminum alloys stressed in pure NaCl, crack arrest and frequency-history dependence are likely, as reported for constant  $\Delta K$  experiments with 7075-T7X1<sup>3, 4</sup>. Addition of chromate eliminated such crack closure by restricting crack-wake corrosion for this overaged 7075 case. For C47A-T87<sup>15, 24, 28</sup> and 7075-T651<sup>3, 4, 34</sup> stressed in pure NaCl at constant  $\Delta K$ ,  $da/dN$  was invariably constant with time in solution during a single-constant frequency segment. The possibility of crack closure contributing to decreasing  $da/dN$  was examined for a similar Al-Cu-Mg alloy (C433-T351) which exhibited self inhibition in pure NaCl;  $da/dN$  was constant with exposure time at constant  $\Delta K$  and immediately changed with increasing frequency, which is characteristic of minimal corrosion product closure at lower  $f$  levels<sup>24</sup>. For C47A-T86 stressed in pure NaCl and NaCl + 0.6M  $\text{Na}_2\text{MoO}_4$ , non-linear crack length versus  $N$  at constant  $\Delta K$  and  $f$ , and crack arrest at low  $f$ , were not observed for applied potentials of between -750 mV<sub>SCE</sub> and -500 mV<sub>SCE</sub> (Figure 203), as amplified in Figure 209. Crack growth rate reduction with time in solution at constant  $\Delta K$  and  $f$  was observed for NaCl- $\text{Na}_2\text{MoO}_4$  exposure with the -400 mV<sub>SCE</sub> anodic polarization and loading frequency of 3 Hz (Figure 203 and Figure 204), but not for other frequencies at this potential and crack arrest was never observed. The transient-reduced  $da/dN$  at -400 mV<sub>SCE</sub> is likely due to a change in crack tip passive film stability rather than corrosion product closure<sup>34</sup>, as discussed in an ensuing section. However, since a comparable experiment with a -400 mV<sub>SCE</sub> anodic polarization was not conducted for pure NaCl, this interpretation is speculative.

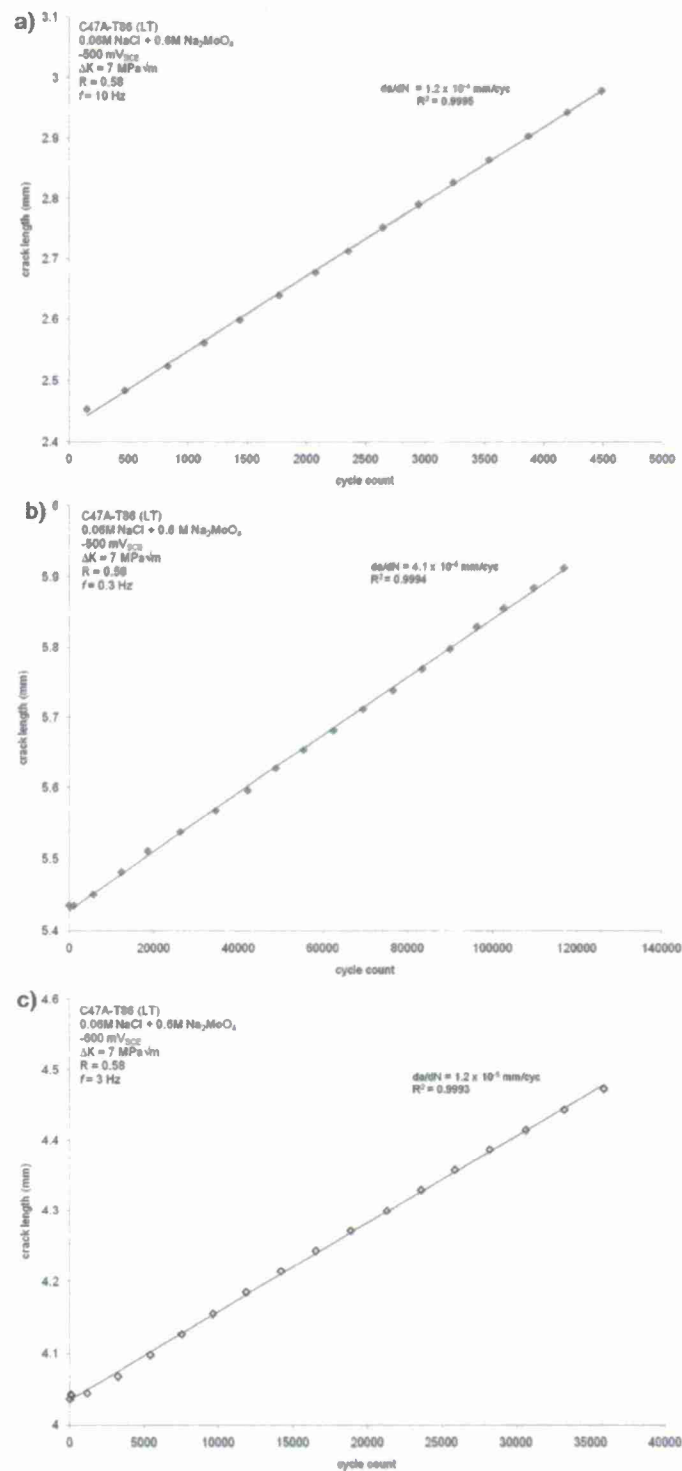


Figure 209. Crack length versus fatigue loading cycles for C47A-T86 (L-T) stressed in 0.06M NaCl + 0.6M Na<sub>2</sub>MoO<sub>4</sub> at constant  $\Delta K$  of 7 MPa $\sqrt{\text{m}}$  and  $R$  of 0.58 with polarizations and  $f$  of (a) - 500 mV<sub>SCE</sub> and 10 Hz, (b) -500 mV<sub>SCE</sub> and 0.3 Hz, and (c) -600 mV<sub>SCE</sub> and 3 Hz.



### 1.10.6.2 Effect of Frequency

For C47A-T86, addition of 0.6M  $\text{Na}_2\text{MoO}_4$  to 0.06M NaCl effectively inhibits EFCP by reducing  $da/dN$  by close to two orders of magnitude over the frequency range from 6 Hz to 0.1 Hz ( $8.3 \times 10^{-5}$  mm/cyc to  $2.6 \times 10^{-6}$  mm/cyc respectively), and by almost an order of magnitude when compared to growth rates typical of alloy-induced inhibition in pure NaCl ( $1.1 \times 10^{-5}$  mm/cyc to  $2.6 \times 10^{-5}$  mm/cyc respectively), as shown in Figure 202. As in  $\text{MoO}_4^{2-}$  inhibition of EFCP in 7075-T651, the effect of environment on FCP was eliminated completely at  $f_{\text{critLB}}$  of 0.1Hz, as evidenced by vacuum level  $da/dN$  ( $2.6 \times 10^{-6}$  mm/cyc). This suggests that molybdate is a robust EFCP inhibitor that is capable of eliminating the environmental acceleration of FCP in multiple age-hardenable aluminum alloys, at least for the molybdate to chloride ratio examined in this study.

Because fatigue loading mechanically destabilizes the crack tip passive film by one or more rupture events when strain accumulated at the crack tip exceeds the critical level required for film rupture, the observed  $f$  dependence for C47A-T86 in chloride-molybdate solutions is a consequence of the interplay between rupture and repassivation of the  $\text{MoO}_4^{2-}$  stabilized passive film. Therefore, the  $f$  dependence for  $\text{MoO}_4^{2-}$  inhibition of EFCP in C47A-T86 (Figure 202) is described as follows: Below an  $f_{\text{critLB}}$  of about 0.1 Hz, the crack tip strain rate ( $\dot{\epsilon}_{\text{tip}}$ , which controls the rate of film rupture and is proportional to  $f$  and  $\Delta K$ ) is sufficiently low to maintain stability of the crack tip passive film against mechanical damage. Additionally, upon an isolated rupture event at low frequencies near  $f_{\text{critLB}}$ , crack tip solution conditions are such that molybdate acts as a pH buffer to consume any  $\text{H}^+$  generated and maintain a neutral to alkaline pH<sup>28, 34</sup>. As  $f$  increases above  $f_{\text{critLB}}$ ,  $\dot{\epsilon}_{\text{tip}}$  is sufficient for mechanical destabilization of the crack tip passive film and rupture occurs leaving the crack tip unprotected until repassivation. As  $\dot{\epsilon}_{\text{tip}}$  increases in this  $f$  regime,  $t_{\text{repass}}$  remains the same while  $t_{\text{rup}}$  decreases causing H production and uptake to increase with increasing  $\dot{\epsilon}_{\text{tip}}$  and  $f$  for a constant  $\Delta K$ . For frequencies at and above  $f_{\text{critUB}}$ , which is between 3 and 6 Hz for  $\text{MoO}_4^{2-}$  EFCP inhibition in C47A-T86 (Figure 202), the time between rupture events is insufficient to allow for significant repassivation of the crack tip passive film; basically  $t_{\text{repass}}$  is greater than  $t_{\text{rup}}$ , and molybdate inhibition is lost. Because the presence of  $\text{Al}^{3+}$  which hydrolyzes to produce  $\text{H}^+$  increases as  $f$  increases above  $f_{\text{critLB}}$ , pH buffering to near neutral is overwhelmed and not available to assist EFCP inhibition at high  $f$ <sup>28, 34</sup>.

Molybdate ion-assisted inhibition of C47A-T86 produces an abrupt decrease in  $da/dN$  at or near  $f_{\text{critUB}}$  (Figure 202). This abrupt transition was not seen in alloy-induced inhibition of C47A-T86 or C433-T351<sup>24, 28</sup>, an Al-Cu-Mg alloy, nor in molybdate or chromate ion-assisted inhibition of 7075-T651<sup>4, 28, 34</sup>. A speculative explanation is that EFCP rates for C47A are more sensitive than 7075 to small changes in the FPZ H concentration. This H concentration dependence of  $da/dN$  will interact with the amount of crack tip H produced for the various environmental conditions studied. Research on fatigue crack growth rate as a function of environmental exposure, ranging from ultra high vacuum with various pressures of water vapor ( $P_{\text{H}_2\text{O}}$ ) to full immersion in aqueous sodium chloride solutions for both 7075-T651<sup>28, 34, 45</sup> and C47A-T86<sup>14-16</sup>, supports this interpretation. A reproduction of the exposure dependence ( $P_{\text{H}_2\text{O}}/f$ ) for both 7075-T651<sup>28, 34, 45</sup> and C47A-T86<sup>14-16</sup> is shown in Figure 210, along with arrows indicating  $da/dN$  levels for full immersion in several NaCl and NaCl- $\text{Na}_2\text{MoO}_4$  electrolytes from Figure 202. C47A shows an abrupt change in  $da/dN$  with a small change in  $P_{\text{H}_2\text{O}}/f$  in Regime II, while no such abrupt transition is seen for 7075-T651. Overall, large changes in exposure parameter, proportional to crack tip H concentration, produce a larger change in  $da/dN$  for C47A-T86 compared to 7075-T651 (Figure 210). Furthermore, crack growth rates for C47A-T86 stressed under full immersion in chloride-molybdate solution at 6 Hz and greater correspond to Regime

IV crack growth rates, while those for 3 Hz and below correspond to Regimes I and II crack growth rates which are below the abrupt transition in  $da/dN$ . These measured crack growth rates for C47A in chloride-molybdate solutions (arrows in Figure 210) at  $f$  equal to and below 3 Hz correspond to those in Regimes I and II and suggest that the  $\text{MoO}_4^{2-}$  stabilized passive film reduced the H concentration to an effective  $P_{\text{H}_2\text{O}}/f$  of between  $10^{-2}$  Pa·s and 1 Pa·s, below that expected for full immersion and high humidity air. Additionally, crack growth rates for C47A-T86 in pure chloride solution at  $f_{\text{critLB}}$  correspond to those in the lower bound of Regime III. This comparison in Figure 210 suggests that the native aluminum passive film responsible for alloy-induced inhibition<sup>24</sup> does not reduce H production and uptake to the extent that the  $\text{MoO}_4^{2-}$  stabilized passive film does, and provides an explanation as to why an abrupt decrease in  $da/dN$  was not seen for pure chloride. While there is not a wealth of data for 7075-T651 in Figure 210, the trend lines in each regime have been established for several aluminum alloy systems<sup>14-16</sup>.

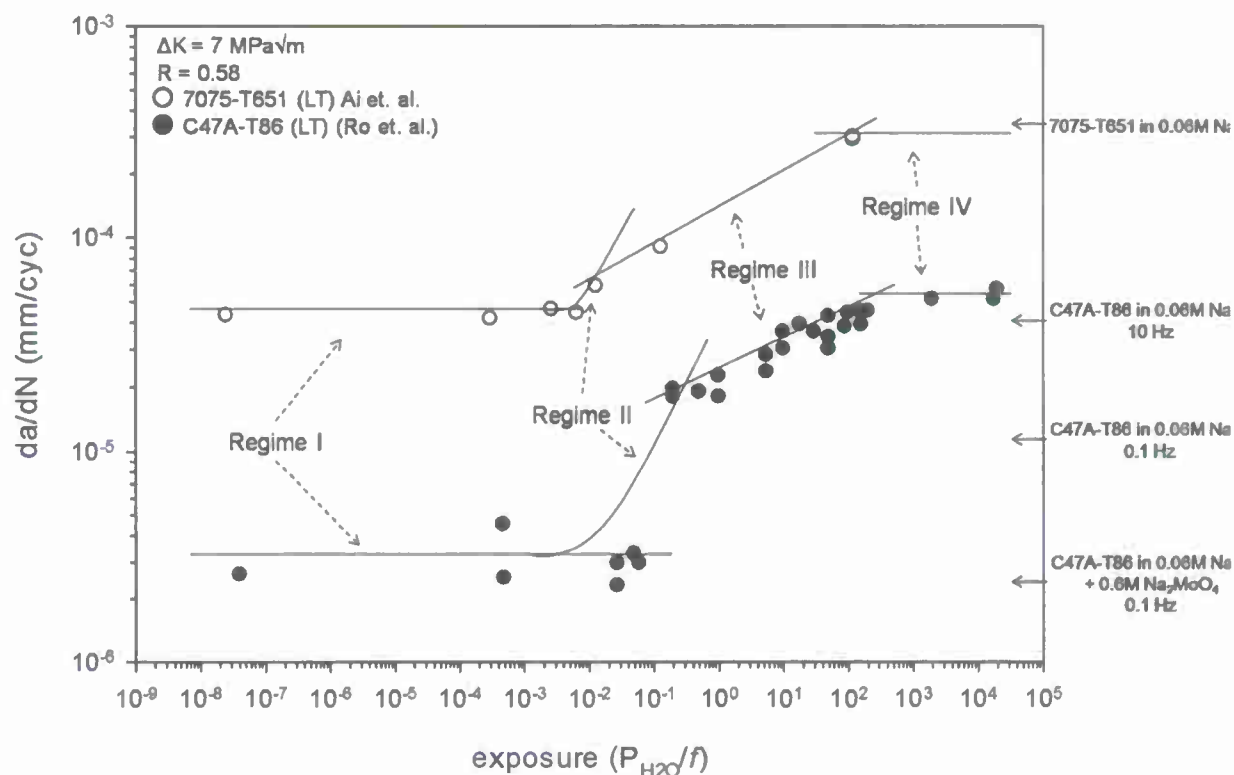


Figure 210. Water vapor exposure dependence of  $da/dN$  for C47A-T86 and 7075-T651 at a  $\Delta K$  of 7 MPa $\sqrt{m}$  and  $R$  of 0.58.

The C47A results (•) were reported by Ro et al.<sup>14-16</sup>, 7075 data (o) reported by Ai et al.<sup>45</sup>, and the data for 7075 full immersion in NaCl and C47A full immersion in chloride and chloride-molybdate solutions were reported by Warner et al.<sup>28, 34</sup> and represented as arrows at measured levels of  $da/dN$ .

As  $f_{critUB}$  is the point where passive film rupture becomes too rapid for sufficient repassivation, bare surface repassivation kinetics can be compared to the calculated time between rupture events ( $t_{rup}$ ) to validate the film rupture-H embrittlement mechanism.  $t_{rup}$  can be estimated by the ratio of the film rupture strain (uncertain, but likely on the order of 1% for a passive film on Al<sup>46, 47</sup>) to the crack tip strain rate ( $\dot{\epsilon}_{tip}$ )<sup>29-31</sup>. Analytical and experimental approaches estimated the average  $\dot{\epsilon}_{tip}$  during cyclic loading as<sup>12</sup>:

$$\frac{\partial \epsilon}{\partial t_{tip}} = \beta (\Delta K)^\lambda f \quad \text{Equation 1}$$

The material constants,  $\lambda$  and  $\beta$ , were determined for fatigue loading of 7075-T6 using *in situ* SEM stereo-imaging measurements of crack tip opening displacement, and are 3.2<sup>48, 49</sup> and 1.2x10<sup>-4</sup><sup>49</sup> respectively. These constants are relevant to  $\dot{\epsilon}_{tip}$  in units of s<sup>-1</sup> with  $\Delta K$  as MPa $\sqrt{m}$  and  $f$  as Hz. As the values for these coefficients are unknown for C47A-T86, the 7075-T6 values are used to estimate  $\dot{\epsilon}_{tip}$  and  $t_{rup}$ , and thus the inferred  $t_{repass}$ . Using the maximum

possible  $f_{\text{critUB}}$  (6 Hz in Figure 202), Equation 1 gives an  $\dot{\epsilon}_{\text{tip}}$  of  $0.36 \text{ s}^{-1}$ . From this,  $t_{\text{repass}}$  is 0.028 s. This is consistent with the  $t_{\text{repass}}$  of 0.022 s that was estimated by the same procedure applied to measured  $f_{\text{critUB}}$  for molybdate inhibition of 7075-T651<sup>28, 34</sup>. Unfortunately, there are no published data on repassivation transients for bare Al or Al-Cu-Li alloys in chromate or molybdate solutions; but the repassivation behavior of Al in chloride-free electrolytes provides a lower bound approximation for repassivation times. Without chloride, literature results show that Al repassivates in benign electrolytes at times on the order of 0.002 to 0.003 s<sup>50, 51</sup>. Given the range of frequencies between  $f_{\text{critUB}}$  and  $f_{\text{critLB}}$ , and the chemical/electrochemical differences between the crack tip and repassivation experiments, this order of magnitude in the repassivation time is consistent with the values of 0.028 s and 0.022 s inferred from  $f_{\text{critUB}}$ .

The  $f_{\text{critLB}}$  of 0.1 Hz in Figure 202 corresponds to an  $\dot{\epsilon}_{\text{tip}}$  of  $0.006 \text{ s}^{-1}$  using Equation 1. The  $\dot{\epsilon}_{\text{tip}}$  which corresponds to the  $f_{\text{critLB}}$  for  $\text{MoO}_4^{2-}$  inhibition in 7075-T651 is  $0.001 \text{ s}^{-1}$ <sup>28, 34</sup>. This difference implies that the Mo-bearing passive film on Al-Cu-Li is stable to higher crack tip strain rates and more resistant to mechanical degradation than the Mo-bearing passive film on 7075-T651. If  $\dot{\epsilon}_{\text{tip}}$  at  $f_{\text{critLB}}$  was equivalent to that for 7075-T651 ( $0.001 \text{ s}^{-1}$ ), then the lower bound critical frequency which would be expected for the loading conditions in this study is 0.016 Hz. This is an order of magnitude lower than that suggested by the limited low-frequency data given in Figure 202.

Above  $f_{\text{critUB}}$ , addition of 0.6M  $\text{Na}_2\text{MoO}_4$  to 0.06M NaCl at -500 mV<sub>SCE</sub> mildly accelerated  $da/dN$  in C47A-T86, as shown in Figure 202. This implies that addition of  $\text{Na}_2\text{MoO}_4$  to pure chloride solution minimized alloy-induced inhibition. This is expected due to the fact that alloy-induced inhibition is attributed to increased cathodic reaction kinetics in the crack wake from Cu enrichment after localized corrosion of anodic crack wake  $\text{Al}_2\text{CuLi}$  precipitates<sup>24, 28</sup>. As molybdate is a localized corrosion inhibitor<sup>52-55</sup>, addition of  $\text{Na}_2\text{MoO}_4$  should inhibit the corrosion of crack wake  $\text{Al}_2\text{CuLi}$ ; and thus, impede alloy-induced inhibition. If alloy-induced inhibition is eliminated by molybdate, then  $da/dN$  measured at 6 Hz and greater ( $1.1 \times 10^{-4} \text{ mm/cyc}$ ) represents crack growth when no crack tip passive film is present. Therefore, the crack growth rates associated with 6 Hz and greater in chloride-molybdate solutions represent the  $f$  independent regime predicted by H diffusion modeling<sup>3, 4</sup>; where no passive film is present on the crack tip, crack tip reaction rates and diffusion of H are not rate limiting, and rapid dissolution of bare Al is prevented by a crack tip gel<sup>19, 56, 57</sup>. As such, the  $f$ -dependence for the pure NaCl data at all polarizations shown in Figure 202 and Figure 203, and alloy-induced EFCP inhibition of C47A-T86, is better represented by the trend line plotted in Figure 211. This interpretation shows that alloy-induced inhibition is sustainable to higher  $f$  than was assumed in Figure 202. That is, the plateau  $da/dN$  shown in Figure 202 and Figure 203, expected based on H diffusion modeling<sup>3</sup>, is not real given the higher plateau supported by the data for the chloride-molybdate solution. While this interpretation supports the trend line in Figure 211, the true trend line remains uncertain.) More important, the behavior shown in Figure 211 suggests that ionic and alloy-induced inhibition mechanisms are not synergistic at any frequency. Rather, molybdate inhibition eliminates alloy-induced inhibition of EFCP by reducing corrosion of Cu-rich crack wake phases.



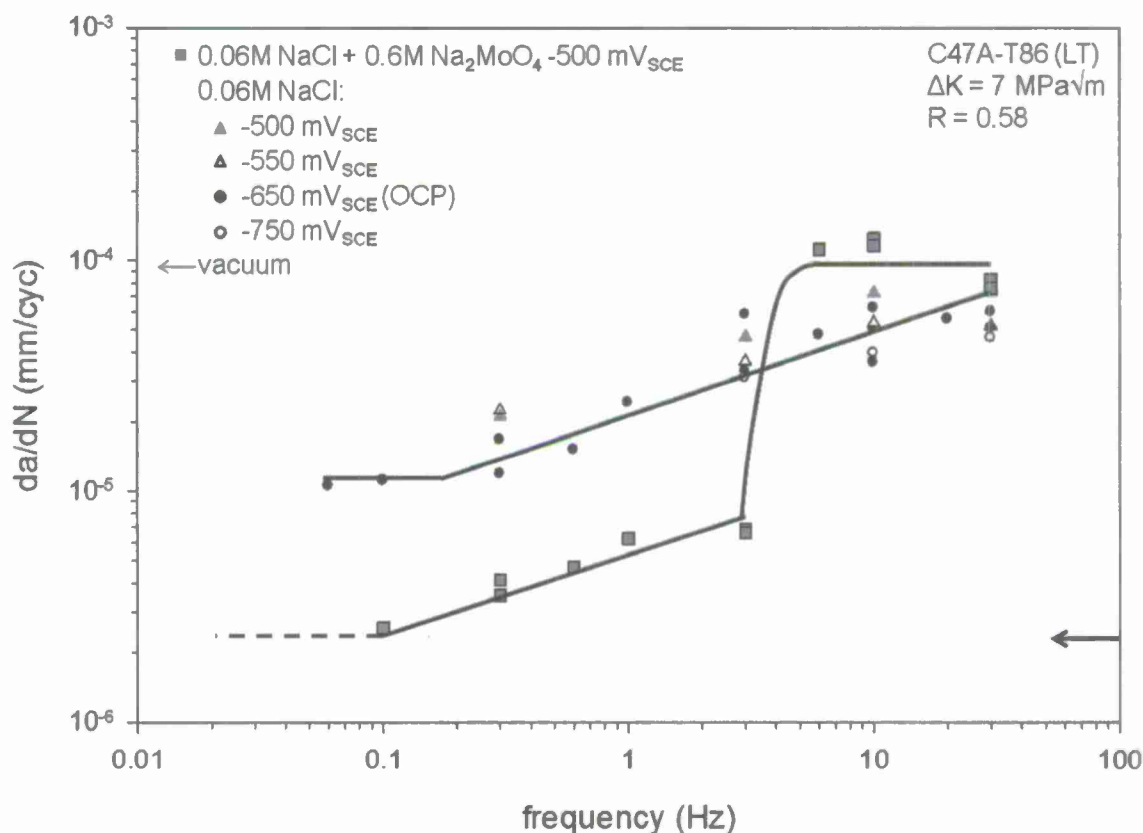


Figure 211. Loading frequency dependence of  $da/dN$  for C47A-T86 (L-T) stressed in solutions of chloride and chloride-molybdate, replotted from Figure 202.

The trend line for pure NaCl alloy induced inhibition is redrawn to reflect the argument that molybdate inhibits alloy induced inhibition that occurs in pure NaCl. Therefore, the high  $f$  molybdate behavior is based on plateau-saturated crack growth in the absence of crack tip passivity.

#### 1.10.6.3 Effect of Applied Potential

The effect of applied polarization on molybdate inhibition of C47A-T86 parallels that reported for 7075-T651<sup>28, 34</sup>. Figure 203 shows that inhibition below  $f_{critUB}$  is possible under slight anodic and cathodic polarizations; but inhibition is enhanced by anodic polarization as  $f_{critLB}$  increases from 0.1 Hz to about 0.3 Hz. Enhanced  $MoO_4^{2-}$  inhibition with anodic polarization was also reported for 7075-T651<sup>28, 34</sup>. This behavior can be explained<sup>28, 34</sup> through consideration of the Mo and Al Pourbaix diagrams<sup>58</sup> and expected crack tip electrochemical conditions<sup>19-21</sup>. Essentially,  $Al_2O_3$  is breached by  $Cl^-$  to allow H production and uptake to occur when molybdate is not in solution. When molybdate is present, crack tip chemical and electrochemical conditions which favor the stability of  $MoO_2$  (Mo-IV) or Mo (because electrodeposition of Mo is unlikely and  $MoO_2$  persists in the Mo stability regime<sup>59</sup>) over  $MoO_4^{2-}$  (Mo-VI) will promote crack tip passivity; and hence, reduce H production and uptake to reduce  $da/dN$ . Crack tip pH and E deviate from that in the bulk solution and applied to the external surface<sup>19-21</sup>. Due to the lack of a strong electrical

connection between the crack tip and external surface, the crack tip potential remains slightly below OCP (IR drop decreases  $E$  to slightly below OCP) unless severely anodically or cathodically polarized<sup>19-21</sup>. In contrast, crack tip pH decreases significantly to a pH as low as 2 under applied anodic polarization, and increases to a pH as high as 12 for applied cathodic polarization<sup>19-21</sup>. These electrochemical conditions pull the crack tip towards the  $\text{MoO}_2$  and Mo stability regime when the bold surface is anodically polarized, and towards the  $\text{MoO}_4^{2-}$  stability regime upon cathodic polarization, as argued for molybdate inhibition of EFCP in 7075-T6<sup>28, 34</sup>.

Figure 203 shows that above the  $f_{\text{critUB}}$  of about 6 Hz there is no effect of applied polarization on  $da/dN$ . According to the film rupture-H embrittlement mechanism, the crack tip passive film is mechanically destabilized above  $f_{\text{critUB}}$ , and there is insufficient time for repassivation between rupture events ( $t_{\text{rup}} \leq t_{\text{repass}}$ ). Therefore, no effect of applied polarization on inhibition is expected unless polarization changes  $t_{\text{repass}}$ . Although applied polarization may affect  $t_{\text{repass}}$ <sup>60, 61</sup>, and subsequently alter  $f_{\text{critUB}}$ , the crack tip potential is not significantly affected by external polarization<sup>19-21</sup>; therefore, no significant effect of polarization on inhibition is expected at and above  $f_{\text{critUB}}$ . This high  $f$  behavior supports the argument that crack growth rates at and above 6 Hz in chloride-molybdate solutions are representative of crack growth in the absence of a crack tip passive film, and supports the NaCl trend lines in Figure 211. Similar high  $f$  polarization behavior was observed in the prior molybdate study on 7075-T651<sup>28, 34</sup>.

#### 1.10.6.4 Fractographic Implications

Research by Ro et al. on EFCP in C47A-T86 quantified fatigue crack surface morphology and crack growth rate as a function of environmental exposure using quantitative SEM-stereology coupled with Electron Backscatter Diffraction (EBSD)<sup>14-16, 39, 43</sup>. The exposure dependence of  $da/dN$  was summarized in Figure 210 (●). The SEM-EBSD established the crystallographic facet orientations on the fracture surface in environments ranging from ultra-high vacuum with various partial pressures of pure water vapor ( $P_{\text{H}_2\text{O}}$ ) to full immersion in aqueous chloride solution for the precise C47A-T86 alloy and loading conditions employed in the current study. Ro et al. found three regimes of behavior: (1) ultra-high vacuum and extremely low water vapor exposures up to  $0.001 \text{ Pa}\cdot\text{s}$  ( $P_{\text{H}_2\text{O}}/f$ ) where the fatigue crack surface was composed of over 90 % slip band cracking (SBC:  $\{111\}$  facets); (2) exposures of 0.05 to  $0.2 \text{ Pa}\cdot\text{s}$  where  $\{110\}$  and  $\{100\}$  facets increasingly replaced  $\{111\}$  features as  $P_{\text{H}_2\text{O}}/f$  increased; and (3) exposures at and above  $0.2 \text{ Pa}\cdot\text{s}$  where the remainder of  $\{111\}$  facets were replaced by high index  $\{hkl\}$  facets. This latter regime includes full immersion in pure NaCl solution. Figure 212 summarizes the percentage of each facet type for each regime.

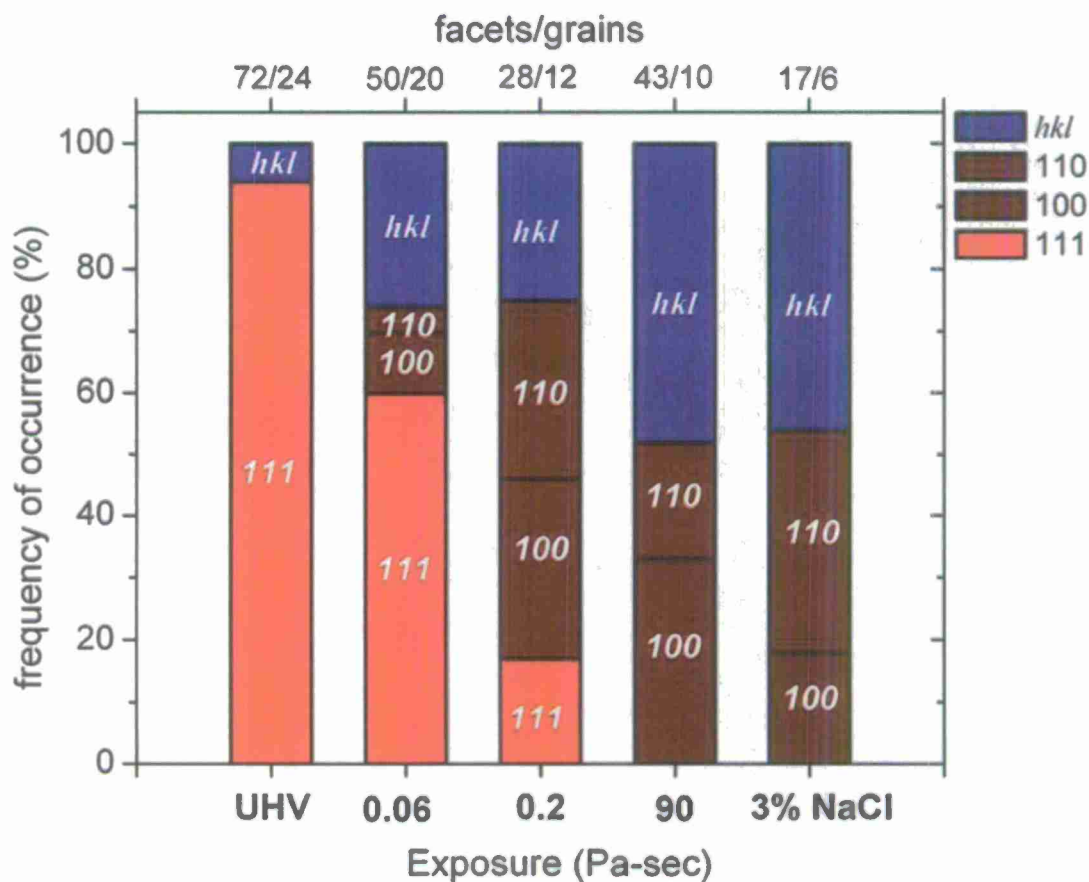


Figure 212. Summary of results from Ro et al.<sup>14-16, 39, 43</sup> for measured crack surface crystallography as a function of water vapor exposure for the lot of Al-Cu-Li alloy used in the present study.

The results for measured crack growth rate as a function of water vapor exposure were summarized in Figure 210.

The environmental contribution to fatigue can be assessed by examination of the crack surface morphology and crystallography because {111} facet features are characteristic of inert environment SBC driven by plasticity without an environmental influence; while {110}, {100}, and {hkl} features are characteristic of HEE<sup>16</sup>. Although corrosion product severely hindered analysis of the crack surface morphology for a majority of the loading conditions in Figure 202 and Figure 203, the last experimental segment generated for NaCl-Na<sub>2</sub>MoO<sub>4</sub> solution at  $f$  of 0.3 Hz and an applied potential of -600 mV<sub>SCE</sub> was not obscured by corrosion product. The  $da/dN$  measured under these loading conditions was  $6.7 \times 10^{-6}$  mm/cyc (Figure 203), which correlates to an exposure level of about  $10^{-1}$  Pa·s in the middle of Regime 2 shown in Figure 210. Figure 212 shows that this Regime 2 is characterized by crack facets which are 30% {100}, 30% {110}, 25% {hkl}, and 15% {111} SBC<sup>16</sup>. The crack surface morphology for C47A-T86 stressed in 0.06M NaCl + 0.6M Na<sub>2</sub>MoO<sub>4</sub> at 0.3 Hz and -600 mV<sub>SCE</sub> shown in Figure 208 is qualitatively consistent these Regime 2 proportions. This supports the claim that the crack tip passive film can impede H production and uptake, but is not a sufficient barrier at this loading frequency and applied potential to completely eliminate HEE (0.3 Hz is above  $f_{critLB}$  and below  $f_{critUB}$  for -600

mV<sub>SCE</sub> polarization). For  $f \leq f_{critLB}$ , it would be expected that essentially all of the crack surface facets in this heterogeneous planar slip alloy would be parallel to {111}.

#### 1.10.6.5 Implementation

Molybdate offers the ability to both eliminate the effect of environment on FCP at sufficiently low  $f$ , and be released in the proper oxidation state through dissolution of metallic Mo<sup>58</sup>; both of which have not been reported for chromate. Additionally, the results from this study suggest that EFCP inhibition for Al-Cu-X alloys can be achieved via release of an ionic inhibitor from a pigmented paint much like the release provided by chromate conversion coatings in use today<sup>62</sup>. The high molybdate concentration studied here is not representative of the low concentrations expected after release from a coating. The leach rate of chromate from a commercial coating varies greatly depending on the primer and pigments used<sup>62</sup>. At the high end, concentrations of chromate leached into small occluded solution volumes like those found in a lap joint may be as high as 0.01 to 0.03M based on leach rates reported by Petry et. al<sup>62</sup>. The prior 7075 molybdate study showed effective inhibition for molybdate concentrations as low as 0.03M when loading under high stress ratios<sup>28, 34</sup>. For full immersion or large solution volumes, significantly lower inhibitor concentrations would be expected after inhibitor leaching. Experiments are in progress to examine the impact of these low expected inhibitor concentrations on EFCP in aerospace aluminum alloys stressed under either full immersion or with coverage by a thin electrolyte layer.

The long term implementation path for this work requires additional stages of research. First, the effect of very low molybdate and chromate inhibitor concentrations on EFCP must be quantified. Second, coatings must be formulated, and the ionic-inhibitor release kinetics and capacity must be determined. Third, the measurements in these two former tasks must be extended to the case of atmospheric thin-film electrolytes typical of airframe applications. Fourth, the repassivation kinetics pertinent to the proposed inhibition mechanism must be established. This 4<sup>th</sup> aspect of the implementation work is ongoing in a task sponsored by OuSD and lead by Professor Scully. The former three tasks are being researched by Ms. Sarah Galyon Dorman as part of her PhD degree program, sponsored by OuSD through the United States Air Force Academy under contract to SAFE. Professor Robert Kelly is collaborating on these three tasks. The results of these studies will be reported in the final reports associated with each of these OuSD grant programs.

#### 1.10.7 Conclusions

- Molybdate ion addition effectively inhibits environmental fatigue crack propagation in a modern peak aged Al-2.6Cu-1.6Li alloy (wt pct, 2199-T86) stressed during full immersion in chloride solution, as understood by the film rupture-hydrogen embrittlement mechanism.
- Molybdate fully inhibits EFCP at sufficiently low frequencies for 2199-T86 by reducing crack growth to that typical of ultra-high vacuum, suggesting that a Mo-bearing passive film at the crack tip is a sufficient barrier relative to the required-critical amount of H production and uptake.
- Ion-assisted inhibition destabilizes alloy-induced inhibition, as addition of molybdate to chloride solution accelerates crack growth in Al-Cu-Li alloys for fatigue loading frequencies that prohibit sufficient repassivation of the Mo-bearing passive film. This is



likely due to molybdate inhibiting localized corrosion of  $\text{Al}_2\text{CuLi}$  precipitates in the crack that otherwise lead to Cu replating/enrichment, and suggests that ionic and alloy-induced inhibition mechanisms are not synergistic at any frequency.

- Anodic polarization enhances molybdate inhibition of EFCP and increases the frequency at which complete elimination of the environmental contribution to FCP is achieved.
- When considering replacements for chromate-based coating systems, corrosion inhibitors should not only be evaluated in the context of localized corrosion, but also for their impact on the pit to crack transition and fatigue crack propagation kinetics.

#### 1.10.8 Bibliography

1. J. A. Feeney, J. C. McMillan and R. P. Wei, Environmental Fatigue Crack Propagation of Aluminum Alloys at Low Stress Intensity Levels, *Metallurgical Transactions*, 1 (1970), 1741-1757.
2. M. Gao, R. P. Wei and P. Pao, Chemical and Metallurgical Aspects of Environmentally Assisted Fatigue Crack Growth in 7075-T651 Aluminum Alloy, *Metallurgical and Materials Transactions A*, 19 (1988), 1739-1750.
3. Z. Gasem and R. P. Gangloff, Rate-Limiting Processes in Environmental Fatigue Crack Propagation in 7000-series Aluminum Alloys, R. H. Jones, (Ed.), *Chemistry and Electrochemistry of Corrosion and Stress Corrosion Cracking*, (Warrendale, PA, TMS-AIME, 2001, p. 501-521).
4. Z. M. Gasem, "Frequency Dependent Environmental Fatigue Crack Propagation in the 7XXX Alloy/Aqueous Chloride System" University of Virginia, 1999).
5. A. Hartman, On the Effect of Oxygen and Water Vapor on the Propagation of Fatigue Cracks in 2024-T3 Alclad Sheet, *International Journal of Fracture Mechanics*, 1 (1965), 167-188.
6. P. S. Pao, M. Gao and R. P. Wei, Environmentally Assisted Fatigue-Crack Growth in 7075 and 7050 Aluminum Alloys, *Scripta Metallurgica*, 19 (1985), 265-270.
7. J. Ruiz and M. Elices, Effect of Water Vapor Pressure and Frequency on Fatigue Behaviour in 7017-T651 Aluminium Alloy Plate, *Acta Materialia*, 45 (1997), 281-293.
8. R. P. Wei, Fatigue-Crack Propagation in a High-Strength Aluminum Alloy, *International Journal of Fracture Mechanics*, 4 (1968), 159-168.
9. R. P. Wei, Some Aspects of Environment-Enhanced Fatigue-Crack Growth, *Engineering Fracture Mechanics*, 1 (1970), 633-651.
10. R. P. Wei and R. P. Gangloff, Environmentally Assisted Crack Growth in Structural Alloys: Perspectives and New Directions, R. P. Wei and R. P. Gangloff, Eds., *Fracture Mechanics: Perspectives and Directions*, ASTM STP 1020, (West Conshohocken, PA, ASTM International, 1989, p. 233-264).
11. T. Broom and A. Nicholson, Atmospheric Corrosion Fatigue of Age Hardenable Aluminum Alloys, *Journal of the Institute of Metals* 89 (1960-1961), 183-190.
12. R. P. Gangloff, Corrosion Fatigue Crack Propagation in Metals, R. P. Gangloff and M. B. Ives, Eds., *Environment Induced Cracking of Metals*, (Houston TX, NACE, 1989, p. 55-109).
13. R. P. Gangloff, Environment Sensitive Fatigue Crack Tip Processes and Propagation in Aerospace Aluminum Alloys, A. Blom, (Ed.), *Fatigue '02*, (West Midlands, UK, Engineering Materials Advisory Services, 2002, p. 3401-3433).

14. Y. Ro, S. R. Agnew, G. H. Bray and R. P. Gangloff, Environment-Exposure-Dependent Fatigue Crack Growth Kinetics for Al-Cu-Mg/Li, *Materials Science and Engineering: A*, 468-470 (2007), 88-97.
15. Y. J. Ro, "Characterization of Exposure Dependent Fatigue Crack Growth Kinetics and Damage Mechanisms for Aluminum Alloys" University of Virginia, (2008),
16. Y. J. Ro, S. R. Agnew and R. P. Gangloff, Environmental Exposure Dependence of Low Growth Rate Fatigue Crack Damage in Al-Cu-Li/Mg, J. E. Allison, J. Wayne Jones, J. M. Larsen and R. O. Ritchie, Eds., *Fourth International Very High Cycle Fatigue Conference*, (Warrendale, PA, TMS, 2007, p. 409-420).
17. Y. J. Ro, S. R. Agnew and R. P. Gangloff, Effect of Environment on Fatigue Crack Wake Dislocation Structure in Al-Cu-Mg, *Metallurgical and Materials Transactions A*, in review (2011).
18. R. P. Wei, P. S. Pao, R. G. Hart, T. W. Weir and G. W. Simmons, Fracture Mechanics and Surface Chemistry Studies of Fatigue Crack Growth in an Aluminum Alloy, *Metallurgical and Materials Transactions A*, 11A (1980), 151-158.
19. K. R. Cooper, "Chemistry and Electrochemistry of Environment-Assisted Cracking of an Al-Zn-Mg-Cu Alloy" University of Virginia, (2001),
20. K. R. Cooper and R. G. Kelly, Using Capillary Electrophoresis to Study the Chemical Conditions within Cracks in Aluminum Alloys, *Journal of Chromatography A*, 850 (1999), 381-389.
21. K. R. Cooper and R. G. Kelly, Crack Tip Chemistry and Electrochemistry of Environmental Cracks in AA 7050, *Corrosion Science*, 49 (2007), 2636-2662.
22. R. S. Piascik and R. P. Gangloff, Environmental Fatigue of an Al-Li-Cu Alloy: Part I. Intrinsic Crack Propagation Kinetics in Hydrogenous Environments, *Metallurgical and Materials Transactions A*, 22 (1991), 2415-2428.
23. N. J. H. Holroyd and D. Hardie, Factors Controlling Crack Velocity in 7000 Series Aluminium Alloys During Fatigue in an Aggressive Environment, *Corrosion Science*, 23 (1983), 527-531, 533-546.
24. J. S. Warner and R. P. Gangloff, Alloy Induced Inhibition of Fatigue Crack Growth in Age-hardenable Al-Cu alloys, *International Journal of Fatigue*, in press: doi: 10.1016/j.ijfatigue.2011.04.013 (2011).
25. F. Menan and G. Henaff, Influence of Frequency and Exposure to a Saline Solution on the Corrosion Fatigue Crack Growth Behavior of the Aluminum Alloy 2024, *International Journal of Fatigue*, 31 (2009), 1684-1695.
26. F. Menan and G. Henaff, Influence of Frequency and Waveform on Corrosion Fatigue Crack Propagation in the 2024-T351 Aluminium Alloy in the S-L Orientation, *Materials Science and Engineering: A*, 519 (2009), 70-76.
27. R. S. Piascik and R. P. Gangloff, Aqueous Environment Effects on Intrinsic Corrosion Fatigue Crack Propagation in an Al-Li-Cu Alloy, R. P. Gangloff and M. B. Ives, Eds., *Environment Induced Cracking of Metals*, (Houston, TX, NACE, 1989, p. 233-239).
28. J. S. Warner, "Inhibition of Environmental Fatigue Crack Propagation in Age-Hardenable Aluminum Alloys" University of Virginia, (2010),
29. F. P. Ford, Effect of Metallurgical and Mechanical Factors on Cracking in Ductile Alloy/Aqueous Environment Systems, R. P. Gangloff, (Ed.), *Embrittlement Localized Crack Environment*, (Warrendale, PA, Metallurgical Society AIME, 1984, p. 117-147).
30. F. P. Ford and P. L. Andresen, Corrosion Fatigue of Pressure Boundary Materials, K. Salema, (Ed.), *Advances in Fracture Research*, (Oxford, UK, Pergamon Press, 1989, p. 1571-1584).
31. F. P. Ford and P. L. Andresen, Electrochemical Effects on Environmentally-Assisted Cracking, S. M. Bruemmer, E. I. Meletis, R. H. Jones, W. W. Gerberich, F. P. Ford and

- R. W. Staehle, Eds., Parkins Symposium on Fundamental Aspects of Stress Corrosion Cracking, (Warrendale, PA, TMS, 1992, p. 43-67).
32. T. Ramgopal, P. Schmutz and G. S. Frankel, Electrochemical Behavior of Thin Film Analogs of  $Mg(Zn, Cu, Al)_2$ , *Journal of The Electrochemical Society*, 148 (2001), B348-B356.
  33. J. S. Warner, S. Kim and R. P. Gangloff, Ionic Inhibition of Environmental Fatigue Crack Growth in 7075-T6, *Key Engineering Materials*, 345-346 (2007), 989-994.
  34. J. S. Warner, S. Kim and R. P. Gangloff, Molybdate Inhibition of Environmental Fatigue Crack Propagation in Al-Zn-Mg-Cu, *International Journal of Fatigue*, 31 (2009), 1952-1965.
  35. C. M. A. Brett, I. A. R. Gomes and J. P. S. Martins, The Electrochemical Behavior and Corrosion of Aluminum in Chloride Media: The Effect of Inhibitor Anions, *Corrosion Science*, 36 (1994), 915-925.
  36. R. J. Cinderey and G. T. Burstein, The Repassivation Potential of Aluminium in Water, *Corrosion Science*, 33 (1992), 499-502.
  37. H. J. Raetzer-Scheibe and C. D. S. Tuck, The Polarization and Repassivation Behavior of the Aluminum-Zinc-Magnesium-Copper Alloy 7010, *Corrosion Science*, 36 (1994), 941-956.
  38. C. Giummarra, B. Thomas and R. J. Rioja, New Aluminum Lithium Alloys for Aerospace Applications, *Proceedings of the Light Metals Technology Conference*, (2007).
  39. Y. J. Ro, "Fatigue Crack Surface Crystallography of Precipitation Hardened Aluminum Alloys" University of Virginia, (2004),
  40. H. Tada, P. C. Paris and G. R. Irwin, *The Stress Analysis of Cracks Handbook*, (St. Louis, MO: Paris Productions Inc., 1985), p. pp. 2.10-12.12.
  41. R. P. Gangloff, D. C. Slavik, R. S. Piascik and R. H. Van Stone, Direct Current Electrical Potential Measurement of the Growth of Small Cracks, J. M. Larsen and J. E. Allison, Eds., *Small Crack Test Methods*, ASTM STP1149, (Philadelphia, PA, ASTM, 1992, p. 116-168).
  42. J. K. Donald and J. Ruschau, Direct Current Potential Difference Fatigue Crack Growth Measurement Techniques, K. J. Marsh, R. A. Smith and R. O. Ritchie, Eds., *Fatigue Crack Measurement: Techniques and Applications*, (West Midland, UK, EMAS, 1991, p. 11-38).
  43. Y. Ro, S. R. Agnew and R. P. Gangloff, Crystallography of Fatigue Crack Propagation in Precipitation-Hardened Al-Cu-Mg/Li, *Metallurgical and Materials Transactions A*, 38 (2007), 3042-3062.
  44. Y. Ro, S. R. Agnew and R. P. Gangloff, Environmental Fatigue-Crack Surface Crystallography for Al-Zn-Cu-Mg-Mn/Zr, *Metallurgical and Materials Transactions A*, 39 (2008), 1449-1465.
  45. J. Ai, Y. Lee, J. T. Burns, R. Bush and R. P. Gangloff, unpublished research. University of Virginia, 2010
  46. K. R. Morasch and D. F. Bahr, Nanomechanical Testing for Fracture of Oxide Films, *Journal of Materials Research*, 20 (2005), 1490-1497.
  47. M. Pang, D. E. Wilson and D. F. Bahr, The Strength and Fracture of Passive Oxide Films on Metals, *Materials Research Society Symposium Proceedings*, 594, p. 501-506, (MRS, 2000).
  48. D. L. Davidson and J. Lankford, The Effects of Aluminum Alloy Microstructure on Fatigue Crack Growth, *Materials Science and Engineering*, 74 (1985), 189-199.
  49. D. Williams, D. Davidson and J. Lankford, Fatigue-Crack-Tip Plastic Strains by the Stereoimaging Technique, *Experimental Mechanics*, 20 (1980), 134-139.

50. F. P. Ford, G. T. Burstein and T. P. Hoar, Bare Surface Reaction Rates and their Relation to Environment Controlled Cracking of Aluminum Alloys. I. Bare Surface Reaction Rates on Aluminum-7 Weight Percent Magnesium in Aqueous Solutions, *Journal of the Electrochemical Society*, 127 (1980), 1325-1331.
51. G. S. Frankel, C. V. Jahnes, V. Brusic and A. J. Davenport, Repassivation Transients Measured with the Breaking-Electrode Technique on Aluminum Thin-Film Samples, *Journal of the Electrochemical Society*, 142 (1995), 2290-2295.
52. M. A. Jakab, "Corrosion Inhibition by Metal Ions Delivered from Amorphous Alloys" University of Virginia, 2006),
53. M. W. Kendig and R. G. Buchheit, Corrosion Inhibition of Aluminum and Aluminum Alloys by Soluble Chromates, Chromate Coatings, and Chromate-Free Coatings, *Corrosion*, 59 (2003), 379-400.
54. S. Oleinik and Y. Kuznetsov, Corrosion Inhibitors in Conversion Coatings. IV, Protection of Metals, 43 (2007), 391-397.
55. M. S. Vukasovich and J. P. F. Farr, Molybdate in Corrosion Inhibition - A Review, *Polyhedron*, 5 (1986), 551-559.
56. G. S. Frankel, Pitting Corrosion of Metals. A Review of the Critical Factors, *Journal of the Electrochemical Society*, 145 (1998), 2186-2198.
57. A. Sehgal, D. Lu and G. S. Frankel, Pitting in Aluminum Thin Films, *Journal of the Electrochemical Society*, 145 (1998), 2834-2840.
58. M. Pourbaix, *Atlas of Electrochemical Equilibria in Aqueous Solutions*, (Houston, TX: NACE, 1974),
59. A. Brenner, *Electrodeposition of Alloys*, (New York: Academic Press, 1963),
60. J. Kim and S. Pyun, Effects of Electrolyte Composition and Applied Potential on the Repassivation Kinetics of Pure Aluminium, *Electrochimica Acta*, 40 (1995), 1863-1869.
61. S. I. Pyun and E. J. Lee, Effect of Halide Ion and Applied Potential on Repassivation Behavior of Al-1wt.Percent-Si-0.5wt.Percent-Cu Alloy, *Electrochimica Acta*, 40 (1995), 1963-1970.
62. L. Petry, D. W. Barrington and J. F. Dante, Evaluation of the Inhibitor Leaching Performance of Chromated Primers by Capillary Ion Analysis and Electrochemical Impedance Spectroscopy, Tri-Service Conference on Corrosion, (NACE, Houston, TX, 2003).